UNIVERSITY COLLEGE LONDON

Faculty of Mathematics and Physical Sciences
Department of Physics & Astronomy

CHARACTERISING THE DENSE MOLECULAR GAS IN EXCEPTIONAL LOCAL GALAXIES

LAYING THE FOUNDATIONS FOR FUTURE MILLIMETRE OBSERVATIONS

Thesis submitted for the Degree of Doctor of
Philosophy of University College London

by
Richard C. A. Tunnard

Supervisors:	Examiners:
Thomas R. Greve	Ian Howarth
Serena Viti	Susanne Aalto

August 11, 2016

I, Richard Tunnard, confirm that the work presented in this thesis is my own. Where information has been derived from other sources, I confirm that this has been indicated in the thesis.

Abstract

The interferometric facilities now coming online (the Atacama Large Millimetre Array (ALMA) and the NOrthern Extended Millimeter Array (NOEMA)) and those planned for the coming decade (the Next Generation Very Large Array (ngVLA) and the Square Kilometre Array (SKA)) in the radio to sub-millimetre regimes are opening a window to the molecular gas in high-redshift galaxies. However, our understanding of similar galaxies in the local universe is still far from complete and the data analysis techniques and tools needed to interpret the observations in consistent and comparable ways are yet to be developed.

I first describe the Monte Carlo Markov Chain (MCMC) script developed to empower a public radiative transfer code. I characterise both the public code and MCMC script, including an exploration of the effect of observing molecular lines at high redshift where the Cosmic Microwave Background (CMB) can provide a significant background, as well as the effect this can have on well-known local correlations.

I present two studies of ultraluminous infrared galaxies (ULIRGs) in the local universe making use of literature and collaborator data. In the first of these, NGC 6240, I use the wealth of available data and the geometry of the source to develop a multi-phase, multi-species model, finding evidence for a complex medium of hot diffuse and cold dense gas in pressure equilibrium. Next, I study the prototypical ULIRG Arp 220; an extraordinary galaxy rendered especially interesting by the controversy over the power source of the western of the two merger nuclei and its immense luminosity and dust obscuration. Using traditional grid based methods I explore the molecular gas conditions within the nuclei and find evidence for chemical differentiation between the two nuclei, potentially related to the obscured power source.

Finally, I investigate the potential evolution of proto-clusters over cosmic time with sub-millimetre observations of 14 radio galaxies, unexpectedly finding little to no evidence for cluster evolution.

Acknowledgements

This thesis would not have been possible without the help and guidance of my supervisor, Thomas Greve, to whom I extend my sincerest thanks. His patience, network of collaborators and easy going attitude have been invaluable throughout. The freedom he gave me to explore my own ideas led to much of the work in this thesis.

I thank Serena Viti for her counsel and guidance in the study of molecular lines and chemistry, and for her healthy scepticism which greatly improved the work presented in this thesis.

Zhi-yu Zhang was instrumental in instructing me in the use and limitations of RADEX and contributed much to discussions on the geometry of Arp 220. Additional thanks to the DeMoGas team, in particular Manolis Xilouris and Ioanna Leonidaki for making me welcome and helping me to develop my understanding of radiative transfer.

Special thanks go to Santiago García-Burillo, Javier Graciá Carpio and Asunción Fuente for sharing their data with me, making the the studies of Arp 220 and NGC 6240 possible and setting the direction of this thesis. I must also thank them, as well as Jackie Fischer and Eduardo González-Alfonso for their help and guidance in interpreting and modelling molecular lines.

I also wish to thank the organisers and sponsors of the Imperial College Centre for Inference and Cosmology workshop 2014. As well as being a thoroughly enjoyable experience the workshop introduced me to the Monte Carlo Markov Chain, used extensively in this thesis, and provided me my first real introduction to Bayesian statistics. For this, I will be forever grateful.

A highlight of the past three years was observing with the JCMT on the summit of Mauna Kea. Thank you to all of the scientists and staff at the EAO for this opportunity, but especially Iain Coulson, Harriet Parsons, Callie Matulonis and William Montgomerie.

I thank the staff at the University College London Observatory (UCLO, previously ULO) for the opportunity to teach and demonstrate. This allowed me to explore old ideas with new eyes and find new ways of interpreting observations.

Finally, thank you to Claudia, for staying by my side and acting as a sounding board for my thoughts throughout.

"Deep in the human unconscious is a pervasive need for a logical universe that makes sense. But the real universe is always one step beyond logic."

Frank Herbert

Contents

This page was intentionally left nearly blank.

List of Figures

This page was intentionally left nearly blank.

List of Tables

This page was intentionally left nearly blank.

Chapter 1

Introduction

> *"Our knowledge of stars and interstellar matter must be based primarily on the electromagnetic radiation which reaches us. Nature has thoughtfully provided us with a universe in which radiant energy of almost all wavelengths travels in straight lines over enormous distances with usually rather negligible absorption."*
>
> Lyman Spitzer, Jr.

While the electronic transitions of CH and CN have been seen in absorption since the late 1930s (Swings & Rosenfeld, 1937; McKellar, 1940; Adams, 1941) it was not until the late 1960s that the rotational emission of molecules, the mainstay of modern molecular astronomy, was observed (Weaver et al., 1965; Weinreb et al., 1965; Cheung et al., 1968; Weaver et al., 1968; Wilson et al., 1970; Rydbeck et al., 1974). In particular, the detection of ^{12}CO in the Orion nebula by Wilson et al. marked the beginning of a new era in astronomy with previously invisible cold molecular gas, the precursor to star formation, becoming visible for the first time. No longer constrained to the luminiferous stars and ionised nebulae, a wealth of new information poured forth.

Since these humble beginnings molecular astronomy has exploded with the development of increasingly sensitive millimetre single-dish telescopes and interferometric arrays. Low-excitation molecular rotational emission lines lie in the millimetre regime with energies in the realm of $10\,\mathrm{K}-100\,\mathrm{K}$; sufficiently low to be easily excited in cold gas clouds. Conveniently, this low-energy regime, hosting many key astrophysical molecular tracers, also lies in a region of high atmospheric transmission: see Figure 1.1.

Despite, or perhaps because of, the wealth of information obtained over the past 40 years the fundamental physics and chemistry guiding processes in the interstellar medium (ISM) are still not well understood. While progress has been made, the great complexity and divergent nature of the chemical processes in the ISM with respect to those on Earth has grossly retarded advancement of the field. A major contributor to this is the dramatic difference between the prevailing conditions in interstellar molecular clouds and those on Earth. By number, approximately $90-95\%$ of the baryonic matter in the universe is hydrogen and in the molecular regions of interest temperatures are low ($10\,\mathrm{K}-100\,\mathrm{K}$) and densities are between 10 and $10^6\,\mathrm{cm}^{-3}$ (Tennyson, 2003). This leads to a highly saturated two-body chemistry, distinct from the chemistry seen on Earth where hydrogen is already locked up in molecules and densities are sufficient for three-body reactions to dominate. Kinetic isotope effects arise due to the different masses of isotopes leading to different bond energies, which in turn affects reaction rates. In particular, the low temperatures found in some dense molecular clouds render kinetic isotope effects significant, further complicating analyses and chemical pathways (Langer et al., 1978, 1984; Langer & Penzias, 1993; Milam et al., 2005; Henkel et al., 2010, 2014; Ritchey et al., 2011; Szűcs et al., 2014; Roueff et al., 2015).

Given these complications, it has to be asked whether the study of molecular emission is worth the effort. Fortunately, the answer is unequivocally *yes.* From a practical point of view, molecular

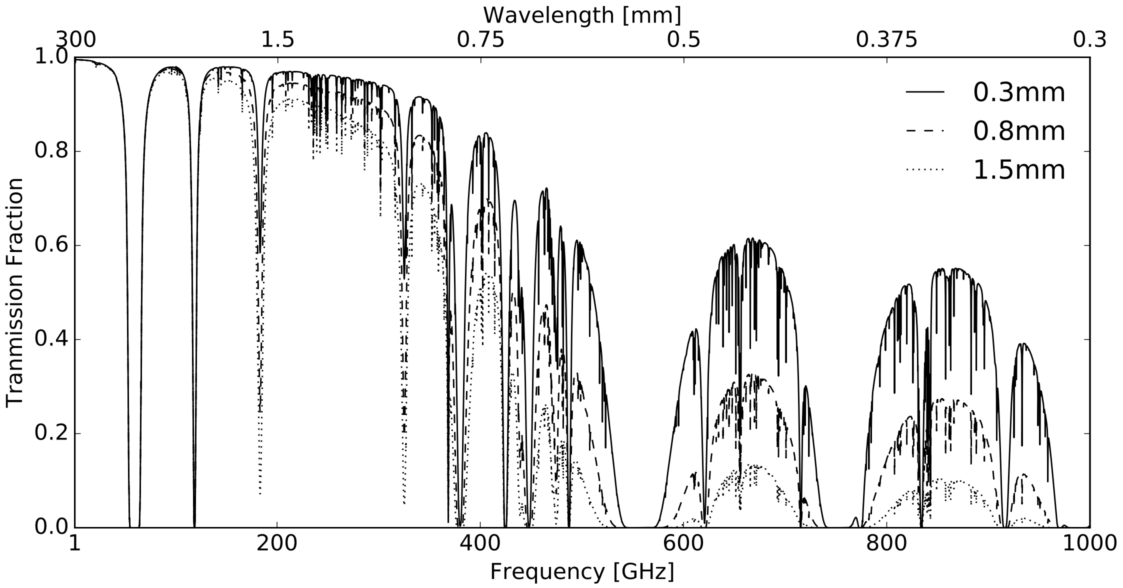

Figure 1.1: The atmospheric transmission curve for zenith at the site of the IRAM Plateau de Bure Interferometer and a range of precipitable water vapours, calculated with the IRAM program ASTRO. With the exception of a couple of pressure broadened O_2 and H_2O absorption lines transmission is excellent below 400 GHz, convenient for the observation of low excitation CO and other molecular rotational emission in the local universe.

emission allows us to peer behind the veil of dust that hides much of the universe at optical wavelengths, and permits us to constrain the physical conditions of the emitting (or absorbing) gas. In dark clouds in the Milky Way, believed to be the sites of future star formation, molecular studies reveal new information for star-formation theory and models (Caselli et al., 1993, 2002; Keto et al., 2015). In “hot cores” complex organic molecules, including prebiotics, have been discovered, which, combined with the observations of over 200 amino acids in solar system objects, has potentially enormous implications for the origins of life (Chyba et al., 1990; Beltrán et al., 2009; Calcutt et al., 2014; Fedoseev et al., 2015). Molecular lines allow for measurements of the gas content and properties of galaxies, placing powerful constraints on models of galaxy evolution and star formation (e.g., Saintonge et al., 2011a,b; Kauffmann et al., 2012). In galaxies other than the Milky Way molecular lines not only provide unique information on the cold gas reservoirs and kinematics but may also be tracers of active galactic nuclei (AGN) activity. These molecular line diagnositcs could then be used, for example, to identify buried AGN, undetectable in the X-ray or optical due to the Compton thick ($N_{\mathrm{H}_2} > 1 \times 10^{24}\,\mathrm{cm}^{-2}$) hydrogen column densities and dust obscuration (Jackson et al., 1993; Sternberg et al., 1994; Tacconi et al., 1994; Kohno et al., 2001; Usero et al., 2004; Kohno, 2005; Imanishi et al., 2007a; Krips et al., 2008; Davies et al., 2012; Izumi et al., 2016a; Imanishi et al., 2016). The extensive range of information obtainable from molecular observations renders them an indispensable component of modern astrophysics.

While molecular lines can, in principle, originate from even diffuse molecular gas, in practice almost all lines other than CO are observed only in dense molecular gas. While densities $n_{\mathrm{H}_2} \sim 10^3\,\mathrm{cm}^{-3}$ are sometimes referred to as dense, in the remainder of this thesis the term “dense gas” is customarily used to refer to molecular gas with $n_{\mathrm{H}_2} \gtrsim 10^4\,\mathrm{cm}^{-3}$, which is the typical density of molecular cloud cores bound by their self-gravity (e.g., Lada, 1992). This phase offers significant shielding against photo-dissociation, while being heated and partially ionised by cosmic rays, leading to chemistry distinct from gas elsewhere in the ISM (Williams & Viti, 2013a). It is best traced by the rotational transitions of molecules such as HCN, HCO^+, and CS, which can reach high abundances relative to H_2 ($10^{-8} - 10^{-6}$) under these conditions (Nguyen et al., 1992; Solomon et al., 1992; Boger & Sternberg, 2005) and the low-J transitions of which are readily collisionally excited at these densities. This phase also encompasses molecular gas involved in slow, C-type shocks, where magnetic fields propagating ahead of the shock front ameliorate the shock jump. This leads to less extreme heating than without the magnetic front, allowing dust mantles and grains to be evaporated and sputtered, but also allowing for molecules to survive and be seen in emission. Dense molecular gas is the site of star formation, generates unusual chemistry and is arguably the most interesting phase of the ISM, and is the focus of the work presented in this thesis.

1.0.1 The Changing of the Guard

The trend over the past 50 years in physics and astronomy has been towards ever larger and more expensive projects as part of the constant march for greater energies, better resolution and higher sensitivity. Specifically within radio and millimetre astronomy this has given birth to the now operational Atacama Large Millimetre Array (ALMA) in Chile and, in the next few years, the Square Kilometre Array (SKA) will begin to operate across South Africa and Australia. Upgrades to existing facilities such as the Jansky Very Large Array (JVLA) in the USA and the Plateau de Bure Interferometer (PdBI) in France are set to transform them into the Next Generation Very Large Array (ngVLA) and the NOrthern Extended Millimetre Array (NOEMA), with increased collecting area, resolution and frequency ranges. Single dish (sub)millimetre telescopes in commissioning, such as the Large Millimetre Telescope Alfonso Serrano (LMT) in Mexico, and under development, such as the Cerro Chajnantor Atacama Telescope (CCAT) in Chile, will provide high sensitivity and large fields of view suitable for survey mapping to identify interferometric follow-up targets. The CCAT in particular will, for the first time, enable a comprehensive survey of cold, low mass molecular clouds in the Milky Way, providing a complete census of star formation down to the lowest mass stars.

The increased sensitivity becoming available in the (sub)millimetre regime opens up molecular astronomy in three ways. Firstly, it is becoming possible to study molecular lines at higher and higher redshifts, with CO now routinely detected at redshifts $1-2$ with the PdBI (Combes, 2013) while ALMA ‘blind’ spectral scans have successfully been used to identify galaxies out to $z = 5.6$, and in principle out to $z = 8$ (Weiß et al., 2013; Carilli & Walter, 2013). While surveys of molecular lines at $z > 2$ are still challenging even with ALMA, the proposed ngVLA will be able to sample molecular gas reservoirs at multiple redshifts simultaneously in HCN, HCO^+ and HNC as well as CO (Casey et al., 2015). This will revolutionise galaxy-evolution studies, providing direct probes of the molecular reservoirs of star formation across cosmic time with statistically useful sample sizes.

The second enormous change in the field, already being realised by ALMA, the EMIR receiver on the IRAM 30m telescope and the Sub-Millimetre Array (SMA), is the detection of a plethora of molecules in local galaxies, enabled by the combination of high sensitivity and large bandwidths. Spectral scans with the IRAM 30m and the SMA have detected a vast array of molecules, posing challenges for baselining the data (due to line forests and potential emission obscuring the continuum level, e.g., Costagliola et al., 2011; Martín et al., 2011; Aladro et al., 2013; Costagliola et al., 2015). Even ALMA Cycle 0 observations, before all dishes were incorporated into the array, revealed staggering degrees of molecular complexity in the local galaxies NGC 1068 and NGC 4418 (García-Burillo et al., 2014; Viti et al., 2014; Costagliola et al., 2015). In particular, the spectral scans of Costagliola et al. (2015) detected 317 emission lines from 45 different molecular species over 70.7 GHz, presenting new challenges in data analysis and scientific interpretation. The transformative aspect of ALMA is the ability to spatially resolve the complex molecular emission in these galaxies, and to run highly sensitive spectral scans across tens of GHz. This allows for much more detailed and meaningful modelling of the line emission, where it is starting to become possible to take into account the significant variations in the gas conditions across a galaxy (García-Burillo et al., 2014; Viti et al., 2014). Nevertheless, the tens of milli-arcsecond resolution now regularly achieved by ALMA covers tens of parsecs in local active galaxies, encompassing a wide range of physical conditions, molecular abundances and excitation profiles, all of which are conflated into a single beam.

The third change has been underway for some time, but is still in the process of being fully utilised, namely, the introduction of heterodyne receiver arrays such as the Heterodyne Array Receiver Program (HARP) and Auto-Correlation Spectral Imaging System (ACSIS) on the JCMT (Buckle et al., 2009) and the HEterodyne Receiver Array (HERA) on the IRAM 30-meter telescope

(Schuster et al., 2004)[1]. These arrays represent the next step in increasing observing efficiency: instead of seeking to continue improving the sensitivity of individual detectors, heterodyne arrays add more detectors. This allows for rapid spectral mapping of molecular gas, but these telescopes are still somewhat hampered by their relatively poor spatial resolution, rendering them only really suitable for mapping of gas within the Milky Way or in galaxies in the local universe.

We are in the middle of a major shift in extragalactic molecular astronomy that began in the last decade. The field is moving from small, single-molecule, time-consuming studies of the brightest galaxies such as the NUGA project (García-Burillo et al., 2003), to the era of large-scale single-molecule surveys of local galaxies such as COLD GASS (Saintonge et al., 2011a) and in the future to large scale multi-molecule surveys of local galaxies and galaxies at higher redshift. However, the methods and techniques necessary to interpret these new data, especially complex spectral scans, are not yet mature, with challenges including the reliable identification of the continuum level, the identification of lines and associating them with molecules, and the identification of the physical and chemical conditions traced by multiple molecular lines simultaneously. The problem is similar to that seen in Milky Way molecular astronomy where the number of lines and potential molecules can be overwhelming, but is exacerbated by the much larger line widths due to bulk motions in the target galaxy, the larger regions being probed and the potential for divergent chemistry and non-LTE excitation. While significant progress has been made by some authors (Martín et al., 2011; Aladro et al., 2011, 2013, 2015; Costagliola et al., 2015) there are still no clear routes to reliable line identification without the significant and suspect assumptions of LTE and 'standard' molecular abundances.

1.1 Active Galaxies Near and Far

Active galaxies are, by definition, aberrations from the norm. They represent either rare or transient phases of galaxy evolution (Soifer et al., 1987b), and as such can provide unique insights into astrophysical processes and galaxy evolution. The majority of this thesis focuses on local Ultra-Luminous Infrared Galaxies (ULIRGs), while chapter 7 explores the potential high-z analogues of local ULIRGs: sub-millimetre galaxies (SMGs) and high-redshift radio galaxies (HzRGs). Before discussing these particular types of galaxies I present below a brief overview of the prevailing theory of galaxy evolution to better frame the discussion of these aberrations.

1.1.1 Galaxy Formation, Evolution, and the Galaxy Main Sequence

The prevailing picture of galaxy formation is that of hierarchical structure formation, as opposed to monolithic collapse. Within this paradigm, pre-inflation quantum fluctuations create the initial overdensities into which dark matter begins to collapse while baryonic matter is coupled to photons and therefore prevented from falling into the gravitational wells; a situation which persists until the inter-galactic medium becomes neutral (the epoch of the surface of last scattering). This leads to many small dark-matter halos that then merge into the massive halos seen today, with the contemporaneous accretion of baryonic matter (Peebles, 1982; Bond & Szalay, 1983; Blumenthal et al., 1984; Lacey & Cole, 1993; Kampakoglou et al., 2008). This model is able to reproduce the galaxy luminosity function, although it requires the addition of star-formation feedback and quasar mode AGN feedback to correct excesses in the theory over the observations at the low and high ends respectively (e.g., Silk, 1977; Li & White, 2009). A thorough review of the theory of galaxy formation can be found in Silk & Mamon (2012).

Studies have found that the rate of star formation in the universe is not constant, and that it peaked between redshift $1.0 - 2.5$: see Figure 1.2 (Madau et al., 1996; Madau, 1997; Madau et al., 1998; Heavens et al., 2004). Current evidence suggests that this is in large part simply due to there being a higher dense molecular gas fraction in galaxies over this redshift range, and not due to a change in the star-formation efficiency (Daddi et al., 2010; Tacconi et al., 2010; Geach et al., 2011). More recent studies by Saintonge et al. (2013) and Tacconi et al. (2013) have found evidence for a decrease in the molecular gas fraction at redshifts $\gtrsim 3$, consistent with both the decreasing

---

[1] A point of clarification: ACSIS is the backend for several JCMT receivers, of which HARP is one. There is no such distinction for HERA.

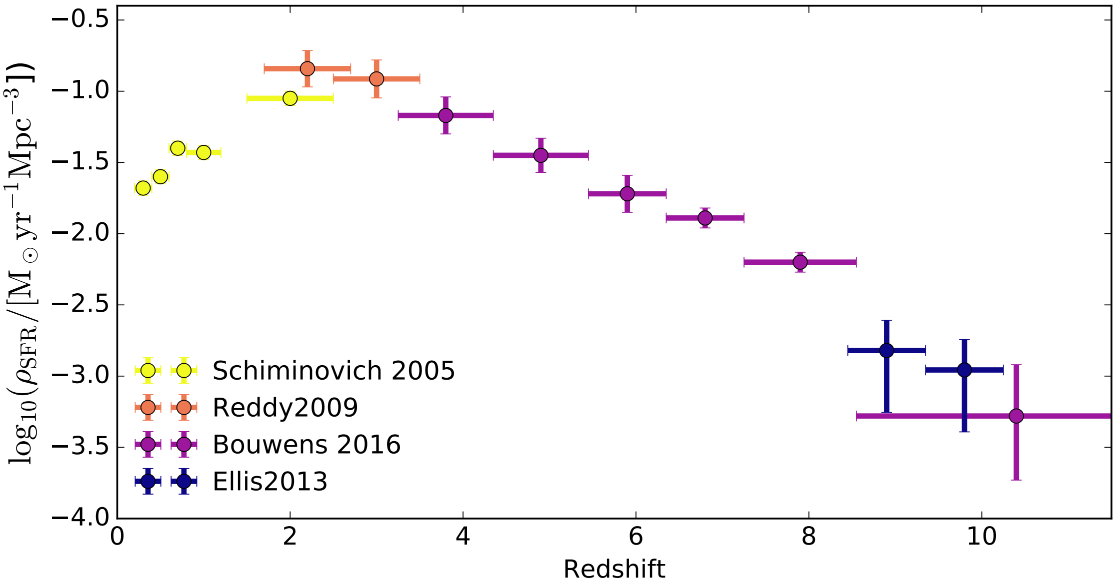

Figure 1.2: The star-formation-rate density of the universe out to redshift ten, reproduced from Bouwens et al. (2016) using data from Schiminovich et al. (2005); Reddy & Steidel (2009); Ellis et al. (2013); Bouwens et al. (2016). The epoch of peak star formation around $1.5 < z < 3$ is clearly visible.

star formation at these redshifts and the hypothesis that the star-formation rate is driven by the molecular gas fraction.

The advent of the Sloan Digital Sky Survey (SDSS) allowed for statistical examinations of galaxy properties on an unprecedented scale. One of the key results of the SDSS has been the discovery of a strong relationship between star-formation rate and stellar mass dubbed the star forming main sequence, with 'red and dead' elliptical galaxies with high stellar mass and low star-formation rate forming a separate population on the diagram (Brinchmann et al., 2004; Daddi et al., 2007; Elbaz et al., 2007; Noeske et al., 2007; Salim et al., 2007; Schiminovich et al., 2007; Pérez-González et al., 2008; Peng et al., 2010). This main sequence has been well characterised out to $z \sim 3$, and has been found to evolve with redshift, with the whole relation moving to higher star-formation rates at higher redshifts: see Figure 1.3 (Karim et al., 2011; Rodighiero et al., 2011). However, Mannucci et al. (2010) introduced gas phase metallicity as a third variable and found that not only did this account for most of the scatter in the relationship, but that once metallicity was included there was no evolution in this fundamental main sequence, at least out to $z \simeq 2.5$. Furthermore, very recently, Bothwell et al. (2016) showed that, at least for the 227 galaxies they studied, the metallicity was entirely determined by stellar mass and molecular gas mass. In other words, that the fundamental stellar-mass−SFR−metallicity relation of Mannucci et al. (2010) is in fact entirely a by product of the underlying relation between stellar mass, star-formation rate, and molecular gas mass.

The aberrations that are the focus of this thesis, that is local ULIRGs, SMGs and HzRGs, all lie above, or at least at the upper end of, the galaxy star-forming main sequence at their redshifts (Genzel et al., 2010; da Cunha et al., 2015). In the case of local ULIRGs this is almost certainly driven by merger activity and while for SMGs the situation is less clear a similar picture is emerging. HzRGs, as is discussed below, are thought to trace the most over-dense regions at their redshift, and as such their departure from the main sequence is to be expected. How rare are these rare galaxies? The answer is largely redshift dependent, with Murphy et al. (2011) finding the space density of LIRGs rises from $\sim 2 \times 10^{-5}\,{\rm Mpc}^{-3}$ at $z \simeq 0$ to a peak of $1.5 \times 10^{-3}\,{\rm Mpc}^{-3}$ at $z \sim 1$ before potentially falling again to $\sim 1 \times 10^{-3}\,{\rm Mpc}^{-3}$ at $z \geq 2.5$, largely consistent with the increases in the star-formation-rate density of the universe and the star forming main sequence. ULIRGs on the other hand are very rare in the local universe, with space densities

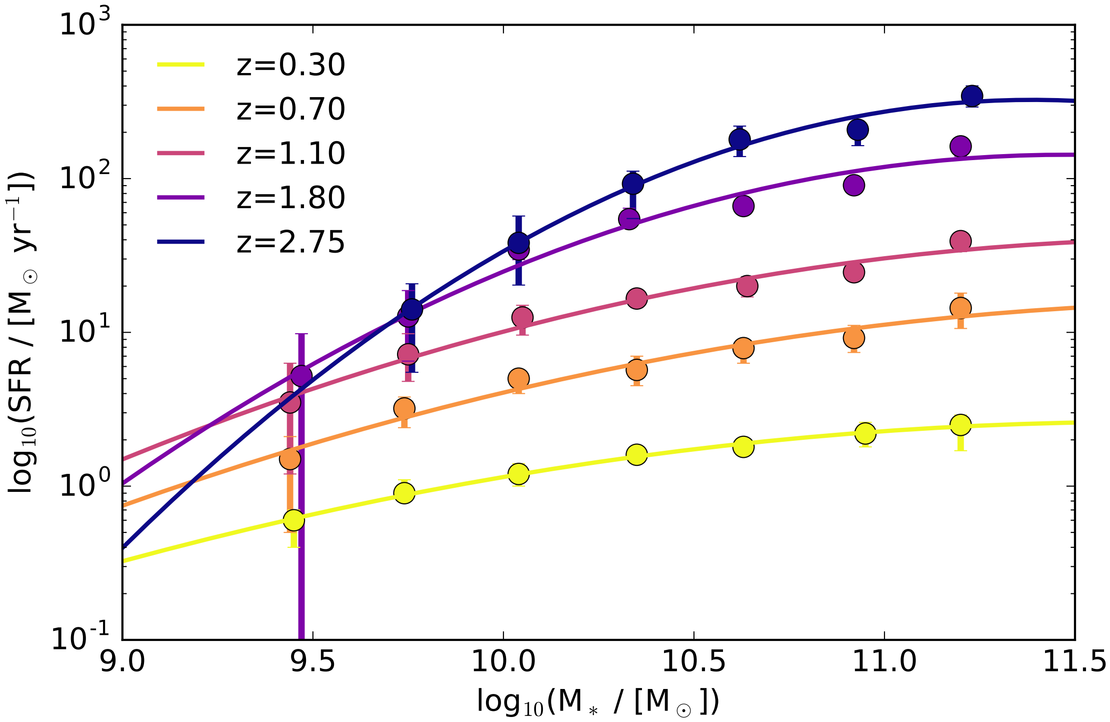

Figure 1.3: The evolution of the galaxy star forming main sequence with redshift using data from Karim et al. (2011). Shown are the logarithm of the star-formation rate and stellar mass for more than 10^5 galaxies from the COSMOS field divided into five redshift bins. The points indicate the data binned by redshift, SFR and stellar mass; the lines show the quadratic fits to the data in log-space and serve only to guide the eye. The redshift evolution of the star forming main sequence is clear. ULIRGs and SMGs lie above the main sequence at their redshift.

$\sim 1 \times 10^{-7} - 1 \times 10^{-8}\,\mathrm{Mpc}^{-3}$, rising rapidly to $\sim 5 \times 10^{-5}\,\mathrm{Mpc}^{-3}$ at $z \sim 1$ and $\sim 3 \times 10^{-4}\,\mathrm{Mpc}^{-3}$ at $z \sim 2.5$ (Kim, 1995; Sanders & Mirabel, 1996; Murphy et al., 2011). HzRGs however are rare at all redshifts, with space densities rising from $\sim 10^{-11}\,\mathrm{Mpc}^{-3}$ locally to $\sim 10^{-9} - 10^{-8}\,\mathrm{Mpc}^{-3}$ at $z \geq 2$ (Jarvis et al., 2001; Venemans et al., 2007). The relative contributions of 'normal' galaxies, LIRGs and ULIRGs to the star-formation-rate density as a function of redshift are shown in Figure 1.4.

1.1.2 Luminous and Ultraluminous Infrared Galaxies

(U)LIRGs are defined as galaxies with $L_{8-1000\,\mu\mathrm{m}} > 10^{11(12)}\,L_\odot$ and were first identified by the Infrared Astronomical Satellite (IRAS) in 1983 (Soifer et al., 1987a; Sanders & Mirabel, 1996), and dominate the population of $L_{\mathrm{bol}} > 10^{11}\,L_\odot$ galaxies in the local universe. ULIRGs in the local universe are all mergers, and out to $z \sim 1.5$ there is evidence that both the star-formation rate and the specific star-formation rate increase with neighbour proximity (Hwang et al., 2011; Zamojski et al., 2011; Larson et al., 2016). However, at $z \sim 2$ the majority of ULIRGs are likely to be disk-like star forming galaxies without major mergers, where high SFRs are driven by enhanced gas fractions (Elbaz et al., 2011; Kartaltepe et al., 2012).

In local ULIRGs, early suspicions that the majority of their luminosity ($30\% - 100\%$) arises from extremely compact structures on the scale of $100 - 300\,\mathrm{pc}$ were confirmed by interferometric CO observations and high-resolution mid-IR imaging (e.g. Downes & Solomon, 1998; Soifer et al., 2000), as well as from the analysis of molecular absorption lines in the far-IR (González-Alfonso et al., 2012, and references therein). In some cases this compact source is found to be a dust enshrouded active galactic nucleus (AGN) (e.g. Soifer et al., 1999; Lonsdale et al., 2006), but in many the extraordinary dust obscurations and column densities have made it impossible to

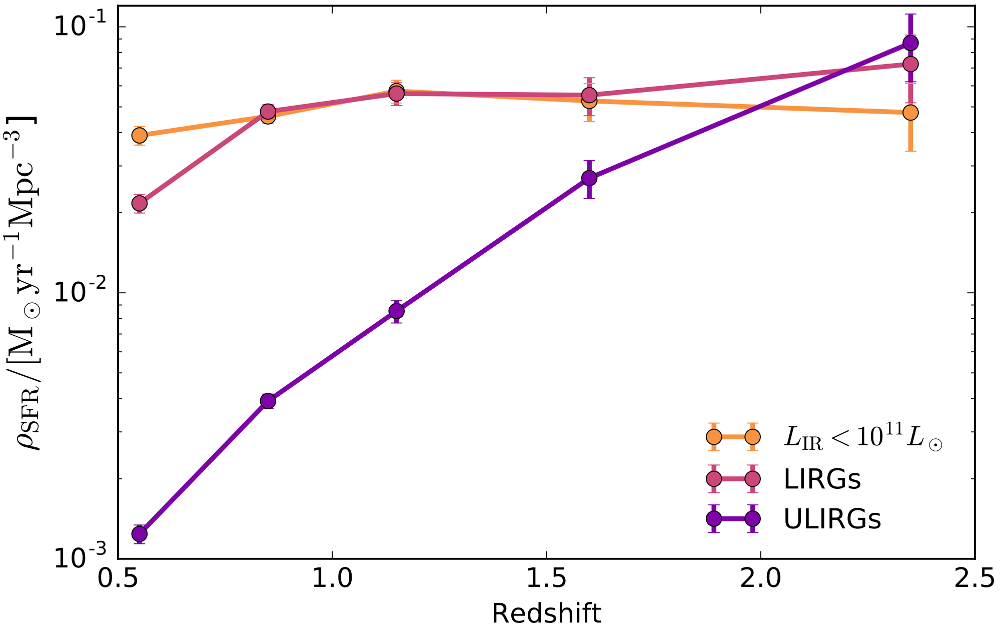

Figure 1.4: The relative contributions of 'normal' galaxies, LIRGs and ULIRGs to the star-formation-rate density as a function of redshift, using data from Murphy et al. (2011). The ULIRG contribution increases rapidly with redshift as the star forming main sequence rises and galaxies that are exceptional in the local universe become much more common.

distinguish between an AGN and a compact starburst, similar in star-formation rate to entire galaxies and with surface brightnesses comparable to globular clusters (Soifer et al., 2000). When AGN are present they appear to frequently dominate the luminosity of the galaxy: in Seyfert type I[2] ULIRGs the AGN contribution to the bolometric luminosity can be as high as 75% (Veilleux et al., 2009).

For some time AGN have been suspected to play a pivotal role in galaxy evolution due to the observed correlation between the mass of the central supermassive black hole (SMBH) and that of its host spheroid (Magorrian et al., 1998; Ferrarese & Merritt, 2000; Tremaine et al., 2002; Gültekin et al., 2009; McConnell & Ma, 2013). AGN feedback is thought to be responsible for the observed sharp cutoff at the upper end of the galactic mass function (Silk & Rees, 1998). While AGN provide an excess of energy for quenching star formation (~ 80× the gravitational binding energy of their host galaxies; Fabian, 2012), it is uncertain how this energy is coupled to the ISM and surrounding dust, and in particular whether there is sufficient momentum coupling to evacuate the central regions of gas. Nevertheless, massive molecular outflows from AGN residing in local ULIRGs have recently been observed (Cicone et al., 2014, and references therein), while ionised outflows have been found to be not only ubiquitous, but also to exist with sufficient outflow rates to shape galaxy evolution (Harrison et al., 2014). These results have confirmed that AGN can drive outflows in excess of the host starburst, but that frequently most of the mass in these outflows is moving slower than the galactic escape velocity, perhaps leading to future bursts of star formation as the gas falls back onto the host. Feedback from star formation in the form of stellar winds and supernovae also has a significant role to play in galaxy evolution, although this is predominantly in low-mass galaxies where it is responsible for the low-mass turnover in the the galactic mass function. Nevertheless, it may significantly contribute to feedback and outflows in massive galaxies by heating of the ISM (Efstathiou, 2000). Finally, while the immense potential power of AGN implies that they drive the SMBH−spheroid mass correlation it is also possible that causality runs in the other direction, and the star formation determines the feeding of the SMBH

---

[2] Seyfert galaxies are AGN where the host galaxy is clearly visible, and the AGN component has $M_B > -21.51 + 5\log(h_0)$. Seyfert I galaxies present both broad and narrow high ionisation emission lines in their optical spectra: Seyfert II galaxies present narrow lines only (Schmidt & Green, 1983).

with the increased pressure and instabilities from star formation driving gas towards the centre of the galaxy. Or indeed, the correlation could be due to both star formation and AGN accretion sharing a mutual underlying dependence, such as the inflow rate onto the galaxy of pristine atomic gas from the intergalactic medium.

Despite their rarity LIRGs and ULIRGs contribute significantly to the star-formation history of the universe. Murphy et al. (2011) found that for $0.85 \leq z \leq 1.6$ LIRGs contribute between 40% and 50% of the star formation in the universe, while for $z > 2$ ULIRGs contribute comparably to LIRGs. Understanding the molecular gas, in particular the dense star-forming molecular gas in (U)LIRGs, is therefore extremely important for understanding the processes behind the build up of a large fraction of the stars in the universe. Yet in these galaxies the presence of an AGN, which could bias star formation estimates, is difficult to diagnose due to them often being deeply buried by nuclear gas and dust (Hopkins et al., 2005, 2006; Debuhr et al., 2011).

The definitive study of (U)LIRGs in the local universe is the Great Observatories All-sky LIRG Survery (GOALS), which combines data from the NASA space telescopes Spitzer, Hubble, Chandra and GALEX, providing unparalleled coverage of the EM spectrum from the near-IR through to X-rays in 200 local (U)LIRGs (Armus et al., 2009). GOALS is complemented by the Herschel Comprehensive ULIRG Emission Survey (HerCULES, PI: van der Werf): a study of 29 of the brightest local (U)LIRGs and with data presented in Rosenberg et al. (2015). HerCULES provides observations of the mid to far-IR covering key emission lines such as the forbidden transition lines [C II - 157 μm], [O I - 63 μm, 145 μm] and [C I - 370 μm, 609 μm], as well as the CO rotational transitions from $J = 4 - 3$ through to and including $J = 13 - 12$.

An extensive review of ULIRGs can be found in Lonsdale et al. (2006), with an update focussing on more recent IR observations to be found in Alonso-Herrero (2013).

1.1.3 Sub-millimetre Galaxies

Sub-Millimetre Galaxies were first observed with the Sub-millimetre Common User Bolometer Array (SCUBA) on the James Clerk Maxwell Telescope (JCMT) (Smail et al., 1997; Barger et al., 1998; Blain, 1999; Hughes et al., 1998; Eales et al., 1999). They have since been the subject of extensive observing campaigns to discern their properties and number counts making use of, amongst others, SCUBA, the Max-Planck Millimetre Bolometer (MAMBO) array on the IRAM 30-meter telescope and the Large Apex BOlometer CAmera (LABOCA) on APEX (Bertoldi et al., 2000, 2002; Carilli et al., 2001; Scott et al., 2002; Borys et al., 2003; Greve et al., 2004; Chapman et al., 2005; Pope et al., 2005; Coppin et al., 2006; Scott et al., 2006; Knudsen et al., 2008; Weiß et al., 2009).

SMGs are, in principle, readily observed between $z = 1.5$ and $z \sim 10$ due to the large negative K correction in the sub-millimetre regime (Blain & Longair, 1993; Blain, 1999; Blain et al., 2002). That is to say, longward of $\sim 250\,\mu$m, as we probe larger and larger redshifts the peak of the dust spectral energy distribution (SED) is redshifted closer to the sub-millimetre bands. This largely compensates for the increasing faintness due to the increasing distance and cosmological effects such as redshift dimming and the curvature of the universe. In practice there are additional issues related to galaxy evolution, dust temperature, selection effects, and the additional cosmological reduction in surface brightness. These effects, combined with the potential rarity of these galaxies at $z > 5$, makes observations beyond $z = 5$ much more challenging.

SMGs at $z \gtrsim 1.5$ show many similarities to local ULIRGs such as their extreme far-IR luminosity and star-formations rates (SFRs). In the few cases where they have been resolved with kinematic information (from Hα or CO) at least half show signs of merger activity (Swinbank et al., 2006; Tacconi et al., 2006, 2008; Bothwell et al., 2010; Engel et al., 2010; Alaghband-Zadeh et al., 2012; Menéndez-Delmestre et al., 2013), suggesting that they may be driven by similar processes and physics to local ULIRGs (Blain et al., 2002). On the other hand, in the resolved Hα studies it is found that SMGs show multiple luminous knots of star formation, whereas in local ULIRGs the star formation is much more concentrated in the nuclei. Furthermore, using simulations Hayward et al. (2011) found that since starbursts shift the SED peak by heating the dust, a 24 times increase in the star-formation rate only increases the sub-millimetre flux by a factor of ~ 2. This implies that SMGs must be massive ($> 6 \times 10^{10}\,\mathrm{M}_{\odot}$) star forming galaxies due to the inefficient 850 μm flux increase in compact starbursts due to dust destruction and heating. A concomitant conclusion is that the confusion of two non-interacting galaxies in the sub-millimetre beam boosts the flux much more effectively than simply doubling the star-formation rate in a single galaxy. In summary, the current evidence suggests that SMGs are the progenitors of local massive, 'red and dead', early-type galaxies (Brodwin et al., 2008; Viero et al., 2009; Daddi et al., 2009; Aravena et al., 2010; Capak et al., 2011; Amblard et al., 2011; Toft et al., 2014).

An extensive review of the current state of SMG observations may be found in Casey et al. (2014).

1.1.4 High-redshift Radio Galaxies

High-redshift radio galaxies are radio sources at $z > 2$ with a rest-frame $L_{500\,\mathrm{MHz}} > 10^{27.5}\,\mathrm{W\,Hz^{-1}}$ and are identified by their steep radio spectra, small angular size, K-band magnitudes and near-IR $R-K$ colour (Miley & De Breuck, 2008). Observationally, these radio sources are usually Fanaroff-Riley II objects (Fanaroff & Riley, 1974), with large edge brightened double lobes and are almost certainly powered by AGN (Miley, 1980; Carilli et al., 1994, 1997; Pentericci & Venemans, 2007). K-band luminosities imply that HzRGs are old ($> 1\,\mathrm{Gyr}$) and massive (up to $10^{12}\,\mathrm{M_\odot}$) galaxies (Best et al., 1998; Jarvis et al., 2001; Willott et al., 2003; Rocca-Volmerange et al., 2004), a fact confirmed by *Spitzer* SED fitting in the rest frame near-IR by Seymour et al. (2007), who also found that the HzRG stellar mass was largely independent of redshift. As well as hosting old, massive stellar populations, some HzRGs are often undergoing star formation, evidenced by their UV spectra and dust SEDs (e.g., Dey et al., 1997; Herbert et al., 2010, 2011; Hardcastle et al., 2013; Drouart et al., 2014).

HzRGs are thought to lie at the cores of galaxy proto-clusters, with Carilli et al. (1997) and Athreya et al. (1998) finding very large rest-frame rotation measures, implying electron densities $\sim 0.05\,\mathrm{cm^{-3}}$, comparable to measurements in local clusters. Companion galaxy overdensities have been identified around HzRGs out to $z = 5$ using Lyα galaxies, spectroscopically confirming their relationship with the HzRG-centred proto-clusters and showing overdensities between 5 and 15 times field densities, with proto-cluster sizes between 2 and 5 Mpc (Kurk et al., 2000; Venemans et al., 2002, 2004, 2005; Intema et al., 2006; Venemans et al., 2007; Pentericci & Venemans, 2007), although Jones et al. (2015) found SMG overdensities extending out to 10 Mpc. Complementary efforts to identify companion galaxies in the near to mid-IR have also found that HzRGs are generally in overdense regions (Galametz et al., 2012; Mayo et al., 2012; Wylezalek et al., 2013a), while far-IR studies have found SMG overdensities around HzRGs, although these have historically been limited by small fields of view (Ivison et al., 2000; Smail et al., 2003; Stevens et al., 2003, 2010; Carrera et al., 2011; Wylezalek et al., 2013b). More recent observations have begun to extend these studies to larger radii. Rigby et al. (2014) presented large ($\sim 400\,\mathrm{arcmin^2}$) fields around 26 HzRGs observed in the 200, 350, and 500 μm SPIRE bands, finding evidence for moderate overdensities within 6 Mpc and $\pm 0.2(1+z)$ ($\lesssim 2$ times the field counts) around HzRGs with $L_{500\,\mathrm{MHz}} \gtrsim 10^{29}\,\mathrm{W\,Hz^{-1}}$ and $z < 3$. Dannerbauer et al. (2014) used LABOCA to observe an $11.4'$ radius field around the HzRG MRC 1138−262 (the Spiderweb galaxy) and found an overdensity of SMGs tracing the filamentary proto-cluster structure. Multi-wavelength follow up observations allowed them to confirm the redshifts and cluster association of these galaxies, firmly identifying the sub-millimetre selection as a potential tool for identifying proto-clusters at $z \gtrsim 1.5$.

A thorough review of the history and properties of HzRGs can be found in Miley & De Breuck (2008).

1.2 Chemistry in Active Galaxies

One of the most interesting, and most complicated, aspects of the study of molecular gas is the complex chemistry of this phase of the ISM. While not the focus of this thesis, interstellar molecular chemistry not only motivates but is also necessary to explain the results of later chapters. I therefore include here a concise overview of the relevant aspects of the field.

1.2.1 Isotope Fractionation

Since different nuclear reactions are responsible for the production of ^{12}C and ^{13}C, if the [^{12}C]/[^{13}C] abundance ratio can be accurately measured, it can be a powerful diagnostic of the evolutionary state of a galaxy, with a high [^{12}C]/[^{13}C] abundance ratio being evidence for a young, unprocessed ISM (Milam et al., 2005; Henkel et al., 2010). Alternatively, it has been suggested by Papadopoulos et al. (2011) that a high [^{12}C]/[^{13}C] ratio might be evidence for a cosmic ray dominated star-formation paradigm, leading to a more top heavy stellar initial mass function than is prevalent in the Milky Way and the local group. In both cases the ^{12}C production is via the triple alpha process in young, massive stars whereas ^{13}C production is via the CNO cycle in evolved Asymptotic Giant Branch (AGB) stars. Typical values of [^{12}C]/[^{13}C] in the local universe are ~ 25 in the central Milky Way, 68 in the Milky Way as a whole, up to ~ 100 in local starbursts and potentially $\gtrsim 100$ in high redshift ULIRGs (Milam et al., 2005; Henkel et al., 2010, 2014). Typically, these ratios are measured using a combination of observations of CN, ^{13}CN, CO, ^{13}CO and C^{18}O lines.

The measurement of [^{12}C]/[^{13}C] is non-trivial due to chemical effects leading to isotope fractionation under a variety of circumstances. Chemical reactions rates are sensitive to the particular isotope involved in the reaction, ostensibly due to the altered zero-point energy of the formed molecular bond (due in turn to the altered reduced mass of the system). Since, in a gross approximation, the zero-point energy of a bond is proportional to the harmonic vibrational frequency, which is in turn inversely proportional to the square root of the reduced mass, a slightly more massive isotope will have a slightly lower bond energy, leading to preference for the replacement of lighter with heavier isotopes in cold environments for reactions with a low activation barrier. In particular, in cool ($< 35\,\mathrm{K}$) molecular clouds the isotope charge exchange (ICE) reaction

$$^{13}\mathrm{C}^{+} + {}^{12}\mathrm{CO} \rightarrow {}^{13}\mathrm{CO} + {}^{12}\mathrm{C}^{+} \tag{1.1}$$

is strongly favoured (Watson et al., 1976), while under some conditions and for $T_{\mathrm{k}} < 9\,\mathrm{K}$ the reaction

$$^{13}\mathrm{CO} + \mathrm{H}^{12}\mathrm{CO}^{+} \rightarrow \mathrm{H}^{13}\mathrm{CO}^{+} + {}^{12}\mathrm{CO} \tag{1.2}$$

becomes favourable (Langer et al., 1984). The high abundance of CO leads to the depletion of the ^{13}C reservoir, so that other carbon-bearing species formed from or in equilibrium with this ^{13}C-depleted ISM obtain a higher [^{12}C]/[^{13}C] ratio than inherent to the ISM. This leads to a "bracketing" of the true, elemental [^{12}C]/[^{13}C] ratio in the ISM as:

$$[\mathrm{CO}]/[^{13}\mathrm{CO}] \leq [^{12}\mathrm{C}]/[^{13}\mathrm{C}] \leq [\mathrm{HCN}]/[\mathrm{H}^{13}\mathrm{CN}] \tag{1.3}$$

(Langer et al., 1984), where HCN has been introduced to represent the remaining carbon-bearing molecules and, for example, the [HCN]/[H^{13}CN] ratio can be $2\times - 3\times$ higher than [CO]/[^{13}CO] (Roueff et al., 2015). HCO^{+} can be fractionated in either direction depending upon kinetic temperature, density, ionisation fraction and abundance (Langer et al., 1978, 1984). While in regions with high FUV fluxes selective photodissociation can lead to [CO]/[^{13}CO] being elevated (as FUV photodissociation of CO is a line process where self-shielding plays an important role: Ritchey et al., 2011), Casoli et al. (1992) and Papadopoulos et al. (2014) argued strongly on empirical and theoretical grounds against this having a significant effect in (U)LIRGs.

There are additional observational difficulties in discerning the true isotope abundance ratios. For relatively abundant molecular species, such as CO, HCN and HCO^{+}, the ^{12}C isotopologue is most often optically thick, while the rarer isotopologues are not. This severely complicates the interpretation of the observed line brightnesses, due to a degeneracy between the isotope ratio and the optical depths. Solutions involve observations of multiple transitions of the isotopologues and modelling the line emission/radiative transfer.

1.2.2 Chemical Tracers of Buried AGN

Murphy et al. (2011) showed that while in the local universe LIRGs and ULIRGs are negligible contributors to the total star formation due to their rarity, from redshift $\gtrsim 1$ LIRGs, and for $z \gtrsim 2.3$ ULIRGs, dominate the star formation in the universe. Furthermore, there is considerable evidence for the co-evolution of AGN and ULIRGs (Magorrian et al., 1998; Sajina et al., 2007; Pope et al., 2008; Coppin et al., 2010; Kirkpatrick et al., 2012). The identification of AGN and characterisation of the physical conditions within these active galaxies is therefore of great importance for understanding the evolution of galaxies.

In the local and low-redshift universe, AGN are usually identified by one of three techniques: optical ionisation line diagnostic diagrams or 'BPT diagrams' (Baldwin et al., 1981; Kewley et al., 2006), multi-wavelength SED modelling from X-ray through to radio but especially the mid-IR, and spatially resolved kinematic modelling (e.g., Downes & Eckart, 2007). The first of these, the BPT diagrams, plots the ratio of ([OIII] $\lambda5007$)/(Hβ $\lambda4861$) against a range of lower-ionisation forbidden lines such as ([NII] $\lambda6584$) (the traditional BPT diagram), ([SII] $\lambda6717, 6731$) and ([OI] $\lambda6300$), taken in ratio with (Hα $\lambda6563$). Since in the local universe AGN have a much harder radiation spectrum than HII regions associated with star formation they separate out in the diagrams, which are essentially a measure of the hardness of the ionising radiation. There are many variations on the theme of the BPT diagram, comparing ionisation with stellar mass (the MEx diagram Juneau et al., 2011, 2014), rest frame $U - B$ colour (the CEx diagram Yan et al., 2011) and rest frame $g - z$ colour (the TBT diagram, Trouille et al., 2011). Nevertheless, there are signs that at $z \gtrsim 1$ more vigorous star formation leads to star-forming clumps contaminating the AGN regions of the diagram (Kewley et al., 2013; Juneau et al., 2014; Kewley et al., 2015). Furthermore, as we probe higher redshifts the emission lines shift further and further into the near-IR, seriously complicating observations. Finally, the rest-frame optical lines are severely attenuated by dust obscuration, rendering the BPT diagram and its variations essentially useless for identifying dust obscured AGN.

The second technique, multi-wavelength SED modelling, requires extensive and expensive observations. X-rays can identify AGN obscured in the optical but are biased against low-mass galaxies (Xue et al., 2010; Aird et al., 2012), and over the history of the universe approximately half of all AGN are likely to be Compton thick ($N_\mathrm{H} > 10^{23}\,\mathrm{cm}^{-2}$) and so undetectable with X-rays (Buchner et al., 2015), although mild obscuration ($10^{22} < N_\mathrm{H} < 10^{23}\,\mathrm{cm}^{-2}$) can be countered by the addition of mid-IR observations: Mendez et al. (2013). Radio is an extremely powerful and precise tool (especially when combined with the far-IR flux: Yun et al., 2001) for identifying (rare) high-mass AGN but is less accurate when identifying the much more common low-mass AGN where high star-formation rates can confuse the matter. There is also the problem that only 10% of AGN are radio luminous (White et al., 2000). Rest frame near to mid-IR SED modelling or even photometry can in principle identify AGN based on their hot dust emission (Lacy et al., 2004; Stern et al., 2005; Spoon et al., 2007; Veilleux et al., 2009; Jarrett et al., 2011; Kirkpatrick et al., 2015; Secrest et al., 2015). Yet even the IR diagnostics are not always sufficient, with dust extinctions $A_\mathrm{v} > 1000$ in some ULIRGs (Fischer et al., 1997) obscuring the nuclear source even in the mid-IR, conditions which may have been more common in the early universe.

The third technique, spatially resolved kinematic modelling, is only really useful in nearby galaxies due to the extremely high spatial resolutions required: the AGN sphere of influence is $< 100\,\mathrm{pc}$ in radius, corresponding to approximately 10 milliarcseconds at $z = 2$. Identification of an AGN therefore requires milli to sub milliarcsecond resolution, but is then model and inclination dependent and cannot easily distinguish between a quiescent super-massive black hole and an AGN (although kinematic evidence of outflows can help in some cases, Riffel & Storchi-Bergmann, 2011).

The difficulties in applying these AGN identification techniques to dusty galaxies and at high redshift have driven the search for molecular line diagnostics of AGN/starburst (SB) activity. Molecular lines, especially the mid-J transitions of HCN, HCO$^+$ and CS, are within existing ALMA bands out to $z \sim 3$, while the JVLA provides coverage at higher redshift. The far more significant issue is the faintness of these lines once redshifted, which may be alleviated in the future by the increased collecting area of the ngVLA and the SKA. Nevertheless, redshifts out to $\sim 1 - 2$ are already being studied with ALMA, driving the search for molecular-line equivalents of the BPT diagrams with the potential to identify AGN without dust bias.

The identification of effective molecular diagnostic lines has been troublesome. Graciá-Carpio et al. (2008a) found enormous variation in HCN and HCO^+ line ratios for similar galaxies, whereas Krips et al. (2008) found, for a smaller number of galaxies, but more transitions of HCN and HCO^+, tentative trends for HCN and HCO^+ excitation depending on SB or AGN dominance. Costagliola et al. (2011) used the EMIR on the IRAM 30m to observe 23 galaxies, including LIRGs and ULIRGs, and analysed the results with line ratios and a Principle Component Analysis (PCA) of the HNC/HCN, HCO^+/HCN and C_2H/HCN lines ratios; the $9.7\,\mu$m silicate absorption feature strength, polycyclic aromatic hydrocarbon emission (PAH) and the $25/100\,\mu$m flux ratio. As in Krips et al. (2008) they found that the HCO^+/HCN intensity ratio appears to correlate weakly with galaxy type, being > 1 in SB dominated galaxies and < 1 in AGN. However, also as in Krips et al. (2008), the trend was weak and complicated by the uncertain source sizes. HC_3N was identified as a potential diagnostic of SB dominated galaxies but was also seen in NGC 1068 which, while having an extensive SB ring (García-Burillo et al., 2014) is also a classical Seyfert galaxy.

The most successful approach to date has been that of Izumi et al. (2013, 2016b), who have developed an AGN/SB diagnostic plot using the HCN$(4-3)$/HCO+$(4-3)$ and HCN$(4-3)$/CS$(7-6)$ line ratios. They found that when observed at sufficient spatial resolution to exclude SB rings ($< 500\,$pc) AGN are readily identified by an excess of HCN$(4-3)$ emission, arguing for mechanically heated gas driving HCN favourable chemistry as the source of this excess based on single component LVG modelling of the excitation of HCN and HCO^+. The use of the $J = 4 - 3$ line alleviates concerns that the hot dust ($> 50\,$K) surrounding ULIRG nuclei (whether starburst or AGN driven) could lead to moderate pumping of the low$-J$ HCN, but not CS, lines. However, given that even their high resolution sample includes hundreds of parsecs within a single pointing, encompassing a wide range of physical conditions, it is hard to say conclusively whether their observations really point to an HCN abundance enhancement or are in fact due to HCN, HCO^+ and CS tracing different physical conditions. Recently however, Imanishi et al. (2016) found new evidence for a real HCN abundance enhancement around the AGN hosting ULIRG IRAS $20551 - 4250$ by studying the vibrationally excited and unexcited HCN and HCO^+ $J = 3 - 2$ lines, lending more credibility to the proposed diagnostic plots.

The apparent success of AGN diagnostic diagrams based on molecular line ratios is not without theoretical justification. The extreme luminosity of accreting AGN implies significant heating of the surrounding ISM, including any originally cold molecular gas. Owing to their smaller scattering cross section cosmic rays penetrate further into molecular clouds than UV or even X-ray radiation, leading to a greater heating in the denser, UV-shielded regions. This significantly affects the chemistry within these clouds (Tielens & Hollenbach, 1985; Maloney et al., 1996; Meijerink & Spaans, 2005; Meijerink et al., 2006, 2007; Harada et al., 2010; Meijerink et al., 2011; Harada et al., 2013; Williams & Viti, 2013b). In principle therefore, if an accreting black hole were the dominant energy source in a galactic nucleus it could significantly alter the molecular chemistry in the centre of the galaxy. Since the molecular emission from the galactic nuclei usually dominates the total emission single-dish integrated measurements could, at least in principle, distinguish between AGN and starburst dominated nuclei.

Despite these apparent successes there are concerns with HCN as a tracer of AGN. Solomon et al. (1992); Gao & Solomon (2004a); Wu et al. (2005, 2010) found that the HCN$(1 - 0)$ line is extremely well correlated with the IR luminosity, $L_{\rm IR}$, with $\log L_{\rm IR} = 1.00 \log L_{\rm HCN} + 2.90$, from Milky Way star forming clumps out to ULIRGs over 10 orders of magnitude. This was interpreted by Wu et al. (2005) as evidence that the HCN emission in starburst galaxies is well described by an optically thin ensemble of Milky-Way-like star-forming clumps of dense gas. In this scenario star formation in ULIRGs is fundamentally similar to that in the Milky Way, but with a higher fraction of dense gas and therefore also many more star forming clumps, but importantly not an enhanced specific star-formation rate (sSFR). The concern with HCN as an AGN tracer is that it is hard to reconcile the putative Gao-Solomon relation with the work of Izumi et al. (2016b), as HCN tracing AGN would imply a departure from the Gao-Solomon relation, or that AGN contribute to the IR and HCN luminosities in accordance with the Gao-Solomon relation, i.e., imitating star formation. The latter is possible, as it could be AGN induced star formation leading to the HCN$(4 - 3)$ luminosity enhancement. However, this alone would not explain the separation of starbursts and AGN in the Izumi et al. (2016b) diagnostic diagram. It is not yet clear how

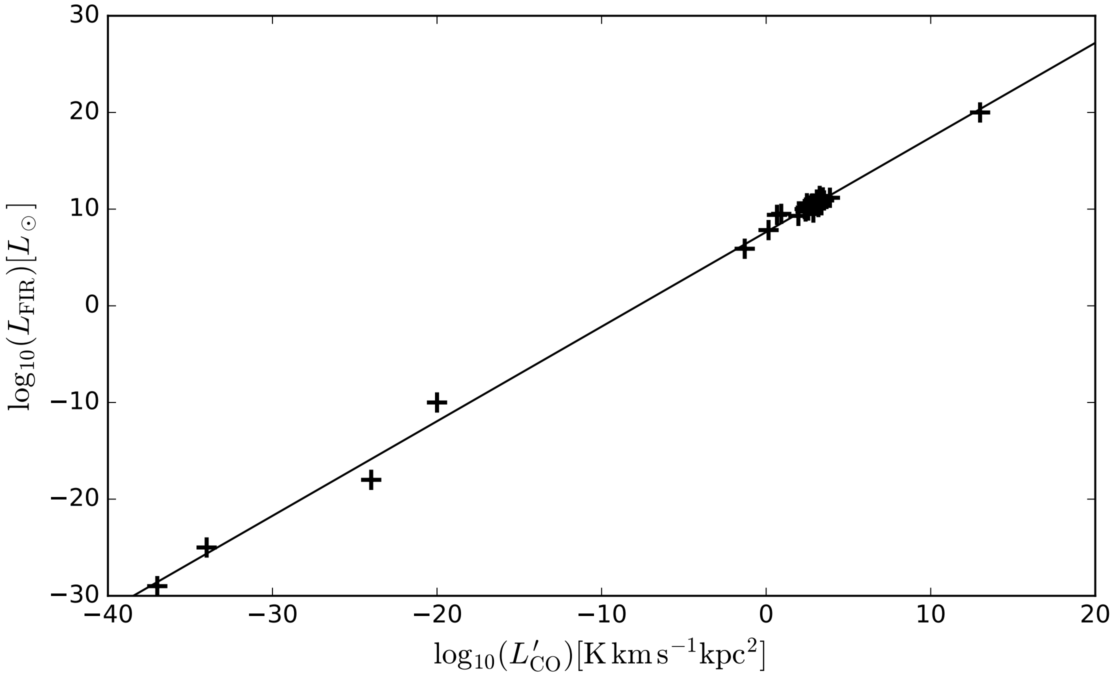

Figure 1.5: The correlation over almost 50 orders of magnitude between CO$(1-0)$ line luminosity and $L_{\rm FIR}$. Reproduced from/plotted using data from Thronson & Shull (1990), Page 421, Figure 5.b. Plotted are, in order of increasing luminosity, a burning cigar, a Jeep Cherokee, the 1988 Yellowstone forest fire, Venus, observed galaxies (Tacconi & Young, 1987; Solomon & Sage, 1988) and finally the observable universe.

to reconcile these two strands of research, although the answer probably lies in a combination of molecular abundances and excitation. It is noteworthy that Costagliola et al. (2011) and others have found that the chemistry in galactic nuclei is most reminiscent of galactic hot cores as modelled by Bayet et al. (2008), potentially suggesting extensive star formation as the dominant source of molecular luminosity. More exotically, it could be the case that the nuclei of these galaxies are in fact physically and chemically similar to enormously scaled up hot cores, although this is only likely in the most obscured nuclei, the Compact Obscured Nuclei (CON) (Costagliola & Aalto, 2010; Aalto et al., 2015b).

With all of these studies it is important to remember that we expect a correlation between any two luminosities on galaxy scales simply because bigger things are, in general, brighter (e.g., Kennicutt, 1989; Thronson & Shull, 1990): see Figure 1.5. This is not to say that the correlations are uninformative. Indeed, the slope of the correlation is of great interest, and potentially also the intercept (Greve et al., 2014). It is simply a reminder that a correlation is expected based on physical scaling and logarithmic plotting/analysis alone: it is the details of and departures from the correlation that are scientifically interesting.

It has been noted that (U)LIRGs may form a separate population in star-formation-rate surface density ($\Sigma_{\rm SFR}$) – dense gas surface density ($\Sigma_{\rm dense}$) space (traced by $L_{\rm IR} - L'_{\rm HCN(1-0)}$) (García-Burillo et al., 2012), although not in $\log_{10}(L_{\rm IR}) - \log_{10}(L_{\rm HCN(1-0)})$ space. Apparent discrepancies in the gradient of the $\log_{10}(L_{\rm FIR}) - \log_{10}(L'_{\rm mol})$ relations between works, with some authors finding linear relations even in the high-J CO transitions (Kamenetzky et al., 2015) and others sublinear slopes (Greve et al., 2014), appear to be due to (U)LIRGs, with sublinear slopes found for (U)LIRGs alone, whereas studies including 'normal' star forming galaxies are dominated by the low luminosity end of the relationship, which is indeed linear. The sublinearity in (U)LIRGs is likely due to the existence of a warm, dense molecular gas phase which is capable of exciting the high-J CO lines but does not contribute to the far-IR emission: such a phase is likely mechanically heated, consistent with the merger dominated nature of local ULIRGs (Greve et al., 2014).

Silicon monoxide, SiO, is another particularly interesting molecule both in the Milky Way and extragalactically. It is well established that silicates (such as fosterite, Mg_2SiO_4, and olivine, $MgFeSiO_4$) are a key component of interstellar dust (Kamijo, 1963; Gilman, 1969; Knacke et al., 1969; Hackwell et al., 1970). In Milky Way star forming regions SiO emission is unquestionably associated with strong shocks and the associated sputtering of the silicate dust (Gueth et al., 1998; Martin-Pintado, 1992; Meier & Turner, 2005; Guillet et al., 2009; Jiménez-Serra et al., 2010), yet in other galaxies the situation is not so clear cut. Similarly, extensive SiO emission is observed in the Central Molecular Zone (CMZ) of the Milky Way, which may be associated more with widespread turbulence and not specifically with individual star forming cores (Jones et al., 2012; Ginsburg et al., 2015; Tsuboi et al., 2015), and in proto-stellar outflows a fraction of the SiO emission appears to be unexplained and inconsistent with other shock tracers (Widmann et al., 2016). In external galaxies it appears that SiO may be related to X-ray chemistry or large scale turbulence, potentially providing a complimentary tracer of buried AGN (García-Burillo et al., 2000; Usero et al., 2004; García-Burillo et al., 2010). It may however simply be the case that SiO is tracing large scale outflows, shocks and turbulence associated with the AGN and any AGN induced star formation, as well as large scale bulk motions in mergers (Usero et al., 2006; Meier & Turner, 2012; García-Burillo et al., 2014; Meier et al., 2015; Tunnard et al., 2015b).

There is a strong and natural desire to find molecules that act as tracers of a single specific excitation mechanism, which has been the resounding ethos behind much of the past two decades of extragalactic molecular astronomy. Unfortunately, it is becoming ever clearer that this approach is not only limited but perhaps also counterproductive. The combination of various chemistries and excitation conditions which are then confused within even interferometric beams leads to an extreme wealth of degeneracies. This is further complicated by the different sizes of emitting regions of different species and of the transitions within a species. Even when the disk of a galaxy is resolved the constituent molecular clouds are not, and within molecular clouds themselves lies even greater complexity: e.g., Liu et al. (2015b); Zhang et al. (2015). This is in contrast to optical tracers such as ionisation line ratio diagrams, where there are clear and unique physical processes determining the galaxy's position in the diagram, which can be averaged over a galaxy without many of the complications inherent in molecular lines. The advent of ALMA alleviates the problems to some extent, but then only in the closest and brightest galaxies (García-Burillo et al., 2014; Viti et al., 2014; Meier et al., 2015), and even then the solution is incomplete. Finding new ways to interpret molecular emission and developing a better understanding of the collective processes are essential if the field is to make significant progress in the coming years.

1.3 An Interferometric Aside

The observations presented in this thesis were almost exclusively obtained using the Institut de Radioastronomie Millimétrique (IRAM) Plateau de Bure Interferometer (PdBI). There are a few peculiarities of interferometry that are important for interpreting the results of chapters 4 and 5, which I shall briefly discuss here. I do not provide a comprehensive description of the technique and refer the interested reader to the excellent expositions on the subject to be found in the NRAO Essential Radio Astronomy Course[3] and the course notes for the NRAO Synthesis Imaging Summer Schools[4]. Special note should also be given to the ESO introduction to interferometry by Andreas Glindemann[5], which while aimed towards optical and near-IR interferometry provides an excellent introduction to the general theory in common to both optical and radio interferometry.

1.3.1 A Simplified View of Interferometry

The full theory of millimetre radio astronomy is extensive and well beyond the scope of this thesis. Nevertheless, significant insights can be obtained by considering an extremely simplified

---

[3] `https://www.cv.nrao.edu/course/astr534/PDFnew.shtml`

[4] e.g., `www.phys.unm.edu/~gbtaylor/astr423/s98book.pdf`

[5] `https://www.eso.org/sci/facilities/paranal/telescopes/vlti/tuto/tutorial_spatial_interferometry.pdf`

'cartoon' of the process. As well as the technicalities of calibration and specific instrumental effects I neglect issues arising from the rotation of the Earth, the inherent bandwidth of all radiation (i.e., I make the unphysical assumption that the radiation is monochromatic) and I will focus on the one-dimensional case.

Each pair of antennas in an array defines a baseline, $\mathbf{b}$, and there is a time delay between light of frequency $\nu = \omega/2\pi$ arriving at the two antennas from a distant point source of $\tau_g = \mathbf{b} \cdot \hat{\mathbf{s}}/c$, where $\hat{\mathbf{s}}$ is the unit vector between the antenna and the source position on the sky. The response of each antenna is then of the form $V \cos(\omega\, t)$, and the product of the two antenna responses is:

$$\begin{aligned} R &= V^2 \cos(\omega\, t) \cos(\omega\,(t - \tau_g)), \\ &= V^2 \cos(\omega\, t) \left[\cos(\omega\, t) \cos(\omega\, \tau_g) + \sin(\omega\, t) \sin(\omega\, \tau_g)\right], \\ &= \frac{V^2}{2} \left[\cos(\omega\, \tau_g) + \cos(\omega\, \tau_g) \cos(2\omega\, t) + \sin(2\omega\, t) \sin(\omega\, \tau_g)\right], \\ &= \frac{V^2}{2} \left[\cos(\omega\, \tau_g) + \cos(2\omega\, t - \omega\, \tau_g)\right]. \end{aligned}$$

If one then takes the time averaged product of the antenna responses over a time $t \gg (2\omega)^{-1}$ one obtains:

$$R \propto \cos(\omega\, \tau_g) = \cos\left(\frac{\omega\, \mathbf{b} \cdot \hat{\mathbf{s}}}{c}\right). \tag{1.4}$$

One immediate result of this is that the response is independent of the actual positions of the antennas, depending only on the baseline between them. With the explicit dependence on $\hat{\mathbf{s}}$ the above equation holds for any position on the sky (assuming a perfectly isotropic antenna), and the total response to an extended source brightness distribution, $I_\nu(\hat{\mathbf{s}})$, is:

$$R_{\text{even}} = \int I_\nu(\hat{\mathbf{s}}) \cos\left(\frac{\omega\, \mathbf{b} \cdot \hat{\mathbf{s}}}{c}\right) \mathrm{d}\Omega. \tag{1.5}$$

The cosine term renders this integral insensitive to any antisymmetric (odd) components of $I_\nu(\hat{\mathbf{s}})$, so an additional delay of $\pi/2$ is added and passed to a separate correlator giving an antisymmetric term:

$$R_{\text{odd}} = \int I_\nu(\hat{\mathbf{s}}) \sin\left(\frac{\omega\, \mathbf{b} \cdot \hat{\mathbf{s}}}{c}\right) \mathrm{d}\Omega \tag{1.6}$$

and the complex visibility is given by:

$$V \equiv R_{\text{even}} - i\, R_{\text{odd}} = A\, e^{-i\phi} = \left(R_{\text{even}}^2 + R_{\text{odd}}^2\right)^2 e^{-i \arctan(R_{\text{even}}/R_{\text{odd}})}. \tag{1.7}$$

Therefore, the response of the 2-element, planar, monochromatic and isotropic interferometer to an extended source is:

$$V_\nu = \int I_\nu(\hat{\mathbf{s}}) e^{-i\, 2\, \pi \mathbf{b} \cdot \hat{\mathbf{s}}/\lambda} \mathrm{d}\Omega. \tag{1.8}$$

I.e., the complex visibility is the Fourier transform of the sky brightness distribution. The complex visibility is a function of $\mathbf{b}/\lambda$, the components of which are conventionally termed u, v and w. For small arrays and small angles away from the pointing direction the dot product can be expanded in terms of u and v and their associated directional cosines, l and m. The complex visibility then reduces to:

$$V_\nu(u, v) = \iint I_\nu(l, m) e^{-i\, 2\, \pi(ul + vm)} \mathrm{d}l \mathrm{d}m, \tag{1.9}$$

which is a realisation of the Van Cittert-Zernike theorem, and has the formal inversion:

$$I_\nu(l,m) = \iint V_\nu(u,v) e^{i\,2\,\pi(ul+vm)} \mathrm{d}u\mathrm{d}v. \tag{1.10}$$

I.e., with a complete sampling of the complex visibility in the (u,v) plane it would be possible to perfectly recover the sky brightness distribution. In practice this is of course impossible, and there are the additional complexities such as finite bandwidth which introduces a modulating sinc-like function[6] due to a loss of coherence at large angles away from the pointing centre. The rotation of the Earth introduces rapid oscillations in the visibilities and the anisotropy of the antenna primary beam introduces another envelope function. Furthermore, Fourier inversion of the visibilities is very rarely the best approach in practice and numerous algorithms exist to generate images from visibilities, and it is often advantageous to work with the visibilities directly.

1.3.2 Resolution and Largest Observable Angular Scale

Having outlined the simplified fundamental principles of interferometry I now discuss the issues of angular resolution and the challenges presented by incomplete (u,v) plane coverage, using one dimensional top-hat brightness distributions to illustrate the problem.

The crux of the matter is summarised in Figure 1.6. I have plotted, for narrow and wide top-hats, the sky brightness distribution, the (analytic) Fourier transforms and an example sampling of visibility for four unique baselines. Given the extremely sparse sampling of the visibilities neither of these brightness distributions would be well recovered. The relevant point is that the wide top-hat is completely 'resolved out' in this case - without shorter baselines the wide top-hat is simply undetectable. This has significant implications for observations of molecular lines in galaxies and especially when comparing single dish and interferometric fluxes, as depending upon the array configuration it is entirely possible to resolve out emission on scales larger than the primary beam, so simply have missing flux in images.

Nevertheless, it should be noted that the precise amount of flux that is lost is extremely uncertain due to the highly non-linear nature of practical observation and data reduction techniques, as well as depending upon the shape of the brightness distribution. Furthermore, the significant ($> 10\%$) absolute flux calibration uncertainties for both single dish and interferometric millimetre observations hinder empirical efforts to quantify the extent to which flux is resolved out in real applications.

The issue is reversed for small structures in the sky brightness distribution: as a feature becomes smaller its visibility tends more towards a single value, requiring larger and larger baselines to detect the drop in visibility indicative of a resolved object. This is less of a concern however, as the total flux is not significantly affected in this case, although as with single dish observations it is only possible to place lower limits on the source surface brightness if it is unresolved.

Some of the work presented in this thesis makes use of data reduced by collaborators. Where this is the case I have endeavoured to make this abundantly clear. The structure of the thesis is as follows. In chapter 2 I discuss some radiative transfer theory and the theory behind Large Velocity Gradient (LVG) modelling, before introducing Monte Carlo Markov Chains (MCMC) and the MCMC script developed for use in this thesis. Chapter 3 presents an extensive and quantitative assessment of the accuracy and precision of LVG models and concludes with an introduction to the effects of the CMB on molecular line emission. Chapter 4 explores the effect of the CMB on molecular-line − IR-luminosity relations as we begin to explore high redshifts. Chapters 5 and 6 present case studies of the local ULIRGs NGC 1068 and Arp 220, using molecular lines from PdBI observations and literature data to characterise the gas conditions and chemistry within these galaxies. Chapter 5 also allows for an exposition of the MCMC-LVG code presented in chapters 2 and 3. Chapter 7 steps away from much of the work in the thesis, focussing on 850 μm continuum observations instead of molecular lines. In it, I explore the potential evolution of proto-clusters

---

[6] A finite, non-zero bandwidth is introduced as an integral over the frequency: for a perfect top-hat bandpass this will introduce a sinc function. Realistic bandpasses are top-hat like, introducing sinc-like envelope functions.

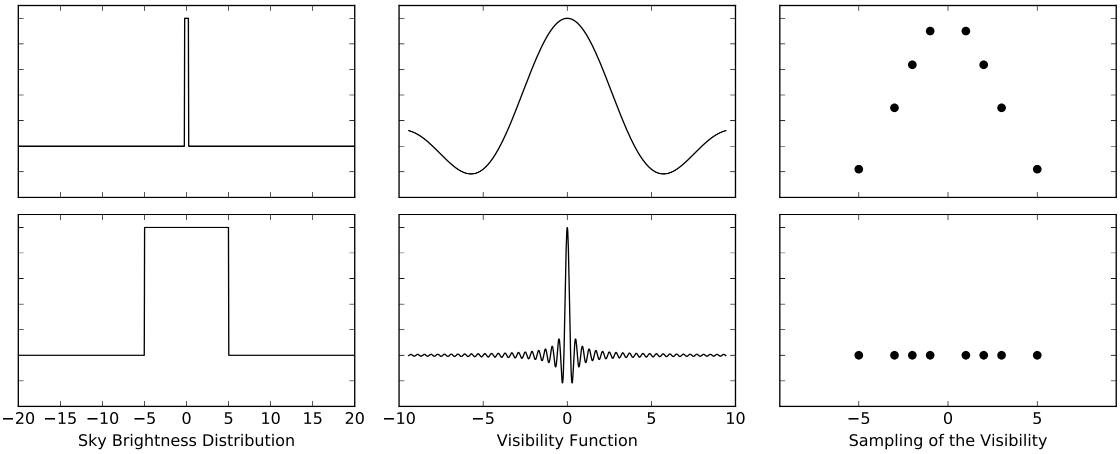

Figure 1.6: A one dimensional example of how interferometers sampling the Fourier transform of the sky brightness distribution leads to a largest detectable angular scale. The sky complex visibility functions (centre panel) have been sampled by four unique baselines (right). The extended top-hat brightness has a narrow visibility function which is not sampled by the baselines: detection would require a shorter baseline. The narrower distribution on the other hand is well sampled. N.B., while the plots are to scale the x-axis values are in arbitrary units.

around HzRGs via SMG overdensities and radial overdensity profiles between $z = 1.5 - 4.5$. The conclusions of the thesis are summarised in chapter 8.

This page was intentionally left nearly blank.

Chapter 2

Large-Velocity-Gradient Modelling

"I'm not a zebra. I'm the Doppler effect"

Sheldon Cooper, The Big Bang Theory

2.1 Theory

Despite the potential advent of neutrino and gravitational wave astronomy, it remains a fundamental truth that the primary tool of the astronomer is the electromagnetic spectrum propagated across the complex and various phases of interstellar and intergalactic space. It is therefore essential to understand not only how electromagnetic radiation is affected by the conditions giving rise to its emission, but also by the media it passes through between the source and the observer.

This thesis makes extensive use of Large Velocity Gradient (LVG) models to interpret observations of molecular rotational lines. I devote this chapter to introducing the theory of radiative transport, molecular line emission, and the means of interpreting this emission. The chapter concludes with an introduction of the Monte Carlo Markov Chain (MCMC) model I developed and go on to use in chapters 4 and 5.

2.1.1 Radiative Transfer

The following section draws heavily on both the RADEX manual (van Langevelde & van der Tak) and the undergraduate lecture notes of Professor Paul Alexander, Cavendish Laboratory, Cambridge. For a similar didactic including the details of line profiles (which are not modelled by RADEX and not included here) see Peters et al. (2012).

The essential theory of radiative transfer is remarkably simple, with the devil lying in the details. Beginning with some basic definitions the *specific intensity* or spectral brightness, I_ν, is defined as the rate at which energy flows perpendicularly through an area $\mathrm{d}A$ into a solid angle $\mathrm{d}\Omega$, i.e.,

$$\mathrm{d}E = I_\nu \, \mathrm{d}A \, \mathrm{d}t \, \mathrm{d}\Omega \, \mathrm{d}\nu, \tag{2.1}$$

with an additional $\cos(\theta)$ term if the ray is not perpendicular to the surface (Beer-Lambert's Law).

We can further define the emission coefficient, j_ν, as the rate at which energy is emitted into a solid angle $\mathrm{d}\Omega$ from a volume $\mathrm{d}V$:

$$\mathrm{d}E = j_\nu \, \mathrm{d}V \, \mathrm{d}t \, \mathrm{d}\Omega \, \mathrm{d}\nu, \tag{2.2}$$

and similarly an absorption coefficient, α_ν, which is the amount of energy removed from a ray as it passes through a distance ds:

$$\mathrm{d}I_\nu = -\alpha_\nu \, I_\nu \, \mathrm{d}s. \tag{2.3}$$

With these terms defined we can proceed to derive the iconic transfer equation, which states that the change in the specific intensity over a distance ds is simply the combination of the absorption and emission terms:

$$\frac{\mathrm{d}I_\nu}{\mathrm{d}s} = -\alpha_\nu \, I_\nu + j_\nu. \tag{2.4}$$

The more common form of this equation is

$$\frac{\mathrm{d}I_\nu}{\mathrm{d}\tau_\nu} = -I_\nu + S_\nu, \tag{2.5}$$

where

$$\tau_\nu\left(s\right) = \int^{s} \alpha_\nu\left(s'\right)\,\mathrm{d}s' \tag{2.6}$$

and $S_\nu = j_\nu/\alpha_\nu$ is the source function, which encompasses the majority of the physics involved. There exists a formal integral solution to equation 2.5, although for most realistic source functions the integral is analytically intractable, and must be solved computationally:

$$I_\nu\left(\tau_\nu\right) = I_{\nu,0}e^{-\tau_\nu} + \int_0^{\tau_\nu} e^{-\left(\tau_\nu - \tau'_\nu\right)} S_\nu\left(\tau'_\nu\right)\mathrm{d}\tau'_\nu. \tag{2.7}$$

2.1.2 Molecular Rotational Line Emission

Asymmetric molecules may posses significant electric dipole moments and as such their rotation generates a sinusoidally varying electric field, which in turn implies that the rotation of a polar molecule generates radiation. Molecular rotation is quantised so the molecular rotational radiation must also be quantised, and the eigenvalues of the Schröedinger equation are given by:

$$E_{\mathrm{rot}} = \frac{J(J+1)\hbar^2}{2I}, \tag{2.8}$$

where J is the angular momentum quantum number and I is the moment of inertia of the molecule. While higher order corrections to this energy term exist, describing the effects of bond stretching and other such effects, these are negligible in the extragalactic studies that are the focus of this thesis (Jennings et al., 1987; Gordy & Cook, 1984). Furthermore, the transitions between rotational states are restricted by transition selection rules such that $\Delta J = \pm 1$ and

$$h\nu = \Delta E_{\mathrm{rot}} = \left[J(J+1) - J(J-1)\right]\frac{\hbar^2}{2I} = \frac{\hbar^2 J}{I}. \tag{2.9}$$

Transitions between these states can be fully described by simulated emission, spontaneous emission, photo-absorption and molecular collisions, and can be related to the emission and absorption coefficients through the introduction of the Einstein coefficients:

$$j_{\nu_{J,J-1}} = \frac{h\nu_0}{4\pi} n_J A_{J,J-1}\phi(\nu) \tag{2.10}$$

and

$$\alpha_\nu = \frac{h\nu_{J,J-1}}{4\pi}\left(n_{J-1}B_{J-1,J} - n_J B_{J,J-1}\right)\phi(\nu), \tag{2.11}$$

where $\nu_{J,J-1}$ is the frequency for a transition from $J \rightarrow J-1$ and $\phi(\nu)$ is the line profile, normalised such that

$$\int_0^{+\infty} \phi(\nu)\mathrm{d}\nu = 1. \tag{2.12}$$

There are several key relationships necessary for us to progress that I will now simply quote here. Firstly, switching from $J, J+1$ notation to i, j notation to allow for more concise generalisation, it is a general statement that for $j > i$:

$$\frac{n_j}{n_i} = \frac{g_j}{g_i} \exp\left(-\frac{(E_j - E_i)}{kT_{\mathrm{ex}}}\right), \tag{2.13}$$

where g_i denotes the statistical weight of level i (for a linear rotor such as CO this is equal to $2J+1$) and if the system is in thermodynamic equilibrium the excitation temperature, T_{ex}, equals the kinetic temperature (T_{k}). We also need the relations between the Einstein coefficients themselves, the derivation of which is postponed to the end of this section:

$$g_i B_{ij} = g_j B_{ji} \tag{2.14}$$

$$A_{ji} = \frac{2h\nu_{ji}^3}{c^2} B_{ji}. \tag{2.15}$$

With these relations one can immediately see that the source function for the line transition $j \rightarrow i$ can be written as:

$$S_{ji} = \frac{j_{\nu_{ji}}}{\alpha_{\nu_{ji}}} = \frac{n_j A_{ji}}{n_i B_{ij} - n_j B_{ji}}, \tag{2.16}$$

$$= \frac{2h\nu_{ji}^3}{c^2} \frac{1}{\frac{n_i g_j}{n_j g_i} - 1}, \tag{2.17}$$

$$= \frac{2h\nu_{ji}^3}{c^2} \frac{1}{\exp\left(\frac{h\nu_{ji}}{kT_{\mathrm{ex}}}\right) - 1} \tag{2.18}$$

(e.g., Wilson et al., 2009). Then, to solve the radiative transfer problem it is necessary to solve for the level populations subject to the rate equation:

$$\frac{\mathrm{d}n_i}{\mathrm{d}t} = \sum_{j>i} A_{ji} n_j - \sum_{j<i} A_{ij} n_i + \sum_{j \neq i} \left(B_{ji} n_j - B_{ij} n_i\right) U_{ji} + \sum_{j \neq i} \left(C_{ji} n_j - C_{ij} n_i\right), \tag{2.19}$$

where U_{ji} is the local radiation field at the frequency of the transition $j \rightarrow i$, and C_{ji} is the rate of collisionally induced transitions from level $j \rightarrow i$ *without* the emission or absorption of a photon (Deguchi, 1981). The challenge of solving molecular, and indeed all, radiative transfer problems is the simultaneous solution of the rate equations for rotational levels coupled with the radiation field.

2.1.3 Derivation of the Einstein Coefficient Relations

Derivation of the Einstein coefficient relations relies upon the fact that since the coefficients describe the rate of transitions for individual atoms/molecules they cannot depend upon whether a system is in thermodynamic equilibrium (TE). Therefore, any relations derived under the assumption of thermodynamic equilibrium must also hold under non-LTE conditions. Then, if we consider the system to be in TE, the net rate of transitions into and out of a level must be zero, and by detailed balance:

$$A_{ji} n_j = (B_{ij} n_i - B_{ji} n_j) U_{ji}. \tag{2.20}$$

Since we assume TE we also have the relation (compare with Eqn 2.13):

$$\frac{n_i}{n} = \frac{g_i e^{-E_i/k_\mathrm{B}T_\mathrm{k}}}{Z}, \tag{2.21}$$

where Z is the partition function. Substituting, rearranging, recalling that $E_j - E_i = h\nu_{ji}$ and noting that since the system is in TE the radiation field can be described by a black body with temperature equal to the kinetic temperature, one obtains:

$$A_{ji} g_j \left(e^{h\nu_{ji}/k_\mathrm{B}T_\mathrm{k}} - 1 \right) \frac{c^2}{2h\nu_{ji}^3} = B_{ij} g_i e^{h\nu_{ji}/k_\mathrm{B}T_\mathrm{k}} - B_{ji} g_j. \tag{2.22}$$

The only terms in this equation with temperature dependence lie in the exponentials, but the equation must hold for all temperatures, and as such the temperature bearing terms must cancel. For this to be the case the right hand side of the above equation must rearrange to something of the form $X\left(e^{h\nu_{ji}/k_\mathrm{B}T_\mathrm{k}} - 1\right)$. This is only possible if $B_{ji}g_j = B_{ij}g_i$, giving the first Einstein relation. Substituting this relation back into Eqn 2.22 yields the second relation.

2.2 Escape Probabilities and the LVG Approximation

One of the most successful and widely used tools for interpreting the physical conditions of gas traced by molecular rotational lines is the LVG model (although Photon Dominated Region (PDR) models should not be forgotten), where the radiative transfer and rotational level populations are decoupled through the introduction of a photon escape probability (Sobolev, 1960; de Jong et al., 1975; Goldreich & Scoville, 1976; Weiß et al., 2005; van der Tak et al., 2007). This approach has two key strengths: **1)** it does not assume Local Thermodynamic Equilibrium (LTE), and **2)** it is fast, allowing for grids of models to be run. There are many implementations of the LVG model, although currently the most widely used in the millimetre and sub-millimetre regime is the publicly available code, RADEX[1] (van der Tak et al., 2007). Technically, RADEX is an escape probability code, for which one form of the escape probability corresponds to the LVG approximation. However, it is common parlance within the community to refer to RADEX as an LVG code, a convention which I continue here.

While far less sophisticated than Monte Carlo models such as RATRAN[2] and LIME[3] (Hogerheijde & van der Tak, 2000; Brinch & Hogerheijde, 2010), which are better able to model radiative transfer in very optically thick environments as well as working in 3D, the much greater speed of LVG codes, and the fact that they do not require models (or assumptions) regarding the distribution of the gas, means that in many instances, especially extragalactic observations, LVG models are still the most practical non-LTE approach. RATRAN and LIME also include the ability to input non-uniform temperatures and densities; while this is in principle possible with the LVG approach there is, so far, no publicly available code providing these features.

One of the most common methods of simultaneously solving the rate equation and transfer equation is to introduce an escape probability, β_{ji}, which is simply the probability that a photon with frequency ν_{ji} escapes from the emitting gas. The specific form of β_{ji} depends upon the assumed geometry, with the traditional LVG or Sobolev approximation for a uniformly expanding (or contracting) spherical cloud:

$$\beta_{ji} = \frac{1 - \exp(-\tau_{ji})}{\tau_{ji}}, \tag{2.23}$$

where τ_{ji} is the optical depth for frequency ν_{ji} (Castor, 1970). While the full derivation of this expression is rather geometrically involved, significant insight can be obtained by considering the simplified, one dimensional case. If one first considers that the absorption coefficient can be described, dimensionally, as the product of a cross section and a number density: $\alpha_{ji} \sim \sigma_{ji} n$, then

---

[1] `http://home.strw.leidenuniv.nl/~moldata/radex.html`

[2] `http://home.strw.leidenuniv.nl/~michiel/ratran/`

[3] `https://github.com/lime-rt/lime`

for an optical depth of unity the path length, $s = 1/\sigma_{ji} n$, i.e., the classical mean free path for a single scattering. The photon escape probability will then be, approximately, the average value of $e^{-\tau_{ji}}$ over the path (temporarily neglecting subscripts for readability):

$$\beta \sim \left\langle e^{-\tau} \right\rangle = \frac{1}{\tau} \int_0^{\tau} e^{-\tau'} \mathrm{d}\tau' = \frac{1 - e^{-\tau}}{\tau}. \tag{2.24}$$

The simplicity of this expression is largely due to a great deal of complexity being obfuscated inside of, and then integrated over, the optical depth. Expressions have also been derived for a uniform slab of gas (Scoville & Solomon, 1974; de Jong et al., 1975):

$$\beta = \frac{1 - e^{-3\tau}}{3\tau}, \tag{2.25}$$

and for a uniform, homogeneous sphere (Osterbrock & Ferland, 2006):

$$\beta = \frac{3}{4\tau} \left[1 - \frac{1}{2\tau^2} + \left(\frac{1}{\tau} + \frac{1}{2\tau^2} e^{-2\tau} \right) \right]. \tag{2.26}$$

The specific choice for the form of the escape probability has to be made according to the investigation at hand. It has been argued, based on results in Henkel et al. (2010), that the choices have little effect on the results. The interpretation of 'little' here is ambiguous: Henkel et al. (2010) found that the choice changes the parameter ranges by almost half a dex. Nevertheless, given the integration over an entire galaxy with multiple gas phases and geometries the choice is indeed unlikely to significantly bias results, and a reliable determination of a representative geometry for the emission from an entire galaxy is likely impossible.

The underlying assumption of the escape-probability approach is that the local radiation field within the cloud can be described by the sum:

$$U_{ji} = S_{ji}(1 - \beta_{ji}) + B_{ji}(T_{\mathrm{bg}})\beta_{ji}, \tag{2.27}$$

where $B(T_{\mathrm{bg}})$ is the black body background radiation with temperature T_{bg}. The rate equation can then be greatly simplified by the substitution of the radiation field and recalling Eqn 2.16:

$$\begin{aligned}
\frac{\mathrm{d}n_i}{\mathrm{d}t} &= \sum_{j>i} A_{ji} n_j - \sum_{j<i} A_{ij} n_i + \sum_{j \neq i} \left(B_{ji} n_j - B_{ij} n_i \right) U_{ji} + \sum_{j \neq i} \left(C_{ji} n_j - C_{ij} n_i \right), && (2.28) \\
&= \sum_{j>i} A_{ji} n_j - \sum_{j<i} A_{ij} n_i + \sum_{j<i} \left(B_{ji} n_j - B_{ij} n_i \right) U_{ji} - \sum_{j>i} \left(B_{ij} n_i - B_{ji} n_j \right) U_{ji} \\
&\qquad + \sum_{j \neq i} \left(C_{ji} n_j - C_{ij} n_i \right), && (2.29) \\
&= \sum_{j>i} \beta_{ji} A_{ji} n_j - \sum_{j<i} \beta_{ji} A_{ij} n_i + \sum_{j \neq i} \beta_{ji} B_{ji}(T_{\mathrm{bg}}) \left(B_{ji} n_j - B_{ij} n_i \right) \\
&\quad + \sum_{j \neq i} \left(C_{ji} n_j - C_{ij} n_i \right). && (2.30)
\end{aligned}$$

The simplification arises from that fact that the calculation of the rate equation is now decoupled from that of the radiation field, allowing for the two to be solved iteratively.

Finally, it should be noted that RADEX has several significant limitations. It does not allow for modelling of line profiles, treating all lines as top-hat profiles. Since the enhanced optical depth around the line centre of a Gaussian line has significant effects on the level populations this is a significant limitation of the code. Furthermore, there are localised regions in the parameter space where RADEX does not converge, notably a thin plane in $n_{\mathrm{H}_2} - T_{\mathrm{k}} - N_{\mathrm{mol}}$ space where RADEX will reliably fail (Z. Zhang, private communication). A small jittering of the parameters about the failure point is generally sufficient for convergence to be obtained, but it is another limitation of the code.

2.3 The Monte Carlo Markov Chain Approach

Traditionally, RADEX has been used to generate two-dimensional grids of line ratios as functions of physical parameters which are then compared to observations. This is the method I use in Chapter 5, and this remains a powerful tool, especially when there are few lines available. However, the increase in both affordable computer power and molecular line observations now allows for more complex modelling. This was first attempted by Kamenetzky et al. (2014), who used the code Multinest (Feroz et al., 2013) and RADEX to model the line emission directly (i.e., not line ratios) for two gas phases.

Here, I present a Monte Carlo Markov Chain (MCMC) code I developed to run RADEX for an arbitrary number of gas phases and combinations of molecular species. This code is used to test the usefulness of the LVG approximation itself in Chapter 3, and to model the molecular gas in NGC 6240 in Chapter 4.

MCMC is a powerful technique for sampling the posterior probability distributions of analytically intractable problems (Hastings, 1970; Link et al., 2002). While extensively used in other fields and in cosmology and extrasolar planetary research, it has not been widely adopted in molecular astronomy despite having enormous potential for interpreting the profusion of molecular lines now accessible with ALMA, NOEMA and the JVLA. It requires only a likelihood function and priors, and for the posterior distribution to be continuous, although for best results the posterior should also be singly peaked.

The algorithm calculates the likelihood of a point in the N-D phase space, randomly samples a nearby point and calculates its likelihood. If the likelihood of the new point is greater the chain moves to the new point. If it is less, it moves to the point if a uniform random number $[0, 1)$ is less than the ratio of the likelihoods; else the chain remains where it is. This chance of jumping to a less likely point is the key step in the process: it allows for the system to, given infinite time, reach a statistical equilibrium. As has been shown by mathematicians far more accomplished than I, for an infinitely long run the density of samples in the N-D phase space will be equal to the posterior probability distribution.

One of the main differences between realisations of this algorithm is the method chosen for sampling the new point. In the simplest case, one simply chooses an N-D random vector, centred on the previous point and with a normalisation in each dimension equal to a scaling parameter or step size, which is tuned to maximise the MCMC efficiency. This can be changed to an N-variate normal distribution with a covariance array equal to the covariance of the trace[4] of a short first run, or in fact to any arbitrary probability distribution, as long as the new distribution depends only on the current location. This can lead to much faster convergence of the chain. This Metropolis-Hastings method of sampling points is easy to code and, more importantly, to test, which led to it being adopted for the present code (Metropolis et al., 1953; Hastings, 1970).

While there exist potentially improved sampling methods such as adaptive sampling and the Gibbs sampler, these are significantly more complex and much more susceptible to the curse of dimensionality (Casella & George, 1992; W. R. Gilks, 1992; Görür & Teh, 2011). Since the purpose of this MCMC is to explore potentially many gas phases and molecular species simultaneously the code could be used for many dimensions. As such I do not discuss these alternative samplers further.

2.3.1 Convergence

I have mentioned the issue of convergence of MCMCs and slightly brushed over the issue that MCMC is only truly correct when the trace is infinitely long. In practice it is necessary to check that the MCMC has converged onto a solution. While there are various methods to test for convergence they often are as time intensive as the MCMC itself, with no guarantee of accuracy for an arbitrary posterior.

There are two potential convergence issues. The first is that the MCMC cannot converge at all: for a classical minimisation problem the MCMC should converge to the minimum of the likelihood function, with the reversibility condition leading to oscillations about this minimum,

---

[4] The trace of an MCMC run is the output in the form of each of the N variables at each step of the chain.

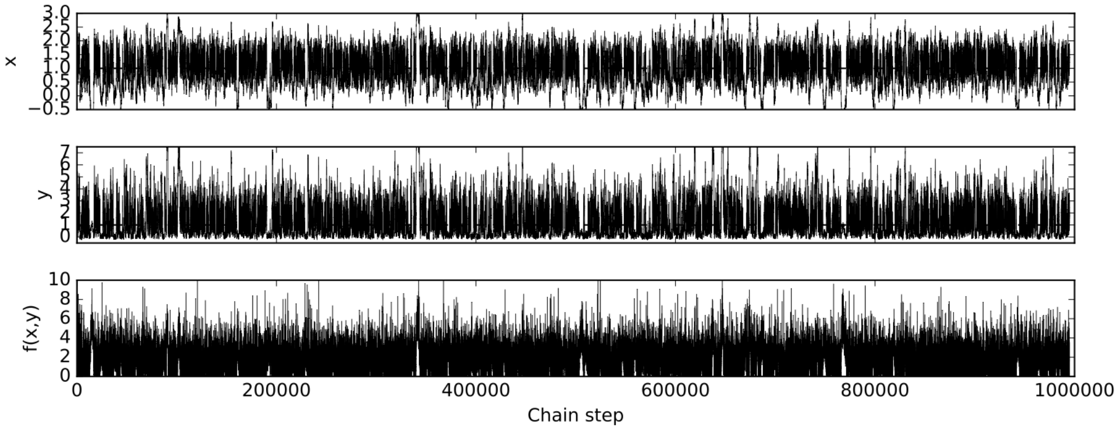

Figure 2.1: The MCMC traces, post burn-in, for the 2D Rosenbrock function, which has a minimum value of 0 at $(x, y) = (1, 1)$ for the values used here. While the x value oscillates around the minimum at 1, the y value and the function values converge on 1 and 0 respectively, but also 'bounce' back. This allows for a thorough characterisation of the parameter space.

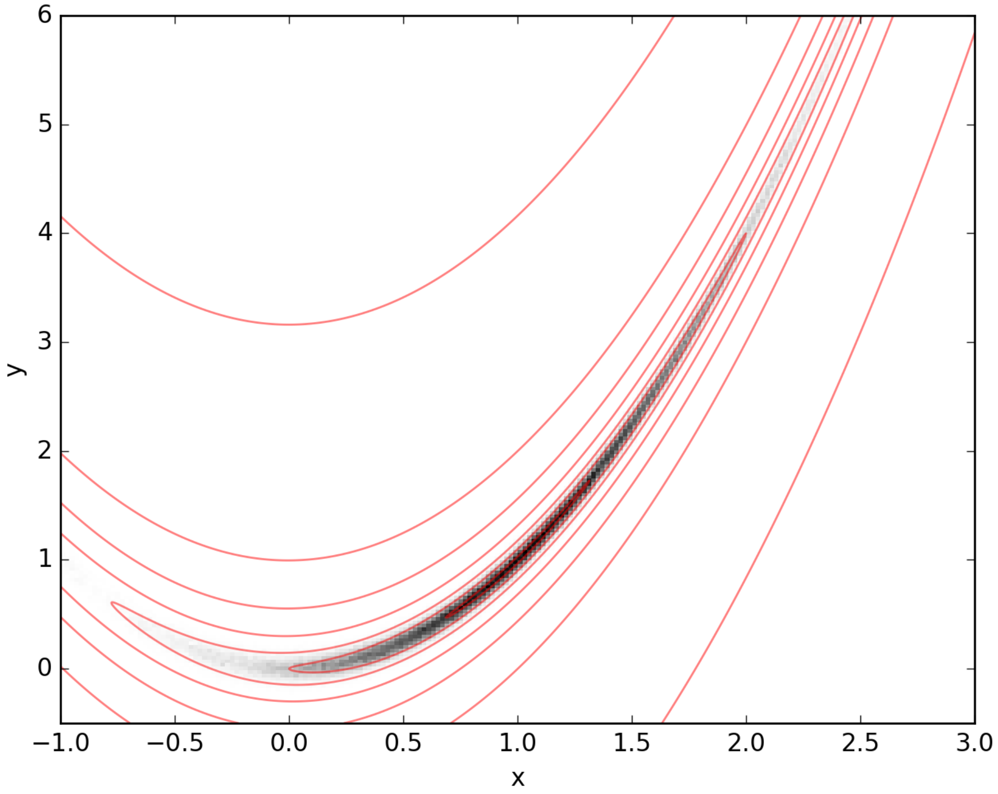

Figure 2.2: The 2D Rosenbrock function with $a, b = 1, 100$ (red contours) and the density of points for the MCMC (greyscale shading). The MCMC not only finds the minimum of the function but also measures well the shape of the function's PDF about the minimum.

as in Figure 2.1. This issue is easily diagnosed, as the resultant trace has no mean about which is oscillates. The much more problematic and much harder to identify case is when the MCMC becomes trapped in a local minimum. The MCMC traces appear to have converged, but the global minimum can be completely unsampled. For an infinitely long trace the MCMC would eventually escape the local minimum. One of the simplest and most effective ways to test for this second kind of non-convergence is to run multiple traces with randomised starting positions. However, this does not guarantee finding the global minimum if there are many local minima. This is one of the limitations of MCMC.

2.3.2 Testing and the Rosenbrock Function

One of the many performance tests for optimisation algorithms is finding the minimum of the Rosenbrock function (Rosenbrock, 1960):

$$f(x,y) = (a-x)^2 + b(y-x^2)^2, \tag{2.31}$$

which has a minimum value of 0 at $f(a, a^2)$. Typically, $a = 1$ and $b = 100$. This function has the useful property that the approximate minimum, given by a quadratic arc passing through $(0, 0)$, is trivial to find, yet the global minimum at $(1, 1)$ is much harder. It is therefore a useful test function for codes designed to be used on less than trivial PDFs, such as the complex multi-molecule and multi-phase models presented later. I used the Rosenbrock function to test the performance of the MCMC, defining the likelihood function to be:

$$\mathcal{L} \propto \exp\left(-f(x,y)\right), \tag{2.32}$$

thereby corresponding to a maximum likelihood of unity at the minimum of the function. Running the MCMC for 10^6 steps with a burn-in of 5000 steps I recovered the traces and 2D PDF shown in Figures 2.1 and 2.2 respectively. The code rapidly and accurately homes in on the minimum, and traces out the surrounding PDF well. The traces in Figure 2.1 indictate convergence on the minimum.

The MCMC can also use the difference in the log-likelihoods, instead of the ratio of the likelihoods, to decide upon the next step in the chain. The choice between the two is essentially decided by the steepness of the function as it approaches a minimum. The Rosenbrock function is very steep and using the log-likelihoods leads to the MCMC very rapidly finding the global minimum. However, once found, the MCMC extremely rarely leaves this minimum so even the PDF close to the minimum is very poorly sampled. For functions with a single minimum this is perhaps acceptable for some situations: for the forthcoming exploration of the complex molecular phase space it is not. The key point here is that while being exceptionally powerful MCMC is a blind tool: its results must be inspected to ensure they are well behaved and explore reasonable parameter spaces, and this is before entering into a discussion of the physical and chemical constraints.

The number of jumps to a new point as a fraction of the total number of steps in the chain is indicated by R. This jump ratio is a powerful (but in no way absolute) indicator of the robustness of the chain: $R \ll 1$ implies that the PDF is not being sampled well. Either the chain is broken, trapped in a small local minimum, or the step size is too large. On the other hand, $R \simeq 1$ implies that the chain is jumping far too frequently, and is still to find the minimum. It could be the case that the step size is too small, the PDF does not have a clear minimum, or that the PDF does not fall sharply enough. It is therefore a delicate process to tune the MCMC according to the problem at hand in order to maximise its efficiency, a problem that would not exist if the MCMC were to be run indefinitely.

2.3.3 An MCMC–LVG Model

The MCMC code was written to serve as a replacement for grid methods when using RADEX. With the plethora of molecular lines being observed in nearby galaxies with modern telescope arrays it is becoming possible to model many line ratios simultaneously, allowing for more degrees of freedom and fewer modelling assumptions. However, while running 2D grids of line ratios is fast and effective, it quickly becomes infeasibly slow and cumbersome to interpret when extended to higher dimensions, such as when exploring kinetic temperature, density and molecular abundance simultaneously. The MCMC code allows for just such a high-dimensionality exploration.

For each RADEX run several physical parameters are necessary. Specifically: the gas kinetic temperature (T_k [K]), the gas density (n_{H_2} [cm^{-3}]), the background radiation temperature (T_bg [K]), the line width (Δv [km s^{-1}]), and the molecular column density *of the emitting/absorbing species* (N_mol [cm^{-2}]). However, there are a number of relationships between the parameters which allow for much more meaningful and efficient modelling. Immediately:

$$N_\mathrm{mol} = X_\mathrm{mol}\, N_{\mathrm{H}_2} = \frac{3.086\times 10^{18}\, n_{\mathrm{H}_2}\, \Delta v\, X_\mathrm{mol}}{\mathrm{d}v/\mathrm{d}r}, \tag{2.33}$$

where $\mathrm{d}v/\mathrm{d}r$ is the velocity gradient of the gas in km s^{-1} pc^{-1}. Separating the molecular hydrogen column density from the molecular abundance allows for clearer comparisons between abundances when modelling multiple molecular species while ensuring that all emission from a given gas phases shares the same physical parameters. Secondly, I make use of the virial parameter, K_vir (e.g., Greve et al., 2009; Papadopoulos et al., 2012, 2014):

$$K_\mathrm{vir} = \frac{\mathrm{d}v/\mathrm{d}r}{(\mathrm{d}v/\mathrm{d}r)_\mathrm{vir}} = \frac{1.54}{\sqrt{\alpha}}\frac{\mathrm{d}v}{\mathrm{d}r}\left(\frac{n_{\mathrm{H}_2}}{1000\,\mathrm{cm}^{-3}}\right)^{-0.5}. \tag{2.34}$$

The geometric coefficient α ranges from $1-2.5$ and adopting a uniform pdf over this range for α implies an expectation value $\langle\sqrt{\alpha}\rangle = 1.312$. Given the small range in α compared to the orders of magnitude changes in the other parameters I adopted $\langle\sqrt{\alpha}\rangle = 1.312$ for the modelling. The velocity gradient, $\mathrm{d}v/\mathrm{d}r$, describes the change in line-of-sight velocity through the cloud. K_vir is equal to unity for a virialised cloud, while for turbulent but still bound gas K_vir could be much higher. Due to the highly dynamic conditions in the centres of ULIRGs Papadopoulos et al. (2014) argued that values of up to 20 are very reasonable even for the putative dense gas tracers HCN and HCO$^+$.

The core of the code can be broken down into three parts: the sampler, the RADEX interfacing, and the likelihood function. The sampler was described and tested above. A key additional step is the addition of K_vir restrictions, which required an alteration of the sampler and were one of the reasons for developing a custom MCMC code. This was implemented by repeatedly sampling new points as normal, but only accepting the trial parameters if they corresponded to an acceptable K_vir. When they did not, all of the trial parameters were discarded and redrawn. While not ideal for computational efficiency this was to avoid biasing the results as would be the case if the code first sampled a new n_{H_2} (for example), and then selected $\mathrm{d}v/\mathrm{d}r$ based on n_{H_2} and the K_vir restrictions. In the worst case, of a single allowed K_vir, this could permanently exclude a significant region of the $\mathrm{d}v/\mathrm{d}r$ parameter space. Resampling in the case of unacceptable K_vir values avoids this problem and associated biases, while not introducing a significant overhead[5].

The second component, the RADEX interfacing, was based on the sample scripting files included in the RADEX distribution and uses text files and system calls to RADEX. RADEX can run many models from a single input script, and although this number is limited the limit is sufficient for 3 gas phases and 6 molecules. The RADEX output files are then read by the MCMC script.

The likelihood function is fundamentally the same as described above, using the χ^2 estimator. The χ^2 is calculated for all independent observed molecular line ratios and errors input to the model. When multiple lines have been observed in the same spectrum, as in the study of NGC 6240 presented later in this thesis, it is preferable to set these ratios by hand, as their ratio is not subject to the (significant) calibration uncertainties inherent to millimetre observations. Otherwise, and as in the more general code used in Chapter 3, the ratios are simply ordered as the line data are passed to the program which then creates all of the independent line ratios in an arbitrary order.

---

[5] Speed tests on the code, not included in this thesis as they add nothing of scientific value or interest, showed that for any reasonable trial the code spent between 95% and 98% of the runtime in RADEX.

The choice to use line ratios, instead of fitting to line brightnesses, was motivated by the combination of data from many different telescopes with different beam sizes. To some extent, these effects cancel out in line ratios (see Chapter 4), whereas attempts to correct for the beam and source size requires extensive assumptions or a beam filling factor for each line used, neither of which is desirable. In principle, however, it is simple to adjust the code to fit to each line individually.

The code is functional but there are numerous steps for potential improvement. The easiest step would be the introduction of multiple 'walkers', so that there are multiple chains exploring the parameter space simultaneously. This would help alleviate concerns regarding local maxima in the likelihood function which are currently addressed by repeated runs with randomised starting positions. A much more extensive alteration would be the complete rewriting of the LVG code in modern FORTRAN, wrapped into the Python code using F2PY[6], which allows FORTRAN functions to be run natively by Python. This would offer significant speedups as currently much time is spent interfacing with RADEX, although some headway has been made in this direction for the complex models by generating a single RADEX input script for all molecules and gas phases for each MCMC step. In the case of such an undertaking it would be desirable to include the physics of dust inside the gas, and even perhaps the possibility of multiple gas phases along the line of sight and the introduction of line profiles with 1D kinematics. These extensions are far beyond the current needs of the code, and beyond the scope of this thesis.

---

[6] `http://docs.scipy.org/doc/numpy-dev/f2py/index.html`

Chapter 3

How Wrong is Wrong? Testing LVG Models

> *"[A]ll models are wrong, but some are useful."*
>
> George Box & Norman Draper: Empirical Model-Building and Response Surfaces

This chapter was published in a similar form in Tunnard & Greve (2016).

3.1 Introduction

As was discussed in Chapter 2, in millimetre astronomy one of the most widely used simple radiative-transfer codes is RADEX. When it was introduced, RADEX was recommended as a tool for interpreting molecular line ratios, primarily through diagnostic plots. However, since then it and other LVG codes have become extensively used as general-purpose tools for extracting gas conditions, especially in extragalactic targets; e.g., Krips et al. (2008); Greve et al. (2009); Rangwala et al. (2011); Kamenetzky et al. (2014); Papadopoulos et al. (2014); Viti et al. (2014); Tunnard et al. (2015a,b), where the plethora of molecular lines now being observed by the state-of-the-art single-dish telescopes and interferometer arrays are allowing for modelling of multiple line ratios, and therefore more complex physical models.

Despite the wide spread use of LVG models, there have been no published studies on the ability of LVG models to recover the true gas parameters. I present here such a study, using an unmodified version of RADEX[1] to explore the precision and accuracy of LVG models as a means for recovering gas parameters. The work in this chapter was published in Tunnard & Greve (2016).

In the second half of this chapter I explore the effects of the CMB on molecular rotational lines. CO spectral-line energy distributions (SLEDs) of star-forming galaxies are a topic of active research and are of great interest for the study of star formation over cosmic times. As such they have been extensively studied, including with sophisticated hydrodynamic modelling including radiative transfer post-processing (Narayanan et al., 2009, 2010; Narayanan & Krumholz, 2014; Olsen et al., 2015), as well as analytically by Shirley (2015). However, while these papers present state of the art models of the galaxies and their molecular emission, the effect of the CMB temperature is given only a cursory discussion. In cold molecular environments in high-redshift galaxies the effects of the CMB on the low$-J$ CO lines can become highly significant at $z > 2$ where the CMB

---

[1] There are some known issues with convergence in RADEX (Z. Zhang, private communication) and some authors (e.g., Rangwala et al., 2011) have altered the FORTRAN code to address these issues. These alterations are not public however.

temperature begins to exceed the energy of the $J = 1 - 0$ line (5.53 K), similar to the suppression of molecular lines in local ULIRGs (Papadopoulos et al., 2010a), where the hot dust leads to a very significant reduction in the observed molecular flux. This in turn leads to apparently under-excited CO SLEDs unless corrected for the effects of dust. The effect of the CMB as a function of redshift has been modelled by da Cunha et al. (2013) for single lines of sight for both dust and CO, and Shirley (2015) showed that for heavy rotor molecules (such as HCN and HCO^+) the effect of the CMB on line excitation is very small, although the loss of contrast due to a higher CMB is not explored in their paper.

The outline of this chapter is as follows. I describe the models, assumptions and techniques in §3.2. I begin by demonstrating both the accuracy of grids and MCMCs with and without a 10% observation uncertainty and then show how the addition of ^{13}C isotopologue line observations can improve the results. I then investigate whether it is better to assume a canonical molecular abundance or introduce the abundance as a free parameter, before repeating this for the [HCN]/[H^{13}CN] abundance ratio. Finally, I use two toy models to explore the potential effects of the CMB at high redshifts, including galaxy integrated effects. The results of this investigation are presented in §3.3, and discussed in §3.4.

3.2 Models and Methods

In order to test the recoverability of LVG parameters I introduce a highly idealised scenario in that I generate lines using RADEX, from which I then attempt to recover the input parameters. With modern millimetre and sub-millimetre line observations there is a ubiquitous absolute calibration uncertainty of $\sim 10-20\%$ in both interferometric and single-dish observations and this uncertainty usually dominates the overall uncertainty in the line flux. I explore the recovery accuracy both with zero errors and where all lines are given an (optimistic) uncertainty of 10%.

It should be noted that in practice there are additional significant potential sources of error, beyond the scope of this work. In the case of single-dish observations there are complications arising from an unknown source size and hence uncertain (and likely different for different molecular lines) beam coupling factors. While interferometers can, to some extent, alleviate these issues by resolving the source they are in turn susceptible to spatial filtering (the resolving out of large scale emission discussed in Chapter 1) as well as to synthesised beam side-lobe artefacts. Nevertheless, the vastly improved (u, v) plane coverage of ALMA and the ngVLA will significantly alleviate these issues, even with snapshots[2].

3.2.1 Generating Lines

For all of the tests I generate artificial lines using RADEX and collision rates from the Leiden Lambda database (van der Tak et al., 2007; Dumouchel et al., 2010; Yang et al., 2010). The specifics depend upon the investigation in question, but the features common to most of the models are:

- The physical free parameters are drawn from a uniform distribution in log space.
- I restrict the thermal pressure, $P/k_{\rm B}$, of the models to be $< 1 \times 10^8\,{\rm K\,cm^{-3}}$. Higher thermal pressures are very unlikely/rare (even ULIRGs only exhibit thermal pressures $\sim 10^7\,{\rm K\,cm^{-3}}$: Dopita et al., 2005), but also RADEX tends to fail at high thermal pressures, biasing the results[3].
- The virial parameter, $K_{\rm vir}$, is set to unity (corresponding to virialised clouds), so that for a given $n_{\rm H_2}$ dv/dr is determined, and not a free parameter. It is however kept as a (constrained) free parameter when attempting to recover input parameters with the Monte Carlo Markov Chain (MCMC) models.

---

[2] Short observations that do not make use of terrestrial rotation to increase the sampling of the (u, v) plane.

[3] The specific error seems to vary, but the result is that high thermal pressure inputs are recovered extremely poorly, with a ~ 4 dex underestimate of kinetic temperature and a ~ 2 dex overestimate of density. There is also a region of high thermal pressure where all fluxes are zero.

3.2.2 Introducing Errors

I introduce random statistical errors to the lines produced by RADEX. The motivation is to emulate reality, where there is a true, unknown, value of the line brightness temperature, but the observed value may be larger or smaller, primarily due to calibration uncertainties. In these tests the true value is used to generate the randomised values.

For the tests including observation calibration uncertainty I randomise the flux of each line individually, such that the new, uncertain flux is drawn from a Normal distribution with mean equal to the artificial line brightness temperature and with a standard deviation equal to 0.1 times the artificial line brightness temperature. I calculate line ratios using randomised line brightnesses, propagating the uncertainties so that the uncertainty in the line ratios is $\sim 14\%$. This is the uncertainty used when calculating χ^2 in the grids and MCMC traces.

In all but one of the cases I work entirely in line brightness temperature, the exception being when I plot SLED fluxes. This is a further idealisation, as it does not take into account the additional errors when observing galaxies due to spatial variations in molecular excitation across the target which can lead to source sizes varying as a function of line transition.

3.2.3 Grids and MCMC

I explore two methods for recovering parameters from line ratios using RADEX: grids and MCMCs. I first adopt the traditional grid based method before demonstrating the capabilities and limitations of an MCMC approach.

The grid method is, in principle, uniquely simple: a grid of input parameters is generated, and RADEX fluxes and line ratios generated for each point. Lines or line ratios are then fitted (minimum χ^2) to the grid, and the best fit parameters thus recovered. Some authors extend this by generating a full likelihood grid (Ward et al., 2003; Kamenetzky et al., 2011; Rangwala et al., 2011; Papadopoulos et al., 2014). The grid must be trimmed of spurious points where either RADEX or the LVG framework breaks down (due to extremely high optical depths). This is accomplished with appropriate checks of the RADEX output when generating the grid.

I also use an MCMC model to recover the parameters, as in Tunnard et al. (2015a) and similar to Kamenetzky et al. (2014) who adopted a Nested Sampling approach for two phase modelling of CO emission. Instead of fitting to a discrete grid the MCMC explores the continuous parameter space, sampling the posterior probability distribution. This also allows for the modelling of much more complex parameter spaces than is easily achievable with the grid method. Furthermore, it has the advantage of naturally producing posterior probabilities and being trivial to marginalise.

The results of the MCMC are a chain of parameter values (called a trace): for a converged MCMC using the Metropolis-Hastings sampler the results should oscillate about the most probable values (assuming a singly peaked posterior), so that the mean of each parameter value over the trace corresponds to the most probable parameter (e.g., Hanson, 2001). I present both the means and the parameters corresponding to the minimum χ^2 set of parameters.

The MCMC method is slower than grids for low dimensional parameter spaces, presenting a significant overhead when running for many realisations of the randomised line ratios. Its true power lies in the ability to simultaneously fit multiple species and gas phases, avoiding the bias inherent in fitting multiple gas phases sequentially or by eye (Kamenetzky et al., 2014). Here, I run all models for 5×10^3 steps with a burn in of 1×10^3 steps, based off preliminary tests on convergence rates. This is less than ideal, but necessary to be able to run a large number of trials in a reasonable time.

For the grid recovery models I generate 10^5 trials, each with physical parameters drawn randomly from the parameter space and recorded, subject to the pressure upper limit. For the MCMC only 1000 trials are generated due to the much greater run time of the MCMC. Since I am not directly comparing the grid and MCMC methods this is not a significant concern.

3.2.4 Model Descriptions

I present four simple models for testing the precision and accuracy of the LVG approach:

1. A general randomised model, which randomly selects parameters from uniform distributions in log space and uses a single molecular species.
2. As above, but using a molecular species and its ^{13}C isotopologue lines. I explore how well I can recover the isotopologue abundance ratio, and the variation when using a single ^{13}C line and when using four ^{13}C lines. This model is only run with the MCMC due to the long runtime of the higher dimensional grid space.
3. A study of the effects of assuming an erroneous molecular abundance, relative to adopting the molecular abundance as a free parameter.
4. A study of the effects of assuming an erroneous isotopologue abundance ratio when including a single ^{13}C isotopologue line with four main isotopologue lines, relative to adopting the isotopologue abundance ratio as a free parameter.

and two investigations of the effects of background radiation:

5. An exploration of the effect of the background radiation blackbody temperature, $T_{\rm bg}$, on line emission of HCN and CO.
6. A toy model of the effects of varying CMB temperatures on galaxy integrated CO and HCN emission.

These models represent a wide range of conditions and provide essential estimates of the optimal accuracy of LVG models. All of these model are run with and without the 10% randomisation errors to distinguish between inherent and random noise induced offsets and uncertainties.

For the LVG testing I fix $T_{\rm bg} = 3\,{\rm K}$. For all comparison grids and MCMCs I adopt the parameter ranges $3 \leq T_{\rm k} \leq 1000$ and $10^2 \leq n_{\rm H_2} \leq 10^8$. For the grids $K_{\rm vir}$ is set to unity, while for the MCMC runs I also adopt $0.1 \leq {\rm d}v/{\rm d}r \leq 1000$, $0.5 \leq K_{\rm vir} \leq 2.0$ and for the models including ^{13}C isotopologues $10 \leq X_{^{12}{\rm C}}/X_{^{13}{\rm C}} \leq 1000$.

The MCMC models require initial positions to either be provided or randomly generated. In this work, I generate random initial conditions for each MCMC, with each parameter, θ_i, drawn from from a uniform random distribution centred on the middle of the prior range and with a width 0.3 times the parameter prior range (in log space).

3.2.5 Randomised, Single Species

The general model explores randomised $T_{\rm k}$ and $n_{\rm H_2}$, with fixed molecular abundances[4], $T_{\rm bg} = 3\,{\rm K}$ and $K_{\rm vir} = 1$. The model was run separately for HCN and CO, with and without the 10% randomisation errors on the lines fluxes, and the input parameters were recovered using both grid and MCMC methods.

This model serves to explore the ability of LVG models to recover the true input parameters under the simplest and most ideal conditions.

For HCN I use only the $J = 1-0$ to $J = 4-3$ transitions, as these are the most commonly available lines (although all four lines are available in the literature for only a few sources). For CO I use the full SLED up to the $J = 13-12$ transition, as is available for many galaxies but in particular those in the Herschel Comprehensive ULIRG Emission Survey (HerCULES, PI: van der Werf, van der Werf et al., 2010; Rosenberg et al., 2015; Kamenetzky et al., 2015). However, in reality this full SLED covers a wide continuum of physical conditions: here they all sample a single parameter set. Therefore, the derived uncertainties are a lower limit on the true uncertainties when interpreting real observations. Indeed, fitting a single gas phase to the full CO SLED of a galaxy is rarely possible, and never reliable. I leave an investigation into the effects of reducing a continuum of gas phases across a galaxy to a two- or three-phase model to future work.

---

[4] $X_{\rm HCN} = 2 \times 10^{-8}$, $X_{\rm CO} = 5 \times 10^{-5}$.

3.2.6 Randomised, with Isotopologues

This model is identical to the Randomised, Single Species case, except that I now only use HCN and include $H^{13}CN$ lines. I only run these models with the MCMC as the grid becomes a cube and starts to take prohibitively long to generate and compare with the synthetic line ratios. The [HCN]/[$H^{13}CN$] abundance ratio is entered into the model as a free parameter, while I keep $X_{\mathrm{HCN}} = 2 \times 10^{-8}$ for both line generation and parameter recovery.

I run these tests using both the complete $H^{13}CN$ SLED from $J = 1-0$ up to $J = 4-3$ as well as just the $J = 1-0$ line. It is rare enough to have a single $H^{13}CN$ observation in a galaxy: to have four lines is currently unheard of. Nevertheless I explore the four-line case to assess the potential benefit of obtaining additional lines.

3.2.7 Assumed X_{HCN}

It is standard practice with LVG modelling (and indeed for any interpretation of molecular lines) to assume a canonical molecular abundance. As well as simply being frequently necessitated by a paucity of observed lines this has a physical justification in that LVG models are only sensitive to the combination $X_{\mathrm{mol}}\,(\mathrm{d}v/\mathrm{d}r)^{-1}$, not to either individually. This is sometimes then used in the RADEX native form $N_{\mathrm{mol}}/\Delta v$. However, since

$$N_{\mathrm{mol}} = X_{\mathrm{mol}} N_{\mathrm{H_2}} = \frac{3.086 \times 10^{18}\, X_{\mathrm{mol}}\, n_{\mathrm{H_2}}\, \Delta v}{\mathrm{d}v/\mathrm{d}r}, \tag{3.1}$$

fixing $N_{\mathrm{mol}}/\Delta v$ actually enforces certain tacit assumptions about the virial state of the gas[5]. Due to these complications I explore whether model parameters are better recovered assuming a canonical, but potentially incorrect, X_{mol}, or whether better results are obtained by leaving X_{mol} as a free parameter.

This should not be seen as a claim that the molecular abundance can be recovered accurately when only a single species is observed. What I am investigating is whether the recovery of T_{k} and $n_{\mathrm{H_2}}$ is seriously affected by assuming a canonical X_{mol}.

To this end I generate HCN lines with physical parameters drawn from the aforementioned parameter ranges, but I now also draw X_{HCN} from the range $10^{-12} - 10^{-4}$. However, when recovering the parameters with the MCMC I run two cases: the first where X_{HCN} is introduced as a free parameter, and the second where I fix X_{HCN} to the canonical value of 2×10^{-8}.

3.2.8 Assumed [HCN]/[$H^{13}CN$]

When only a single ^{13}C isotopologue line is available it is common to assume a canonical molecular abundance and/or isotopologue abundance ratio. However, these values are poorly constrained for CO, let alone less abundant molecular species such as HCN. Furthermore, isotopologue selective chemical effects such as selective photodissociation and isotope charge exchange reactions can lead to isotope fractionation. When coupled with real variations in the elemental isotope abundances, such as in accreted primordial gas or cosmic ray dominated star formation paradigms, can lead to large variations in the isotopologue abundance ratios from species to species and galaxy to galaxy (Henkel et al., 2010, 2014; Papadopoulos et al., 2010c, 2011; Ritchey et al., 2011; Roueff et al., 2015). I therefore explore the effects of assuming an incorrect abundance ratio on the recovered T_{k} and $n_{\mathrm{H_2}}$, using HCN.

The [HCN]/[$H^{13}CN$] ratio is drawn from the range 10 to 1000 (as a uniform random variable in log space), and I recover the parameters assuming [HCN]/[$H^{13}CN$]= 60 and adopting a fixed $X_{\mathrm{HCN}} = 2 \times 10^{-8}$. This tests whether assuming a canonical value is reasonable, or whether it is in fact better to introduce [HCN]/[$H^{13}CN$] as a free parameter (as in the Randomised, with Isotopologues model), even when there is only a single $H^{13}CN$ line available.

---

[5] The numerical prefactor is just the parsec to cm conversion.

3.2.9 $T_{\rm bg}$

The exploration of the effects of $T_{\rm bg}$ on the lines is not a test of the abilities of LVG models to recover input parameters. Rather, it is a demonstration of the effects of background radiation on the molecular lines. I generate line fluxes for $T_{\rm bg} = 3$, 5, 10, 15, 20, 25 and 30 K. For each $T_{\rm bg}$ I generate SLEDs from $J = 1-0$ to $J = 4-3$ for HCN and from $J = 1-0$ to $J = 13-12$ for CO, with constant density $n_{\rm H_2} = 1 \times 10^4\,{\rm cm^{-3}}$ (HCN) and $1 \times 10^3\,{\rm cm^{-3}}$ (CO), and $X_{\rm HCN} = 2 \times 10^{-8}$ and $X_{\rm CO} = 5 \times 10^{-5}$, for $T_{\rm k} = 3$, 5, 10, 50, 100, 300, 500 and 1000 K. For the CO lines I reduce the density to $1 \times 10^3\,{\rm cm^{-3}}$ since at $1 \times 10^4\,{\rm cm^{-3}}$ many lines, but in particular the $J = 5-4$ line, present pathological fluxes (e.g., for $T_{\rm bg} = 3$ K and $T_{\rm k} \geq 500$ K RADEX fails to converge, ultimately because the column density and associated optical depth becomes too large). This is also more representative of the likely conditions of the CO on galactic scales. I also generate grids to explore the effect of $T_{\rm bg}$ on the line brightness ratios, with high resolution in $T_{\rm bg}$ and $T_{\rm k}$.

I am also interested in how the CO and HCN line peak brightness temperatures, $T_{\rm B,peak}$, are affected by the CMB, as a function of the kinetic temperature of the emitting gas. This is applicable for the detectability of cold gas reservoirs at high z. For five redshifts (0, 2, 4, 6 and 8) I run RADEX for the physical conditions above for 1000 values of $T_{\rm k}$ distributed evenly in log-space from 1000 K to 3 K. Other physical parameters are kept as for the models above.

3.2.10 Toy Galaxy Models

I now extend the functional models above to a very simple 1D toy galaxy model in order to explore the effect of CMB temperature on potential galaxy integrated SLEDs.

The model uses a $1/r$ temperature profile falling from 100 K at $r = 0$ down to 10 K at the galaxy edge, and the profile is sampled with 10^4 molecular clouds distributed with radius according to an exponential distribution. All clouds share the same density: $10^3\,{\rm cm^{-3}}$ for the CO models and $10^5\,{\rm cm^{-3}}$ for the HCN models, and the clouds are assumed to be virialised. The total emission from all of the clouds in the galaxy is then integrated to give a total ‘single-dish’ SLED. I do not explicitly include dust, but I do set $T_{\rm CMB}$ as a lower limit on $T_{\rm k}$. It is however still dust free, as RADEX does not include dust *within* the gas: dust can only be added as a source of background radiation incident on the cloud. This toy model allows us to demonstrate the significant effects of the CMB on CO and HCN emission and on their line ratios at high z.

These toy models are much less complex than the work of da Cunha et al. (2013) and Narayanan & Krumholz (2014), with an emphasis lying somewhere between the two. While da Cunha et al. (2013) focussed heavily on the theory of line excitation as a function of redshift, they did not investigate galaxy wide trends. On the other hand, Narayanan & Krumholz (2014) focussed almost entirely on detailed modelling of galaxy emission, with little investigation of the effect of the CMB at high redshift (although see their Figure 12). Our approach here is to simply demonstrate the possibility of unifying the two approaches.

3.3 Results

I present the results of the models in the following sections. For the sake of readability, for the recoverability tests I present the results in tables in the main text and include the figures at the end of the chapter.

3.3.1 Randomised, Single Species

The results of the Randomised, Single Species models are presented in Figures 3.1, 3.10 and 3.11 (the last two may be found at the end of the chapter), where I plot the histograms of the logarithm of the ratio of the recovered over true parameters (hereafter the “deviation”). Numerical results are included in Table 3.1. For the grid models I also plot the deviation of the product $T_{\rm k} \times n_{\rm H_2}$, which is well known to be more tightly constrained than $T_{\rm k}$ or $n_{\rm H_2}$ alone. I record the means and standard deviations of the deviations, as well as the bootstrap estimated mean and standard deviation of the median of the deviations.

Table 3.1: Deviations of Recovered Parameters from Grid Models

	Statistical			Bootstrap Median		
	T_{k}	$n_{\mathrm{H_2}}$	$T_{\mathrm{k}} \times n_{\mathrm{H_2}}$	T_{k}	$n_{\mathrm{H_2}}$	$T_{\mathrm{k}} \times n_{\mathrm{H_2}}$
HCN	-0.2 ± 0.5	0.3 ± 0.8	0.1 ± 0.5	-0.085 ± 0.001	0.194 ± 0.002	0.058 ± 0.001
HCN-noE	-0.02 ± 0.20	0.05 ± 0.37	0.03 ± 0.29	0.0001 ± 0.0003	0.0007 ± 0.0003	0.0038 ± 0.0003
CO	-0.2 ± 0.5	0.2 ± 0.9	0.0 ± 0.9	-0.058 ± 0.001	0.071 ± 0.001	0.024 ± 0.001
CO-noE	-0.1 ± 0.4	0.0 ± 0.5	-0.1 ± 0.7	-0.0120 ± 0.0003	0.0081 ± 0.0004	0.0013 ± 0.0003

Table 3.2: Deviations of Recovered Parameters from MCMC Models.

	Statistical			Bootstrap Median		
	T_{k}	$n_{\mathrm{H_2}}$	$\mathrm{d}v/\mathrm{d}r$	T_{k}	$n_{\mathrm{H_2}}$	$\mathrm{d}v/\mathrm{d}r$
HCN Best fit	-0.2 ± 0.6	0.2 ± 0.9	0.1 ± 0.6	-0.013 ± 0.003	0.07 ± 0.02	0.07 ± 0.02
HCN Mean	-0.2 ± 0.6	0.2 ± 1.0	0.1 ± 0.5	-0.015 ± 0.003	0.04 ± 0.01	0.03 ± 0.01
HCN-noE Best fit	-0.3 ± 0.7	0.2 ± 1.0	0.1 ± 0.6	-0.0010 ± 0.0003	0.004 ± 0.002	0.009 ± 0.003
HCN-noE Mean	-0.3 ± 0.7	0.2 ± 1.1	0.1 ± 0.6	-0.004 ± 0.001	0.02 ± 0.01	0.031 ± 0.009
CO Best fit	-0.5 ± 0.9	0.5 ± 1.8	0.3 ± 0.9	-0.010 ± 0.003	0.05 ± 0.02	0.11 ± 0.03
CO Mean	-0.5 ± 0.9	0.5 ± 1.8	0.3 ± 0.9	-0.011 ± 0.003	0.08 ± 0.01	0.11 ± 0.02
CO-noE Best fit	-0.6 ± 1.0	1.0 ± 2.0	0.6 ± 1.0	-0.005 ± 0.001	0.06 ± 0.02	0.09 ± 0.03
CO-noE Mean	-0.6 ± 1.0	1.1 ± 1.9	0.6 ± 1.0	-0.018 ± 0.005	0.34 ± 0.07	0.29 ± 0.03

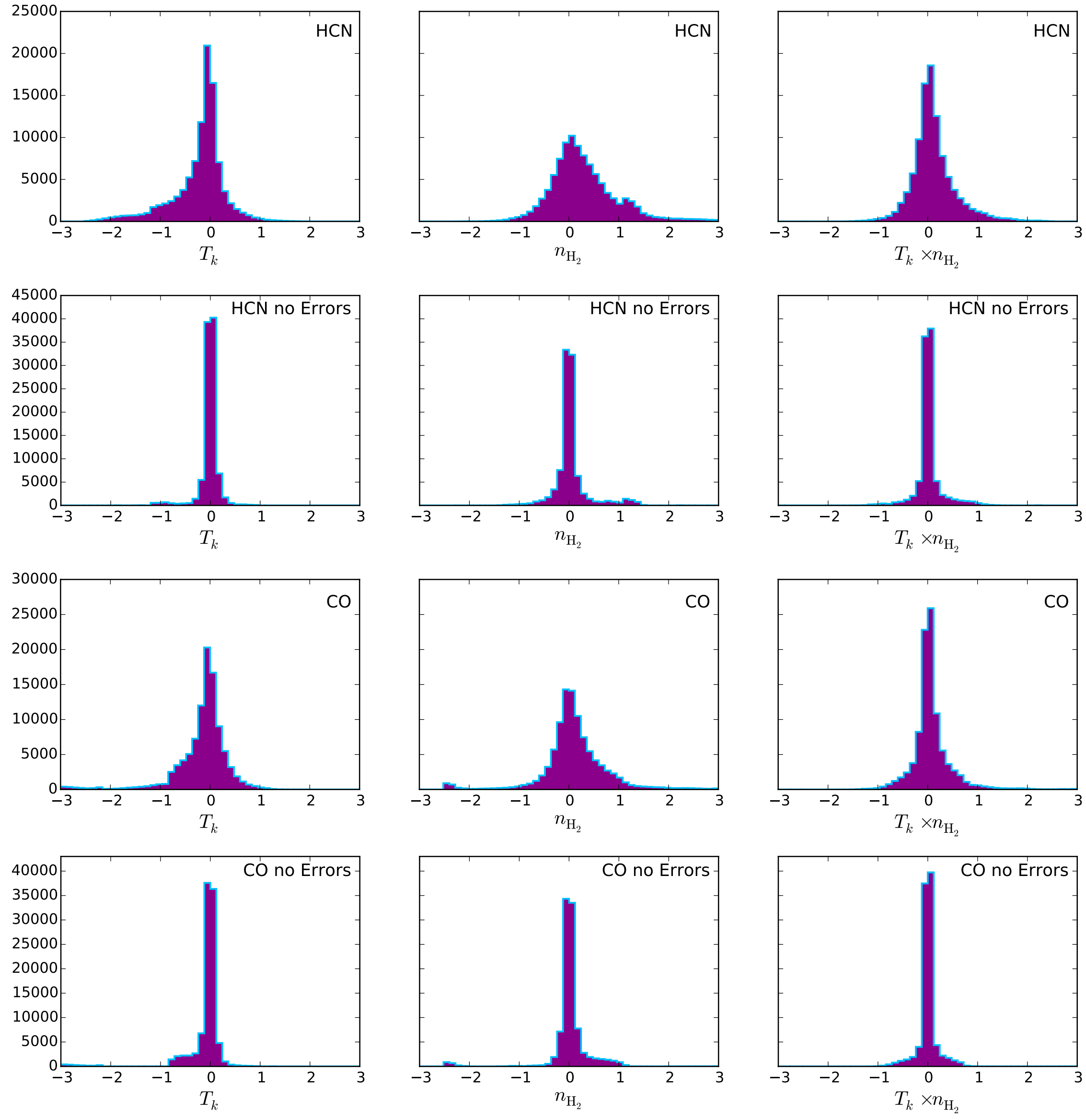

Figure 3.1: The logarithm of the ratio of the recovered to true parameters for HCN and with and without 10% errors as indicated in the upper right corner of each plot, drawn from a pressure restricted parameter range and recovered with a grid with a log step size of 0.1.

The numerical results for the grid models are shown in Table 3.1. I include the statistical mean and standard deviations of the deviations, as well as the bootstrap estimated means and standard deviations of the medians of the deviations. Reassuringly, all parameters are recovered without bias for the no-error cases. There is a trend for both HCN and CO, when line uncertainties are added, to underestimate T_{k} and overestimate n_{H_2}. This trend is far weaker in the medians, suggesting that it is due to the rare but extreme outliers. There is no sign that the CO model, with 9 more lines than the HCN model, obtained improved recovery rates above those of HCN.

The thermal pressure, $T_{\mathrm{k}} \times n_{\mathrm{H}_2}$, is better determined than either of T_{k} or n_{H_2} alone. The effects of increasing T_{k} and increasing n_{H_2} are not identical, but they are partially degenerate, leading to the improved recovery of thermal pressure.

The results show that the recovery rates are worryingly low. Without any errors there is a spread of $0.05 - 0.10$ dex in all of the recovered parameters. I.e., even if I knew the line ratios perfectly, in a spatial resolved, virialised gas cloud of uniform density, temperature and velocity gradient, with a uniform and known molecular abundance, one should not expect to recover parameters with a precision better than $\sim$ 10%. Keeping all other idealisations and introducing 10% observational uncertainties this falls to between 50% and 300%. These are lower limits on the true uncertainties. The accuracies are very good in the no error cases, but for the randomised cases the *systematic* offsets can be as large as a factor of 2.

The MCMC results are recorded in Table 3.2. For the MCMC I have results for both the trace mean parameters and the minimum χ^2 parameters. I also record the median of the standard deviations of the traces for each parameter, as these are one measure of the uncertainty in the MCMC mean results. The systematics seen in the grids are also present here, and once again it is readily apparent that they are due to outliers.

The MCMC results are particularly interesting. The MCMC appears to have much less Gaussian deviation distributions, being very strongly peaked about the true parameters, but with low levels of extreme outliers. For example, in the no error case in Figure 3.11 between 55% and 68% of the $T_{\rm k}$ values were recovered very nearly perfectly, but there is a low level tail of underestimates extending out to a factor of 300.

The mean parameters of the MCMC traces should be more meaningful than the best fit parameters. This is consistent with the $\mathrm{d}v/\mathrm{d}r$ deviations for the randomised MCMC model, where the best fit values almost form a top-hat distribution, while the mean values are very nearly Normally distributed.

The CO results are consistently worse than the HCN results, with a far greater tendency towards extremely low $T_{\rm k}$ and high $n_{\rm H_2}$. It is not clear why this is the case, although further examination revealed that the outliers all had very poor MCMC traces due to non-physical synthetic fluxes. These arose even when RADEX converged and optical depths were reasonable: there were specific parameter combinations which appear to produce pathological fluxes (as was found for some combinations in the $T_{\rm bg}$ exploration). Small variations away from the specific input parameters leads to the recovery of realistic SLEDs. While no method was found to reliably exclude these values from the synthetic fluxes I do not consider this of great concern: when fitting to real data the MCMC will find very poor fits for these values and so exclude them, jumping to a nearby point. Since the surrounding phase space will produce good fits this excludes only an N-dimensional delta-function from the trace, and the results are still reliable. This is supported by the *inability* of the MCMC to fit these pathological synthetic fluxes: if the responsible phase-volume was non-zero the MCMC would still be able to "home in" on it. Therefore, this is only a problem for the synthetic fluxes and not for real observations. For the synthetic fluxes it produces the extreme outliers, which are clearly distinguishable post-hoc. The pseudo-Gaussian spread in the deviations is unrelated to this issue, and is due to many-to-one relationship between physical conditions and line ratios which is the focus of this work.

These grid and MCMC results demonstrate that even under ideal conditions a 10% calibration uncertainty corresponds to uncertainties in LVG derived parameters of approximately 0.5 dex / a factor of 3. This is believed to be due to both the slow variation of the line ratios across the parameter space and the many-to-one relationship between physical conditions and line ratios.

3.3.2 Randomised, with Isotopologues

The results of the Randomised, with Isotopologues trials with four $\rm H^{13}CN$ lines and one $\rm H^{13}CN$ line are shown in Figures 3.12 and 3.13 respectively, and the numerical results are collated in Table 3.3.

The figures demonstrate the (well known) power of adding isotopologue lines. Even with the additional free parameter of $\rm [HCN]/[H^{13}CN]$ the model places much tighter and more accurate constraints on $T_{\rm k}$ and $n_{\rm H_2}$, as well as placing very tight constraints on $\rm [HCN]/[H^{13}CN]$. This is not simply an effect of having more lines to work with since the fits are better than those obtained using the 13 CO lines. The good $T_{\rm k}$ results are due to the strong degeneracy between $T_{\rm k}$ and $\rm [HCN]/[H^{13}CN]$. This can be roughly understood as follows: $T_{\rm k}$ and $n_{\rm H_2}$ set the primary shape of the SLEDs of HCN and $\rm H^{13}CN$ - with this determined the model can then find $\rm [HCN]/[H^{13}CN]$ since, to first order, this corresponds to a scaling of the SLED but not a change in shape[6]. Put

---

[6] Although second order effects come into play due to the differing optical depths and line trapping.

Table 3.3: Deviations of Recovered Parameters from MCMC ^{13}C Isotopologue Models. Values in parenthesis are the MCMC standard deviations.

		Four H^{13}CN lines		One H^{13}CN line	
		Best	Mean	Best	Mean
Statistical	T_k	$-0.1 \pm 0.4(0.04)$	$-0.1 \pm 0.4(0.04)$	$-0.1 \pm 0.5(0.1)$	$-0.1 \pm 0.5(0.1)$
	n_{H_2}	$-0.0 \pm 0.7(0.14)$	$-0.1 \pm 0.7(0.14)$	$0.0 \pm 0.6(0.2)$	$0.0 \pm 0.6(0.2)$
	$\mathrm{d}v/\mathrm{d}r$	$0.0 \pm 0.4(0.18)$	$0.0 \pm 0.4(0.18)$	$0.0 \pm 0.4(0.2)$	$0.0 \pm 0.3(0.2)$
	$\frac{[\mathrm{HCN}]}{[\mathrm{H^{13}CN}]}$	$0.01 \pm 0.21(0.03)$	$0.01 \pm 0.22(0.03)$	$0.05 \pm 0.28(0.05)$	$0.05 \pm 0.29(0.05)$
Median	T_k	-0.003 ± 0.002	-0.005 ± 0.002	-0.006 ± 0.003	-0.010 ± 0.003
	n_{H_2}	-0.019 ± 0.015	-0.025 ± 0.010	0.015 ± 0.016	-0.007 ± 0.012
	$\mathrm{d}v/\mathrm{d}r$	-0.063 ± 0.016	-0.034 ± 0.009	0.029 ± 0.016	-0.006 ± 0.010
	$\frac{[\mathrm{HCN}]}{[\mathrm{H^{13}CN}]}$	0.002 ± 0.002	-0.001 ± 0.003	0.005 ± 0.003	0.009 ± 0.003

another way: iso-ratio contours for HCN and H^{13}CN intersect roughly perpendicularly in $T_\mathrm{k} - n_{\mathrm{H}_2}$ plots. None of this needs to be entered into the model: it explores the posterior probability space, without needing to understand the underlying relationships. With a single H^{13}CN line the ability to uniquely identify a T_k is lost, due again to the degeneracy between T_k and [HCN]/[H^{13}CN].

The 'four H^{13}CN lines, no error' results are exceptionally good, with the models recovering the correct T_k and [HCN]/[H^{13}CN] in almost 100% of the cases, and n_{H_2} and $\mathrm{d}v/\mathrm{d}r$ being exceptionally well constrained. There are however a few extreme outliers, which are responsible for the statistical deviations in Table 3.3 being so much greater than those of the medians. The single H^{13}CN line fits are still very good; although worse than the 4 H^{13}CN line fits they are still better than the HCN only models, despite the additional free parameter.

The value of multiple ^{13}C isotopologue lines is clear. However, despite only being $10 - 15\times$ fainter than the ^{12}C lines[7] the acquisition of even one H^{13}CN line in a local galaxy ($z \leq 0.1$) represents a significant time investment, even with ALMA. The small size of these sources, coupled with the inherent faintness of the ^{13}C lines, leads to them being washed out by beam dilution, requiring even longer to observe with single-dish instruments. The one exception to this is ^{13}CO, which is sufficiently abundant to emit relatively brightly and be quite easily detectable. In cases where accurate and precise non-LTE gas parameters are desired from molecular observations it is imperative that ^{13}C isotopologue lines be observed.

3.3.3 Assumed X_HCN

The results of the third model, with free and fixed X_HCN, are shown in Figure 3.14 and Table 3.4. Note in particular the much wider ranges of the x-axes than in the previous plots.

There is no clear sign of any difference in the recoverability of T_k or n_{H_2} in either model. Furthermore, the molecular abundance in the free parameter case is essentially unconstrained and although the model is slightly able to recover the true value there is a huge spread in the results as well as a systematic offset of almost -1 dex. It would appear therefore to be perfectly acceptable to assume a canonical molecular abundance. If two species are available, and their abundance ratios are of interest, it should therefore be acceptable to fix one abundance and have as a free parameter the abundance ratio itself, thereby removing a free parameter. Further testing is needed however to see whether this result holds when the synthetic line ratios emerge from clouds with $K_\mathrm{vir} \neq 1$.

3.3.4 Assumed [HCN]/[H^{13}CN]

The results of the Assumed [HCN]/[H^{13}CN] model using one H^{13}CN line and with 10% errors are shown in Figure 3.15 and Table 3.5.

The striking result here is that the parameters are recovered much more poorly than in Figure 3.13, where I ran the same model but without fixing [HCN]/[H^{13}CN] to an assumed value. Simultaneously, the MCMC trace reports much smaller errors. In other words, the MCMC fixes very

---

[7] Even when 100× less abundant, due to optical depth effects.

Table 3.4: Deviations of recovered parameters from MCMC models for the free and assumed X_{HCN}.

		Free X_{HCN}		Fixed X_{HCN}	
		Best	Mean	Best	Mean
Statistical	T_{k}	$-0.1 \pm 0.7(0.06)$	$-0.1 \pm 0.6(0.06)$	$0.0 \pm 0.7(0.08)$	$0.0 \pm 0.6(0.08)$
	n_{H_2}	$0.5 \pm 1.4(0.4)$	$0.5 \pm 1.3(0.4)$	$0.0 \pm 1.2(0.2)$	$-0.1 \pm 1.2(0.2)$
	$\mathrm{d}v/\mathrm{d}r$	$0.2 \pm 0.7(0.3)$	$0.3 \pm 0.7(0.3)$	$0.0 \pm 0.7(0.2)$	$0.0 \pm 0.6(0.2)$
	X_{HCN}	$-0.7 \pm 2.4(0.7)$	$-1.2 \pm 2.1(0.7)$	0.2 ± 2.3	0.2 ± 2.3
Median	T_{k}	-0.001 ± 0.003	-0.011 ± 0.004	0.044 ± 0.005	0.035 ± 0.003
	n_{H_2}	0.32 ± 0.05	0.34 ± 0.05	-0.10 ± 0.04	-0.12 ± 0.04
	$\mathrm{d}v/\mathrm{d}r$	0.15 ± 0.03	0.18 ± 0.03	-0.05 ± 0.03	-0.05 ± 0.02
	X_{HCN}	-0.63 ± 0.13	-1.07 ± 0.09	0.06 ± 0.14	0.05 ± 0.13

Table 3.5: Deviations of Recovered Parameters from MCMC Models for an Assumed [HCN]/[H^{13}CN].

		Assumed [HCN]/[H^{13}CN]	
		Best	Mean
Statistical	T_{k}	$-0.1 \pm 0.7(0.03)$	$-0.1 \pm 0.7(0.03)$
	n_{H_2}	$-0.3 \pm 0.9(0.1)$	$-0.3 \pm 0.9(0.1)$
	$\mathrm{d}v/\mathrm{d}r$	$-0.2 \pm 0.6(0.1)$	$-0.2 \pm 0.6(0.1)$
	$\frac{[\mathrm{HCN}]}{[\mathrm{H}^{13}\mathrm{CN}]}$	-0.3 ± 0.6	-0.3 ± 0.6
Median	T_{k}	-0.042 ± 0.014	-0.032 ± 0.009
	n_{H_2}	-0.20 ± 0.04	-0.23 ± 0.04
	$\mathrm{d}v/\mathrm{d}r$	-0.29 ± 0.03	-0.232 ± 0.026
	$\frac{[\mathrm{HCN}]}{[\mathrm{H}^{13}\mathrm{CN}]}$	-0.282 ± 0.028	-0.281 ± 0.029

tightly on the wrong point in $T_{\mathrm{k}} - n_{\mathrm{H}_2}$ space; i.e., one is actually better off adding [HCN]/[H^{13}CN] as a free parameter. This does not induce as dramatic reductions in the parameter space as can be seen by fixing the [HCN]/[H^{13}CN] ratio, but it is also less likely to exclude the true parameters.

Fixing [HCN]/[H^{13}CN] to a canonical value causes three problems: 1) due to the degeneracy between [HCN]/[H^{13}CN] and T_{k}, fixing [HCN]/[H^{13}CN] artificially restricts T_{k}, and if [HCN]/[H^{13}CN] is not close to the canonical value this then offsets T_{k}. However, since T_{k} and n_{H_2} are also partially degenerate, this also offsets n_{H_2}. Then, since the virial state of the gas is dependent upon n_{H_2} and $\mathrm{d}v/\mathrm{d}r$, $\mathrm{d}v/\mathrm{d}r$ is also affected (for a fixed K_{vir}). 2) as well as increased deviations, there is a systematic offset introduced into the physical parameters. 3) an incorrectly assumed [HCN]/[H^{13}CN] can force T_{k}, and hence n_{H_2}, into unphysical regions where RADEX becomes unstable, leading to wildly incorrect parameter recovery.

When using an MCMC there is a further issue, which is that the MCMC will dramatically understate the true uncertainty on the recovered parameters. Fixing [HCN]/[H^{13}CN] is a very strong prior, so that the MCMC will show only small oscillations about the mean parameters. This is precisely why ^{13}C isotopologue line observations are so powerful: they are extremely good at breaking the degeneracies found in single species models. However, this means that if the wrong isotopologue abundance ratio is assumed then the recovered parameters will be forced to be incorrect. *This effect is so large that you can actually be worse off assuming a canonical isotopologue abundance ratio than if you had no isotopologue lines at all.*

3.3.5 T_{bg}

The HCN and CO SLEDs for ranges of T_{bg} and T_{k} are shown in Figure 3.2. Each panel corresponds to the indicated T_{bg}, increasing from left to right, and I plot the line flux in arbitrary units against the J_u of the line transition. All panels share the same vertical scale. The colour corresponds to T_{k} from cold (10 K, sky blue) to hot (1000 K, dark magenta). While it is usually the case that $T_{\mathrm{k}} \geq T_{\mathrm{dust}} \geq T_{\mathrm{CMB}}$ I include regions where the kinetic temperature is lower than the incident blackbody radiation temperature for completeness.

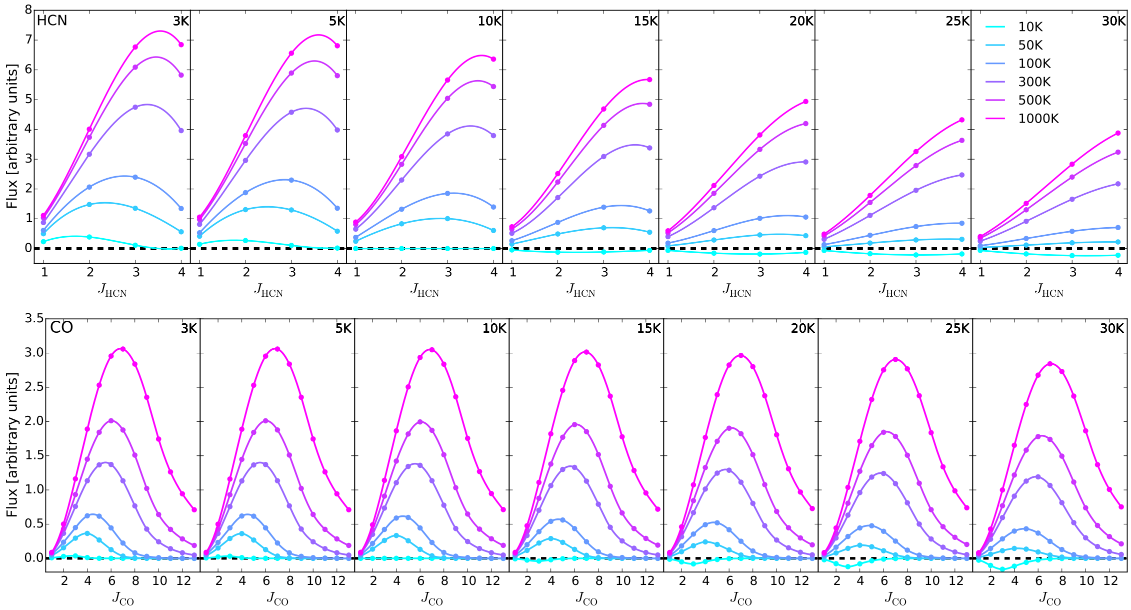

Figure 3.2: The effect of increasing the background radiation temperature from 3 K to 30 K on the HCN SLED (top) and CO SLED (bottom) for a range of kinetic temperatures from 10 K to 1000 K (legend is common to both plots). $T_{\rm bg}$ increases from left to right as indicated, and $T_{\rm k}$ varies by colour, from sky blue (cold) to dark magenta (hot). Within each species all plots are to the same, arbitrary, flux scale.

It is important to note that these are the observable fluxes; i.e., the line flux seen in excess of the continuum level, which RADEX provides by default. This "loss of contrast" is the primary cause of the "shrinking" of the SLEDs as $T_{\rm bg}$ increases.

As expected, the SLEDs fall into absorption when their $T_{\rm k}$ is less than $T_{\rm bg}$. All of the fluxes fall as $T_{\rm bg}$ increases: this is due to the reduced contrast of the line emission against the hotter background radiation field (e.g., Papadopoulos et al., 2010a). The CO SLEDs display fundamentally similar, if offset, behaviour to the HCN SLEDs.

This model is, as ever, a gross simplification of reality, where hot background radiation fields on 10 pc scales are usually due to AGN- or starburst-heated dust which also emits significantly in the mid-IR, leading to optical pumping of molecular vibrational lines (Aalto et al., 2007; González-Alfonso et al., 2013a; Aalto et al., 2015a,b). Nevertheless, the low $T_{\rm bg}$ SLEDs, where the background temperature of 10 K is reached by the CMB at $z = 2.3$ demonstrate that *line ratios indicative of certain behaviours in the local universe are not necessarily applicable in high-redshift galaxies.* Similarly, any investigation into correlations between line ratios and galaxy properties must take into account variation in the incident radiation field, as well as variation within individual galaxies.

It is noteworthy that since RADEX presents the line brightness in excess of the background, if there is a hot background field, but it is completely obscured by the foreground gas and dust, then the background temperature should be added back onto the line brightness produced by RADEX. On the other hand, this very specific geometry is probably rare in nature, and may be hard to identify. Furthermore, in these cases it is highly likely that only the outer edges of the very dense clouds are visible, where the gas is not exposed to the full force of the intense background field, further complicating the analysis.

Line ratios are frequently invoked where there are few line observations of a source. In principle, they allow an exploration of the molecular gas conditions and there have been extensive efforts to develop diagnostic molecular line ratios, e.g., as a means of distinguishing between obscured AGN and obscured starbursts (Kohno, 2003, 2005; Meijerink & Spaans, 2005; Meijerink et al., 2007; Imanishi et al., 2006; Krips et al., 2008). More recently, Izumi et al. (2013) have attempted to develop diagnostic plots using the HCN$(4-3)$/HCO$^+(4-3)$ and HCN$(4-3)$/CS$(7-6)$ line

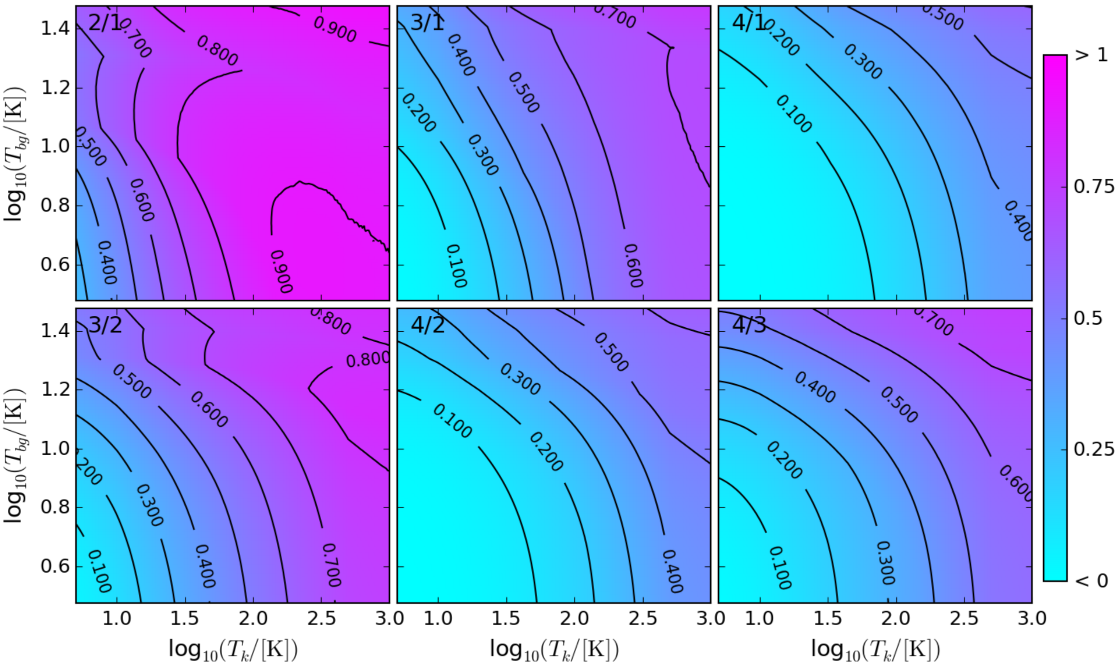

Figure 3.3: The effect of increasing the background radiation temperature from 3 K to 30 K on the HCN line ratios for a range of kinetic temperatures from 10 K to 1000 K. The line ratio is given in the top right corner of each plot.

ratios. However, these studies are frequently single-dish observations of entire galaxies. There are therefore potential concerns that gas and dust temperature gradients in the galaxies may have significant effects on the integrated line ratios[8], especially if the ratios are dependent on $T_{\rm bg}$, which, in active galaxies in the local universe, is usually dominated by dust emission. If these effects are varying between galaxies then this may lead to either scatter in true relationships or anomalous relationships where none exist. Furthermore, extending these line ratios to higher redshift, where $T_{\rm CMB}$ is elevated, could present further problems.

I present 2D plots of the HCN line ratios as functions of $T_{\rm k}$ and $T_{\rm bg}$ in Figure 3.3. There is a clearly visible degeneracy between $T_{\rm k}$ and $T_{\rm bg}$, especially in ratios with the $J = 4-3$ line. While the low$-J$ line ratios do not change significantly, the HCN$\frac{(4-3)}{(3-2)}$ line ratio changes dramatically between $T_{\rm bg} = 3\,{\rm K}$, $T_{\rm k} = 10\,{\rm K}$ and $T_{\rm bg} = 30\,{\rm K}$, $T_{\rm k} = 1000\,{\rm K}$, rising rapidly.

The results of the model exploring the effect of $T_{\rm bg}$ on $T_{\rm B,peak}$ as a function of $T_{\rm k}$ are shown in Figures 3.4 and 3.5 where I plot the peak brightness temperature for the first 9 CO rotational transitions and first 6 HCN rotational transitions as functions of $T_{\rm k}$ for a range of redshifts. The models demonstrate how cooler molecular gas, such as the at outer edges of molecular reservoirs or in interclump regions, can become indistinguishable from the CMB. If galaxies at high z possess kinetic temperature gradients or harbour cold molecular gas environments, the aforementioned effect could lead to a bias in the gas morphologies inferred from low-J CO lines. This is not a new or surprising result; from a purely analytical approach this is to be expected since the total intensity is:

$$I_\nu^{J_u} \propto S_\nu^{J_u}\left(1 - e^{-\tau_\nu^{J_u}}\right) + B_\nu(T_{\rm CMB})e^{-\tau_\nu^{J_u}}, \tag{3.2}$$

where S is the source function, and therefore that the intensity in excess of the background field (here just the CMB) is:

---

[8] On the other hand, in active galaxies the molecular line emission is dominated by emission from centre of the galaxy.

$$\Delta I_\nu^{J_u} \propto S_\nu^{J_u}\left(1-e^{-\tau_\nu^{J_u}}\right)+B_\nu(T_{\rm CMB})\left(e^{-\tau_\nu^{J_u}}-1\right), \tag{3.3}$$

$$=\left(1-e^{-\tau_\nu^{J_u}}\right)\left(S_\nu^{J_u}-B_\nu(T_{\rm CMB})\right), \tag{3.4}$$

so that when the gas is emitting approximately thermally, or $T_{\rm ex} \simeq T_{\rm CMB}$, then $S_\nu^{J_u} \simeq B_\nu(T_{\rm ex})$, and the line becomes indistinguishable from the CMB (e.g., Wilson et al., 2009; da Cunha et al., 2013). This will introduce an additional bias towards detecting hotter, more excited gas as redshift increases.

The effect is more pronounced for HCN: this is due to the lines being naturally fainter than the CO lines (due to the much lower abundance of HCN cf CO), and so the fall in contrast against the CMB in much more pronounced. There is also a similar effect for dust, with the same associated implications on observability (da Cunha et al., 2013).

3.3.6 Toy Galaxy Models

The results of the toy model are shown in Figures 3.6, 3.7 and 3.8. As described in §3.2.10, this model distributes 10^4 clouds exponentially with radius across an artificial galaxy, with the clouds identical except for their $T_{\rm k}$, which is determined by their radius. The galaxy is then placed at a range of redshifts and the galaxy wide emission integrated. The SLED in Figure 3.6, left, shows how the flux, relative to the background, decreases with redshift, but also how the peak of the SLED shifts to higher J. These results are consistent with da Cunha et al. (2013).

The right hand SLED of Figure 3.6 shows the same data, but with the SLED presented relative to the intensity of the $J = 1-0$ line. These SLEDS are in turn consistent with Narayanan & Krumholz (2014). Note however that da Cunha et al. (2013) and Figure 3.6, left, show that the increase of the SLED with redshift, defined relative to the $J = 1-0$ line, is primarily due to the much greater reduction in line contrast of the low$-J$ lines. While the increasing $T_{\rm bg}$ does indeed raise the high$-J$ lines this effect is small in comparison to the contrast reduction of the low$-J$ lines.

This reduction in the overall SLED is important, as it leads to a higher $\alpha_{\rm CO}$[9], e.g., equation 1 in Ivison et al. (2011) and equations 17 and 18 in Bolatto et al. (2013). Since the molecular-gas mass of these models is identical at all redshifts, and since $L'_{\rm CO(1-0)}$ "de-redshifts" emission (i.e., for two identical SLEDs at $z = 0$ and $z = 2$, excluding CMB effects, $L'_{\rm CO(1-0)}$ will be identical) any difference in $L'_{\rm CO(1-0)}$ in these models is solely due to changes in the CO$(1-0)$ line flux, which is solely due to the CMB. I show these effects in Figure 3.7, where I plot the line luminosities relative to the $z = 0$ line luminosities (left) and the line luminosities relative to the $z = 0$ CO$(1-0)$ line luminosity. For the adopted temperature profile and cloud distribution profile this effect is very large, with 80% of the mass recovered at $z = 2$ if a standard $\alpha_{\rm CO}$ is adopted, 60% at $z = 4$, and by $z = 8$ only 35% of the mass is recovered.

It is important to note that while Figure 3.7 left shows that the high-J line luminosity increases significantly with redshift, Figure 3.7 right shows that it still only traces a small fraction of the gas (for this toy model). The CO$(1-0)$ line at $z = 0$ traces all of the molecular clouds, so the fraction of this luminosity recovered is directly comparable to the mass that would be estimated if a standard $z = 0$ $\alpha_{\rm CO}$ factor was used. The HCN emission only traces the dense molecular gas, so the fall in the HCN integrated emission is representative of the dense gas that would be missed, not the total molecular mass.

In Figure 3.8 I present the line-brightness temperature CO and HCN line ratios for the toy model galaxy. I present a selection of line ratios only. It is clear that there is very little variation in the galaxy-integrated line ratios with redshift, except for in the $\frac{5-4}{1-0}$ and $\frac{4-3}{1-0}$ line ratios, although in all cases there is greater variation in the HCN ratios than the the CO ratios. This is, as in the $T_{\rm bg}$ investigation above, due to HCN simply being fainter than CO, so is more strongly affected by the brightening of the CMB. However, these ratios are specific to the galaxy excitation model used here,

---

[9] $\alpha_{\rm CO} = M_{\rm mol}/L'_{\rm CO(1-0)}$

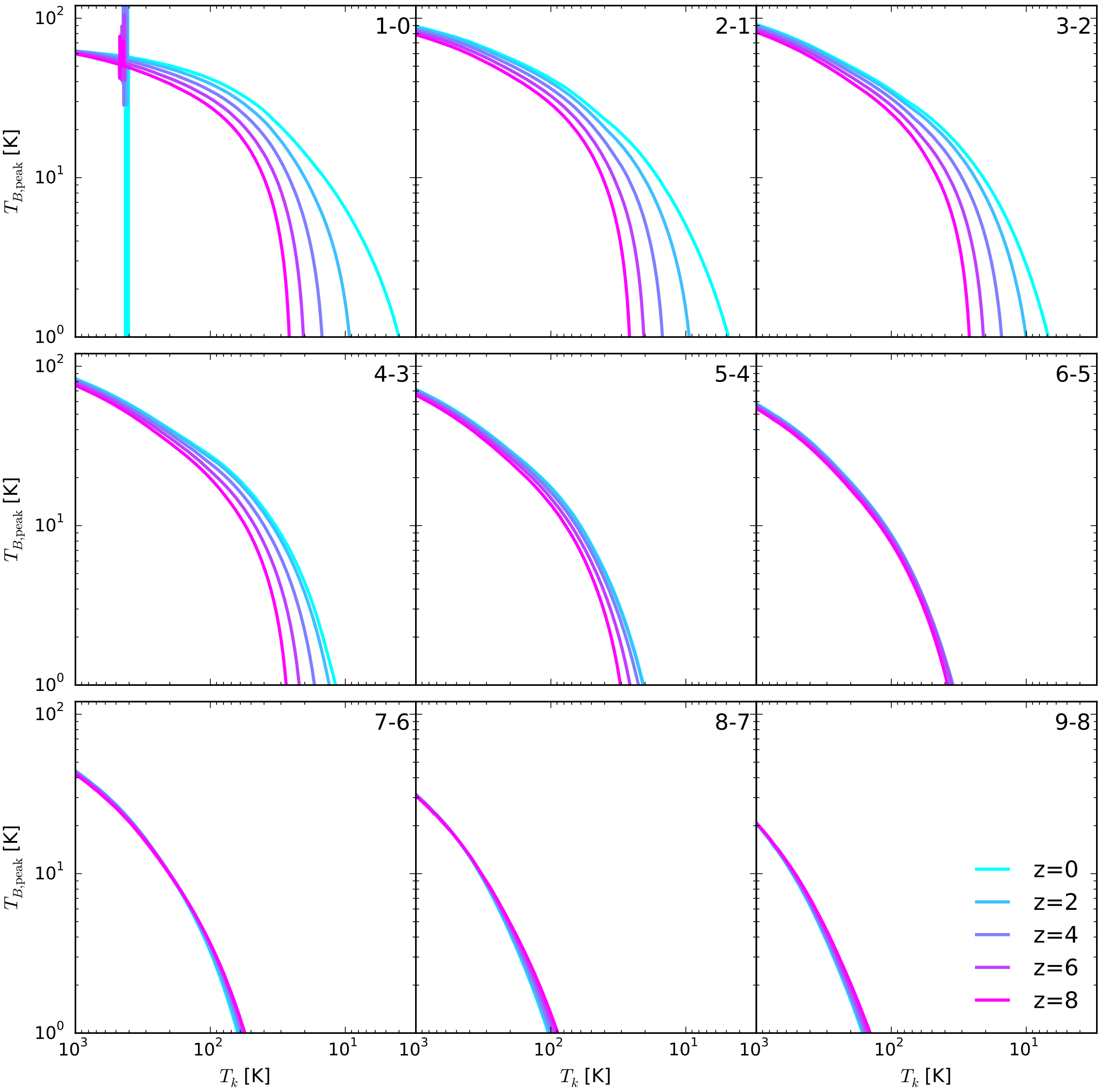

Figure 3.4: The effect of $T_{\rm bg}$ on rest frame CO rotational line emission as a function of gas kinetic temperature. Note that the x-axis decreases from left to right. The rotational transition is given in the upper right corner of each subplot. The discontinuities in the $1-0$ plot are due to localised non-convergences in RADEX.

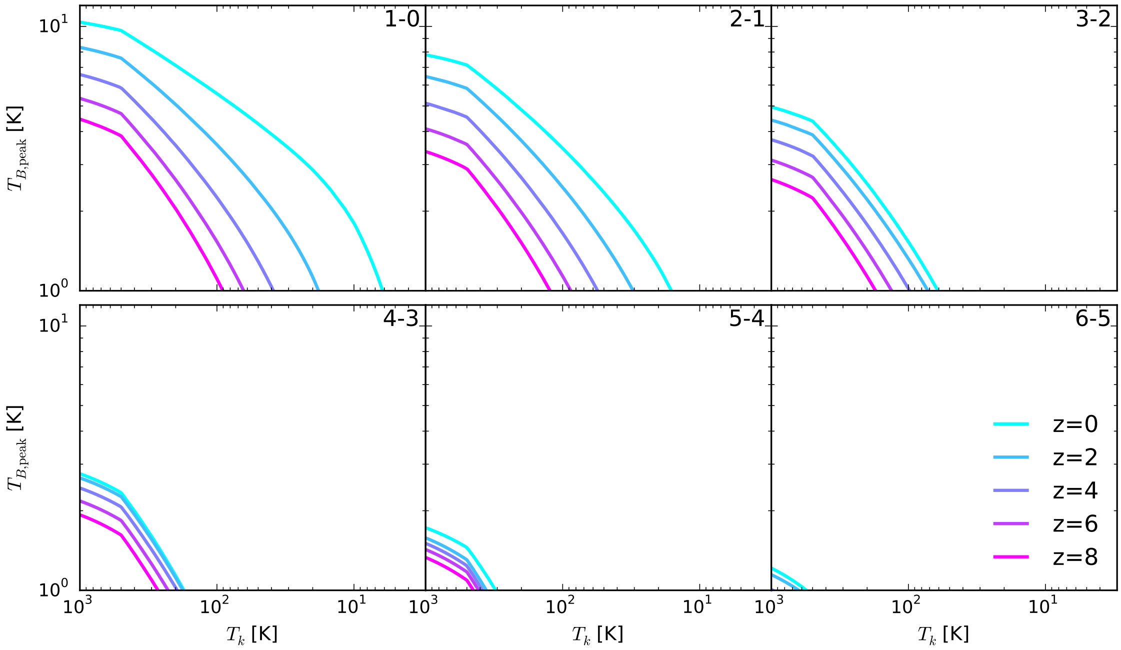

Figure 3.5: The effect of $T_{\rm bg}$ on rest frame HCN rotational line emission as a function of gas kinetic temperature. Note that the x-axis decreases from left to right. The rotational transition is given in the upper right corner of each subplot. The kink at $T_{\rm k} > 500\,{\rm K}$ is due to the lack of collisional rate data above this temperature for HCN.

and are not generally applicable: there is likely to be a set of ratios which vary significantly, but the particular ratios will depend upon the peaks of the galaxy SLEDs, which in turn depends upon excitation conditions. The excitation conditions used here are rather weak, especially compared to the very active star forming models of Narayanan & Krumholz (2014). In general however, the galaxy-integrated line ratios appear to be rather robust to changes in redshift, unlike the individual line of sight HCN brightness temperature ratios in §3.3.5.

3.4 Discussion

3.4.1 Are LVG Model Results Reliable?

LVG models are quick and easy to run, and have been used to a varying extent in Galactic, local-universe and high-redshift studies of molecular gas. One of most common, and indeed most reliable uses of the models is to generate grids of results, then overlaying either χ^2 or likelihood contours (e.g., García-Burillo et al., 2000; Rangwala et al., 2011). This graphically illustrates the reasonable parameter ranges, and does not necessarily claim specific values. However, even these methods are susceptible to assumptions, which can bias the results in unexpected and unusual ways, especially if canonical abundances or abundance ratios are assumed. For example, assuming an [HCN]/[H^{13}CN] ratio of 60 actually imposes strong constraints on the possible $T_{\rm k}$ range. If the true [HCN]/[H^{13}CN] ratio is closer to 300 (such as in NGC 6240: Papadopoulos et al., 2014; Tunnard et al., 2015a), then the assumptions can throw off $T_{\rm k}$ by over a dex. Furthermore, when multiple lines and species are available these approaches can be restrictive: they cannot be used to explore higher dimensional parameter spaces.

One great reassurance of the tests presented here is that there is no significant systemic offset in the model deviations, with most trials returning centrally peaked deviation distributions. In almost all models there was a small set of extreme outliers, almost always with an underestimate of $T_{\rm k}$ and concomitant overestimate of $n_{\rm H_2}$. These outliers are greatly exacerbated by including regions

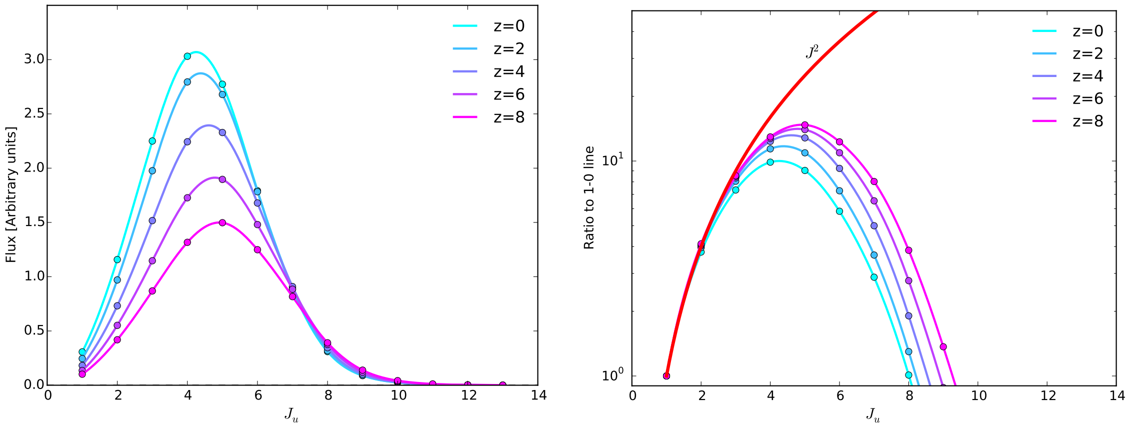

Figure 3.6: Galaxy integrated CO SLEDs from 10^4 clouds distributed exponentially with radius for five sample redshifts. The SLEDs are presented as arbitrary fluxes observed from the same distance (left), and as line intensity ratios to CO$(1-0)$ line (right), as in Narayanan & Krumholz (2014). The thick red line in the right hand plot is the thermalised J^2 limit. The trend of increasing excitation relative to the CO$(1-0)$ line in the high-J lines as a function of redshift is due to the combination of reduced CO$(1-0)$ emission observable against the hotter CMB *and* a small, real increase in the high-J excitation due to the hotter CMB.

with a thermal pressure $> 10^8\,\mathrm{K\,cm^{-3}}$. This regime is so extreme that its exclusion is unlikely to remove many realistic regions with significant emission, especially when integrated across a galaxy.

The concern arises when model parameters are interpreted as hard and fast values, or as being known better than within a factor of 3. Even in the most optimistic scenarios and with zero observational uncertainties LVG models cannot be expected to provide answers more accurately than ± 0.2 dex. The real uncertainties on the results are most likely much higher, presenting real and significant concerns with any possible precision uses of LVG models.

A topic I have not mentioned until now is that of the collisional rate constants. LVG models require these (temperature dependent) rates which are primarily determined in laboratory experiments. The models presented here should be largely insensitive to any errors in these rates, as I am using the same rates for generating both the original lines and comparison lines (whether they be in grids or MCMC). In real-world observations however, these errors could be significant, especially for the less well studied molecules (such as HNC, a chemically interesting isomer of HCN). Furthermore, RADEX does not extrapolate the rate constants beyond the provided data, keeping them constant instead[10]. I am not suggesting that this is the wrong approach; indeed any extrapolation of rate constants must be performed with utmost caution. It is simply being noted that this should be appreciated as a limitation of LVG, and indeed any molecular-line radiative-transfer models, including LIME. Nevertheless, I have no means of quantifying these potential errors with the models, and as such consider the issue beyond the scope of this paper, leaving it as a further reason to consider the model precisions presented here as best cases only.

No discussion of the reliability of LVG models would be complete without mentioning chemistry. The LVG framework does not include chemistry; chemistry can be added to LVG models ante hoc, post hoc or iteratively, but in all cases this is just altering the molecular abundances. In other words, LVG codes, e.g., RADEX, can find excellent fits for completely unrealistic physical conditions and molecular abundances.

To some extent unrealistic physical conditions may be excluded by the use of appropriate priors. Similarly, a sceptical interpretation of the LVG results is essential, preferably including an examination of the appropriateness of the derived molecular abundance ratios for the physical conditions. A potentially very powerful technique for this would be post hoc chemical modelling or comparison with lookup tables, to examine whether the results are self consistent, somewhat

---

[10] See `http://home.strw.leidenuniv.nl/~moldata/radex.html`

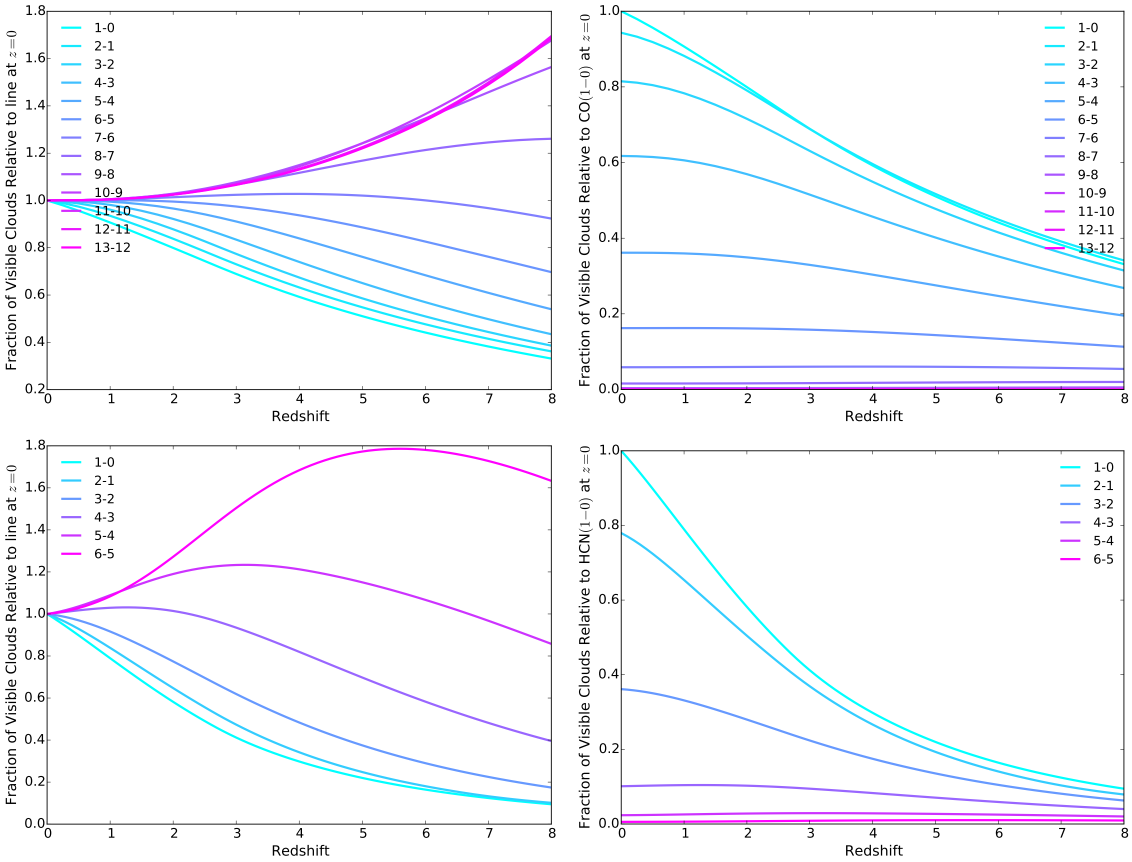

Figure 3.7: Ratios of observed line luminosity relative to the line luminosity at $z = 0$ (left) and relative to the $1 - 0$ line at $z = 0$ (right) for the toy galaxy model, with CO (top) and HCN (bottom). Since the model has the same mass at all redshifts the CO$(1-0)$ track in these plots may be interpreted as one over the $\alpha_{\rm CO}$ correction factor necessary to account for the hotter CMB. Unlike the plots of da Cunha et al. (2013), which showed the effect of the CMB background on the intrinsic emission from the galaxy, these plots show the differences due to both decreased CMB contrast and the changes in line excitation due to the hotter CMB.

in the fashion of Viti et al. (2014). Unlike running chemistry for every step in the MCMC, this method would not add significantly to the run time while providing significantly more physical insight and potentially highlighting interesting results.

I also point to the risks of modelling emission from entire galaxies as single clouds. Not only is this physically unmotivated, it produces unrealistic column densities and masses. Dynamically motivated and self consistent methods exist which are also physically meaningful, and although they may require prior assumptions these assumptions are in all cases more reasonable than the tacit assumptions implicit in the single cloud alternative (see appendices in Papadopoulos et al., 2012; Tunnard et al., 2015a).

3.4.2 An Aside on $K_{\rm vir}$

There are some subtleties associated with assuming a virial state for the modelled gas. Since, for a uniform density cloud, the mass (in kg) is given by:

$$M_{\rm cloud} = \frac{4\pi}{3}\left(\frac{\zeta\,\Delta v}{2{\rm d}v/{\rm d}r}\right)^3 n_{\rm H_2}\,\mu_{\rm H_2}, \tag{3.5}$$

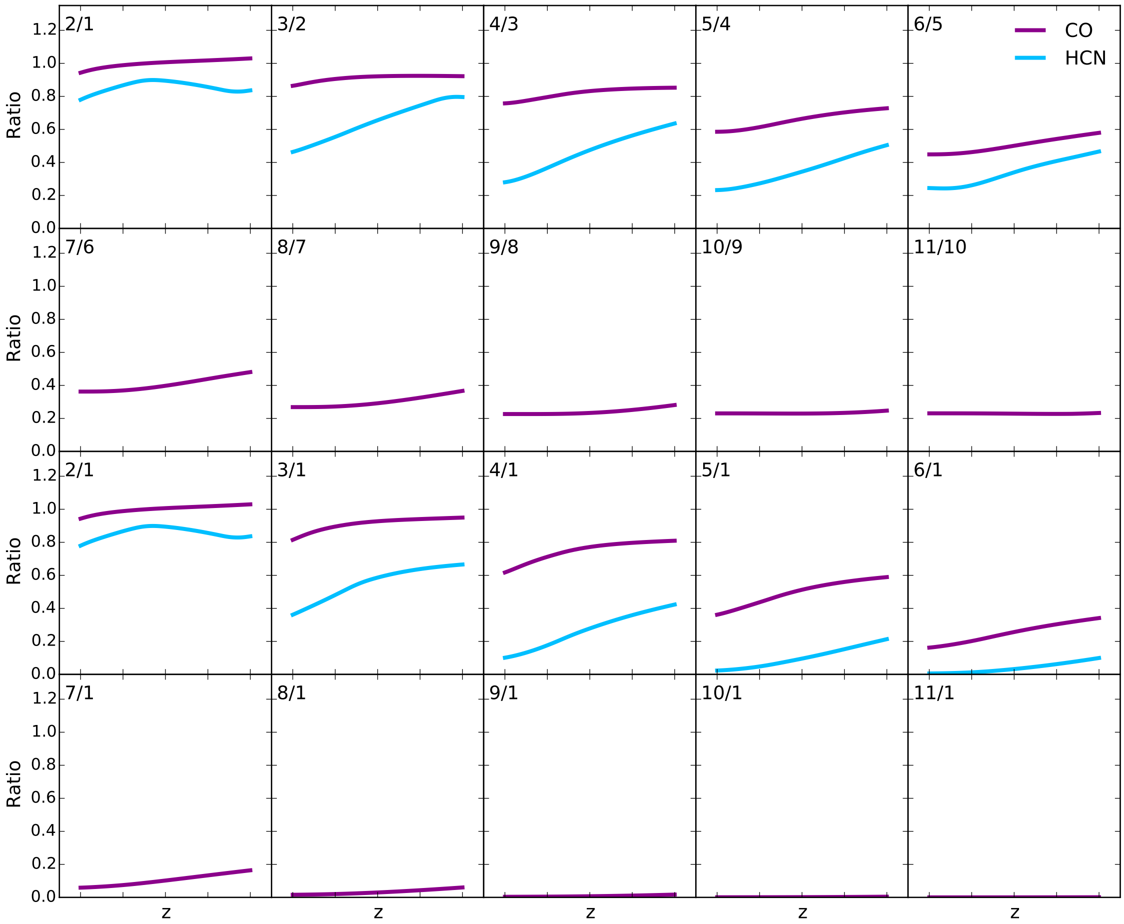

Figure 3.8: Line brightness ratios for a selection of CO and HCN line ratios as functions of redshift, generated using the galaxy integrated model. The line ratios are indicated in the top left of each subplot. There is very little variation with redshift, except for in the $5-4/1-0$ and $4-3/1-0$ line ratios. These ratios are specific to the galaxy excitation model used here, and are not generally applicable. They are however indicative of the expected scale of the variation in the line ratios with redshift.

where μ_{H_2} is the helium corrected mass per H_2 molecule, and $\zeta = 3.08 \times 10^{18}\,\mathrm{cm\,pc}^{-1}$, or equivalently that:

$$r_{\mathrm{cloud}} = \frac{\zeta\,\Delta v}{2\mathrm{d}v/\mathrm{d}r}. \tag{3.6}$$

The issue is that if a virial state is assumed, then for an observed line width the size of the cloud is fixed. Therefore, if the assumed virial state of the cloud is changed (through $\mathrm{d}v/\mathrm{d}r$), and all other variables held constant, then the size of the cloud has also been changed. This subtlety is important both for resolved and extragalactic observations: if the size of the cloud is known from observations then this should be fixed in the modelling. If the size of the cloud is unknown, then there is a degeneracy between the size of the cloud and multiple clouds distributed in velocity space across the galaxy.

Further discussion of this topic can be found in Papadopoulos et al. (2012) and Tunnard et al. (2015a). Here, I simply present a comparison of the peak brightness temperature from RADEX models where K_{vir} is varied, first without any constraint on the cloud size, and then with the cloud size constrained to be 1 pc, with the results shown in Figure 3.9. In the unconstrained case there is less emission in all lines as K_{vir} increases: this is due to the cloud shrinking, and the column density of CO falling. In the $r = 1\,\mathrm{pc}$ case however there is a pivot around the $J_u \simeq 5-6$ lines,

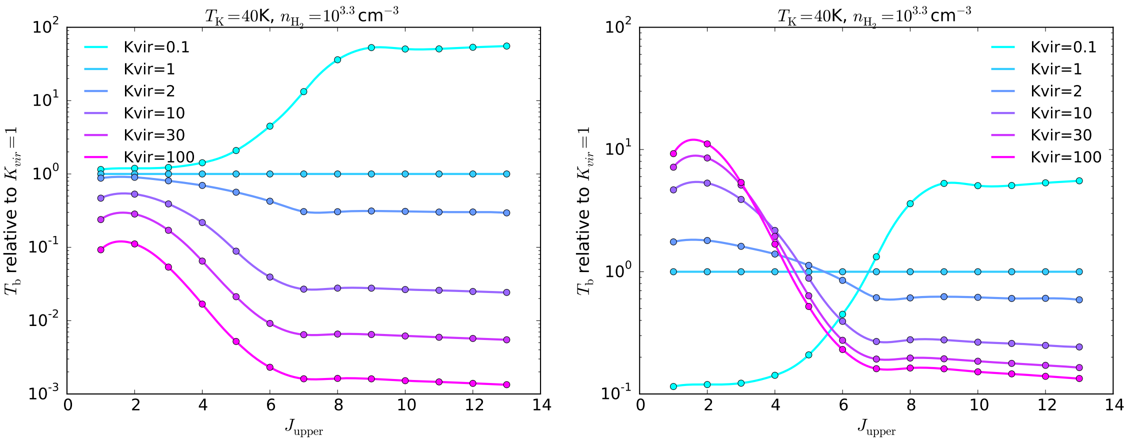

Figure 3.9: The effect of varying $K_{\rm vir}$ without constraining cloud size (left) and constraining the cloud size to be 1 pc (right). The peak brightness temperatures are presented relative to the $K_{\rm vir} = 1$ case.

with emission increasing with $K_{\rm vir}$ at lower J and decreasing at higher J. Here, the column density is the same but the lines become less optically thick as $K_{\rm vir}$ increases, so more of the column can be seen, and emission increases.

The key point here is that there are strong variations in the line emission as well as the relative line emission with variations of $K_{\rm vir}$ and dependent upon the underlying assumptions. In situations where the cloud size is known this can be particularly important.

3.4.3 How important is $T_{\rm bg}$?

I have presented several models of the potential effects of the background radiation field on LVG model results. These models do not, and cannot, account for dust within the emitting gas, as this is not a feature included in RADEX. They can however model gas illuminated by a separate hot dust background, and the effects of the CMB at higher redshift.

As I have noted, it is also important to recognise that RADEX presents line results as line brightnesses in excess of the background field. When dealing with the CMB this is ideal, however, when dealing with a hot dust source that is completely obscured by cooler, intervening dust this is misleading. In these cases it may be more appropriate for the applied background field to be re-added to the line brightnesses. On the other hand, due to the high column depths and line optical depths of compact obscured nuclei (CONs) it is only possible to observe the cooler, shielded outer layers in the major isotopologue lines (Aalto et al., 2015b) at which point the background dust has cooled significantly and a high $T_{\rm bg}$ is not actually incident on the observable regions.

I have demonstrated the well known degeneracy between $T_{\rm k}$ and $T_{\rm bg}$, and demonstrated the effects of a hot dust background on HCN and CO SLEDs (Figure 3.2). These effects can be huge, including the effects on the line ratios. However, these conditions are likely to be significant in a minority of objects, and more comprehensive modelling of dust included in the gas phase is beyond the scope of this paper. Papadopoulos et al. (2010a) argued that if the gas and dust are in thermal equilibrium, then any heating of the dust will increase the line and continuum brightness equally, thereby reducing the line/continuum contrast. While essential when analysing objects such as Arp 220, this is unlikely to be a concern in most galaxies.

At $z = 4$ both CO$(4-3)$ and CO$(5-4)$ lie in ALMA Band 3 while the lower J lines, observed by Carilli et al. (2010, 2011); Hodge et al. (2012), require the JVLA. These studies have revealed a clumpy medium: precisely what is expected if the real conditions are GMC-like clumps embedded in an extended diffuse medium. The low excitation diffuse medium becomes undetectable against the hotter CMB and only the high density clumps are seen (see also Casey et al., 2015). The effects on planned blind surveys of CO with the ngVLA and SKA are more complex, but will risk introducing a significant redshift bias on both the low-J CO luminosity function and the H_2 mass fractions, as well as the cosmological $\Omega(H_2)$ (Casey et al., 2015; Leroy et al., 2015). How significant this effect will be is not clear, as it depends heavily on the kinetic temperature of the molecular gas at high z. If large fractions of the molecular reservoirs are $\lesssim 20\,\mathrm{K}$ then the effects are likely to be very significant as early as $z \simeq 3-4$. However, if high z molecular reservoirs are mostly $\geq 30\,\mathrm{K}$ then there is no reason to expect any significant effect even out to $z = 8$.

The change in α_{CO} with redshift highlights the importance of dynamical mass estimates for high z line observations (Carilli et al., 2010, 2011; Hodge et al., 2012), and presents new challenges for high z mergers, where dynamical mass estimates may no longer be meaningful. Our model, while very simple, demonstrates that even at $z = 2$ there are risks of significantly underestimating the molecular masses of galaxies due to the loss of contrast against the CMB, including the potential invisibility of the coldest, yet perhaps in some cases also the densest, regions of the galaxies.

The line ratios most affected by the higher CMB are those including the low$-J$ lines, so that higher J line ratios should remain relatively robust even at redshifts as high as $z = 8$, depending upon the galaxy excitation.

3.5 Conclusions

I have presented tests of the ability of grid and MCMC methods to recover the true input parameters of LVG models using line ratios generated by the same LVG model. I have shown that without any additional errors there is a factor of $2-3$ uncertainty in most derived parameters. When a 10% absolute flux calibration error is applied to the synthetic lines the parameter uncertainty can expand to a factor of 10, even when making very generous assumptions.

I have shown that the MCMC approach, used in Tunnard et al. (2015a) and similar to that of Kamenetzky et al. (2014), produces results comparable to or better than the grid method, while also being easily extended to accommodate additional parameters, molecules and gas phases. In a future work I intend to examine the potential biases involved when observing an entire galaxy, reducing the continuum of conditions to three phase models.

Most importantly, I have demonstrated that assuming an isotopologue abundance ratio will lead to less accurate results than modelling it as a free parameter. Incorrect assumptions with regards to the isotopologue abundance ratio can have disastrous consequences for the accuracy of recovered T_{k} and $n_{\mathrm{H_2}}$ (and of course [HCN]/[H^{13}CN]). *This effect is so large that you can actually be worse off assuming a canonical isotopologue abundance ratio than if you had no isotopologue lines at all.*

By examining the effect of the background radiation temperature on molecular line ratios I have demonstrated the potential for significant effects on line ratios due to hot dust backgrounds and the high z CMB. Using toy models to explore the effects of the CMB on CO SLEDs with increasing redshift I demonstrate that for galaxies with molecular gas components with $T_{\mathrm{k,z=0}} \leq 20\,\mathrm{K}$ both morphologies and masses inferred from low$-J$ CO lines are likely to be affected when $z \geq 5.5$, while if there are molecular gas components with $T_{\mathrm{k,z=0}} \leq 10\,\mathrm{K}$ there are large effects as early as $z \geq 2$. The specific values of the biases are dependent upon the galactic T_{k} profile. Nevertheless, I find that galaxy integrated CO line ratios are likely to be fairly robust even out to $z = 8$, whereas the line of sight line brightness ratios vary very strongly (see also da Cunha et al., 2013). Furthermore, it is imperative when modelling molecular rotational lines that the redshift is taken into account through the inclusion of the CMB. When modelling line ratios it is still important to include the CMB, but less so than when modelling the lines themselves.

The potentially very strong effect of the CMB on the recovered line flux has worrying implications for the application of α_{CO} to high redshift studies, adding another complication to the already difficult mix of kinematic state, metallicity and chemistry.

3.6 Additional Plots

Here I include plots described throughout the chapter which have been moved to improve the readability of the main text.

3.7 Free X_{mol}

I include a final model of less general interest, but which is nevertheless important for appreciating the limitations of LVG codes. I explore the case where one has four HCN lines and four $H^{13}CN$ lines, and where both X_{HCN} and [HCN]/[$H^{13}CN$] are free parameters.

One of the key parameters necessary to predict the dominant heating source in a gas (PDRs, XDRs, MDRs etc.) is the molecular abundance. While a single molecular abundance is not particularly informative, with reliable estimate of the abundances of several species significant progress can be made (e.g., Meijerink & Spaans, 2005; Meijerink et al., 2007, 2011; Bayet et al., 2008; Viti et al., 2014), especially when observing with spatial resolutions sufficient to distinguish individual molecular clouds. An interesting question therefore is whether LVG models can in fact be used to reliably recover molecular abundances. While I showed in the main body of the chapter that with single isotopologue lines alone this is not possible, I now investigate whether the addition of $H^{13}CN$ improves the situation.

Due to the degeneracy between X_{mol} and $\mathrm{d}v/\mathrm{d}r$ it is not possible to recover the molecular abundance with a single species, unless one is willing to assume a fixed value of K_{vir} and the observed cloud is spatially and spectrally resolved. If K_{vir} is assumed or known, then for a given n_{H_2} $\mathrm{d}v/\mathrm{d}r$ is determined. However, even this is not necessarily enough, due to the degeneracy between T_{k} and n_{H_2}. Furthermore, the assumption of a fixed K_{vir} is dubious, especially in luminous infrared galaxies where K_{vir} is very likely elevated (Papadopoulos et al., 2014). This is before ones takes into account that even high resolution interferometric extragalactic observations (in all but the closest galaxies) will confuse multiple gas phases within the beam.

One possible solution, at least to the alleviate the degeneracy, appears to lie in isotopologue lines. Here, I present a model with four HCN lines and four $H^{13}CN$ lines, with the free parameters T_{k}, n_{H_2}, $\mathrm{d}v/\mathrm{d}r$, X_{HCN} and [HCN]/[$H^{13}CN$]. The results are shown in Figure 3.16. Unfortunately, while T_{k} and [HCN]/[$H^{13}CN$] are well determined, n_{H_2}, $\mathrm{d}v/\mathrm{d}r$ and X_{HCN} are not. The conclusion here is that while LVG models cannot reliably estimate molecular abundances they *can* very reliably estimate abundance ratios. This is not a revolutionary result, but rather a relevant reminder that has now been accurately assessed.

3.8 CO Line Ratios

As a continuation of the discussion of the effect of T_{bg} on the observed line fluxes and line brightness ratios in §3.3.5 I present the CO line ratios in Figures 3.17 and 3.18. It is not practical to present all 78 possible line ratios, so I include only the most relevant: the 12 ratios with the $J = 1-0$ line and the 12 $J + 1/J$ line ratios.

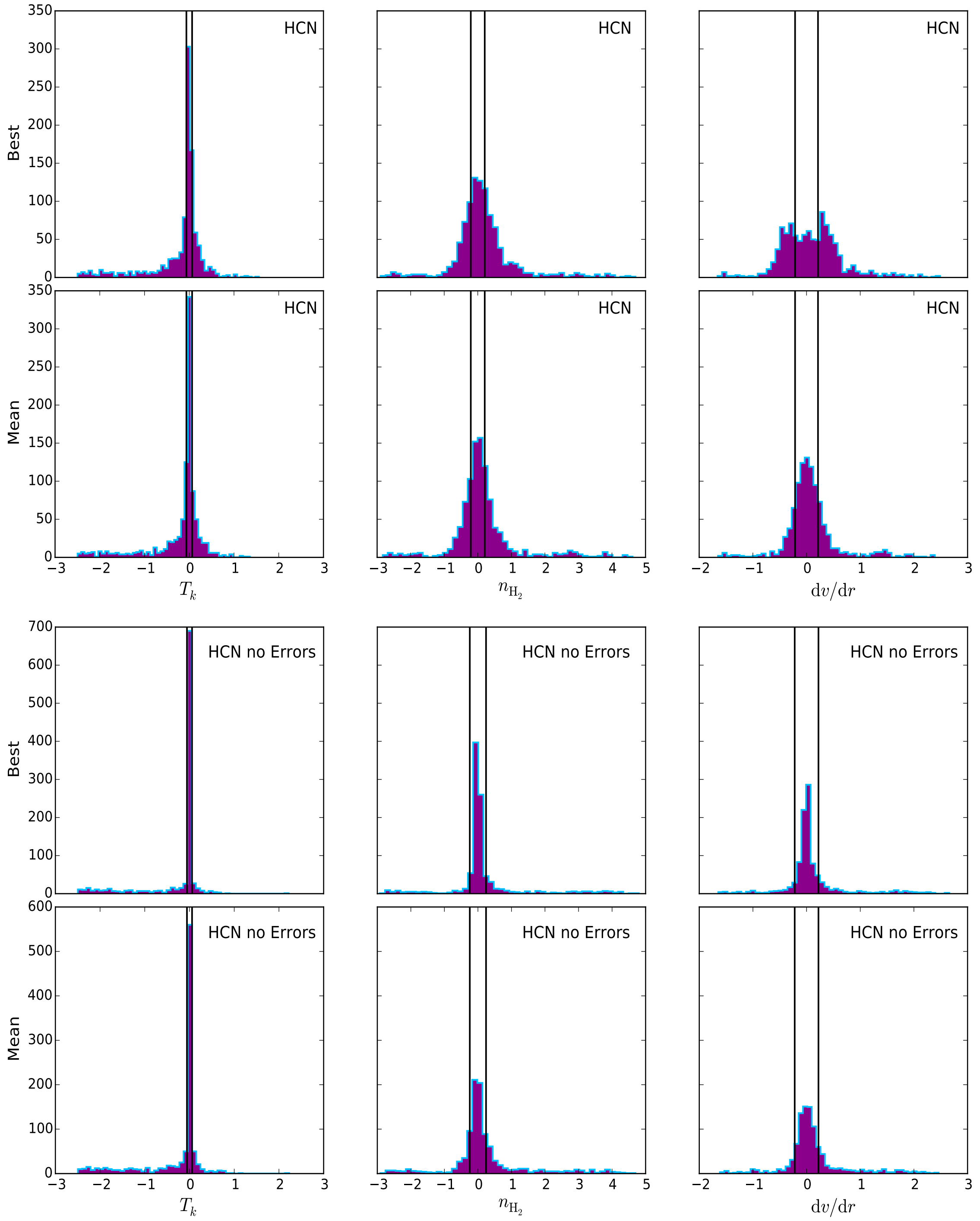

Figure 3.10: The logarithm of the ratio of the recovered to true parameters with (upper panel) and without (lower panel) 10% errors for HCN, drawn from a pressure restricted parameter range and recovered with an MCMC. The best fit (top row) and mean (bottom row) recovered parameters are reported.

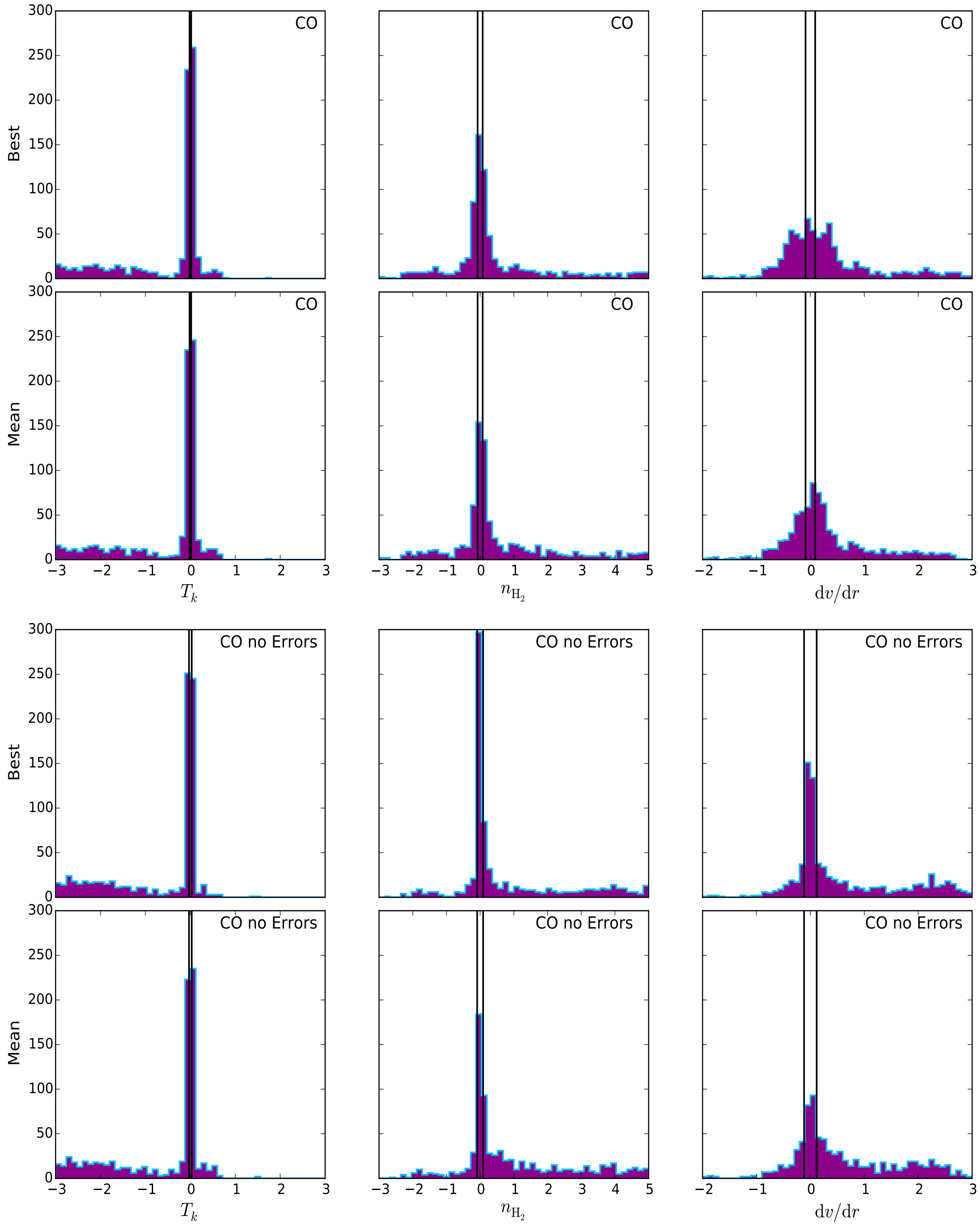

Figure 3.11: The logarithm of the ratio of the recovered to true parameters with (upper panel) and without (lower panel) 10% errors for CO, drawn from a pressure restricted parameter range and recovered with an MCMC. The best fit (top row) and mean (bottom row) recovered parameters are reported.

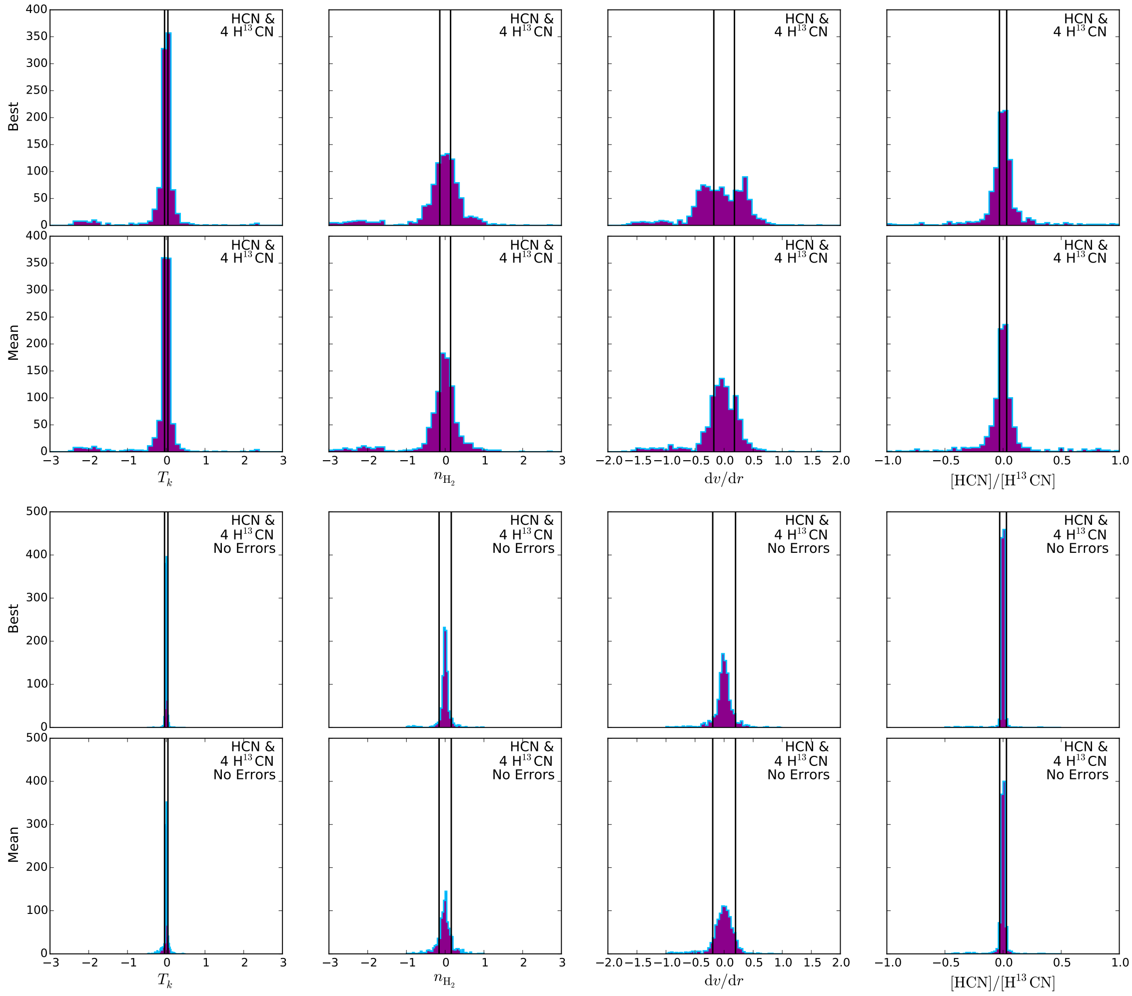

Figure 3.12: The logarithm of the ratio of the recovered to true parameters with (upper panel) and without (lower panel) 10% errors for four HCN lines and four H^{13}CN lines, drawn from a pressure restricted parameter range and recovered with an MCMC. The best fit (top) and mean (bottom) recovered parameters are reported. The $\pm 1\sigma$ standard deviations of the MCMC traces are indicated by the vertical, solid black lines.

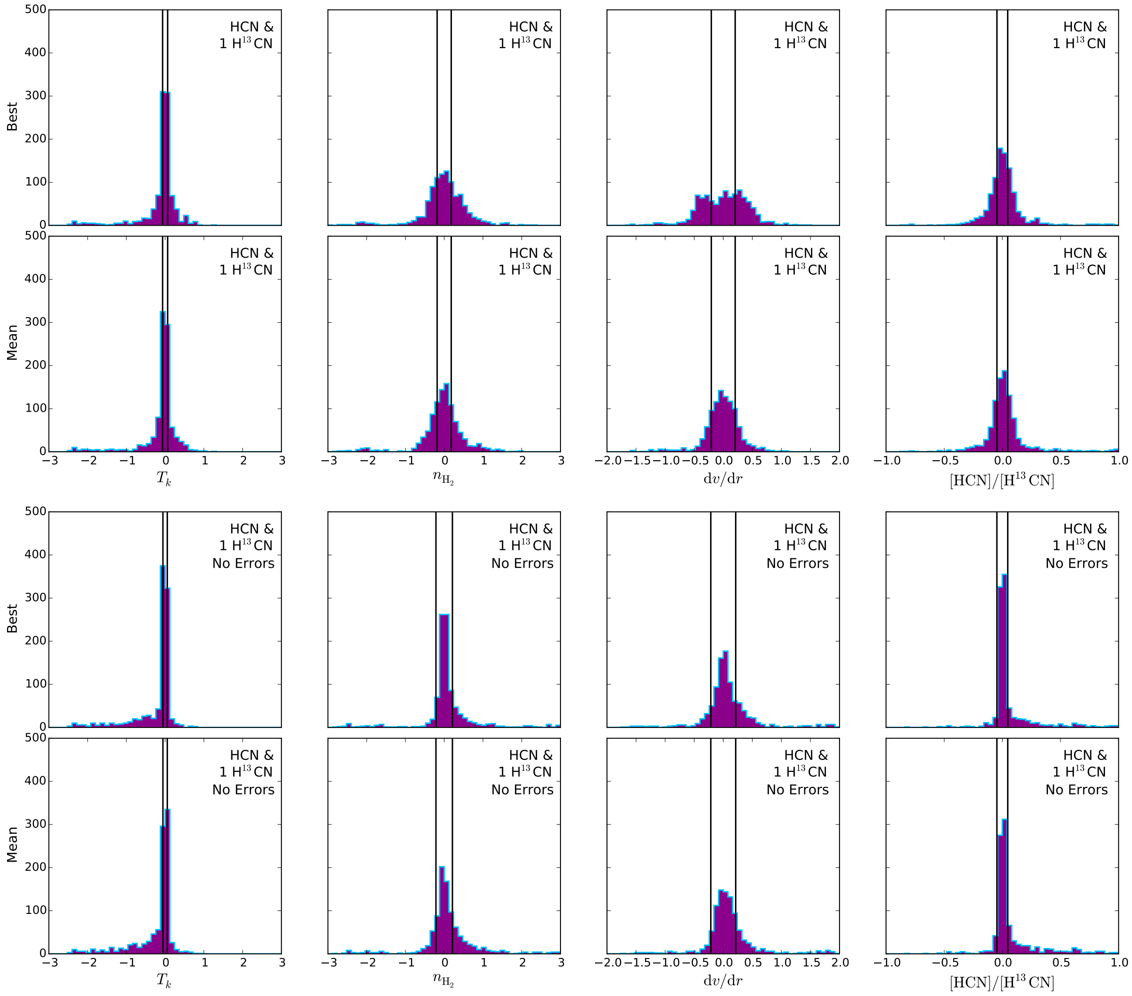

Figure 3.13: The logarithm of the ratio of the recovered to true parameters with (upper panel) and without (lower panel) 10% errors for four HCN lines and one H^{13}CN line, drawn from a pressure restricted parameter range and recovered with an MCMC. The best fit (top) and mean (bottom) recovered parameters are reported. The $\pm 1\sigma$ standard deviations of the MCMC traces are indicated by the vertical, solid black lines.

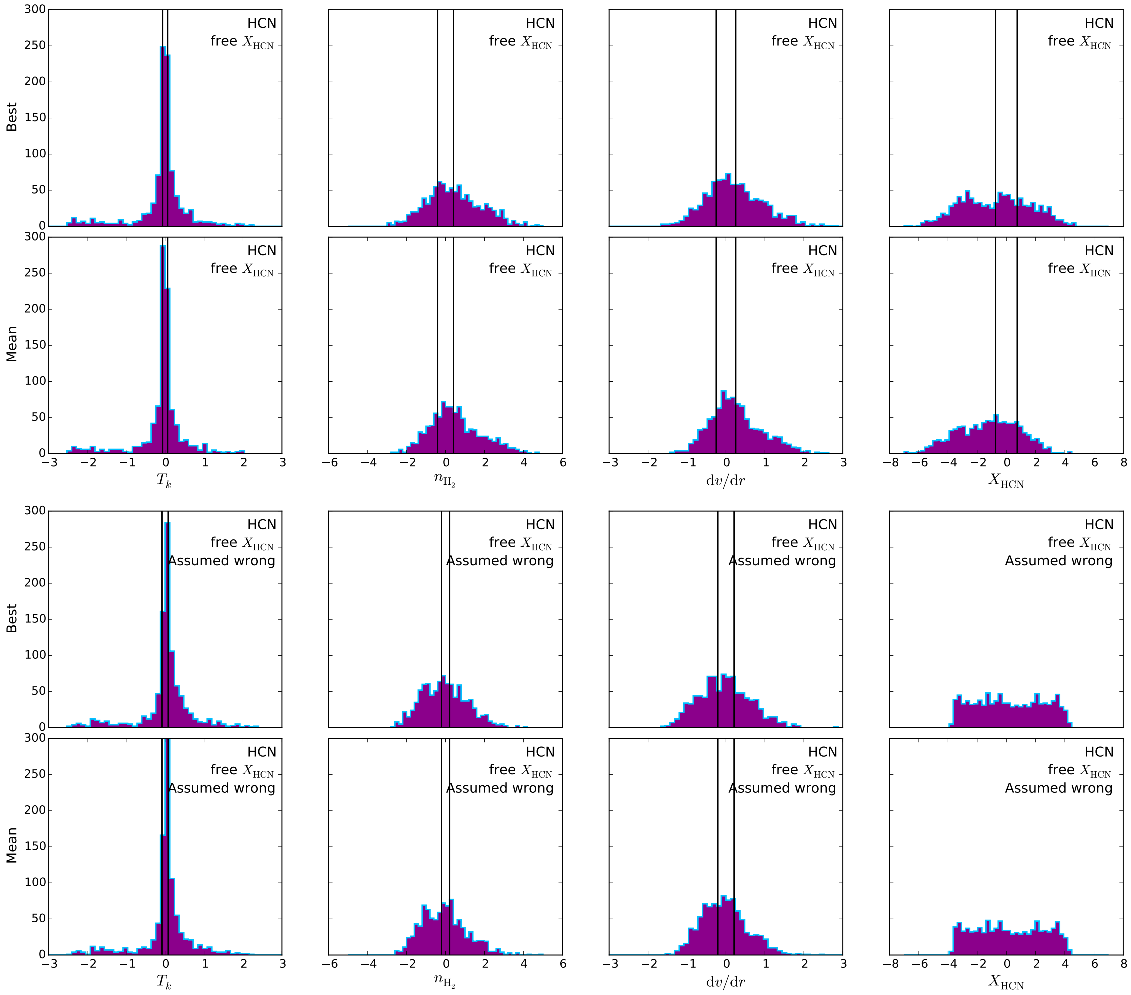

Figure 3.14: The logarithm of the ratio of the recovered to true parameters with 10% errors for four HCN lines, drawn from a pressure restricted parameter range and recovered with an MCMC. In all cases X_{HCN} is a random variable when generating the lines; in the top panel X_{HCN} is a free parameter in the recovery, while in the lower I attempt to recover parameters assuming $X_{\mathrm{HCN}} = 2 \times 10^{-8}$. The best fit (top row) and mean (bottom row) recovered parameters are reported. The $\pm 1\sigma$ standard deviations of the MCMC traces are indicated by the vertical, solid black lines, except for X_{HCN} which was a fixed parameter in the MCMC. T_{k} and n_{H_2} are recovered equally well in both cases.

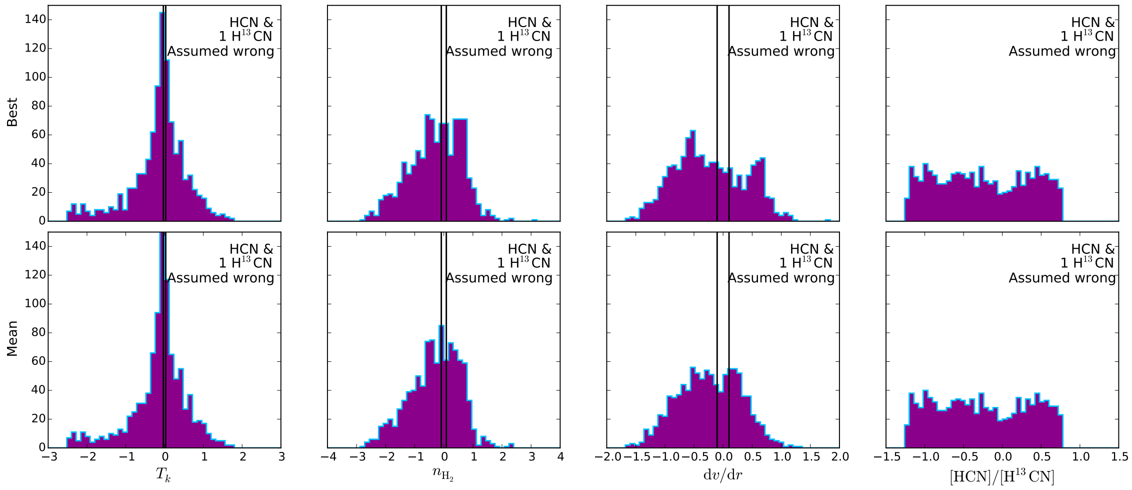

Figure 3.15: The logarithm of the ratio of the recovered to true parameters with 10% errors for four HCN lines and one H^{13}CN line, drawn from a pressure restricted parameter range and recovered with an MCMC, assuming [HCN]/[H^{13}CN]= 60. The best fit (top) and mean (bottom) recovered parameters are reported. The ±1σ standard deviations of the MCMC traces are indicated by the vertical, solid black lines, except for [HCN]/[H^{13}CN] which was a fixed parameter in the MCMC.

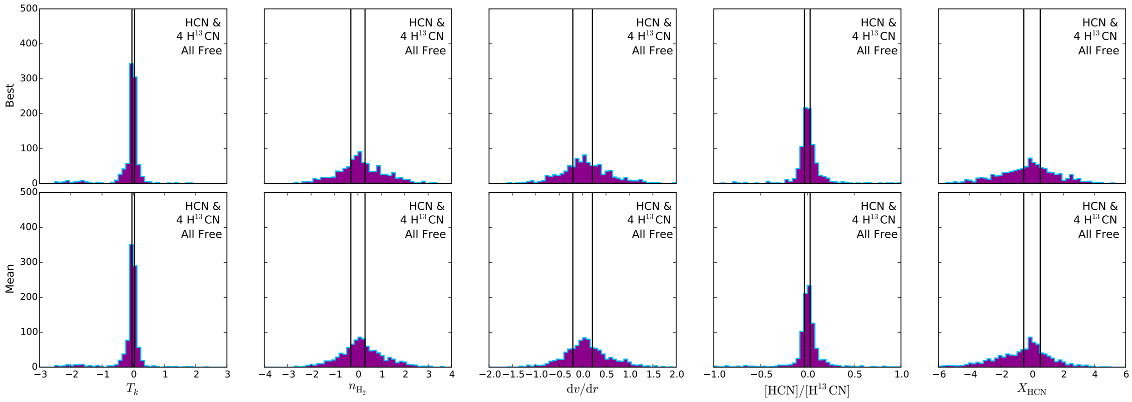

Figure 3.16: The logarithm of the ratio of the recovered to true parameters with 10% errors for four HCN lines and four H^{13}CN lines, drawn from a pressure restricted parameter range with free X_{HCN} and recovered with an MCMC. The best fit (top) and mean (bottom) recovered parameters are reported. The ±1σ standard deviations of the MCMC traces are indicated by the vertical, solid black lines. The model is not able to reliably recover the HCN abundance.

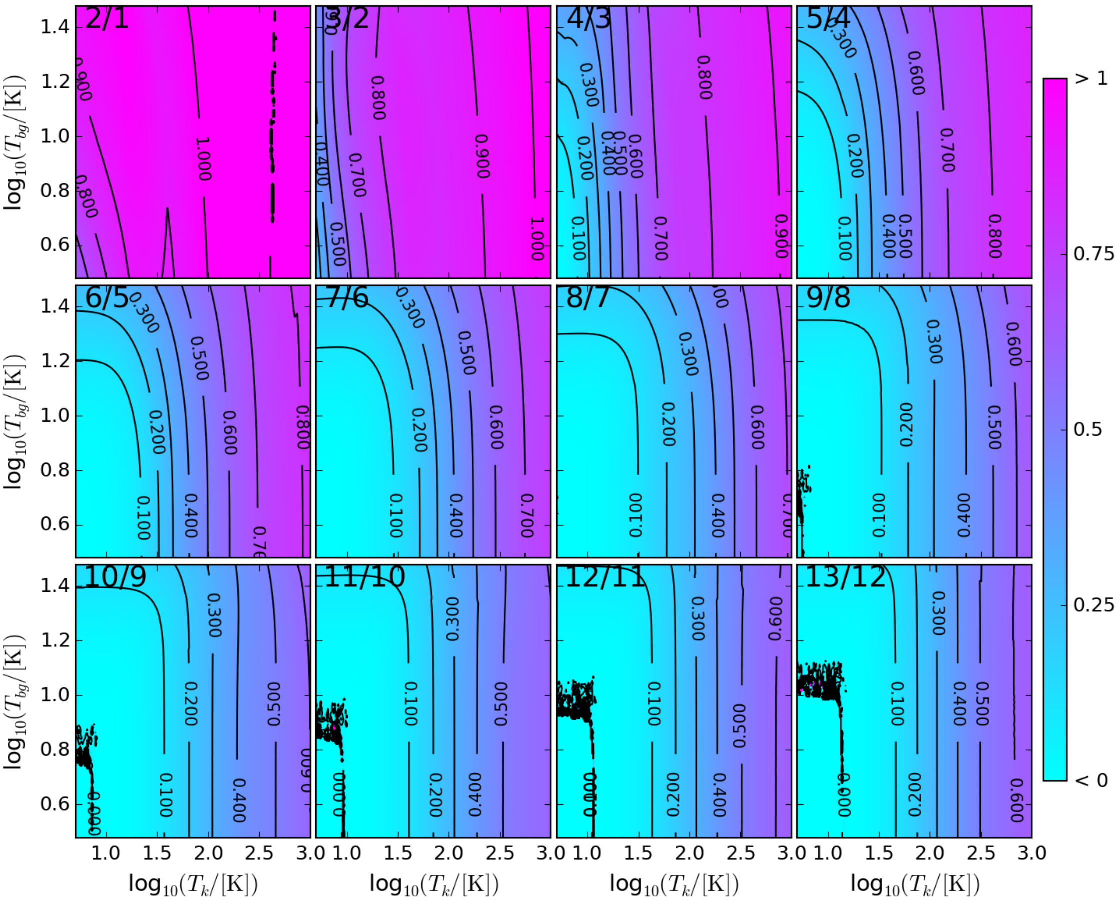

Figure 3.17: The effect of increasing the background radiation temperature from 3 K to 300 K on a selection of CO line ratios for a range of kinetic temperatures from 10 K to 1000 K. The line ratio is given in the top right corner of each plot. I plot contours at ratio levels of −10, −5, −2, −1, −0.5, 0, 0.1, 0.2, 0.3, 0.4, 0.5, 0.6, 0.7, 0.8, 0.9, 1, 2, 5 and 10.

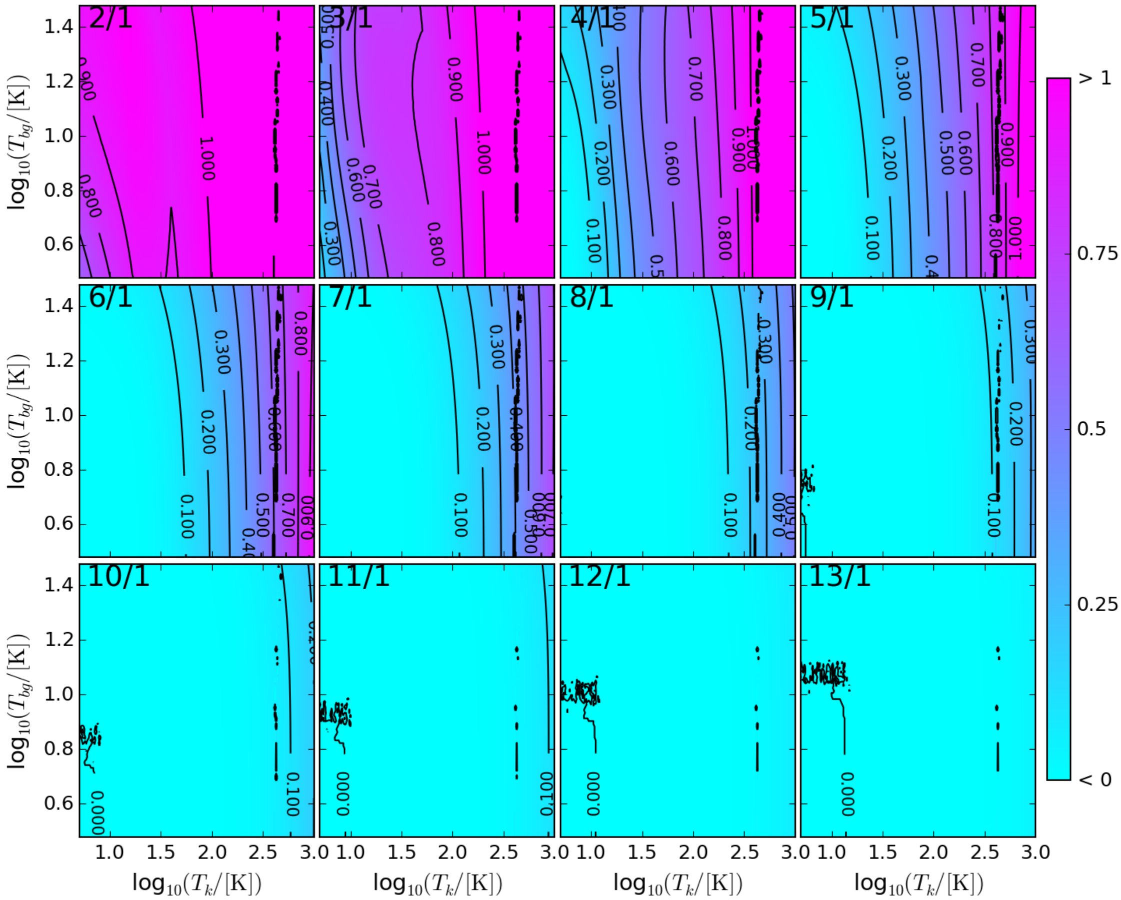

Figure 3.18: The effect of increasing the background radiation temperature from 3 K to 300 K on a selection of CO line ratios for a range of kinetic temperatures from 10 K to 1000 K. The line ratio is given in the top right corner of each plot. I plot contours at ratio levels of −10, −5, −2, −1, −0.5, 0, 0.1, 0.2, 0.3, 0.4, 0.5, 0.6, 0.7, 0.8, 0.9, 1, 2, 5 and 10.

Chapter 4

The Role of the CMB in Redshift–Related Departures from the Gao–Solomon Relation

> *"Omnia profecto, cum se a cœlestibus rebus referet ad humanas, excelsius magnificentiusque et dicet et sentiet."*
>
> *"The contemplation of celestial things will make a person both speak and think more sublimely and magnificently when he descends to human affairs."*
>
> Marcus Tullius Cicero

4.1 Introduction

Studies have found the HCN$(1-0)$ line emission from the molecular medium in galaxies to be extremely well correlated with the IR emission (e.g., Solomon et al. (1992); Gao & Solomon (2004); Gao & Solomon (2004b); Wu et al. (2005, 2010); García-Burillo et al. (2012); Bigiel et al. (2015)). This correlation is most often expressed in terms of the canonical Gao-Solomon luminosity relation between IR and HCN$(1-0)$ line luminosity: $\log L_{\rm IR} = 0.99 \log L'_{\rm HCN} + 2.90$, which was first derived from integrated luminosities of nearby star-forming galaxies, from normal disk galaxies to ultraluminous infrared galaxies (ULIRGs), but subsequently shown to extend, without modification, all the way down to individual star-forming clumps in the Milky Way. This 'universality', spanning more than 10 orders of magnitude in luminosity, was interpreted by Wu et al. (2005) as evidence that the HCN emission in starburst galaxies is well described by an optically thin ensemble of Milky Way like star-forming clumps of dense gas. This interpretation is also consistent with 500 pc resolution observations in the Antennae galaxies (Bigiel et al., 2015). In this scenario star formation in ULIRGs is fundamentally similar to that in the Milky Way, but with many more star-forming clumps, and therefore also a higher fraction of dense gas, but importantly not a significantly shorter gas depletion time-scale ($t_{\rm depl} \sim M_{\rm gas}/{\rm SFR}$). This interpretation was further supported by analyses of *Herschel* observations of the CO$(5-4)$ through to $(13-12)$ transitions of normal star-forming galaxies, which show linear trends with $L_{\rm FIR}$ over 13 orders of magnitude, with only $0.2-0.3$ dex of scatter (Kamenetzky et al., 2015; Liu et al., 2015a). Only ULIRGs show deviations from linearity for these high-J transitions, owing to the significant contribution from mechanical heating to the excitation of these lines (see discussion in Greve et al., 2014).

Extending the $L_{\rm IR} - L'_{\rm HCN}$ relation to higher redshifts has proven challenging owing to the faintness of the HCN lines (typically $\sim 5-10\times$ fainter than CO). Both Gao et al. (2007) and Riechers et al. (2007) found that extremely luminous galaxies at high redshift ($z \sim 2.7$ and $z = 6.4$

respectively) show a deviation from the Gao-Solomon relation, lying about a factor of 2 above the $z = 0$ relation (cf. Greve et al., 2006). This excess far-IR emission was interpreted as evidence that luminous galaxies at high redshift are forming stars more efficiently than their counterparts in the local universe.

A further complication arises from the increasing AGN fraction with redshift (e.g., Eastman et al., 2007). Since AGN contribute more to the continuum luminosity than to the HCN luminosity they have the potential to systematically offset galaxies from the Gao-Solomon relation, especially in the most luminous galaxies. This should be contrasted with the potential for AGN activity to induce star formation, and the potential stimulation of HCN emission via mid-IR pumping as well as chemical abundance enhancement of HCN by obscured AGN (Kohno, 2005; Lintott & Viti, 2006; Gaibler et al., 2012; Aalto et al., 2015b; Izumi et al., 2016b; Imanishi et al., 2016).

While it is now clear that high-z galaxies have higher dense-gas fractions (as indeed is seen in local ULIRGs) (Daddi et al., 2010; Tacconi et al., 2010), due to the greater turbulence, there is little and conflicting evidence beyond the offsets from the Gao-Solomon relation to suggest that they have intrinsically higher star-formation efficiencies (e.g., Combes, 2013; Magdis et al., 2014).

In this chapter, building upon the work of da Cunha et al. (2013) and chapter 3, I examine to what extent the hitherto undiscussed effect of the Cosmic Microwave Background (CMB) on the HCN$(1-0)$ emission can account for the observed deviations in the $L_{\rm FIR} - L'_{\rm HCN}$ relation at high redshifts. Throughout this chapter I discuss the line luminosity[1], $L'_{\rm HCN(1-0)}$, which I abbreviate to $L'_{\rm HCN}$. For plotting I adopt cosmological parameters $h = 0.75$, $\Omega_{\rm m} = 0.3$ and $\Omega_{\rm vac} = 0.7$; the choice of values for these parameters have no effect on the conclusions of this chapter.

4.2 Modelling

I explore the effects of the rising CMB in two ways. First, the effect on single lines of sight. I then explore a more complex model where I set up a toy model of the local active galaxy NGC 1068 and push this model back to higher redshifts. For much of the analysis in this chapter I use the non-LTE molecular line radiative transfer code RADEX (van der Tak et al., 2007) with collisional data from the Leiden Lambda database, specifically HCN collisional rates (Dumouchel et al., 2010) and CO collisional rates (Yang et al., 2010).

For reasons that become evident in §4.2.2 I do not repeat the exploration of the Gao-Solomon relation for CO in the main body of the chapter. Essentially, the range of possible densities and temperatures distributions of CO across galaxies leads to much larger random variations on a galaxy-by-galaxy basis than are seen for HCN. Nevertheless, I include similar single line of sight redshift adjusted plots of the $L_{\rm FIR} - L'_{\rm CO}$, relation as well as a very brief examination of the potential effects on the $L'_{\rm HCN} - L'_{\rm CO}$ relation, at the end of the chapter.

4.2.1 Single Lines of Sight

The increasing temperature of the CMB with redshift can significantly affect both the dust and molecular line emission from galaxies, especially at $z > 2$ (e.g., da Cunha et al., 2013; Narayanan & Krumholz, 2014; Tunnard & Greve, 2016; Zhang et al., 2016). There are two key effects that come into play depending upon the optical thickness of the line. In low-optical-depth regions the CMB photons help pump the low-J transitions when the CMB temperature approaches the line excitation temperature. In higher-optical-depth regions the effect of the CMB on the line emission is negligible; instead there is a significant loss of contrast due to the higher-temperature background, which does not propagate through the line emitting gas due to the high optical depth.

I investigate whether a hotter CMB can account for the departure from the Gao-Solomon relation seen by Gao et al. (2007); Riechers et al. (2007). To this end I take the observed relation at $z = 0$ and extrapolate to higher redshifts assuming an average kinetic temperature, HCN abundance and H_2 density. Under the null hypothesis that there is no evolution in the star-formation efficiency with redshift the inherent HCN and FIR emission will lie on the Gao-Solomon relation, with the redshift related deviation being due to the CMB effects. Therefore, for a given $L_{\rm FIR}$, I

---

[1] $L'_{\rm mol} = 3.25 \times 10^7 \left(\frac{\nu_{\rm obs}}{[\rm GHz]}\right)^{-2} \left(\frac{D_L}{[\rm Mpc]}\right)^2 (1+z)^{-3} \frac{\int S_{\rm mol}\Delta v}{[\rm Jy\,km\,s^{-1}]}$, (Solomon et al., 1992).

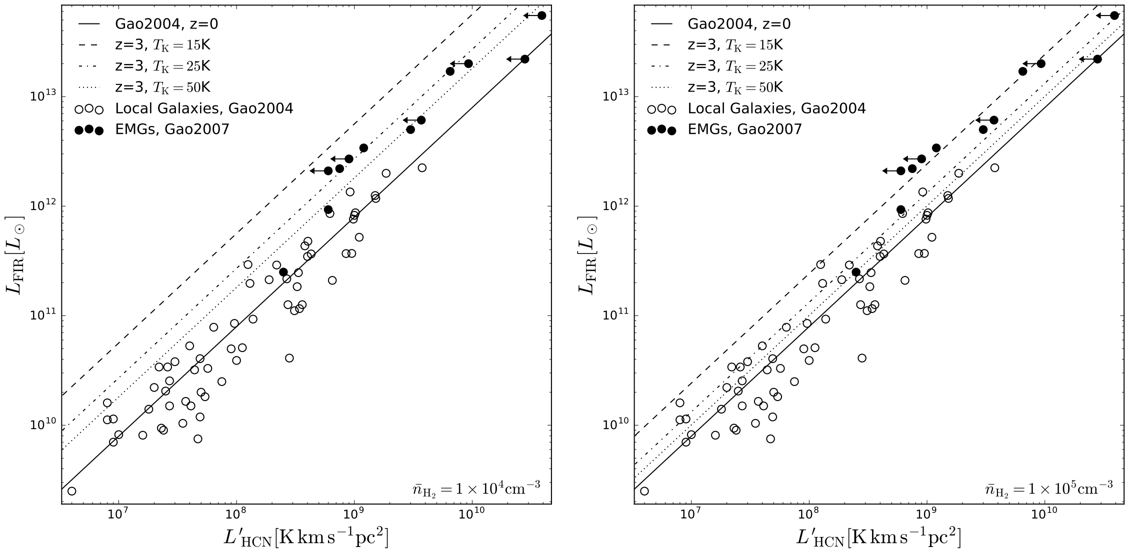

Figure 4.1: The effect of the CMB on the Gao-Solomon relation at $z = 3$ for a range of kinetic temperatures with $\bar{n}_{\mathrm{H}_2} = 1 \times 10^4\,\mathrm{cm}^{-3}$ (left) and $\bar{n}_{\mathrm{H}_2} = 1 \times 10^5\,\mathrm{cm}^{-3}$ (right), calculated using RADEX. Data from Gao et al. (2007) and references therein: Beelen et al. (2006); Carilli et al. (2005); Solomon & Vanden Bout (2005); Wagg et al. (2005); Egami et al. (2000); Riechers et al. (2006); Isaak et al. (2004); Greve et al. (2006).

assume the same quantity of dense gas, but alter its excitation and observability by increasing the CMB temperature. This leads to an evolution of the Gao-Solomon relation from its local universe form:

$$\log_{10}(L_{\mathrm{FIR}}) = 0.99 \log_{10}(L'_{\mathrm{HCN}}) + 2.90 \tag{4.1}$$

(Gao & Solomon, 2004; Gao et al., 2007), to the form that would be observed at redshift z:

$$\log_{10}(L_{\mathrm{FIR}}) = 0.99 \log_{10}\left(L'_{\mathrm{HCN}} \frac{T_{\mathrm{b}}(z)}{T_{\mathrm{b}}(z=0)}\right) + 2.90, \tag{4.2}$$

where T_{b} is the line brightness temperature. These adjusted relations are shown in Figure 4.1 for $z = 3$, two different average densities ($\bar{n}_{\mathrm{H}_2} = 1 \times 10^4\,\mathrm{cm}^{-3}$ and $\bar{n}_{\mathrm{H}_2} = 1 \times 10^5\,\mathrm{cm}^{-3}$), an HCN abundance with respect to H_2 of 2×10^{-8} and assuming virialised gas. These two values of the density were chosen as the critical density of the HCN$(1-0)$ lines is approximately $1 \times 10^5\,\mathrm{cm}^{-3}$ (e.g., Greve et al., 2014), but the *effective* critical density, when taking into account the potential for line trapping, can be as low as $\sim 1 \times 10^4\,\mathrm{cm}^{-3}$ (Shirley, 2015). It should be noted that both of these values are kinetic temperature sensitive but that RADEX was used to calculate the CMB affected brightness temperatures, which calculates the level populations without assuming a critical density.

For local galaxies Gao & Solomon (2004) reported L_{IR} $(8 - 1000\,\mu\mathrm{m})$, but in later works (including Gao et al., 2007) it has become conventional to use L_{FIR} $(40 - 500\,\mu\mathrm{m})$. Therefore the local galaxies used in this chapter had to have L_{FIR} recalculated; for this purpose I used the IRAS flux definition of L_{FIR} from Sanders & Mirabel (1996)[2] and use the galaxy luminosity distances from Gao & Solomon (2004) for consistency and comparability with their L'_{HCN}.

In Figure 4.2 I plot the $T_{\mathrm{b},z}/T_{\mathrm{b},z=0}$ surfaces themselves as a function of redshift and kinetic temperature for the same parameters as used in Figure 4.1. These may be thought of as the generalised correction factor surfaces for the vertical offset in the Gao-Solomon relation due to the two CMB effects discussed above. The surfaces show the expected rapid fall to zero observability

---

[2] $L_{\mathrm{FIR}} = L_{40-500\,\mu\mathrm{m}} = 4\pi\, D_L^2\, C\, \left[1.26 \times 10^{-14}\{2.58\, f_{60} + f_{100}\}\right]$ where D_L is the luminosity distance in metres, and f_{60} and f_{100} are the respective IRAS fluxes in Jy. C is a correction factor lying between 1.4 and 1.8; I adopt an average value of 1.6 here as I am not actually fitting to the galaxies.

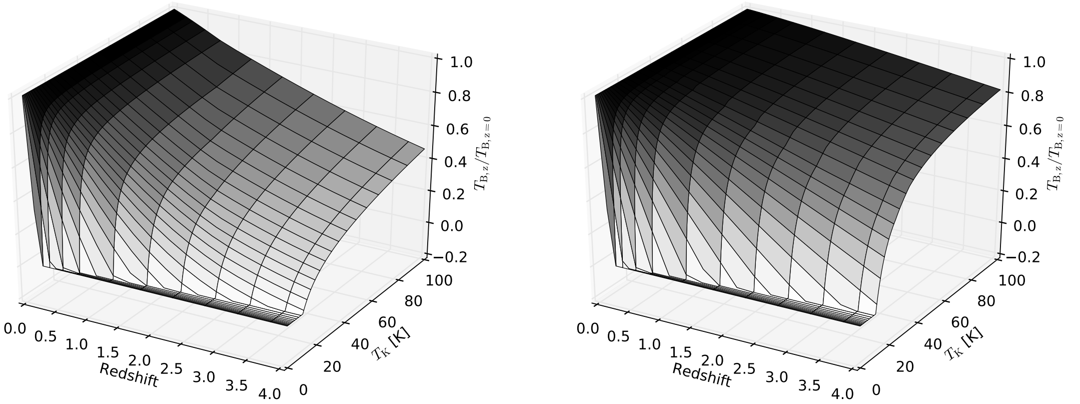

Figure 4.2: Surface plots of the line brightness ratios as functions of redshift and $z = 0$ brightness for the HCN$(1-0)$ line and $\bar{n}_{H_2} = 1 \times 10^4\,\mathrm{cm}^{-3}$ (left) and $\bar{n}_{H_2} = 1 \times 10^5\,\mathrm{cm}^{-3}$ (right), calculated using RADEX.

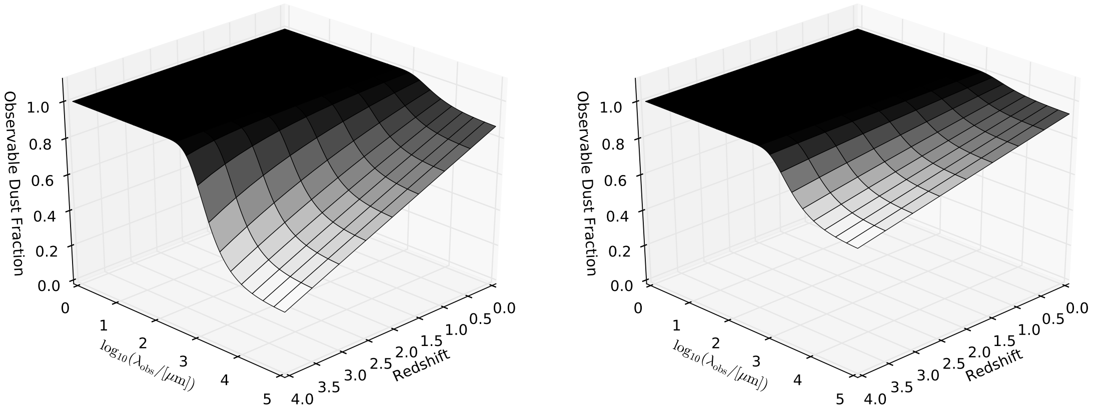

Figure 4.3: Surface plots of the observable fraction of the dust as functions of redshift and the *observed* wavelength, for a dust temperature of 20 K (left) and 40 K (right). See also Figure 3 in da Cunha et al. (2013).

as the kinetic temperature of the gas approaches that of the CMB, with a general trend towards decreased observability with increasing redshift. The lower density surface is much more strongly affected by the CMB as the HCN in this gas is sub-thermally excited. Nevertheless, even in the dense case if the kinetic temperature of the gas is approaching that of the CMB (as it indeed does in cold pre-stellar GMCs) then the loss of contrast becomes very significant.

Given that I am searching for a shift in observable HCN, I must confirm that there is not also a compensating reduction in L_{FIR}. In Figure 4.3 I plot the observable fraction of the dust brightness temperature against the CMB as a function of redshift and *observed* wavelength for dust temperatures of 20 K and 40 K. The surfaces are calculated following the discussion and Equation 18 in da Cunha et al. (2013). The plots in Figure 4.1 have not been adjusted to include this effect as it depends on the method used to observe and calculate L_{FIR} which varies for each galaxy. The dust in luminous high-z galaxies is primarily at temperatures $30 - 50$ K, more closely represented by the 40 K surface than the 20 K. Nevertheless, even for the 20 K case, at $z = 3$ and an *observing* wavelength of 1 mm the CMB only reduces the observed dust temperature by 10%. For the much more realistic parameters of 40 K dust and an 850 μm measurement the reduction is less than 0.5%. Therefore, while care should be taken to ensure that the CMB is not affecting the dust observations of a specific galaxy it is extremely unlikely to be having any effect on the observations as a whole.

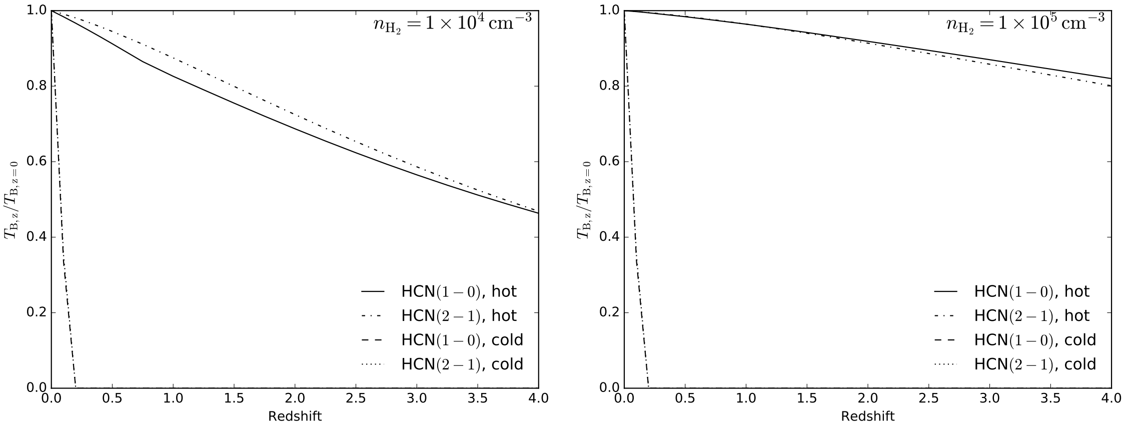

Figure 4.4: A demonstration that the loss of contrast against a hot CMB is not much alleviated for single lines of sight by using the HCN(2 − 1) line. For the parameters discussed in §4.2.1 the HCN(2 − 1) line is affected almost identically to the HCN(1 − 0) line. Results shown here for the hot and cold limits on the earlier models for $\bar{n}_{\mathrm{H}_2} = 1 \times 10^4\,\mathrm{cm}^{-3}$ (left) and $\bar{n}_{\mathrm{H}_2} = 1 \times 10^5\,\mathrm{cm}^{-3}$ (right).

Note that using a naïve analytical approach to the loss of contrast significantly overestimates the effect of the CMB. That is, if one assumes high optical depth and that:

$$T_z \simeq T_0 - (T_{\mathrm{CMB},z} - T_{\mathrm{CMB},0}) = T_0 - z\,T_{\mathrm{CMB},0}, \tag{4.3}$$

then one can significantly underestimate the observable HCN, due to a combination of optical depth effects and the hotter CMB contributing to exciting the low-J lines. This is not an issue in the current analysis as RADEX takes the incident background radiation field and its propagation through the gas column into account.

Sensitivity to line transition

Due to difficulties in observing the highly redshifted HCN(1 − 0) line its strength is often estimated from observations of higher transitions which are then converted (with implicit assumptions regarding excitation) to the 1 − 0 line. While I do not explore the effects of the assumptions here, I do assess how much weaker the effect of the CMB on the 2 − 1 line is. The results are shown in Figure 4.4. For the 2 − 1 line there is no significant difference over the parameter range explored for the single lines of sight. However, for the galaxy-integrated emission the effects become much more complicated due to partial stimulation of the line by the CMB and excitation gradients across the galaxy. Nevertheless, the line tends to be similarly affected (Tunnard & Greve, 2016), and the stimulated emission is a small effect (Shirley, 2015). Higher-J transitions will be much less affected by the CMB due to the rapid fall off of the blackbody spectrum with decreasing wavelength, although attempts to use these lines as proxies for the $J = 1 - 0$ line are plagued by uncertainties in the excitation of the gas which render them extremely uncertain.

CO

So far I have focussed on the effect of the CMB on the HCN(1 − 0) line. However, there is undoubtedly also an effect on the CO lines (e.g., da Cunha et al., 2013). I therefore repeated the previous analysis but for CO, assuming an abundance of 5×10^{-5} with respect to H_2 and adjusting the local universe relation. The results are shown in Figure 4.5. I find that at $z = 3$ only in the most diffuse gas is the effect significant when compared to the intrinsic scatter in the relationship. Since the luminosity weighted CO(1 − 0) emission is biased towards the denser regions this implies that while the effect should not be neglected, it is less significant than for the fainter HCN.

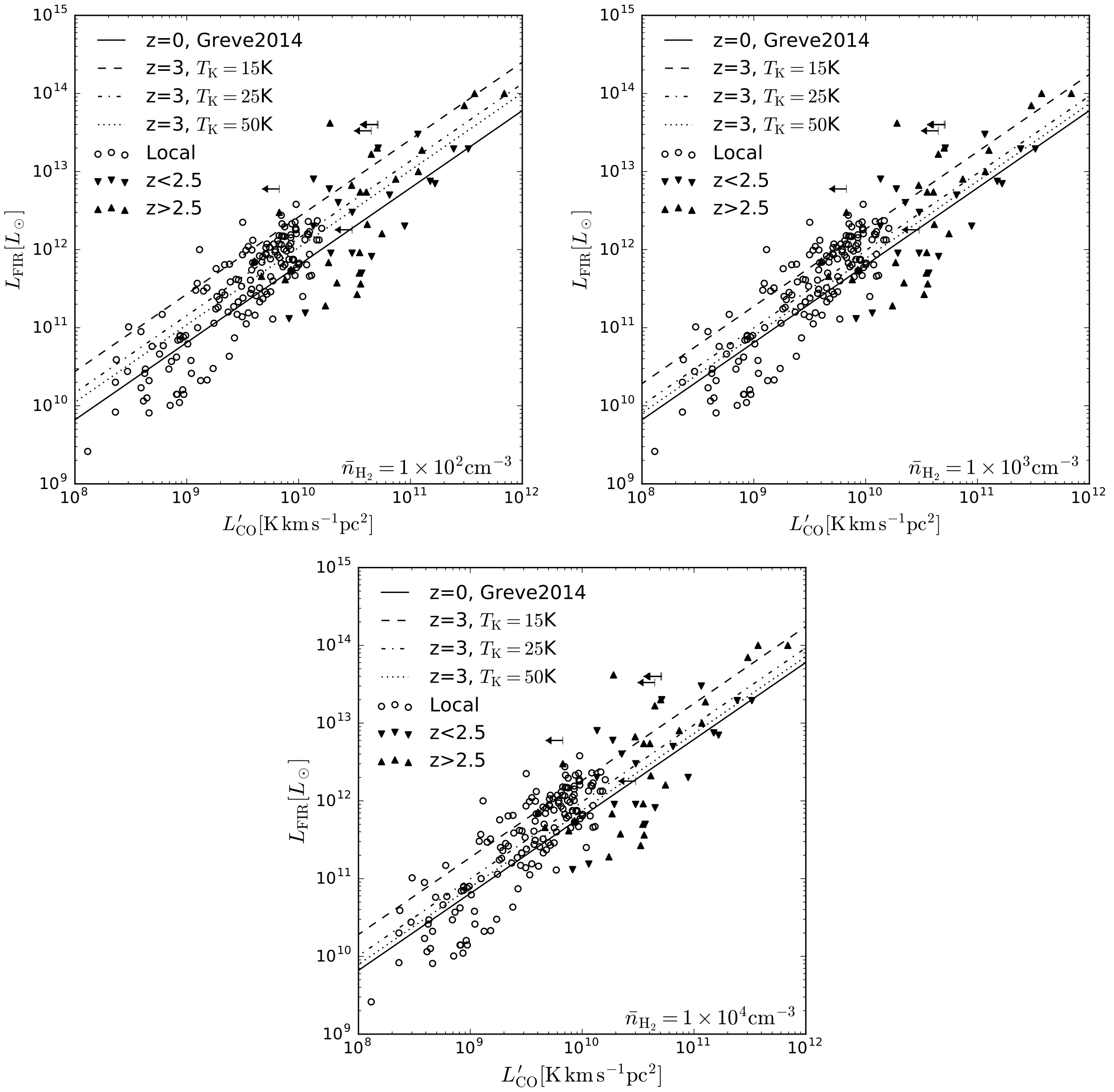

Figure 4.5: The effect of the CMB on the $L_{IR} - L'_{CO}$ relation at $z = 3$ for a range of kinetic temperatures with $\bar{n}_{H_2} = 1 \times 10^3\,\mathrm{cm}^{-2}$ (left), $\bar{n}_{H_2} = 1 \times 10^3\,\mathrm{cm}^{-3}$ (right), and $\bar{n}_{H_2} = 1 \times 10^4\,\mathrm{cm}^{-3}$ (bottom) calculated using RADEX. Data from Sanders et al. (1991); Solomon et al. (1997); Gao & Solomon (2004); Chung et al. (2009).

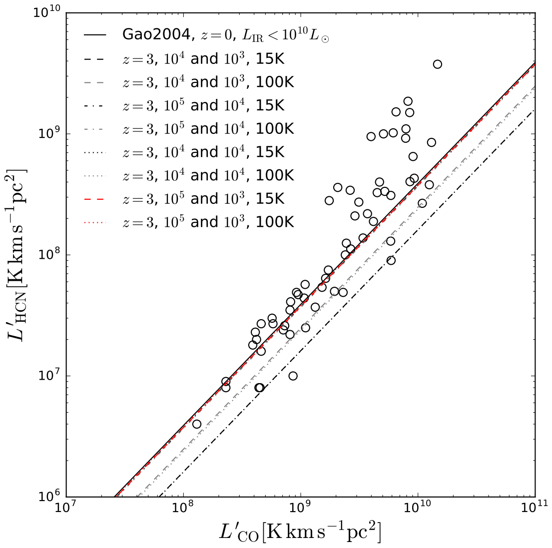

Figure 4.6: The effect of the CMB on the $L'_{\rm HCN}/L'_{\rm CO}$ ratio, a proxy for the dense gas fraction, for a select sample of parameters. The effect is negligible for most parameters, with the greatest effect seen when HCN is least affected. Different temperatures, densities and indeed galaxy integrated measurements will affect this plot, but it is extremely hard to find a realistic set of conditions that could lead to observations overestimating the dense gas fraction.

HCN-CO ratios

Secondary to the discussion at hand but nevertheless interesting is the question of whether and in what way the CMB affects the $L'_{\rm HCN}/L'_{\rm CO}$ ratio. This is harder to model without full galaxy simulations due to the increased range of possible parameters, and I do not investigate all possibilities here. However, I plot in Figure 4.6 a selected sample of conditions at $z = 3$, adjusting the empirical relation found by Gao & Solomon (2004).

This very simple exploration does not include temperature effects, in particular different temperatures for the two species. Furthermore, it does not take into account the structure and density gradients present in real galaxies which will introduce additional, potentially significant, offsets. For example, see Figure 6 in Viti et al. (2014), where the HCN$(1-0)$/CO$(1-0)$ ratio varies by a factor of 10 across NGC 1068. This makes the problem of extrapolating to high redshift far more complicated than for a single species alone and requires careful modelling of a galaxy to achieve reliable results.

4.2.2 Galaxy Averaged Effects

The local active galaxy NGC 1068 has been extensively studied and modelled, most recently by García-Burillo et al. (2014); Viti et al. (2014). Here, I use the physical conditions from Viti et al. (2014), found by modelling the HCN and CO line emission, to generate a toy model galaxy which I then shift to higher redshifts. The toy model is based upon that used in Tunnard & Greve (2016), and uses RADEX to generate an optically thin ensemble[3] of 10^4 putative clouds distributed across analytically defined temperature and density gradients, with the clouds exponentially radially distributed. Note that while the ensemble is optically thin there are no such restrictions on the emission from the clouds themselves.

The toy galaxy is separated into two radial regimes: the AGN dominated core out to $r = 400\,{\rm pc}$ followed by the starbursting spiral arms out to $r = 1750\,{\rm pc}$. Since I only include the effects of the CMB in our model; i.e., I do not consider the effects of cosmological dimming, the radii are largely arbitrary. Over the AGN region the kinetic temperature falls linearly from 200 K to 60 K, and then

---

[3] I.e., the clouds are either non-overlapping or kinematically decoupled. I assume that the unresolved galaxy kinematics lead to a Gaussian profile: I do not model the galaxy kinematics or otherwise include them in the analysis.

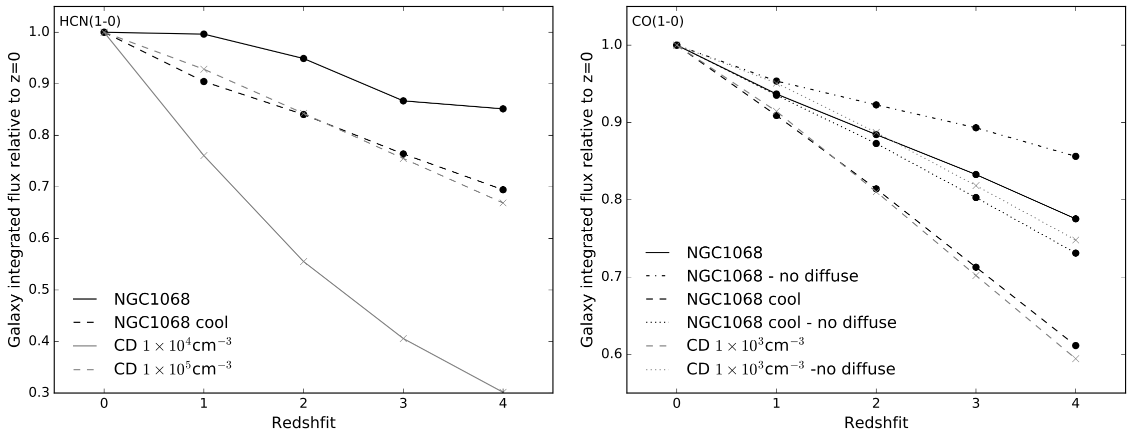

Figure 4.7: Galaxy integrated line emission as functions of redshift for the toy models. Left: HCN$(1-0)$. Right: CO$(1-0)$. The loss of contrast against the CMB is evident even for the NGC 1068 analogue. In both subplots the constant density model (CD) is also plotted in grey with crosses.

down to 40 K at the edge of the starburst. Density falls linearly in log-space, over the same radii as the kinetic temperature, from $10^6\,\mathrm{cm}^{-3}$ to $10^5\,\mathrm{cm}^{-3}$ and then $10^4\,\mathrm{cm}^{-3}$. Throughout I assume $X_{\mathrm{HCN}} = 2 \times 10^{-8}$ and virialised gas.

To examine the effect in less active galaxies I include a cooler version of the model, which is identical but with kinetic temperature pivot points of 100 K, 40 K and 10 K. Note that in no case is the kinetic temperature allowed to fall below the CMB temperature at the model redshift.

The toy models are also run with CO using the same physical parameters as for HCN (except for $X_{\mathrm{CO}} = 5 \times 10^{-5}$), but also adding a diffuse CO field in the form of an additional 10^4 clouds with $n_{\mathrm{H}_2} = 5 \times 10^2\,\mathrm{cm}^{-3}$ and $T_{\mathrm{K}} = 15\,\mathrm{K}$.

The results of the models are shown in Figure 4.7 where the integrated galaxy emission is plotted for the various models. Included in Figure 4.7 are three comparison models with constant temperature and density. These models have uniform temperature of 50 K and uniform densities of $n_{\mathrm{H}_2} = 1 \times 10^4\,\mathrm{cm}^{-3}$ and $n_{\mathrm{H}_2} = 1 \times 10^5\,\mathrm{cm}^{-3}$ for HCN, and $n_{\mathrm{H}_2} = 1 \times 10^3\,\mathrm{cm}^{-3}$ for CO.

Importantly these toy models allow us to begin to account for variations in the physical parameters across the galaxies, as opposed to assuming a constant temperature and density. This approach avoids the potentially problematic assumption of a constant gas density and temperature across the disk, which can overestimate the effect of the CMB as the hot, dense galactic nuclei are far less affected by the loss of contrast than the cooler outer regions. Unsurprisingly, for CO the biggest effect is the assumption of a constant temperature, since for reasonable column densities the line is approximately thermalised at densities as low as $1 \times 10^3\,\mathrm{cm}^{-3}$, whereas HCN is sub-thermally excited even at $1 \times 10^4\,\mathrm{cm}^{-3}$. The effect of the hotter central regions of the galaxy, whether they be heated by an AGN, mechanical turbulence (as is the case for the Central Molecular Zone in our own galaxy; Ginsburg et al., 2015), or a greater surface density of star formation, is important to consider when trying to predict or interpret high redshift observations.

4.3 Discussion

I have shown that, to a lesser or greater extent, the loss of contrast against the CMB with increasing redshift can lead to a shift in the Gao-Solomon relation upwards, increasing the logarithmic intercept. This shift applies whatever the intrinsic trend may be, whether it is super linear, bimodal or indeed if there is no change in the intrinsic relation (García-Burillo et al., 2012; Usero et al., 2015). These results complements the findings of Lintott & Viti (2006) who argued that the apparent HCN deficit in high-z galaxies might be due to metallicity evolution; i.e., suggesting that there is no intrinsic evolution in the Gao-Solomon relation with redshift. Nevertheless, the CMB effects do not appear to be significant in galaxies at least as active as NGC 1068, requiring cooler or less-dense gas to be prevalent in order to exceed the natural scatter in the relationship.

Interestingly, this could lead to a second-order effect on the Gao-Solomon relation at high redshift: if more luminous galaxies are, on average, denser and warmer than less luminous galaxies, then, as redshift increases there will be a gradual shifting of not only the intercept but also the *gradient* of the Gao-Solomon relation. That is to say, if there is no inherent evolution of the Gao-Solomon relation with redshift then one should observe the gradient decreasing and the intercept increasing due to redshift related effects alone. Unfortunately this prediction is extremely challenging to test as it requires statistically significant sampling of less luminous galaxies at high redshift; an observationally unachievable aim at the current time.

The reduced observability of molecular lines at high redshift has further implications, and when considering an entire galaxy there is the additional complication of variations in density and temperature throughout and across a galaxy. Therefore, if a significant fraction of the HCN emission in a galaxy originates from cool gas near the effective critical density, with a core of much denser gas near the galactic centre (reminiscent of the Central Molecular Zone in the Milky Way) this can lead to large fractions of the gas being lost against the CMB. Furthermore, if there is a radial density profile across the galaxy, with the average density at the outer edges much lower than the centre, this will inevitably bias size measurements with the edges much harder to distinguish from the CMB. This would also likely lead to an artificially high Star Formation Efficiency (SFE) being observed towards the edges of high-z galaxies in future resolved studies. The local observation of Gao & Solomon (2004); Wu et al. (2010); Kepley et al. (2014) found that for resolved galaxies the $L_{\rm FIR}/L'_{\rm HCN}$ ratio increases towards the galactic centres, probably due to increased star-formation efficiency (Leroy et al., 2013), suggesting that at high-z the loss of the outskirts is very possible. This last point is currently controversial with the exact opposite trend seen by Usero et al. (2015); Bigiel et al. (2016), who found that the $L_{\rm IR}/L'_{\rm HCN}$ ratio *decreases* towards the centres of local galaxies. In particular, Bigiel et al. (2016) found that star formation does not care for the total density but rather the local density contrast.

A more general but related side note is that the increasing CMB will bias molecular gas detections towards hotter gas. This is not a new result, but is important to keep in mind in the coming decade as next-generation instruments allow for more regular observations of high-z molecular lines.

Some 'observations' of HCN$(1-0)$ at high-z are observations of HCN$(2-1)$ or higher lines which are then converted to HCN$(1-0)$ by making assumptions about the excitation of the gas or by using locally calibrated conversions. Not only are these inherently uncertain, but they will be affected by the CMB differently. For the HCN$(2-1)$ line I show in the appendix that this effect is not significant over the parameter space discussed for the single lines of sight, with the fractional loss in HCN$(2-1)$ brightness temperature closely following that of HCN$(1-0)$. The mid to high-J lines however are far less significantly affected, although they are troubled by potentially being biased by AGN, especially the $J = 4-3$ line (Izumi et al., 2016b; Imanishi et al., 2016).

The toy galaxy models, which attempt to introduce a description of the continuum of physical conditions present within a galaxy, generate contributions from 'clouds' with a single density and temperature. The real effect of the CMB may be greater or smaller than predicted here depending upon the temperature, density and abundance distributions within the observed galaxy. Starburst heated gas and dust is usually cooler and less dense than AGN heated gas (see for example the resolved modelling of NGC 1068 in Viti et al., 2014), which means that starburst galaxies are more susceptible to CMB effects than those dominated by the activity of the central AGN, while normal star-forming galaxies will be the most seriously affected. Furthermore, the presence of an extensive but relatively diffuse CO reservoir tracing $n_{\rm H_2} \sim 5\times10^2-10^3\,{\rm cm}^{-3}$ will be extremely hard to detect above $z \sim 3$ with the fraction of flux that is observable falling to less ~ 0.3 at $z = 3$ and ~ 0.1 at $z = 4$, further biasing attempts to trace molecular gas at these redshifts. Note that the addition of similar diffuse clouds to the HCN toy model has no effect on the maps and integrated emission, as expected given the low column and volume densities. On the other hand, cold and dense gas not yet heated by protostars, not included in the toy models, could contribute significantly to the HCN emission at low-z: this gas would be much more susceptible to the increased CMB at high-z.

The toy galaxy models show that it is important to account for the non-uniform temperatures and densities in galaxies when extrapolating to higher redshift. Even with a generously hot galaxy the affect of the CMB on the integrated emission is non-negligible and must be considered when discussing deviations from the Gao-Solomon relation. The effects on galaxy morphology are far more sensitive to non-uniformities in the kinetic temperature and density than the galaxy integrated line emission, with the cooler and less dense regions lost much more quickly than the hotter and denser regions. The ideal solution to this problem is a suite of SPH simulation with comprehensive chemical and radiative transfer modelling for which the radiative transfer can be calculated for a range of redshifts.

The CO toy galaxy models include a diffuse layer of CO emission spread throughout the disk. While this is reasonable in the local universe, at high-z where UV fields may be significantly enhanced with respect to local values the CO may be efficiently photo-dissociated in low density regions. This would exacerbate the effect seen here.

4.4 Conclusions

In this chapter I have described the hitherto unexplored affect of the CMB on the Gao-Solomon relation with a perspective on explaining the apparent offset observed in high redshift galaxies. This effect has been examined both for single representative lines of sight and for toy galaxy models including a realistic range of physical conditions. While the extent of the effect is strongly sensitive to the temperature and density of the emitting gas there is a systematic offset at $z = 3$ for all reasonable physical conditions, although for the warm, dense gas associated with ongoing star formation this effect is small and is much less than the scatter in the Gao-Solomon relation.

The increasing significance of the CMB on the HCN$(1-0)$ line measurement in cooler galaxies may lead to further variation in the observed Gao-Solomon relation. The cooler, low luminosity end of the relation may rise (being more strongly affected by the CMB), leading to a sub-linear slope. However, if the Gao-Solomon relation is indeed due to galaxy wide HCN and FIR emission from individual star-forming cores then as the temperature of the cores is largely determined by a (presumably universal) star formation process the kinetic temperature of the emitting HCN will also be universal, even between low luminosity normal star-forming galaxies and ULIRGs, and there would be no sub-linear slope. On the other hand, if there is substantial mechanical heating of HCN, as in the galactic Central Molecular Zone, the effect may be pronounced.

While the systematic effect of the CMB unlikely to be important when extending the Gao-Solomon relation to higher redshifts, owing to it being less than the intrinsic scatter in the relation, the effect may still be important for individual galaxies, especially when resolved. By $z = 3$, even the NGC 1068 model lost 10% of the integrated flux, while the cooler model lost more than 20%; in both cases the flux is preferentially lost in the cooler outer regions. This will have significant implications for resolved dense gas studies at $z \gtrsim 2$ unless it is properly accounted for.

Radial temperature and density gradients in galaxies combined with the CMB effects may lead to apparent radial variations in the SFE in high-z galaxies, with the suppression of the HCN line in cooler gas emulating an enhanced SFE in the outer regions of galaxies.

Further study of the effect of the CMB on the observability of galaxy integrated low-J line emission is essential, in particular a full suite of SPH model galaxies with chemical modelling and radiative transfer would allow for a meaningful exploration of the systematic effects of the CMB on unresolved HCN$(1-0)$ observations. The assumption of single 'average' densities and temperatures to represent a galaxy can have significant effects on conclusions compared to more realistic ranges of parameters.

This study demonstrates that a single unresolved line is insufficient when observing at high redshift, as the additional affect of the CMB enormously complicates the interpretation. With the HCN$(1-0)$ line alone it is impossible to distinguish between a compact, hot galaxy where all of the dense molecular gas is observed and an extended, cooler galaxy with significant loss of observable emission against the hotter CMB, a problem not found in the local universe or at other wavelengths.

Chapter 5

Between the Jaws of the Beast: The Molecular Gas in NGC 6240

> *"[W]hen people thought the earth was flat, they were wrong. When people thought the earth was spherical, they were wrong. But if you think that thinking the earth is spherical is just as wrong as thinking the earth is flat, then your view is wronger than both of them put together."*
>
> Isaac Asimov, "The Relativity of Wrong"

This chapter was published in a similar form in Tunnard et al. (2015a).

5.1 Background

In this chapter I will use the MCMC-LVG code discussed and tested in chapters 2 and 3 to study the LIRG merger NGC 6240. The work in this chapter was published in Tunnard et al. (2015a), and makes use of PdBI data reduced to (u, v) visibility tables by R. Neri.

Single-dish surveys of primarily the HCN, but also the HCO$^+$, $J = 1-0$ line towards samples of local (ultra)luminous infrared galaxies ((U)LIRGs) suggest that a larger fraction of the molecular gas in these galaxies is in a dense state compared to that of normal star forming galaxies (Solomon et al., 1992; Gao & Solomon, 2004; García-Burillo et al., 2012), where the HCN/CO $J = 1-0$ luminosity ratio is adopted as a proxy of the dense gas mass fraction (typically ~ 0.1 in LIRGs/ULIRGs cf. ~ 0.03 in normal star-forming galaxies, Gao & Solomon, 2004; Greve et al., 2014). However, to date, only a handful of sources have been analysed using multi-line data-sets of dense gas tracers, in conjunction with radiative transfer analyses, to constrain the dense-gas mass (Krips et al., 2008; Greve et al., 2009; Papadopoulos et al., 2014).

Gas mass conversion factors typically assume: **1)** something about the kinematical state of the gas; typically that it resides within virialized clouds (Bolatto et al., 2013, although see Papadopoulos et al., 2012 for a formulation that allows for a generalised kinematic state): perhaps not unreasonable for dense gas tracers but certainly questionably for CO. **2)** that the lines are optically thick, which is generally a good assumption, at least for the $J = 1-0$ lines. **3)** metallicity and/or molecular abundances. These are particularly uncertain, being strongly affected by the environment the emission is tracing, e.g., photon-dominated regions (PDRs), X-ray dominated regions (XDRs), hot-cores or cold, dark clouds, and are usually a subject of interest in themselves. There are also possible contaminations from other sources, such as mid-IR pumping of HCN (and perhaps HNC and HCO$^+$), which increases the low$-J$ HCN line intensity (Aalto et al., 2007, 2012, 2015a). As we move to higher redshifts the effect of the CMB becomes noticeably non-linear, with the greatest effects on the low$-J$ CO lines, and even in the local universe bright continuum backgrounds could be having significant effects on observed lines and line ratios (Papadopoulos et al., 2000, 2010b). HCO^+ is also subject to a complicated network of ion chemistry reactions, as well as photochemical reactions, making it particularly complicated molecular tracer (Viti et al., 2002; Papadopoulos, 2007).

Optically-thin dense-gas tracers, in particular isotopologues of the main species (e.g., $H^{13}CN$ and $H^{13}CO^+$), can be especially powerful as they provide much tighter constraints on large velocity gradient (LVG) models when combined with their ^{12}C isotopologues. Although usually $40-100\times$, and perhaps up to $\sim 500\times$, less abundant than their ^{12}C isotopologues, optical-depth effects mean that these lines are usually only $\sim 10-15\times$ fainter, and are detectable with the IRAM Plateau de Bure Interferometer (PdBI) and certainly with the Atacama Large Millimeter/submillimeter Array (ALMA) for the closest LIRGs and ULIRGs.

NGC 6240 is an early-stage major-merger galaxy in the constellation of Ophiuchus. Hosting two active supermassive black holes and possessing an infra-red luminosity $L_{8-1000\mu\mathrm{m}} = 10^{11.73}\,L_\odot$ it is a luminous infrared galaxy (LIRG) and a LINER (low-ionization nuclear emission-line region) (Komossa et al., 2003; Lutz et al., 2003; Sanders et al., 2003; Véron-Cetty & Véron, 2006). Studies by Tacconi et al. (1999) and Tecza et al. (2000) have shown that while star formation is concentrated in two nuclei, the molecular gas is predominantly in a turbulent, thick disk between the nuclei. They also demonstrated that the extremely luminous infrared H_2 $S(0)$ and $S(1)$ emission ($L(H_2) \sim 2\times10^9\,L_\odot$) is most likely due to slow C shocks between gas clouds in this dense, turbulent disk; a finding confirmed by the study of the CO spectral line energy distribution (SLED) by Meijerink et al. (2013).

As one of the closest LIRGs the molecular emission in NGC 6240 has been extensively studied. The finding of Greve et al. (2009) that the CO SLED required at least a two-component fit has been extended upon by Papadopoulos et al. (2014), who fitted the CO SLED of CO from $J = 1-0$ to $J = 13-12$ with an "inside out" decomposition, where the results of HCN and HCO^+ $J = 1-0$ to $J = 4-3$ SLED fits are used to constrain the high$-J$ CO lines under the assumption that the high$-J$ CO lines originate in the same dense gas as HCN and HCO^+. Two of their key findings for NGC 6240 were a very high $[^{12}C]/[^{13}C]$ ratio of $300-500$ and that most of the H_2 gas mass is inconsistent with self-gravitating and photoelectrically heated gas, requiring either cosmic ray or turbulent heating. Indeed, Meijerink et al. (2013) model the CO SLED as being entirely due to shock-heated gas. An independent two-phase analysis was also conducted by Kamenetzky et al. (2014), who used a nested-sampling routine to model only the CO SLED, finding a hot, diffuse phase and a cold, dense phase.

As well as presenting a striking CO SLED, NGC 6240 was shown to possess massive ($\sim 120\,\mathrm{M}_\odot\,\mathrm{yr}^{-1}$) molecular outflows at -600, $+800\,\mathrm{km\,s^{-1}}$ by Feruglio et al. (2013) in CO$(1-0)$, while Wang et al. (2014) found that the extended (5 kpc) hard X-ray spectrum (~ 6 keV) is due to $\sim 2200\,\mathrm{km\,s^{-1}}$ outflows, which they ascribe to the nuclear starburst with a supernova rate of $\sim 2\,\mathrm{yr}^{-1}$.

This combination of extreme conditions make NGC 6240 a unique laboratory for star-formation physics under unusual conditions, while the extensive previous molecular observations make this an ideal target for more-complex molecular-line modelling of the ISM.

The outline of this chapter is as follows: I describe the observations and their analysis in § 5.2 and the line extraction in § 5.3. I use the MCMC LVG model discussed in the previous chapter and present the results in § 5.4. The results are discussed in § 5.5 and I outline the conclusions in § 5.6. I adopt cosmological parameters $h = 0.70$, $\Omega_\mathrm{m} = 0.3$ and $\Omega_\Lambda = 0.7$, giving a luminosity distance of 107 Mpc and an angular scale of $0.494\,\mathrm{kpc}/''$ at $z = 0.0245$ (Wright, 2006a; Papadopoulos et al., 2014). To avoid confusion, I note that throughout this chapter, unless explicitly stated otherwise, I present results as x_b^a, where a and b denote the values at the upper and lower limits on the 68% credible interval.

5.2 Observations

Observations of $H^{13}CN(1-0)$, $H^{13}CO^+(1-0)$ and SiO$(2-1)$ in NGC 6240 were obtained with the Plateau de Bure Interferometer (PdBI) on 2008 February 21 and 2008 March 7 in the most extended configuration (PI: J. Graciá-Carpio), obtaining minimum and maximum baselines of 59.7 m (16.8 kλ) and 760 m (215.8 kλ) respectively, centred on the sky frequency of 84.6 GHz. With natural weighting to maximise sensitivity the observations reach a synthesised beam of $1.86'' \times 0.74''$.

The initial data reduction was performed by R. Neri in CLIC, part of the IRAM software package GILDAS[1], while I undertook the (u, v) analysis and imaging using the GILDAS program, MAPPING.

5.3 Spectrum Extraction and Data Analysis

Due to poor signal-to-noise in the (u, v) visibilities I analysed the data independently in both the (u, v) plane and in the final imaged datacube. These two methods are outlined below, and produced spectra consistent on a channel-by-channel basis, within the channel uncertainties.

Elliptical Gaussian and disk models were fitted to the (u, v) visibilities on a channel-by-channel basis, using the GILDAS task UV_FIT and 30 MHz channels. The fitted fluxes and fit rms's were identical for the two models and I adopted the elliptical Gaussian model. Fitting of channels narrower than 30 MHz was attempted but produced pathological fits in multiple channels, presumably due to the poor S/N of the visibilities. The spectrum obtained is shown in Figure 5.1, where I fit two Gaussian profiles and a constant baseline[2]. The SiO$(2-1)$ line is clearly detected and there is a possible detection of H^{13}CN$(1-0)$. The significance of this detection is quantified in § 5.3.2 below. Channel errors are shown at the $\pm 1\sigma$ level and are evaluated individually for each channel, based on uncertainty in the fitted flux. The channel median error is ± 0.8 mJy.

A concern with the (u, v) fit to each channel is the possibility of fitting to a different spatial centre, and thereby unintentionally applying a spatial pseudo-averaging across the channels. I note that most channels were fitted with a centre consistent within the uncertainties ($\sim \pm 0.06''$), while the full range is $0.3''$ in Dec and $0.1''$ in RA, dominated by four outlying channels. These offsets are $< 25\%$ of the fitted FWHMs, and $< 5\%$ of the aperture used for extracting the spectrum from the imaged spectrum (see below), and so this is not a significant effect here.

For imaging, I first continuum-subtracted the data. I extracted the visibilities from the 210 MHz line-free region from 86.47 GHz to 86.67 GHz (rest frame) to define the continuum and subtracted these channel averaged visibilities in the (u, v) plane. The visibilities were imaged in MAPPING and the spectrum extracted in CASA (McMullin et al., 2007) with an elliptical aperture $5.58'' \times 2.22''$, PA $= 162^\circ$ (three times the clean beam), centred on the phase centre RA$= 16^{\rm h}52^{\rm m}58^{\rm s}.890$, Dec$= +02^\circ 24' 03''.90$. This includes conversions from mJy beam^{-1} to mJy and allows for a slightly extended source.

The noise in the imaged cube was estimated with the GILDAS task NOISE to be 0.2 mJy beam^{-1}. To estimate the noise in the spectrum I placed eight apertures, identical to that used for the spectrum extraction, arranged around the science aperture so as to create a regular 3×3 grid with the science spectrum in the centre. I then extracted the spectra from within these eight apertures. Since the cube is continuum subtracted, the signal in these apertures should be entirely noise (both thermal, and artificial from the CLEANing). For each spectrum the rms about zero was found, and then these eight rms's were averaged to produce a final rms for the imaged spectrum of 0.6 mJy channel^{-1}. The spectrum and a single-Gaussian fit are shown in Figure 5.2. I fitted a single Gaussian to the SiO$(2-1)$ line and find a reduced χ^2 of 2.12. Attempts to fit a second Gaussian component consistently lead to pathological results due to all of the putative H^{13}CN$(1-0)$ flux lying in a single channel.

The (u, v) fitted and imaged spectra are compared in Figure 5.3. The channel errors have been offset horizontally for clarity. Every channel is consistent between the two spectra within 1σ rms and there is a good qualitative similarity between the two spectra.

---

[1] `http://www.iram.fr/IRAMFR/GILDAS/`.

[2] All reasonable fits with a linear baseline had a gradient of almost zero. However, due to the randomised starting conditions I use to check for convergence, some solutions with a 1$^{\rm th}$-order polynomial were pathological, and I adopt instead the stable 0$^{\rm th}$ order.

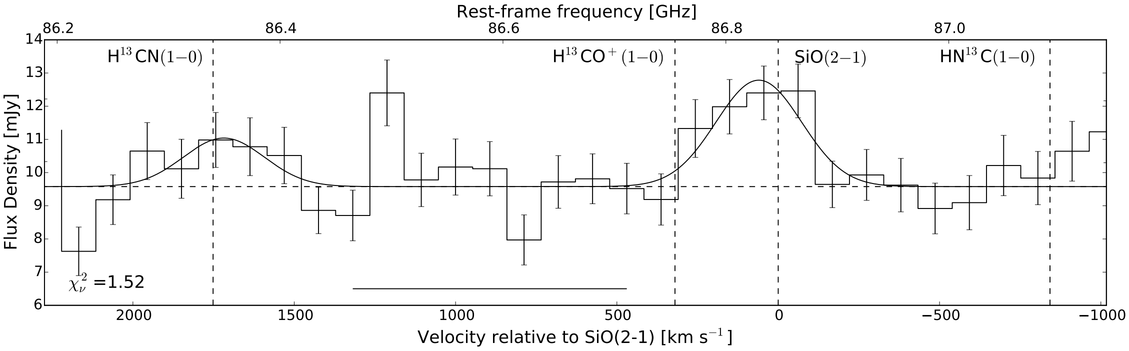

Figure 5.1: The (u, v) fitted spectrum and the least squares two Gaussian plus baseline fit. Velocities are relative to the SiO$(2-1)$ line centre, and rest-frame frequencies in GHz are given at the top of the plot. The 1σ channel uncertainties (median ± 0.8 mJy) from the (u, v) fitting are shown, and do not include the absolute flux calibration uncertainty. The horizontal bar indicates the region identified as line free and used for the continuum subtraction in the imaging step. The reduced χ^2 of the fit is 1.52.

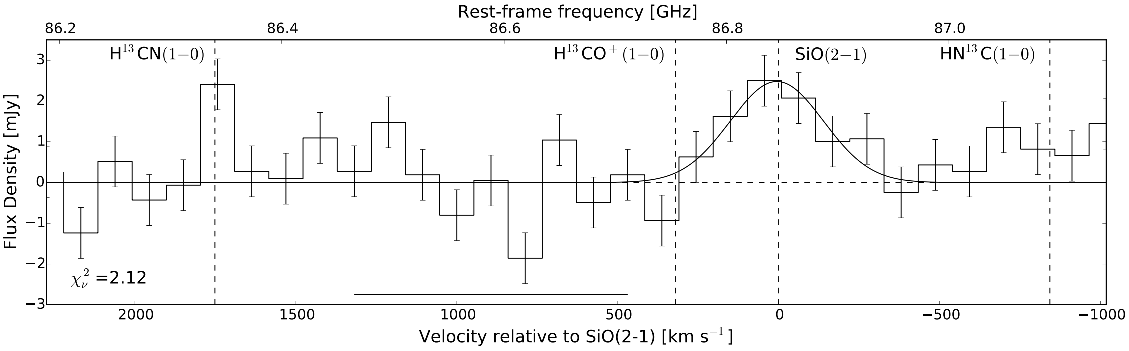

Figure 5.2: The imaged spectrum, extracted with an aperture as described in § 5.3, and the least squares Gaussian fit to the SiO$(2-1)$ line. Velocities are relative to the SiO$(2-1)$ line centre, and rest frame frequencies in GHz are given at the top of the plot. The 1σ rms channel uncertainties (± 0.6 mJy) are shown, and do not include the absolute flux calibration uncertainty. The horizontal bar indicates the region used for the continuum. The reduced χ^2 of the fit is 2.12.

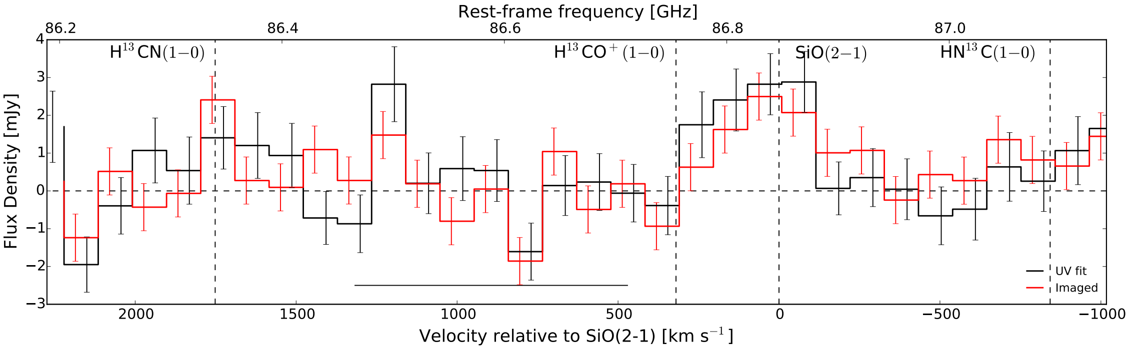

Figure 5.3: A comparison of the (u, v) fitted and Imaged spectra. Axes are as in Figures 5.1 and 5.2. The (u, v) fitted spectrum has been continuum subtracted using the baseline fitted simultaneously with the Gaussian lines. Channel uncertainties have been offset left and right for clarity.

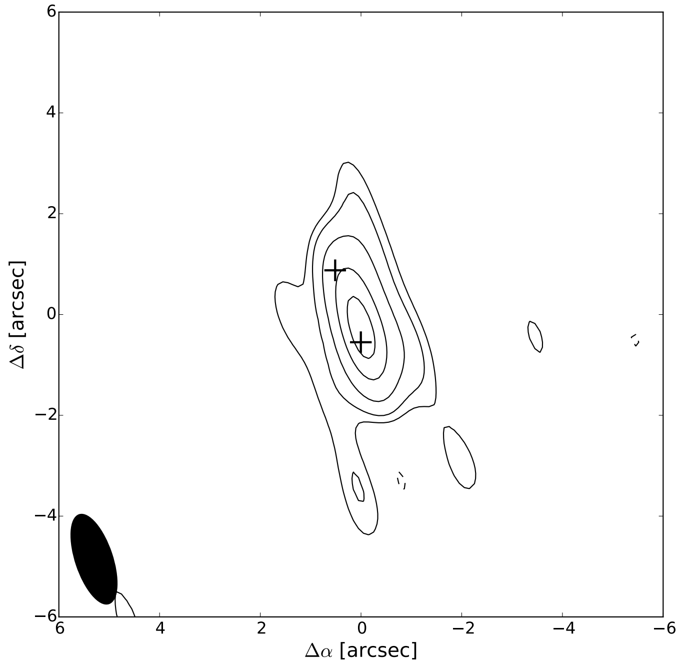

Figure 5.4: The NGC 6240 continuum. Black crosses mark the positions of the AGNs as reported in Hagiwara et al. (2011). Contours are at −3, 3, 5, 10, 20 and 30σ, where $\sigma = 1.63 \times 10^{-4}$ Jy beam^{-1}.

5.3.1 Continuum

We used the 210 MHz region from 86.47 GHz to 86.67 GHz (rest frame) to define the continuum. This region, expected to be line free, was verified as such by an inspection of the (u, v) fitted spectrum. The imaged continuum is shown in Figure 5.4 and I find an aperture extracted flux density of 11.3 ± 1.7 mJy (using the same aperture and method as for the spectrum extraction). This is noticeably larger than the flux density of the elliptical Gaussian fitted to the continuum (u, v) visibilities, which gives a flux density of 9.70 ± 0.29 mJy (9.7 ± 1.5 mJy including the 15% absolute flux calibration uncertainty), although it is still consistent within 1σ. This is in part due to the extended irregularly shaped emission to the south-east of the pointing centre, which is not accounted for in the single component (u, v) fit. Ideally I would fit further components to the residual visibilities (see e.g., Feruglio et al., 2013), but the poor signal to noise ratio of the data prevents meaningfully fitting additional components.

An estimate of the continuum was also provided by the baseline fitted to the (u, v) fitted spectrum. This measured a continuum flux density of 9.58 ± 0.19 mJy, or, including the 15% absolute flux calibration uncertainty, 9.6 ± 1.5 mJy.

The continuum flux density is slightly lower than expected: Nakanishi et al. (2005) found 16.6 ± 1.7 mJy at comparable wavelengths (~ 266 GHz rest-frame) with the Nobeyama Millimeter Array and RAINBOW interferometers. Their measurement is consistent with the imaged continuum at the 2σ level. Expanding the aperture used for the imaged continuum does not significantly change the recovered flux density.

5.3.2 Spectral Lines

Given the low signal to noise ratio of the observations I adopt an elementary statistical approach to line identification. A priori, I expect to detect $\mathrm{H^{13}CN}(1-0)$ and $\mathrm{H^{13}CO^{+}}(1-0)$ based on previous detections of HCN and $\mathrm{HCO^{+}}$ in NGC 6240, while I expect to detect $\mathrm{SiO}(2-1)$ based on comparisons with other LIRGs and major mergers. I give basic parameters for these lines in Table 5.1.

Only $\mathrm{SiO}(2-1)$ is clearly detected in both the (u, v) fitted and imaged spectra. The $\mathrm{H^{13}CN}(1-0)$ line appears to be present in the (u, v) fitted spectrum, but not clearly so in the imaged spectrum, and there is no sign of $H^{13}CO^+(1-0)$ in either. While, if detected, it would be at least partially blended with the $SiO(2-1)$ line, there is absolutely no sign of emission redwards of the $H^{13}CO^+(1-0)$ line centre, or bluewards in the residuals of the $SiO(2-1)$ line fit.

For the statistical test of the line detections I treat the channel uncertainties as being Gaussian distributed. I then sum the channels within $\pm 400\,\mathrm{km\,s^{-1}}$ of the line centre and sum the channel rms's in quadrature, to create a single 'detection' channel and quantify this signal in units of σ_{detect}, the rms of the detection channel. I define the upper limit on the flux density, S_{max}, as the flux density which has a 2% chance of being measured at the value I see or less if the line is in fact present, i.e.,

$$S_{\mathrm{max}} = \left[S_{\mathrm{detect}} + \sqrt{2\sigma^2}\mathrm{erf}^{-1}(2\mathrm{p}-1)\right], \tag{5.1}$$

where S_{detect} is the measured signal in the detection channel, p is the 0.02 probability and erf is the Gauss error function. For $\mathrm{p} = 0.02$ this gives $S_{\mathrm{max}} = S_{\mathrm{detect}} + 2.054\sigma$ (Masci 2011)[3].

Table 5.1: Observed line parameters

Line	ν_0 [GHz]	E_u/k [K]	S_{line} $((u,v))$ [$\mathrm{Jy\,km\,s^{-1}}$]	S_{line} (imaged) [$\mathrm{Jy\,km\,s^{-1}}$]
$H^{13}CN(1-0)^a$	86.340	4.14	0.46 ± 0.07	< 0.8
$H^{13}CO^+(1-0)^a$	86.754	4.16	< 0.4	< 0.4
$SiO(2-1)^b$	86.847	6.25	1.10 ± 0.15	0.90 ± 0.09

[a] Spectral Line Atlas of Interstellar Molecules (SLAIM, Remijan et al., 2007).
[b] The Cologne Database for Molecular Spectroscopy (CDMS, Müller et al., 2005).

I use two measures to test whether the line is actually detected. Firstly, I test against the null hypothesis that one sees a signal at least as bright as in the data, given that there is no line present, i.e., assuming that there is no chance of absorption. This is a one-tailed test with probability

$$\alpha = \frac{1}{2}\left[1 - \mathrm{erf}\left(\frac{x-\mu}{\sqrt{2\sigma^2}}\right)\right], \tag{5.2}$$

and a value consistent with no line is 0.5.

Secondly, I test against the null hypothesis that one sees a signal with an absolute value at least as great as is seen, given that there is no line present, i.e., allowing for absorption. This is a two-tailed test with probability

$$\alpha = 1 - \mathrm{erf}\left(\frac{|x-\mu|}{\sqrt{2\sigma^2}}\right), \tag{5.3}$$

and a value consistent with no line is 1. While the one-tailed test specifically searches for *emission* lines, the two-tailed test makes no such distinction.

For the aperture-extracted $SiO(2-1)$ line and continuum region I found one-tailed values of 7.0×10^{-7} and 0.53 respectively, precisely as expected for a clear line detection and a flat continuum. The two-tailed values are 1.4×10^{-6} and 0.95, again consistent with a clear line detection and a flat continuum. For the imaged $H^{13}CN(1-0)$ line the one and two-tailed tests gave 0.014 and 0.028 respectively, while the (u,v) fitted line gave 0.014 and 0.004. While not entirely conclusive, these tests argue for a detection of the $H^{13}CN(1-0)$ line in the (u,v) fitted spectrum. For $H^{13}CO^+(1-0)$ I subtracted the $SiO(2-1)$ line fit from the spectrum before running the tests. In all cases I find values completely consistent with no line detection with one and two-tailed tests giving 0.51 and 0.98 respectively.

For the $H^{13}CN(1-0)$ line I find an upper limit $S_\nu dv < 0.8\,\mathrm{Jy\,km\,s^{-1}}$ from the imaged spectrum and $S_\nu dv < 0.9\,\mathrm{Jy\,km\,s^{-1}}$ from the (u,v) fitting. The imaged spectrum cannot be well fitted with a

---

[3] `wise2.ipac.caltech.edu/staff/fmasci/UpperLimits_FM2011.pdf`

Gaussian due to almost all of the flux residing in one channel, but for the (u,v) fitted spectrum the Gaussian fit to the line gives $S_\nu \mathrm{d}v = 0.46 \pm 0.07\,\mathrm{Jy\,km\,s^{-1}}$. The SiO$(2-1)$ line was clearly detected in both spectra, and was fitted with line fluxes of $S_\nu \mathrm{d}v = 1.10 \pm 0.15\,\mathrm{Jy\,km\,s^{-1}}$ and $S_\nu \mathrm{d}v = 0.90 \pm 0.09\,\mathrm{Jy\,km\,s^{-1}}$ in the (u,v) fitted and imaged spectra respectively (not including the 15% absolute calibration uncertainty). For H^{13}CO$^+(1-0)$ I first subtracted the SiO$(2-1)$ Gaussian line fit before summing the channel fluxes. I obtain an upper limit of $S_\nu \mathrm{d}v < 0.4\,\mathrm{Jy\,km\,s^{-1}}$ for both spectra. Attempts to simultaneously fit two Gaussians to the SiO$(2-1)$ and H^{13}CO$^+(1-0)$ line centres consistently reported zero line flux for H^{13}CO$^+(1-0)$, consistent with a non-detection/upper limit. All of these measured fluxes and upper limits for the lines are recorded in Table 5.1.

We present 30 MHz channels maps for H^{13}CN$(1-0)$, H^{13}CO$^+(1-0)$ and SiO$(2-1)$ in Figure 5.5. H^{13}CN$(1-0)$ is seen only in the channel over the line centre, at a peak level of 3σ. It is concentrated between the two nuclei, as was seen for HCN$(1-0)$ by Nakanishi et al. (2005). There is no sign of H^{13}CO$^+(1-0)$ in any of the channels, consistent with the non-detection in the (u,v) fitted and imaged spectra. Finally, SiO$(2-1)$ appears at the 3 and 4σ level in the 0 and $-110\,\mathrm{km\,s^{-1}}$ channels centred on the southern nucleus, with a possible 3σ detection in the $+110\,\mathrm{km\,s^{-1}}$ channel about the northern nucleus.

We briefly note than there is no sign of HN^{13}C$(1-0)$ in either of the spectra. Also, if the line were detected it would extend beyond the edge of the spectrum, hindering its analysis. I mark the line frequency in Figures 5.1 and 5.2 for reference.

5.3.3 Spatial Filtering and Missing Flux

Interferometers discretely sample spatial frequencies, and as such may underestimate the true flux of a source. As there are no single-dish observations of any of the targeted lines there is no direct means of measuring the fraction of recovered flux. Instead, I use comparisons with other line and continuum measurements from the literature. Nominally, the observations should only resolve out emission on scales larger than $12''$, three times larger than the largest line and continuum structures seen by Nakanishi et al. (2005), Iono et al. (2007) and Scoville et al. (2015), so it is unlikely that there is a significant loss of flux. However, given the detection of CO on scales $\sim 25''$ by Feruglio et al. (2013) I proceed with caution, despite not expecting HCN or HCO$^+$ emission to be extended on the same scales.

Nakanishi et al. (2005) found the HCN$(1-0)$ line to be more compact than both the continuum and HCO$^+(1-0)$, suggesting that the H^{13}CN$(1-0)$ line in very unlikely to suffer from significant spatial filtering. The HCO$^+(1-0)$ line was slightly more extended, but still only out to scales $\sim 4''$. It is of course possible that the observations of Nakanishi et al. (2005) are also filtering a significant fraction of the flux, and indeed their single-dish flux to interferometric flux ratio was 0.68 for HCN$(1-0)$, using the single-dish data of Solomon et al. (1992). However, the single-dish fluxes are extremely inconsistent, and comparisons with more recent single dish observations give flux ratios of 1.1 ± 0.4 (Greve et al., 2009) and 0.9 ± 0.4 (Krips et al., 2008). I therefore do not believe that the observations are resolving out large scale emission in these lines.

The high-spatial-resolution ($0.5''$) interferometric (ALMA) HCN$(4-3)$ observations of Scoville et al. (2015) have single dish (APEX) counterparts from Papadopoulos et al. (2014). Here the flux ratio is 0.90 ± 0.16, i.e., it is completely consistent with no spatial filtering/almost complete flux recovery. While extrapolating from the $J = 4-3$ transition to the $J = 1-0$ transitions is unacceptably unreliable, combined with the very compact HCN$(1-0)$ emission and the comparisons in the previous paragraph this comparison does argue for the observations recovering most of the H^{13}CN$(1-0)$ flux.

We note that, when comparing ALMA observations with JCMT fluxes Scoville et al. (2015) raised significant concerns regarding the calibration accuracy of the single-dish measurements.

Wang et al. (2013) observed SiO$(2-1)$ in a six local galaxies with the IRAM 30m, including NGC 6240. They found a double peaked line profile, with a combined flux of $0.72 \pm 0.30\,\mathrm{Jy\,km\,s^{-1}}$[4], consistent with the observations. Wang et al. (2013) also observe what may be a marginal H^{13}CO$^+$

---

[4] Converted from the T_A^* fluxes in their Table 1, using their quoted $F_\mathrm{eff} = 95\%$ and the 30m conversion factor $S/T_\mathrm{A}^* = 3.06 F_\mathrm{eff}/A_\mathrm{eff}\,\mathrm{Jy\,K^{-1}}$, with $A_\mathrm{eff} = 0.63$ from `http://www.iram.es/IRAMES/mainWiki/Iram30mEfficiencies`.

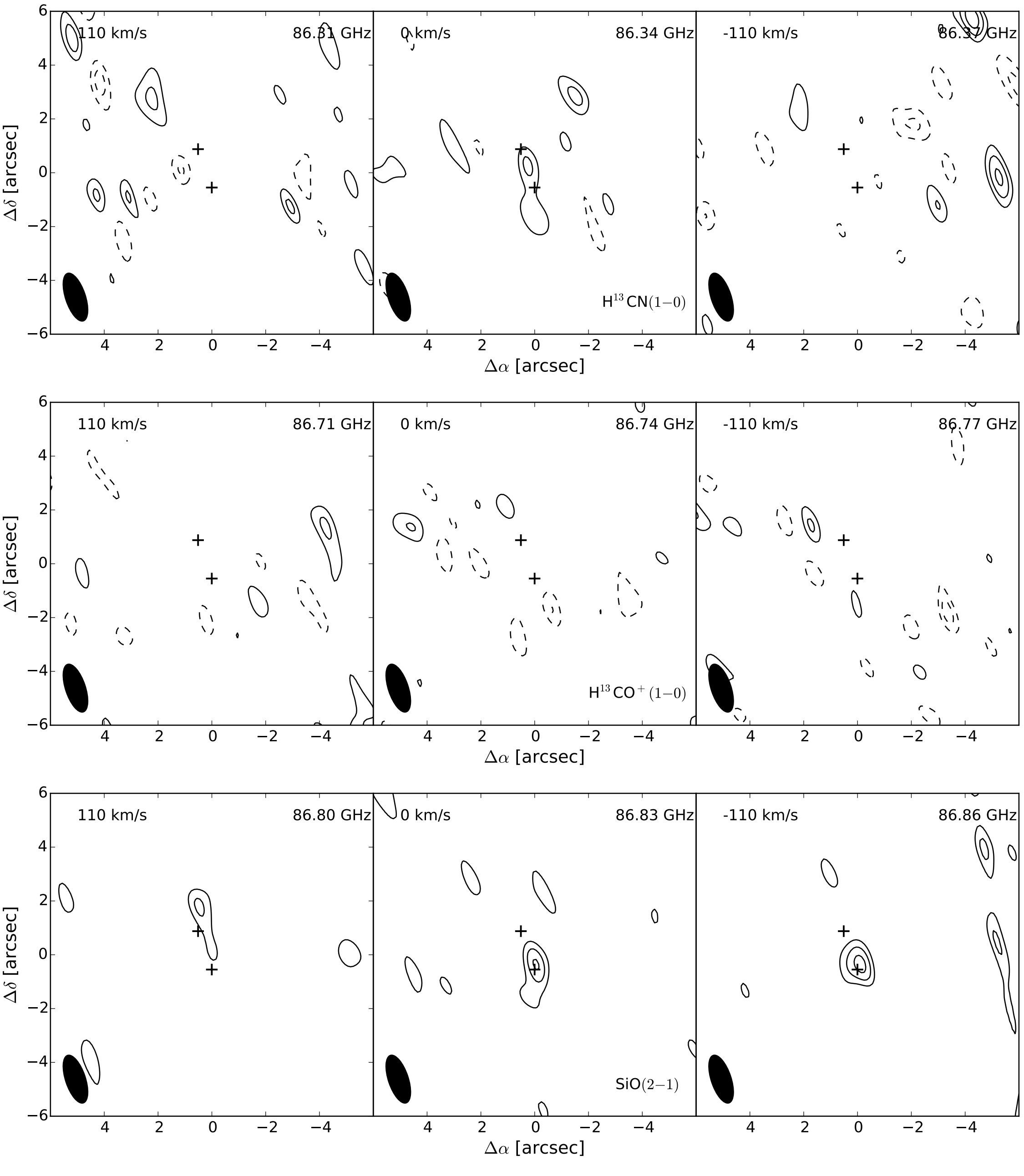

Figure 5.5: Continuum-subtracted channel maps for H^{13}CN$(1-0)$, H^{13}CO$^{+}(1-0)$ and SiO$(2-1)$. Black crosses mark the AGN as reported in Hagiwara et al. (2011) Contours are at −3, −2, 2, 3 and $4\,\sigma$, where $\sigma = 3.9 \times 10^{-4}$ Jy beam^{-1}. H^{13}CN$(1-0)$ appears to be located between the two nuclei, co-located with the the HCN$(1-0)$ (Nakanishi et al., 2005). SiO$(2-1)$ on the other hand appears to be concentrated around the more active southern nucleus.

detection, with a peak $T_{\rm A}^* \simeq 0.55\,{\rm mK}$. I approximate this as corresponding to $\simeq 0.08\,{\rm Jy\,km\,s^{-1}}$, consistent with the upper limit on the line of $0.4\,{\rm Jy\,km\,s^{-1}}$.

5.3.4 The LTE limit

One of the results of Papadopoulos et al. (2014) was the discovery of an extremely high [^{12}C]/[^{13}C] abundance ratio ($300-500$) in NGC 6240, derived from the [CO]/[^{13}CO] ratio. Here I test whether this ratio is compatible with the observed H^{13}CN$(1-0)$ line flux under the simplifying assumption of local thermodynamic equilibrium (LTE).

I compare the H^{13}CN$(1-0)$ line flux to an aggregate of literature measurements of the HCN$(1-0)$ line using

$$S_\nu = \frac{2kT_{\rm A}\nu^2}{c^2}\Omega_{\rm A}, \tag{5.4}$$

$$T_{\rm A}{\rm d}v = \frac{hc^3}{8\pi k\nu^2}N_u A_{ul}\left(\frac{\Omega_{\rm s}}{\Omega_{\rm A}}\right)\left(\frac{1-e^{-\tau}}{\tau}\right), \tag{5.5}$$

where $\Omega_{\rm A,s}$ is the solid angle of the primary beam and source respectively, N_u is the column density of the species in level u in cm^{-2} and A_{ul} is the Einstein A coefficient for the transition between levels u and l (Goldsmith & Langer, 1999). Combining these equations and assuming that HCN and H^{13}CN share the same excitation temperature ($T_{\rm ex}$), so that $N_{{\rm HCN},J}/N_{{\rm H^{13}CN},J} =$ [HCN]/[H^{13}CN], I obtain for the $J = 1-0$ transition:

$$\frac{S_1{\rm d}v_1}{S_2{\rm d}v_2} = \frac{[{\rm HCN}]}{[{\rm H^{13}CN}]}\frac{A_{1,1-0}}{A_{2,1-0}}\frac{\tau_2\,(1-e^{-\tau_1})}{\tau_1\,(1-e^{-\tau_2})}, \tag{5.6}$$

where the subscripts 1 and 2 refer to HCN and H^{13}CN respectively, Therefore, the lower limit on [HCN]/[H^{13}CN] for a given flux ratio is found when both lines are optically thin[5]. In this optically thin LTE case and using the upper limit on the H^{13}CN$(1-0)$ line flux, I find [HCN]/[H^{13}CN]≥ 12. However, exploring a range of optical depths I find that constrained by the $J = 1-0$ lines alone the [HCN]/[H^{13}CN] could be as large as 1000, completely consistent with the high values found by Papadopoulos et al. (2014). I further constrain the isotopologue ratio in § 5.4 using LVG modelling.

A high [^{12}C]/[^{13}C] ratio, leading to high [HCN]/[H^{13}CN] and [HCO$^+$]/[H^{13}CO$^+$] ratios, is also consistent with SiO$(2-1)$ being brighter than both H^{13}CN$(1-0)$ and H^{13}CO$^+(1-0)$ (SiO$(2-1)$/H^{13}CO$^+(1-0) > 3$); SiO$(2-1)$ is not over-luminous, rather the low abundances of the ^{13}C isotopologues leads to unusually faint H^{13}CN$(1-0)$ and H^{13}CO$^+(1-0)$ lines. Usero et al. (2004) found SiO$(2-1)$/H^{13}CO$^+(1-0)$ intensity ratios of about 3 in some regions of NGC 1068, but this galaxy is unusually bright in SiO.

5.4 LVG Modelling

I use the publicly available code RADEX[6] (van der Tak et al., 2007) with collisional data from the Leiden LAMBDA database (Green & Thaddeus, 1974; Flower, 1999; Dayou & Balança, 2006; Lique et al., 2006; Dumouchel et al., 2010; Yang et al., 2010) to model spectral line ratios as a function of the gas phase conditions. I first explore simple, single species (and isotopologue) models before exploring a higher order parameter space. The high dimensionality of the latter precludes the use of a grid method[7], and I use the MCMC LVG model introduced earlier in this thesis to explore the parameter space.

The data from the PdBI were combined with literature data for HCN, HCO$^+$ and CS, shown in Table 5.2. I have available to me the complete HCN and HCO$^+$ ladders from $J = 1-0$ to

---

[5] Assuming that the optical depth of HCN$(1-0)$ is always greater than that of H^{13}CN$(1-0)$ - a safe assumption.

[6] `http://home.strw.leidenuniv.nl/~moldata/radex.html`

[7] At least a naïve one. In principle the grid could be subdivided and parallelised to complete in a reasonable time. However, the total computational overhead would be unchanged.

$J = 4-3$ except for $\mathrm{HCO^+}(2-1)$. The CS lines are more sparsely sampled, with the $2-1$, $3-2$, $5-4$ and $7-6$ lines measured or possessing an upper limit.

In collecting data from a range of telescopes and a range of frequencies it is essential to consider whether there is a common putative source size and whether the single-dish beam-coupling factor of the source and antenna varies significantly between observations. I first convert the line fluxes from the observations and the literature into line luminosities as:

$$L' = 3.25 \times 10^7 \left(\frac{\nu_{\mathrm{obs}}}{\mathrm{GHz}}\right)^{-2} \left(\frac{D_{\mathrm{L}}}{\mathrm{Mpc}}\right)^2 (1+z)^{-3} \left(\frac{\int_{\Delta v} S_v \mathrm{d}v}{\mathrm{Jy\,km\,s^{-1}}}\right), \tag{5.7}$$

where D_{L} is the luminosity distance of the source and L' has units of $\mathrm{K\,km\,s^{-1}\,pc^2}$ (Solomon et al., 1992). Ideally I would have a complete, spatially resolved sample of lines so that I could precisely compare the line brightnesses at specific positions in the source, ensuring that I was comparing cospatial regions of equal size. Working instead with almost entirely unresolved single dish observations I make the following approximations.

Beam coupling: Interferometric observations of the dense-gas tracers exist for only the $J = 1-0$ and $J = 4-3$ HCN and $\mathrm{HCO^+}$ lines, and the CS$(7-6)$ line. Convolved source sizes range from $4''$ to $1''.5$ as frequency increases, with the deconvolved low$-J$ source sizes being quite uncertain, but with very compact high$-J$ deconvolved sizes: $1''.1 \times 0''.6$ for HCN$(4-3)$ (Scoville et al., 2015), and even these most likely being composed of multiple unresolved cores. Even if the low-J emission is more widespread it will still be much smaller than the single dish beam sizes at the associated sky frequencies, so that the beam coupling corrections are $\lesssim 1.05$ and as such are much less significant than the single dish calibration uncertainties ($> 10\%$). Also, this would be a systematic underestimate of the flux, so is accounted for to first order when using line ratios.

Source size: In all of the observations, except for the HCN$(4-3)$ and CS$(7-6)$ of Scoville et al. (2015), the source size is so uncertain that I cannot make any convincing estimates of the source size beyond the flat assumption that there is a common size to all J levels. This could potentially introduce a bias into the models, with the lower$-J$ lines being integrated over a larger area than the high$-J$. However, this acts in the opposite sense to any potential beam coupling errors, which reduce the measured low$-J$ fluxes if the low$-J$ lines are significantly more extended. To some extent these opposing errors correct for any inaccuracies introduced by assuming a common source size and not attempting to account for changes in the beam coupling.

In addition to the observed line ratios I use the dynamical parameter K_{vir} (see Eqn. 2.34) to constrain the models (e.g., Greve et al., 2009; Papadopoulos et al., 2012, 2014). In galactic GMCs in virial equilibrium K_{vir} is ~ 1; however, as was pointed out by Papadopoulos et al. (2014), in the extreme environments of LIRGs and ULIRGS it is very likely that due to unusual GMCs and unbound gas a wider K_{vir} range is necessary to capture the true environment. I therefore follow Papadopoulos et al. (2014) and adopt limits of 0.5 and 20.0 on the allowed K_{vir} values for the models.

5.4.1 MCMC

The MCMC modelling was broken down into a series of runs of increasing complexity, to check for consistency both with existing data and between models. I ran four models with single species and their respective isotopologues: HCN & $\mathrm{H^{13}CN}$ with the detected $\mathrm{H^{13}CN}(1-0)$ line flux, HCN & $\mathrm{H^{13}CN}$ with the upper limit on the $\mathrm{H^{13}CN}(1-0)$ line flux, $\mathrm{HCO^+}$ & $\mathrm{H^{13}CO^+}$ and CS only. The introduction of the ^{13}C isotopologue lines allows for tighter constraints on the gas kinetic temperature and density, while simultaneously placing new constraints on the [HCN]/[$\mathrm{H^{13}CN}$] and [$\mathrm{HCO^+}$]/[$\mathrm{H^{13}CO^+}$] abundance ratios. For the last of the single-phase models I run two models with two species combined: HCN, $\mathrm{H^{13}CN}$ & SiO and HCN, $\mathrm{HCO^+}$, $\mathrm{H^{13}CN}$ & $\mathrm{H^{13}CO^+}$. These models allow for the exploration of the abundances of HCN, $\mathrm{HCO^+}$ and SiO relative to $\mathrm{H_2}$, but more meaningfully the derivation of robust abundance ratios for the species.

Table 5.2: LVG line inputs

Line	ν_0 [GHz]	$S_{\rm line}$ [$\rm Jy\,km\,s^{-1}$]	References[a]
HCN$(1-0)$	88.63	14 ± 2	1, 2, 3, 4
HCN$(2-1)$	177.3	44 ± 7	3
HCN$(3-2)$	265.9	74 ± 7	3, 4, 5
HCN$(4-3)$	354.5	41 ± 6	5
H^{13}CN$(1-0)$	86.34	0.46 ± 0.07	x
HCO$^+(1-0)$	89.19	21 ± 3	2
H^{13}CO$^+(1-0)$	86.75	< 0.44	x
HCO$^+(3-2)$	267.6	141 ± 21	5
HCO$^+(4-3)$	356.7	74 ± 9	2, 5
CS$(2-1)$	97.98	7.5 ± 1.5	5
CS$(3-2)$	145.0	9 ± 2	5
CS$(5-4)$	239.1	54 ± 6	6
CS$(7-6)$	342.9	7.4 ± 1.0	7
SiO$(2-1)$	86.85	1.10 ± 0.15	x

[a]1 = Nakanishi et al. (2005), 2 = Greve et al. (2009), 3 = Krips et al. (2008), 4 = Graciá-Carpio et al. (2008b), 5 = Papadopoulos et al. (2014), 6 = Wang et al. (2011), 7 = Scoville et al. (2015), x = this work.

The limits on the [HC(N/O$^+$)]/[H^{13}C(N/O$^+$)] range were taken from the analysis of the HCN$(1-0)$/H^{13}CN$(1-0)$ line ratio in § 5.3.4 to be 10 and 1000, while the limits on $T_{\rm k}$, $n_{\rm H_2}$ and dv/dr are chosen to be consistent with Papadopoulos et al. (2014). The temperature of the background blackbody, $T_{\rm bg}$, is set to 3 K. For the models with an abundance range I adopted a large range of $-12 < \log_{10}(X_{\rm mol}) < -4$. The model applies the limits as uniform top hat priors in log-space. The full list of models and input parameters/parameter ranges is given in Table 5.3 and the recovered results in Table 5.5. It is one of the successes of the models that they are able to extract realistic results for $X_{\rm mol}$ from this broad, flat prior range, although I caution that the abundance ratios are far better constrained than the abundances themselves due to multiple degeneracies in LVG models.

Table 5.3: MCMC model input parameter ranges.

		All values $\log_{10}$							
		T_k	n_{H_2}	dv/dr	$[^{12}C]/[^{13}C]$	X_{HCN}	X_{SiO}	X_{HCO^+}	X_{CS}
Model	ID	[K]	[cm^{-3}]	[$km\,s^{-1}\,pc^{-1}$]					
HCN & $H^{13}CN$, measured . . .	1a	$0.5-3$	$2-8$	$0-3$	$1-3$	-7.70	...	...	...
HCN & $H^{13}CN$, upper limit . .	1b	$0.5-3$	$2-8$	$0-3$	$1-3$	-7.70	...	...	...
HCO^+ & $H^{13}CO^+$	2	$0.5-3$	$2-8$	$0-3$	$1-3$	...	...	-8.10	...
HCN, $H^{13}CN$ & SiO	3	$0.5-3$	$2-8$	$0-3$	$1-3$	$-12--4$	$-12--4$	...	...
HCN, HCO^+, $H^{13}CN$ & $H^{13}CO^+$	4	$0.5-3$	$2-8$	$0-3$	$1-3$	$-12--4$	...	$-12--4$	...
CS	5	$0.5-3$	$2-8$	$0-3$	...	...	...	...	-9.00

Table 5.4: Three-phase input ranges. All values $\log_{10}$.

Parameter	Hot, shocked	Diffuse	Cold, dense
T_k	$2.0-3.5$	$1.0-3.0$	$0.5-1.5$
n_{H_2}	$1-6$	$1-6$	$4-8$
dv/dr		$-1-3$	
$[CO]/[^{13}CO]$		$1-3$	
$[HCN]/[H^{13}CN]$	–	–	$1-3$
X_{CO}		$-8--2$	
X_{HCN}	–	–	$-12--4$
X_{HCO^+}	–	–	$-12--4$
f	$-2-0$	–	$-2-0$

5.4.2 MCMC Results

The results of the models are presented in Table 5.5. The tabulated results include the means of the 1D marginalised posterior pdfs bounded by the 68% credible interval boundaries, as well as the most likely overall solution[8]. However, when marginalising over parameters subtle relations and correlations between parameters are lost. I therefore also present pair grids with all 2D and 1D pdfs with the 68%, 95% and 99% credible interval boundaries illustrated with contours for the 2D pdfs and vertical lines for the 1D pdfs. In some cases the 1D posterior pdf is doubly peaked: in these cases there is no clear, meaningful way to compress the information into three numbers, so the tabulated results for these cases should be interpreted with caution.

HCN & H^{13}CN - detection

For HCN & H^{13}CN with the detected flux value the MCMC results are shown in Figure 5.6. T_k and n_{H_2} are both relatively well constrained, but due to the introduction of [HCN]/[H^{13}CN] as a free parameter they are much more poorly constrained than for fixed [HCN]/[H^{13}CN]. The value of [HCN]/[H^{13}CN] is moderately constrained, and is most likely greater than 100, and possibly as high as 1000.

Note in particular the strong degeneracy between T_k and [HCN]/[H^{13}CN]. This highlights the dangers of assuming a canonical [^{12}C]/[^{13}C] ratio and applying this as the [HCN]/[H^{13}CN] ratio - such an assumption massively reduces the allowed range of T_k. Therefore if the [HCN]/[H^{13}CN] ratio is indeed know a priori, it is very effective at identifying the true T_k. However, if the wrong [HCN]/[H^{13}CN] is assumed, this will very significantly bias the T_k results.

HCN & H^{13}CN - upper limit

Using only an upper limit on the H^{13}CN$(1-0)$ line flux I obtain the results in Figure 5.7. The resulting pdfs are extremely similar to the detection case with the clear exception of [HCN]/[H^{13}CN], which is no longer peaked but rather unbound at the upper limit of the [HCN]/[H^{13}CN] range. The interesting result here is that while for any given [HCN]/[H^{13}CN] ratio the H^{13}CN$(1-0)$ line is an extremely powerful discriminant of T_k and n_{H_2}, this effect is “absorbed” by allowing [HCN]/[H^{13}CN] to be a free parameter. On the other hand, if the [HCN]/[H^{13}CN] ratio can be well determined from other line ratios an upper limit on an isotopologue flux can be almost as effective at constraining T_k and n_{H_2} as a clear detection.

HCO$^+$ & H^{13}CO$^+$

We present the results of the HCO$^+$ & H^{13}CO$^+$ MCMC in Figure 5.8. Like the second HCN & H^{13}CN model above, I have only an upper limit on the H^{13}CO$^+(1-0)$ line flux, but am still able to use this to place reasonably tight constraints on the model parameters. The mean n_{H_2} is slightly lower than for HCN, as is perhaps expected given the slightly lower critical density of HCO$^+$. The kinetic temperature is better constrained than for HCN, and while the mean of the posterior gives a lower T_k ($\sim$ 25 K cf. 30 K for HCN), the peak of the pdf is slightly higher, at $\sim$ 20 K cf. $\sim$ 10 K for HCN. As with the other upper limit, the [HCO$^+$]/[H^{13}CO$^+$] posterior peaks at the edge of the range allowed by the priors. Uniquely amongst the models however, HCO$^+$ shows a preference for $K_\mathrm{vir} < 2$ in the $\mathrm{d}v/\mathrm{d}r$ vs n_{H_2} posterior pdf. While not significant enough to merit strong conclusions, it might be interpreted as a sign that HCN is present in both dense clouds and shocked regions, while HCO$^+$ is present only in relatively quiescent dense cores (similar to the situation in Arp 220: Tunnard et al., 2015b). The K_vir results for all of the single phase models can be found in § 5.7.1.

The HCO$^+$ model appears to have two loci in $T_\mathrm{k} - n_{\mathrm{H}_2} - \mathrm{d}v/\mathrm{d}r$ space, visible in the top three pair plots of Figure 5.8. This could be indicative of HCO$^+$ tracing two different gas phases with $\sim$ 1 dex difference in density. However, test runs of the MCMC LVG code with artificial lines also show this distribution when some of the line fluxes are shifted by up to ±10% (to emulate mild

---

[8] Note that the most likely solution for the full model, in n-dimensional parameter space, is not the same as the peaks of the individually marginalised posterior pdfs.

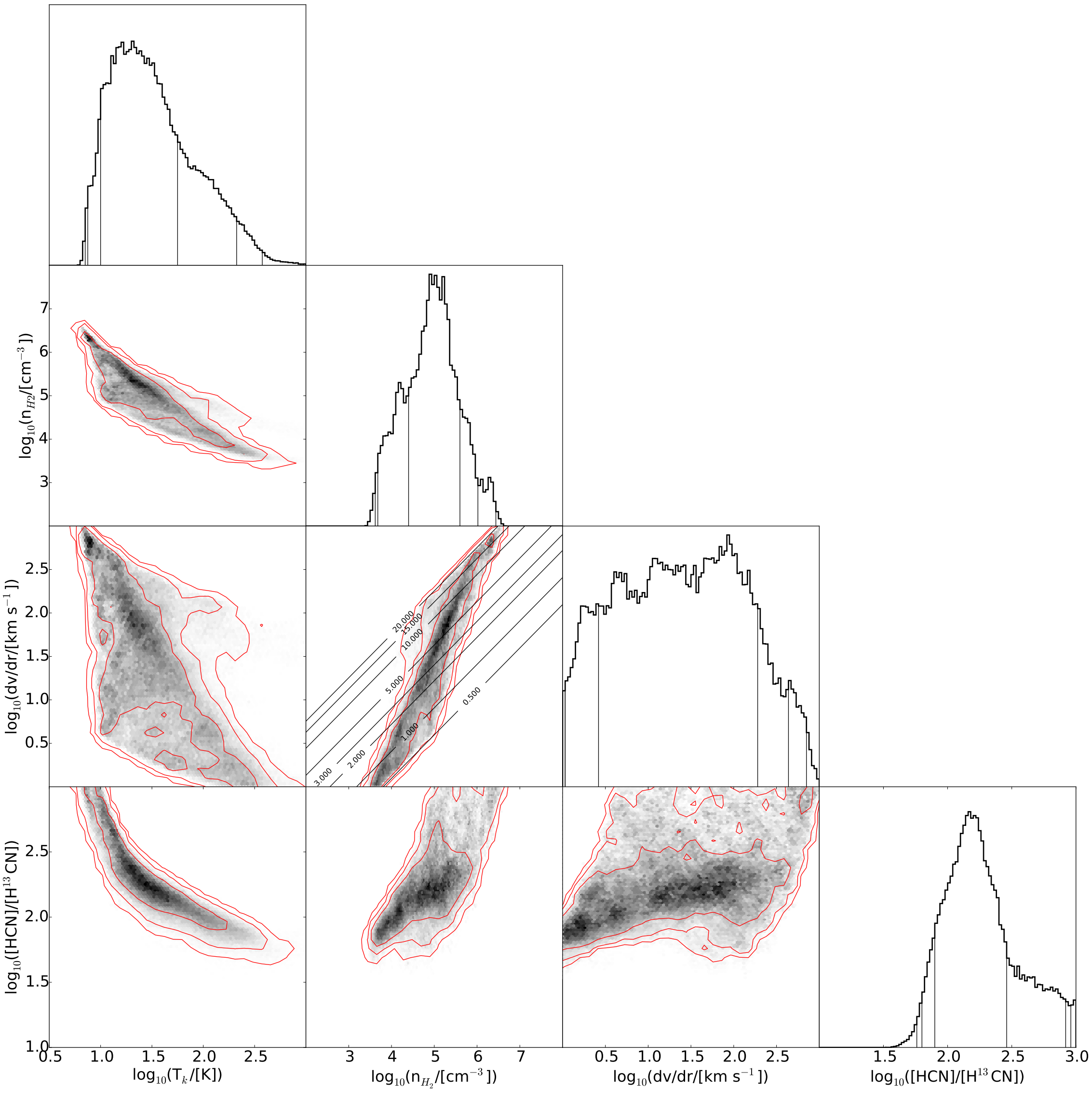

Figure 5.6: HCN & H^{13}CN detection. The lower half and diagonal present the 2D and 1D marginalised posterior pdfs. The 0.68, 0.95 and 0.99 credible-interval levels are marked by the contours in the 2D plots and by the vertical lines in the histograms. Contours of constant $K_{\rm vir}$ have been overlaid on the pdf of dv/dr vs $n_{\rm H_2}$ at levels of 0.5, 1, 2, 3, 5, 10, 15 and 20.

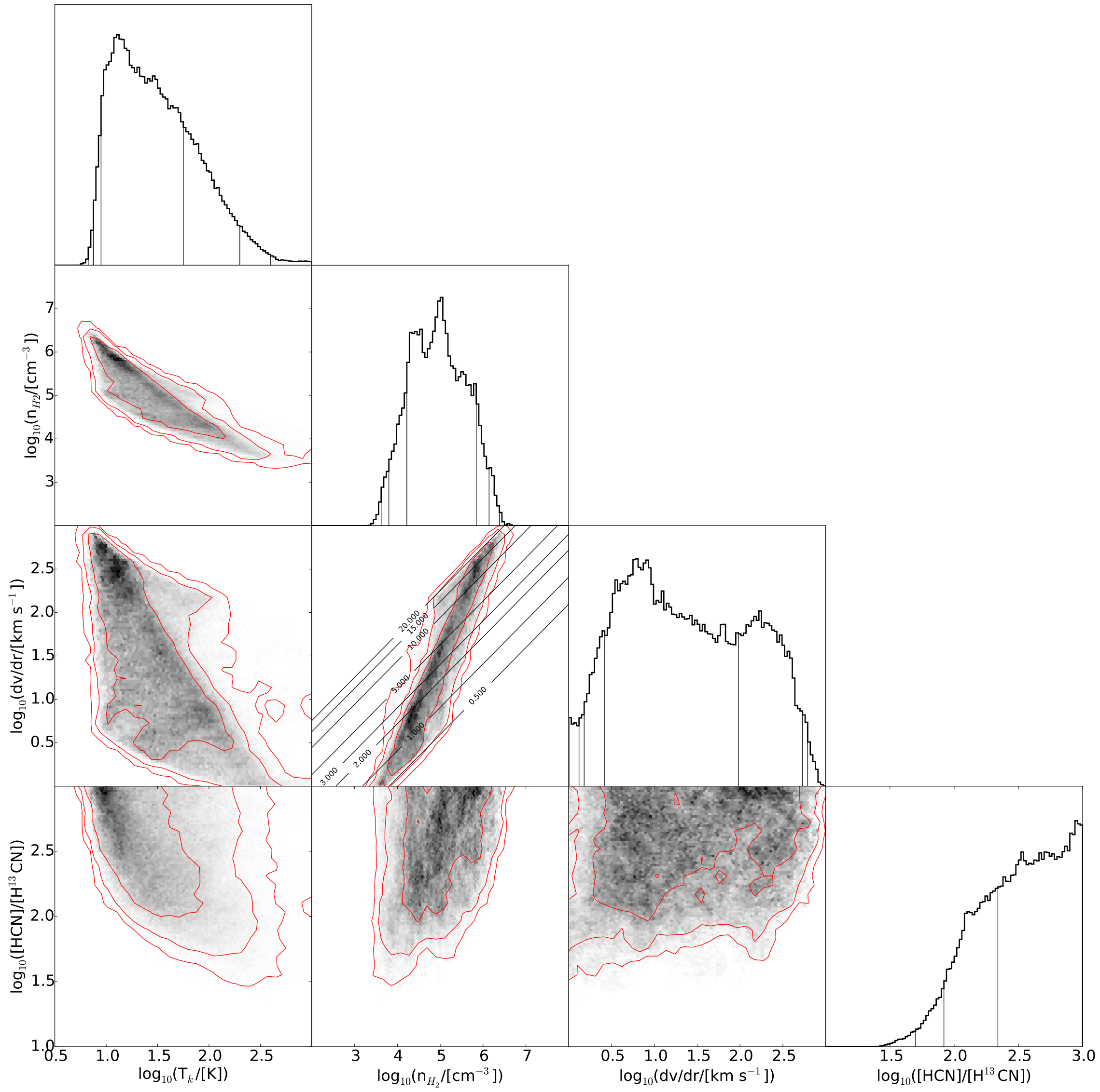

Figure 5.7: HCN & H^{13}CN limit. The lower half and diagonal present the 2D and 1D marginalised posterior pdfs. The 0.68, 0.95 and 0.99 credible-interval levels are marked by the contours in the 2D plots and by the vertical lines in the histograms. Contours of constant $K_{\rm vir}$ have been overlaid on the pdf of dv/dr vs $n_{\rm H_2}$ at levels of 0.5, 1, 2, 3, 5, 10, 15 and 20.

calibration errors in observed data). This bi-modality may therefore simply be due to uncertainties in the line observations.

HCN, H^{13}CN & SiO

The results of the first of the multi-species models is shown in Figure 5.9. The constraints from this model are much worse than those of any of the single species model above, which is most likely a sign that HCN and SiO are tracing significantly different environments in NGC 6240. T_k and n_{H_2} are poorly constrained, as is [HCN]/[H^{13}CN] although the latter still suggests an elevated value > 100.

In the bottom right of Figure 5.9 the pdfs of the abundances X_HCN and X$_\mathrm{SiO}$ are shown. Both possess the expected degeneracy with n_{H_2}, and the ratio between them is approximately constant, with over a dex of scatter in the relationship. The abundance ratio is $\sim 10-100$, but I place more meaningful constraints on this in § 5.4.5. The HCN abundance peaks around 10^{-7}, but extends towards the unphysically high levels of 10^{-4}. This is extremely unlikely (implying an *abundance* ratio [CO]/[HCN] ~ 1), and a clear warning sign that combining HCN and SiO in a single phase is inappropriate in NGC 6240, although the 2D pdfs also reveal that these extremely high abundances are only obtained for the lowest n_{H_2} values. With more SiO lines I would extend this analysis to allow for two separate gas phases, but with only one SiO line this is too poorly constrained to be remotely meaningful.

Other than an exploration of the SiO abundance I do not examine SiO further, as without additional SiO lines the MCMC will simply assign SiO the conditions of any other species it is combined with.

HCN, H^{13}CN, HCO$^+$ & H^{13}CO$^+$

The results of the other mutli-species model: HCN, HCO$^+$ and their isotopologues, are shown in Figure 5.10. This model provides the tightest constraints on all parameters, but the validity of these results rests upon the assumption that the majority of HCN and HCO$^+$ are tracing the same environments. As with the HCN, H^{13}CN & SiO model, I defer a discussion of the validity of this assumption to § 5.5.1.

While T_k and n_{H_2} are more tightly constrained than in any of the single species models, T_k is lower by $\sim 10\,\mathrm{K}$ and $\log_{10}(n_{\mathrm{H}_2})$ higher by ~ 0.4, however the values are consistent between all models within 1σ. I adopt a single isotopologue abundance ratio to encompass [HCN]/[H^{13}CN] and [HCO$^+$]/[H^{13}CO$^+$] and find that it is constrained to lie between 210 and 500, peaking at 350. This relatively high value appears consistent with that found by Papadopoulos et al. (2014) based on CO isotopologue lines if I neglect isotope fractionation. The X_HCN and X_{HCO^+} abundances are tightly constrained around $10^{-8.32}$ and $10^{-9.04}$ respectively, similar to, but perhaps slightly lower than, values I would expect a priori. The abundance ratio [HCN]/[HCO$^+$] is found to be slightly elevated at ~ 5.

5.4.3 CS

The final single phase MCMC model, CS only, is presented in Figure 5.11. The CS results are extremely unusual, requiring high T_k and low n_{H_2} inconsistent with the other "dense gas tracers" and with the expectation that CS will trace denser gas than HCO$^+$ and HCN. This result was checked with grid methods to guarantee that it is not an issue with the MCMC itself; the grids produced indistinguishable results. The collisional rates for CS from the LAMBDA database only extend to 300 K, with RADEX keeping rates constant above this temperature[9], whereas for the other species I have collisional rates up to at least 1000 K. This may go some way to explaining the unusual results, although I do not consider it likely to be the dominant cause.

Papadopoulos et al. (2014) argued that the upper limit on the CS$(7-6)$ line flux precludes the presence of large gas reservoirs with $n_{\mathrm{H}_2} > 10^5\,\mathrm{cm}^{-3}$, consistent with the CS results here, although not with the other species models. Investigating the runs of the model excluding individual CS lines I find that both the CS$(5-4)$ line and the CS$(7-6)$ upper limit contribute considerably to

---

[9] `http://home.strw.leidenuniv.nl/~moldata/radex.html`

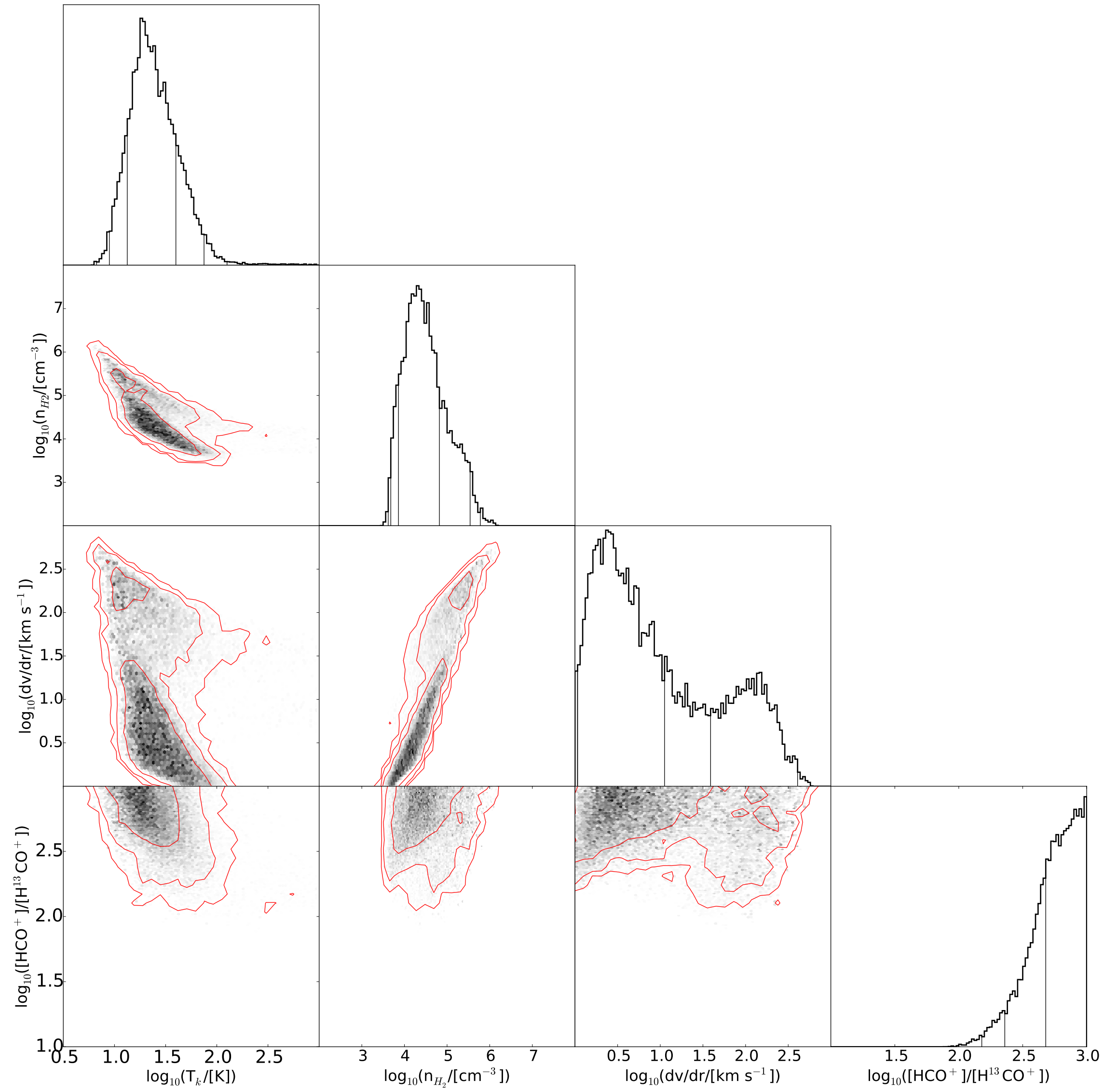

Figure 5.8: HCO$^+$ & H^{13}CO$^+$. The lower half and diagonal present the 2D and 1D marginalised posterior pdfs. The 0.68, 0.95 and 0.99 credible-interval levels are marked by the contours in the 2D plots and by the vertical lines in the histograms. I caution that in the multi-peaked 1D pdfs the credible-interval levels may be unreliable. Contours of constant $K_{\rm vir}$ have been overlaid on the pdf of dv/dr vs $n_{\rm H_2}$ at levels of 0.5, 1, 2, 3, 5, 10, 15 and 20.

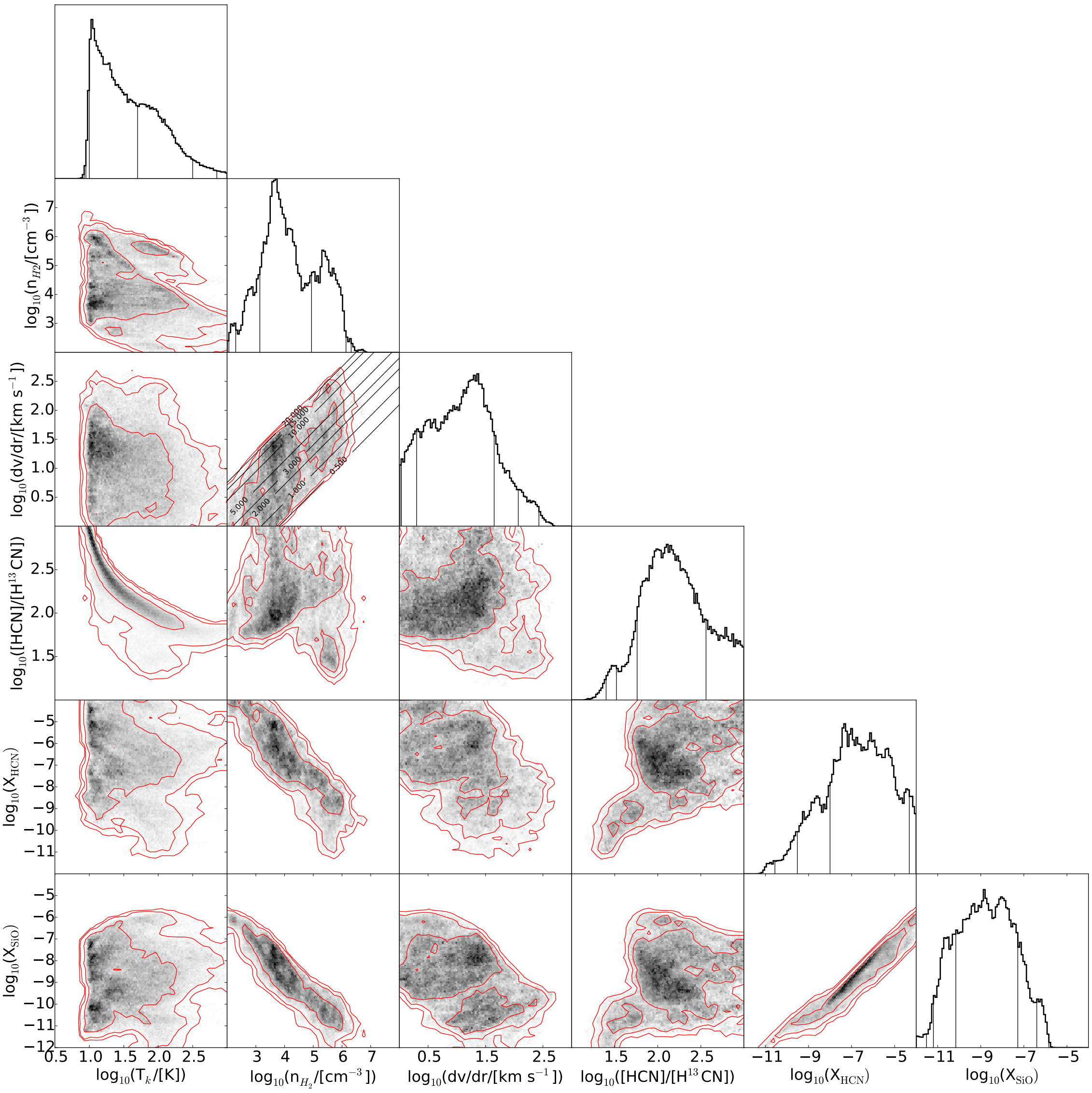

Figure 5.9: HCN, H^{13}CN & SiO. The lower half and diagonal present the 2D and 1D marginalised posterior pdfs. The 0.68, 0.95 and 0.99 credible-interval levels are marked by the contours in the 2D plots and by the vertical lines in the histograms. I caution that in the multi-peaked 1D pdfs the credible-interval levels may be unreliable. Contours of constant $K_{\rm vir}$ have been overlaid on the pdf of dv/dr vs $n_{\rm H_2}$ at levels of 0.5, 1, 2, 3, 5, 10, 15 and 20.

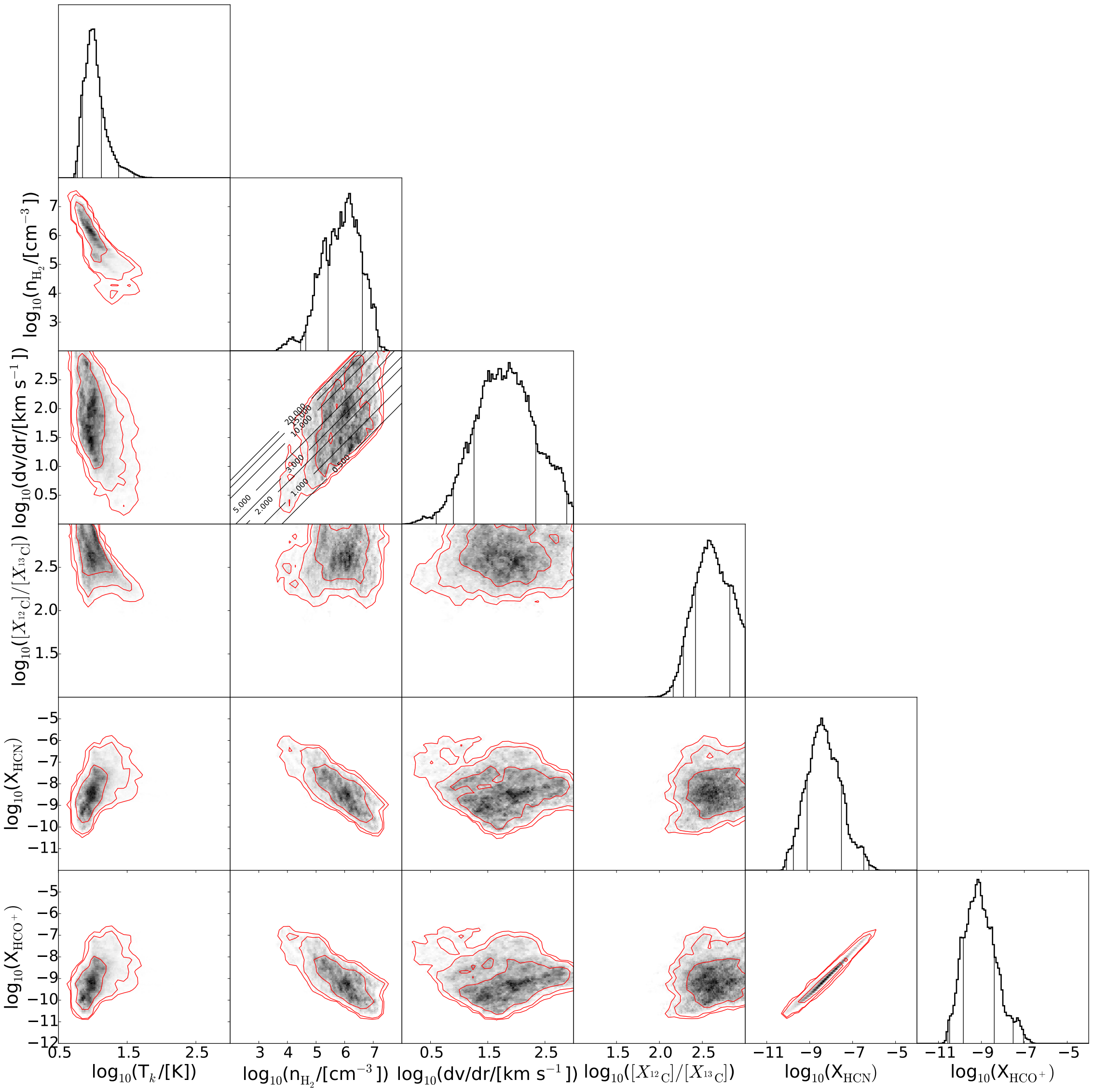

Figure 5.10: HCN, H^{13}CN, HCO^{+} & H^{13}CO^{+}. The lower half and diagonal present the 2D and 1D marginalised posterior pdfs. The 0.68, 0.95 and 0.99 credible-interval levels are marked by the contours in the 2D plots and by the vertical lines in the histograms. Contours of constant $K_{\rm vir}$ have been overlaid on the pdf of dv/dr vs $n_{\rm H_2}$ at levels of 0.5, 1, 2, 3, 5, 10, 15 and 20.

excluding the low$-T_\mathrm{k}$, high$-n_{\mathrm{H}_2}$ regime, but that even excluding both I still find the vast majority of probability density lying in the high T_k, low n_{H_2} region.

Further investigation revealed that the CS model is extremely sensitive to the applied background temperature, with a strong anti-correlation between the background blackbody temperature T_bg and the derived gas kinetic temperature T_k, such that increasing T_bg by 2 K shifts $\log_{10}(T_\mathrm{k})$ from being a limit > 2 to a defined region $1.5 < \log_{10}(T_\mathrm{k}) < 2.5$, and with $T_\mathrm{bg} = 10\,\mathrm{K}$ $1.0 < T_\mathrm{k} < 1.8$. Throughout, the fitted density remains essentially unchanged. This effect is not seen in the single phase HCN models (although I have seen this have extremely significant effects with other line fluxes from other galaxies), suggesting that while the HCN results are relatively robust to changes in T_bg, the CS in NGC 6240 is not.

I also experimented with setting T_bg to be a free parameter, but these runs are too poorly constrained with the current line fluxes and were not found to produce useful results.

We do not compare the CS results to the other species as the results are highly suspect, and if they are accurate then CS is tracing regions with significantly different properties to the other species. In § 5.5.5 I present an alternative explanation for the unusual CS results, consistent with the other species models.

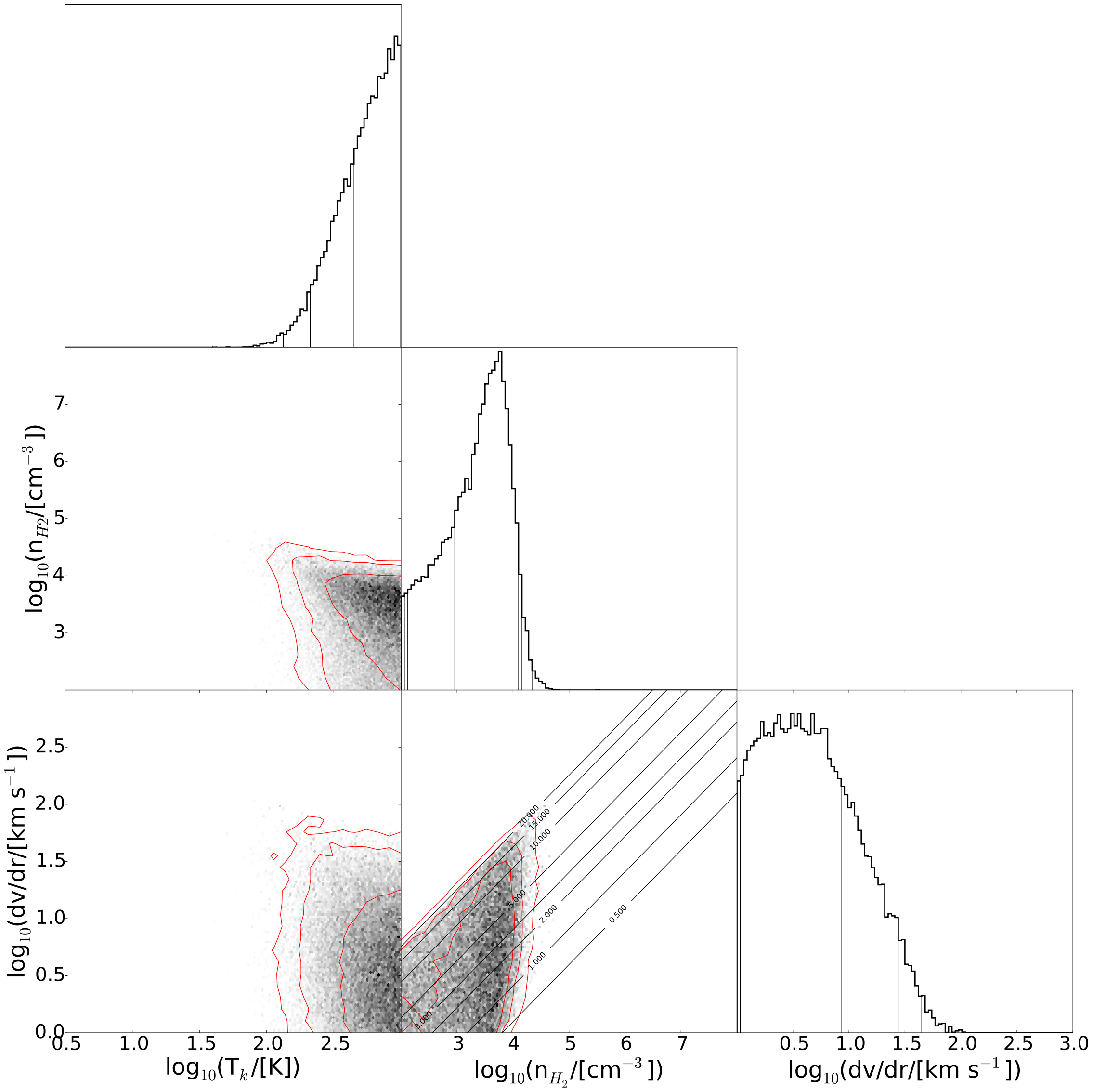

Figure 5.11: CS. The lower half and diagonal present the 2D and 1D marginalised posterior pdfs. The 0.68, 0.95 and 0.99 credible-interval levels are marked by the contours in the 2D plots and by the vertical lines in the histograms. Contours of constant $K_{\rm vir}$ have been overlaid on the pdf of dv/dr vs $n_{\rm H_2}$ at levels of 0.5, 1, 2, 3, 5, 10, 15 and 20.

Table 5.5: MCMC Results

Posterior mean results and the upper and lower limits on the 68% credible interval.

					All values $\log_{10}$			
Model	Model ID	T_{k} [K]	$n_{\mathrm{H_2}}$ [cm^{-3}]	dv/dr [km s^{-1} pc^{-1}]	$\frac{[\mathrm{HC(N/O^+)}]}{[\mathrm{H^{13}C(N/O^+)}]}$	X_{HCN}	X_{SiO}	$X_{\mathrm{HCO^+}}$
HCN & $H^{13}CN$, measured ...	1a	$1.52^{1.75}_{1.00}$	$4.93^{5.60}_{4.40}$	$1.28^{2.28}_{0.42}$	$2.27^{2.46}_{1.90}$	...	...	...
HCN & $H^{13}CN$, upper limit ..	1b	$1.50^{1.75}_{0.95}$	$4.95^{5.84}_{4.22}$	$1.39^{1.98}_{0.42}$	$2.49^{3.00}_{2.34}$	...	...	...
HCO^+ & $H^{13}CO^+$	2	$1.39^{1.60}_{1.13}$	$4.51^{4.82}_{3.86}$	$1.00^{1.05}_{0.03}$	$2.74^{3.00}_{2.68}$	...	...	...
HCN, $H^{13}CN$ & SiO	3	$1.60^{1.70}_{1.00}$	$4.20^{4.94}_{3.14}$	$1.10^{1.65}_{0.30}$	$2.20^{2.56}_{1.76}$	$-6.80^{-4.32}_{-8.00}$	$-8.80^{-7.28}_{-10.16}$	...
HCN, HCO^+, $H^{13}CN$ & $H^{13}CO^+$	4	$1.04^{1.13}_{0.85}$	$5.87^{6.62}_{5.42}$	$1.81^{2.34}_{1.26}$	$2.61^{2.82}_{2.42}$	$-8.32^{-7.52}_{-9.12}$	...	$-9.04^{-8.4}_{-9.84}$
CS	5	$2.71^{3.0}_{2.65}$	$3.3^{4.1}_{3.0}$	$0.68^{0.93}_{0.03}$	...	...	...	...

Joint maximum likelihood results.

					All values $\log_{10}$			
Model	Model ID	T_{k} [K]	$n_{\mathrm{H_2}}$ [cm^{-3}]	dv/dr [km s^{-1} pc^{-1}]	$\frac{[\mathrm{HC(N/O^+)}]}{[\mathrm{H^{13}C(N/O^+)}]}$	X_{HCN}	X_{SiO}	$X_{\mathrm{HCO^+}}$
HCN & $H^{13}CN$, measured ...	1a	0.86	6.3	2.7	3.0	...	...	...
HCN & $H^{13}CN$, upper limit ..	1b	0.88	6.3	2.7	3.0	...	...	...
HCO^+ & $H^{13}CO^+$	2	1.1	4.8	1.1	3.0	...	...	...
HCN, $H^{13}CN$ & SiO	3	0.94	6.0	2.0	2.9	−8.0	−10.5	...
HCN, HCO^+, $H^{13}CN$ & $H^{13}CO^+$	4	0.96	6.3	1.7	2.6	−9.0	...	−9.8
CS	5	3.0	3.5	0.1	...	...	...	...

5.4.4 SLEDs

In Figure 5.12 I present the model fits to the observed SLEDs. These provide a qualitative means of inspecting the quality of the model fits. I compare the observed SLEDs to the SLEDs of the maximum-likelihood solutions, fitted with a cubic spline to guide the eye. Since I am fitting line ratios I do not obtain an absolute scaling of the SLED, only the shape, and so the model SLEDs are normalised to the mean of the observed lines.

In the SiO model the fit to the HCN SLED is significantly worse than for HCN alone, lying very far from the observed SLED. In model 4, both HCN and HCO^+ are fitted quite well, but the fits for both are slightly worse than the single species fits. This is not surprising: I have forced the two to occupy the same gas phase while the two additional degrees of freedom, X_{HCN} and X_{HCO^+}, will only, to first order, shift the SLEDs of HCN and HCO^+ relative to one another.

These results for model 3 raise further questions regarding the accuracy of this particular model, and suggest that a single phase treatment of HCN and SiO is insufficient. Similarly, the slightly worse fits of the model 4 SLEDs suggests that two phases may be necessary, even for these two dense gas tracers. Therefore, in § 5.4.6 I explore an elementary two phase approach for model 4. The single SiO line prohibits this approach for model 3.

5.4.5 Abundance Ratios

The molecular abundances in Figures 5.9 and 5.10 are quite poorly constrained, largely due to degeneracies with n_{H_2} and $\mathrm{d}v/\mathrm{d}r$. The fitted values (Table 5.5) are slightly lower than the adopted canonical values of $X_{\mathrm{HCN}} = 2 \times 10^{-8}$ and $X_{\mathrm{HCO}^+} = 8 \times 10^{-9}$. However, the pair plots reveal that the abundance *ratios* are much better constrained. The pdfs of these ratios are shown in Figure 6.16.

From models 3 and 4 I find abundance ratios $[\mathrm{HCN}]/[\mathrm{SiO}] = 80^{330}_{10}$ and $[\mathrm{HCN}]/[\mathrm{HCO}^+] = 5.2^{7.0}_{4.7}$ respectively. While the $[\mathrm{HCN}]/[\mathrm{HCO}^+]$ ratio is very well constrained, [HCN]/[SiO] is very uncertain, due largely to having only a single SiO line but also likely because HCN and SiO are not actually tracing the same gas. While the relationship in Figure 5.9 appears to be relatively tight, the “blobbing” of the 2D pdf at both high and low ends leaves the ratio poorly determined.

5.4.6 Model Extensions

One of the strengths of the MCMC LVG model is the ease with which it can be extended to explore additional parameters. Below, I examine five extensions: varying the background radiation field temperature, T_{bg}, adding a second gas phase to the model, adding a second gas phase and the CO and ^{13}CO lines, a study of the $[^{12}\mathrm{C}]/[^{13}\mathrm{C}]$ abundance ratio and finally a three-phase model. In particular these extensions allow me to explore two key questions: **1)** is there an elevated $[^{12}\mathrm{C}]/[^{13}\mathrm{C}]$ ratio in NGC 6240? **2)** what are the mass−luminosity conversion factors, α_{CO} and α_{HCN}, in NGC 6240?

The effect of $\mathbf{T_{bg}}$

First, I explore whether a slight to moderate increase in the background radiation field above that of the CMB can improve the fits of the two species model 4: the HCN + HCO^+ single phase model. The models were rerun with fixed background temperatures of 10, 20 and 50 K. I explored introducing T_{bg} as a free parameter, but found that this introduced huge scatter in all parameters.

For some very active galaxies, with luminous dust emission, the background radiation from the dust may significantly affect the line ratios (Papadopoulos et al., 2010a). For dense molecular gas tracers, neglecting this can lead to extremely unusual solutions from RADEX fits to the line ratios. I explored this possibility in NGC 6240 considering the 52 K black body dust temperature described by Tacconi et al. (1999), but found no consistent solutions over multiple runs, and pathological fits to the SLEDs. This is in fact consistent with the inconsistencies between the CO and 1.3 mm continuum estimates of gas mass commented on by Tacconi et al. (1999): they find that the dust co-located with the dense gas was most likely significantly cooler (perhaps 20-25 K), and furthermore that the shock heated gas is thermally decoupled from the cooler dust.

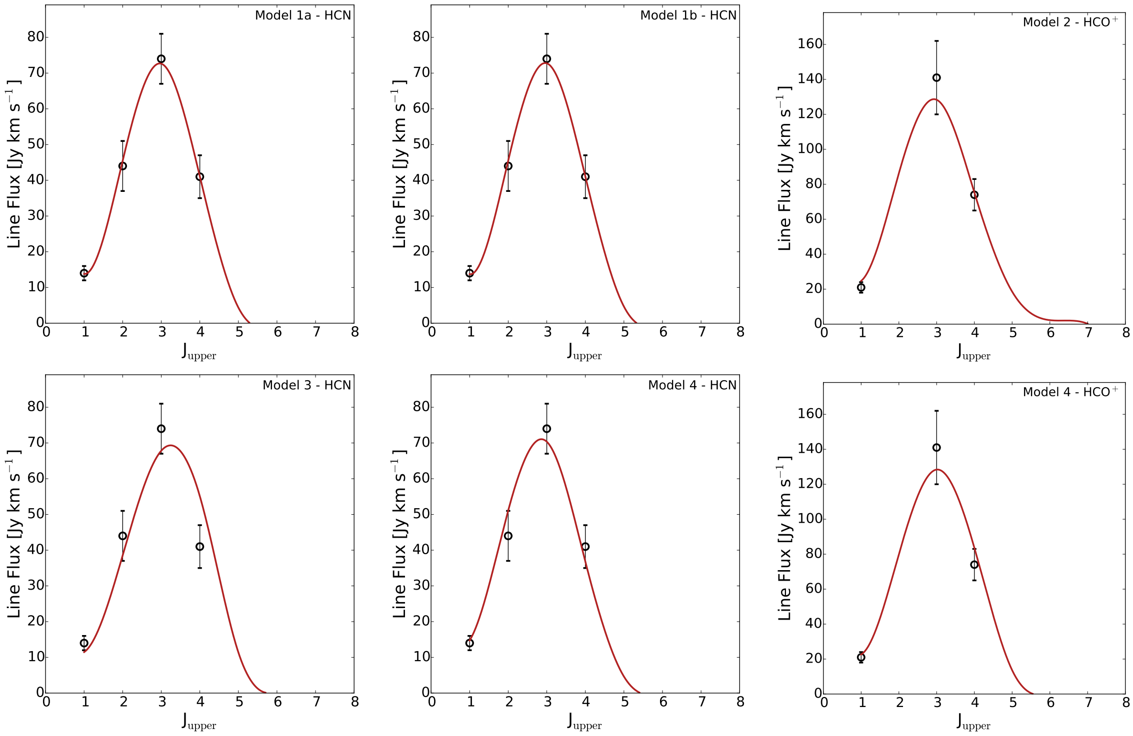

Figure 5.12: SLED fits for models (clockwise from top left) 1a, 1b, 2, 4 (HCO^+), 4 (HCN) and 3. The single species models all fit the SLEDs very well.

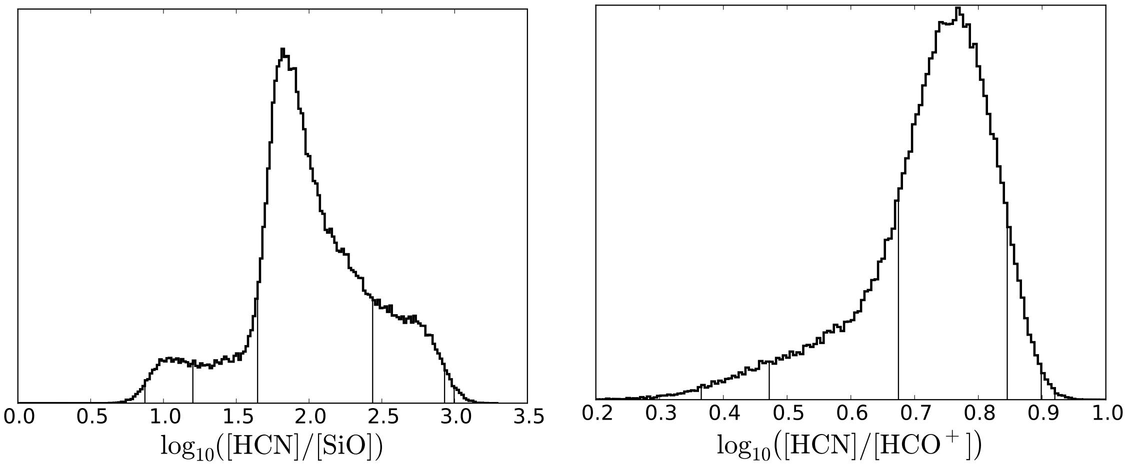

Figure 5.13: Marginalised posterior pdfs for the [HCN]/[SiO] and [HCN]/[HCO^+] abundance ratios from models 3 and 4 respectively. The 68%, 95% and 99% credible intervals are indicated by the vertical lines. The [HCN]/[HCO^+] is particularly well constrained as $5.2^{7.0}_{4.7}$.

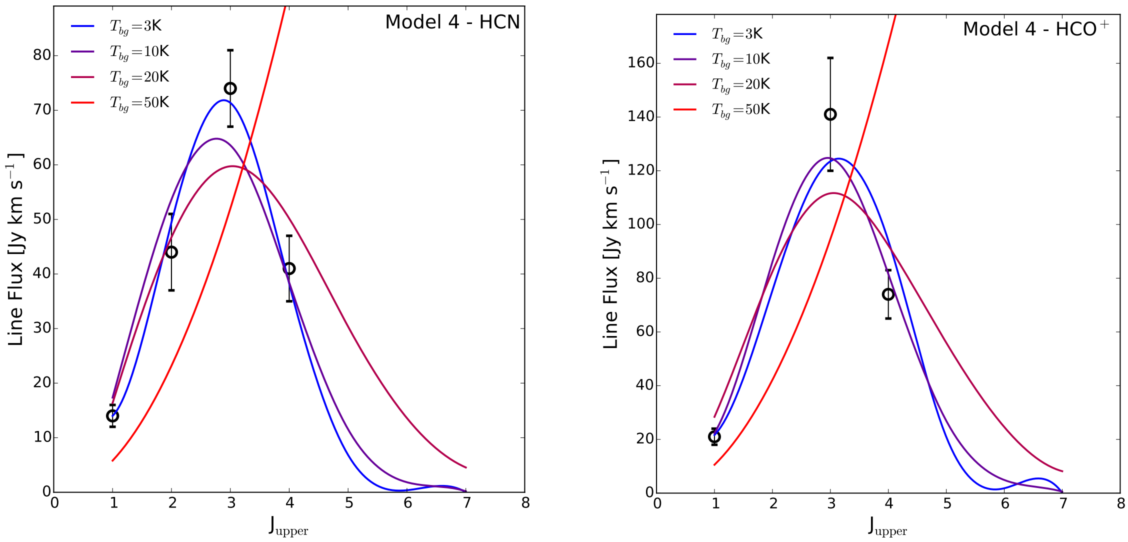

Figure 5.14: SLED fits for the HCN & HCO$^+$ single phase model, with $T_{\rm bg}$ increasing as 3, 10, 20 and 50 K. The best fits are from the 3 K background, and the two observationally motivated background temperatures (20 and 50 K) both produce much worse fits.

I find that increasing $T_{\rm bg}$ to 10 K marginally improves the HCO$^+$ SLED fit, at the expense of a sightly worse HCN SLED fit. To match observations the solutions are constrained to give positive fluxes, which indirectly constrains the gas kinetic temperature in these models to be $\gtrsim T_{\rm bg}$. The results push against this limit, so that $T_{\rm k}/T_{\rm dust} \sim T_{\rm k}/T_{\rm bg} \simeq 1$, which is unlikely to be reasonable in the extensively shocked environment of NGC 6240 (Meijerink et al., 2013; Papadopoulos et al., 2014), unless the HCN and HCO$^+$ are located not in shocks but in cold, dense cores. As $T_{\rm bg}$ is increased, the fits become progressively worse, with 50 K not remotely fitting the SLED and producing $\chi^2 > 1300$ (cf. $4-6$ for $T_{\rm bg} = 3-10$ K). The SLED fits for these models are shown in Figure 5.14.

The inability of the results to find good a solution for a 50 K background is unsurprising, but the poor solution at 20 K is slightly more interesting. One possible, and I would argue likely, explanation could simply be that the HCN and HCO$^+$ emission are tracing the relatively quiescent, (potentially cosmic ray heated) regions of shielded, dense gas, i.e., they are performing as classical dense gas tracers. This is consistent with the marginal improvement (worsening) of the SLED fit of HCO$^+$ (HCN) when $T_{\rm bg}$ is increased from 3 K to 10 K, as HCO$^+$ is probably more extended and less shielded than HCN, so subject to a slightly stronger background radiation field. It is also consistent with the very high HCN/CN line ratio of 2 found by Aalto et al. (2002), which is evidence of large reservoirs of (u, v)-shielded gas (Fuente et al., 1995; Greaves & Church, 1996).

From these results I conclude that there is no evidence to support using a greater than CMB background radiation field in the models of NGC 6240, and proceed with the 3 K CMB field used thus far.

Two-phase modelling - HCN & HCO$^+$

As was shown in § 5.4.4, the models for HCN and HCO$^+$ in a single gas phase and a CMB background were able to simultaneously reproduce the HCN and HCO$^+$ SLEDs, but with worse fits than with each species fitted independently. Here, I extend the model to include a second, non-interacting gas phase. This is strongly physically motivated as single dish observations across the galaxy are sampling multiple non-interacting gas phases confused within the beam.

Each of the two phases has their own kinetic temperature, density, and velocity gradient while they share common HCN and HCO$^+$ abundances, as well as a single [HC(N/O$^+$)]/[H^{13}C(N/O$^+$)] abundance ratio[10]. The fluxes from the two phases are added, weighted by a free parameter,

---

[10] While this is undesirable, I am forced to use shared abundances to minimise the number of free parameters I attempt to constrain with the few line ratios. A model was attempted with free abundances in each phase, but this

Table 5.6: HCN & HCO$^+$ Two-Phase Model Solutions. All values $\log_{10}$.

Parameter	Mean	min χ^2
$T_{\mathrm{k},1}$	$1.8^{2.8}_{1.1}$	1.8
$T_{\mathrm{k},2}$	$1.1^{1.2}_{0.9}$	1.1
$n_{\mathrm{H_2},1}$	$3.9^{4.3}_{2.4}$	3.9
$n_{\mathrm{H_2},2}$	$5.6^{6.4}_{5.1}$	5.6
$(\mathrm{d}v/\mathrm{d}r)_1$	$1.0^{1.4}_{0.2}$	1.0
$(\mathrm{d}v/\mathrm{d}r)_2$	$1.8^{2.6}_{1.2}$	1.8
$\frac{[\mathrm{HCN}]}{[\mathrm{H^{13}CN}]} = \frac{[\mathrm{HCO^+}]}{[\mathrm{H^{13}CO^+}]}$	$2.6^{2.8}_{2.3}$	2.6
X_{HCN}	$-8.1^{-7.3}_{-8.7}$	-8.1
$X_{\mathrm{HCO^+}}$	$-8.8^{-8.1}_{-9.5}$	-8.8
f	$-1.2^{-0.2}_{-2.0}$	-1.2

$0.01 < f < 1$, such that:

$$S = S_1 f + S_2(1 - f), \tag{5.8}$$

where S_1 and S_2 are the RADEX fluxes for phase 1 and 2 respectively, in a simplified version of the method used in (Zhang et al., 2014). Either of S_1 and S_2 may be negative, but the combined fluxes S are constrained to be positive as per observations. It is extremely important to appreciate that f is *NOT* the fraction of flux densities S emerging from the first phase, as S_1 may intrinsically be much greater (or smaller) than S_2. It is merely a free parameter to allow the MCMC to scale the significance of the two phases, and is indirectly related to the beam filling factor for the phase. Furthermore, there is no line transfer between the two phases: they emulate two phases confused in the imaging beam, not two phases along the same line of sight (unless they are decoupled by a sufficiently large velocity offset). Following the results of the exploration of T_{bg} above I adopt $T_{\mathrm{bg}} = 3\,\mathrm{K}$ for both phases.

The results of this initial two-phase model are shown in Figure 5.15, the SLED fits in Figure 5.16 and the K_{vir} posteriors are given in Figure 5.17. Numerical results are tabulated in Table 5.6. It is clear from Figures 5.15, 5.16 and 5.17 that I have an underdetermined model, with the available lines unable to either constrain both phases or clearly exclude one. Interestingly, even though I am completely unable to constrain the kinetic temperature, density or velocity gradient the abundances still appear to be relatively well determined. Similarly, the abundance ratio is still quite well constrained.

The $[\mathrm{HC(N/O^+)}]/[\mathrm{H^{13}C(N/O^+)}]$ ratio in this model is again elevated. It is almost definitely unsuitable to have a single $[\mathrm{HC(N/O^+)}]/[\mathrm{H^{13}C(N/O^+)}]$ ratio for both phases and both HCN and HCO$^+$; unfortunately, as is shown by the degeneracy of the two phases, I do not have sufficient observations nor are observations of sufficient precision to constrain two phases. Further observations of the H^{13}CN and H^{13}CO$^+$ SLEDs, in particular the $J = 3 - 2$ line, would go a long way towards solving this issue.

Two-phase modelling - HCN, HCO$^+$ & CO

The previous two-phase model failed due to the paucity of available molecular lines and the large uncertainties in those available. In lieu of additional ^{13}C isotopologue line observations, which would place much tighter constraints on the models, I explore the addition of CO and ^{13}CO to the two-phase models. I take the line fluxes directly from Papadopoulos et al. (2014), and do not make corrections for source size: the f scaling parameter allows the model to account for different beam filling factors due to the different sizes of the HCN and CO emitting regions, while the two phases allow for non-cospatial emission.

---

was unable to converge on any solutions as the problem is underdetermined. I discuss the validity of this step in § 5.5.2.

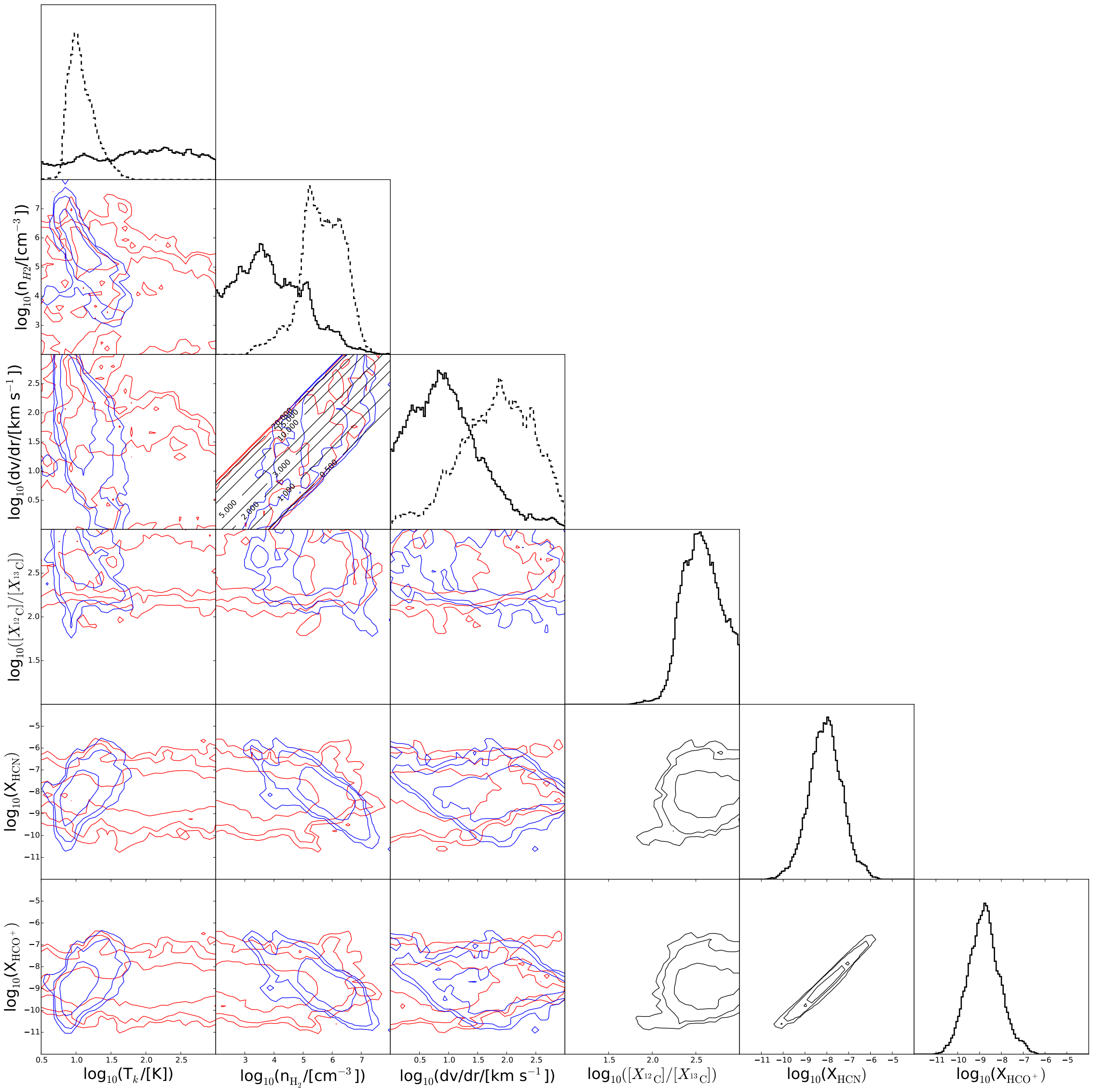

Figure 5.15: The modified step plot for the two phase HCN & HCO$^+$ model. Contours are at the 68%, 95% and 99% credible intervals. Red/solid and blue/dashed contours are phases 1 and 2, with $T_{\rm bg}$ = 3 and 3 K respectively. [^{12}C]/[^{13}C], $X_{\rm HCN}$ and $X_{\rm HCO^+}$ are kept the same in the two phases, so have only one set of black contours. The two phases are completely degenerate - unsurprising given the good fits of the single-phase models.

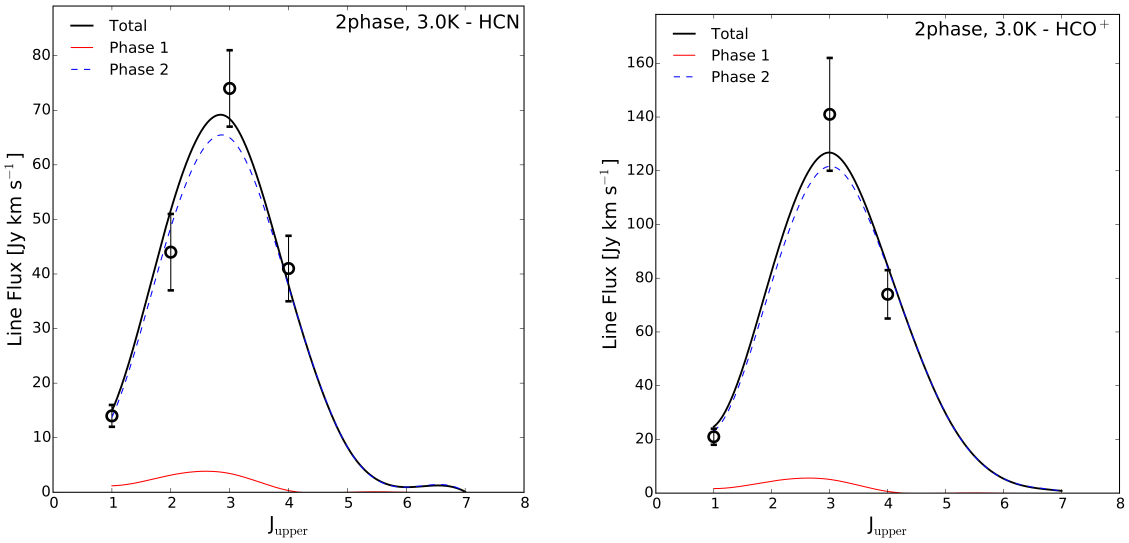

Figure 5.16: SLED fits for the two phase HCN & HCO$^+$ model, showing the relative contribution of each gas phase. In this case these contributions are not particularly meaningful, given the almost complete degeneracy between the two phases.

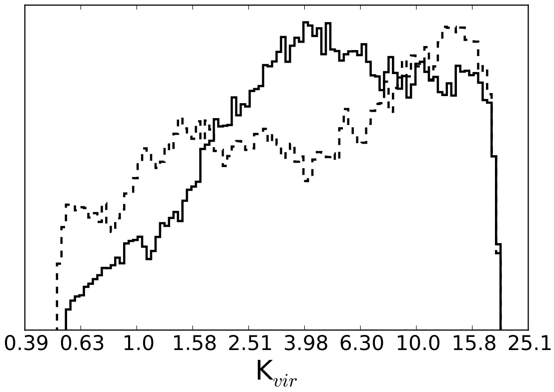

Figure 5.17: $K_{\rm vir}$ for the two phase HCN & HCO$^+$ model. Solid and dashed contours are phases 1 and 2. The model appears underdetermined, with no constraints on $K_{\rm vir}$.

With the additional lines I am able to extend the model complexity significantly, so that the free parameters include $X_{\rm CO}$, $X_{\rm HCN}$, $X_{\rm HCO^+}$ and $[X_{^{12}\rm C}]/[X_{^{13}\rm C}]$ in each gas phase. Once again, the model is unable to simultaneously fit free $X_{\rm mol}$ and $[X_{^{12}\rm C}]/[X_{^{13}\rm C}]$ ratios for every species in both phases, forcing the use a single $[X_{^{12}\rm C}]/[X_{^{13}\rm C}]$ ratio in each phase for all species. Even with these restrictions the code can take many steps to converge, and the output chains were carefully inspected to exclude unstable runs. Of the runs that converged, all converged onto the same locus, which is presented here. The results are tabulated in Table 5.7 and shown in Figures 5.18 (parameter pdfs), 5.19 (SLEDs), 5.20 (abundance ratios) and 5.21 ($K_{\rm vir}$ pdf).

It is clear from Table 5.7 and Figure 5.18 that this model provides very tight constraints on the two gas phases, although the tightness of the constraints is no guarantee of accuracy. The model spontaneously separates into a hot, diffuse, CO dominated phase and a cold, dense, HCN dominated phase. This result is robust to randomised chain initial positions over multiple MCMC runs and is similar to the findings of Kamenetzky et al. (2014) who used only CO. $T_{\rm k}$ and $n_{\rm H_2}$ are the best constrained parameters, with less than ± 0.1 dex spread in the 68% credible intervals. In the diffuse phase $X_{\rm HCN}$ falls rapidly, and Figure 5.19 confirms that HCN has no contribution from the diffuse gas phase, so that $X_{\rm HCN}$ in this phase is an upper limit only. In both phases $X_{\rm CO}$ is slightly lower than the canonical value of 2×10^{-4} presenting instead 4×10^{-5} and 6×10^{-6}. In particular the latter

Table 5.7: HCN, HCO^+ & CO Two-Phase Model Solutions. All values $\log_{10}$.

Parameter	Mean	min χ^2
$T_{k,1}$	$3.2^{3.3}_{3.1}$	3.2
$T_{k,2}$	$0.9^{0.9}_{0.8}$	0.8
$n_{H_2,1}$	$3.6^{3.8}_{3.5}$	3.5
$n_{H_2,2}$	$6.6^{6.8}_{6.3}$	6.5
$(\mathrm{d}v/\mathrm{d}r)_1$	$0.8^{1.5}_{1.1}$	1.2
$(\mathrm{d}v/\mathrm{d}r)_2$	$2.4^{3.0}_{2.3}$	2.9
$\left(\frac{[\mathrm{HCN}]}{[\mathrm{H^{13}CN}]} = \frac{[\mathrm{HCO^+}]}{[\mathrm{H^{13}CO^+}]} = \frac{[\mathrm{CO}]}{[\mathrm{^{13}CO}]}\right)_1$	$1.8^{2.0}_{1.7}$	1.9
$\left(\frac{[\mathrm{HCN}]}{[\mathrm{H^{13}CN}]} = \frac{[\mathrm{HCO^+}]}{[\mathrm{H^{13}CO^+}]} = \frac{[\mathrm{CO}]}{[\mathrm{^{13}CO}]}\right)_2$	$2.7^{3.0}_{2.7}$	2.9
$X_{\mathrm{HCN},1}$	$-10.8^{-10.4}_{-11.9}$	-10.0
$X_{\mathrm{HCN},2}$	$-8.6^{-7.9}_{-9.0}$	-7.7
$X_{\mathrm{HCO^+},1}$	$-9.3^{-6.7}_{-10.6}$	-6.6
$X_{\mathrm{HCO^+},2}$	$-9.3^{-8.7}_{-9.6}$	-8.6
$X_{\mathrm{CO},1}$	$-5.3^{-4.5}_{-6.0}$	-4.4
$X_{\mathrm{CO},2}$	$-6.1^{-5.4}_{-6.3}$	-5.2
f	$-0.9^{-0.7}_{-1.2}$	-1.2

value, corresponding to the dense gas phase, is quite low, giving [CO]/[HCN]$\sim$ 300 (Figure 5.20). However, the spread in X_{CO} is very large, especially in the hot phase. While the dense phase ratios are well constrained, the diffuse phase ratios extend over almost 6 dex - principally due to the uncertainty of HCN and HCO^+ values (not the CO abundance) in this phase, which arises because they contribute virtually none of the diffuse phase flux.

The K_{vir} pdfs in Figure 5.21 are once again rather poorly constrained, although the cold phase pdf does appear to be slightly bimodal, peaking around 1.5 and 10, whereas the hot phase pdf is generally unconstrained, although it does perhaps tend towards higher K_{vir} values. As in the previous models, the prior on K_{vir} is a relatively informative prior, and a smaller permitted K_{vir} range would increase the precision, but not necessarily the accuracy, of the results, in particular the molecular abundances and $\mathrm{d}v/\mathrm{d}r$.

The $[^{12}C]/[^{13}C]$ ratio: evidence for fractionation?

Even with the addition of the CO and ^{13}CO lines I am unable to constrain two gas phases with free CO, HCN and HCO^+; ^{13}CO, $H^{13}CN$ and $H^{13}CO^+$ abundances in each phase. In the quest to identify whether the $[^{12}C]/[^{13}C]$ ratio found by Papadopoulos et al. (2014) is real, or due to biased SLED fitting, I ran a model with X_{CO}, X_{HCN} and $X_{\mathrm{HCO^+}}$ fixed to the best fit parameters of the previous run (see Table 5.7 for values). I then introduce as free parameters $[\mathrm{CO}]/[^{13}\mathrm{CO}]_1$, $[\mathrm{CO}]/[^{13}\mathrm{CO}]_2$, $[\mathrm{HCN}]/[\mathrm{H^{13}CN}]$ and $[\mathrm{HCO^+}]/[\mathrm{H^{13}CO^+}]$. The single ratio for HCN and HCO^+ is motivated by only having the $J = 1 - 0$ line for the $H^{13}CN$ and $H^{13}CO^+$ and the $J = 1 - 0$ line has a negligible contribution in the hot phase - I exclude $H^{13}CN$ and $H^{13}CO^+$ from the hot phase (see Figure 5.19).

The expectation is that if fractionation is responsible for the apparently elevated $[^{12}C]/[^{13}C]$ ratio then I should find high $[\mathrm{HCN}]/[\mathrm{H^{13}CN}]$ and low $[\mathrm{CO}]/[^{13}\mathrm{CO}]$ in the cold, dense phase, but normal/low $[\mathrm{CO}]/[^{13}\mathrm{CO}]$ in the hot, diffuse phase. The $[\mathrm{HCO^+}]/[\mathrm{H^{13}CO^+}]$ ratio is more ambiguous, as it can be fractionated in either direction depending upon the physical and chemical conditions (Langer et al., 1984), but in either case the fractionation should be less extreme than exhibited by CO or HCN. This should then provide a "bracketing" of the true $[^{12}C]/[^{13}C]$ ratio in the galaxy as:

$$[\mathrm{CO}]/[^{13}\mathrm{CO}] \leq [^{12}\mathrm{C}]/[^{13}\mathrm{C}] \leq [\mathrm{HCN}]/[\mathrm{H^{13}CN}]. \tag{5.9}$$

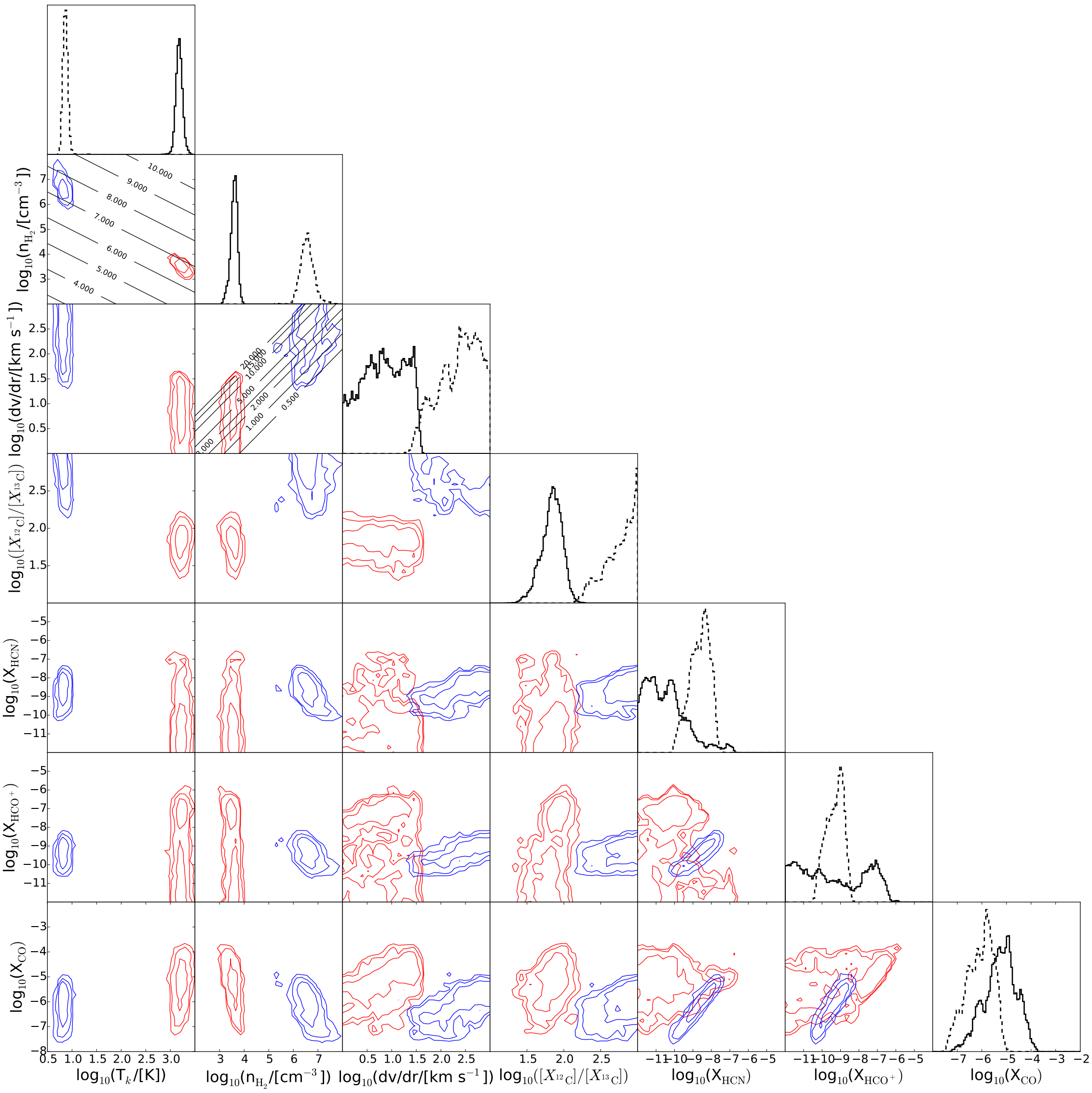

Figure 5.18: The modified step plot for the two-phase HCN, HCO^{+} & CO model. Contours are at the 68%, 95% and 99% credible intervals. Red/solid and blue/dashed contours are phases 1 and 2, with $T_{\rm bg}$ = 3 and 3 K respectively. Contours of constant pressure have been included in the $T_{\rm k} - n_{\rm H_2}$ plot at intervals of one dex. There is a very clear, robust and spontaneous separation into a hot, diffuse and cold, dense gas phase.

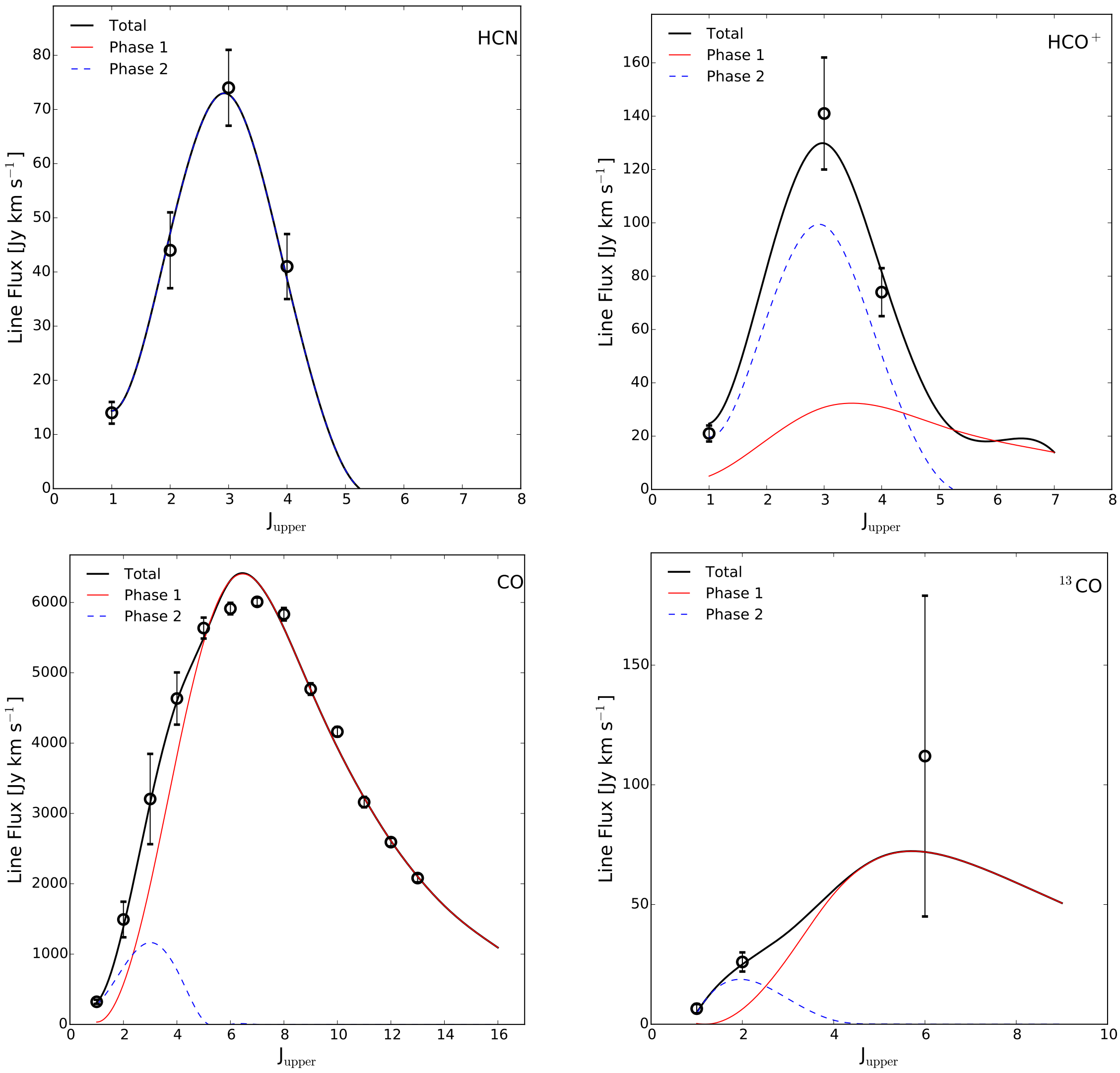

Figure 5.19: SLED fits for the two-phase HCN, HCO$^+$ & CO model, showing the relative contribution of each gas phase. The same normalisation has been used for the CO and ^{13}CO SLEDs.

The results of the [^{12}C]/[^{13}C] investigation model are shown in Figure 5.22. It is immediately clear that the model recovers very similar $T_{\rm k}$, $n_{\rm H_2}$ and dv/dr as the previous model. As I have fixed the main isotope abundances this is not surprising, but it is important as it confirms that the isotopologue abundance ratios I derive here are in fact compatible with the less restricted two-phase model; by fixing some parameters and freeing others I have not inadvertently moved into a very different locus in parameter space.

The [HCN]/[H^{13}CN] and [HCO$^+$]/[H^{13}CO$^+$] ratios are both very high, while the [CO]/[^{13}CO] ratio is $\sim 100 - 200$ in *both* phases. However, the abundance ratios are correlated, so that the spread in ([CO]/[^{13}CO]$_2$)/([HCN]/[H^{13}CN]) is extremely small, strongly peaking at $2{-}3$, consistent with Roueff et al. (2015). These results should be interpreted with caution: the fixing of the molecular abundances could be biasing the results. However, it is expected to bias them towards the values found in the previous model, so [CO]/[^{13}CO]$_2$ lying much lower, while [HCN]/[H^{13}CN] and [HCO$^+$]/[H^{13}CO$^+$] both lie higher, suggests that this is a real effect and not a bias due to the fixed abundances. This is evidence for a “standard” [^{12}C]/[^{13}C] abundance ratio (for (U)LIRGs) of ~ 100 in NGC 6240. The high ratio found by Papadopoulos et al. (2014) is explained by their attribution of the high$-J$ CO lines to the dense gas phase, whereas the simultaneous fitting and the addition of the H^{13}CN and H^{13}CO$^+$ lines/limits leads to the model spontaneously fitting these

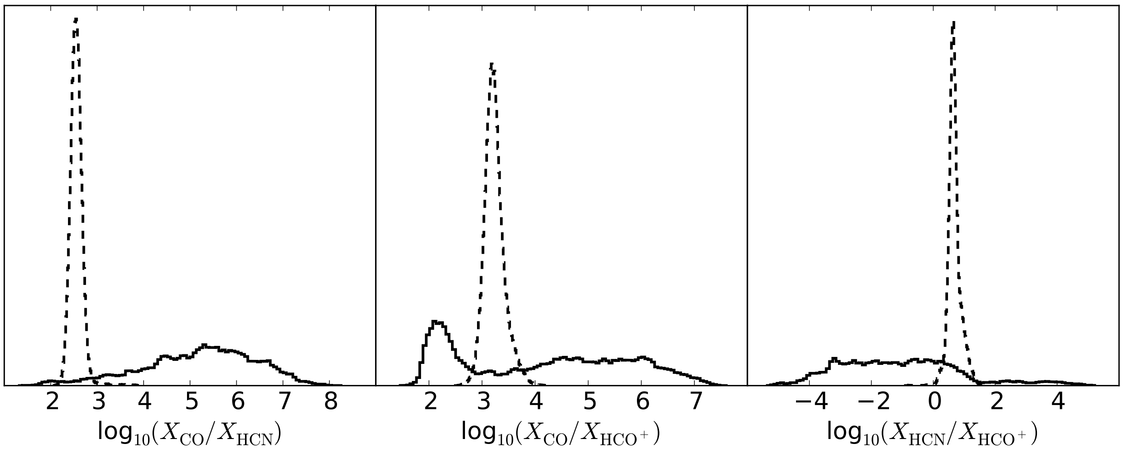

Figure 5.20: Abundance ratios for the two-phase model including CO. Solid and dashed contours are phases 1 (hot) and 2 (cold) respectively. The abundance ratios are very well determined in phase 2, but are essentially unconstrained in the hot phase.

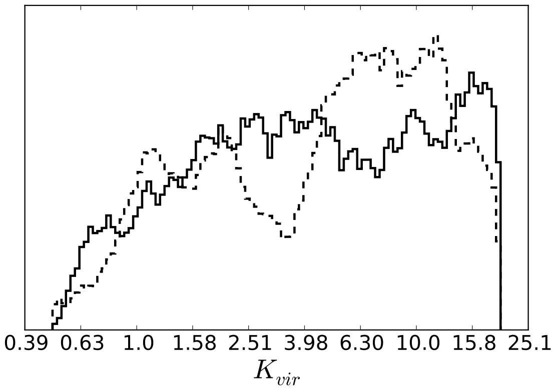

Figure 5.21: $K_{\rm vir}$ for the two-phase HCN, HCO$^+$ & CO model. Solid and dashed contours are phases 1 (hot) and 2 (cold) respectively.

high$-J$ lines to a hot, diffuse phase, as did the two phase CO model of Kamenetzky et al. (2014). The high observed [HCN]/[H^{13}CN] and [HCO$^+$]/[H^{13}CO$^+$] ratios are explained by chemical effects (ICE) in the very cold, dense gas.

Three-phase modelling

One of the major concerns regarding the two-phase-model approach is that I know that CO$(1-0)$ is far more extended that any other molecular species (Feruglio et al., 2013), yet I am artificially constraining it to lie in the same phase as HCN and HCO$^+$. Here, I use a three-phase model with some physically motivated constraints to alleviate this concern.

If I allow all species to vary freely in every phase, the addition of a third phase introduces too many free parameters to constrain with the current observations. To reduce the number of free parameters I enforce certain simplifying assumptions based on the results of the earlier models. I restrict HCN and HCO$^+$ to one gas phase, and force this phase to be the cold, dense phase by reducing the prior ranges on $T_{\rm k}$ and $n_{\rm H_2}$. This is largely motivated by the absence of HCN emission from the shocked phase in the two-phase models above, however the same logic suggests that I should be including HCO$^+$ in the shocked and/or diffuse phase, as it shows evidence both in the two-phase model SLEDs and the single phase model 2 2D pdfs of arising from at least two phases. The choice to force HCO$^+$ into the dense phase only is a pragmatic one: I simply do not yet have enough observed lines to constrain a more accurate model of HCO$^+$. This should not

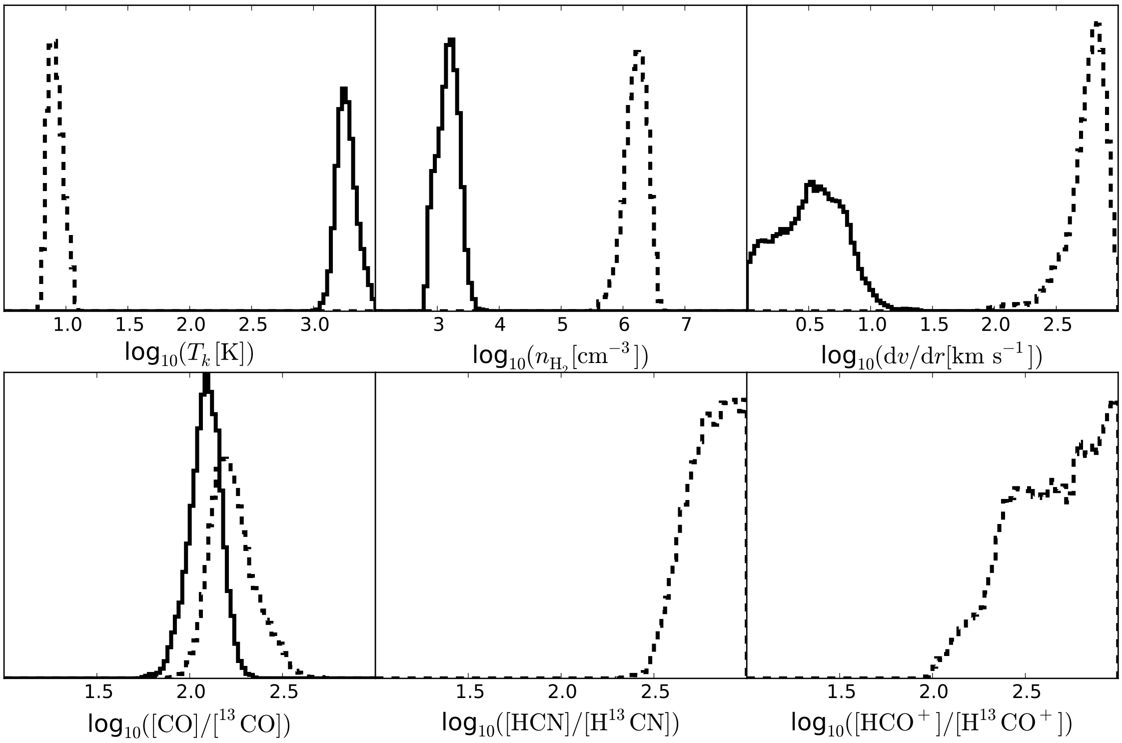

Figure 5.22: 1D marginalised-posterior pdfs for the gas-phase parameters of the $[^{12}\mathrm{C}]/[^{13}\mathrm{C}]$ investigatory model. The gas parameters are very similar to those of the HCN, $\mathrm{HCO^+}$ & CO two-phase model. The $[\mathrm{CO}]/[^{13}\mathrm{CO}]$ abundance ratios are similar in both phases, and are in the "standard" region for (U)LIRGs, suggesting that the high $[\mathrm{HCN}]/[\mathrm{H^{13}CN}]$ and $[\mathrm{HCO^+}]/[\mathrm{H^{13}CO^+}]$ ratios are due to isotope fractionation in the cold gas phase.

Table 5.8: $[^{12}\mathrm{C}]/[^{13}\mathrm{C}]$ Study Two-Phase Model Solutions. All values $\log_{10}$.

Parameter	Mean	min χ^2
$T_{k,1}$	$3.3^{3.4}_{3.2}$	3.3
$T_{k,2}$	$0.9^{1.0}_{0.9}$	0.8
$n_{\mathrm{H_2},1}$	$3.2^{3.4}_{3.0}$	3.0
$n_{\mathrm{H_2},2}$	$6.2^{6.4}_{6.1}$	6.5
$(\mathrm{d}v/\mathrm{d}r)_1$.....	$0.5^{0.8}_{0.3}$	0.3
$(\mathrm{d}v/\mathrm{d}r)_2$.....	$2.7^{2.9}_{2.7}$	3.0
$[\mathrm{CO}]/[^{13}\mathrm{CO}]_1$ ..	$2.1^{2.2}_{2.0}$	2.2
$[\mathrm{CO}]/[^{13}\mathrm{CO}]_2$ ..	$2.2^{2.3}_{2.1}$	2.3
$[\mathrm{HCN}]/[\mathrm{H^{13}CN}]$.	$2.8^{3.0}_{2.7}$	3.0
$[\mathrm{HCO^+}]/[\mathrm{H^{13}CO^+}]$	$2.6^{3.0}_{2.6}$	3.0
f	$-1.1^{-1.0}_{-1.2}$	-1.1

significantly affect the results however as the CO lines are in any case the primary determinants of the conditions in the diffuse and shocked phases.

CO is present in all three phases, and in each phase there is an independent [CO]/[^{13}CO] ratio. In the cold, dense phase there is also an [HCN]/[H^{13}CN] ratio, which is shared with HCO^{+}. All three phases have $T_{\rm bg} = 3\,{\rm K}$. The fluxes from the three phases are linked by two free scaling factors f_1 and f_2, such that:

$$S = S_{\rm shocked} f_1 + S_{\rm diffuse} + S_{\rm dense} f_2. \tag{5.10}$$

The full list of parameter ranges is given in Table 5.4 in the appendix. The temperature and density ranges are chosen so as to force each phase to be hot, diffuse or dense respectively, while still allowing a significant range for each parameter to explore.

The results of the three-phase modelling are shown in Figures 5.23, 5.24 and 5.25, while the numerical values are tabulated in Table 5.9. The model successfully splits into three clear phases, without any tension against the parameter ranges. The cold, dense phase pdfs are very similar to those of model 4 (Figure 5.10) despite the addition of CO to the phase. $X_{\rm CO}$ varies greatly between the gas phases, being greatest in the diffuse phase lying near the canonical value of 2×10^{-4}, before dropping slightly to around 1×10^{-5} in the shocked phase and then dropping rapidly to around $10^{-6} - 10^{-7}$ in the cold, dense phase: very much the behaviour I would expect.

The isotopologue abundance ratios are also largely as I would expect: both the shocked and the dense gas phases have relatively low [CO]/[^{13}CO] ratios of $30 - 100$, likely representative of the true [^{12}C]/[^{13}C] ratio in the galaxy. The diffuse phase present a slightly elevated ratio of $\sim 100 - 200$, consistent with this ubiquitous gas phase being influenced by the nuclear starbursts and some degree of selective photodissociation. Finally the [HCN]/[H^{13}CN] ratio is the highest, at around 300, consistent with isotope fractionation in cold, dense molecular cores.

We note that there is some tension in the [CO]/[^{13}CO] ratios, in that the shocked phase has a sizeable portion of its pdf below the [CO]/[^{13}CO] ratio of the dense phase. Isotope fractionation in the dense phase should lower the [CO]/[^{13}CO] ratio while increasing the [HCN]/[H^{13}CN] ratio: it is therefore contradictory if the hot, shocked phase, where there is no isotope fractionation, presents a lower [CO]/[^{13}CO] ratio than the dense phase. However, there is still a region of parameter space within 1σ of the mean values where the [CO]/[^{13}CO] ratio is lower in the dense phase, so while there is tension it is not that great, and the model is still consistent with isotope fractionation.

The SLEDs in Figure 5.24 show exceptionally good fits to the observed lines. The cold, dense phase has very little contribution to the CO or ^{13}CO SLEDs, and in both of these the shocked phase dominates the emission at $J \gtrsim 4$, while the low$-J$ lines are set by the ubiquitous diffuse phase.

The $K_{\rm vir}$ pdfs are shown in Figure 5.25. Both the diffuse and dense phases present doubly peaked pdfs, in particular with a peak about $K_{\rm vir} = 1$, while the shocked phase pdf steadily increases towards the upper limit of $K_{\rm vir} = 20$. $K_{\rm vir}$ is generally a poorly constrained parameter in the models, but this is strongly suggestive of approximately virialised gas dominating the diffuse and dense gas phases, while the shocked phase is highly turbulent.

For each gas phase I am able to derive $\alpha_{\rm mol}$ factors for CO and, for the dense phase, for HCN. These are presented, along with the corresponding masses, in Figure 5.26. The spread in each of the $\alpha_{\rm CO}$ pdfs is between 1.5 and 2 dex, with the centres shifting to increasing $\alpha_{\rm CO}$ as I move from the diffuse phase, through the shocked phase and onto the dense phase. There is less spread in the masses, and in particular the HCN derived and CO derived dense gas masses are very consistent with almost identical pdfs but for a systematic shift of $\sim -0.2\,{\rm dex}$ on the CO mass estimates. These are discussed more thoroughly in § 5.5.4.

5.4.7 Comparison to the Literature

The dense, HCN-bearing molecular gas in NGC 6240 has been modelled previously, by Krips et al. (2008), Greve et al. (2009) and Papadopoulos et al. (2014) (Kamenetzky et al., 2014 only modelled

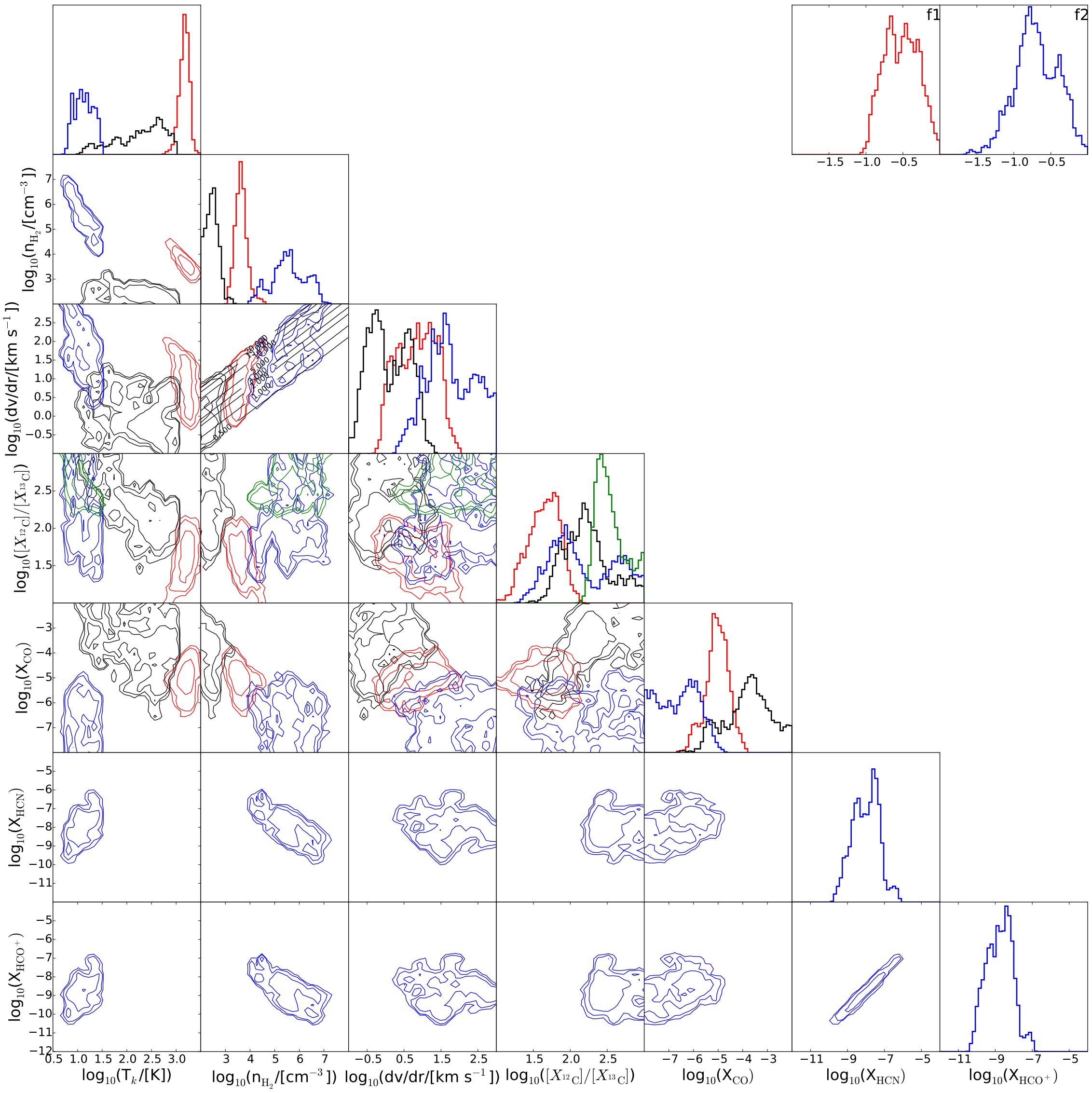

Figure 5.23: The step plot for the three-phase HCN, HCO$^+$ & CO model. Contours are at the 68%, 95% and 99% credible intervals. Red, black and blue contours are the shocked-, diffuse- and dense-gas phases respectively. In the $[X_{^{12}\mathrm{C}}]/[X_{^{13}\mathrm{C}}]$ plots the green contours correspond to the [HCN]/[H^{13}CN] abundance ratio, and the blue the [CO]/[^{13}CO] ratio, both in the cold, dense phase.

Table 5.9: Three-Phase Results. All values $\log_{10}$. Values in parenthesis are the best fit values.

Parameter	Hot, shocked	Diffuse	Cold, dense
T_k	$3.2^{3.3}_{3.1}(3.2)$	$2.3^{2.9}_{1.8}(2.4)$	$1.1^{1.3}_{1.0}(0.9)$
n_{H_2}	$3.6^{3.9}_{3.4}(3.5)$	$2.5^{2.7}_{2.2}(2.4)$	$5.6^{6.5}_{5.0}(6.6)$
$\mathrm{d}v/\mathrm{d}r$	$0.8^{1.0}_{0.1}(0.2)$	$0.1^{0.4}_{-0.6}(0.2)$	$1.8^{1.9}_{1.1}(1.5)$
$\frac{[\mathrm{CO}]}{[^{13}\mathrm{CO}]}$	$1.6^{1.9}_{1.5}(1.8)$	$2.2^{2.4}_{1.9}(2.2)$	$2.2^{2.8}_{1.6}(2.5)$
$\frac{[\mathrm{HCN}]}{[\mathrm{H}^{13}\mathrm{CN}]}$	–	–	$2.5^{2.7}_{2.3}(2.6)$
X_CO	$-5.0^{-4.5}_{-5.4}(-5.1)$	$-3.8^{-2.7}_{-5.4}(-3.7)$	$-6.6^{-5.6}_{-7.5}(-7.4)$
X_HCN	–	–	$-8.0^{-7.2}_{-7.9}(-9.6)$
X_{HCO^+}	–	–	$-8.8^{-8.0}_{-9.0}(-10.2)$
f	$-0.5^{-0.3}_{-0.7}(-0.6)$	–	$-0.7^{-0.5}_{-1.0}(-0.2)$

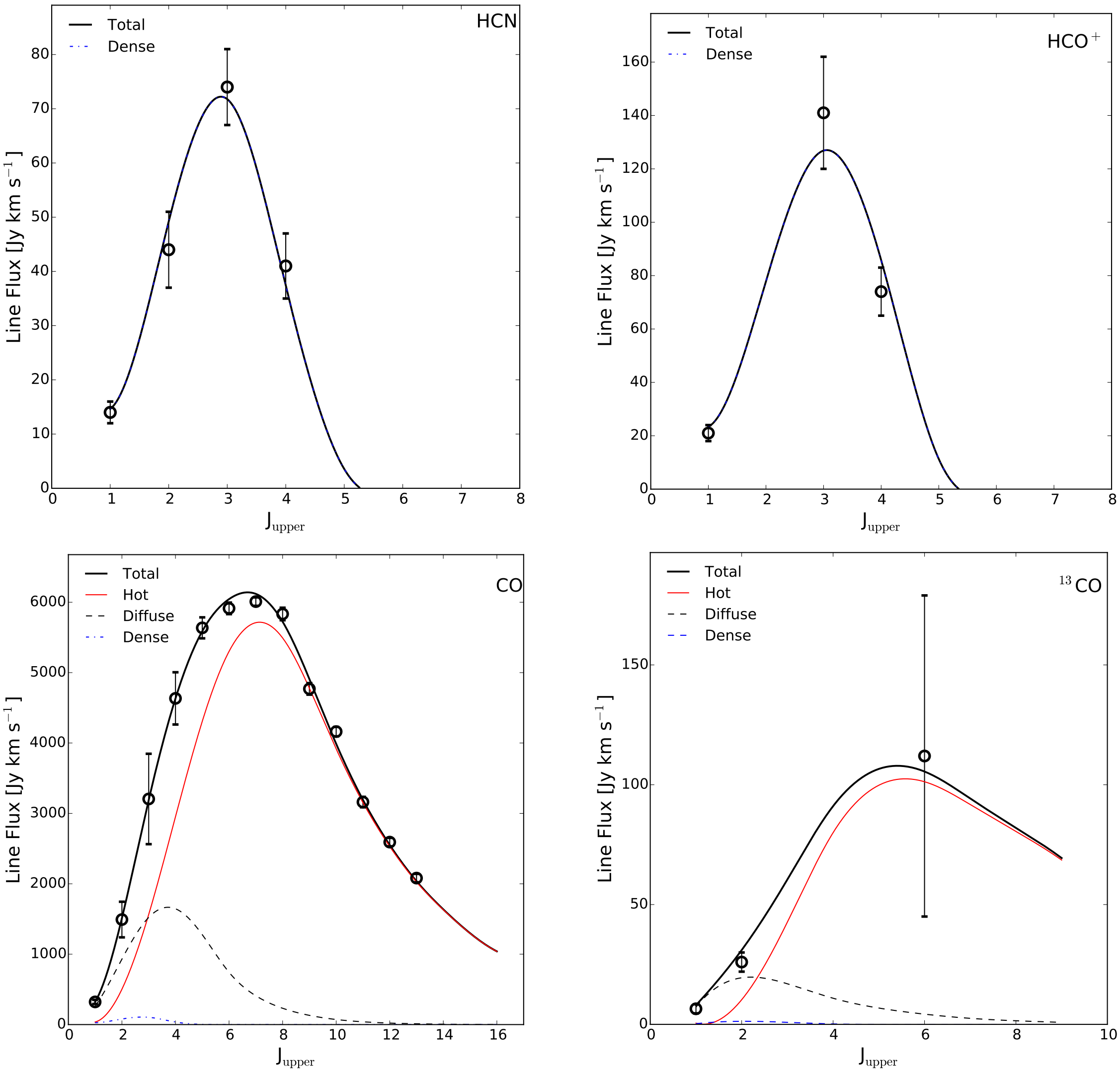

Figure 5.24: SLED fits for the three-phase HCN, HCO$^+$ & CO model, showing the relative contribution of each gas phase. The same normalisation has been used for the CO and ^{13}CO SLEDs.

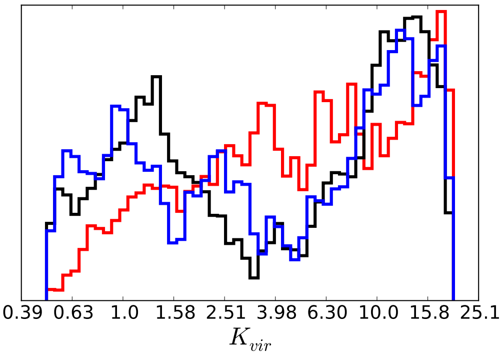

Figure 5.25: The $K_{\rm vir}$ pdfs for the three-phase model. Colours are as in Figure 5.23, with red, black and blue correspond to the shocked, diffuse and dense phases respectively. Both the diffuse and dense phases present doubly-peaked pdfs, in particular with a peak about $K_{\rm vir} = 1$, while the shocked-phase pdf steadily increases towards the upper limit of $K_{\rm vir} = 20$.

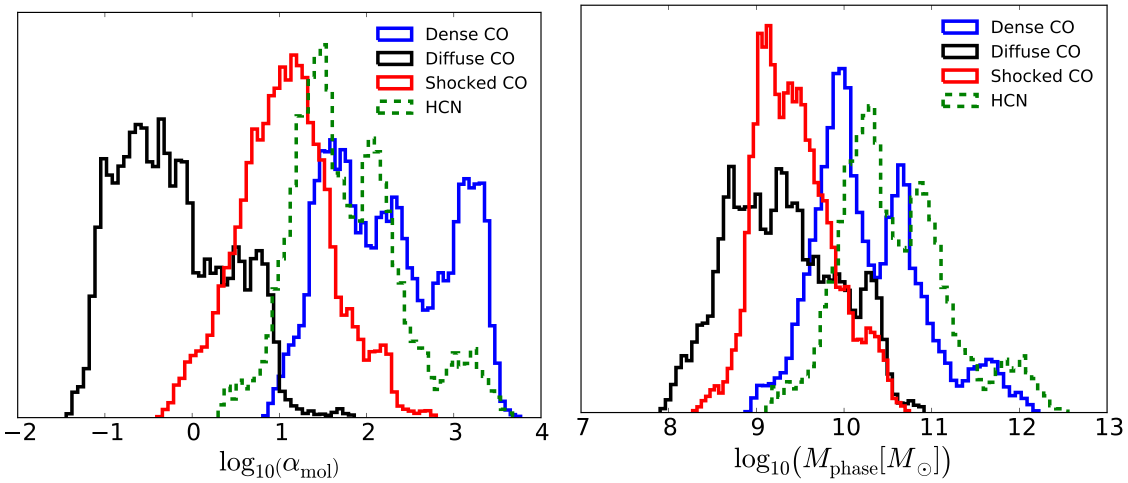

Figure 5.26: The $\alpha_{\rm CO}$ factor for each of the gas phases of the three-phase model and the $\alpha_{\rm HCN}$ (encompassing the dense phase) (left), and the corresponding mass of the gas phase (right). The diffuse and shocked phases are consistent with the "standard" $\alpha_{\rm CO}$ values of between 0.5 and 4, while the dense gas phase is considerably higher. While contributing a very small fraction of the CO$(1-0)$ line flux the dense gas phase dominates the molecular gas mass in the galaxy. The CO estimate and the HCN estimate of the mass of the dense phase are very consistent.

the CO SLED). While Krips et al. (2008) modelled a single gas phase for both HCN and HCO^+, Greve et al. (2009) and Papadopoulos et al. (2014) fitted HCN and HCO^+ independently, each with their own gas phase parameters, as in models 1 and 2.

While Krips et al. (2008) and Greve et al. (2009) both found similar gas kinetic temperature ranges ($20-120\,$K and $60-120\,$K respctively), Greve et al. (2009) found much larger n_{H_2} in the HCN phase of $\sim 10^5\,\mathrm{cm}^{-3}$, cf. $10^{3.5}-10^{4.5}\,\mathrm{cm}^{-3}$ found by Krips et al. (2008). On the other hand, the HCO^+ phase had an n_{H_2} of $\sim 10^4\,\mathrm{cm}^{-3}$, consistent with the results of Krips et al. (2008).

Papadopoulos et al. (2014) present their results as 2D pdfs, finding degenerate "bananas" ranging from $n_{\mathrm{H}_2} \simeq 10^6\,\mathrm{cm}^{-3}/T_\mathrm{k} \simeq 8\,$K to $n_{\mathrm{H}_2} \simeq 10^4\,\mathrm{cm}^{-3}/T_\mathrm{k} \simeq 1000\,$K, although the HCN pdf appears to peak at the high-density, low-T_k end of the "banana".

The results are broadly consistent with these previous works. The models argue for relatively cool ($10-30\,$K), dense ($10^{4.5}-10^6\,\mathrm{cm}^{-3}$) gas dominating the HCN and HCO^+ emission. The single phase models echo the trend seen by Greve et al. (2009) and Papadopoulos et al. (2014) of HCO^+ preferring a $\sim 0.5\,$dex lower n_{H_2} than HCN while sharing a similar kinetic temperature. The [HCN]/[HCO^+] abundance ratio of $5.3^{7.0}_{4.7}$ is slightly lower than that of Krips et al. (2008) who found "around 10", but still generally consistent.

The multiple phases of the molecular gas in NGC 6240 have been characterised previously, including by Armus et al. (2006, using Spitzer observations of H_2 vibrational lines), Papadopoulos et al. (2014, using the aforementioned spectral decomposition of the CO SLED) and Kamenetzky et al. (2014, using a two-phase MCMC model of the CO SLED). The models presented in this chapter are the first to simultaneously fit multiple species in both single and multiple gas phases. As was pointed out by Kamenetzky et al. (2014), and as I found here comparing to the results of Papadopoulos et al. (2014), it is important to simultaneously fit multiple components to SLEDs to prevent the introduction of additional biases.

From modelling of H_2 vibrational lines Armus et al. (2006) found two highly excited phases of the molecular gas, with $6.7\times10^6\,M_\odot$ at $T_\mathrm{k} = 957\,$K and $1.6\times10^9\,M_\odot$ at $T_\mathrm{k} = 164\,$K respectively. Papadopoulos et al. (2014) first fitted the HCN and HCO^+ SLEDs, before using these results to fit high$-J$ components of the CO SLED, then fitting the residual CO SLED. This produces three gas phases with densities $\log_{10}(n_{\mathrm{H}_2}) = 5.0$, 4.3 and 3.0 and kinetic temperatures $\log_{10}(T_\mathrm{k}) = 1.5$, 2.6 and 2.0. The model of Kamenetzky et al. (2014) used a nested sampling algorithm to fit two gas phases to the CO SLED, finding a hot and a cold phase with best fit densities $\log_{10}(n_{\mathrm{H}_2}) =$ 4.1 and 5.8 and kinetic temperatures $\log_{10}(T_\mathrm{k}) = 3.1$ and 1.2. These are reassuringly similar to the results of the multi-species, multi-phase analysis.

5.5 Discussion

5.5.1 Validity of Multi-species Models

An important question of this analysis is whether or not it is appropriate to model multiple species as sharing the same gas phase. In reality there is almost a continuum of gas conditions within any radio beam and any single-phase (or even two- or three-phase) model is only an approximation of the conditions dominating the emission, which will vary from molecule to molecule. Nevertheless, combining molecular species which are likely to trace similar regions is a powerful tool for estimating molecular abundance ratios and gas conditions.

The combination of two or more species in a single model is a compromise, with the extent of the assumptions dependent upon how similar the regions traced by the different species are likely to be. This raises particular concerns for the combination of HCN and SiO. While these two species are usually considered to be present in the same phases, their emission peaks in dramatically different regions. HCN is generally seen to trace dense, and perhaps turbulent, gas in molecular clouds, where SiO is present but with an abundance $\sim 10^{-12}$. SiO on the other hand emits most brightly in strongly shocked regions, where its abundance can be as high as 10^{-8} due to sputtering of dust grains. This would suggest that treating their emission as emerging from the same phase is an egregious error, a fact supported by the extremely poorly constrained posterior pdfs in Figure 5.9. However, I am already averaging over a wide range of HCN emitting phases with the single species models; a fact which is unavoidable in all but the closest extragalactic observations. Furthermore, due to line trapping[11], I cannot assume that optically thick HCN is only tracing regions near its critical density, and not just high column density regions. Therefore, I argue that while being a poor solution, as evidenced by the chaotic and extended pdfs in almost all of the parameters in this model and the SLED fit, this is an acceptable compromise for deriving the [HCN]/[SiO] abundance ratio only, with even this being very poorly constrained. The other parameters in this fit are not thought to be meaningful.

Model 4, the combination of models 1a and 2, is a very different case to the HCN+SiO combination of model 3. HCN and HCO^+ are far more likely to trace similar regions than HCN and SiO (although there is a strong ionisation state dependence for the HCO^+: e.g., Fuente et al., 2005), so in principle this should be a more reasonable combination. Model 4 places the tightest constraints on the main parameters as well as providing a very well constrained [HCN]/[HCO^+] abundance ratio. However, the SLED fit for HCO^+ is slightly worse than that for HCO^+ alone, and the $T_\mathrm{k} - n_{\mathrm{H}_2}$ pdf lies at the far edges of the individual HCN and HCO^+ pdfs.

It is possible that I am combining two partially overlapping pdfs, producing artificially tight constraints. Examining the pdfs and the results in Table 5.5 this seems unlikely: T_k is lower for model 4 than either 1a or 2, and n_{H_2} is higher. The [^{12}C]/[^{13}C] ratio on the other hand hand is in between 1a and 2. While it is hard to gauge the effects of combining two 4-D parameter spaces with degeneracies, it does not appear to be the case that the improved constraints are due to combining two partially overlapping pdfs. This does not guarantee the validity or accuracy of the model, but it does rule out one major concern.

5.5.2 Two-Phase Models

In the first of the two-phase models I allowed the HCN and HCO^+ abundances and the [^{12}C]/[^{13}C] ratio to vary freely, but used a single common value for both phases. This was necessitated by a paucity of line ratios to place constraints on any more free parameters, and even with these restrictions the model was unable to constrain a second gas phase. Models with separate free HCN and HCO^+ abundances for each phase, as well as models with separate [HCN]/[$H^{13}CN$] and [HCO^+]/[$H^{13}CO^+$] for each phase were trialled but did not converge. In these models the contributions of the second gas phase HCN and HCO^+ lines to the total SLEDs is less than 10% in any line, so that I am simply unable to constrain a second gas phase using HCN and HCO^+ without greater precision observations. A more comprehensive HCN/HCO^+ model, with fewer assumptions, needs more $H^{13}CN$ and $H^{13}CO^+$ observations, as well as observations of HCN and HCO^+ $J = 5-4$ and higher transitions.

The introduction of the contrast factor, f, allows for the abstraction of the issue that different molecular species usually present different beam filling factors, while the two phases also allow for the separate regions where only one of the species is present. For example, the situation where HCO^+ is significantly more extended that HCN can be described by two gas phases with similar T_k, n_{H_2} and $\mathrm{d}v/\mathrm{d}r$, but with an appropriate contrast factor scaling the emission. For the unresolved single dish observations this is essential, but even for high resolution interferometric observations this is a desirable property, allowing for that fact that the ISM can vary significantly over parsec scales (barely resolvable with ALMA in even the closest galaxies).

Adding CO

The first extension of the two-phase model was the addition of the CO and ^{13}CO lines. This large dataset allows for more complex modelling while providing tighter constraints on some of the derived parameters. In all of the models, but especially these models, the molecular abundance ratios are much better constrained than the molecular abundances themselves due to multiple degeneracies within the LVG framework, in particular the degeneracy between X_mol and $\mathrm{d}v/\mathrm{d}r$.

We noted in § 5.4.6 that the two phase, HCN+HCO^++CO model was less stable than the single phase models: I expand upon this here. The single phase models were all found to rapidly converge onto a single locus in the N-D parameter space, and this locus was robust to randomised

---

[11] For a recent didactic article on the subject see Shirley (2015).

initial positions over multiple MCMC runs[12]. Convergence was assessed by autocorrelation for the short chains and visual inspection of each parameter as a function of chain step. After burn-in the parameters showed clean oscillation about the mean parameter value, as expected for a converged Metropolis-Hastings MCMC. For the two phase, HCN+HCO^++CO model however, some chains failed to converge after 5×10^5 steps, showing dramatic swings in the parameters across more than half of the prior range. These chains (and subsets of these chains) produced very poor SLED fits, as well as usually non-sensical parameters and very high χ^2 cf. the converged chains. However, all of the chains for this model that did converge converged onto the same locus and had converged by 10^4 steps - the length of the burn-in. This is the locus presented in this work in § 5.4.6, and was found for a wide range of initial parameters[13].

A significant concern with this model is the large spatial extension of about 30% of the CO$(1-0)$ line flux seen by Feruglio et al. (2013), tracing an outflow out to almost $30''$. The two-phase model places almost all of the CO$(1-0)$ flux in the cold, dense, HCN dominated gas phase, but the HCN emission only extends out to $\lesssim 2''$. This apparent contradiction arises because the model is restricted to two phases: the high$-J$ lines drive a hot, diffuse phase arising from the slow shocks in the turbulent internuclear disk (Meijerink et al., 2013), while the HCN lines force a very dense, cold phase. This is accounted for in the three-phase model by including a diffuse CO emitting phase, able to account for CO throughout the galaxy and in the outflow.

The issue of poor convergence was far less significant with the three-phase model. Here, the runs converged very quickly (well within the first 10^4 steps I typically used for a (particularly zealous) burnin) and consistently, although some converged to regions of lower likelihood than the results presented here. In these cases the SLED fits were much worse, in particular the CO SLED, and had higher χ^2 values for the fits to the observed line ratios. The improved convergence rates over the two-phase models are likely a combination of more free parameters in the fits and the third phase allowing the model to more accurately represent the true conditions of the molecular gas in NGC 6240, in particular the diffuse CO phase.

Interestingly, as shown in Figure 5.18, the derived thermal pressure of both gas phases $P/k \sim 10^7\,\mathrm{K\,km\,s^{-1}}$ - the same value that Dopita et al. (2005) found necessary to fit the SED in NGC 6240 and the value found for the hot, diffuse phase in Kamenetzky et al. (2014). This makes sense in light of the three-phase model: the diffuse CO and shocked CO dominate the CO SLED, so when Kamenetzky et al. (2014) fitted to the CO SLED only they recovered these phases. However, the diffuse phase is only partially co-located with the shocked phase so is not in pressure balance, whereas the dense phase, identified here by fitting HCN, HCO^+ and CO simultaneously, *is* co-located with the shocked phase, and in pressure balance with it. This highlights the importance of simultaneously fitting not only multiple phases, but also multiple species.

5.5.3 The $[^{12}C]/[^{13}C]$ Abundance Ratio in NGC 6240

Papadopoulos et al. (2014) constrained the high$-J$ CO lines using the LVG solutions for HCN and HCO^+ before fitting a third phase to the remaining lines. When they compared these to their ^{13}CO data, a very high $[CO]/[^{13}CO]$ abundance ratio of $300-500$ was required for consistency, and they argued for that this was evidence for a similarly elevated $[^{12}C]/[^{13}C]$ ratio. Here, I have used the new observations of $H^{13}CN$ and $H^{13}CO^+$ in combination with the ^{12}C isotopologue lines from the literature to place independent constraints on the $[^{12}C]/[^{13}C]$ abundance ratio. A naïve approach, simply taking the 68% credible intervals on $[CO]/[^{13}CO]$ and $[HCN]/[H^{13}CN]$ as the brackets on the $[^{12}C]/[^{13}C]$ ratio, puts the ratio somewhere between 100 and 1000: however, this does not account for the much greater abundance of CO with respect to HCN nor the dominance by mass of the dense phase. If I instead adopt a mass- and abundance-weighted average I find that $[^{12}C]/[^{13}C] = 98^{230}_{65}$. The pdf of the ratio is shown in Figure 5.27. The ratio is strongly peaked at "normal" ULIRG values of about 100, although there is a long extended tail out to 1000. Nevertheless, I find that the model is actually compatible, within the 68% credible interval, with even a Galactic value, whereas the upper limit of the 95% credible interval is at 550. I therefore have strong evidence against a super-ULIRG elevated $[^{12}C]/[^{13}C]$ abundance ratio, but cannot conclusively exclude the

---

[12] Each initial parameter was drawn independently from a uniform distribution over its allowed prior range.

[13] The initial parameters were usually random, but to check whether the (non-)convergences were due to a specific set of initial conditions I explored the initial conditions by hand as well.

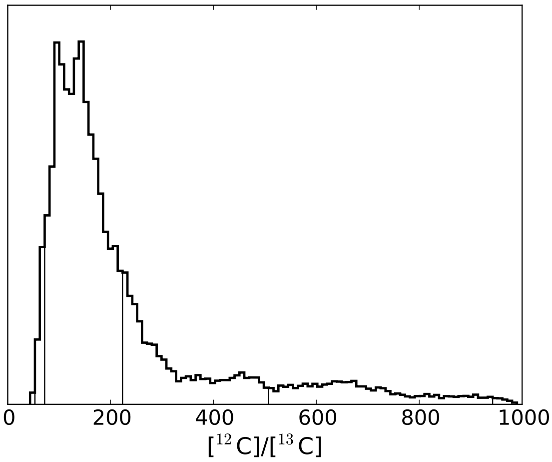

Figure 5.27: The posterior pdf for the [^{12}C]/[^{13}C] ratio in NGC 6240, derived from the three-phase model in § 5.4.6 using a mass and abundance weighted average. The ratio shows some signs of being slightly elevated, but the upper 68% credible interval is less than half the value found by Papadopoulos et al. (2014).

range found by Papadopoulos et al. (2014). The ideal solution, a full chemical model, is beyond the scope of this paper. Nevertheless, it appears that the [^{12}C]/[^{13}C] ratio in NGC 6240 is most similar to other ULIRGs.

As was pointed out by Papadopoulos et al. (2014), a high [^{12}C]/[^{13}C] (300-500) abundance ratio would imply the existence of a very unusual environment in NGC 6240. It would be either a sign of a prolonged period of star formation with a very top heavy initial mass function (IMF) or an inflow of unprocessed gas from the outer edges of the galaxy. However, the massive, wide outflow in CO observed by Feruglio et al. (2013) in NGC 6240 suggests that an extensive inflow of gas would be difficult to maintain. That being said, García-Burillo et al. (2014) observed simultaneous inflows and outflows into/from the circumnuclear disk of NGC 1068, so this option cannot be entirely ruled out. Nevertheless, I believe it to be unlikely in the case of NGC 6240.

5.5.4 Line-Luminosity–to–Gas-Mass Conversion Factors

The ratio between line luminosity and gas mass, α, is of great interest as it provides a means of estimating galaxy gas fractions from observations of a single molecular line, usually CO. However, the determination of a general α_{CO} is particularly complicated, with dependences on luminosity (Solomon et al., 1987) and metallicity, leading to a range of values from 0.3 to almost 300, and a typical Milky Way value of 4.8 dropping to about 1 in $z = 2$ SMGs and 0.8 in (U)LIRGs[14] (Downes & Solomon, 1998; Bolatto et al., 2013). Nevertheless, it has recently been argued that α_{CO} may be underestimated in (U)LIRGs, and a Galactic value may be more accurate (Papadopoulos et al., 2012), due to gas over-densities arising from over-pressurisation due to turbulence.

There is interest in α_{HCN} as a possible estimator of the *dense* molecular gas mass, which may be more robust over a wide range of luminosities and may more accurately trace the specifically star forming gas (Gao & Solomon, 2004; Greve et al., 2009; García-Burillo et al., 2012). This in turn has been complicated by high resolution studies of ULIRGs which suggest that HCN emission may in many cases be dominated by shocked, X-ray heated or infra-red pumped emission (Aalto et al., 2007; Sakamoto et al., 2010; Aalto et al., 2012; García-Burillo et al., 2014; Viti et al., 2014; Aalto et al., 2015a; Martín et al., 2015; Tunnard et al., 2015b)

The MCMC LVG models allow for the calculation of α_{mol} and the corresponding mass for each gas phase. The values for the three-phase model are shown in Figure 5.26 where I plot α_{CO} for each of the three gas phases, and α_{HCN} for the dense phase, as well as the corresponding masses. The α_{CO} pdfs are relatively broad, with spans of about $1.5 - 2$ dex. The diffuse and shocked

---

[14] Downes & Solomon (1998) found a range for α_{CO} from 0.3 to 1.3 in ULIRGs.

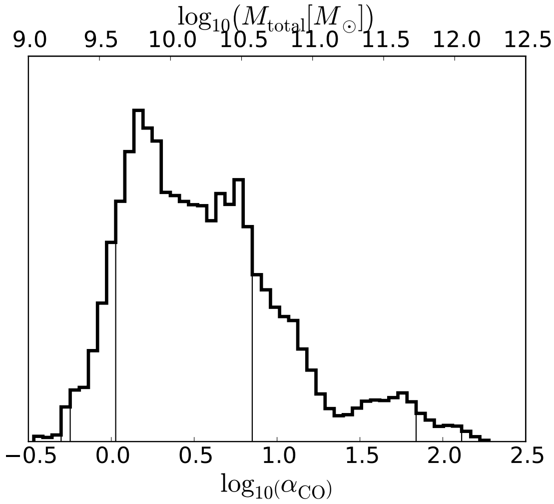

Figure 5.28: The global $\alpha_{\rm CO}$ for NGC 6240 derived from the three-phase model with the corresponding total molecular gas mass.

phases both cover the range $\alpha_{\rm CO} = 1 - 10$, while the diffuse phase extends down to 0.1. The dense phase $\alpha_{\rm CO}$ is much higher, due to a lower $X_{\rm CO}$, higher $n_{\rm H_2}$ and higher $\mathrm{d}v/\mathrm{d}r$ in this phase, all of which contribute to an increased $\alpha_{\rm CO}$. Despite contributing $< 5\%$ of the CO$(1-0)$ line flux, the dense phase accounts for almost all of the molecular gas mass. The dense phase gas masses derived using HCN and using CO are consistent but for a systematic offset of ~ -0.2 dex on the CO mass estimate. The $\alpha_{\rm HCN}$ pdf peaks around 30, higher than the canonical value of 10 but similar to the $13 - 31.1$ found by Papadopoulos et al. (2014), although some regions of their Figure 14 do extend to $\alpha_{\rm HCN} = 60$. Gao & Solomon (2004) predicted $\alpha_{\rm HCN} \sim 25$ for $X_{\rm HCN} = 2 \times 10^{-8}$ and $\mathrm{d}v/\mathrm{d}r = 5\,\mathrm{km\,s^{-1}\,pc^{-1}}$: the lower $X_{\rm HCN}$ and higher $\mathrm{d}v/\mathrm{d}r$ are responsible for the slightly higher $\alpha_{\rm HCN}$.

The $\alpha_{\rm HCN} = 32^{89}_{13}$, and thus is not very tightly constrained. While the upper limit on the 68% credible interval is very high, the best fit and lower limit on the 68% credible interval are completely consistent with Greve et al. (2009), who found $\alpha_{\rm HCN} = 17 - 37$ in NGC 6240.

We derive a global $\alpha_{\rm CO}$ by calculating the sum of the masses of each gas phase, and dividing by the total CO$(1-0)$ line luminosity. The resultant $\alpha_{\rm CO}$ pdf and the corresponding mass pdf for NGC 6240 is shown in Figure 5.28. This global $\alpha_{\rm CO}$ is much more tightly constrained than the those of the individual phases, and I find $\alpha_{\rm CO} = 1.5^{7.1}_{1.1}$: consistent with a Galactic $\alpha_{\rm CO}$, as predicted by Papadopoulos et al. (2012), but perhaps more consistent with the canonical $\alpha_{\rm CO}$ of starbursts (0.8, Downes & Solomon, 1998). The low luminosity dense phase contributes the majority of this gas mass.

The high $\alpha_{\rm HCN}$ I derive is contrary to the findings of García-Burillo et al. (2012), who argued for a lower $\alpha_{\rm HCN}$ in (U)LIRGs, matching the lower $\alpha_{\rm CO}$. It is very possible that this contradiction is simply due to the extremely unusual properties of NGC 6240; NGC 6240 is perhaps not even representative of other (U)LIRGs, existing in a class of its own.

5.5.5 Dense Gas and Star Formation in NGC 6240

The results of the LVG models present an intriguing picture of the dense molecular gas in NGC 6240. I appear to be finding large quantities of very cold (~ 8 K) gas within the internuclear molecular disk, which is also host to extensively shocked and very hot (~ 2000 K) molecular gas. The question is how can such a large quantity of cold, dense gas coexist with the hot phase. I have argued that the isotopologue abundance ratios in NGC 6240 are explained by chemical effects in cold, dense clouds, but these effects require active chemistry: CO and HCO$^+$ undergo isotope charge exchange (ICE) reactions which can alter the ratio as long as the gas is partially ionised (e.g., due to galactic-background cosmic-ray flux), while HCN exists in an equilibrium with HNC, and can be fractionated post production both by ICE and by the neutral reaction:

$$\mathrm{C} + \mathrm{HNC} \rightarrow \mathrm{HCN} + \mathrm{C} \tag{5.11}$$

(Loison et al., 2014). Furthermore, star formation in NGC 6240 is not found in the internuclear molecular disk; it is instead concentrated in the two nuclei. If I truly have almost $10^{10}\,M_\odot$ of cold, dense gas then I must be able to explain why this gas is not actively forming stars.

An insight is offered if I apply an upper limit to the H_2 column density of the dense phase. There is an inherent degeneracy within the LVG model between a single, large cloud and multiple, small clouds distributed in velocity space across the large scale velocity field of the galaxy. However, for the dense gas phase a single cloud implies column densities in excess of $10^{26}\,\mathrm{cm}^{-2}$, which are extremely unlikely. If instead I assume that the column densities of the clouds are $\simeq 10^{23}\,\mathrm{cm}^{-2}$ then I am instead seeing multiple small ($0.1 - 0.01\,\mathrm{pc}$) dense clouds.

We therefore propose the following situation. Within the turbulent internuclear disk instabilities lead to rapid, localised cooling of pockets of gas, leading to multiple small, cold, dense clouds embedded in pressure equilibrium with the hot, diffuse phase. This rapid cooling leads to an active chemistry, potentially with molecules less stable than CO destroyed in the high temperatures of the shocks reforming as the gas cools. These clouds are still turbulent however, and may indeed be transient, explaining the lack of star formation.

In the two and three-phase HCN, HCO^+ & CO models the CO abundance is significantly lower in the cold, dense phase than in the hot phase or diffuse phase. This is consistent with the many cold clouds interpretation above, with freeze out of CO onto dust grain mantles depleting the gas phase CO in cold, dense clouds - as observed in Milky Way cold cores (Kramer et al., 1999; Tafalla et al., 2002; Liu et al., 2013; Ripple et al., 2013). This might also explain the very strange CS model solutions (Figure 5.11): CS is depleted along with CO (Tafalla et al., 2002), so the only CS I observe is in the hot gas phase. Unfortunately this is highly speculative, and cannot be confirmed without much higher spatial resolution observations able to resolve the high density molecular clouds. Such observations were proposed and awarded time in ALMA Cycle 3, but are yet to be observed. This trend is even more pronounced in the three-phase model, where I have almost a continuum of X_{CO}, from the the diffuse phase value of $\sim 10^{-4}$, falling to $\sim 10^{-5}$ in the shocked phase and then to $\sim 10^{-6}$ in the dense phase. However, the $\pm 1\sigma$ spread in these values is almost ± 1 dex, so as I have stated throughout the paper, the absolute abundances should be interpreted with caution.

While the majority of the dense gas and the ongoing star formation are separate in NGC 6240 (Tacconi et al., 1999), I explore the galaxy averaged star formation efficiency. Combining the star formation rate (SFR) of $60 \pm 30\,M_\odot\,\mathrm{yr}^{-1}$ (Yun & Carilli, 2002; Feruglio et al., 2013) with $\alpha_{\mathrm{HCN(1-0)}}$ and $L'_{\mathrm{HCN(1-0)}}$ I can obtain estimates of the star formation efficiency (SFE) in NGC 6240. I am constrained by the dynamical mass within 600 pc of $\sim 10^{10}\,M_\odot$ found by Tacconi et al. (1999). Models 1a, 1b, 3 and 4 are all able to produce dense gas masses within 1σ of this limit (Figure 5.30), while models 2 and 5 have -1σ masses of $1.7 \times 10^{10}\,M_\odot$ and $4.3 \times 10^{10}\,M_\odot$ respectively. In all cases except model 5 the $+1\sigma$ mass is within 0.5 dex of the $10^{10}\,M_\odot$ limit. The three-phase model recovers very similar values.

The dynamical mass places the tightest constraints on the derived dense gas mass, and as such it also dominates the SFE estimates, effectively constraining the gas depletion time to between 10^7 and 10^8 years. All of the models, except for the exceptionally dubious model 3, push against this limit, with gas depletions times between 8×10^7 and 1.5×10^8 years as 1σ lower limits. Models 2 and 5 (HCO^+ and CS respectively) are unable to produce dense gas masses within 1σ of the limit, and so produce correspondingly higher gas depletion times.

With $n_{\mathrm{H}_2} \sim 1 \times 10^5$, a uniform density profile and spherical gas distribution the dynamical mass implies an upper limit on the dense gas volume filling factor of 0.002 within the central 600 pc of NGC 6240. This is consistent with the image, presented above, of the molecular disk being almost entirely filled with hot, shocked gas, but with the majority (by mass) of the molecular gas surviving in cold, dense clouds embedded within the hot phase.

I do however question whether the dynamical mass is in fact particularly meaningful in the central regions of NGC 6240. This galaxy is an ongoing major merger, so it is not clear that the velocity dispersion should actually correlate with the mass. Estimating the mass from the velocity dispersion assumes either virialisation or stable orbital rotation, neither of which is necessarily true for the central gas in NGC 6240, which is dissipating turbulent energy from the merger (Tacconi et al., 1999) and is most likely a transient feature itself. It is very possible that this explains the super-dynamical masses suggested by some regions of the results and a large region of the parameter space in Papadopoulos et al. (2014).

5.5.6 Implications of the [HCN]/[SiO] and [HCN]/[HCO$^+$] Abundance Ratios

I have found abundance ratios [HCN]/[SiO] = 80^{330}_{10} and [HCN]/[HCO$^+$] = $5.3^{7.0}_{4.7}$ in NGC 6240. This compares favourably to the value of "around 10" found by Krips et al. (2008). NGC 6240 is frequently compared to Arp 220, where Tunnard et al. (2015b) found [HCN]/[SiO] = $35 - 50$ and [HCN]/[HCO$^+$] > 18 in the western nucleus (WN) and [HCN]/[SiO] = $10 - 40$ and [HCN]/[HCO$^+$] $0.5 - 5$ in the eastern nucleus (EN)[15]. The abundances for NGC 6240 appear to me most consistent with the less luminous EN, which is dominated by star formation (whereas Arp 220 WN may contain an energetically significant AGN).

However, in NGC 6240 the comparison is probably less meaningful. Unlike in most of the galaxies of Krips et al. (2008), the majority of the molecular gas is spatially separated from the starbursts and putative AGNs in the two nuclei. As Krips et al. (2008) pointed out, the extreme conditions in NGC 6240 make it quite unique, and the abundance ratios may not carry the same meaning as they do in other galaxies and Arp 220 (which may itself be in a unique class of galaxies possessing Compact Obscured Nuclei (CONs), which generate unique chemistries Costagliola et al., 2015). In the context of Krips et al. (2008), the results place NGC 6240 in the intermediate region between a starburst and AGN dominated galaxy. The derived n_{H_2} is higher than the usual $< 10^{4.5}\,\mathrm{cm}^{-3}$ for AGNs, while the [HCN]/[HCO$^+$] ratio is higher than the $0.01 - 1$ of starburst but lower than the > 10 of AGN. Given the separation of the starburst and AGN nuclei from the bulk of the molecular gas (which lies between the two nuclei) the fact that NGC 6240 does not fit clearly into any specific category is not surprising.

The high [HCN]/[SiO] abundance is rather poorly constrained due to having only a single SiO line. It appears to be elevated nevertheless, which is consistent with most of the dust in NGC 6240 not being co-located with with molecular gas, as evidenced by the offsets between the continuum and dense gas tracers (e.g., in Nakanishi et al., 2005; Scoville et al., 2015).

5.6 Conclusions

In this chapter I have:

- presented the first observations of the low-optical-depth "dense gas" tracer H^{13}CN$(1-0)$ and an provide a strong upper limit on H^{13}CO$^+(1-0)$ in NGC 6240, as well as observations of SiO$(2-1)$.
- combined these observations with literature data as inputs for an MCMC wrapper for RADEX to find the conditions of the gas in NGC 6240. This code is extremely flexible, easily being extended to model multiple gas phases and species, with the greatest limitations being the divergences in RADEX itself and the paucity of, and uncertainties in, available line data.
- presented a two-phase, multi-species model which simultaneously fits both phases to the observed line ratios, and "spontaneously produces" a cold, dense phase and a hot, diffuse phase, which provide good fits to the HCN, HCO$^+$, CO and ^{13}CO SLEDs. This model was extended to three semi-prescribed phases to account for shocked molecular gas, extended diffuse molecular gas and cold, dense molecular gas.

---

[15] The [HCN]/[SiO] ratios were derived from the reported [H^{13}CN]/[SiO] ratios and an assumed [^{12}C]/[^{13}C] abundance ratio of 60.

- used my MCMC code and the new ^{13}C observations to show that the very high [^{12}C]/[^{13}C] ratio in NGC 6240 found by Papadopoulos et al. (2014) was due to assuming that the high$-J$ CO lines originate in the dense gas traced by HCN, whereas in NGC 6240 they probably originate in shocks (Meijerink et al., 2013), and the HCN lines are dense-gas dominated. These models suggest instead that the [^{12}C]/[^{13}C] ratio is "standard" for ULIRGs (98^{230}_{65}). The high [HCN]/[H^{13}CN] and [HCO^{+}]/[H^{13}CO^{+}] ratios (300^{500}_{200}) are due to isotope fractionation in cold, dense gas.
- derived $\alpha_{\rm CO}$ values for the diffuse, shocked and dense gas phases in NGC 6240, and combined these to produce a global $\alpha_{\rm CO} = 1.5^{7.1}_{1.1}$.

5.7 Additional Plots

Here I include additional plots from the MCMC LVG analysis in this chapter, but which for the sake of readability and concision have removed from the main text.

5.7.1 $K_{\rm vir}$ and Mass-Luminosity Ratios

For each point in the MCMC chain one can calculate $K_{\rm vir}$ and $\alpha_{\rm mol(1-0)}$, where $\alpha_{\rm mol(1-0)}$ is the ratio of dense gas mass to the $J = 1-0$ line luminosity of the species[16]. Using equation A4 for optically thick gas from Papadopoulos et al. (2012)[17] to derive $\alpha_{\rm mol(1-0)}$ for HCN and HCO^{+}, where $M_{\rm dense} = \alpha_{\rm mol(1-0)} L'_{\rm mol(1-0)}$. I also derived $\alpha_{\rm CS(1-0)}$, but this value is extremely uncertain given the caveats discussed previously for the CS results, and $\log_{10}\left(\alpha_{\rm CS(1-0)}\right)$ ranges from about 2.2 to 4.2, rendering it essentially meaningless. Given the extreme uncertainties in interpreting $\alpha_{\rm CS(1-0)}$ I neither include the pdf here nor explore it further, focussing instead on HCN and HCO^{+}.

I also derived $\alpha_{\rm mol(1-0)}$ using the general case of finite optical depths (Eqn. A15 in Papadopoulos et al., 2012, with changes to account for HCN and HCO^{+} instead of CO), and found the results are almost identical to the optically thick method, but systematically lower by 0.04 dex. This change is negligible relative to the general spread in the pdfs, but requires significantly more time to compute.

The posterior pdfs for $K_{\rm vir}$ are shown in Figure 5.29. All of the models with HCN show no preference for any $K_{\rm vir}$, but the HCO^{+} model shows a strong peak between 0.5 and 1, which is what we would expect for virialised molecular gas clouds. While this is far from conclusive, it is reminiscent of recent findings (e.g., Martín et al., 2015) of HCN in shocked regions as well as in quiescent clouds. Nevertheless, the very poor fit with SiO, as well as the cool, dense parameters of the HCN fits suggests that this may not be the case in NGC 6240. A cursory principle component analysis (PCA) of the chain shows the composite vector containing the majority of the variation (i.e., the least constraining composite vector) is almost entirely $n_{\rm H_2}$ and dv/dr, indicating that $K_{\rm vir}$ is not well constrained by the model (and therefore that the prior on $K_{\rm vir}$ is a strong prior). It is therefore not very meaningful to draw conclusions from these $K_{\rm vir}$ pdfs.

The posterior pdfs for $\log_{10}\left(\alpha_{\rm mol(1-0)}\right)$ and $\log_{10}\left(M_{\rm dense}[M_\odot]\right)$ are shown in Figure 5.30. For all of the models both $\alpha_{\rm HCN(1-0)}$ and $\alpha_{\rm HCO^{+}(1-0)}$ peak at $\sim 30\,M_\odot\left(\rm K\,km\,s^{-1}\,pc^2\right)^{-1}$, but also present multiple secondary peaks. The HCN pdfs have FWHM of almost a dex, and the model 3 $\alpha_{\rm HCN(1-0)}$ pdf has an FWHM almost 3 dex wide. HCO^{+} presents a narrower central peak, but more extended structure. These pdfs are particularly hard to decompose, to isolate the parameter spaces responsible for the various structures, so we simply note that the extremely wide pdf of model 3 further questions the validity of combining HCN and SiO in a single phase, while the HCN and HCO^{+} pdfs are not significantly worse than their single species counterparts.

The masses implied by these $\alpha_{\rm mol(1-0)}$ are centred in the range $10^{10.0}$ - $10^{10.5}$ $M_\odot$.

Numerical results for $K_{\rm vir}$ and $\alpha_{\rm mol(1-0)}$ are tabulated in Table 5.10. Table 5.10 presents the $K_{\rm vir}$ and $\alpha_{\rm mol(1-0)}$ values corresponding to the means of the pdfs.

---

[16] Units of $M_\odot\left(\rm K\,km\,s^{-1}\,pc^2\right)^{-1}$.

[17] $\alpha_{\rm mol(1-0)} = \frac{3.25}{\sqrt{\alpha}} \frac{\sqrt{\langle n_{\rm H_2}\rangle}}{\langle T_{b,1-0}\rangle} K_{\rm vir}^{-1}$

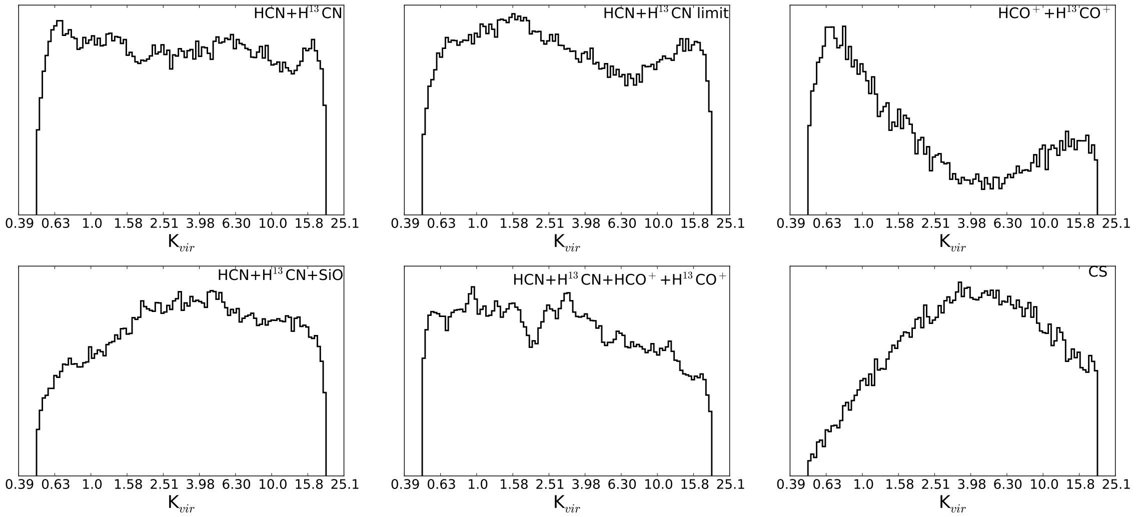

Figure 5.29: Marginalised posterior pdfs for K_{vir} in the single phase models. Note the logarithmic abscissa. None of the models with HCN show a preference for any K_{vir}, but the HCO$^+$ model 3 shows a strong peak between 0.5 and 1, which is what one would expect for virialised molecular gas clouds.

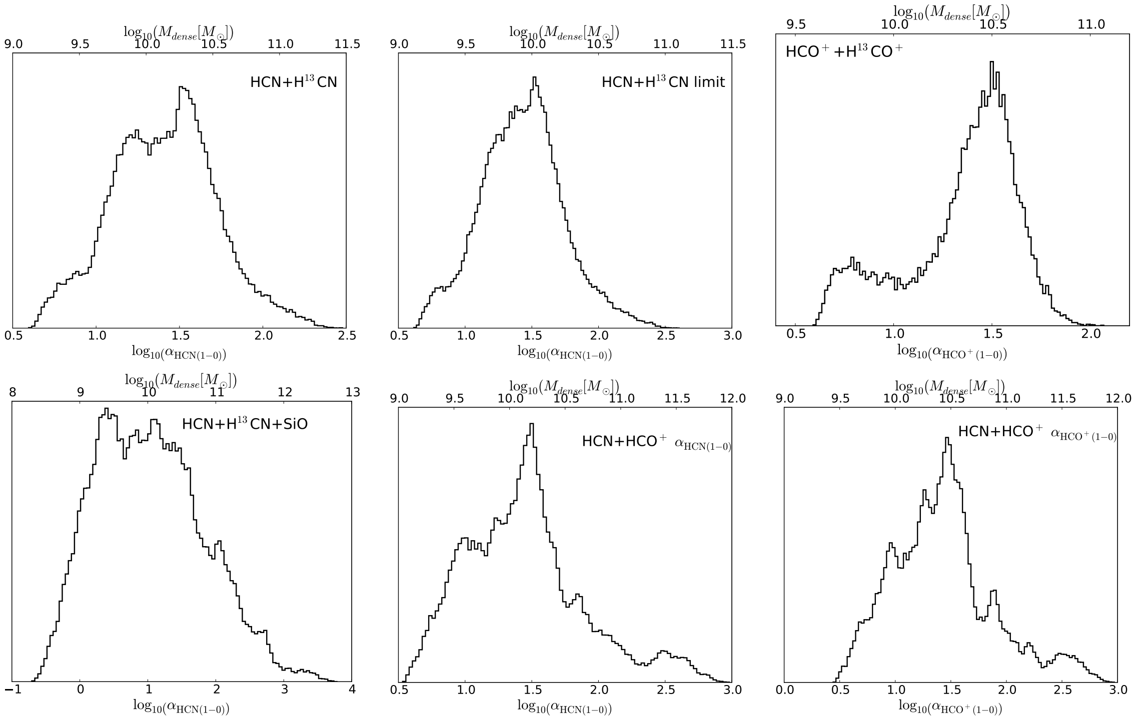

Figure 5.30: Posterior pdfs for $\log_{10}\left(\alpha_{\mathrm{mol}(1-0)}\right)$, with the implied dense gas mass indicated on the upper axis. All of the models and species peak strongly around $\sim 30\,M_\odot\left(\mathrm{K\,km\,s^{-1}\,pc^2}\right)^{-1}$, except for the already dubious HCN+H^{13}CN+SiO case of model 3. In all cases except model 3 the pdf peaks between $10^{10.0}$ $M_\odot$ and $10^{10.5}$ $M_\odot$ of dense gas.

Table 5.10: $K_{\rm vir}$ and $\alpha_{\rm mol(1-0)}$ mean values from their marginalised posterior pdfs.

Model ID	$K_{\rm vir}$	$\alpha_{\rm mol(1-0)}$ $[M_\odot\,(\mathrm{K\,km\,s^{-1}\,pc^2})^{-1}]$
1a	3.1	HCN: 26_{13}^{51}
1b	3.0	HCN: 27_{14}^{51}
2	2.0	HCO$^+$: 22_{18}^{50}
3	5.4	HCN: 11_{1}^{47}
4	2.7	HCN: 28_{8}^{51} HCO$^+$: 27_{7}^{51}
5	4.1	CS: 440_{150}^{720}

5.8 Cloud Kinematic Separation

The MCMC LVG model only fits line ratios, so while it is ideal for identifying the dominant conditions of the sampled gas phases it is poorly adapted for identifying the masses within each phase. A simple but inelegant solution would be to identify the CO line luminosity from each gas phase and then use an $\alpha_{\rm CO}$ factor to estimate the mass of the phase. This is however extremely susceptible to uncertainties in the $\alpha_{\rm CO}$ factor. Instead, I attempt to derive an alternative method, self-consistent with the MCMC LVG model. In this framework, one could apply a physically motivated upper limit on $N_{\rm H_2}$, thereby applying a limit on Δv per cloud.

It is readily apparent that a single gas cloud representing the galaxy is inadequate, since the column density of H$_2$ can be written as:

$$N_{\rm H_2} = \frac{3.086\times10^{18} n_{\rm H_2}\Delta v}{\mathrm{d}v/\mathrm{d}r}, \tag{5.12}$$

which for the high density gas phase leads to column densities in excess of $10^{26}\,\mathrm{cm^{-2}}$! This is because the dense gas is not in a single cloud, but distributed across the galaxy in many much smaller clouds, so that Δv is overwhelmed by the large scale motion in the galaxy, and does not correspond to the LVG Δv which is the line width of the putative emitting cloud.

What would be ideal would be to be able to separate the emission into multiple identical clouds and thereby obtain more realistic estimates of the mass of the gas phase. I start my attempt to do such by noting that it is a general statement that for a cloud of uniform density:

$$M_{\rm cloud} = \frac{4\pi}{3}\left(\frac{\zeta\Delta v}{2\,\mathrm{d}v/\mathrm{d}r}\right)^3 n_{\rm H_2}\mu_{\rm H_2}, \tag{5.13}$$

where $\zeta = 3.08\times10^{18}$ is the parsec to cm conversion factor, Δv is the FWHM line width of the cloud, $\mathrm{d}v/\mathrm{d}r$ is the velocity gradient of the cloud in $\mathrm{km\,s^{-1}\,pc^{-1}}$, $n_{\rm H_2}$ is the hydrogen number density in $\mathrm{cm^{-3}}$ and $\mu_{\rm H_2}$ is the helium adjusted ISM mass per H$_2$ molecule.

Separately, one can also make the general statement of beam dilution that for a Gaussian surface brightness with peak $T_{\rm b}$ and a Gaussian beam much larger than the size of the cloud, that

$$T_{\rm b,d} = \frac{1.133\,T_{\rm b}\,\chi^2}{\Omega_{\rm beam}}\left(\frac{\Delta v}{2\,\mathrm{d}v/\mathrm{d}r}\right)^2, \tag{5.14}$$

where $\chi = \frac{1}{494}$ arcsec/pc is the angular scale for NGC 6240 and $\Omega_{\rm beam}$ is in arcsec^2. In this case, $T_{\rm b}$ is a result of RADEX runs, which give optically thick clouds for the HCN and CO $J=1-0$ lines.

For a Gaussian line or a line which can be described as a combination of Gaussians the number of clouds is the ratio of the area ($T\Delta v$) of the observed line to the diluted area per cloud:

$$n_{\rm clouds} = \frac{T_{\rm obs}{\rm FWHM}}{T_{\rm b,d}\Delta v} = \frac{T_{\rm obs}\Omega_{\rm beam}{\rm FWHM}}{1.133\,T_{\rm b}\,\Delta v\,\chi^2\left(\frac{\Delta v}{2\,{\rm d}v/{\rm d}r}\right)^2}. \tag{5.15}$$

Therefore the total mass in the galaxy in this gas phase is:

$$M = M_{\rm cloud}\;n_{\rm clouds} \tag{5.16}$$

$$= \frac{4\pi}{3}\left(\frac{\zeta\Delta v}{2{\rm d}v/{\rm d}r}\right)^3 n_{\rm H_2}\mu_{\rm H_2}\frac{T_{\rm obs}\Omega_{\rm beam}{\rm FWHM}}{1.133\,T_{\rm b}\,\Delta v\,\chi^2\left(\frac{\Delta v}{2\,{\rm d}v/{\rm d}r}\right)^2} \tag{5.17}$$

$$= \frac{1.85\,\zeta^3\mu_{\rm H_2}}{\chi^2}\frac{T_{\rm obs}\Omega_{\rm beam}}{T_{\rm b}}\frac{n_{\rm H_2}}{{\rm d}v/{\rm d}r}{\rm FWHM} \tag{5.18}$$

$$= 0.123\frac{T_{\rm obs}\Omega_{\rm beam}}{T_{\rm b}\,\chi^2}\frac{n_{\rm H_2}}{{\rm d}v/{\rm d}r}{\rm FWHM} \qquad [M_\odot] \tag{5.19}$$

This in fact corresponds to the same equation for $\alpha_{\rm mol}$ as that derived by Papadopoulos et al. (2012) by considering iso-velocity surfaces across a galaxy. Also, I find that the mass is independent of the chosen upper limit on $N_{\rm H_2}$, which is reassuring given that GMCs are likely to present a range of column densities (Vázquez-Semadeni et al., 1997).

Chapter 6

Behind the Veil of Dust: the ULIRG Arp 220

"Shall any gazer see with mortal eyes, Or any searcher know by mortal mind? Veil after veil will lift -but here must be Veil upon veil behind."

Edwin Arnold

This chapter was published in a similar form in Tunnard et al. (2015b).

6.1 Background

In the previous chapter I made use of an extensive suite of molecular lines to model dense molecular gas in NGC 6240, where the majority of the molecular gas lies in a dense molecular disk between the two merger nuclei. In the ULIRG Arp 220 however, the majority of the molecular gas is centred on the two nuclei which may possess significantly different dominant energy sources and chemistries. This limits the utility of the MCMC-LVG code for this galaxy and poses additional challenges when combining the different beam sizes of the available single dish and interferometric data. The work in this chapter was published in Tunnard et al. (2015b), and the PdBI observations and initial data reduction (to (u, v) visibility tables) were conducted by R. Neri and J. Graciá-Carpio.

.

The prototypical ULIRG Arp 220 (aka NGC 4027 and IC 4553, $z = 0.01818$) has been extensively studied across the entire EM-spectrum, revealing an extraordinarily dense and massive galactic merger (Soifer et al., 1984; Emerson et al., 1984; Young et al., 1984; Scoville et al., 1991; McDowell et al., 2003). It is a late-stage merger with two high-column-density ($N_{\mathrm{H}_2} \gtrsim 1 \times 10^{25}\,\mathrm{cm}^{-2}$), counter-rotating disks (separation $\simeq 400\,\mathrm{pc}$ along the east-west axis) orbiting within a much larger gas disk (radius $\simeq 0.25 - 1.5\,\mathrm{kpc}$, average molecular gas density $\sim 10^3\,\mathrm{cm}^{-3}$), potentially with an extended galactic halo (Sakamoto & Scoville, 1999; Mundell et al., 2001; Sakamoto et al., 2008; Engel et al., 2011; González-Alfonso et al., 2012). Arp 220 is extremely dusty with $A_{\mathrm{V}} > 1000\,\mathrm{mag}$ towards the central nuclear region (Fischer et al., 1997), and possesses at least three distinct stellar populations: a 10 Myr old starburst, a $\gtrsim 1\,\mathrm{Gyr}$ old population and a nascent, $\lesssim 7\,\mathrm{Myr}$ old non-starburst component, all distributed across the kiloparsec scale merger(Wilson et al., 2006; Rodríguez Zaurín et al., 2008; Engel et al., 2011).

There is mounting evidence for an AGN in the western nucleus (WN) of Arp 220 (Downes & Eckart, 2007, and references therein) as well as a nuclear starburst revealed with Very Long Baseline Interferometry (VLBI) (Rodríguez Zaurín et al., 2008; Batejat et al., 2011). In particular,

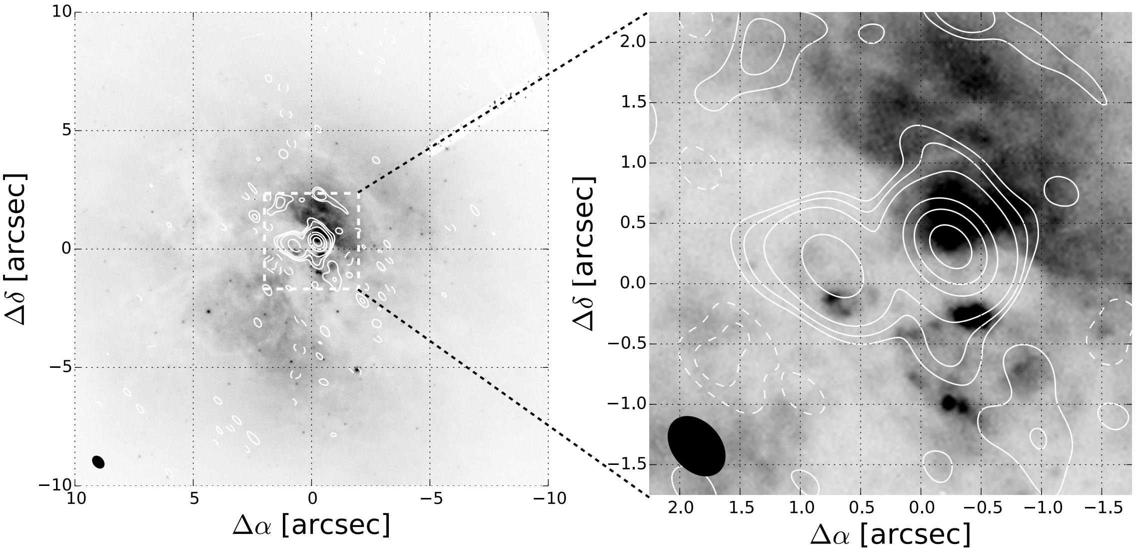

Figure 6.1: Hubble ACS/HRC F814W image with the 1.2 mm continuum contours overlaid. The compact red emission demonstrates the highly obscured nature of the central regions of Arp 220. The right hand image shows a $4'' \times 4''$ extract centring on the millimetre continua. The 1.2 mm continuum contours (in white) are overlaid at −5, −3, 3, 5, 10, 50, 100, 200 and 300σ and the 1.2 mm beam ($0.52'' \times 0.37''$) is shown in the bottom left hand corners. The HST image was created with the help of the ESA/ESO/NASA FITS Liberator, and has a nominal astrometric accuracy of $0.3''$.

the mass, luminosity and dust temperatures have previously been used in attempts to identify an AGN. Sakamoto et al. (2008) and Engel et al. (2011) found dynamical masses in the WN and eastern nucleus (EN) from CO and stellar kinematics respectively. Within 100 pc of the continuum centres of each nucleus they agree that the masses are on the order of $\sim 1 \times 10^9\,M_\odot$, although Engel et al. (2011) found masses closer to $\sim 5 \times 10^9\,M_\odot$. When Wilson et al. (2014) combined these results with their own high resolution ALMA observations of the nuclear continua, they obtained luminosity-mass ratios $540\,L_\odot\,M_\odot^{-1}$ and $30\,L_\odot\,M_\odot^{-1}$ for the WN and EN respectively: they conclude that the high WN ratio could be an AGN, or a hot starburst. Dust temperatures in the WN have been found from millimetre continuum measurements to be $\sim 180 - 200\,$K, once accounting for optical depth effects (Downes & Eckart, 2007; Wilson et al., 2014), while far-IR absorption lines suggest temperatures as high as 400 K (González-Alfonso et al., 2012). Such temperatures are usually associated with dusty toroids around AGN (e.g. Weiß et al., 2007). Attempts to identify an AGN from X-ray observations have also been unsuccessful, but due to the Compton thick H_2 column density ($\sim 1 \times 10^{25}\,\mathrm{cm}^{-2}$) towards the WN any X-ray emission would be almost completely attenuated (Wilson et al., 2014). Molecular outflows have been observed in OH^+, H_2O^+ and H_2O by Rangwala et al. (2011); González-Alfonso et al. (2012) and in $CO(3-2)$, $HCO^+(4-3)$ and $(3-2)$ by Sakamoto et al. (2009), although these could be driven by either an AGN or a starburst. Mangum et al. (2013) confirmed a hot, dense gas phase through NH_3 thermometry, finding solutions including $T_\mathrm{k} \sim 300\,$K at $n_{\mathrm{H}_2} \sim 10^6\,\mathrm{cm}^{-3}$.

Sakamoto et al. (2009) observed the $HCO^+(3-2)$, $(4-3)$ and $CO(3-2)$ lines at high resolution ($\sim 0.3''$) with the Sub-Millimetre Array (SMA), identifying prominent P Cygni profiles in both nuclei in the HCO^+ lines as well as absorption about the $CO(3-2)$ line centre. All of their WN lines displayed redshifted emission out to $+500\,\mathrm{km\,s^{-1}}$, while the HCO^+ lines showed maximum absorption around $-100\,\mathrm{km\,s^{-1}}$, but with some signs of blueshifted absorption out to $-500\,\mathrm{km\,s^{-1}}$, mixed with some blueshifted emission. The $HCO^+(4-3)$ lines in both nuclei presented much cleaner P Cygni profiles than the $(3-2)$ lines, although they still showed extended redwards emission.

The warm, dense dust in the WN (Sakamoto et al., 2009 found $T_\mathrm{d} \simeq 130\,$K, Matsushita et al., 2009 suggested T_d could be as high as 310 K and optically thick at 435 μm while González-Alfonso et al. (2012) found $T_\mathrm{d} \simeq 90 - 120\,\mathrm{K}$ and that the dust could be optically thick out to 2.4 mm) provides a powerful radiation source against which absorption in molecular outflows can be clearly seen. In particular Sakamoto et al. (2009) and Papadopoulos et al. (2010a) noted that the unusually high dust temperature favours the observation of higher frequency rotational transitions in absorption, and in the case of CO$(6-5)$ Papadopoulos et al. (2010a) found that the optical thickness of the dust in Arp 220 suppresses emission in higher transitions.

In this work I present a P Cygni profile, seen in SiO$(6-5)$ for the first time in this galaxy, towards the western nucleus (WN) of Arp 220. I also report PdBI observations of SiO$(2-1)$, H^{13}CN and H^{13}CO$^+$ $(3-2)$ and $(1-0)$; HN^{13}C and HC^{15}N $(3-2)$ and SO(6_6-5_5). The lower optical depths of the ^{13}C isotopologues provide a better measure of abundances than the ^{12}C isotopologues, while the millimetre observations allow us to see through much of the dust enshrouding the nuclear disks of Arp 220. This combination of effects allows us to probe deeper into the driving regions of Arp 220 than has previously been possible. The observations are outlined in §6.2 and the continuum and line identification are discussed in §6.3. I outline the details of the lines in each nuclei in §6.4 and §6.5, before entering into a more complete analysis in §6.6. Finally I discuss the significance of the results in §6.7.

I assume a flat universe with the 2013 Planck cosmological parameters (Planck Collaboration et al., 2014): $h = 0.673$, $\Omega_m = 0.315$ and $\Omega_\Lambda = 0.685$. For Arp 220 at $z_\mathrm{co} = 0.01818$ (V_co(WN) $=$ $5355 \pm 15\,\mathrm{km\,s^{-1}}$, V_co(EN) $= 5415 \pm 15\,\mathrm{km\,s^{-1}}$, radio, LSR, Sakamoto et al., 2009) this gives a scale of 384 pc/″ and a luminosity distance $D_\mathrm{L} = 82.1$ Mpc (Wright, 2006a). The longest baseline for the 1.2 mm data was 382.5 kilowavelengths and 218.1 kilowavelengths at 3.5 mm, giving a maximum resolution $\simeq 0.37''$, or ~140 pc at 1.2 mm and $\simeq 0.70''$, or ~270 pc at 3.5 mm.

6.2 Observations and Data Reduction

Two datasets were obtained from the IRAM Plateau de Bure Interferometer (PdBI) at 3.5 mm (2007 February 1 and 2007 March 14 in the A configuration (beam $1.44'' \times 0.70''$, $PA = 22°$, maximum angular scale $\sim 5.7''$)) and one at 1.2 mm (2011 January 11 in the B configuration (beam $0.52'' \times 0.37''$, $PA = 44°$, maximum angular scale $\sim 9.1''$)). All six antennas were available for all observations. Total on source time for 3.5 mm was 17550 s and 21690 s for 1.2 mm.

For both 2007 observations the bandpass was classed as excellent, with excellent and good amplitude calibrations in the February and March observations respectively. The correlator was centred on 85.0474 GHz sky frequency, corresponding to 85.2783 GHz in the $z_\mathrm{co} = 0.01818$ rest frame, and had a bandwidth of 965 MHz. Bandpass calibrators were 3C273 and 3C454.3, amplitude and phase calibration used 1611+343 and radio seeing was 0.30″. The data were reduced to UV tables by J. Graciá-Carpio and R. Neri using CLIC. The UV tables were analysed and mapped by R. Tunnard using the MAPPING program in the IRAM proprietary software GILDAS[1] (Guilloteau & Lucas, 2000). These observations targeted SiO$(2-1)$, H^{13}CN$(1-0)$ and H^{13}CO$^+$$(1-0)$ in both nuclei.

The 1.2 mm data used the full 3.6 GHz bandwidth of the WideX correlator, centred on 255.127 GHz sky frequency, corresponding to 259.765 GHz in the $z_\mathrm{co} = 0.01818$ rest frame, with spectral channels of width 3.9 MHz (~$4.59\,\mathrm{km\,s^{-1}}$), with the aim of mapping H^{13}CN$(3-2)$, H^{13}CO$^+$$(3-2)$ and SiO$(6-5)$. The observations were phase centred at RA: $15^\mathrm{h}34^\mathrm{m}57^\mathrm{s}24$, Dec: $23°30'11''2$. The data were imaged from UV tables using natural weighting.

For both frequencies I estimate a 10% uncertainty in the absolute flux calibration. The Hogbom CLEAN algorithm (Högbom, 1974) was used to produce data cubes, cleaning down to a flux level of ~$0.5\,\sigma$. I obtain rms. noise levels of $3.3\,\mathrm{mJy\,beam^{-1}}$ at 1.2 mm with channels of $4.59\,\mathrm{km\,s^{-1}}$ and $1.60\,\mathrm{mJy\,beam^{-1}}$ at 3.5 mm with channels of $8.81\,\mathrm{km\,s^{-1}}$.

---

[1] `http://www.iram.fr/IRAMFR/GILDAS`

6.3 Results

6.3.1 Continuum

Interpretation of the line profiles and implied kinematics requires knowledge of the dust properties of the source, and in particular to what extent dust is obscuring the observations. The continuum emission is dominated by dust, so provides a means of studying the dust properties in Arp 220. Furthermore, it is necessary to confirm that the detected continuum is consistent with previous observations to ensure that the sub-continuum absorption is real.

The GILDAS task UV_FIT was used to fit two elliptical gaussians to the 1.2 mm and 3.5 mm continuum UV tables. Elliptical gaussians were chosen to facilitate meaningful comparisons with the literature. These produced good fits, with flux densities consistent with those obtained from the imaged data. Elliptical disks fit the data with the same rms. error, while point sources provide inferior fits. The residual UV table, after subtraction of the fitted components, was imaged and is consistent with noise. The peak intensity in the imaged residual data cube is 4% of that of the imaged continuum, at the same level as the main beam side lobes, and is not associated with any structure in the map. The fitted parameters, with nominal errors, are presented in Table 6.1, along with comparable continuum measurements from the literature.

Table 6.1: Continuum data for Arp 220 in the millimetre regime. Data from Martín et al. (2011) are not included as the resolution of the observations precludes individual nuclear size or position measurements.

Source	ν_0 [GHz]	RA	Dec	Size[a] [arcsec]	S_ν [b] [mJy]
This work: WN	86.6	$15^{\mathrm{h}}34^{\mathrm{m}}57^{\mathrm{s}}23$	$23^\circ30'11''50$	$0.53(0.06) \times 0.27(0.05)$	$17(8) \pm 2$
This work: EN		$15^{\mathrm{h}}34^{\mathrm{m}}57^{\mathrm{s}}30$	$23^\circ30'11''32$	$0.43(0.09) \times 0.32(0.07)$	$11(6) \pm 1$
Scoville et al. (1991): both	110.3	−−	−−	−−	30 ± 3
Downes & Eckart (2007): WN	230	$15^{\mathrm{h}}34^{\mathrm{m}}57^{\mathrm{s}}2226$	$23^\circ30'11''46$	0.19×0.13	106 ± 2
Scoville et al. (1997): both	229.4	−−	−−	1.07×0.63	192 ± 20
This work: WN	260	$15^{\mathrm{h}}34^{\mathrm{m}}57^{\mathrm{s}}22$	$23^\circ30'11''50$	$0.194(0.004) \times 0.1546(0.0021)$	$200(196) \pm 20$
This work: EN		$15^{\mathrm{h}}34^{\mathrm{m}}57^{\mathrm{s}}29$	$23^\circ30'11''34$	$0.258(0.008) \times 0.183(0.007)$	$71(69) \pm 7$
Sakamoto et al. (2009): WN	273	−−	−−	−−	200 ± 20
Sakamoto et al. (2009): EN					70 ± 7
Aalto et al. (2009):WN	277	$15^{\mathrm{h}}34^{\mathrm{m}}57^{\mathrm{s}}230$	$23^\circ30'11''50$	−−	152 ± 19
Aalto et al. (2009):EN		$15^{\mathrm{h}}34^{\mathrm{m}}57^{\mathrm{s}}310$	$23^\circ30'11''40$	−−	57.6 ± 16
Sakamoto et al. (2008): WN	344.6	$15^{\mathrm{h}}34^{\mathrm{m}}57^{\mathrm{s}}215$	$23^\circ30'11''45$	0.28×0.22	380 ± 60
	349.6			0.16×0.13	360 ± 50
Sakamoto et al. (2008): EN	344.6	$15^{\mathrm{h}}34^{\mathrm{m}}57^{\mathrm{s}}285$	$23^\circ30'11''27$	0.31×0.25	200 ± 30
	349.6			0.27×0.14	190 ± 30
Wilson et al. (2014): WN	691	$15^{\mathrm{h}}34^{\mathrm{m}}57^{\mathrm{s}}22$	$23^\circ30'11''5$	$0.21 \times \leq 0.19$	1810 ± 270
Wilson et al. (2014): EN		$15^{\mathrm{h}}34^{\mathrm{m}}57^{\mathrm{s}}29$	$23^\circ30'11''3$	0.34×0.2	1510 ± 230

---

[a] Numbers in parentheses are the nominal uncertainties from UV fitting.

[b] Numbers in parentheses are the estimated synchrotron subtracted flux densities. The errors are dominated by the 10% estimated uncertainty in the absolute flux calibration.

The 1.2 mm continuum was obtained from the central $443\,\mathrm{km\,s^{-1}}$ wide line free region from $259.388 - 259.765$ GHz, WN rest frame, and the 3.5 mm continuum was found from the central $511\,\mathrm{km\,s^{-1}}$ wide line free region from $85.925 - 86.623$ GHz, WN rest frame. These regions are line free in both nuclei. Continuum contours for the 1.2 mm nuclei are shown in Fig. 6.1. The two nuclei are at best marginally resolved, so I worked in the UV plane to constrain the continuum parameters of the two nuclei. Fitting elliptical gaussians with the GILDAS task UV_FIT I found 1.2 mm continuum centres and sizes, and fluxes (RA=$15^{\mathrm{h}}34^{\mathrm{m}}57^{\mathrm{s}}220$, Dec=$23°30'11''50$, FWHM=$0.19'' \times 0.15''$, $S_{1.2\,\mathrm{mm}} = 200 \pm 20$ mJy and $S_{3.5\,\mathrm{mm}} = 17 \pm 2$ mJy for the WN and RA=$15^{\mathrm{h}}34^{\mathrm{m}}57^{\mathrm{s}}291$, Dec=$23°30'11''34$, FWHM=$0.26'' \times 0.18''$, $S_{1.2\,\mathrm{mm}} = 71 \pm 7$ mJy and $S_{3.5\,\mathrm{mm}} = 11 \pm 1$ mJy for the EN). These results and comparable measurements from the literature are included in Table 6.1. The fitted continuum centres at 1.2 mm are precisely in agreement with those that Wilson et al. (2014) found at much higher resolution ($0.363'' \times 0.199$") with ALMA. The 1.2 mm flux densities are consistent with the 1.1 mm flux densities of Sakamoto et al. (2009) who found 200 mJy and 70 mJy with 15% uncertainties. Subtracting synchrotron emission I find flux densities 196 ± 20 mJy and 69 ± 7 mJy for the WN and EN at 1.2 mm and 8 ± 2 mJy and 6 ± 1 mJy for the WN and EN at 3.5 mm.

The global (i.e., WN and EN, combined) dust optical depth and spectral index found from SED fitting of the continuum measurements and data from the literature were $\tau_{258\mathrm{GHz}} = 0.06$ and $\beta = 1.5$, with a turnover frequency ~ 1600 GHz. This is similar to the global fit of Rangwala et al. (2011), who found a turnover frequency of 1277 GHz and $\beta = 1.8$. However, compared with the four component SED fits of González-Alfonso et al. (2012), who for $\beta_{\mathrm{WN}} = 1 - 2$ predict $\tau_{258\mathrm{GHz}} = 2 - 0.4$ and $\tau_{86\mathrm{GHz}} = 0.7 - 0.04$ in the WN, the value is low, most likely due to fitting only two components (González-Alfonso et al., 2012 used four). Due to the more sophisticated modelling of González-Alfonso et al. (2012) I use their dust optical depths.

SED fitting

Using data from the literature including the fluxes in Table 6.1, Eales et al. (1989) and Rangwala et al. (2011), as well as Wide-field Infrared Survey Explorer (WISE) measurements of Arp 220, I fitted two grey-body models to the SED (Fig. 6.7). The WISE flux densities were corrected assuming a 100 K blackbody, as per Wright et al. (2010). I fitted the function:

$$S_{i,\nu} = \left(1 - e^{-\left(\frac{\nu}{\nu_{0,i}}\right)^{\beta_i}}\right) \frac{A_i \nu^3}{e^{\frac{h\nu}{kT_i}} - 1}, \tag{6.1}$$

$$S_\nu = S_{1,\nu} + S_{2,\nu}, \tag{6.2}$$

where ν_0 is the turnover frequency where the dust becomes optically thin, β is the dust emissivity spectral index, T is the dust temperature and A is an absolute normalisation. I performed a naturally weighted fit of these 8 free parameters to the SED, finding $\nu_{0,1} = 1.6 \times 10^3$ GHz (190μm), $\beta_1 = 1.5$, $A_1 = 4.9 \times 10^{-32}\,\mathrm{mJy\,Hz^{-3}}$ and $T_1 = 62$ K for the main component, and $\nu_{0,2} = 1.0$ GHz, $\beta_2 = 1.6$, $A_2 = 3.8 \times 10^{-37}\,\mathrm{mJy\,Hz^{-3}}$ and $T_2 = 340$ K. This fit has a reduced χ^2 (45 degrees of freedom) of 6.8. I note that $\nu_{0,2}$ is unphysically low, suggesting a blackbody spectrum. This should not be interpreted literally, since I am combining four known dust components (González-Alfonso et al., 2012) into a simple 2 element model. As I am only interested in $\nu_{0,1}$ and β_1 this is sufficient for the purposes. I find a global optical depth at 258 GHz of 0.06. For comparison, González-Alfonso et al. (2012) developed a complex, 4 component model of the dust in Arp 220 including a hot component, an extended component and models for the WN and EN. They found the greatest optical depth in the WN, with $\tau_{200\mu\mathrm{m}} = 6 - 12$. Assuming "worst case" parameters: $\tau_{200\mu\mathrm{m}} = 12$ and $\beta_{\mathrm{WN}} = 1 - 2$ gives $\tau_{258\mathrm{GHz}} = 2 - 0.4$ and $\tau_{86\mathrm{GHz}} = 0.7 - 0.04$. It seems reasonable then to assume that for the 3.5 mm observations the dust is almost entirely optically thin, although it may still be optically thick at 1.2 mm. The optical depth is significantly lower ($7 - 33\times$ lower) than that obtained by González-Alfonso et al. (2012) for the WN. This is probably due to the much simpler fit and averaging across both nuclei. The lower best-fit temperature (62 K cf. $90 - 130$ K) suggests that the low-optical-depth, high-luminosity extended dust component ($\tau_{200\mu\mathrm{m}} = 0.17$, $T_{\mathrm{d}} = 90 - 40$ K,

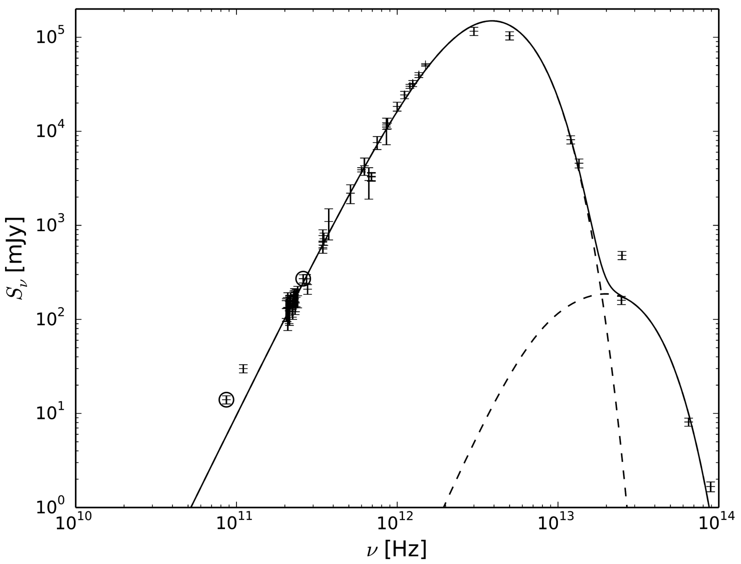

Figure 6.2: Continuum fluxes for Arp 220 from Table 6.1, Martín et al. (2011), Rangwala et al. (2011) and WISE data. I fit the data with two grey bodies. The continuum measurements are circled. I find best fit parameters $\nu_{0,1} = 1.6 \times 10^3$ GHz (190μm), $\beta_1 = 1.5$, $A_1 = 4.9 \times 10^{-32}$ mJy Hz^{-3} and $T_1 = 62$ K for the main component, and $\nu_{0,2} = 1.0$ GHz, $\beta_2 = 1.6$, $A_2 = 3.8 \times 10^{-37}$ mJy Hz^{-3} and $T_2 = 340$ K for the hotter component.

diameter ~ 650 pc $\simeq 1.7''$ González-Alfonso et al., 2012) could be having a significant effect upon the fit.

6.3.2 Line Identification

Within the bandwidth of the WideX correlator I detected a plethora of wide, high S/N lines in emission towards both nuclei of Arp 220, the frequencies and upper level energies of which are given in Table 6.3. The continuum subtracted spectra, including the multiple component Gaussian line fits, are shown in Figs. 6.3 to 6.6. The fitting derived line parameters are given in Table 6.4, and a full list of the fitted components is given in Table 6.2.

Since there is at least one pair of blended lines, and possibly two, I used multiple component Gaussian fits to parameterise the observed lines and to provide a handle for spectral deblending. Each of the boxes in the middle rows of Figs. 6.3-6.6 presents an individual fitting, which ranged from single to up to five components. I checked that randomised starting parameters (±50%) converged to the same final fits, demonstrating that the fits are robust. The number of fitting components was chosen such that χ^2_ν was closest to unity without having consecutive residuals above $\pm 1\sigma$. The rms. uncertainty in each channel was included in the fitting.

I include below in Table 6.2 the details of the Gaussian fitting to the spectra. These Gaussians should not be interpreted literally as the line profiles, but rather as well defined parametric descriptions of lines' peaks and areas. Reduced χ^2 is between 0.2 and 0.7 for all fits.

Uncertainties in the fitting were derived from the covariance matrixes. For functions making use of more than one fitting parameter (such as the flux of a component or the total flux of a line summed over all components) the correlations in the covariance matrices were taken into account when calculating uncertainties.

Lines were identified using the Cologne Database for Molecular Spectroscopy (CDMS) (Müller et al., 2005) and the Spectral Line Atlas of Interstellar Molecules (SLAIM) (Remijan et al., 2007), as well as the SMA line survey of Martín et al. (2011). The final line list consists of $H^{13}CN(1-0)$ and $(3-2)$, $HN^{13}C(3-2)$, $SiO(2-1)$ and $(6-5)$, $H^{13}CO^+(1-0)$ and $(3-2)$, $SO(6_6-5_5)$ and $HC^{15}N(3-2)$. The WN $HN^{13}C(3-2)$ line extends beyond the end of the spectrum. I see the blue edge of what is likely the $SO(2_2-1_1)$ in the 3.5 mm spectra, but almost the entire line is beyond

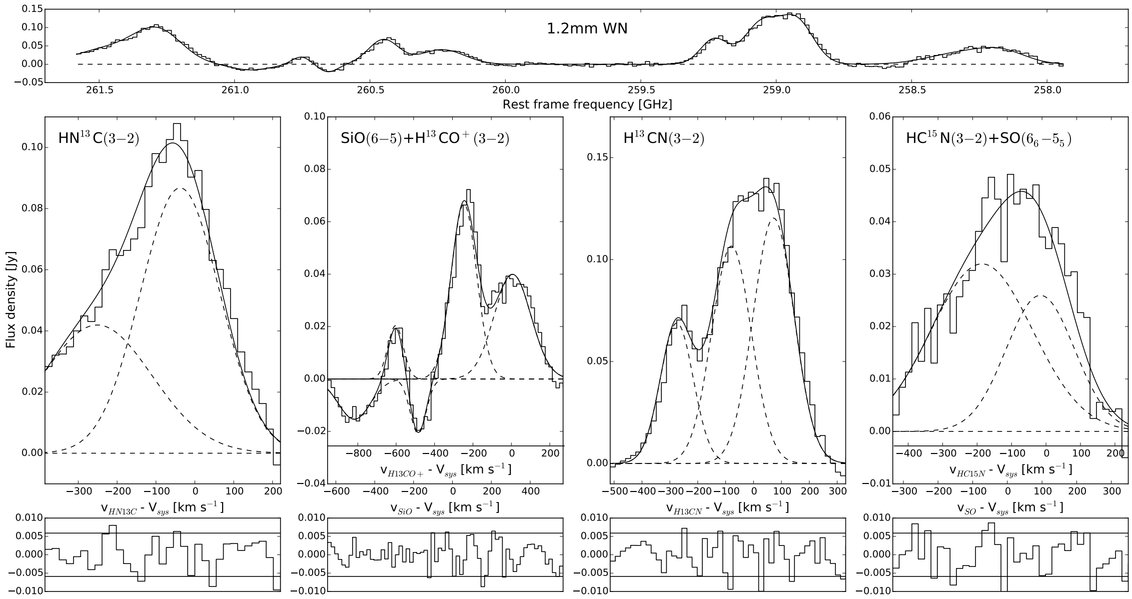

Figure 6.3: Continuum subtracted spectrum of Arp 220 WN extracted using a 1″ diameter circular apertures centred on the continuum centre. Top: the whole spectrum with the fitted lines overlaid. Frequencies are rest frame with $z = 0.01818$. Middle: multiple component Gaussian fits to the observed lines, with velocities shown relative to the line centres. Bottom: residuals from the fitting. The horizontal lines indicate the $\pm1\sigma$ rms. noise level (5.9 mJy). Reduced χ^2 values range from 0.25 to 0.7.

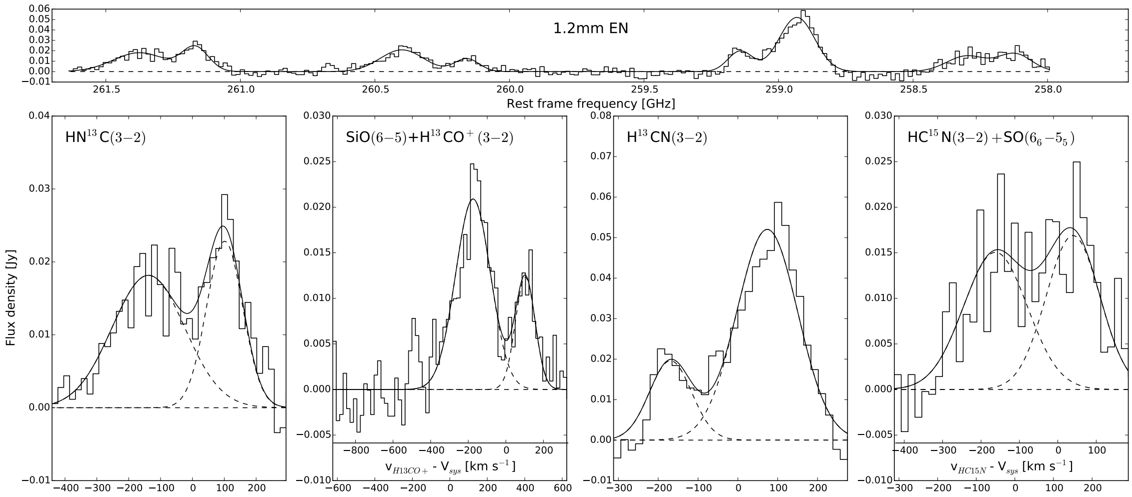

Figure 6.4: Continuum subtracted spectrum of Arp 220 EN extracted using a 1″ diameter circular apertures centred on the continuum centre. Top: the whole spectrum with the fitted lines overlaid. Frequencies are rest frame with $z = 0.01839$. Middle: multiple component Gaussian fits to the observed lines, with velocities shown relative to the line centres. Bottom: residuals from the fitting. The horizontal lines indicate the $\pm1\sigma$ rms. noise level (5.9 mJy). Reduced χ^2 values range from 0.25 to 0.7.

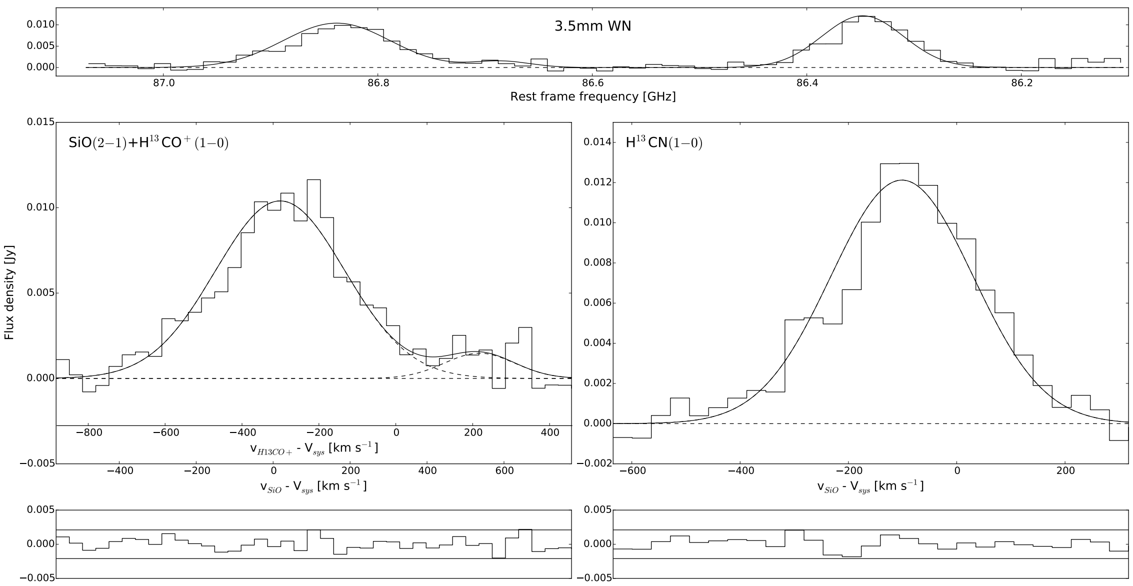

Figure 6.5: Continuum subtracted spectrum of Arp 220 WN extracted using elliptical apertures with major and minor axes equal to scaled FWHMs of the 3.5 mm beam, centred so as to minimise inter-nuclear contamination (RA: $15^{\rm h}34^{\rm m}57^{\rm s}226$, Dec: $23^{\circ}30'11''613$, scaling = 1.8). Top: the whole spectrum with the fitted lines overlaid. Frequencies are rest frame with $z = 0.01818$. Middle: multiple component Gaussian fits to the observed lines, with velocities shown relative to the line centres. Bottom: residuals from the fitting. The horizontal lines indicate the $\pm 1\sigma$ rms. noise level (2.1 mJy). Reduced χ^2 values range from 0.4 to 0.5.

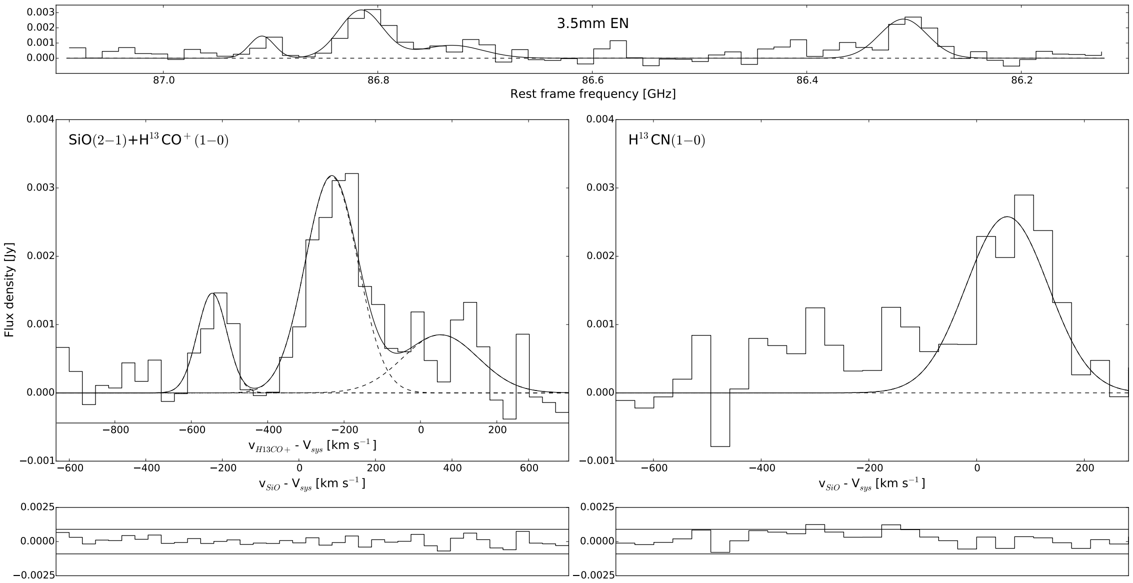

Figure 6.6: Continuum subtracted spectrum of Arp 220 EN extracted using elliptical apertures with major and minor axes equal to scaled FWHMs of the 3.5 mm beam, centred so as to minimise inter-nuclear contamination (RA: $15^{\rm h}34^{\rm m}57^{\rm s}302$, Dec: $23^{\circ}30'11''415$, scaling = 1.2). Top: the whole spectrum with the fitted lines overlaid. Frequencies are rest frame with $z = 0.01839$. Middle: multiple component Gaussian fits to the observed lines, with velocities shown relative to the line centres. Bottom: residuals from the fitting. The horizontal lines indicate the $\pm 1\sigma$ rms. noise level (0.9 mJy). Reduced χ^2 values range from 0.2 to 0.5.

Table 6.2: Details of Gaussian line fitting. Errors are determined from the fitting covariance matrices.

WN

Line	Component	S_ν	Centre[a]	FWHM	Area[b]
		[mJy]	[GHz]	[$\mathrm{km\,s^{-1}}$]	[$\mathrm{Jy\,km\,s^{-1}}$]
$SO(6_6 - 5_5)$	1	32 ± 20	253.69	350 ± 300	$12 \pm 18(18)$
$HC^{15}N(3 - 2)$	1	30 ± 60	253.55	230 ± 40	$6 \pm 15(15)$
$SiO(6 - 5)$	1	39.9 ± 2.5	255.589	223 ± 23	$9, 5 \pm 0.5(1.1)$
	2	66.8 ± 3.0	255.800	153 ± 11	$10.9 \pm 0.9(1.4)$
	3	-20.8 ± 3.8	256.000	97 ± 36	$-2.1 \pm 0.9(0.9)$
	4	20.3 ± 4	256.099	90 ± 40	$2.0 \pm 1.1(1.1)$
	5	-15.4 ± 2.7	256.280	190 ± 50	$-3.1 \pm 0.3(0.5)$
$H^{13}CN(3 - 2)$	1	173 ± 19	254.304	159 ± 18	$22 \pm 6(6)$
	2	69 ± 4	254.600	141 ± 13	$10.3 \pm 1.5(1.8)$
	3	110 ± 15	254.433	170 ± 30	$20 \pm 7(7)$
$HN^{13}C(3 - 2)$	1	42 ± 20	256.789	330 ± 300	$15 \pm 20(20)$
	2	90 ± 40	256.617	240 ± 40	$22 \pm 18(18)$
$H^{13}CN(1 - 0)$	1	12.1 ± 1.0	84.806	310 ± 30	$4.0 \pm 0.07(0.4)$
$SiO(2 - 1)$	1	10.4 ± 0.9	85.288	410 ± 40	$4.49 \pm 0.12(0.5)$
	2	1.5 ± 1.2	85.137	220 ± 220	$0.35 \pm 0.07(0.08)$

EN

Line	Component	S_ν	Centre[a]	FWHM	Area[b]
		[mJy]	[GHz]	[$\mathrm{km\,s^{-1}}$]	[$\mathrm{Jy\,km\,s^{-1}}$]
$SO(6_6 - 5_5)$	1	15 ± 4	253.636	201 ± 28	$3.2 \pm 1.2(1.2)$
$HC^{15}N(3 - 2)$	1	16.9 ± 2.3	253.460	170 ± 60	$3.1 \pm 1.1(1.2)$
$SiO(6 - 5)$	1	12 ± 3	255.460	120 ± 40	$1.63 \pm 0.19(0.25)$
	2	20.9 ± 2.5	255.697	220 ± 30	$4.87 \pm 0.19(0.5)$
$H^{13}CN(3 - 2)$	1	52.0 ± 2.7	254.256	182 ± 12	$10.06 \pm 0.26(1.0)$
	2	20 ± 3	254.463	125 ± 26	$2.60 \pm 0.18(0.31)$
$HN^{13}C(3 - 2)$	1	23 ± 4	256.451	133 ± 27	$3.2 \pm 1.1(1.2)$
	2	18.2 ± 2.3	256.655	270 ± 60	$5.2 \pm 0.6(0.8)$
$H^{13}CN(1 - 0)$	1	2.6 ± 0.6	84.751	180 ± 50	$0.497 \pm 0.018(0.053)$
$SiO(2 - 1)$	1	0.9 ± 0.5	85.165	240 ± 200	$0.22 \pm 0.06(0.06)$
	2	3.2 ± 0.6	85.248	170 ± 40	$0.56 \pm 0.16(0.17)$
	3	1.5 ± 0.8	85.339	90 ± 60	$0.145 \pm 0.013(0.019)$

---

[a] In the sky frame.

[b] Errors in parentheses include the 10% calibration error. These errors also account for the correlations between the component peaks and widths.

Table 6.3: Lines Observed in Arp 220 in Present Observations

Line	ν^{a} [GHz]	E_u/k [K]
$H^{13}CN(1-0)$	86.340	4.1
$H^{13}CO^{+}(1-0)$	86.754	4.2
$SiO(2-1)$	86.847	6.3
$HC^{15}N(3-2)$	258.157	24.8
$SO(6_6-5_5)$	258.256	56.5
$H^{13}CN(3-2)$	259.012	24.9
$H^{13}CO^{+}(3-2)$	260.255	25.0
$SiO(6-5)$	260.518	43.8
$HN^{13}C(3-2)$	261.263	25.1

[a] Rest frame frequency.

the red edge of the spectrum. The relative contributions of $SO(6_6-5_5)$ and $HC^{15}N(3-2)$ in the 1.2 mm spectrum are highly uncertain.

Vibrationally excited molecular absorption and emission (including HCN) was detected in Arp 220 by Salter et al. (2008) and Martín et al. (2011) respectively, suggesting that there may be some contribution from the vibrationally excited $H^{13}CN(v_2 = 1, J = 3-2, l = 1e \ \& \ 1f)$ lines at 258.936 GHz and 260.225 GHz respectively. However, the ratios of the predicted line intensities for the $v_2 = 0$ to $v_2 = 1$ transitions at 75 K and 300 K from the CDMS database (Müller et al., 2005) are $1 : 10^{-6}$ and $1 : 35$ respectively. This suggests that even with considerable mid-IR pumping (Aalto et al., 2007; Sakamoto et al., 2010; Rangwala et al., 2011) the vibrational lines should be below the noise level. Whether the effect of mid-IR pumping on the $v_{1,2} = 0$ rotational transitions is significant is still unclear (Rangwala et al., 2011; González-Alfonso et al., 2012).

SiO & $H^{13}CO^{+}$

There is significant uncertainty regarding the identification of SiO and $H^{13}CO^{+}$ in the spectra. At both observing frequencies and in both nuclei there is the possibility that all of the line components shown in the SiO+$H^{13}CO^{+}$ boxes in Figs. 6.3–6.6 are due to SiO, with no significant $H^{13}CO^{+}$ detection. Therefore, I examine the kinematic, spatial and line-brightness evidence in an attempt to constrain the contribution of $H^{13}CO^{+}$ at 3.5 mm and at 1.2 mm. While Sakamoto et al. (2009) provide a comprehensive benchmark with their $HCO^{+}(3-2)$ observations there are no published observations of $HCO^{+}(1-0)$ in Arp 220 resolving the two nuclei. Although Imanishi et al. (2007b) present interferometric observations of the line the two nuclei are completely unresolved in their observations. Therefore, the following analysis of $H^{13}CO^{+}$ contribution focusses on the $(3-2)$ transition in the 1.2 mm data.

Kinematically, a comparison with the $HCO^{+}(3-2)$ spectra of Sakamoto et al. (2009), shown in Fig. 6.7, reveals startlingly similarities between the line profiles of their $HCO^{+}(3-2)$ and those of the $SiO(6-5)$–$H^{13}CO^{+}(3-2)$ line complex, in both nuclei. Particularly in the WN, the line profiles are extremely similar, with all five of the fitted Gaussian line components in Fig. 6.3 having an equivalent in the $HCO^{+}(3-2)$ spectrum. I rule out that the lines are entirely $H^{13}CO^{+}(3-2)$ based on the significant ($\sim$ 320 km s^{-1}) velocity offset from the observed systemic velocity that this would require, but the kinematics cannot exclude the possibility that the lines are entirely $SiO(6-5)$.

In the 3.5 mm spectra there are multiple fitted components that are significant only at the 1 σ level, currently attributed to $H^{13}CO^{+}(1-0)$ (line centre +250 km s^{-1} in the WN and line centre +50 km s^{-1} in the EN, see Figs. 6.5 and 6.6). Given the low significance of these components, as well as their considerable offset from their line centres, it is highly uncertain whether they are (a) real detections and (b) not an extended red component of the the $SiO(2-1)$ lines.

To search for spatial clues I produced line integrated velocity maps for all of the lines. Shown in Fig. 6.8, one can see that all of the 1.2 mm lines, except for $H^{13}CO^{+}(3-2)$ and $SiO(6-5)$ are

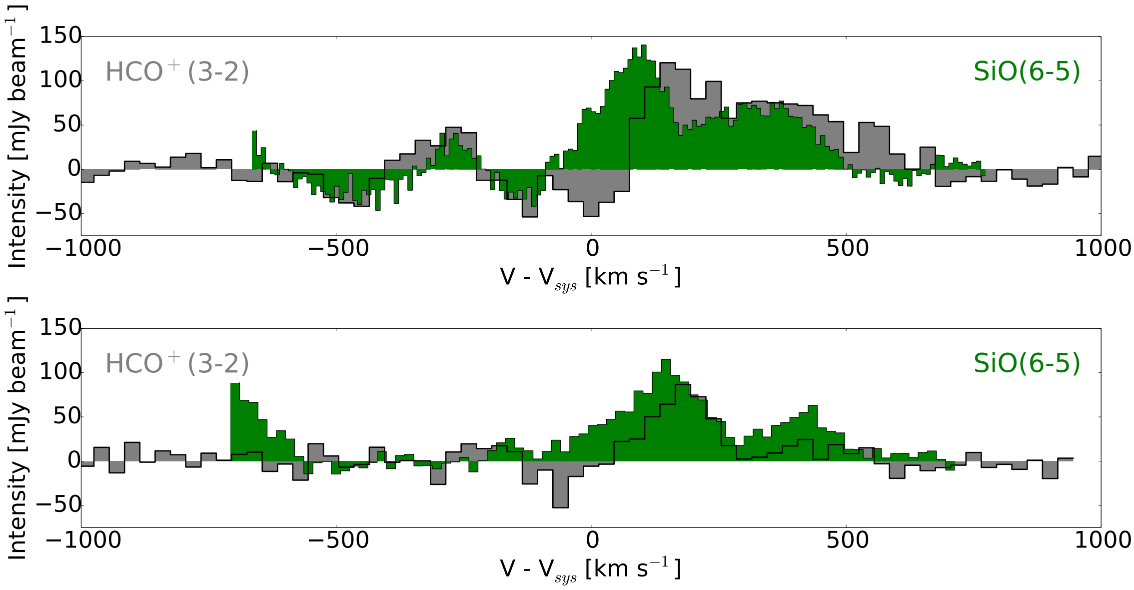

Figure 6.7: The $HCO^+(3-2)$ spectra from Sakamoto et al. (2009), with the $SiO(6-5)$-$H^{13}CO^+(3-2)$ spectra scaled by a factor of 8 and overlaid. The WN lines (top) are centred on $V_{\rm sys}(\rm WN) = 5355\,\rm km\,s^{-1}$, the EN (bottom) on $V_{\rm sys}(\rm EN) = 5415\,\rm km\,s^{-1}$. The similarity between the profiles, in particular in the WN, suggests that the spectrum may be predominantly $SiO(6-5)$, with no more than a minor contribution from the blended $H^{13}CO^+(3-2)$ component at $+317\,\rm km\,s^{-1}$. The $H^{13}CO^+(3-2)$ line centre is $+317\,\rm km\,s^{-1}$ redwards of $SiO(6-5)$, so cannot be the dominant contributor given the $HCO^+(3-2)$ profile.

tightly bound around the nuclear continua, while the $SiO(6-5)$–$H^{13}CO^+(3-2)$ line complex is strongly asymmetric about the WN continuum centre, highlighting it as a line of interest. The 3.5 mm lines are observed at too low a spatial resolution for us to derive any solid conclusions on the spatial distribution of the emission. Spatially, Sakamoto et al. (2009) found the line integrated $HCO^+(3-2)$ emission to be tightly collocated with the continuum emission, just as is seen for the $H^{13}CN(3-2)$ and $HN^{13}C(3-2)$ lines, but contrary to what is seen for the $SiO(6-5)$–$H^{13}CO^+(3-2)$ line complex, which in the WN is offset north of the continuum centre (Fig. 6.8). While it is possible that $H^{13}CO^+(3-2)$ is tracing very different regions from $HCO^+(3-2)$, possibly due to optical depth effects, it is far more likely, especially in light of the kinematic evidence presented above, that the explanation for this unique spatial arrangement is that the line integrated emission is dominated by $SiO(6-5)$.

As well as the kinematic and spatial comparisons discussed above, I also consider the brightness temperature ratios implied with detection and non-detection of $H^{13}CO^+$, using simple LTE estimations and $HCO^+(3-2)$ data from Sakamoto et al. (2009) to identify whether non-detections of $H^{13}CO^+(3-2)$ are physically viable.

Quantitatively, I use the $HCO^+(3-2)$ data to estimate the predicted $H^{13}CO^+(3-2)$ contribution. From Sakamoto et al. (2009) (data kindly provided by Sakamoto) I have the peak brightness temperature, optical depth and FWHM of the best fit Gaussian to the emission region of the line profile. The optical depth is found for the absorbing column, where the observed fractional absorption,

$$f_a = \frac{I_{\rm out}}{I_{\rm in}} - 1, \tag{6.3}$$

gives the optical depth of the absorption component:

$$\tau_a = -\log(1 + f_a). \tag{6.4}$$

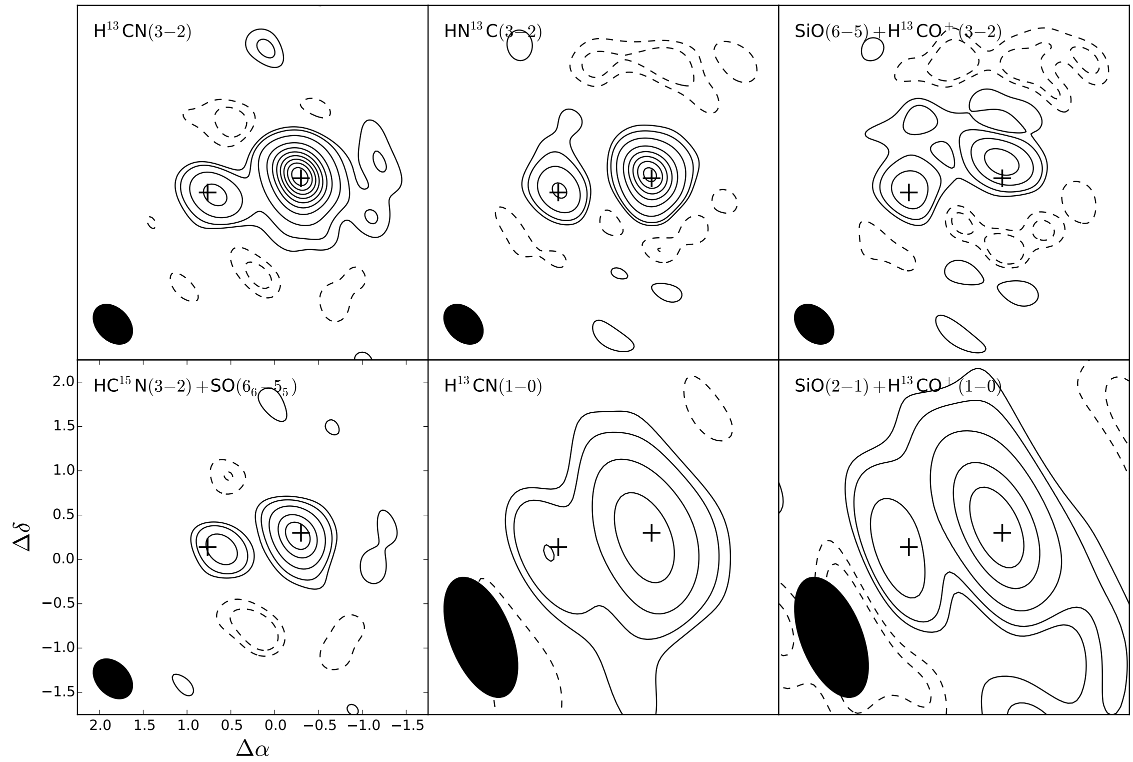

Figure 6.8: Line integrated contour plots of the observed species. Contours are at -5, -3, 3, 5 and $10n\sigma$, for $n = 1, 2...10$. The synthesised beams are $0.52'' \times 0.37''$ and $1.44'' \times 0.70''$ and are shown in the bottom left corners of the plots. Crosses mark the continuum centres. The 5σ sidelobe contours suggest that the observations are dynamic range limited.

For an integrated line emission intensity:

$$W = \int T_{\rm B} {\rm d}v \simeq 1.064\, T_{\rm B,peak}\, v_{\rm FWHM}, \tag{6.5}$$

I have an upper level column density:

$$N_u = \frac{8\pi k \nu^2 W}{hc^3 A} \left(\frac{\Delta\Omega_a}{\Delta\Omega_s}\right) \left(\frac{\tau}{1 - e^{-\tau}}\right), \tag{6.6}$$

where A is the Einstein coefficient and $\Delta\Omega_a$ and $\Delta\Omega_s$ are the beam and source sizes respectively. If one assumes that $[\mathrm{HCO^+}]/[\mathrm{H^{13}CO^+}] \simeq 60$, that the two isotopologues trace similar regions and share similar excitation properties then if the source sizes are the same for both isotopologues or if they are beam filling sources we have:

$$W_{13} = \frac{1}{60} \frac{\nu_{12}^2}{\nu_{13}^2} \frac{\tau_{12}}{1 - e^{-\tau_{12}}} \frac{1 - e^{-\tau_{13}}}{\tau_{13}} W_{12}. \tag{6.7}$$

Here the subscripts 12 and 13 refer to the $\mathrm{H^{12}CO^+}$ and $\mathrm{H^{13}CO^+}$ properties respectively, and ν is the frequency of the $(3-2)$ rotational transition. For the WN peak $T_{\rm B}$ and FWHM I find $W_{12} \sim 2500\,\mathrm{K\,km\,s^{-1}}$, so with $\tau_{12} = 0.36$ and our fitted width of $180\,\mathrm{km}^{-1}$ to the emission region of the suspected $\mathrm{H^{13}CO^+}(3-2)$ line I have a predicted peak $T_{\rm B} = 0.27\,\mathrm{K} \simeq 2.9\,\mathrm{mJy\,beam^{-1}}$. I.e. the peak contribution from $\mathrm{H^{13}CO^+}(3-2)$ is expected to be $\simeq 1\sigma$. It is worth noting that the $\mathrm{HCO^+}(3-2)$ and $\mathrm{SiO}(6-5)$ FWHMs are significantly larger (closer to $500\,\mathrm{km\,s^{-1}}$), suggesting a lower peak, but also that the optical depth has been derived from absorption, so the true optical depth is likely larger, raising the peak. The estimate is therefore quite uncertain, but demonstrates the possibility of $H^{13}CO^{+}(3-2)$ being seen in the WN. In the EN, Sakamoto et al. (2009) found a significantly higher $HCO^{+}(3-2)$ effective optical depth of 3.7. This yields an $H^{13}CO^{+}(3-2)$ peak intensity of 10.5 mJy beam^{-1} in the EN, which is readily detected, and is in fact very similar to the observed peak near the line centre.

Sakamoto et al. (2009) report peak $HCO^{+}(3-2)$ $T_{\mathrm{B}} \sim 20\,\mathrm{K}$, with nuclear averaged values closer to 13.5 K for the WN and 10 K for the EN. Assuming that the component centred on the $H^{13}CO^{+}(3-2)$ line centre in Fig. 6.3 is entirely $H^{13}CO^{+}(3-2)$, I have corresponding temperatures of 2.5 K and 1 K in the WN and EN respectively, giving T_{B} ratios in the WN between 8 and 13.5. Assuming a $[^{12}C]/[^{13}C]$ abundance ratio of 60 (e.g. Langer & Penzias, 1993), I find a minimum optical depth $\tau_{12} \geq 4.5$ (with $\tau_{13} << 1$), where τ_{12} and τ_{13} denote the optical depths of the ^{12}C and ^{13}C $HCO^{+}(3-2)$ isotopologue lines respectively. For a T_{B} ratio of 8 I find $\tau_{12} \geq 7$. This is almost 20 times higher than the optical depth measured in absorption in the WN by Sakamoto et al. (2009). If I instead use the optical depth for the WN from Sakamoto et al. (2009) (0.36), I find a predicted $H^{13}CO^{+}(3-2)$ $T_{\mathrm{B}} \sim 0.27\,\mathrm{K}$, approximately at the 1σ noise level, as calculated above. In this case, the $H^{13}CO^{+}(3-2)$ WN line would be completely blended with $SiO(6-5)$, its contribution wholly undetectable, and the $SiO(6-5)$ would extend redwards to $+500\,\mathrm{km\,s^{-1}}$, almost far as $HCO^{+}(3-2)$. I interpret this as weak evidence for an insignificant $H^{13}CO^{+}(3-2)$ contribution in the WN.

In the EN, Sakamoto et al. (2009) observed a much higher optical depth in absorption $\tau_{12} = 3.7$. This predicts an $H^{13}CO^{+}(3-2)$ $T_{\mathrm{B}} \sim 1.0\,\mathrm{K}$, exactly as is observed in the data.

While these estimates are extremely uncertain, including multiple simplifying assumptions, they do offer the tantalising possibility that while the $H^{13}CO^{+}(3-2)$ line in the EN is real, and accurately determined, the line that is suspected to be $H^{13}CO^{+}(3-2)$ in the WN is almost entirely $SiO(6-5)$, with $H^{13}CO^{+}(3-2)$ contributing at the same level as random noise.

The evidence from the above kinematic, spatial and line brightness analyses casts doubt on the identification of $H^{13}CO^{+}(3-2)$ in the WN, but I do not believe that it is sufficient to rule it out entirely. It seems much more likely that $H^{13}CO^{+}(3-2)$ has been observed in the EN, but this conclusion rests upon numerous assumptions. As I cannot rule clearly for one side or another, in either nucleus, I therefore proceed working with two limiting cases which can apply to each nucleus independently:

- **Case 1**: there is no detection of $H^{13}CO^{+}$ in either the $(1-0)$ or $(3-2)$ transition.
- **Case 2**: the fitted components near the $H^{13}CO^{+}(1-0)$ and $(3-2)$ line centres are purely $H^{13}CO^{+}$, with no contamination (other than that from the other fitted components).

6.4 Western Nucleus

The WN line profiles all share similar features, although there is a significant variation between the 3.5 mm and 1.2 mm spectra. The 1.2 mm lines show a distinct asymmetry, peaking just redwards of the line centre but with the majority of the velocity integrated emission bluewards of the line. Of particular interest are $H^{13}CN$ and SiO, which are not only the brightest lines, but those with the most complex line profiles.

The $SiO(6-5)$ line is especially complex, both spectrally (requiring 5 Gaussian components including the possible $H^{13}CO^{+}(3-2)$ component), and spatially, with multiple components in the WN. The intriguing spatial distribution seen in Fig. 6.8 is explored in Fig. 6.9 where I present the $SiO(6-5)$ channel maps. The overall peak emission and absorption are $\sim 0.1''$ north and south of the continuum centre and in the $+115\,\mathrm{km\,s^{-1}}$ and $-115\,\mathrm{km\,s^{-1}}$ channels respectively, while the full $SiO(6-5)$ data cube has 1σ continuum absorption extending as far north as the peak of the $SiO(6-5)$ emission. The peak emission and absorption in the $0\,\mathrm{km\,s^{-1}}$ channel map only has an even greater separation, almost $0.4''$, clearly indicating that the offset is real, and not due to radio seeing effects. The north-western offset of the $SiO(6-5)$ emission peak from the continuum centre was also seen in $CO(2-1)$ observations by Downes & Eckart (2007). Fractional absorption against

Table 6.4: Line parameters in the two nuclei of Arp 220.

WN: RA 15:34:57.220, Dec 23:30:11.50

Line	Flux[a] [Jy km s^{-1}]	L'[b] [10^8 K km s^{-1} pc^2]	$T_{\rm B,\,peak}$[c] [K]	FWZI [km s^{-1}]	FWHM[d] [km s^{-1}]
$H^{13}CN(3-2)$.	52 ± 5	1.66 ± 0.24	11.2 ± 1.1	775±25	464±5
$H^{13}CN(1-0)$.	4.0 ± 0.4	1.15 ± 0.12	1.94 ± 0.22	800±50	285±27
$HC^{15}N(3-2)$.	6 ± 14	0.2 ± 0.5	1.86 ± 0.28	−−	220±40
$SO(6_6-5_5)$ . .	12 ± 16	0.4 ± 0.6	2.8 ± 0.4	−−	320±270
$SiO(6-5)^2$ . .	17.1 ± 2.5	0.54 ± 0.08	5.75 ± 0.61	1200±100	730±30
$SiO(6-5)^3$ . .	7.6 ± 2.0	0.24 ± 0.06	5.75 ± 0.61	950±50	−−
$SiO(2-1)^e$ . .	4.8 ± 0.5	1.38 ± 0.14	1.62 ± 0.20	803±22	440±50
$SiO(2-1)^f$ . .	4.5 ± 0.5	1.28 ± 0.13	1.62 ± 0.20	−−	370±40
$H^{13}CO^+(3-2)^f$	9.5 ± 1.1	0.30 ± 0.03	2.77 ± 0.29	500±50	205±21
$H^{13}CO^+(1-0)^f$	0.35 ± 0.08	0.100 ± 0.022	0.22 ± 0.11	350±50	200±200
$HN^{13}C(3-2)$.	37 ± 4	1.16 ± 0.13	7.72 ± 0.80	−−	350±100

EN: RA 15:34:57.291, Dec 23:30:11.34

Line	Flux[a] [Jy km s^{-1}]	L'[b] [10^8 K km s^{-1} pc^2]	$T_{\rm B,\,peak}$[c] [K]	FWZI [km s^{-1}]	FWHM[d] [km s^{-1}]
$H^{13}CN(3-2)$.	12.7 ± 1.3	0.41 ± 0.04	4.91 ± 0.53	550±50	523±10
$H^{13}CN(1-0)$.	0.50 ± 0.05	0.144 ± 0.015	0.57 ± 0.12	450±100	170±40
$HC^{15}N(3-2)$.	3.1 ± 1.2	0.10 ± 0.04	1.50 ± 0.26	−−	160±60
$SO(6_6-5_5)$ . .	3.2 ± 1.1	0.10 ± 0.04	1.10 ± 0.24	−−	186±26
$SiO(6-5)^e$ . .	6.5 ± 0.7	0.206 ± 0.029	2.48 ± 0.33	740±80	410±20
$SiO(6-5)^f$ . .	4.9 ± 0.5	0.155 ± 0.017	2.48 ± 0.33	600±50	200±30
$SiO(2-1)^e$ . .	0.92 ± 0.14	0.26 ± 0.04	0.72 ± 0.13	800±100	539±11
$SiO(2-1)^f$ . .	0.70 ± 0.17	0.20 ± 0.06	0.72 ± 0.13	500±50	−−
$H^{13}CO^+(3-2)^f$	1.63 ± 0.25	0.052 ± 0.008	1.15 ± 0.24	300±50	110±40
$H^{13}CO^+(1-0)^f$	0.22 ± 0.06	0.062 ± 0.018	0.16 ± 0.11	450±50	220±190
$HN^{13}C(3-2)$.	8.4 ± 1.0	0.26 ± 0.03	2.22 ± 0.31	700±50	408±10

[a] Fluxes are estimated from the Gaussian fitting components in Figs. 6.3 to 6.6, which are listed in Table 6.2. Uncertainties in the fluxes and L' are estimated from the fitting covariance matrices and the absolute flux calibration (10%). While the total flux in the $HC^{15}N(3-2)+SO(6_6-5_5)$ line blend is relatively well constrained, the contribution of each species is extremely uncertain, indicated by their $> 200\%$ uncertainties.

[b] For consistency with HCN single dish data used in the analysis I include source integrated L' values (Solomon et al., 1992):

$$L' = 3.25 \times 10^7 \left(\frac{\nu_{\rm obs}}{\rm GHz}\right)^{-2} \left(\frac{D_L}{\rm Mpc}\right)^2 (1+z)^{-3} \left(\frac{\int_{\Delta v} S_v {\rm d}v}{\rm Jy\,km\,s^{-1}}\right),$$

[c] Peak of the line profile extracted from single spaxels towards the continuum centres. Relative errors on 1.2 mm data are ±0.21 K, on the 3.5 mm data are ±0.11 K, but in almost all cases these are insignificant compared to the absolute 10% calibration uncertainty. [d] Where multiple Gaussian components are required to fit the line, I use a non-parametric FWHM derived from the intensity weighted mean width inspired by Bothwell et al. (2013), defined in the discreet form as:

$${\rm FWHM_{iwm}} = 2\sqrt{2\ln 2}\left(\frac{\sum_i (v-\bar{v})^2\,|I_i|\Delta v}{\sum_i |I_i|\Delta v}\right)^{0.5}.$$

Note that this method is very sensitive to both the location of the line centre (and hence to the assumed redshift) and to noise at the ends of the fainter lines: this method becomes increasingly susceptible to noise at low S/N.

the continuum implies a lower limit for the optical depth, $\tau_{\mathrm{SiO}(6-5)} \geq 0.25$ towards the absorption peak.

In Fig. 6.10 I show position-velocity slices across the two nuclei. Slices are 1.2″ long, centred on the continuum centres and taken at 270° across the WN (east to west) and 225° across the EN (south-east to north-west) to be consistent with Sakamoto et al. (2009). The velocity slices have been smoothed with a Gaussian kernel for clarity. While the EN signal is too weak to identify any clear trends, the WN $\mathrm{H^{13}CN}(3-2)$ and $\mathrm{SO}(6_6-5_5)$ lines both display evidence of disk-like rotation. The $\mathrm{SiO}(6-5)$ line shows signs of a strong, kinematically extended outflow with the P Cygni like absorption at negative velocities mixed with an emission signature at $\sim -300\,\mathrm{km\,s^{-1}}$, coincident with the peak blueshifted emission in the $\mathrm{H^{13}CN}(3-2)$ line. There is a clear systemic velocity offset between the two nuclei, as reported in the literature, potentially as large as $90\,\mathrm{km\,s^{-1}}$ based on the data, but the asymmetry and width of the lines makes reliably identifying the precise value of the offset highly uncertain. I therefore adopt the $60\,\mathrm{km\,s^{-1}}$ CO derived offset of Sakamoto et al. (2009), which is reliably determined from narrow, on line centre, absorption in the CO lines.

Fig. 6.10 reveals the bluewards absorption extending all the way out to $-600\,\mathrm{km\,s^{-1}}$, with no equivalent redshifted emission, even in the case 1 limit. However, if I temporarily exclude the blueshifted emission peak at $-300\,\mathrm{km\,s^{-1}}$ the emission and absorption appear symmetric about a point $\sim -50\,\mathrm{km\,s^{-1}}$. This profile is suggestive of a symmetric outflow, traced by SiO, merged with SiO emission from the nuclear disk itself.

In case 2 the reddest peak in the $\mathrm{SiO}(6-5)$ line profile is attributed entirely to $\mathrm{H^{13}CO^+}(3-2)$. This case seems unlikely as the emission at these velocities is concentrated north of the continuum (Fig. 6.9), whereas the $\mathrm{HCO^+}(3-2)$ emission of Sakamoto et al. (2009) is continuum centred and spatially very similar to the $\mathrm{H^{13}CN}(3-2)$ line (Fig. 6.8). It is clear from Fig. 6.10 that case 1 implies that SiO reaches higher velocities than $\mathrm{H^{13}CN}$, but it is still not as extended in velocity as $\mathrm{HCO^+}$ (Fig. 6.7), which extends almost $200\,\mathrm{km\,s^{-1}}$ further redwards in emission.

It is worth noting that while $\mathrm{SiO}(6-5)$ shows significant absorption in the WN, $\mathrm{SiO}(2-1)$ has no sign of continuum absorption. As was noted in Sakamoto et al. (2009), the high brightness temperature of the dust in the WN implies that higher frequency transitions are more likely to be seen in absorption against the dust continuum, and indeed in the far-IR almost all molecular lines are observed in absorption (González-Alfonso et al., 2004; González-Alfonso et al., 2012), so the lack of absorption in the $\mathrm{SiO}(2-1)$ line could simply be due to the drop in dust SED between 1.2 mm and 3.5 mm. Sakamoto et al. (2009) further noted that the Einstein coefficients for photo-absorption could be having an effect. Assuming detailed balance:

$$\mathrm{B}_{lu} = \frac{g_u}{g_l}\mathrm{A}_{ul}\left(\frac{2\mathrm{h}\nu^3}{c^2}\right)^{-1}, \tag{6.8}$$

which for the rotational transitions of linear diatomic molecules may be written as:

$$\mathrm{B}_{J,J+1} = \frac{2J+3}{2J+1}\mathrm{A}_{J+1,J}\left(\frac{2\mathrm{h}\nu^3}{c^2}\right)^{-1}, \tag{6.9}$$

gives for SiO $\mathrm{B}_{56}/\mathrm{B}_{12} \simeq 1$, with similar results in other lines (since $\mathrm{A}_{ul} \propto \nu^3$): this effect is most significant when comparing similar frequency transitions of different molecules. This suggests that the absence of absorption in the $\mathrm{SiO}(2-1)$ lines is more likely a dust brightness effect. It does not appear to be a beam size issue: the absorption is still clearly visible when the $\mathrm{SiO}(6-5)$ cube is smoothed to the 3.5 mm beam size. Finally, I consider the possibility that there is an angularly extended “screen” of blueshifted emission in front of the WN which is being spatially filtered in the 1.2 mm observations. The minimum baselines were 22.6 kλ and 36.4 kλ at 1.2 mm and 3.5 mm respectively, so nominally the observations resolve out emission on angular scales greater than 9.1″ and 5.7″. Therefore the baselines are not likely to be responsible for the absence of absorption: the 3.5 mm observations will resolve out emission before the 1.2 mm, whereas the line profiles could only be explained if the 1.2 mm observations were resolving out large-scale, blueshifted emission.

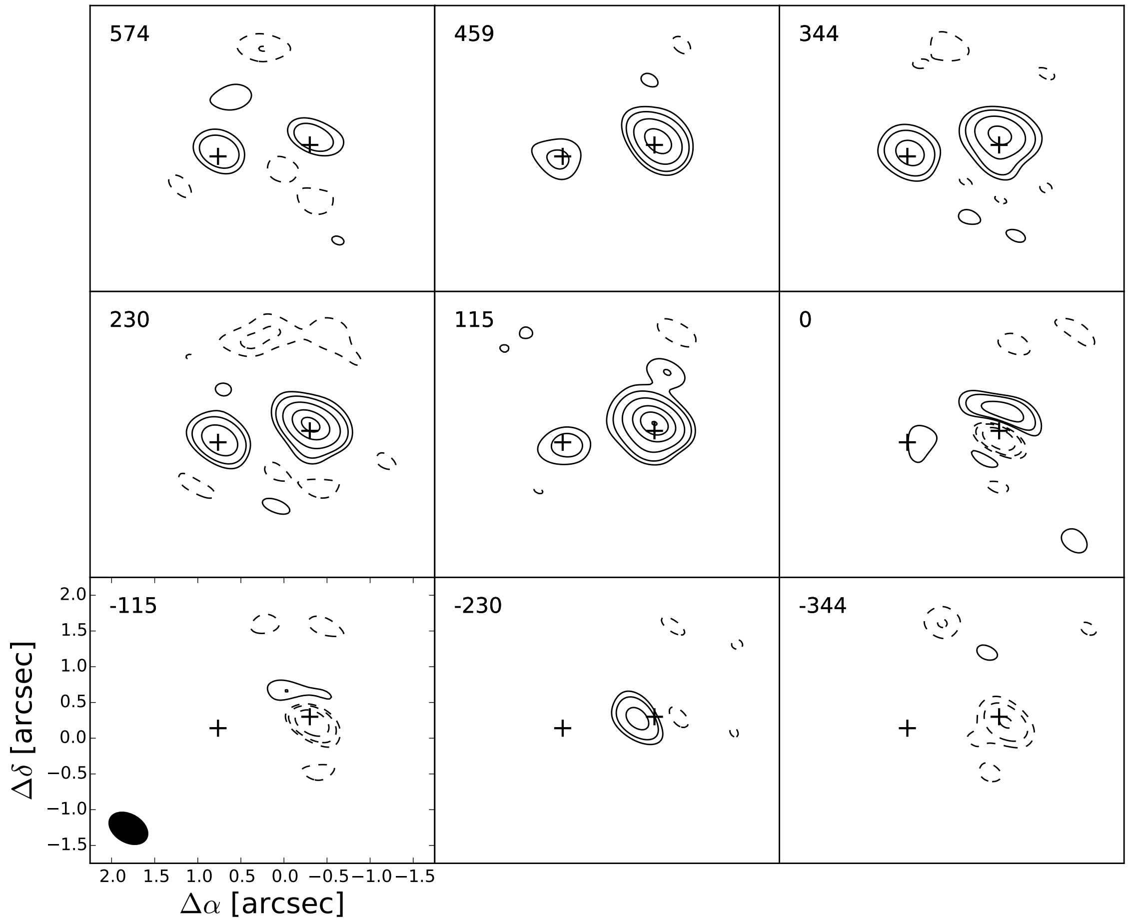

Figure 6.9: Channel maps for the SiO(6 − 5) line complex, including the subsidiary emission (at $-230\,\mathrm{km\,s^{-1}}$) and absorption (at $-344\,\mathrm{km\,s^{-1}}$). Channels have been averaged to $115\,\mathrm{km\,s^{-1}}$. Contours are at −10, −5, −3, 3, 5, and $10n\sigma$ intervals ($1\sigma = 0.63\,\mathrm{mJy\,beam^{-1}}$). The mean velocity of each channel relative to the line centre is given in the top left corners of the plots. Note the eastwards offset of the emission at $-230\,\mathrm{km\,s^{-1}}$ and the colocation of the sub-continuum absorption red and bluewards of this subsidiary peak ($-115\,\mathrm{km\,s^{-1}}$ and $-344\,\mathrm{km\,s^{-1}}$). The $0.52'' \times 0.37''$ synthesised beam is shown in the bottom left panel. The crosses mark the continuum centres.

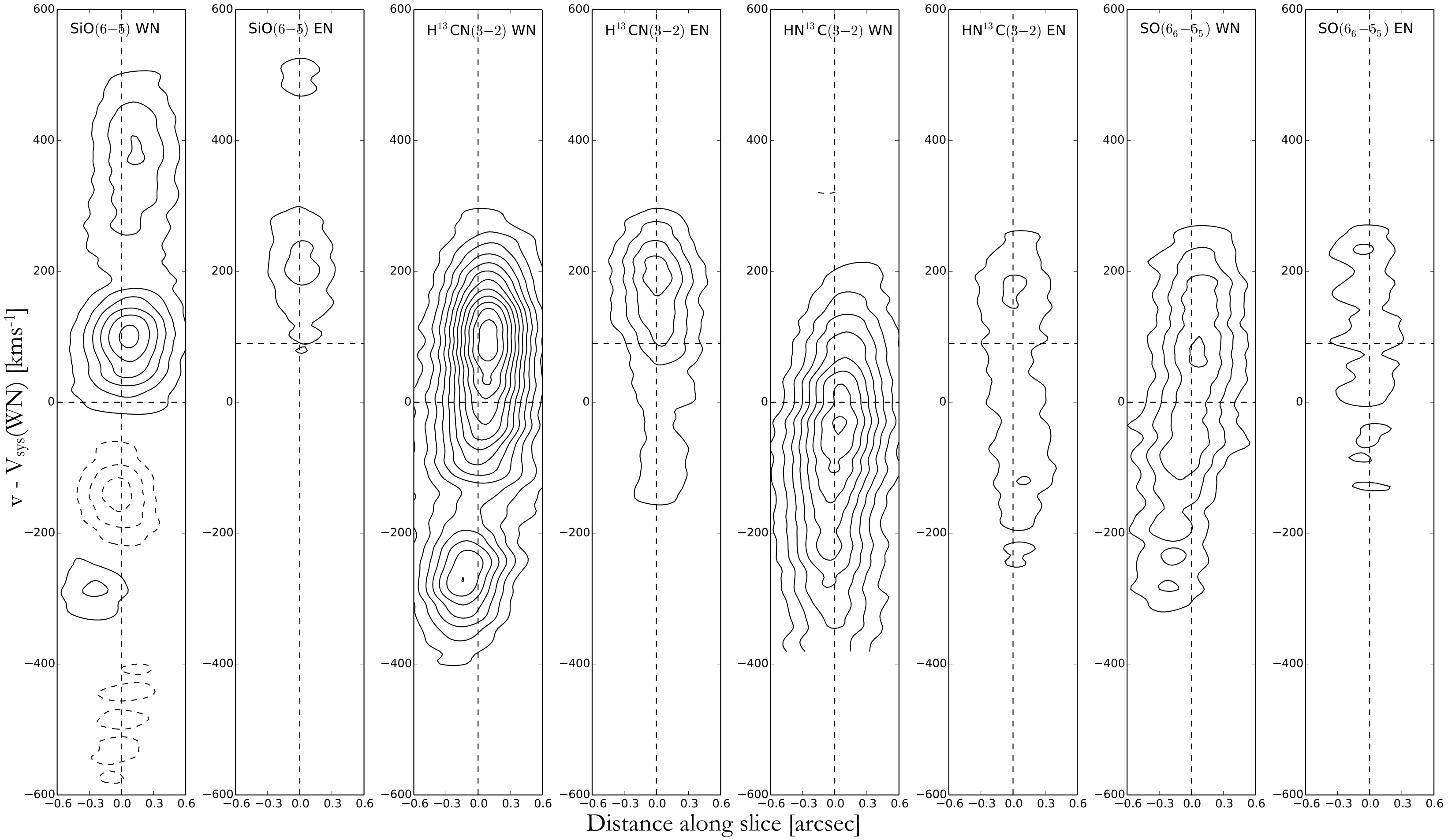

Figure 6.10: Velocity slices across the two nuclei of Arp 220. Slices are centred on the systemic velocity (radio, LSR) of the WN, 5355 $\mathrm{km\,s^{-1}}$, to highlight the offsets between the two nuclei. Slices are 1.2″ long, centred on the continuum centres and taken at 270° across the WN (east to west) and 225° across the EN (south-east to north-west) to be consistent with Sakamoto et al. (2009). The horizontal axis corresponds to the angular distance along the slice. Contours are at $\pm 3n\sigma$. The H^{13}CN and SO WN slices suggest disk like rotation. The SiO WN slice could be indicative of rotation, an outflow or a combination of the two. Its prominent P Cygni profile is clearly seen, but the emission peaks at $\sim 100\,\mathrm{km\,s^{-1}}$ and $\sim -300\,\mathrm{km\,s^{-1}}$ and absorption trough at $\sim -150\,\mathrm{km\,s^{-1}}$ are almost precisely coincident with the two peaks and the minimum in the H^{13}CN WN slice, suggesting they are tracing, at least in part, the same kinematics.

The $H^{13}CN(3-2)$ line is the brightest line observed at 1.2 mm. I would expect this line to trace the same high-density star-forming environment traced by $HCN(1-0)$, $(3-2)$ and $(4-3)$ as observed by Greve et al. (2009) and I find the emission strongly correlated with the continuum emission (Fig. 6.8). The $H^{13}CN$ slice (Fig. 6.10) suggests predominantly disk-like rotation, although the spatial resolution is insufficient for successful kinematic modelling. However, comparison with the SiO WN slice with emission peaks at $\sim 100\,\mathrm{km\,s^{-1}}$ and $\sim -300\,\mathrm{km\,s^{-1}}$ and the absorption trough at $\sim -150\,\mathrm{km\,s^{-1}}$ shows that they are almost precisely coincident with the two peaks and the minimum in the $H^{13}CN$ WN slice suggesting they are tracing, at least in part, the same gas. However, if they are tracing the same gas, it is curious that they have such different levels of absorption. The simplest explanation is that while $H^{13}CN(3-2)$ is tracing both the dense, star-forming nuclear disk and an outflow, presenting as a P Cygni profile embedded within a Gaussian line, while $SiO(6-5)$ traces the outflow with only a small component in the star-forming nuclear disk.

I also examine the possibility that $H^{13}CN(3-2)$ and $SiO(6-5)$ are tracing similar regions, but that the different line profiles are driven by the different properties of the transitions. The $H^{13}CN$ $J=3$ and SiO $J=6$ levels have energies of 24.9 K and 43.8 K respectively (Remijan et al., 2007; Müller et al., 2005). Coupled with the fact that higher J transitions are harder to excite, as they need the intermediate J levels to be excited as well, the P Cygni profile in $H^{13}CN(3-2)$ could be less prominent because the $H^{13}CN$ $J=3$ level is easier to excite, so is seen more in emission, while $SiO(6-5)$ is seen in absorption. However, the HCO^+ $J=3$ level has an energy of 25.7 K (Remijan et al., 2007), only 3% higher than that of $H^{13}CN$ $J=3$, and is seen with strong absorption (Sakamoto et al., 2009), suggesting that the energies alone cannot fully explain the differences in the line profiles. Furthermore, it does not appear to be a critical density effect, since the critical densities for $H^{13}CN(3-2)$, $SiO(6-5)$ and $HCO^+(3-2)$ are $2.9\times10^6\,\mathrm{cm^{-3}}$, $2.0\times10^6\,\mathrm{cm^{-3}}$ and $7.8\times10^5\,\mathrm{cm^{-3}}$ respectively. It would appear therefore to be either an optical depth effect, or that the majority of the $H^{13}CN(3-2)$ emission is tracing the nuclear disks, with a small component in the outflow traced by $SiO(6-5)$. This would imply however that there should be the same ±40 pc emission and absorption offset seen in $SiO(6-5)$ in the $H^{13}CN(3-2)$ line, which would shift the integrated contour peak north (as can be seen for $SiO(6-5)$ in Fig. 6.8); this is not seen, but could simply be a sign that $H^{13}CN$ in the outflow is too faint to significantly affect the integrated plots.

$HN^{13}C(3-2)$ emission extends beyond the end of the spectrum, making it impossible to reliably compare it with the $H^{13}CN(3-2)$ emission. The absorption present in $H^{13}CN(3-2)$ appears to be absent in $HN^{13}C(3-2)$. This could be due to errors at the edges of the bandpass, or it could be the same effect as has been seen in single dish spectra, where $HCN(3-2)$ shows absorption but $HNC(3-2)$ does not, possibly due to mid-IR pumping or maser emission in HNC (Aalto et al., 2009). Alternatively, it could be a sign of HCN enhancement (over HNC) in the shocks in the outflow (e.g. Mitchell, 1984; Bachiller & Pérez Gutiérrez, 1997; Martín et al., 2015). This would be consistent with the case above, where $H^{13}CN$ is over abundant in an outflow from the centre of the nucleus as well as being prevalent throughout the nuclear disk. Both isomers trace the circumnuclear disk (CND), but only $H^{13}CN$ would be detectable in the outflow, imprinting a P Cygni profile on to the $H^{13}CN$ line profile but not the $HN^{13}C$.

Like SiO, SO in the Milky Way is a shock tracer (Chernin et al., 1994), ubiquitous in star-forming regions. It is unclear whether these remain reliable shock tracers extragalactically, where excitation and abundance effects could be more significant. Given the uncertainty in the fitting for $SO(6_6-5_5)$ and $HC^{15}N(3-2)$ I cannot reliably separate the two lines and they are not focussed on in this work. Similarly, I see a trace of the $SO(2_2-1_1)$ line at the red end of the 3.5 mm WN spectrum, but this is severely affected by edge effects in the bandpass and is not included in the analysis.

6.5 Eastern Nucleus

While none of the lines in the EN are spatially resolved, $SiO(2-1)$, $SiO(6-5)$, $HN^{13}C(3-2)$ and $H^{13}CN(3-2)$ all show doubly peaked emission with no significant sign of sub-continuum absorption (while in case 1 the SiO$(2-1)$ and $(6-5)$ spectra both show possible signs of the same absorption-emission-absorption structure seen in the WN, this is not spatially correlated across the channels and is below 1σ).

The SiO line profiles in the EN are very similar: the $(6-5)$ line has major and minor peaks at $V_{\rm sys}+140\,{\rm km\,s^{-1}}$ and $V_{\rm sys}-175\,{\rm km\,s^{-1}}$ respectively, cf. $V_{\rm sys}+150\,{\rm km\,s^{-1}}$ and $V_{\rm sys}-200\,{\rm km\,s^{-1}}$ in the $(2-1)$ line. I do not see the prominent P Cygni profiles observed in the HCO$^+(3-2)$ and $(4-3)$ lines in the EN (Sakamoto et al., 2009), although the 3.5 mm spectrum in particular does allow for some degree of bluewards absorption around $-100\,{\rm km\,s^{-1}}$. Only the absolute scaling of the line profile changes across the EN. This may explain the lack of a clear P Cygni profile in the EN, since the resolution of Sakamoto et al. (2009) was almost double ours, I may be smearing out any sub-continuum absorption in the EN. If the $\sim 1\sigma$ signs of continuum absorption in the EN are real, then this implies $\tau_{\rm SiO(6-5)} \simeq 0.03 \pm 0.01$: 1/10 the WN value.

6.6 Analysis

6.6.1 LVG modelling

The LVG code RADEX[5] was used with line ratios, derived from the earlier analysis and presented in Table 6.5, to provide estimates of the molecular hydrogen density ($n_{\rm H_2}$), molecular column density over velocity width ($N_{\rm x}/\Delta v$) and kinetic temperature ($T_{\rm k}$) for the observed species. The column densities provide abundance ratios [H^{13}CN]/[SiO] and [H^{13}CN]/[H^{13}CO$^+$]. These simple models do not account for the potentially significant mid-IR pumping in Arp 220. Since the beam is averaging over $\sim 200\,{\rm pc} \times 140\,{\rm pc}$, I are certainly including a wide range of regions including giant molecular clouds (GMCs), hot cores, shocked regions, photon dominated regions (PDRs) and perhaps an XDR if there is an AGN at the centre of the WN, so the model parameters are at best only representative of the conditions of the dominant emission regions.

I first used HCN and H^{13}CN data from Greve et al. (2009) (which includes data from Solomon et al., 1992 and Krips et al., 2008) and from the work to find the best fitting parameters for Arp 220 as a whole, then used these to model abundance ratios for SiO and H^{13}CO$^+$ in the two nuclei independently.

HCN

I recalculated the L' values of HCN$(3-2)$ and $(1-0)$ as weighted averages of the data reported in Greve et al. (2009) using their quoted $S_\nu{\rm d}v$ values and the adopted cosmological parameters, finding $L'_{\rm HCN(3-2)} = 9.5 \pm 1.1 \times 10^8\,{\rm K\,km\,s^{-1}\,pc^2}$ and $L'_{\rm HCN(1-0)} = 12.1 \pm 1.2 \times 10^8\,{\rm K\,km\,s^{-1}\,pc^2}$.

The background temperature ($T_{\rm bg}$) was set to 45 K and 110 K (Mangum et al., 2013 and González-Alfonso et al., 2012 respectively), and I modelled the kinetic gas temperature ($T_{\rm k}$) as 70, 100, 150, 300, 350 and 450 K. The molecular hydrogen density ($n_{\rm H_2}$) was varied from $10^4-10^8\,{\rm cm^{-3}}$ in $\log_{10}$ steps of 0.02, and $N_{\rm HCN}$ was varied from $6\times10^{14}-6\times10^{17}\,{\rm cm^{-2}}$ in $\log_{10}$ steps of 0.015. I assume throughout that $\Delta v = 100\,{\rm km\,s^{-1}}$. I further assumed [HCN]/[H^{13}CN] = 60 (e.g. Langer & Penzias, 1993), and found χ^2 values for the results grids which are shown in Fig. 6.11.

For both $T_{\rm bg}$ values, the models exclude low kinetic temperatures ($T_{\rm k} \lesssim 100\,{\rm K}$), which can fit the H^{13}CN$(3-2)/(1-0)$ ratios alone but not the very optically thick HCN. For any given $T_{\rm k}$ the models prefer the lower $T_{\rm bg} = 45\,{\rm K}$. I find reduced $\chi^2 = 1.25$ at $T_{\rm k} = 150\,{\rm K}$ and $T_{\rm bg} = 45\,{\rm K}$ and this continues to decrease as $T_{\rm k}$ increases towards 500 K. Above this temperature I have no HCN transition data and the RADEX solutions begin to diverge rapidly. I adopt $T_{\rm k} = 150\,{\rm K}$ and $T_{\rm bg} = 45\,{\rm K}$ as the best fit solution, being wary of over-fitting, but note that the higher $T_{\rm k}$ is consistent with the NH$_3$ thermometry of Mangum et al. (2013). The green band in Fig. 6.11, showing the parameters fitting the observed ratio to within 1σ for the $L'({\rm HCN}(3-2))/L'({\rm HCN}(1-0))$ line ratio, is much wider than for the other lines. This ratio of two optically thick lines is only weakly dependent upon $n_{\rm H_2}$ and $N_{\rm HCN}/\Delta v$ (provided $N_{\rm HCN}/\Delta v$ is high enough for the line to be optically thick), and varies slowly across the explored parameter space. The four solutions shown

---

[5] A non-LTE code for radiative transfer, available here: `http://home.strw.leidenuniv.nl/~moldata/radex.html`.

Table 6.5: Line brightness-temperature ratios for the two nuclei.

L' ratios

Line Ratio	Ratio
$L'(\mathrm{HCN}(3-2))/L'(\mathrm{HCN}(1-0))$	0.79 ± 0.12
$L'(\mathrm{H^{13}CN}(3-2))/L'(\mathrm{H^{13}CN}(1-0))$	1.60 ± 0.24
$L'(\mathrm{HCN}(3-2))/L'(\mathrm{H^{13}CN}(3-2))$	5.0 ± 0.8
$L'(\mathrm{HCN}(1-0))/L'(\mathrm{H^{13}CN}(1-0))$	10.1 ± 1.3

$T_{\mathrm{B}}\mathrm{d}v$ line integrated ratios[a]

Line Ratio	WN	EN
$\mathrm{H^{13}CN}(3-2)/\mathrm{H^{13}CN}(1-0)$	6.7 ± 0.9	5.8 ± 0.9
$\mathrm{H^{13}CN}(3-2)/\mathrm{HN^{13}C}(3-2)$	1.41 ± 0.07	1.51 ± 0.10
Case 1[4]: no $\mathrm{H^{13}CO^+}$		
$\mathrm{H^{13}CN}(3-2)/\mathrm{SiO}(6-5)$	2.32 ± 0.12	2.0 ± 0.3
$\mathrm{H^{13}CN}(1-0)/\mathrm{SiO}(2-1)$	0.826 ± 0.016	0.54 ± 0.07
$\mathrm{H^{13}CN}(3-2)/\mathrm{H^{13}CO^+}(3-2)$	> 41	> 10
$\mathrm{H^{13}CN}(1-0)/\mathrm{H^{13}CO^+}(1-0)$	> 9	> 3
$\mathrm{SiO}(6-5)/\mathrm{SiO}(2-1)$	2.4 ± 0.3	1.61 ± 0.22
Case 2: $\mathrm{H^{13}CO^+}$		
$\mathrm{H^{13}CN}(3-2)/\mathrm{SiO}(6-5)$	4.0 ± 0.5	2.60 ± 0.11
$\mathrm{H^{13}CN}(1-0)/\mathrm{SiO}(2-1)$	0.890 ± 0.027	0.71 ± 0.16
$\mathrm{H^{13}CN}(3-2)/\mathrm{H^{13}CO^+}(3-2)$	4.78 ± 0.23	7.8 ± 0.9
$\mathrm{H^{13}CN}(1-0)/\mathrm{H^{13}CO^+}(1-0)$	11.5 ± 2.3	2.3 ± 0.6
$\mathrm{SiO}(6-5)/\mathrm{SiO}(2-1)$	1.47 ± 0.23	1.6 ± 0.4

$T_{\mathrm{B,peak}}$ ratios[b]

Line Ratio	WN	EN
$\mathrm{H^{13}CN}(3-2)/\mathrm{H^{13}CN}(1-0)$	5.8 ± 0.9	8.6 ± 2.1
$\mathrm{SiO}(6-5)/\mathrm{SiO}(2-1)$	3.4 ± 0.6	2.8 ± 0.7
$\mathrm{H^{13}CN}(3-2)/\mathrm{H^{13}CO^+}(3-2)$	4.1 ± 0.3	1.72 ± 0.13
$\mathrm{H^{13}CN}(1-0)/\mathrm{H^{13}CO^+}(1-0)$	9 ± 5	5 ± 3
$\mathrm{H^{13}CN}(3-2)/\mathrm{SiO}(6-5)$	1.95 ± 0.08	1.98 ± 0.03
$\mathrm{H^{13}CN}(1-0)/\mathrm{SiO}(2-1)$	1.19 ± 0.11	0.79 ± 0.05
$\mathrm{HN^{13}C}(3-2)/\mathrm{H^{13}CN}(3-2)$	0.689 ± 0.023	0.453 ± 0.010

[a] Based on the fitted Gaussian components, using only the emission components. The $\mathrm{H^{13}CN}(3-2)/(1-0)$ and $\mathrm{SiO}(6-5)/(2-1)$ ratios are quoted here without corrections for beam dilution.

[b] Peak of the line profile extracted from single spaniels towards the continuum centres in the unsmoothed maps: these ratios do not account for beam dilution in ratios of 1.2 mm and 3.5 mm lines.

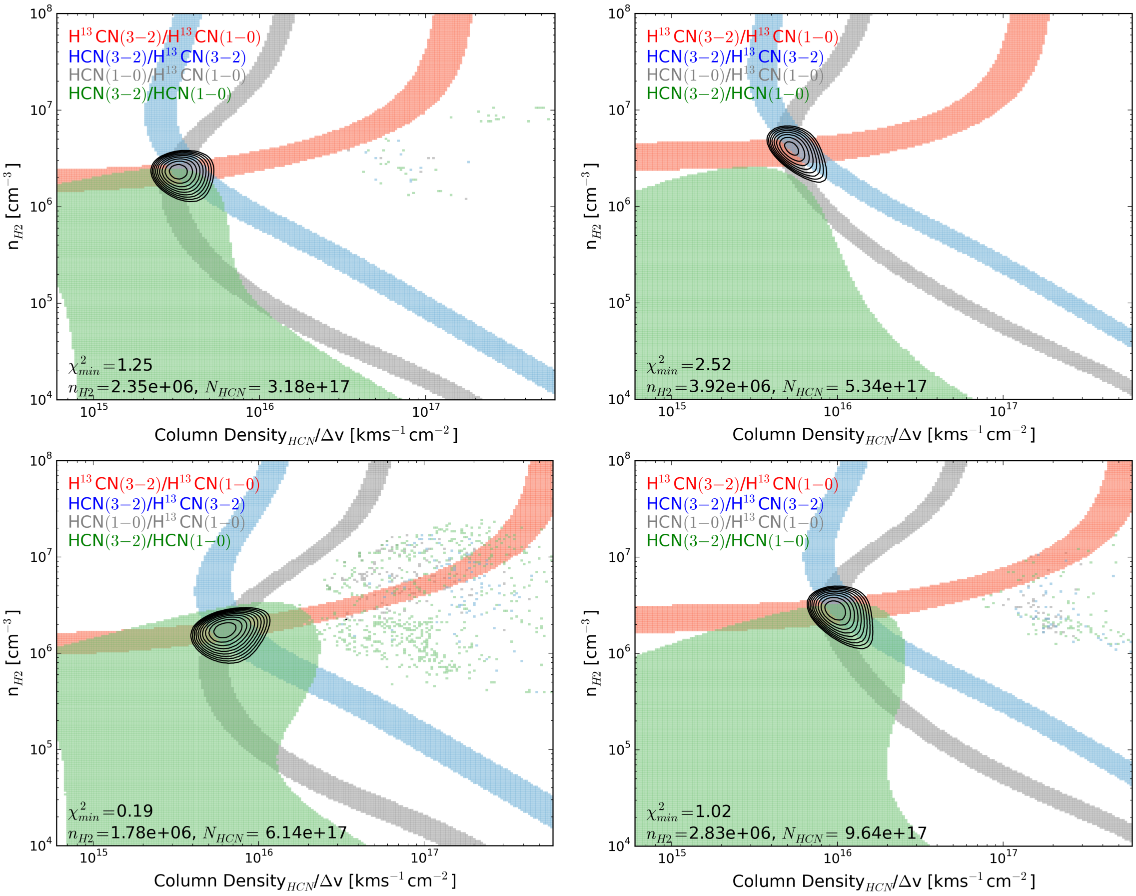

Figure 6.11: The best fitting parameters for the HCN and H^{13}CN ratios. Top: $T_\mathrm{k} = 150\,\mathrm{K}$, bottom $T_\mathrm{k} = 300\,\mathrm{K}$, left $T_\mathrm{bg} = 45\,\mathrm{K}$, right $T_\mathrm{bg} = 110\,\mathrm{K}$. The 1σ regions of individual ratios are highlighted, and the χ^2 contours from 1 to 10 in steps of 1 are shown. The "dotting" in the upper right corner is due to localised non-convergences in the LVG code, and does not affect the results at these temperatures. These results imply $T_\mathrm{k} \geq 150\,\mathrm{K}$ and prefer $T_\mathrm{bg} = 45\,\mathrm{K}$ for all T_k, and as such I identify the $T_\mathrm{k} = 150\,\mathrm{K}$, $T_\mathrm{bg} = 45\,\mathrm{K}$ as the best fit ($\chi^2_\mathrm{min} = 1.25$. The best fit parameters are found from weighted averages of four best fits shown above, and I find $n_{\mathrm{H}_2} = 2.1 \pm 0.6 \times 10^6\,\mathrm{cm}^{-3}$ and $N_\mathrm{HCN}/\Delta v = 6.2 \pm 1.6 \times 10^{15}\,\mathrm{cm}^{-2}\,\mathrm{km}^{-1}\,\mathrm{s}$.

in Fig. 6.11 are the four best fits below 350 K. Given the lack of a clearly superior fit, I find the best fit n_{H_2} and $N_\mathrm{HCN}/\Delta v$ from χ^2_ν weighted averages. I find $n_{\mathrm{H}_2} = 2.1 \pm 0.6 \times 10^6\,\mathrm{cm}^{-3}$ and $N_\mathrm{HCN}/\Delta v = 6.2 \pm 1.6 \times 10^{15}\,\mathrm{cm}^{-2}\,\mathrm{km}^{-1}\,\mathrm{s}$.

Since the χ^2 values for the HCN−H^{13}CN LVG models continue to decrease at higher temperatures, I also consider the case that the HCN and H^{13}CN emission is dominated by shocks. I repeated the following H^{13}CN, H^{13}CO$^+$ and SiO analysis with $T_\mathrm{k} = 450\,\mathrm{K}$ and $T_\mathrm{bg} = 110\,\mathrm{K}$, and find that while the column densities found are a dex higher for all species, the abundance ratios are only slightly changed and are consistent within uncertainties. The abundance ratios presented below are robustly determined, even if the kinetic temperature and background temperatures are not.

The best fit T_k and n_{H_2} are consistent with the maximum-likelihood parameters of Rangwala et al. (2011), which are based on both low J HCN emission and high J absorption seen with Herschel, while the N_HCN is two orders of magnitude higher. They found $T_\mathrm{k} = 320\,\mathrm{K}$, $n_{\mathrm{H}_2} = 2 \times 10^6\,\mathrm{cm}^{-3}$ and $N_\mathrm{HCN} = 2 \times 10^{15}\,\mathrm{cm}^{-2}$. González-Alfonso et al. (2012) found, for $T_\mathrm{bg} = 110\,\mathrm{K}$, $T_\mathrm{k} \sim 150\,\mathrm{K}$, $n_{\mathrm{H}_2} = 4 - 8 \times 10^5\,\mathrm{cm}^{-3}$ and $N_\mathrm{HCN} = 6 - 4 \times 10^{17}\,\mathrm{cm}^{-2}$. While the analysis prefers $T_\mathrm{bg} = 45\,\mathrm{K}$, for the T_bg and T_k of González-Alfonso et al. (2012) I find $n_{\mathrm{H}_2} = 3.6 \pm 1.5 \times 10^6\,\mathrm{cm}^{-3}$ and

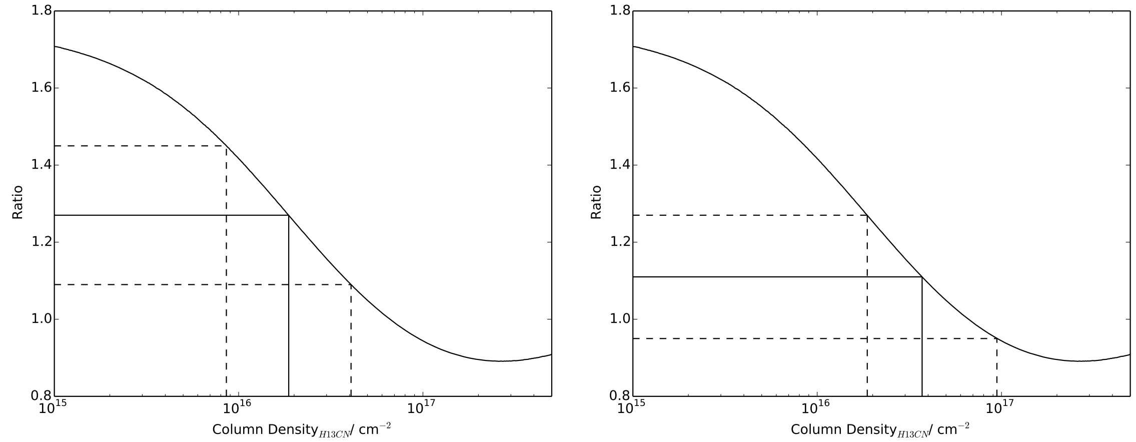

Figure 6.12: The $\mathrm{H^{13}CN}$ column densities found in the WN and EN (left and right respectively). The dashed lines indicate the error bounds. I find column densities $N_{\mathrm{H^{13}CN}}/\Delta v = 1.9^{+2.2}_{-1.0} \times 10^{14}\,\mathrm{cm^{-2}\,km^{-1}\,s}$ and $N_{\mathrm{H^{13}CN}}/\Delta v = 3.7^{+5.7}_{-1.8} \times 10^{14}\,\mathrm{cm^{-2}\,km^{-1}\,s}$ in the WN and EN respectively.

$N_{\mathrm{HCN}} = 6 \pm 3 \times 10^{17}\,\mathrm{cm^{-2}}$. The best fitting model with $T_{\mathrm{bg}} = 45\,\mathrm{K}$ and $T_{\mathrm{k}} = 150\,\mathrm{K}$ gives $n_{\mathrm{H_2}} = 2.1 \pm 0.6 \times 10^{6}\,\mathrm{cm^{-3}}$ and $N_{\mathrm{HCN}}/\Delta v = 6.2 \pm 1.6 \times 10^{15}\,\mathrm{cm^{-2}\,km^{-1}\,s}$, consistent with González-Alfonso et al. (2012). There is some tension with earlier millimetre studies of HCN in Arp 220, which found best-fitting parameters of $45\,\mathrm{K} < T_{\mathrm{k}} < 120\,\mathrm{K}$ and $n_{\mathrm{H_2}} = 0.3 \times 10^{6}\,\mathrm{cm^{-3}}$ (Greve et al., 2009). I note that while Rangwala et al. (2011); Greve et al. (2009) and this work all use simple LVG codes, González-Alfonso et al. (2012) used a more complex, multiphase model including dust attenuation. All of the above used HCN data averaged over the two nuclei, and only González-Alfonso et al. (2012) includes mid-IR pumping. Their results suggested that mid-IR pumping is not having a significant effect on the vibrational ground state, high$-J$ HCN population, but the effect on the low$-J$ transitions may be more significant.

Having found the "average" parameters for the HCN and $\mathrm{H^{13}CN}$ in Arp 220, I use the high resolution of the observations to test for chemical differences between the nuclei. To this end, I ran RADEX again, fixing all parameters to the best fit HCN solution except for the $\mathrm{H^{13}CN}$ column density, and fitted this to the beam dilution corrected $T_{\mathrm{B}}\mathrm{d}v$ ratios for $\mathrm{H^{13}CN}$ $(3-2)/(1-0)$, 1.27 ± 0.18 and 1.11 ± 0.16 in the WN and EN respectively. The results are shown in Fig. 6.12. I find $N_{\mathrm{H^{13}CN}}/\Delta v = 1.9^{+2.2}_{-1.0} \times 10^{14}\,\mathrm{cm^{-2}\,km^{-1}\,s}$ in the WN and $N_{\mathrm{H^{13}CN}}/\Delta v = 3.7^{+5.7}_{-1.8} \times 10^{14}\,\mathrm{cm^{-2}\,km^{-1}\,s}$ in the EN. I note that these solutions are optically thick, with optical depths from 1 to 6.

$\mathrm{H^{13}CO^{+}}$

For $\mathrm{H^{13}CO^{+}}$ I analyse the two nuclei separately, making use of the $T_{\mathrm{B}}\mathrm{d}v$ ratios of $\mathrm{H^{13}CN}(3-2)/\mathrm{H^{13}CO^{+}}(3-2)$ and $\mathrm{H^{13}CN}(1-0)/\mathrm{H^{13}CO^{+}}(1-0)$, which do not require corrections for beam dilution (see Table 6.5). I use a simple two phase model, where the $\mathrm{H^{13}CN}$ column and $n_{\mathrm{H_2}}$ are fixed to the values found above for the WN and EN (with $\Delta v = 100\,\mathrm{km}^{-1}$). In case 1 I fix $n_{\mathrm{H_2}}$ for $\mathrm{H^{13}CO^{+}}$, as with only upper limits I cannot simultaneously constrain the hydrogen density and column density, while in case 2 $n_{\mathrm{H_2}}$ and $N_{\mathrm{H^{13}CO^{+}}}/\Delta v$ for $\mathrm{H^{13}CO^{+}}$ are allowed to vary over the full range described previously for the HCN/$\mathrm{H^{13}CN}$ modelling. In both cases T_{k} and T_{bg} are fixed to the best fit values of 150 K and 45 K respectively from the previous section. I perform the analysis for both case 1 and case 2. I ran grids using the upper, middle and lower values for the $\mathrm{H^{13}CN}$ column density found above, and used the maximum and minimum values of the resultant $\mathrm{H^{13}CO^{+}}$ column density to estimate uncertainties.

Case 1: The column densities permitted by the lower limit ratios are shown in Fig. 6.13. I find upper limits on the $\mathrm{H^{13}CO^{+}}$ column density of $2 \times 10^{11}\,\mathrm{cm^{-2}\,km^{-1}\,s}$ and $2 \times 10^{12}\,\mathrm{cm^{-2}\,km^{-1}\,s}$ in the WN and EN respectively. These correspond to lower limits on the abundance ratio $[\mathrm{H^{13}CN}]/[\mathrm{H^{13}CO^{+}}]$ of 1000 and 200 in the WN and EN respectively. These extremely high limits are dramatically

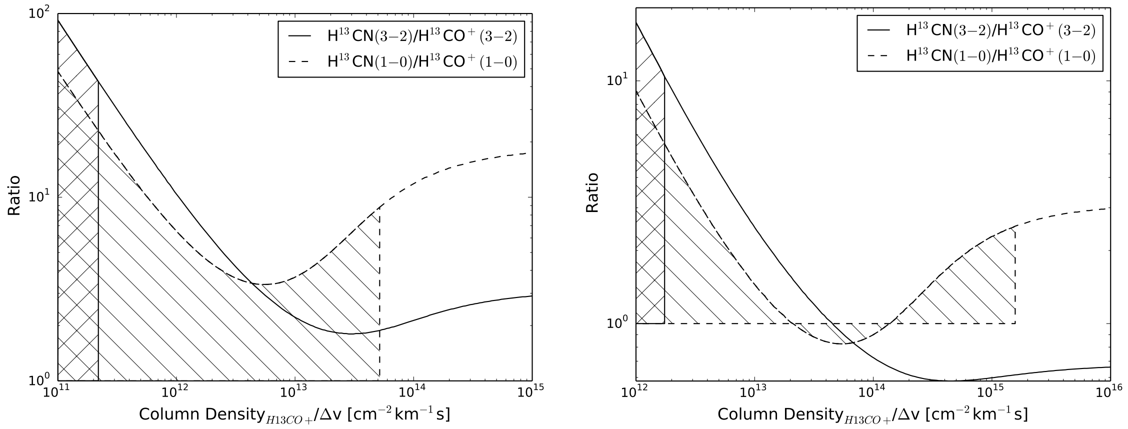

Figure 6.13: The regions of $H^{13}CO^+$ column density permitted by the lower limit ratios of case 1 in the WN (left) and EN (right). The hashed regions indicate the permitted columns for each ratio assuming $n_{H_2} = 2.1 \times 10^6\,\mathrm{cm^{-3}}$. Higher column densities are permitted for lower n_{H_2} values. I find upper limits on the $H^{13}CO^+$ column density of $2 \times 10^{11}\,\mathrm{cm^{-2}\,km^{-1}\,s}$ and $2 \times 10^{12}\,\mathrm{cm^{-2}\,km^{-1}\,s}$ in the WN and EN respectively.

decreased by reducing n_{H_2} in the $H^{13}CO^+$ phase, and at $n_{H_2} = 5 \times 10^4\,\mathrm{cm^{-3}}$ the limits are 44 and 60.

Case 2: I found best fit solutions in the two nuclei $N_{H^{13}CO^+}/\Delta v = 8^{+7}_{-4} \times 10^{12}\mathrm{cm^{-2}\,km^{-1}\,s}$ in the WN and $N_{H^{13}CO^+}/\Delta v = 1.9^{+6.6}_{-1.3} \times 10^{14}\mathrm{cm^{-2}\,km^{-1}\,s}$ in the EN. The grids for the best fit $H^{13}CN$ column densities are shown in Fig. 6.14. The uncertainties are predominantly driven by the uncertainty in the $H^{13}CN$ column density, so that the abundance ratio $[H^{13}CN]/[H^{13}CO^+]$ is relatively well determined as 25^{+16}_{-4} in the WN, and $2.0^{+4.2}_{-1.5}$ in the EN.

SiO

I used the upper, middle and lower $H^{13}CN$ column densities found for each nucleus, and restricted the parameters to $T_k = 150\,\mathrm{K}$, $T_{bg} = 45\,\mathrm{K}$ and $\Delta v = 100\,\mathrm{km\,s^{-1}}$. The maximum and minimum values of the resultant SiO column density were used to estimate uncertainties. I ran grids for the parameter range n_{H_2} for $10^5 - 10^7\,\mathrm{cm^{-3}}$ in $\log_{10}$ steps of 0.01, while N_{SiO} was varied to include the range permitted by the ratios. This was particularly significant for the 3.5 mm ratio in the EN, where the ratio alone cannot exclude extremely low $[H^{13}CN]/[SiO]$ ratios. I used the $T_B dv$ ratios, excluding the negative components of the $SiO(6-5)$ line. The results for both case 1 and 2 are shown in Fig. 6.15. Numerical results for the SiO fitting are collated in Table 6.6.

The results for case 1 and case 2 vary as expected, with higher $[H^{13}CN]/[SiO]$ ratios for case 2, although the ratios are consistent within uncertainties. I find consistent $[H^{13}CN]/[SiO]$ ratios for the two nuclei of $0.74^{+0.11}_{-0.08}$ and $0.28^{+0.50}_{-0.20}$ in the WN and EN respectively for case 1 and $0.87^{+0.11}_{-0.10}$ and $0.67^{+0.99}_{-0.14}$ in the WN and EN respectively for case 2. This would suggest that the elevated $[H^{13}CN]/[H^{13}CO^+]$ abundance ratio in the WN is due to either a process which is elevating the $[H^{13}CN]$ and $[SiO]$ abundances in tandem, or a process which is lowering the $[H^{13}CO^+]$ abundance.

6.6.2 $HC^{15}N(3-2)$ or $SO(6_6-5_5)$?

I attempted to distinguish between $HC^{15}N(3-2)$ and $SO(6_6-5_5)$ by using the HCN parameter results as inputs to LVG models. Assuming $[HCN]/[H^{13}CN] = 60$ and $[HCN]/[HC^{15}N] = 200$, I predict an integrated brightness temperature ratio in the WN for $HC^{15}N(3-2)/H^{13}CN(3-2)$ of 0.4. Using the SO column density from Martín et al. (2011) of $\sim 10 \times 10^{14}\,\mathrm{cm^{-2}}$ the LVG model predicts an integrated ratio $SO(6_6-5_5)/H^{13}CN(3-2) = 0.006$. The observed value of ~ 2, suggesting that the spectral feature may be dominated by $HC^{15}N$ and not SO, or really is a blending of the two. However the ^{15}N isotopic abundance is very uncertain, and could be 3×

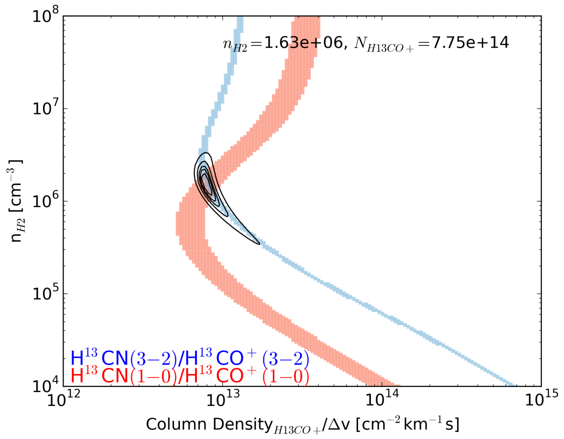

Figure 6.14: The error regions for the modelled $H^{13}CN/H^{13}CO^+$ line ratios in the WN (left) and EN (right). χ^2 contours are overlaid at 1, 2, 3 ,5 and 10. The minimum χ^2 locations are indicated in the top right corners of the plots. Best fits give an abundance ratio $[H^{13}CN]/[H^{13}CO^+]$ of 25^{+16}_{-4} in the WN, and $2.0^{+4.2}_{-1.5}$ in the EN.

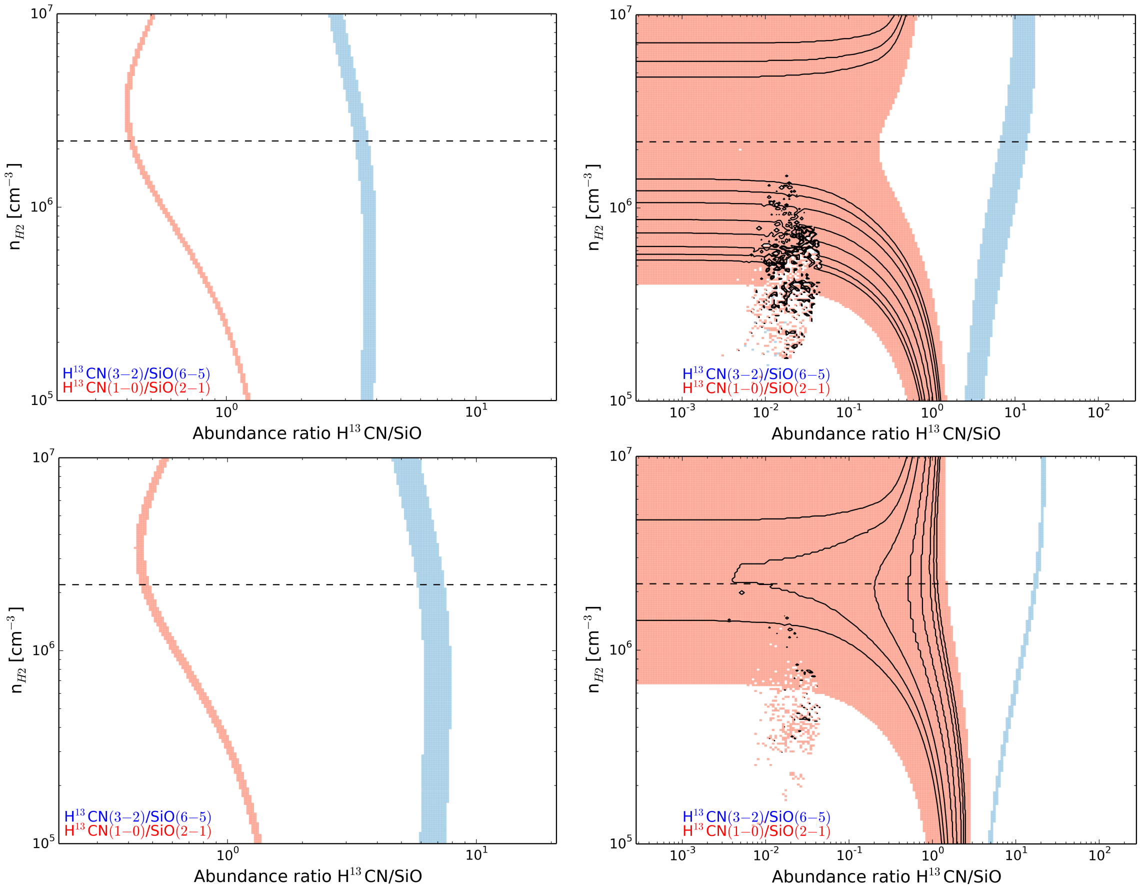

Figure 6.15: The 1σ regions for the modelled $[H^{13}CN]/[SiO]$ abundance ratio in the WN (left) and EN (right) for both case 1 (top) and case 2 (bottom). The dashed horizontal line marks the best fitting n_{H_2} from HCN modelling, and the EN plots show the χ^2 contours for the 3.5 mm component at 0.01, 0.1, 0.2 and 0.3. Numerical results of these models are shown in Table 6.6.

Table 6.6: SiO Abundance Results

	WN		EN	
	$[\mathrm{H^{13}CN}]/[\mathrm{SiO}]$	$N_{\mathrm{SiO}}/\Delta v$ $[10^{13}\mathrm{cm^{-2}\,km^{-1}\,s}]$	$[\mathrm{H^{13}CN}]/[\mathrm{SiO}]$	$N_{\mathrm{SiO}}/\Delta v$ $[10^{13}\mathrm{cm^{-2}\,km^{-1}\,s}]$
	Case 1: no $\mathrm{H^{13}CO^+}$			
1.2 mm	$3.4^{+1.5}_{-0.8}$	$5.6^{+1.7}_{-1.7}$	$3.3^{+3.8}_{-1.2}$	$5.8^{+3.3}_{-3.1}$
3.5 mm	$0.42^{+0.04}_{-0.05}$	46^{+6}_{-4}	$0.15^{+0.35}_{-0.10}$	130^{+250}_{-90}
Mean[a]	$0.74^{+0.11}_{-0.08}$	$25.5^{+3.8}_{-2.9}$	$0.28^{+0.50}_{-0.20}$	70^{+130}_{-50}
	Case 2: $\mathrm{H^{13}CO^+}$			
1.2 mm	$6.4^{+3.9}_{-2.1}$	$3.0^{+1.4}_{-1.1}$	$5.1^{+4.0}_{-1.6}$	$3.7^{+1.7}_{-1.6}$
3.5 mm	$0.47^{+0.05}_{-0.04}$	41^{+4}_{-4}	$0.36^{+0.08}_{-0.22}$	53^{+83}_{-10}
Mean[a]	$0.87^{+0.11}_{-0.10}$	$22.0^{+2.8}_{-2.4}$	$0.67^{+0.99}_{-0.14}$	29^{+42}_{-6}

[a] Since the varied parameter is the SiO column density, the mean here is the arithmetic mean for $N_{\mathrm{SiO}}/\Delta v$, and the harmonic mean for the $[\mathrm{H^{13}CN}]/[\mathrm{SiO}]$ abundance ratio.

Table 6.7: Abundance ratio comparison for $T_{\mathrm{k}} = 150\,\mathrm{K}$, $T_{\mathrm{bg}} = 45\,\mathrm{K}$ and $T_{\mathrm{k}} = 450\,\mathrm{K}$, $T_{\mathrm{bg}} = 110\,\mathrm{K}$

	WN		EN	
	$T_{\mathrm{k}} = 150\,\mathrm{K}$, $T_{\mathrm{bg}} = 45\,\mathrm{K}$			
	$[\mathrm{H^{13}CN}]/[\mathrm{H^{13}CO^+}]$	$[\mathrm{H^{13}CN}]/[\mathrm{SiO}]$	$[\mathrm{H^{13}CN}]/[\mathrm{H^{13}CO^+}]$	$[\mathrm{H^{13}CN}]/[\mathrm{SiO}]$
Case 1	> 950	$0.74^{+0.11}_{-0.08}$	> 185	$0.28^{+0.53}_{-0.20}$
Case 2	25^{+16}_{-4}	$0.87^{+0.11}_{-0.10}$	$2.0^{+4.2}_{-1.5}$	$0.67^{+0.99}_{-0.14}$
	$T_{\mathrm{k}} = 450\,\mathrm{K}$, $T_{\mathrm{bg}} = 110\,\mathrm{K}$			
	$[\mathrm{H^{13}CN}]/[\mathrm{H^{13}CO^+}]$	$[\mathrm{H^{13}CN}]/[\mathrm{SiO}]$	$[\mathrm{H^{13}CN}]/[\mathrm{H^{13}CO^+}]$	$[\mathrm{H^{13}CN}]/[\mathrm{SiO}]$
Case 1	> 640	$0.60^{+0.09}_{-0.07}$	> 180	$0.171^{+0.003}_{-0.092}$
Case 2	23^{+17}_{-6}	$0.70^{+1.0}_{-0.09}$	$2.0^{+3.3}_{-1.7}$	$0.42^{+1.60}_{-0.17}$

lower. Furthermore, the beam size of Martín et al. (2011) is almost 300× greater than ours: if their observed $\mathrm{SO}(5_5 - 4_4)$ emission is as tightly centred about the nuclei as the $\mathrm{SO}(6_6 - 5_5)$, then their LTE analysis could be heavily affected by beam dilution, underestimating the SO column density. Therefore it is not possible to exclude either possibility with these results, but if the spectral feature is dominated by $\mathrm{HC^{15}N}(3-2)$, it is consistent with an abundance ratio $[\mathrm{HCN}]/[\mathrm{HC^{15}N}] \lesssim 200$.

The results of the above LVG analysis are collated in Table 6.7, where the results for $T_{\mathrm{k}} = 450\,\mathrm{K}$ and $T_{\mathrm{bg}} = 110\,\mathrm{K}$ are also shown. I found that while the higher T_{k} and T_{bg} lowered the absolute abundances by over a dex, the abundance ratios are practically unchanged and are consistent within uncertainties. The LVG derived abundance ratios therefore appear to be quite robustly determined over a wide range in kinetic temperature. The column densities over Δv and CO and H_2 abundance ratios for the $T_{\mathrm{k}} = 150\,\mathrm{K}$ and $T_{\mathrm{bg}} = 45\,\mathrm{K}$ results are given in Table 6.8. The quoted uncertainties are propagated from the LVG modelling; the errors due to the uncertainty in T_{k} are not included but, as noted previously, could be as large as a dex.

Table 6.8: LVG Model Abundance Results

	Column densities $N_X/\Delta v$ $[10^{13}\mathrm{cm}^{-2}\,\mathrm{km}^{-1}\,\mathrm{s}]$	Abundance ratios[a] $[X]/[\mathrm{CO}]$[b]	 $[X]/[\mathrm{H_2}]$[c]
HCN	620^{+160}_{-160}	$2.8^{+0.7}_{-0.7} \times 10^{-3}$	$6.2^{+1.6}_{-1.6} \times 10^{-8}$
$\mathrm{H^{13}CN_{WN}}$	19^{+22}_{-10}	$9^{+10}_{-5} \times 10^{-5}$	$1.9^{+2.2}_{-1.0} \times 10^{-9}$
$\mathrm{H^{13}CN_{EN}}$	37^{+57}_{-18}	$1.7^{+2.6}_{-0.8} \times 10^{-4}$	$3.7^{+5.7}_{-1.8} \times 10^{-9}$
Case 1: no $\mathrm{H^{13}CO^+}$			
$\mathrm{H^{13}CO^+{}_{WN}}$	< 0.02	$< 9 \times 10^{-8}$	$< 2 \times 10^{-12}$
$\mathrm{H^{13}CO^+{}_{EN}}$	< 0.2	$< 9 \times 10^{-7}$	$< 2 \times 10^{-11}$
$\mathrm{SiO_{WN}}$	$25.5^{+3.8}_{-2.9}$	$1.16^{+0.17}_{-0.13} \times 10^{-4}$	$2.55^{+0.38}_{-0.29} \times 10^{-9}$
$\mathrm{SiO_{EN}}$	70^{+130}_{-50}	$3.2^{+5.9}_{-2.3} \times 10^{-4}$	$7^{+13}_{-5} \times 10^{-9}$
Case 2: $\mathrm{H^{13}CO^+}$			
$\mathrm{H^{13}CO^+{}_{WN}}$	$0.8^{+0.7}_{-0.4}$	$3.6^{+3.2}_{-1.8} \times 10^{-6}$	$8^{+7}_{-4} \times 10^{-11}$
$\mathrm{H^{13}CO^+{}_{EN}}$	19^{+66}_{-13}	$9^{+30}_{-6} \times 10^{-5}$	$1.9^{+6.6}_{-1.3} \times 10^{-9}$
$\mathrm{SiO_{WN}}$	$22.0^{+2.8}_{-2.4}$	$1.00^{+0.13}_{-0.11} \times 10^{-4}$	$2.20^{+0.28}_{-0.24} \times 10^{-9}$
$\mathrm{SiO_{EN}}$	29^{+42}_{-6}	$1.32^{+1.91}_{-0.27} \times 10^{-4}$	$2.9^{+4.2}_{-0.6} \times 10^{-9}$

[a] Assuming $\Delta v = 100\,\mathrm{km\,s^{-1}}$.
[b] CO column densities are taken from the maximum likelihood estimates of Rangwala et al. (2011) as the sum of the cold and hot phase columns: $N_{\mathrm{CO}} = 2.2 \times 10^{20}\,\mathrm{cm}^{-2}$, i.e. $[\mathrm{CO}]/[\mathrm{H_2}] = 2.2 \times 10^{-5}$. [c] For $N_{\mathrm{H_2}} = 1 \times 10^{25}\,\mathrm{cm}^{-2}$.

6.7 Discussion

6.7.1 Chemical Evidence for an AGN in the WN?

An increasingly common strategy to identify the AGN contribution to the bolometric luminosities of ULIRGs has been to study their HCN/HCO$^+$ integrated intensity ratios (Kohno et al., 2001; Imanishi et al., 2006; Papadopoulos, 2007; Krips et al., 2008; Imanishi et al., 2009). The general trend, as described by Krips et al. (2008) is that of increasing $(J \to J-1)/(J-1 \to J-2)$ intensity ratios for HCN and HCO$^+$ transitions, as well as a decreasing HCN$(J \to J-1)$/HCO$^+$$(J \to J-1)$ ratio, for an increased starburst contribution. These ratios seem to follow a trend from PDR-dominated emission in starbursts, to XDR-dominated emission in the most AGN-dominated galaxies. Krips et al. (2008) single dish analysis of Arp 220 within this framework found it to not fit well with any of their other galaxies (starburst (SB) dominated, SB-AGN composite or AGN dominated), but that it was closest to NGC 6951, an SB dominated galaxy with a weak AGN contribution. The possibility of an AGN has been challenged however by Costagliola et al. (2011), who found strong emission from HC$_3$N, a molecule thought to be readily destroyed in even hard UV environments, let alone XDRs, associated with the highest HCN/HCO$^+$ ratios. Instead, hot-core chemistry models (Bayet et al., 2006, 2008) simultaneously explain both decreased HCO$^+$ and elevated HC$_3$N. Throughout all of this however, it must be remembered that this analysis is averaging over the entire nuclear disk in the beam, covering dense clouds, diffuse gas, hot cores, PDRs and XDRs, all with potentially large cosmic ray contributions (evident from excited OH$^+$ emission González-Alfonso et al., 2013b), due to the observed supernova rate of ~4 a year, so the two-phase LVG model I employ for H^{13}CN and H^{13}CO$^+$ will be an extreme simplification.

Most recently, Martín et al. (2015) have suggested that elevated [HCN]/[HCO$^+$] abundance ratios are due not to XDR or PDR chemistry, but rather extensive shock chemistry in the turbulent regions of the CND. This would be consistent with the kinematics of the the 1.2 mm H^{13}CN and SiO lines in the WN, which suggest an outflow originating close to the continuum centre, as well as the high densities and kinetic temperatures of the LVG fits. García-Burillo et al. (2014) observed an AGN driven molecular outflow in NGC 1068 with an elevated HCN(4−3)/HCO^+(4−3) brightness temperature ratio (~ 2.5) in the regions immediately surrounding the AGN (within 140 pc), but significantly lower (~ 1.3) directly towards the AGN. This is consistent with the elevated HCN/HCO^+ ratios being caused by AGN driven mechanically dominated regions (MDRs), and not XDRs.

Meijerink & Spaans (2005); Meijerink et al. (2007, 2011) extensively modelled PDRs and XDRs over a range of densities and ionisation rates in an attempt to identify unique tracers of the two regions. For the high density environment of the HCN the [$H^{13}CN$]/[$H^{13}CO^+$] ratios are consistent with both PDR and XDR results. Additionally, Meijerink et al. (2011) studied the effects of cosmic rays and mechanical heating, and found evidence that strong mechanical heating can lead to very elevated HCN and HNC abundances (10^{-4} and 10^{-6} respectively) and low [HNC]/[HCN] ratios (1−0.01). While the abundances are very uncertain, the $HN^{13}C$(3−2)/$H^{13}CN$(3−2) line integrated ratios of 0.71 ± 0.04 and 0.66 ± 0.04 are consistent with shock heating, but not with high-density XDRs.

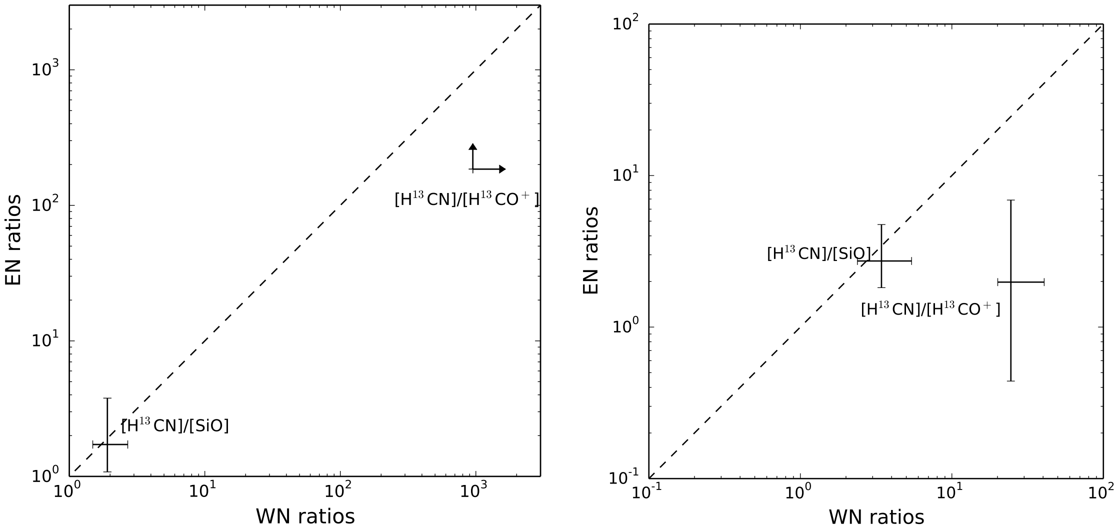

Figure 6.16: The LVG derived abundance ratios [$H^{13}CN$]/[$H^{13}CO^+$] and [$H^{13}CN$]/[SiO] in the two nuclei, for case 1 (left) and case 2 (right). Both show a clear distinction between the two nuclei with [$H^{13}CN$]/[$H^{13}CO^+$] elevated in the WN. The dependent ratio [SiO]/[$H^{13}CO^+$] is similarly elevated in the WN.

The LVG derived abundance ratios in case 1 and case 2 are shown in Fig. 6.16. I omit the dependent ratio [SiO]/[$H^{13}CO^+$] from the plot as it can be calculated trivially from the other two, and lying so close to [$H^{13}CN$]/[$H^{13}CO^+$] including it would significantly obfuscate the figure. I find an elevated [$H^{13}CN$]/[$H^{13}CO^+$] ratio in the WN in both case 1 and case 2. The case-1 ratios are unphysically high for the $H^{13}CN$ derived n_{H_2}, but for $5 \times 10^4\,cm^{-3}$ the ratio of 44 in the WN is entirely physical. The case-2 ratios, based on the upper limit of the $H^{13}CO^+$ contribution, yield lower limits on the [$H^{13}CN$]/[$H^{13}CO^+$] abundance ratios. Therefore the case-2 ratios of 25^{+16}_{-4} and $2.0^{+4.2}_{-1.5}$ in the WN and EN respectively, confirm that the ratio is elevated in the WN not only with respect to the EN, but also with respect to the starburst dominated cases of Krips et al. (2008). I find a conservative (3σ) lower limit on the ratios of 11 and 0.10 in the WN and EN respectively. The WN [$H^{13}CN$]/[$H^{13}CO^+$] is consistent with [HCN]/[HCO^+] ratios found by Krips et al. (2008), who found ratios between 0.01 and 50 (for starburst and AGN dominated galaxies respectively). Empirically therefore, the observations suggest that there is an energetically significant AGN in the WN of Arp 220, while the EN is powered predominantly by a starburst. This is consistent with Engel et al. (2011) who found that the 10 Myr old starburst is more prevalent in the EN.

I note that it is entirely possible that there is case 1 in the WN and case 2 in the EN. The evidence for this is largely the kinematic similarity with $HCO^+(3-2)$ in the WN (which is far more convincing than in the EN) combined with the northwards offset of the case 2 $H^{13}CO^+(3-2)$ line in the EN, which is hard to explain in case 2 but in case 1 implies a symmetry in the SiO outflow with $\pm 500\,km\,s^{-1}$ components. In the EN however the kinematic comparison to Sakamoto et al. (2009) makes it harder to exclude all $H^{13}CO^+(3-2)$ emission, favouring case 2.

The comparison with Krips et al. (2008) is entirely empirical, and cannot distinguish between an XDR and an MDR. Whether the trend of increasing [HCN]/[HCO^+] ratio with increasing AGN contribution is driven by an XDR or MDR does not affect the conclusion that an AGN is likely present in the WN. Nevertheless, the P Cygni profiles, high velocities, high gas kinetic temperatures and densities, as well as the low $HN^{13}C(3-2)/H^{13}CN(3-2)$ line-integrated ratios, point towards extensive shock heating and shock chemistry in Arp 220.

6.7.2 Shocked Gas in a Molecular Outflow? - The Origin of The Species

Based on similar blueshifted absorption in *both* nuclei despite their misaligned disks, Sakamoto et al. (2009) concluded that the P Cygni profiles were evidence of radial outflow in most directions, and not bound non-circular motion along the line of sight. Herschel observations have revealed P Cygni profiles in OH^+, H_2O and HF (Rangwala et al., 2011), as well as high velocity redwards components to the OH and H_2O lines (González-Alfonso et al., 2012). The embedded P Cygni profile of $H^{13}CN(3-2)$ and the P Cygni profile of SiO$(6-5)$, including the high-velocity absorption (seen out to $-600\,km\,s^{-1}$ and troughing about $-500\,km\,s^{-1}$) add to the evidence for an outflow from the Arp 220 WN. Furthermore, the high abundance of SiO and the high [$H^{13}CN$]/[$H^{13}CO^+$] ratio suggests that this outflow contains shocked gas.

Notably, the high-velocity blueshifted absorption seen in $HCO^+(3-2)$ (Sakamoto et al., 2009) and SiO$(6-5)$ has no analogue in blueshifted emission in any observed species, although Sakamoto et al. (2009) did see $\sim 500\,km\,s^{-1}$ redshifted components in both $HCO^+(3-2)$ and CO$(3-2)$. As these are high high$-J$ transitions they require populated $J=2$ and $J=5$ levels respectively to absorb the continuum: future high resolution observations of SiO$(5-4)$ may reveal high velocity emission.

As is discussed in detail in §6.4, I suggest that $H^{13}CN$, with the small P Cygni component is prevalent throughout the CND, but is also elevated in the outflow (e.g. Martín et al., 2015). SiO is almost exclusively present in the outflow, with a small CND component. $H^{13}CO^+$ would be present predominantly in the outflow (evidenced by the line profiles of Sakamoto et al. (2009)), but its abundance is heavily suppressed.

Sakamoto & Scoville (1999) found, on the basis of $0.5''$ CO$(2-1)$ observations, two counter-rotating nuclear discs, each $\sim 100\,pc$ in diameter, embedded in a much larger rotating outer disk. They base the orientation of the WN disk (near-side southwards) on the sharp falloff of light in NICMOS images. More recent work (Wilson et al., 2014) has constrained the continuum sizes to be $76\times < 70\,pc$ for the WN at 53° inclination and $123 \times 79\,pc$ for the EN. The bipolar outflow model presented below requires that the WN disk be oriented near-side northwards.

In stellar P Cygni profiles, the red emission and blue absorption originate along the same line of sight with gas leaving the star roughly isotropically. I see blue absorption across all of the southern half of the WN, i.e. south of the continuum peak, but it peaks $\sim 40\,pc$ south, while the emission peaks $\sim 40\,pc$ north. In the $0\,km\,s^{-1}$ channel of Fig. 6.9 the offset is even greater. This would suggest that while SiO is present mainly in the outflow, there is a disk component which is obscuring the outflow close to the continuum centre. While this could, hypothetically, be due to dust preferentially obscuring low velocity SiO, it is hard to envision the geometry of such a system that is consistent with the spatial profiles at higher velocities.

I propose an outflow geometry similar to the one shown in Fig. 6.17. In this toy model, an outflow leaves the nuclear disk roughly perpendicularly ($\sim 37°$ to the line of sight). As it advances it shocks the dusty medium, liberating SiO through grain sputtering. This leads to a maximum column depth being obtained offset from the disk centre. Since the SiO$(6-5)$ line is only just optically thick, the emission and absorption peaks coincide with the regions of maximum column depth, so I see emission and absorption peaks offset from one another and from the continuum. North of the disk, the redshifted emission behind the disk is attenuated by the optically thick dust

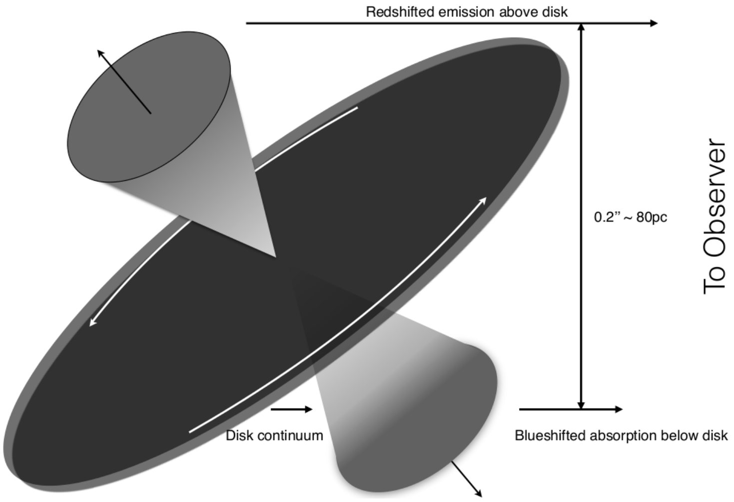

Figure 6.17: Outline of a possible geometry for Arp 220 WN. The highly schematic diagram shows the bipolar outflow scenario, where the north-south offsets of the emission and absorption peaks respectively is explained by a combination of dust opacity and the LoS column density being at a maximum away from the continuum centre. Redshifted emission, behind the disk, is significantly attenuated close to the continuum centre, but as it flows north and away from the disk is increasingly transmitted as thickness of intervening dust decreases. At ~ 40 pc north the light reaching us is maximal: further north the emitting column is decreasing or the excitation conditions are changing faster than transmitted fraction is increasing. South of the continuum centre, the absorption peaks at ~ −40 pc because while the LoS column continues to increase, the continuum emission falls off rapidly further south.

between the outflow and the observer. As it flows north there is less intervening dust, increasing the transmitted fraction until there is a peak at ~ 40 pc north. Beyond this point, either due to column density or the gas properties the emission decreases rapidly. South of the disk, the fraction of the continuum absorbed by the outflow increases as the column density increases, until it reaches the edge of the disk and the continuum falls off rapidly, leaving nothing to be absorbed.

The requirement that the column density increases away from the continuum centre, which by number conservation requires SiO to be either swept up or sputtered from dust, would invalidate the abundance estimates of SiO as the SiO emission would be offset from the peak H_2 column density, implying a much greater SiO abundance than I found in §6.6.1. González-Alfonso et al. (2012) found $3 \times 10^9\,M_\odot$ of dust in an optically thin, extended halo (650 pc diameter) about both nuclei, confirming that there is dust available outside of the WN for this model.

The lack of a P Cygni profile in the SiO$(2-1)$ line can be readily explained by the fainter continuum at 3.5 mm as well as both the dust and the SiO line becoming optically thin at these longer wavelengths.

Sakamoto et al. (2009) noted that the low velocity of the main absorption HCO$^+(3-2)$ is evidence that any outflow is not driven by an accreting supermassive black hole, but rather is either directly related to the nuclear starburst or to the merger super-wind. I see this absorption in SiO$(6-5)$ and H^{13}CN$(3-2)$, but given the high velocity SiO components in both HCO$^+$ and SiO and in light of the chemical evidence presented above, it could be that the outflow is only just beginning to be launched from the luminous core (be it starburst or AGN), and so has not yet all been accelerated to the velocities seen in more extreme outflows (e.g. Cicone et al., 2014). For the proposed geometry projection effects are insignificant: correcting for the ~ 40° angle of the outflow to the line of site only increases the velocities by a factor of 1.15. I propose that the molecular outflow is driven by a nascent/heavily obscured AGN. The geometry of the proposed outflow prohibits an upper limit on the outflow age, it does provide a lower limit of $\sim 6 \times 10^4$ yr, assuming that the outflow was launched at $\sim 500\,\mathrm{km\,s^{-1}}$ and the $150\,\mathrm{km\,s^{-1}}$ absorption is from gas which has been slowed by shocks after escaping the WN. If, as I propose in the chemical discussion above, I have case 1 in the WN, then the SiO$(6-5)$ velocity slice is almost symmetric about $-25\,\mathrm{km\,s^{-1}}$, with emission and absorption extending out to + and $-550\,\mathrm{km\,s^{-1}}$ respectively.

The outflow structure will be investigated further in a future paper, where I will use H_2 kinematic models, and SiO shock chemistry models to better interpret these results. The profusion of supernova remnants and explosions (SNRs and SNe's respectively) observed in the radio Batejat et al. (2011) suggests that shocked gas and mechanically sputtered dust could be extremely prevalent in Arp 220, and LVG codes, even with the addition of mid-IR pumping, may be insufficient to accurately model the abundances in shock-chemistry dominated regions.

6.7.3 SiO Abundance

The intermediate SiO abundance is three orders of magnitude higher than would be expected for quiescent, Galactic, gas (Martin-Pintado, 1992), but one lower than seen in Galactic shocks. However, the extremely dusty Arp 220 may have a higher quiescent gas-phase silicate abundance than the Milky Way. Downes & Eckart (2007) found that if there is a buried AGN at the centre of the WN it must be surrounded by a very thick and dusty torus.

The abundances are consistent with other extragalactic studies of SiO$(2-1)$ and H^{13}CO$^+(1-0)$. García-Burillo et al. (2000); García-Burillo et al. (2001); García-Burillo et al. (2010) and Usero et al. (2006) found SiO abundances in the range $10^{-9}-10^{-10}$ in the circumnuclear disks of NGC 253, M 82, NGC 1068 and IC 342 respectively. These SiO abundances were derived from the SiO/H^{13}CO$^+$ ratios and assumed H^{13}CO$^+$ abundances. For NGC 1068 the abundance was also found from the SiO$(3-2)$/SiO$(2-1)$ ratio and was consistent with that derived from an assumed H^{13}CO$^+$ abundance. In NGC 253 the abundance increases from 1×10^{-10} in the central nuclear disk (CDN) to 5×10^{-10} in the nuclear outflow. M 82 has a particularly complex morphology with a low abundance in the galactic disk (1×10^{-11}), increasing to 1×10^{-10} in a supershell and to 1×10^{-9} in a silicate chimney. NGC 1068 has abundances in the range $1-5\times10^{-9}$ in the CND, while IC 342 has a CND abundance of 2×10^{-10} but this rises to 1×10^{-9} in the spiral arms. Here, in case 2, I find abundances of $2.2^{+0.28}_{-0.24}\times10^{-9}$ and $2.9^{+4.2}_{-0.6}\times10^{-9}$ in the WN and EN CNDs respectively. These uncertainties are nominal, assuming the $T_\mathrm{k}=150\,\mathrm{K}$, $T_\mathrm{bg}=45\,\mathrm{K}$ and $n_{\mathrm{H}_2}=2.1\times10^6\,\mathrm{cm^{-3}}$. For different conditions the abundances can vary by more than a dex.

The SiO column density is $\sim 2-7\times10^{16}\,\mathrm{cm^{-2}}$, while Martín et al. (2011) found, based on LTE modelling of the SiO$(5-4)$ transition, $\sim 1\times10^{14}\,\mathrm{cm^{-2}}$, 100× lower. This is particularly important since the absorption I see in the SiO$(6-5)$ line requires that the $J=5$ level is populated. This difference may be due to the large beam ($8.5''\times7.0''$, 300× the area of the beam) of the SMA configuration used for the line survey of Martín et al. (2011). If the SiO emission is more compact than other lines this would lead to significant dilution, and a reduced column estimate. Higher-resolution observations of the SiO$(5-4)$ line combined with radiative-excitation modelling are needed to obtain a better estimate of the column density.

6.7.4 The Dense-Gas Fraction

Engel et al. (2011) found a dynamical mass within 100 pc of the WN of $6.3\times10^9\,M_\odot$. Using the H_2 density found from the LVG models, including a factor of 1.3 for helium and assuming a single core and a WN disk 75 × 70 × 10 pc, implies a gas mass $\gtrsim 1.7\times10^{10}\,M_\odot$, about 3× the dynamical mass, implying that the HCN and H^{13}CN disk emission is from multiple small, dense cores distributed across the nuclear disk. Repeating this exercise for the EN, dynamical mass $5.8\times10^9\,M_\odot$ leads to the same conclusion. Downes & Solomon (1998) suggested gas masses of $6\times10^8\,M_\odot$ and $1.1\times10^9\,M_\odot$ for the WN and EN respectively, which would suggest that the HCN dense cores cannot have a filling factor greater than 0.1 in the WN disk.

A shell of gas about a single "hot core", powered by the 5 pc-radius 400 K dust continuum found by González-Alfonso et al. (2012), is also possible on dynamical grounds, with a shell 0.1 pc thick having a mass $\sim 3\times10^6\,\mathrm{M_\odot}$.

6.7.5 The HNC/HCN ratio

Aalto et al. (2007) found the line-integrated brightness-temperature ratio HNC(3−2)/HCN(3−2) = 1.9 ± 0.3. This was explained to be due to either mid-IR pumping, where HNC is preferentially pumped over HCN by two orders of magnitude, or XDR chemical effects. I found $T_\mathrm{B}\mathrm{d}v$ ratios for HN^{13}C(3 − 2)/H^{13}CN(3 − 2) = 0.71 ± 0.04 in the WN, and 0.66 ± 0.04 in the EN, and $T_\mathrm{B,peak}$ ratios of 0.689 ± 0.023 and 0.453 ± 0.010 in the WN and EN respectively. Both measures present HN^{13}C as under-luminous with respect to H^{13}CN.

The WN value is uncertain due to the missing blue component of the line, estimated generously to be $\lesssim 25\%$ but not included in the results, but even allowing for a missing 40% on the HN^{13}C(3−2) line the ratio is still ~ 1, as a very generous upper limit. The EN value on the other hand is much more reliable, due to the additional redshift of the EN shifting almost all of the line into the spectrum. This discrepancy between the optically thick HNC/HCN and their much less optically thick ^{13}C isotopologues would suggest that the significantly different ratio is due to optical depth effects. Not only can these lines peer deeper into the high density environments, but the molecules will be less self-shielded against mid-IR pumping. This would lead to us seeing a greater fraction of the HNC and HCN which is hidden in dense cores, and protected against mid-IR pumping. In the “raisin roll” model of Aalto et al. (2007), the mid-IR field in Arp 220 drives widespread HNC emission while the optical depth of the HCN emission, primarily from dense cores, reduces the observed HCN intensity below what would be expected from its true [HNC]/[HCN] abundance ratio and the HNC intensity, leading to the high observed HNC/HCN ratio. When one observes the isotopologues however, one sees a truer representation of the [HNC]/[HCN] abundance ratio as there is no longer optically thick thermal emission from the dense cores.

I note that there might be some concern with extending the logic applicable to the carbon-12 isotopologues to the carbon-13 isotopologues. Measurements of HN^{13}C transitions are few and far between, but data from Harris et al. (2008), and the fact that the energy of the first excited bending mode (which is relevant for mid-IR pumping) has an energy proportional to $\rho^{-0.5}$ where ρ is the reduced mass, suggest any differences should be on the order of 1%. Any arguments based on the susceptibility to mid-IR pumping applicable to the HNC/HCN ratio should also apply to the HN^{13}C/H^{13}CN ratio.

6.8 Conclusions

I have presented spectral imaging of the prototypical ULIRG Arp 220 at 3.5 mm and 1.2 mm from the PdBI. I observe complex molecular lines including H^{13}CN, H^{13}CO$^+$, HN^{13}C and SiO. These results are consistent with previous millimetre studies of Arp 220, while also revealing shocked gas in the molecular outflow, building upon the molecular outflow observed by Sakamoto et al. (2009) in HCO$^+$. A chemical and kinematic analysis suggests that I have non-detections of H^{13}CO$^+$ in the WN, but detections in the EN. Further high-resolution work is needed to study the kinematically complex gas in Arp 220, in particular the SiO transition ladder at frequencies uncontaminated by H^{13}CO$^+$. Observations resolving the molecular emission within the disks are essential, and would allow us to identify whether the emission from different species is segregated to the extent I propose above. Chemical shock models, combined with kinematic and radiative transfer models may be able to shed more light on the environments traced by the complex line profiles observed here.

- I have used HCN(3−2) and HCN(1−0) single-dish data from the literature and the H^{13}CN(3−2) and H^{13}CN(1−0) interferometric data with LVG models to constrain the HCN environment in Arp 220, finding dense ($n_{\mathrm{H}_2} = 2.1 \pm 0.6 \times 10^6\,\mathrm{cm}^{-3}$), hot ($T_\mathrm{k} = 150 - 450\,\mathrm{K}$) gas.

- Working in two limiting cases, where I attribute the reddest components of fitted line profiles to either SiO or H^{13}CO$^+$, I find significant chemical differences between the two nuclei, as well as an elevated [H^{13}CN]/[H^{13}CO$^+$] abundance ratio, in both cases. The lowest [H^{13}CN]/[H^{13}CO$^+$] abundance ratios correspond to the case where the line component is attributed to H^{13}CO$^+$, and I find abundance ratios [H^{13}CN]/[SiO] = $0.87^{+0.11}_{-0.10}$ and $0.67^{+0.09}_{-0.14}$ and [H^{13}CN]/[H^{13}CO$^+$] = 25^{+16}_{-4} and $2.0^{+4.2}_{-1.5}$ in the WN and EN respectively. Therefore the lower limit on the [H^{13}CN]/[H^{13}CO$^+$] abundance ratios, in the limit of a maximal

$H^{13}CO^+$ contribution, are 11 and 0.10 in the WN and EN respectively. If, as I believe is more likely, case 1 (no $H^{13}CO^+$ detections) is a more accurate description of the WN the $[H^{13}CN]/[H^{13}CO^+]$ abundance ratio is significantly larger, most likely > 50.

- The elevated $[H^{13}CN]/[H^{13}CO^+]$ ratio in the WN, compared to the EN and to SB galaxies, suggests (empirically) an energetically significant AGN contribution to the WN luminosity.
- I find a "normal" $(0.1 - 1.0)$ brightness temperature ratio for $HN^{13}C(3-2)/H^{13}CN(3-2)$ in both nuclei, suggesting that the elevated HNC/HCN intensity ratio seen by Aalto et al. (2007) is due predominantly to mid-IR pumping, and not an XDR. Combined with the evidence for an AGN, this implies extensive mechanical heating and shock chemistry in Arp 220.
- I suggest that HCO^+, $SiO(6-5)$ and a fraction of $H^{13}CN(3-2)$ are tracing a dense molecular outflow with a large shocked component, and present a toy model geometry which can explain the north-south offset I observe in the $SiO(6-5)$ emission and absorption, which independently reproduces the size of the WN continuum source seen by Wilson et al. (2014).

Since this work was conducted, ongoing research (Aalto et al., 2015b) has revealed the presence of vibrationally excited HCN in Arp 220, which raises new questions with regards to the spatio-kinematic interpretation of the spectra. This is an open research question, which will require observations at high spatial and spectral resolution of multiple molecular lines and their isotopologue lines with ALMA. Similarly, there is a pressing need for chemical models of molecular gas in outflow conditions, to better inform the observations as well as identifying whether molecules are forming in the outflow itself or are launched from the dusty molecular cores.

Additionally, new ALMA observations (Martín et al., 2016) do not find the spatial offset in the highly blueshifted absorption system, suggesting that the offset seen here is more likely to be an effect of noise in the complex visibility phases. This has little effect on any of the conclusions of this chapter, but does reduce the constraints on the geometry of the outflow.

This page was intentionally left nearly blank.

Chapter 7

And We All Fall Down: The Evolution of HzRG Proto-Clusters

"My dear, here we must run as fast as we can, just to stay in place. And if you wish to go anywhere you must run twice as fast as that."

Lewis Carroll, Alice Through the Looking Glass

7.1 Introduction

As was discussed in chapter 1, high-redshift radio galaxies (HzRGs) are thought to lie at the cores of galaxy proto-clusters, with Carilli et al. (1997) and Athreya et al. (1998) finding extremely large rest frame rotation measures, implying electron densities $\sim 0.05\,\mathrm{cm}^{-3}$, comparable to measurements in local clusters. Companion-galaxy overdensities have been identified around HzRGs out to $z = 5$ using Lyα galaxies, spectroscopically confirming their relationship with the HzRG-centred proto-clusters and showing overdensities between 5 and 15 times field densities, with proto-cluster sizes between 2 and 5 Mpc (Kurk et al., 2000; Venemans et al., 2002, 2004, 2005; Intema et al., 2006; Venemans et al., 2007; Pentericci & Venemans, 2007). Efforts to identify companion galaxies in the mid- to far-IR have found submillimetre galaxy (SMG) overdensities around HzRGs, although these have historically been limited by small fields of view (Ivison et al., 2000; Smail et al., 2003). Rigby et al. (2014) presented large ($\sim 400\,\mathrm{arcmin}^2$) fields around 26 HzRGs observed in the 200, 350, and 500 μm SPIRE bands, finding evidence for slight overdensities around HzRGs with $L_{500\,\mathrm{MHz}} \gtrsim 10^{29}\,\mathrm{W\,Hz}^{-1}$ and $z < 3$.

The *Herschel* Radio Galaxy Evolution Project (Projet HeRGÉ, PI: N. Seymour, Seymour et al., 2007) is the continuation of the *Spitzer* Space Telescope/IRAC ($3.6 - 8\,\mu$m)+MIPS ($24\,\mu$m) survey of 71 HzRGs spanning the redshift range $1 < z < 5.2$. Extensive studies and multi-wavelength follow up observations have analysed the SEDs of these galaxies from $8 - 870\,\mu$m (observed frame), finding that these galaxies are extremely luminous, rapidly star forming galaxies hosting simultaneously accreting supermassive black holes (Seymour et al., 2012; Rocca-Volmerange et al., 2013; Drouart et al., 2014).

In this chapter I explore the overdensity of SMGs around HzRGs and the evolution, or lack thereof, in the overdensities with redshift. Since SMGs are thought to be precursors of modern ellipticals, which are preferentially found near cluster cores (Dressler, 1980), and HzRGs are thought to mark the cores of proto-clusters, I expect to find that there is a significant increase in the SMG overdensity (wrt the field) around HzRGs, especially between $z = 1.5{-}3.0$ when star-formation-rate density of the universe was highest. These galaxies and proto-clusters have significant potential for ALMA follow-up observations, linking them back to work in this thesis.

Throughout this chapter I assume cosmological parameters $H_0 = 71\,\mathrm{km\,s^{-1}\,Mpc^{-1}}$, $\Omega_\mathrm{m} = 0.27$ and $\Omega_\mathrm{vac} = 0.73$, corresponding to physical scales of $8.540\,\mathrm{kpc\,arcsec^{-1}}$ at $z = 1.5$ and 6.734 $\mathrm{kpc\,arcsec^{-1}}$ at $z = 4.5$. The corresponding comoving transverse distance scales are $1.28\,\mathrm{Mpc\,arcmin^{-1}}$ and $2.22\,\mathrm{Mpc\,arcmin^{-1}}$ respectively (Wright, 2006b).

7.2 Observations and Reduction

Sixteen HzRGs were selected from HeRGÉ to be a representative sample in mass and 500 MHz luminosity in the four redshift bands $z = 1.5$, 2.5, 3.5 and 4.5. The selected HzRGs were targeted with JCMT/SCUBA-2, which simultaneously observes at $450\,\mu$m and $850\,\mu$m, in projects M12BU39, M15AI146 and M15BI139 (PI: T. R. Greve). M12BU39 and M15AI146 targeted five galaxies at $z \sim 2.5$ and five at $z \sim 3.5$, while M15BI139 extended the redshift range of the observations with three targets at $z \sim 1.5$ and three at $z \sim 4.5$. All but two of the galaxies were successfully observed, although both of the missing galaxies lie at $z \sim 1.5$. In total, the projects observed for 74.4 hours in weather bands 1 and 2[1]. The redshift, 500 MHz luminosity and stellar masses of the targets in the context of the HeRGÉ sample are shown in Figure 7.1 and the observed fields are listed in Table 7.1.

---

[1] $\tau_{225\,\mathrm{GHz}} \leq 0.08$.

Table 7.1: Positions and redshifts of the HzRG target fields.

Target	Alternative Designation	Redshift	RA	Dec	$\log_{10}(L_{500\,\mathrm{MHz}})$[a]	Repeats[b]	Reference[c]
LBDS 53W091		1.55	$17^{\mathrm{h}}22^{\mathrm{m}}32.^{\mathrm{s}}7$	$+50^\circ06'02''$	27.04	4	1,2,3
TXS 0211−122	LEDA 2823016	2.34	$02^{\mathrm{h}}14^{\mathrm{m}}17.^{\mathrm{s}}4$	$-11^\circ58'46''$	28.48	5	4,5
3C 257	NVSS J112309+053020	2.47	$11^{\mathrm{h}}23^{\mathrm{m}}09.^{\mathrm{s}}2$	$+05^\circ30'19''$	29.16	10	4,6
4C +23.56	LEDA 2819817	2.48	$21^{\mathrm{h}}07^{\mathrm{m}}14.^{\mathrm{s}}8$	$+23^\circ31'45''$	28.93	10	5,7
USS 1558−003	4C −00.62	2.53	$16^{\mathrm{h}}01^{\mathrm{m}}17.^{\mathrm{s}}3$	$-00^\circ28'47''$	28.82	10	4,7,8
USS 0828+193	NVSS J083053+191314	2.57	$08^{\mathrm{h}}30^{\mathrm{m}}53.^{\mathrm{s}}4$	$+19^\circ13'16''$	28.44	3	4,5
B2 0902+34	NVSS J090530+340756	3.38	$09^{\mathrm{h}}05^{\mathrm{m}}30.^{\mathrm{s}}1$	$+34^\circ07'57''$	28.78	5	4,7,9
TN J0205+2242	NVSS J020510+224250	3.51	$02^{\mathrm{h}}05^{\mathrm{m}}10.^{\mathrm{s}}7$	$+22^\circ42'51''$	28.46	5	4,10
TN J0121+1320	NVSS J012142+132058	3.52	$01^{\mathrm{h}}21^{\mathrm{m}}42.^{\mathrm{s}}7$	$+13^\circ20'58''$	28.49	5	4,10
MG J214405+1929	4C +19.71	3.59	$21^{\mathrm{h}}44^{\mathrm{m}}07.^{\mathrm{s}}0$	$+19^\circ29'15''$	29.08	9	4,5,7
TN J2007−1316	MRC 2005−134	3.84	$20^{\mathrm{h}}07^{\mathrm{m}}53.^{\mathrm{s}}2$	$-13^\circ16'45''$	29.13	10	4,11
TN J1338−1942	NVSS J133825−194229	4.11	$13^{\mathrm{h}}38^{\mathrm{m}}26.^{\mathrm{s}}1$	$-19^\circ42'31''$	28.70	6	4,8
8C 1435+635	4C +63.20	4.26	$14^{\mathrm{h}}36^{\mathrm{m}}37.^{\mathrm{s}}3$	$+63^\circ19'13''$	29.40	6	4,5,7
RC J0311+0507	4C +04.11	4.51	$03^{\mathrm{h}}11^{\mathrm{m}}48.^{\mathrm{s}}0$	$+05^\circ08'03''$	29.49	5	7

[a] Units of $\mathrm{W\,Hz^{-1}}$.

[b] Each Pong-900 scan lasts approximately 40 minutes. The total observing time is therefore 40 minutes multiplied by the number of repeats. However, each point on the sky receives different total integration times due to the observing pattern (Holland et al., 2013).

[c] (1): Rigby et al. (2007), (2): Rigby et al. (2008), (3): Kapahi & Kulkarni (1990), (4): Condon et al. (1998), (5): Carilli et al. (1997), (6): van Breugel et al. (1998), (7): White & Becker (1992), (8): Pentericci et al. (2000), (9): Carilli et al. (1994), (10): De Breuck et al. (2000), (11): De Breuck et al. (2010).

The HzRG fields were mapped with Pong-900 observing pattern, which produces a map out to a radius of $900''$. This pattern provides a relatively uniform noise level over the central regions of the map, with the rms increasing smoothly as a function of radius. The noise increases very rapidly over the outer $180''$, and I cropped the maps to $720''$ to remove the most unreliable data. The azimuthally averaged radial noise profiles cropped to $720''$ are shown in Figure 7.2. Cropped thusly, each field covers an area $\sim 452\,\mathrm{arcmin}^2$, with a total area over the 14 fields $\sim 1.8\,\mathrm{degrees}^2$, corresponding to a total comoving area $\sim 23,000\,\mathrm{Mpc}^2$.

7.2.1 Data Reduction Pipeline

The data pipeline developed for this chapter is presented in Figure 7.3. The initial steps of the data reduction followed the methods presented in the SCUBA2 Data Reduction Cookbook[2].

The data were reduced with the STARLINK software packages KAPPA[3] and SMURF[4], and made use of PICARD[5] recipes. First, the calibrator scans and each 40 minute science scan were reduced with *makemap* and the *dimmconfig_blank_field.lis* recipe with pixel sizes of $1''$ (see Chapin et al., 2013, for details on the map making procedure). The resulting maps were calibrated using the mJy/beam flux conversion factors (FCFs) from the matched-filtered calibrators. These FCFs were first checked against the 'standard' SCUBA-2 FCFs to ensure reasonable values (Dempsey et al., 2013). All of the maps of each field were then combined before being matched-filtered with the PICARD recipe SCUBA2_MATCHED_FILTER and then cropped to a radius of $12'$ to remove the high-rms outer edges of the maps. The resulting $850\,\mu$m maps are included in the appendix as Figure A.1.

7.2.2 Source Extraction

A CLEAN-like algorithm was employed to extract point sources from the $850\,\mu$m maps and compile a catalogue of all sources with S/N>3.5. The catalogue is given in Table A.1 in the appendix. The algorithm identifies the most significant pixel in the S/N map and subtracts the telescope point spread function (PSF), appropriate for a point source, from the flux map with peak flux equal to the corresponding pixel in the flux map. This is repeated until there are no pixels with S/N greater than a given threshold (in this case S/N>3.5). The final residual map and a catalogue of sources with S/N, map coordinates, equatorial coordinates, flux and noise are returned.

Note that while the match-filtered PSF is used to extract sources, testing of the routine showed that the the results are robust to small-to-moderate changes in the scale of the extracting PSF.

While it was intended to use $450\,\mu$m fluxes to calculate $850\,\mu$m/$450\,\mu$m colours for photometric redshift estimates, at most one of the sources in each field was also detected at $450\,\mu$m, making this approach impossible.

The $850\,\mu$m maps show clear signs of multiple sources. In the case of USS 1558$-$003 there is also a highly significant negative S/N region as well: this is due to the negative bowling from the matched filtering of the extremely bright and extended source in the South-West quadrant of the map. In TN J0205+2242 there is also a low S/N excess due to a single, unexplained $-11.5\,\sigma$ 'hole' in the map at RA: $02^{\mathrm{h}}04^{\mathrm{m}}34^{\mathrm{s}}.093$, Dec: $22^\circ51'10''.74$, on the North-West edge of the map. While it is not clear what could cause this hole, its proximity to the map edge suggests that it is an isolated error in the map making, and it is excluded from the rest of the analysis.

A Monte-Carlo (MC) analysis was used as an initial test of the robustness of the source counts using the variance maps from *mapmaker*. For each field and frequency 100 source-free maps with noise properties defined by the variance maps were generated as described below in § 7.2.3. These maps were then matched-filtered and cropped as for the real science maps and then CLEANed for a range of S/N thresholds. The average of these MC realisations were compared with the cumulative source counts as functions of the S/N ratio and with the theoretical prediction for Gaussian noise, treating the map as a collection of beams and each beam as an independent Gaussian variable.

---

[2] `http://www.starlink.ac.uk/docs/sc21.htx/sc21.html`

[3] `http://www.starlink.ac.uk/docs/sun95.htx/sun95.html`

[4] `http://www.starlink.ac.uk/docs/sun258.htx/sun258.html`

[5] `http://www.starlink.ac.uk/docs/sun265.htx/sun265.html`

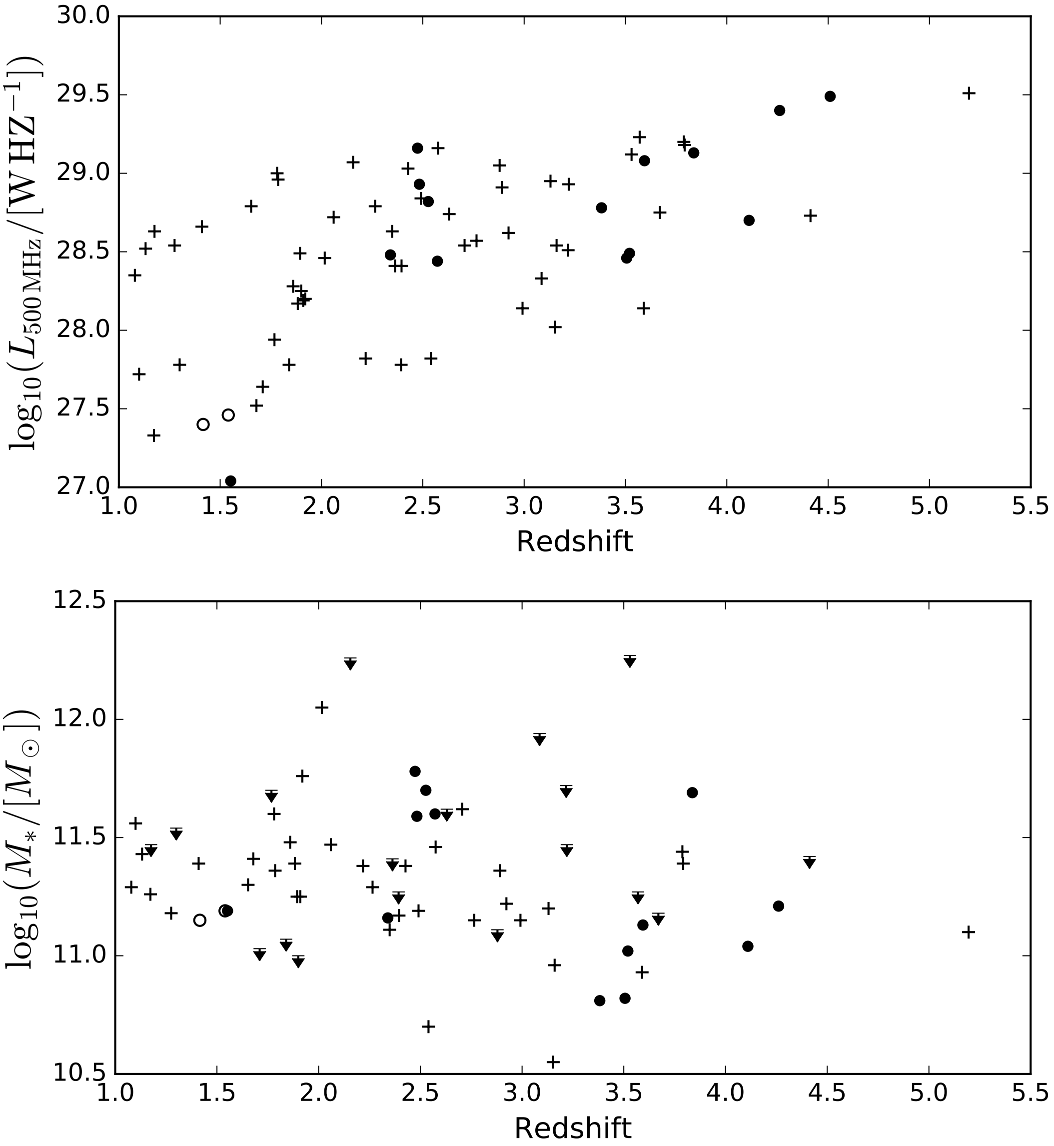

Figure 7.1: The HeRGÉ sample (Seymour et al., 2007; De Breuck et al., 2010) with the SCUBA-2 targets indicated by filled circles. Empty circles indicate the two fields that were proposed but unobserved.

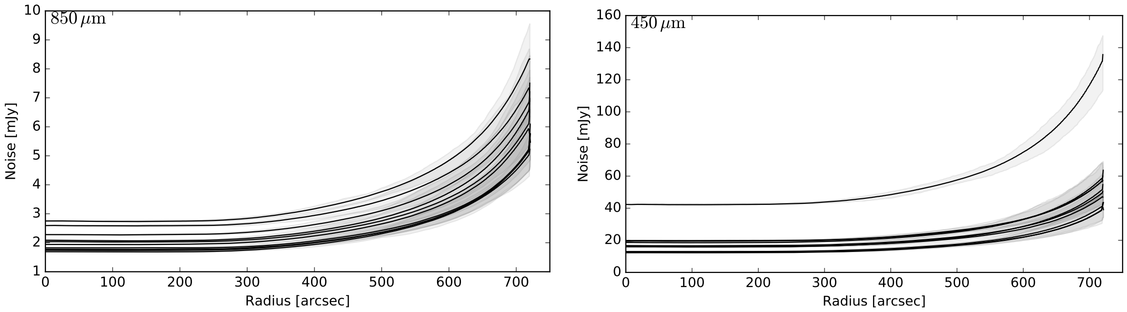

Figure 7.2: The azimuthally averaged radial noise profiles of the 14 HzRG fields, cropped to 720″. The averaged noise profile is shown by the solid lines, with shading marking the upper and lower limits of the noise at a given radius. The very noisy 450 μm field is MG J214405+1929, where one of the 450 μm scans was corrupted.

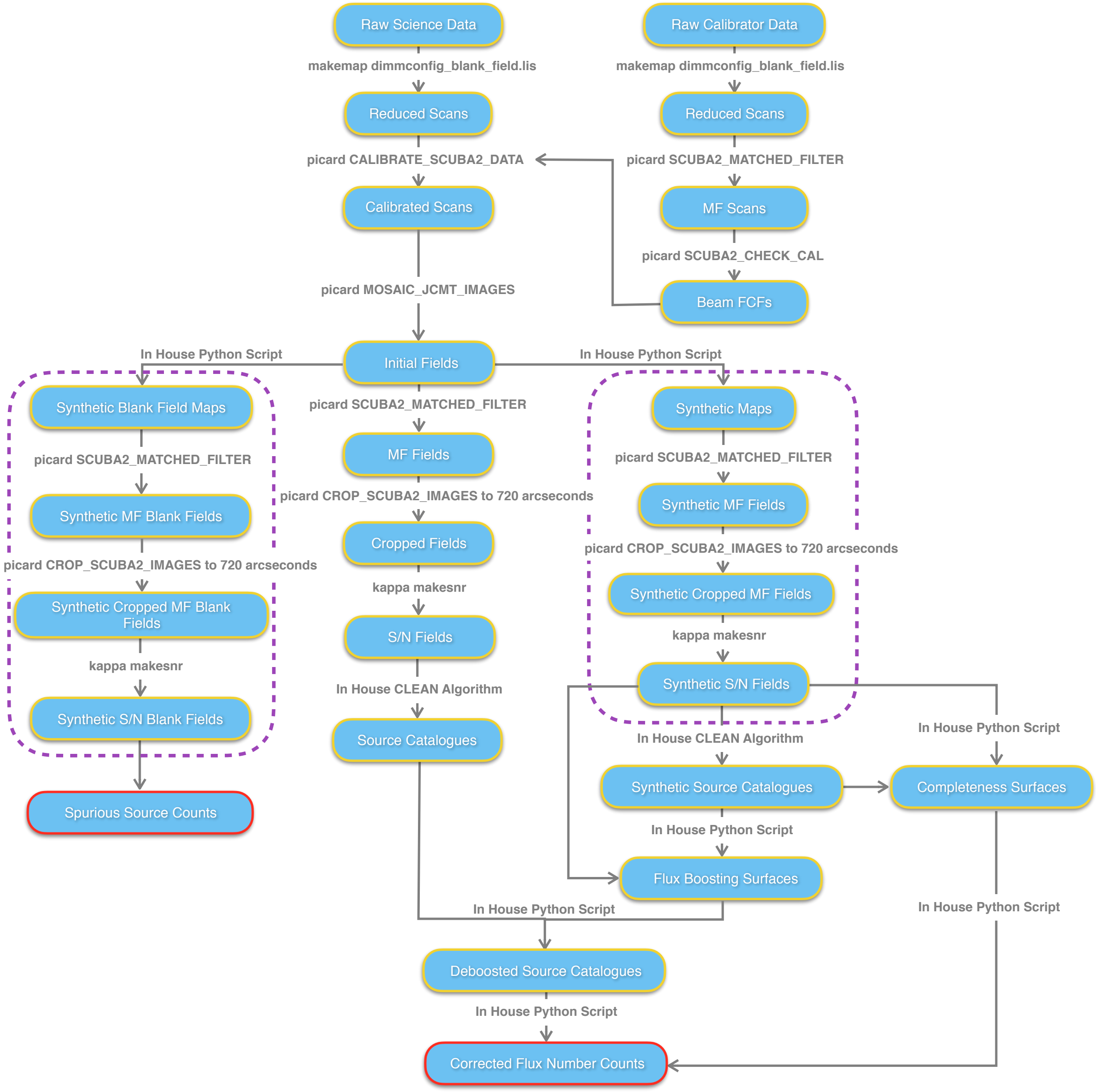

Figure 7.3: Schematic of the data pipeline used to reduce and analyse the SCUBA2 data.

The Gaussian prediction describes the faint ($< 3.5\sigma$) counts well, especially in the 850 μm maps. The 450 μm maps are much better fit by the MC counts which are slightly lower than the Gaussian prediction. This is consistent with the pixel histograms in Figure A.2, where the negative tails of the 850 μm maps are fitted well by Gaussian noise, whereas the 450 μm maps are are more sharply peaked around lower S/N.

7.2.3 Synthetic map production

In order to account for the highly variable noise properties of the maps, while generating completeness surfaces and the data for Bayesian flux deboosting, I create MC realisations of the science maps. Due to the size of the maps it is impossible to store all of the MC maps generated, therefore each MC map is generated, processed, analysed and then discarded. These 'on-the-fly' maps are indicated by the dashed purple boxes in Figure 7.3.

To generate the MC maps I convert the SDF maps to FITS, then use the pixel-by-pixel sky and instrument noise model, generated by the *makemap* reduction, to produce a noisy map. This map has Gaussian noise in each pixel with variance equal to the square of the corresponding pixel noise model.

For tests on blank fields I then export this map with the variance layer and header copied from the input map to a new FITS file. This is converted to SDF for processing with PICARD SCUBA2_MATCHED_FILTER, CROP_SCUBA2_IMAGES and KAPPA *makesnr*. The CLEAN source extraction routine is then run on these blank fields for a range of S/N thresholds to estimate the spurious source counts as a function of S/N threshold for each field.

For the flux boosting and completeness surfaces I add sources to the synthetic maps. Sources are added as point sources (a single PSF) with fluxes chosen from a linearly decreasing distribution over the interval $[-1:35)$ mJy such that:

$$p(S) = \begin{cases} b(1 - S/a) & : \quad -1 \leq S < 35 \\ 0 & : \quad \text{else} \end{cases}$$

for a and b selected to achieve a normalised probability distribution with a compromise between preferentially selecting the more relevant low fluxes and achieving a good sampling of the fluxes.

Sources are distributed uniformly across azimuth but with a radial sampling function such that:

$$r = 720'' \, \zeta^{1/\rho}, \tag{7.1}$$

where ζ is a uniform random variable from the range $[0:1)$ and ρ is selected to achieve as optimal a sampling of the map noise as possible; for the SCUBA-2 maps I place half of the sources with $\rho = 4$ and half with $\rho = 16$. This scaling biases the radial sampling towards the outer edges of the maps where the noise is larger but more relevantly changes most rapidly. This leads to a more uniform sampling of the noise than a scaling of $\rho = 2$, which distributes sources uniformly across the field but oversamples the low noise regions.

The input positions, fluxes and noises are recorded, then the maps passed out for processing as for the blank field maps above. I CLEAN the maps to get an output catalogue, then search for matches between the input and output catalogues with flux and position as match criteria. In the event of multiple potential matches within the flux and position tolerances I select the output with the smallest normalised square deviation in both flux and position. If no matching sources were recovered this is also noted.

To estimate completeness and flux boosting I generated 2000 MC maps for each field, with the same pixel-by-pixel rms as the observed, unsmoothed and unfiltered maps. For each MC map 100 point sources were added as described above. The maps were then processed identically to the science maps and sources extracted with a $3.5\,\sigma$ threshold.

7.2.4 Flux deboosting

Eddington bias describes the preferential boosting of sources with S/N just below a survey cutoff over the boundary due to random noise and a decreasing luminosity function. I use the same MC data generated for the completeness analysis to generate the likelihood and evidence for Bayesian flux deboosting, combined with a Schecter function prior.

To describe the posterior I write:

$$p\left(S_{\mathrm{true}}|S_{\mathrm{obs}},\sigma\right)=\frac{p\left(S_{\mathrm{obs}}|S_{\mathrm{true}},\sigma\right)p\left(S_{\mathrm{true}}|\sigma\right)}{p\left(S_{\mathrm{obs}}|\sigma\right)}, \tag{7.2}$$

and:

$$p\left(S_{\mathrm{true}}|\sigma\right)=p\left(S_{\mathrm{true}}\right) \tag{7.3}$$

since the underlying source flux distribution is not dependent upon the map rms. In the case of the observed source deboosting I estimate $p\left(S_{\mathrm{true}}\right)$ by assuming a Schecter luminosity function with parameters from Coppin et al. (2006).

$p\left(S_{\mathrm{obs}}|\sigma\right)$ can be generated by constructing a 2D histogram of S_{out} vs σ and then finding, for a given σ, the fraction of counts in the S_{obs} bin corresponding to the observed flux. However, this is simply a uniform factor, so does not affect the shape of the recovered posterior. Therefore:

$$p\left(S_{\mathrm{true}}|S_{\mathrm{obs}},\sigma\right)\propto p\left(S_{\mathrm{obs}}|S_{\mathrm{true}},\sigma\right)p\left(S_{\mathrm{true}}\right). \tag{7.4}$$

I generate the likelihood, $p\left(S_{\mathrm{obs}}|S_{\mathrm{true}},\sigma\right)$, from the MC simulations. This necessitates a discrete gridding of the probabilities, and so I first set up a uniformly spaced set of bins for S_{obs}, S_{in} and σ. Using these bins and the known inputs and recovered outputs I bin the output fluxes, S_{obs}, into the cells of a grid defined by S_{in} and σ. The S_{obs} in each grid cell are then themselves binned. The use of the fixed, uniformly spaced bins ensures that the same bins are used for every cell, and that each 3D bin corresponds to the same volume of probability space. Then, the relative likelihood of a flux, S_{obs}, for a given S_{in} and σ, is just the number of counts in the corresponding bin.

With the probabilistic machinery generated for each field, I can then deboost the sources recovered from the science fields. For every source I build the 1D posterior distribution, smooth the distribution with a Gaussian kernel, and adopt the deboosted flux corresponding to the maximum posterior probability.

The Gaussian smoothing kernel is necessitated by the MC noise, which leads to a degree of "spikiness" in the posterior distribution, which can unfairly bias the maximum posterior. Extensive testing on validation sets showed that a 10 bin smoothing kernel optimises both the mean and rms deboosted flux errors. There is a compromise, with the posterior smoothing slightly biasing the recovered S/N towards the observed S/N distribution, and away from the input S/N distribution. The ideal solution would be to increase the number of MC trials, but this is currently impractical due to issues with multiple instances of PICARD running concurrently leading to corruption of config files and the matched filtering step taking approximately a minute for each realisation of the synthetic fields.

Correcting for flux boosting is additionally challenging in the current analysis as there are different noise levels in each field as well as sharply rising radial noise profiles. For the Schecter function with parameters found by Coppin et al. (2006): $S' = 3.3$ and $\alpha = -2.0$. However, the deboosting is not significantly different for any reasonable choice of Schecter function parameters. Note that the absolute scaling of the function, given by N', is irrelevant here as it is only the shape of the prior that matters, not its absolute normalisation.

The results of the Bayesian flux deboosting are shown in Figures 7.5, 7.6 and 7.7. Of 420 sources initially found above 3.5σ 266 (63%) are shifted below this threshold in the deboosting. However, of the 266 sources lost by the deboosting 237 had S/N< 4, and 262 had S/N< 4.5: see Figure 7.6. Similarly, in the uncorrected observations only 67 sources had fluxes with S/N> 4.5. Sources are far more likely to be identified as spurious towards the edges of the maps, where the number of marginal detections increase rapidly.

Figure 7.6 shows the desired clear right-angled distribution of fractional deboosted flux ((observed flux − deboosted flux)/observed flux) vs observed S/N. Similarly, comparing Figure 7.5 left and right shows that the sources most corrected by the deboosting are those found in very high noise regions. However, there does appear to be a slight systematic decrease in the flux for all

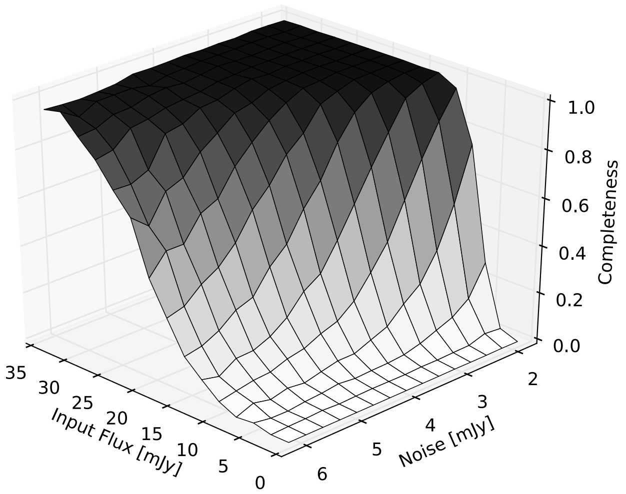

Figure 7.4: The 3C 257 completeness surface as a function of the local map noise and the input flux. Note that the input flux is the true sky flux, which is not necessarily the observed flux.

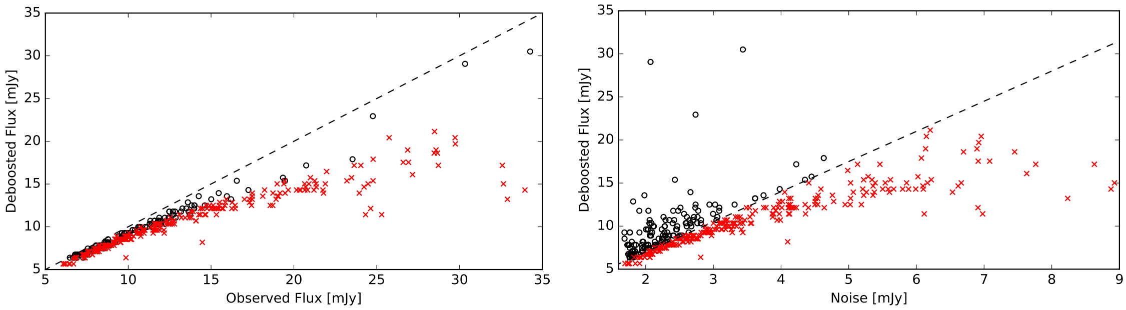

Figure 7.5: Deboosted flux vs the observed flux (left) and Deboosted flux vs the local noise (right). In both figures sources with S/N$< 3.5\sigma$ post deboosting are marked by red crosses; those with S/N$\geq 3.5\sigma$ by black circles. The dashed lines indicate a deboosted/observed flux ratio of 1 on the left, and the 3.5σ cutoff on the right.

sources of between 5 and 10%, which is not seen in the models used to test the flux deboosting. It appears to be due to the Schecter function prior used in the flux deboosting and the relatively high map rms: this leads to high fluxes being pulled low by the prior counts.

7.2.5 Completeness

Due to random noise in the sky, telescope and data reduction some sources with a "true" S/N greater than the survey limit are lost. An attempt was made to correct for this by simulating the observations to derive a model for the completeness.

A catalogue of inputs and outputs from 2000 MC maps per 850 μm field was post processed, binning input sources according to rms and input flux and then counting the fraction of inputs with recovered outputs in each bin, generating a 2D completeness surface. An example of the completeness surface generated is given in Figure 7.4 for the 3C 257 field.

This completeness surface is then used to correct the flux deboosted source counts. The deboosted sources are binned into the corresponding $S_{\rm in} - \sigma$ grid cell, and the counts in that cell are divided by the completeness of that cell. These counts are then summed along the σ axis, leaving binned, deboosted and corrected source counts as a function of source flux.

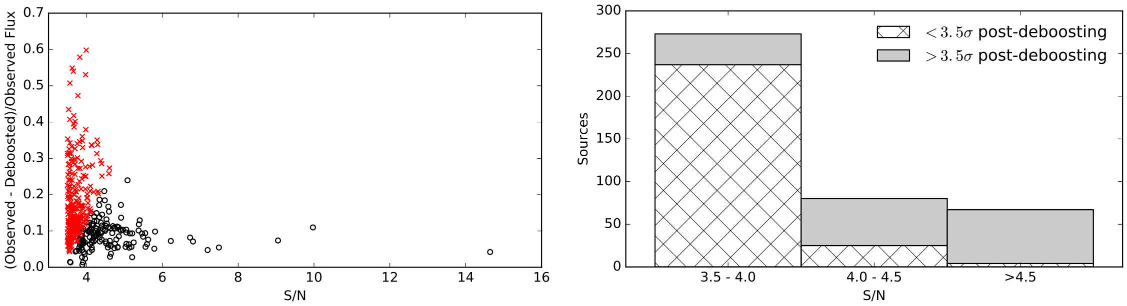

Figure 7.6: Left: the fraction of the flux lost in the deboosting as a function of observed S/N. Sources with S/N$< 3.5\sigma$ post deboosting are marked by red crosses; those with S/N$\geq 3.5\sigma$ by black circles. Right: binned source counts factored by post-deboosting S/N, binned by observed S/N. The vast majority of sources lost post-deboosting had initial S/N less than 4.

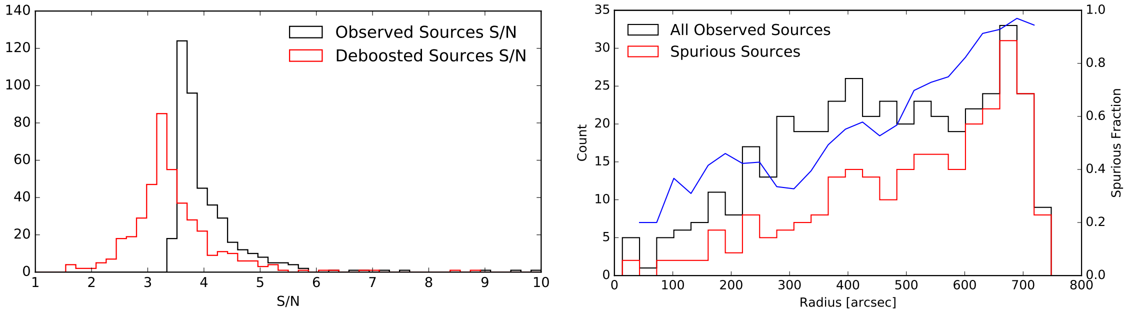

Figure 7.7: Histograms for the source catalogue before and after deboosting, S/N (left) and radius (right). Almost all of the sources pushed below the 3.5σ threshold had observed S/N< 4, and lay at the edges of the maps where the noise is greatest. In the right hand subfigure I over plot the fraction of sources with S/N< 3.5 post deboosting, which I term here spurious sources.

7.3 850 μm Overdensities

I test for overdense fields by comparing the expected field counts in expanding apertures to the observed, deboosted and completeness corrected source counts in the apertures. Any observed sources which, once deboosted, have S/N < 3.5 are not included in this analysis.

Firstly, I parameterise the radial noise profile of the field with a sixth order polynomial. A sixth-order polynomial provides an excellent fit to the noise profile over the range $0'' \leq r \leq 720''$ and avoids difficulties that arise from the radial averaging and spline extrapolation as $r \rightarrow 0''$. Then, for radii from $100''$ out to and including $700''$ in steps of $100''$ I calculate:

$$\langle N(r) \rangle = \int_0^r 2\,\pi\, r'\, \Sigma(S > 3.5\sigma(r'))\, \mathrm{d}r', \tag{7.5}$$

where $\Sigma(S > 3.5\sigma(r))$ is the number of sources per square arcsecond with flux, S, greater than 3.5 times the azimuthally averaged map noise at that radius. The cumulative number counts used to calculate $\Sigma(S > 3.5\sigma(r))$ are from an interpolated average of the sub-millimetre field counts from Scott et al. (2002), Borys et al. (2003), Coppin et al. (2006), Scott et al. (2006), Knudsen et al. (2008) and Weiß et al. (2009).

I then compare the number of completeness-corrected source counts (excluding the radio galaxy where it is detected) within radius r, $N_{\rm obs}(r)$, to the predicted field counts, $\langle N(r) \rangle$, via the standard overdensity estimator (e.g., Rigby et al., 2014):

$$\delta(r) = \frac{N_{\rm obs}(r) - \langle N(r) \rangle}{\langle N(r) \rangle}. \tag{7.6}$$

To calculate the uncertainty in $\delta(r)$ I note that both the observed counts within r and the predicted field counts within r are Poisson variables. Therefore their standard deviations are $\sqrt{N_{\rm obs}(r)}$ and $\sqrt{\langle N(r)\rangle}$ for the observed and background counts, respectively, and propagating errors gives for the uncertainty in δ:

$$\Delta\delta = \sqrt{\frac{N_{\rm obs}}{\langle N\rangle^2}\left(1+\frac{N_{\rm obs}}{\langle N\rangle}\right)}. \tag{7.7}$$

There is an important distinction between the uncertainty on δ and the significance level of any given δ. Equation 7.7 provides the uncertainty on a measured δ due to the natural uncertainty in any Poisson process. However, an overdensity cannot be considered significant simply because $\delta > 0$ within the uncertainty in δ, since due to Poisson noise large δ's are statistically expected to be common when the mean field counts are small.

The $1\,\sigma$ and $3\,\sigma$ significance levels for an overdensity with respect to the field counts are calculated by using the Poisson distribution with mean equal to $\langle N(r)\rangle$ to find the number of counts inconsistent with the mean sky counts at confidence levels of 0.8413 and 0.9987 respectively. The δ corresponding to these counts is then calculated and plotted alongside the observations.

The radial overdensity profiles for each field are shown in in Figure 7.8, and in Figure 7.9 I plot the total overdensities within the fields (i.e., $\delta(r = 700'')$) and within 6 Mpc as functions of redshift, as well as binned into redshift bins. No fields are found to be overdense at the 0.9987 confidence level. 4C +23.56, TN J0121+1320 and LBDS 53W091 all show overdensities between the 0.8413 and 0.9987 confidence levels, however even these are consistent with no overdensity within the uncertainties on the δ's themselves. The current analysis is hampered by the Poisson noise in the central regions, which leads to very large uncertainties on δ. Deeper observations would increase the expected number counts and potentially the observed counts, greatly reducing the Poisson noise on the δ's.

Interestingly, there is a correspondence between the overdensity and the radial profile. I.e., fields which have signs of overdensities tend to have a negative gradient, whereas those that are underdense generally show positive gradients. The gradients are especially useful here, where I lack redshift information on the putative SMGs: the overdensity, δ, can be biased by SMGs within the observed cone but at different redshifts, potentially introducing a systematic bias to all of the recorded δ's. The gradient however is at worst diluted by unassociated line-of-sight galaxies, and any difference in the effect between HzRG fields is a second order effect, unlike the first order offset in δ.

Plots of the total overdensities in the fields as a function of redshift (Figure 7.9) show a very weak trend of decreasing overdensity with increasing redshift. For overdensities calculated out to $r = 700''$ a weighted linear fit gives $\delta = (-0.17 \pm 0.09)z + (0.39 \pm 0.31)$. With the δ's averaged in redshift bins the fit falls slightly to $\delta = -0.12z + 0.29$, although due to only having four points the uncertainties on these coefficients are unconstrained. Given the possibility of field sampling at large radii biasing the results I also plot the total overdensities within comoving projected radii of 6 Mpc at the redshift of the HzRG. This gives weighted linear fits of $\delta = (-0.20\pm0.10)z+(0.4\pm0.4)$ and $\delta = -0.20z + 0.46$ for the unbinned and binned respectively, broadly consistent with the $700''$ fits.

While the question of whether or not the fields are overdense depends upon the chosen number counts, the trend with redshift, at least to first order, does not. This suggests that the uncertainties for the intercepts quoted above are likely underestimates of the true uncertainties. The signs of evolution with redshift are very weak but are consistently seen at the $2\,\sigma$ level irrespective of the chosen cutoff of $700''$ or 6 Mpc. In particular, TN J0121+1320 is by far the densest HzRG field and is the only galaxy more than 1σ from the best fit line, and may be pulling up the high-z end of the $\delta - z$ relation. Either way, the observations here are not sensitive enough to place tight constraints on the evolution one way or the other.

In Figure 7.10 I plot the radial overdensity profiles averaged together by redshift band, both as a function of comoving radial distance and angular radius. While the uncertainties are still too large for any firm conclusions, there is a striking redshift evolution, with clearly underdense HzRG fields at $z \sim 4.5$ evolving towards flat, neither overdense nor underdense fields at $z \sim 3.5$ and

$z \sim 2.5$, before becoming overdense within ~ 7.5 Mpc at $z = 1.55$. I repeat that the uncertainties on these points are too large for this to be a firm conclusion, and they are highly susceptible to stochastic variation in the single low redshift band, but they clearly call for further investigation.

Finally, I investigate whether the counts in the HzRG fields, as a population, are consistent with the expected counts using the exact two-tailed Poisson test in the statistical programming language, R. Out to $700''$ in the 14 fields I detect 209 completeness corrected, flux deboosted sources, compared to a predicted 225. These values are completely consistent with each other, and give a ratio with 95% confidence interval errors on the HzRG/field ratio of $\Sigma / \langle\Sigma\rangle = 0.93^{+0.20}_{-0.16}$. Repeating this analysis limited to 6 Mpc comoving radius gives 29 and 36 counts observed and predicted, respectively, again finding the HzRG fields to be consistent with the literature field number counts and giving $\Sigma / \langle\Sigma\rangle = 0.81^{+0.55}_{-0.33}$, i.e., once again consistent with no overdensity or underdensity within 6 Mpc comoving radius as a population.

7.3.1 Correlations

I plot in Figure 7.11 a range of potential correlations. I define the overdensity gradient, G, as the weighted linear fit to the radial overdensity profiles in Figure 7.8. I find a weak correlation between the overdensity gradient, G, and redshift with $G = (0.0006 \pm 0.0003)z - (0.0015 \pm 0.0012)$, Spearman's $r = 0.42$, $p = 0.13$. There is however a more significant correlation between G and the 500 MHz (rest frame) HzRG luminosity ($G = (0.0013 \pm 0.0006) \log_{10}(L_{500\,\mathrm{MHz}}) - (0.038 \pm 0.017)$, Spearman's $r = 0.61$, $p = 0.02$).

Since the radio luminosity and redshift are also correlated there is some concern that the apparent correlation between G and radio luminosity is due to their mutual dependence on z, or vice versa (an issue identified by Mayo et al., 2012, when considering potential correlations between 24 μm source densities). A partial rank correlation test finds a correlation between G and $L_{500\,\mathrm{MHz}}$ while excluding the effects of redshift of $r_{\mathrm{G,L;z}} = 0.38$. However, an MC permutation analysis suggests a significance of only $p \sim 0.1$, so when accounting for the effects of redshift the correlation between G and $L_{500\,\mathrm{MHz}}$ is not statistically significant.

For completeness' sake I note that I find no correlation between HzRG stellar mass and either G or δ. The interested reader may find the plots in Figure 7.12.

While $\delta(r = 700'')$ and G are essentially uncorrelated, there is a weak negative correlation between $\delta(r = 6\,\mathrm{Mpc})$ and G (not shown), implying that the non-correlation may be due to the washing out of the (over)underdensity signal in overly large apertures.

The single $z = 1.5$ HzRG, LBDS 53W091, is significantly fainter in the radio than the other HzRGs, and as such there may be concern that it is having a significant effect on the linear fits and correlations. For the plots using δ this is not the case, as the large uncertainty on δ in LBDS 53W091 gives it little weight in the weighted linear fits. However, the G for LBDS 53W091 is far better constrained, and so may be of concern. I therefore repeated the weighted fit of $G - \log_{10}(L_{500\,\mathrm{MHz}})$ excluding LBDS 53W091. I found that the slope and intercept are barely affected, but that their uncertainties are both increased by 33%[6]. I therefore do not believe that LBDS 53W091 is biasing the results.

7.4 Discussion

As was discussed by Rigby et al. (2014), the gas and galaxies found within 5 Mpc of cluster cores in the local universe likely originated at radii ~ 20 Mpc at $z \sim 3$. The observations presented in this paper have allowed us to sample comoving radii of this magnitude out to $z = 4.5$. I find galaxy overdensities comparable to those found by Rigby et al. (2014), i.e., very weak signs of potential overdensities, but few that are statistically significant, and I find a similar trend in overdensity with redshift. However, the observations suffer from the lack of 450 μm detections, denying us the photometric redshifts necessary to distinguish between SMGs associated with the HzRG and those coincidentally lying along the line of sight.

Of six HzRG fields at $z < 3$ only one shows no sources within 6 Mpc comoving radius, while of the eight fields at $z > 3$ four show no sources within 6 Mpc comoving radius, potentially suggesting

---

[6] Specifically the fit, excluding LBDS 53W091 is $G = (0.0013 \pm 0.0008) \log_{10}(L_{500\,\mathrm{MHz}}) - (0.038 \pm 0.023)$.

a decrease in star formation at higher redshifts. On the other hand, the most overdense field as measured within 6 Mpc of all 14 fields is TN J0121+1320 at $z = 3.52$. Similarly, the linear regressions, Pearson tests and Spearman rank tests show signs of an evolution in SMG densities around HzRGs over cosmic time, but are not statistically significant.

The most significant relationship I find is between the the radial overdensity gradient and the 500 MHz luminosity, although given the number of correlations investigated and the Spearman rank correlation significance of only $p = 0.05$ this is not statistically significant. Nevertheless, it is consistent with an evolutionary model where as SMGs fall into proto-clusters they begin to cut off or heat up the cold gas streams feeding the radio activity of the HzRG. In this framework the (weaker) correlation between redshift and the radial overdensity gradient, G, is due to the correlations between z and the radio luminosity and the radio luminosity and G. The trend should be compared to the left hand plot in Figure 6 of Rigby et al. (2014), where there is a weak trend of increasing overdensity within 6 Mpc comoving radius with increasing 500 MHz luminosity, the *opposite* trend to what I find.

7.4.1 Star-Formation-Rate Sensitivity

An exceptionally useful property of the SCUBA-2 850 μm band is over the range $1 < z < 5$ it has an almost constant limiting SFR for a given flux limit (e.g., Figure 2 in Drouart et al., 2014). Following Yun & Carilli (2002), in Figure 7.13 I plot the SFR corresponding to the 3.5 σ flux levels at the centres of the 14 HzRG fields for both SCUBA-2 bands and for dust temperatures of 40 K and 60 K.

Our 850 μm observations are sensitive, at the centres of the fields, to SFRs $\gtrsim 1000\,M_{\odot}\,\mathrm{yr}^{-1}$ with negligible variation due to redshift. The 450 μm data are not only less sensitive to SFR but their sensitivity decreases with increasing redshift. It is therefore perhaps unsurprising that I find no significant 450 μm detections corresponding to the 850 μm detections, with the necessary SFRs by $z = 2.5$ rising to $\sim 10,000\,M_{\odot}\,\mathrm{yr}^{-1}$. As a guide, Barger et al. (2014) found that over the range $1.5 < z < 5$ the SFR could be approximated (to within a factor of a few) by the relation:

$$SFR = 200 \times S_{850\,\mu\mathrm{m}}, \tag{7.8}$$

where SFR is in $M_{\odot}\,\mathrm{yr}^{-1}$ and $S_{850\,\mu\mathrm{m}}$ is the observed 850 μm flux in mJy. For the flux limit of ~ 6 mJy this gives $\sim 1200\,M_{\odot}\,\mathrm{yr}^{-1}$, consistent with the values in Figure 7.13.

A persistent problem with single dish sub-millimetre observations is the potential for source blending within the large beam. Karim et al. (2013) have argued, on the basis of high resolution Atacama Large Millimetre Array (ALMA) data, that any sources with SFRs$\gtrsim 1000\,M_{\odot}\,\mathrm{yr}^{-1}$ in single dish observations are in fact multiple confused sources within the beam. However, the most luminous galaxies found in the GOODS-N field by Barger et al. (2014) reached SFRs $\sim 6000\,M_{\odot}\,\mathrm{yr}^{-1}$, and these were confirmed as single sources by combining data from SCUBA-2 and the Karl G. Jansky Very Large Array (JVLA). Without followup interferometric imaging I cannot be certain, but the HzRG fields show no signs of extended emission beyond point sources. The only exceptions are TN J0121+1320 and USS 1558−003: in the former the CLEAN algorithm already separates the slightly extended emission into two sources (one of which is removed by the flux deboosing), in the latter the extended emission is believed to be due to a Hubble Guide Star.

7.4.2 Comparison with the Literature

One of the HzRGs, TN J2007−1316, was studied by Rigby et al. (2014) with SPIRE, looking for 500 μm overdensities. Their overdensity measure is equivalent to ours, and they found $\delta(r = 6\,\mathrm{Mpc}) = -0.79^{+0.45}_{-0.21}$, consistent with the values of $\delta(r = 700'') = -0.25 \pm 0.21$ and $\delta(r = 6\,\mathrm{Mpc}) \geq -1$. Without deboosting I find $\delta(r = 700'') = +0.7 \pm 0.4$, significantly inconsistent with Rigby et al. (2014), although note that the undeboosted is still $\delta(r = 6\,\mathrm{Mpc}) = -1$.

One of the motivations for this work was to expand upon the sensitive but small field of view SCUBA observations of Ivison et al. (2000) and Stevens et al. (2003). It is therefore worthwhile comparing their observations with the sensitivity and completeness of the current observations. The companion SMGs seen in five of the HzRG fields of Stevens et al. (2003) are compared to the most sensitive of the fields (3C 257) and the completeness of the observations at their flux and the deepest (central) region of the 3C357 field. This produces expected counts compared to the Stevens et al. (2003) counts of: 2.2/3, 0.2/1, 1.0/2, 1.7/3 and 0.5/1. In other words, I would only expect to detect approximately the brightest half of the SMGs seen by Stevens et al. (2003). The multi-wavelength analysis of the quasi-stellar object (QSO) RX J0941 by Carrera et al. (2011) found three sub-millimetre sources within $2'$ of the QSO, distinguishing it as a highly star forming group. However, of these three sources only the QSO itself would be detectable in the current data, highlighting that the data are sensitive to only the most star forming galaxies.

Many of the HzRG fields were studied by Mayo et al. (2012) at $24\,\mu$m with MIPS on Spitzer, and also with Spitzer but in the shorter wavelength IRAC bands by Galametz et al. (2012). These studies found that, in general, the $1'$ (IRAC) and $1.75'$ (MIPS) radius cells around the HzRGs were slightly overdense with respect to the Spitzer Wide-area InfraRed Extragalactic Survey (SWIRE, Lonsdale et al., 2003). Of the HzRGs in the study only 4C +23.56 was found to be overdense, with 17 counts in MIPS and 21 in IRAC. Conversely, TN J0121+1320 was found to be one of the least dense fields in MIPS (although still consistent with the SWIRE field counts), whereas in the current work it appears to be one of the most dense fields (see Figure 7.8). That the counts show differing trends is in no way surprising. The MIPS and IRAC observations sample vastly different size regions, different SFRs and have different redshift dependences to the SCUBA-2 data. The SFRs of galaxies detected in the $850\,\mu$m SCUBA-2 data are insensitive to redshift: Figure 7.13. MIPS and IRAC however are extremely strong affected by redshift as well as potential AGN contamination (Drouart et al., 2014). TN J0121+1320 lies at $z = 3.52$, where MIPS sensitivity to SFR is almost an order of magnitude less than at $z = 2$ (e.g., Drouart et al., 2014, Figure 2, right). Furthermore, the far greater sensitivity of the space telescope observations allows them to sample much lower SFRs at low redshift than the current observations, which detect only the most star-forming galaxies.

The putative overdensity around 4C +23.56 in MIPS of 17 counts was reported in Mayo et al. (2012) as $4.7\,\sigma$, based on the mean and standard deviation of a Gaussian fit to the lower half of the SWIRE field counts. Unfortunately, this method significantly overestimates the significance of the overdensity, and the true significance is only 3.8σ. Fitting the lower half of a Poisson process (the number of counts in a cell) with a Gaussian will systematically understimate the true mean by ~ 0.7 counts over the range of true source rate per cell $3 < \Sigma < 10$. Secondly, the Poisson distribution with mean < 10 is noticeably skewed to higher values: the excess of counts in the SWIRE fields over the Gaussian fit for counts greater than 6 per cell is not a sign of clustering. Rather, it is an entirely reproducible effect of fitting the lower half of a histogram of 10,000 samples drawn from a Poisson distribution with a mean of ~ 6. This gives a Gaussian fit with mean 5.2 and standard deviation ~ 2, with some variation at the 0.1 level depending upon the random seed, but consistent with that found by Mayo et al. (2012) (5.28 and 2.52 respectively). The combination of these two effects means that the Poisson equivalent $3\,\sigma$ level (i.e., confidence level of 0.9987) for the SWIRE fields is 15 counts, not 12.84, and almost all of the fields found to be statistically overdense by Mayo et al. (2012) are in fact, not, at least when assessed individually. The overdensity analysis in Galametz et al. (2012) suffers similarly. However, the a one-tailed test for the difference of two Poisson means suggests that the MIPS HzRG fields, considered as a single population, are approximately twice as dense as the SWIRE fields (95% confidence interval $0.0 < \frac{\langle\Sigma_{\rm SWIRE}\rangle}{\Sigma_{\rm HzRG}} < 0.56$) with a p value $< 2\times10^{-16}$ ($> 8\,\sigma$) firmly rejecting the null hypothesis that they have the same source surface density as the SWIRE fields: an important result that was not included in their analysis. Similarly, in Galametz et al. (2012) the same analysis shows the IRAC HzRG fields between $1.5 < z < 3$ to be overdense as a population at the $5.9\,\sigma$ level, with 95% confidence interval $0.0 < \frac{\langle\Sigma_{\rm SWIRE}\rangle}{\Sigma_{\rm HzRG}} < 0.83$. This issue highlights the dangers for describing small number Poisson processes with Gaussian statistics, which are only applicable when the mean of the Poisson distribution is large (> 20).

It is also extremely important to note the different field sizes of the observations. Only five of the fields (TN J0205+2242, TN J0121+1320, 4C +23.56, TXS 0211−122 and TN J1338−1942) have a single detection within $1.75'$ (the size of the MIPS cells) of the HzRG (excluding the HzRG itself), and none have more than one. However, given the much lower sensitivity of the present observations this is again, unsurprising: the detection of multiple galaxies with SFR$>1200\,M_{\odot}\,\mathrm{yr}^{-1}$ within a $1.75'$ radius would be exceptional, even in putative proto-clusters.

Drouart et al. (2014) combined *Herschel* observations from $70\,\mu$m through to $500\,\mu$m with literature measurements from $12\,\mu$m to $870\,\mu$m (observed frame) to model the SEDs of the HeRGÉ sample from $8-1000\,\mu$m (rest frame). The HzRGs in this study with $850-870\,\mu$m detections (as opposed to upper limits) in the collected data in Drouart et al. (2014), from their own observations and those of Archibald et al. (2001) and Reuland et al. (2004), are TN J0121+1320, B2 0902 + 34 and 3C 257; TN J1338−1942, TN J2007−1316, 8C 1435+635 and MG J214405+1929. Of these only TN J0121+1320 and 3C 257 are clearly detected in the current observations. The non-detection of B2 0902 + 34 is expected, given its flux of 2.8 ± 1.0 mJy. TN J2007−1316 has a flux of 5.8 ± 1.5 mJy and as such should be marginally detected. That it is not is not of great concern, as the corresponding completeness of the field at the central noise level and 6 mJy is only ~ 0.5. Furthermore, the $3\,\sigma$ upper limit on the flux of TN J2007−1316 considering the flux detected at the corresponding coordinates is 6.4 mJy, consistent with Drouart et al. (2014). The same is true of MG J214405+1929 where the expected flux was 2.3 ± 0.9 mJy. TN J1338 − 1942 was observed to have a flux 6.9 ± 1.1 mJy. I find a marginal detection of 5.1 mJy, but the noise in this map is slightly higher than the representative level, giving a $3.5\,\sigma$ level of 7.5 mJy, so once again a non-detection is not unexpected. 8C 1435+635 is marginally detected with a flux of 8.9 ± 2.2 mJy cf 7.8 ± 0.8 mJy in the literature. It was however deboosted down to 7.8 mJy be the Bayesian flux deboosting corresponding to a S/N of 3.49, placing it just below the significance cutoff. However, the fact that the deboosting places the flux closer to the literature value is a reassuring validation of the data reduction. Similarly, I find a deboosted flux for 3C 257 of 7.8 ± 1.7 mJy deboosted from 8.3 mJy cf 5.4 ± 1.0 mJy and for TN J0121+1320 I find 7.8 ± 2.0 mJy deboosted from 8.4 mJy cf 7.5 ± 1.0 mJy in the literature (Reuland et al., 2004).

7.5 Conclusions

In this chapter I have presented JCMT/SCUBA-2 observations of 14 HzRG fields with radius $720''$ over the redshift range $1.5<z<4.5$ at $850\,\mu$m and $450\,\mu$m with representative $3.5\,\sigma$ sensitivities of 6 mJy and 70 mJy respectively. Of 420 sources initially identified at $>3.5\,\sigma$ in the $850\,\mu$m maps, 154 were identified as robust detections follow a Monte Carlo Bayesian flux deboosting analysis. The overdensity around the HzRGs was assessed out to radii $700''$ and 6 Mpc (comoving), and the radial overdensity profiles were averaged by redshift bin. I have found no statistically significant overdensity in any field, although two of the fields present weak ($1\,\sigma$) signs of overdensities. The analysis is significantly hampered by the low sensitivity of the maps which, due to the paucity of sources, makes Poisson noise highly significant. Analysing the HzRG fields as a single population also shows no signs of overdensity at the SFR limits probed, with very weak signs of a potential underdensity within 6 Mpc comoving radius.

I find that radial overdensity gradients may be correlated with 500 MHz luminosity and redshift, and that this correlation is much more significant than for the total overdensities out to $700''$ or 6 Mpc comoving. This is promising, as the radial gradients are less affected by foreground contamination than the total overdensity measures. However, a partial rank correlation, which excludes the effect of the correlation between 500 MHz luminosity and redshift, finds that while the correlation between the radial overdensity gradients and 500 MHz luminosity is not statistically significant, with a correlation $r_{\mathrm{G,L;z}}=0.38$ and $p=0.1$. Observations of more fields and to a deeper rms noise level are key to confirming or excluding this relation.

The redshift-band-averaged radial overdensity profiles also show tantalising signs of evolution in both the total overdensity and the radial profile over the redshift range $1.5<z<4.5$, although the trends seen are not statistically significant. This trend is consistent with the correlations found between the radial overdensity gradient and both redshfit and 500 MHz luminosity.

Redshift-band averaging the HzRG field densities gives highly tentative signs of underdensities at $z>4$, broadly consistent with the decreasing SMG traced SFR density at $z>4$ in the GOODS-N field seen by Barger et al. (2014) for galaxies with SFR$>500\,M_{\odot}\,\mathrm{yr}^{-1}$. This may imply that the tend towards underdensity in the high-z fields is due to a global decrease in star formation and not directly a redshift related evolution of HzRG proto-cluster overdensities.

The analysis in this paper has been greatly hindered by the small number of fields, the lack of blank survey fields with the same observing pattern and sensitivity, and the low sensitivity of the observations. More observations would alleviate all of these issues, although this would require many hours of observing time, possibly even reaching the level of a large observing programme.

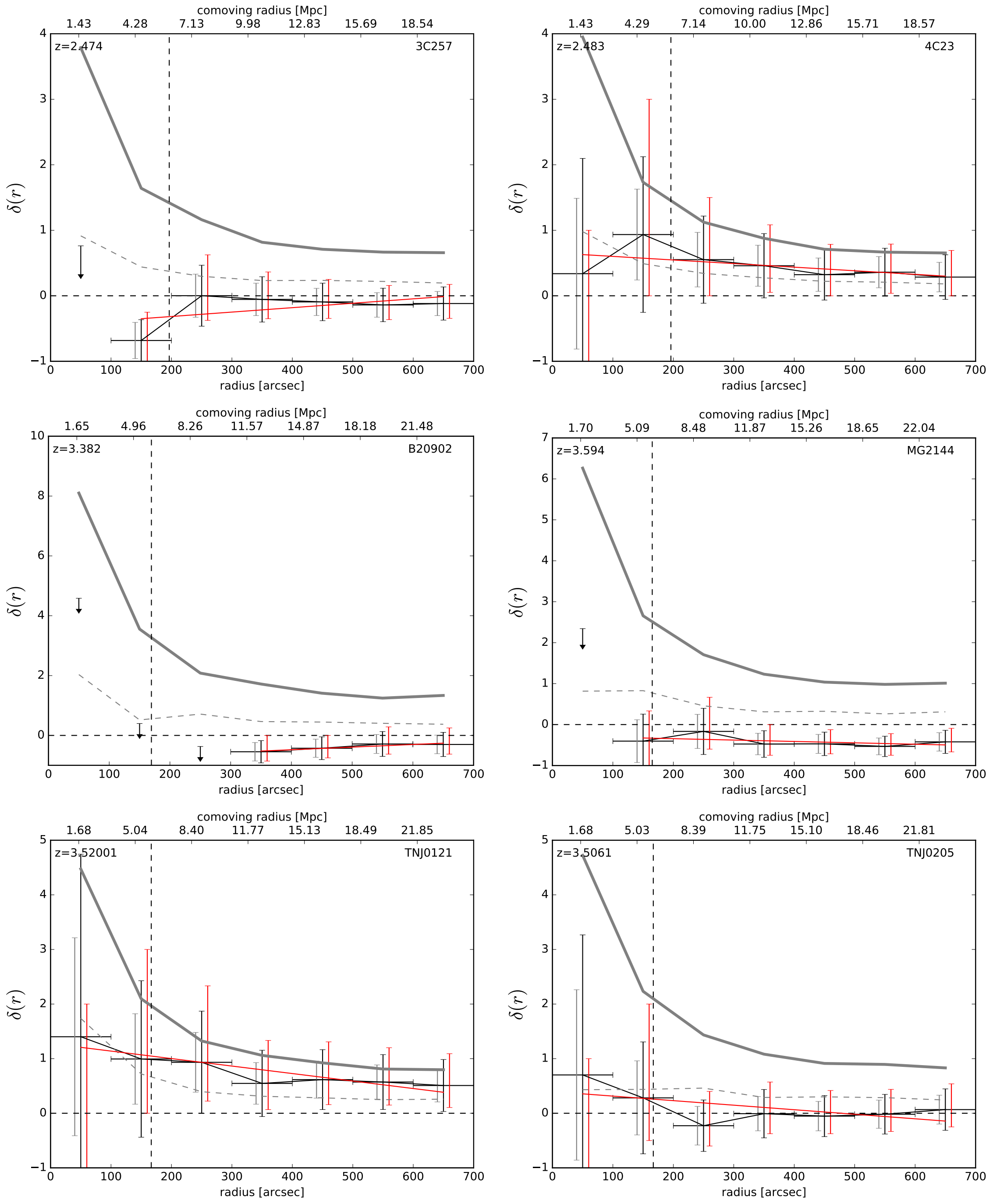

Figure 7.8: Radial overdensities for the individual fields, calculated for increasingly large apertures and with field counts calculated using averaged literature source counts and correcting for flux boosting and completeness. The comoving transverse radii of 6 Mpc at the HzRG redshift is marked by the vertical dashed line. The solid red line shows the weighted linear fit to the overdensity profile. Monte Carlo $\pm 1\,\sigma$ uncertainties are shown by the right offset red errorbars, and uncertainties assuming no Poisson noise in the background counts are shown by the left offset grey errorbars. The solid grey and dashed grey lines indicate the δ corresponding to overdensities at confidence levels of 0.9987 and 0.8413 respectively.

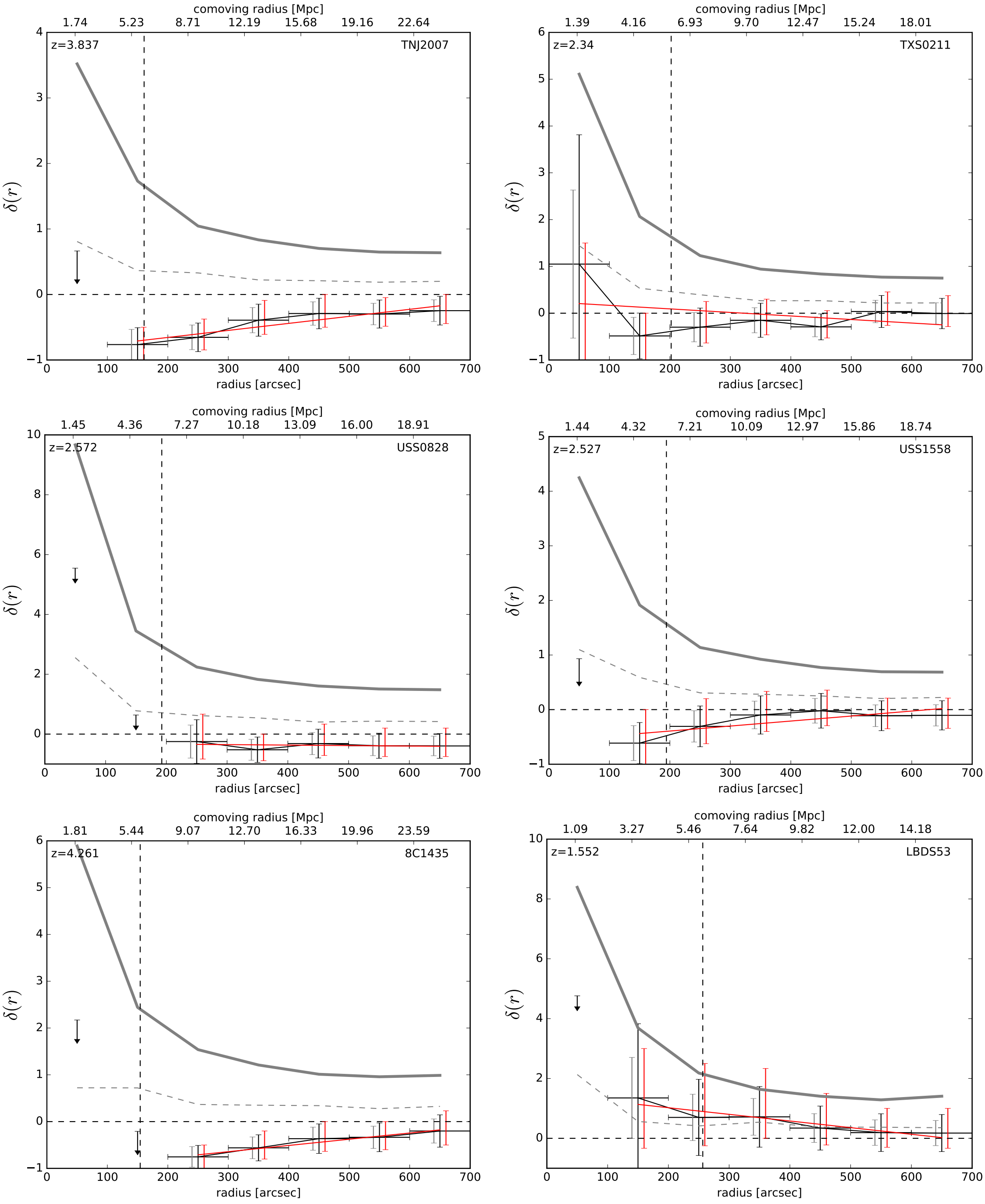

Figure 7.8 (continued)

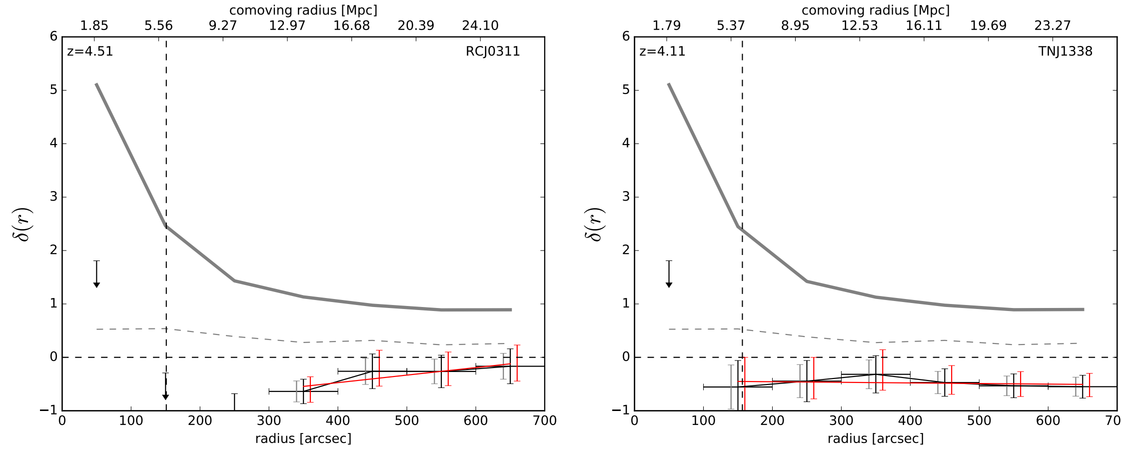

Figure 7.8 (continued)

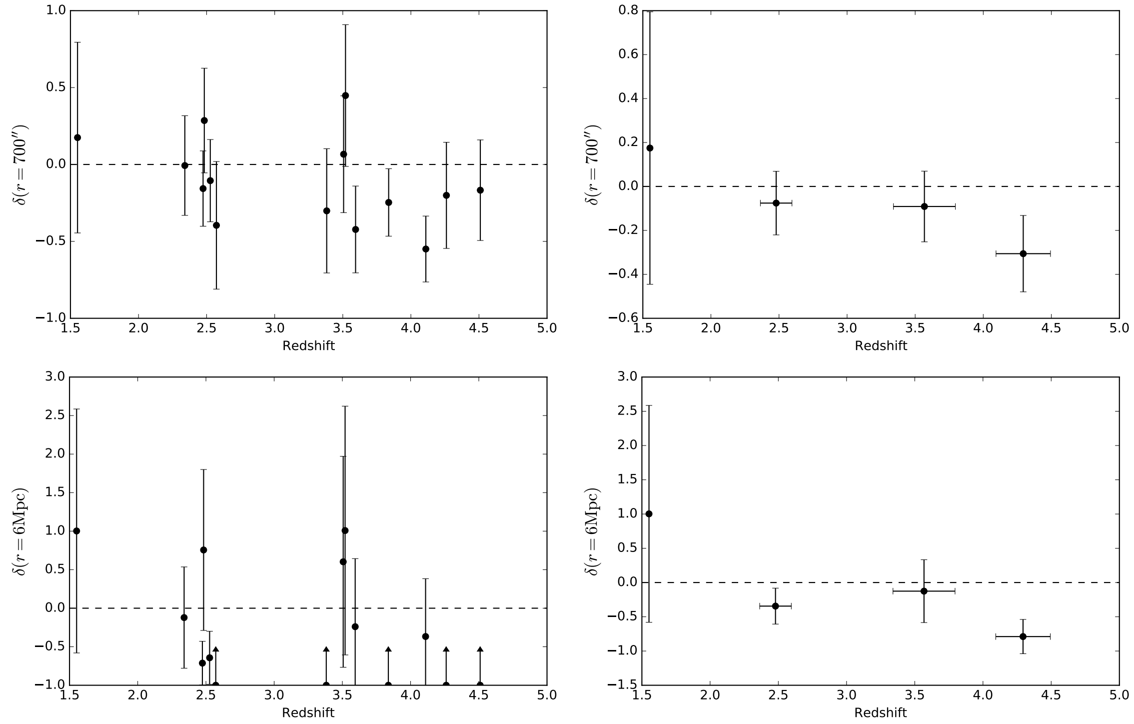

Figure 7.9: Field overdensities as a function of redshift. Top left: the overdensities for each field calculated at $r = 700''$, a weighted linear fit gives $\delta = (-0.17 \pm 0.09)z + (0.39 \pm 0.31)$. Top right: the overdensities binned by redshift calculated at $r = 700''$. Bottom left: the overdensities of the fields calculated at comoving $r = 6\,\mathrm{Mpc}$ at the redshift of the central radio galaxy, a weighted linear fit to the fields with SMGs detected within 6 Mpc (comoving) gives $\delta = (0.1 \pm 0.3)z - (0.8 \pm 0.8)$ while an unweighted fit to all of the fields gives $\delta = (-0.4 \pm 0.3)z + (1.0 \pm 1.0)$. Bottom right: the overdensities binned by redshift calculated at $r = 6\,\mathrm{Mpc}$ at the redshift of the central radio galaxy. The dashed lines guide the eye to the zero level.

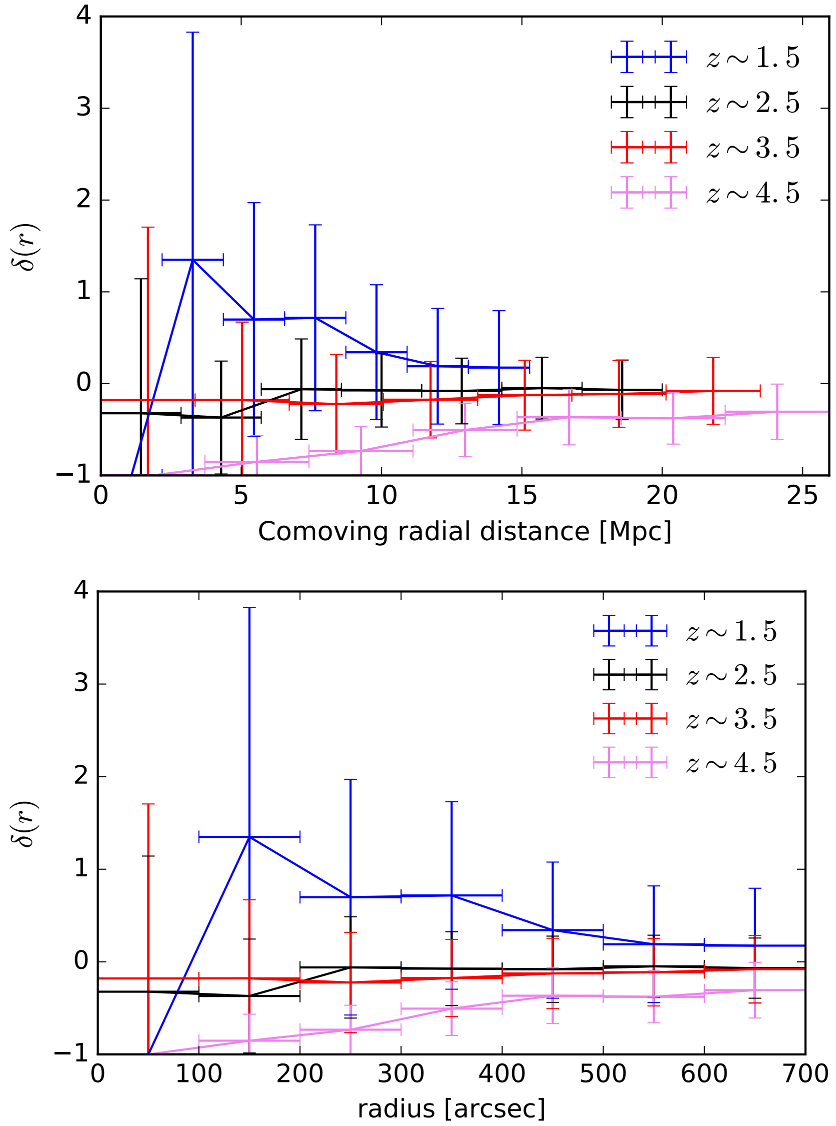

Figure 7.10: Redshift-band-averaged radial overdensity plots as functions of comoving radial distance (left) and angle (right). While the uncertainties on the bins are still too large for any firm conclusions there is a clear trend towards greater and more central overdensity as the redshift decreases, consistent with the infall of galaxies towards HzRGs as clusters form.

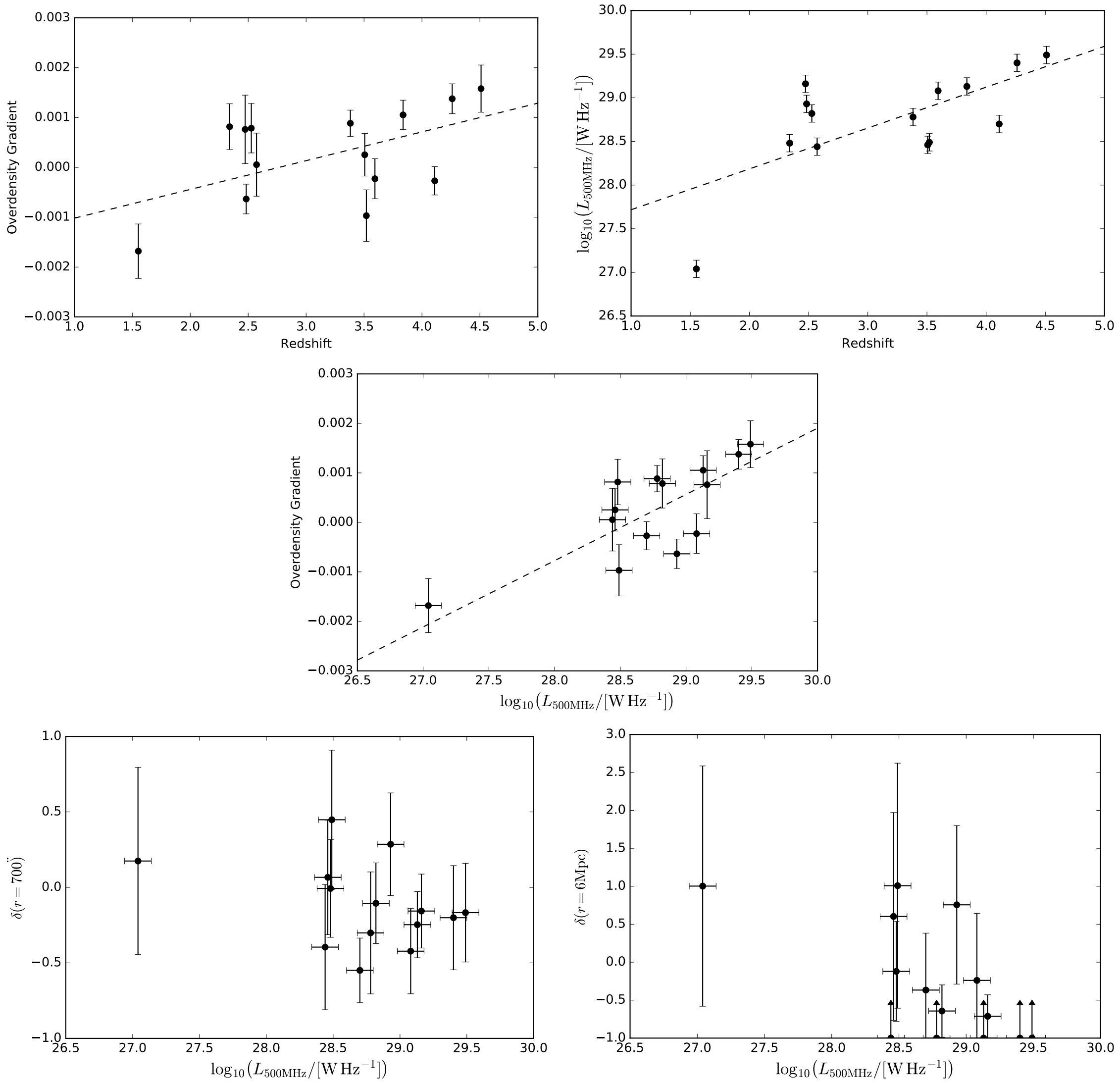

Figure 7.11: Correlation plots for the gradient of the radial overdensity profiles shown in Figure 7.8. Top left: gradient vs HzRG redshift. Top right: HzRG 500 MHz luminosity vs redshift. Middle: gradient vs the HzRG 500 MHz luminosity. Bottom left: $\delta(r = 700'')$ vs the HzRG 500 MHz luminosity. Bottom right: $\delta(r = 6\,\mathrm{Mpc})$ vs the HzRG 500 MHz luminosity. The weighted linear fits are shown by a dashed line.

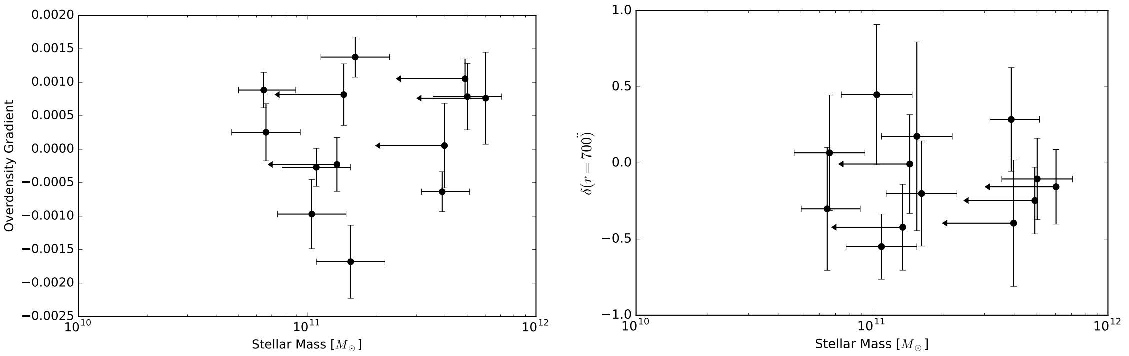

Figure 7.12: The overdensity gradients and total overdensities as functions of the HzRG stellar mass. While no trends are apparent it is impossible to make any firm conclusions given that almost all of the masses are upper limits only.

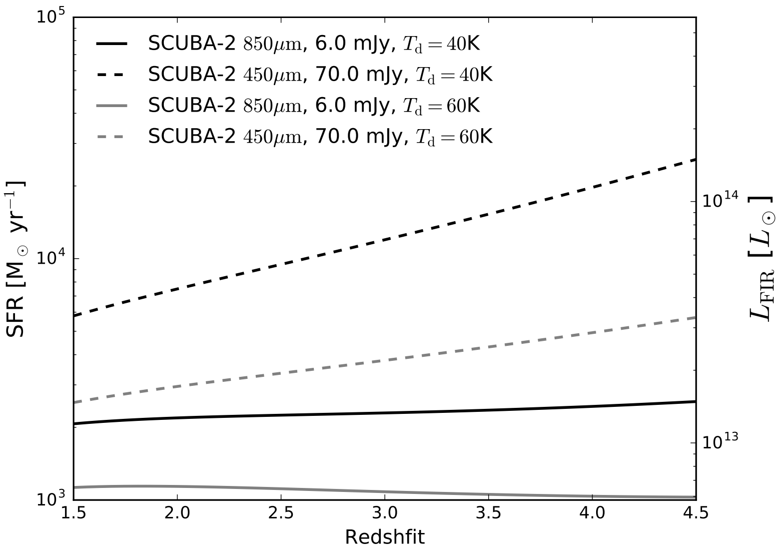

Figure 7.13: The SFR corresponding to the $3.5\,\sigma$ flux limits in the SCUBA-2 $850\,\mu$m and $450\,\mu$m bands over the range $1.5 \leq z \leq 4.5$, assuming dust temperatures $T_\mathrm{d} = 40\,$K and $T_\mathrm{d} = 60\,$K, and a dust emissivity index $\beta = 1.5$. The corresponding L_FIR is also shown. The $850\,\mu$m observations sample almost identical SFR limits over the redshift range of the observations.

Chapter 8

Conclusions and Further Work

"I am not young enough to know everything."

Oscar Wilde

8.1 Summary of Work

In this thesis I have made extensive use of LVG models to explore the molecular gas within two exceptional local galaxies. I have introduced a new MCMC wrapper for RADEX, tested the code and characterised the precision and accuracy of LVG models in general. The effect of the CMB on molecular line emission and on molecular line luminosity relations was also examined. Finally, I presented a novel analysis of SCUBA-2 observations of the potential high$-z$ equivalents of these galaxies.

In Chapter 2, alongside an overview of the theory of radiative transfer, I introduced the MCMC script I developed to interface with the public non-LTE radiative transfer code RADEX. This script allows for exploration of more complex phase spaces than are possible with grid methods alone, while naturally integrating Bayesian priors and producing posterior probability densities. While of limited use when few molecular transitions are available, this code has significant potential for future use with the wealth of molecular lines being, and soon to be, observed with ALMA and other 'next-generation' millimetre and sub-millimetre observatories. The MCMC code was tested against the 2D Rosenbrock function, a typical optimisation test function, and found to perform well.

Chapter 3 presented a series of tests designed to assess the accuracy and precision with which LVG model parameters can be recovered under ideal, and slightly less than ideal, conditions. This analysis demonstrated the inherent limitations of LVG codes due to the slow variation in line ratios with changing physical conditions and the inherent uncertainties in millimetre and sub-millimetre flux calibrations. The chapter also provided an opportunity to assess the performance of the MCMC-LVG code, which was found to perform well compared to traditional grid-based approaches. The chapter concluded with an exploration of the effects of the CMB on CO and HCN emission over the redshift range $0 < z < 8$, including both single line of sight analyses and toy models of integrated galaxy emission. This exploration highlighted the significant challenges faced when observing at high-z.

Chapter 4 examined the potential redshift effects on the Gao-Solomon relation, in particular investigating whether the CMB can account for the apparent HCN deficit seen at $z > 2$. A detailed analysis, including accounting for potential effects on the dust emission, found that while there may be an effect, it is unlikely to be sufficiently significant to account for the observed offset, although this is highly dependent upon the temperature and density of the HCN emitting gas. A toy model analogue of NGC 1068 was almost completely unaffected by redshift in either HCN or

CO, although a cool, diffuse CO reservoir observable at low redshift rapidly becomes lost against the hotter CMB.

Chapter 5 presented the case study of NGC 6240, a ULIRG and major merger with an extensive list of molecular line observations available in the literature. These were combined with new $H^{13}CN$ and $H^{13}CO^+$ observations from the PdBI and the MCMC-LVG code to model the dense molecular gas. I found striking evidence for cold, dense and turbulent clumps of gas condensing out of a much hotter and diffuse CO traced disk. While generally inconsistent with the view of HCN as a tracer of hot ($\sim 100\,\mathrm{K}$), dense molecular gas tracing new star formation this result was consistent with the extraordinary nature of this source, which presents an extremely shocked CO SLED and within which much of the molecular gas lies in a disk between the merger nuclei. This study highlighted some of the challenges associated with interpreting future observations of extreme galaxies at higher redshift.

In chapter 6 I used high-resolution PdBI observations of HCN, HCO^+, their ^{13}C isotopologues, and SiO to search for chemical evidence of an AGN in the western nucleus of Arp 220. The confusion of the two merger nuclei within the beam of most literature observations prohibited the effective use of the MCMC-LVG code and a more traditional grid method was used, with the high-resolution data being used to guide the analysis. I found signs of outflow in the SiO, surprisingly consistent with the HCO^+ outflows seen by Sakamoto et al. (2009), which I interpreted as evidence for an outflow of shocked gas and dust. An analysis using only the high-resolution data found evidence for a chemical difference between the two nuclei, potentially consistent with an obscured AGN lying at the core of the western nucleus. Unfortunately the extreme optical depth of the western nucleus meant that even the ^{13}C isotopologue lines were optically thick, and the kinematics and excitation at the centre of the nucleus remain hidden.

Chapter 7 was a departure from the molecular-gas content of this thesis, and provided an opportunity for me to explore high-redshift analogues of the two local ULIRGs studied in chapters 5 and 6. Using JCMT/SCUBA-2 observations from 2012 through to 2015 I developed a novel Bayesian flux deboosting method to identify spurious sources and account for flux deboosing in the fields with steeply rising noise profiles over the outer half of the maps. Using an integral method to assess the source overdensity accounting for the lack of blank fields and for the radial noise profiles in the maps I identified tentative signs of a redshift related evolution in the radial overdensity profile. Similarly, weak correlations were found between the radial overdensity gradient and the radio flux, but the small number statistics prevented any firm conclusions. The galaxies identified are however excellent candidates for ALMA follow-up observations, as they are selected by the $850\,\mu$m flux limit to be highly star forming ($> 1200\,M_\odot\,\mathrm{yr}^{-1}$) ULIRGs, making them easily observable and offering targets to test the upper luminosity ends of low redshift molecular line relations at high redshift.

8.2 Future Work

An area which this thesis has touched upon but not thoroughly explored is the future of line identification in the ALMA era. Here, there is much to be learned from techniques employed by Milky Way observers studying complex organic molecules in pre-stellar cores. When observed with ALMA and the SMA these regions present spectra of staggering complexity, with multiple transitions of many molecules. Automated recovery in these cases relies upon assumptions of LTE and abundances, with a CLEAN-like procedure iteratively removing calculated molecular spectra. Unfortunately, in extragalactic targets the large velocity dispersions quickly lead to line blending; a problem exacerbated by bulk motions when the galaxy is unresolved. Further work towards a fully Bayesian and non-LTE recovery algorithm, potentially including models for the bulk motions of the gas, would be invaluable over the coming decades.

A significant limitation of any molecular-radiative-transfer code that calculates level populations without the assumption of LTE is the need for collisional rate coefficients. These are found from laboratory experiments, making them difficult, time consuming and expensive to obtain. They are further complicated by being temperature dependent. Nevertheless, *accurate* collisional rate coefficients are essential for accurate modelling of molecular line emission. While there has been significant theoretical effort to calculate molecular line lists, with a focus on near to mid-IR lines for study of exoplanetary atmospheres (Tennyson & Yurchenko, 2012), a similar effort focussed on molecular collisional rate coefficients is currently one of the missing pieces of the puzzle of extragalactic molecular astronomy.

Perhaps the holy grail of the field is to be able to use spatially and spectrally resolved beam-matched observations of a galaxy to accurately and precisely model the molecular-gas density, temperature and species abundances across the galaxy, the first real steps towards which were made by Viti et al. (2014). When combined with similar results from Integral Field Units (IFUs)[1] in the optical this would allow for extremely detailed modelling of the processes driving star formation in galaxies. Studies of this kind in mergers, dwarf galaxies and spirals would do much to extend the current understanding of galaxy evolution. The MCMC-LVG code introduced in this thesis is a significant step towards this goal, by allowing for trivial modelling of multiple species simultaneously. However, both observing times and computing times remain as significant challenges.

It is becoming clear that the mid-IR pumping of molecules commonly thought of as collisionally excited only, such as HCN, HCO^+ and HNC, has significant effects on the vibrational ground state emission, as well as general fluorescence effects due to the hotter CMB as we approach $z = 4 - 5$ (García-Burillo et al., 2006; Aalto et al., 2007; Yamada et al., 2007; González-Alfonso et al., 2012; Aalto et al., 2015a; Imanishi et al., 2016). More accurate studies of resolved AGN tori and shells as well as galactic scale molecular emission in high-z sources will require much more detailed modelling than has regularly been employed in the field, as well as the tools to allow such modelling.

---

[1] IFUs generate velocity cubes like those produced by radio interferometry or spectral maps.

This page was intentionally left nearly blank.

Appendix A

Appendix A: SCUBA-2 Ancillary Data

A.1 850 μm Sources

I include below the 850 μm source catalogue from chapter 7, with 850 μm fluxes before and after flux deboosting. The two sources with a negative deboosted flux and S/N are those which are completely removed by the deboosting.

Table A.1: 850 μm Source Catalogue

Field	S/N	RA [hours]	Dec [deg]	$S_{850\,\mu\text{m,obs}}$ [mJy]	$S_{850\,\mu\text{m,deb}}$ [mJy]	$\sigma_{850\,\mu\text{m}}$ [mJy]	$S_{450\,\mu\text{m}}$ [mJy]	$\sigma_{450\,\mu\text{m}}$ [mJy]
3C257	4.89	11.37756	5.4423	11.9	11.1	2.3	< 74	21
3C257	4.75	11.37880	5.3984	12.5	11.8	2.5	< 91	23
3C257	4.56	11.38638	5.4251	8.7	8.2	1.8	< 40	17
3C257	4.49	11.38595	5.5032	8.3	7.8	1.7	< 48	16
3C257	4.17	11.38412	5.4026	9.2	8.2	2.0	59	18
3C257	4.49	11.38799	5.4662	8.1	7.8	1.7	< 36	16
3C257	4.19	11.37930	5.4532	8.8	8.2	2.0	< 43	17
3C257	3.77	11.39718	5.5160	14.6	12.5	3.3	< 54	28
3C257	3.54	11.37552	5.6269	19.3	15.7	4.5	< 125	43
3C257	3.86	11.37949	5.4951	7.8	7.1	1.8	< 55	17
3C257	3.32	11.39440	5.3523	25.8	20.4	6.1	< 113	47
3C257	3.95	11.39127	5.5229	7.5	7.1	1.8	< 42	16
3C257	3.92	11.38317	5.4273	7.5	7.1	1.8	< 70	16
3C257	3.75	11.38495	5.4245	7.3	6.7	1.8	< 47	16
3C257	3.58	11.37941	5.5824	8.5	7.5	2.1	< 39	20
3C257	3.48	11.37578	5.4887	9.8	8.5	2.5	< 42	24
3C257	1.87	11.39270	5.3345	24.3	11.4	6.1	< -6	46
3C257	3.87	11.38312	5.5541	6.9	6.7	1.7	< 35	16
3C257	3.86	11.38801	5.5657	6.8	6.7	1.7	< 32	16
3C257	3.87	11.38108	5.5054	6.8	6.7	1.7	< 38	16
3C257	2.49	11.38677	5.3069	21.8	13.9	5.6	< 75	45
3C257	3.42	11.38555	5.6508	9.2	8.2	2.4	< 60	22
3C257	3.63	11.39124	5.5816	7.4	7.1	2.0	< 59	17
3C257	3.53	11.39242	5.5649	7.7	7.1	2.0	< 32	18
3C257	3.31	11.37945	5.6500	11.8	10.3	3.1	< 71	30
3C257	3.27	11.38668	5.3776	8.6	7.5	2.3	< 84	20
3C257	3.38	11.39431	5.5863	9.9	8.9	2.6	< 33	22
3C257	3.47	11.38327	5.3973	7.7	7.1	2.0	< 77	18
3C257	2.95	11.38999	5.3208	19.4	15.4	5.2	< 47	42
3C257	3.26	11.38299	5.5416	6.4	5.7	1.7	< 38	16
3C257	3.28	11.37532	5.4999	9.4	8.5	2.6	< 63	25
3C257	3.03	11.37988	5.6583	11.9	10.0	3.3	< 50	32
3C257	3.25	11.38405	5.5404	6.2	5.7	1.7	< 16	16
3C257	3.25	11.38508	5.5454	6.2	5.7	1.7	< 51	16

3C257	2.76	11.39622	5.6222	15.7	12.1	4.4	< 88	43
3C257	3.24	11.38805	5.5557	6.2	5.7	1.7	< 53	16
3C257	2.96	11.38916	5.6002	6.7	5.7	1.9	< 31	17
4C23	7.08	21.11556	23.5354	13.6	12.9	1.8	< 60	17
4C23	6.85	21.12675	23.4756	14.3	13.6	2.0	< 70	19
4C23	5.24	21.12362	23.5640	9.9	9.3	1.8	< 13	17
4C23	5.24	21.12468	23.5207	9.8	9.3	1.8	< 55	17
4C23	4.85	21.11513	23.5796	9.8	9.3	1.9	< 53	18
4C23	4.56	21.12805	23.4523	11.3	10.7	2.3	97	21
4C23	4.42	21.12633	23.4159	11.6	10.7	2.4	< 63	22
4C23	4.45	21.12199	23.5140	8.4	7.8	1.8	< 71	16
4C23	4.37	21.12800	23.4603	10.6	10.0	2.3	< 47	21
4C23	3.99	21.13009	23.5924	11.8	10.3	2.6	< 25	24
4C23	4.22	21.11916	23.5738	8.0	7.5	1.8	< 33	17
4C23	3.90	21.12761	23.5713	8.8	7.8	2.0	< 58	19
4C23	3.95	21.11943	23.3975	9.8	8.9	2.3	< 61	20
4C23	3.88	21.11360	23.4192	11.4	10.3	2.7	< 30	25
4C23	3.89	21.11386	23.5629	8.4	7.8	2.0	< 49	19
4C23	3.70	21.11723	23.4681	7.5	6.7	1.8	< 47	17
4C23	3.69	21.12077	23.3883	9.9	8.9	2.4	< 71	22
4C23	3.40	21.12151	23.6747	9.5	8.2	2.4	< 68	23
4C23	3.81	21.12045	23.5657	7.0	6.7	1.8	< 63	17
4C23	3.66	21.11232	23.5282	8.8	8.2	2.2	< 27	21
4C23	3.62	21.11890	23.5132	6.9	6.4	1.8	< 29	16
4C23	3.78	21.11938	23.4804	6.9	6.7	1.8	< 57	17
4C23	3.63	21.12646	23.5657	7.2	6.7	1.9	< 42	18
4C23	3.67	21.12321	23.4242	7.9	7.5	2.0	< 24	19
4C23	3.35	21.12220	23.7033	12.3	10.7	3.2	< 78	34
4C23	3.51	21.12616	23.5426	6.9	6.4	1.8	< 41	17
4C23	3.50	21.11295	23.5596	8.0	7.5	2.1	< 54	21
4C23	3.35	21.12740	23.4851	7.5	6.7	2.0	< 25	19
4C23	3.22	21.12970	23.4398	10.7	9.3	2.9	< 132	26
4C23	3.37	21.11393	23.6216	8.6	7.8	2.3	< 65	23
4C23	3.09	21.10972	23.5874	12.7	10.7	3.5	< 103	32
4C23	3.11	21.12529	23.6852	10.9	9.3	3.0	< 86	32
4C23	2.75	21.11056	23.6477	16.4	12.5	4.5	< 68	42
4C23	3.10	21.11324	23.5304	7.4	6.4	2.1	< 47	20
4C23	3.09	21.11339	23.5095	7.4	6.4	2.1	< 74	20
4C23	2.90	21.11840	23.3414	15.0	12.1	4.2	< 115	44
4C23	3.52	21.12520	23.5776	6.5	6.4	1.8	< 40	17
B20902	-0.14	9.08058	34.2205	56.7	-0.8	5.9	< 122	39
B20902	5.24	9.08618	34.1087	15.5	13.9	2.7	< 69	20
B20902	4.25	9.09856	34.0998	14.0	12.5	2.9	< 92	22
B20902	3.35	9.09376	33.9514	23.6	17.2	5.1	< 45	46
B20902	3.81	9.09178	34.0076	13.7	11.4	3.0	< 65	22
B20902	3.59	9.10173	34.0959	17.3	14.3	4.0	< 74	30
B20902	2.93	9.10097	33.9909	29.7	20.4	7.0	< 119	57
B20902	3.48	9.08774	33.9942	14.4	12.1	3.5	< 48	27
B20902	3.26	9.08826	34.0715	10.2	8.5	2.6	< 29	20
B20902	3.29	9.09936	34.1941	12.5	11.1	3.4	< 35	25
B20902	3.11	9.08896	34.2141	10.2	8.5	2.7	< 2	20
B20902	2.49	9.09041	33.9503	18.6	12.5	5.0	< 119	46
B20902	3.18	9.08446	34.1132	10.7	9.3	2.9	< 83	23
B20902	3.08	9.09174	34.0270	10.1	8.5	2.8	< 56	20
B20902	2.41	9.08064	34.0573	18.7	12.5	5.2	< 79	37
B20902	2.52	9.09020	33.9420	20.4	14.3	5.7	< 88	53
B20902	3.17	9.08742	34.1863	9.7	8.5	2.7	< −19	20
B20902	2.47	9.07953	34.0801	20.8	14.3	5.8	< 93	42
B20902	2.90	9.09795	34.2366	12.8	10.3	3.6	< 93	26
B20902	3.29	9.09361	34.0879	9.3	8.5	2.6	< 23	20
B20902	2.71	9.08472	34.0084	14.1	10.7	3.9	< 46	30
B20902	2.82	9.08920	33.9898	12.2	9.6	3.4	< 15	27
B20902	2.39	9.09802	33.9636	21.2	14.3	6.0	< 170	54
B20902	2.53	9.09309	33.9533	17.4	12.5	4.9	< 77	45
B20902	3.25	9.09094	34.2038	9.2	8.5	2.6	< 40	20
B20902	2.82	9.08500	34.0429	11.5	9.3	3.3	< 62	25
B20902	2.71	9.08503	34.2872	19.4	15.0	5.5	< 101	43
MG2144	4.07	21.72585	19.3888	20.7	17.2	4.2	< 138	80
MG2144	4.44	21.72736	19.4956	13.3	12.1	2.7	< 115	53
MG2144	3.89	21.73672	19.4450	9.8	8.9	2.3	< 110	42
MG2144	2.75	21.73324	19.2899	28.6	19.0	6.9	< 70	140
MG2144	3.46	21.74175	19.5748	11.6	10.0	2.9	< 73	53

MG2144	3.34	21.73724	19.6312	12.6	10.7	3.2	< 114	61
MG2144	3.52	21.73726	19.4164	9.0	8.2	2.3	< 149	43
MG2144	2.79	21.72294	19.4539	20.7	15.0	5.4	< 96	103
MG2144	3.07	21.73700	19.3538	11.9	9.6	3.1	< −32	56
MG2144	2.92	21.73361	19.6571	15.7	12.1	4.2	< 135	85
MG2144	3.08	21.72779	19.5762	11.7	9.6	3.1	< 67	62
MG2144	3.15	21.74141	19.3522	14.9	12.5	4.0	< 107	69
MG2144	3.39	21.73304	19.3797	9.9	8.9	2.6	< 134	48
MG2144	2.48	21.74410	19.3402	26.6	17.5	7.1	< 157	122
MG2144	3.27	21.73292	19.4567	8.5	7.5	2.3	< 120	42
MG2144	3.20	21.74302	19.4622	10.3	8.9	2.8	< 123	50
MG2144	2.65	21.73241	19.6718	19.5	13.9	5.3	< 217	116
MG2144	3.29	21.73567	19.6109	10.0	8.9	2.7	< 100	51
MG2144	2.60	21.73035	19.6604	19.1	13.6	5.2	< 123	111
MG2144	2.34	21.74404	19.6343	21.8	14.3	6.1	< 213	118
MG2144	2.85	21.73589	19.6515	13.8	11.1	3.9	< 214	77
MG2144	2.44	21.74760	19.5556	21.9	15.0	6.2	< 241	104
MG2144	3.19	21.72998	19.5554	9.1	8.2	2.6	< 201	48
MG2144	2.62	21.74706	19.4692	16.5	12.1	4.6	< 153	77
TNJ0121	14.03	1.36333	13.2823	30.3	29.1	2.1	< 65	13
TNJ0121	8.38	1.37061	13.3376	24.8	22.9	2.7	73	17
TNJ0121	5.77	1.35758	13.3282	12.7	11.8	2.0	< 39	13
TNJ0121	5.03	1.35788	13.3129	11.3	10.3	2.1	< 15	13
TNJ0121	4.75	1.35897	13.3399	10.9	9.6	2.0	< 38	13
TNJ0121	4.72	1.35977	13.3941	10.6	9.6	2.0	< 50	13
TNJ0121	4.45	1.36316	13.2276	12.7	11.4	2.6	< 31	15
TNJ0121	4.13	1.36034	13.5050	14.0	12.5	3.0	< 43	23
TNJ0121	4.07	1.35929	13.4602	10.0	9.3	2.3	< 49	15
TNJ0121	3.84	1.36197	13.3829	8.9	7.8	2.0	< 43	13
TNJ0121	3.82	1.36199	13.5100	13.2	11.8	3.1	< 70	24
TNJ0121	3.78	1.36416	13.2545	9.6	8.5	2.3	51	14
TNJ0121	3.91	1.36963	13.3768	10.4	9.6	2.5	< 18	15
TNJ0121	3.84	1.36598	13.3418	8.5	7.8	2.0	< 33	13
TNJ0121	3.84	1.36179	13.3499	8.4	7.8	2.0	< 36	13
TNJ0121	3.67	1.36890	13.3365	9.6	8.5	2.3	< 54	15
TNJ0121	3.66	1.36177	13.3660	8.3	7.5	2.0	< 52	13
TNJ0121	2.99	1.37402	13.3232	18.1	13.6	4.5	< 86	26
TNJ0121	2.47	1.36855	13.1861	24.8	15.4	6.2	< −8	37
TNJ0121	3.50	1.36731	13.4516	9.9	8.9	2.5	< 34	16
TNJ0121	3.59	1.36288	13.2768	8.1	7.5	2.1	< 37	13
TNJ0121	2.91	1.37389	13.4024	17.3	13.2	4.5	< 73	27
TNJ0121	3.14	1.35095	13.3576	12.5	10.3	3.3	< 27	22
TNJ0121	3.52	1.35764	13.4330	8.4	7.8	2.2	< 50	15
TNJ0121	3.28	1.35576	13.4702	10.5	9.3	2.8	< 55	20
TNJ0121	3.27	1.36938	13.3538	8.9	7.8	2.4	< 9	15
TNJ0121	3.33	1.36303	13.3729	7.5	6.7	2.0	< 39	13
TNJ0121	3.32	1.36688	13.2467	9.8	8.9	2.7	< 49	16
TNJ0121	3.01	1.37013	13.2523	12.5	10.3	3.4	< 43	20
TNJ0121	3.07	1.37011	13.4007	9.6	8.2	2.7	< 77	17
TNJ0121	3.23	1.36914	13.3240	8.6	7.8	2.4	< 22	15
TNJ0121	3.32	1.36440	13.3899	7.2	6.7	2.0	< 40	13
TNJ0121	2.87	1.37394	13.3818	15.5	12.5	4.4	< 68	26
TNJ0121	2.87	1.37357	13.3176	15.0	12.1	4.2	< 51	25
TNJ0121	3.27	1.35988	13.2818	7.3	6.7	2.1	< 40	13
TNJ0121	2.68	1.36362	13.5314	14.1	10.7	4.0	< 22	33
TNJ0121	3.12	1.35480	13.4402	9.3	8.2	2.6	< 67	18
TNJ0121	2.94	1.37324	13.3287	13.7	11.4	3.9	< 52	23
TNJ0205	8.88	2.08083	22.5789	34.3	30.5	3.4	80	25
TNJ0205	5.03	2.08783	22.6923	11.4	10.3	2.1	< 43	16
TNJ0205	3.87	2.07675	22.5962	23.5	17.9	4.6	< 92	35
TNJ0205	4.73	2.08257	22.7646	10.7	10.0	2.1	< 69	16
TNJ0205	4.24	2.08342	22.8491	13.6	11.8	2.8	< 81	22
TNJ0205	4.31	2.08355	22.8272	11.6	10.3	2.4	< 32	19
TNJ0205	4.28	2.08683	22.7115	9.6	8.9	2.1	< 18	16
TNJ0205	4.32	2.08839	22.7240	9.4	8.9	2.1	< 66	16
TNJ0205	4.05	2.07840	22.6937	10.7	10.0	2.5	< 51	19
TNJ0205	3.88	2.08754	22.6173	9.7	8.9	2.3	< 54	17
TNJ0205	3.83	2.09000	22.7844	8.7	8.2	2.1	< 12	16
TNJ0205	2.88	2.09792	22.8096	21.3	15.4	5.3	< 60	41
TNJ0205	2.93	2.08177	22.8889	17.5	13.2	4.5	< 174	43
TNJ0205	3.27	2.08350	22.7382	7.8	6.7	2.1	< 33	16
TNJ0205	3.25	2.09026	22.7507	7.8	6.7	2.1	< 26	16

TNJ0205	3.57	2.08821	22.6204	8.6	8.2	2.3	< 17	17
TNJ0205	2.75	2.09893	22.7415	18.7	13.9	5.1	< 60	36
TNJ0205	2.95	2.09747	22.7707	15.2	12.1	4.1	< 97	29
TNJ0205	3.03	2.08856	22.8702	11.6	9.6	3.2	< 55	28
TNJ0205	3.38	2.07835	22.7452	9.2	8.5	2.5	< 32	20
TNJ0205	2.56	2.09712	22.6242	20.2	14.3	5.6	< 119	38
TNJ0205	3.39	2.08509	22.8138	7.9	7.5	2.2	< 42	17
TNJ0205	3.20	2.09022	22.6779	7.6	6.7	2.1	< 59	16
TNJ0205	2.94	2.08202	22.8614	11.7	9.6	3.3	< 51	28
TNJ0205	2.59	2.09908	22.7557	19.2	13.9	5.4	< 153	39
TNJ0205	2.62	2.09000	22.5575	15.3	11.4	4.4	< −3	31
TNJ0205	2.43	2.09571	22.5920	20.7	14.3	5.9	< 56	41
TNJ0205	3.21	2.09058	22.7593	7.4	6.7	2.1	< 30	16
TNJ0205	3.16	2.09310	22.6365	9.9	8.9	2.8	< 32	20
TNJ2007	5.49	20.13323	-13.2195	9.8	9.3	1.7	< 46	12
TNJ2007	4.96	20.13920	-13.2560	11.4	10.3	2.1	< 29	15
TNJ2007	5.06	20.13492	-13.2768	8.8	8.5	1.7	< 35	12
TNJ2007	4.80	20.12350	-13.2362	10.3	9.6	2.0	< 46	15
TNJ2007	4.52	20.12793	-13.3405	8.7	7.8	1.7	< 49	13
TNJ2007	3.99	20.12677	-13.4011	10.1	9.3	2.3	< 75	18
TNJ2007	3.83	20.13421	-13.1317	11.0	10.0	2.6	< 51	18
TNJ2007	3.85	20.13488	-13.3569	7.6	7.1	1.8	< −0	13
TNJ2007	3.51	20.13245	-13.1097	12.6	10.7	3.0	< 36	21
TNJ2007	3.19	20.14367	-13.3029	17.0	13.2	4.1	< 83	30
TNJ2007	3.91	20.13334	-13.3649	7.4	7.1	1.8	< 30	13
TNJ2007	3.51	20.13416	-13.1890	7.3	6.4	1.8	< 25	13
TNJ2007	3.41	20.14029	-13.2120	9.6	8.5	2.5	< 28	17
TNJ2007	3.59	20.12330	-13.2165	8.3	7.8	2.2	< 55	16
TNJ2007	3.31	20.12956	-13.4294	9.9	8.5	2.6	< 38	20
TNJ2007	3.60	20.12643	-13.2218	6.8	6.4	1.8	< 42	13
TNJ2007	3.28	20.13294	-13.4464	11.9	10.3	3.2	< 42	24
TNJ2007	3.31	20.11959	-13.2737	11.6	10.3	3.1	< 50	24
TNJ2007	3.55	20.13625	-13.3338	6.7	6.4	1.8	< 31	13
TNJ2007	3.21	20.12460	-13.2109	7.3	6.4	2.0	< 42	15
TNJ2007	3.21	20.12560	-13.2518	6.4	5.7	1.8	< 17	13
TNJ2007	3.15	20.13533	-13.4405	12.3	10.7	3.4	< 72	26
TNJ2007	3.39	20.12456	-13.3791	8.3	7.8	2.3	< 51	18
TNJ2007	3.34	20.12715	-13.2804	6.1	5.7	1.7	< 11	12
TNJ2007	3.33	20.13659	-13.2018	6.9	6.4	1.9	< 21	14
TNJ2007	3.53	20.13586	-13.1717	7.6	7.5	2.1	< 32	15
TNJ2007	3.39	20.12424	-13.2757	6.7	6.4	1.9	< 24	14
TNJ2007	2.77	20.12525	-13.4464	14.6	11.4	4.1	< 67	31
TNJ2007	3.36	20.13255	-13.1400	8.2	7.8	2.3	< 11	16
TNJ2007	2.95	20.12141	-13.1862	11.5	9.6	3.3	< 53	26
TNJ2007	3.06	20.13190	-13.1765	6.5	5.7	1.8	< 41	13
TNJ2007	3.26	20.13129	-13.3563	6.1	5.7	1.7	< 18	13
TXS0211	5.20	2.23579	-12.0680	11.6	10.7	2.1	44	14
TXS0211	4.42	2.23467	-11.9018	10.3	9.3	2.1	< 30	13
TXS0211	4.47	2.24294	-12.0332	9.6	9.3	2.1	< 26	13
TXS0211	3.93	2.23414	-11.8400	14.0	12.1	3.1	< 46	18
TXS0211	4.04	2.22837	-12.0049	11.9	10.7	2.6	< 47	18
TXS0211	4.02	2.23836	-11.9215	8.7	7.8	1.9	< 39	13
TXS0211	3.93	2.23032	-12.0560	10.6	9.6	2.4	< 36	17
TXS0211	3.81	2.23375	-12.0805	9.5	8.5	2.2	< 8	15
TXS0211	3.80	2.24613	-11.9065	11.8	10.7	2.8	< 2	17
TXS0211	3.23	2.24726	-11.8770	16.3	12.9	4.0	< 35	22
TXS0211	3.26	2.23504	-11.8253	13.7	11.1	3.4	< 34	19
TXS0211	3.12	2.23225	-11.8153	18.2	14.3	4.6	< 59	28
TXS0211	2.98	2.23267	-11.8033	21.0	15.7	5.3	< 46	32
TXS0211	3.42	2.23199	-11.9482	8.1	7.1	2.1	< 30	13
TXS0211	3.66	2.23858	-11.9646	7.6	7.1	1.9	< 24	12
TXS0211	3.63	2.23460	-12.0207	7.6	7.1	2.0	< 15	13
TXS0211	3.54	2.23073	-12.0730	9.7	8.9	2.5	< 11	18
TXS0211	3.52	2.24190	-12.0721	8.6	7.8	2.2	< 22	15
TXS0211	3.48	2.22999	-12.0474	9.5	8.5	2.5	< 32	17
TXS0211	3.40	2.23249	-12.0438	8.0	7.1	2.1	< 29	14
TXS0211	3.12	2.24779	-11.8937	14.8	12.1	3.9	< 44	22
TXS0211	3.41	2.22891	-12.0149	9.4	8.5	2.5	< 47	17
TXS0211	3.04	2.24779	-11.9184	12.7	10.3	3.4	< −9	19
TXS0211	2.92	2.24852	-12.0655	15.4	12.1	4.2	< 32	29
TXS0211	3.39	2.23456	-11.8798	8.5	7.8	2.3	< 19	15
TXS0211	2.57	2.23844	-11.7811	21.3	15.0	5.9	< 84	32

TXS0211	3.33	2.23662	-11.8400	10.5	9.6	2.9	< 28	17
TXS0211	3.28	2.22973	-11.9521	8.7	7.8	2.4	< 34	15
TXS0211	1.64	2.24935	-11.8703	25.3	11.4	7.0	< 147	39
TXS0211	3.04	2.24192	-11.8134	14.7	12.5	4.1	< 73	22
TXS0211	3.12	2.23918	-11.8273	11.4	10.0	3.2	< 39	18
TXS0211	2.00	2.22635	-11.9307	14.5	8.2	4.1	< 108	29
TXS0211	3.27	2.22860	-11.9123	10.8	10.0	3.1	< 1	20
TXS0211	2.85	2.25000	-11.9662	15.9	12.9	4.5	< 79	28
USS0828	3.74	8.51049	19.2407	12.0	10.3	2.8	< 36	19
USS0828	3.65	8.50843	19.3119	15.0	13.2	3.6	< 69	25
USS0828	3.33	8.50784	19.1570	13.4	11.1	3.3	< 44	23
USS0828	2.93	8.51241	19.0742	16.3	12.1	4.1	< 60	29
USS0828	3.33	8.50902	19.1529	12.0	10.3	3.1	< 36	21
USS0828	3.25	8.50954	19.3260	13.9	11.8	3.6	< 81	25
USS0828	1.61	8.50398	19.3366	33.9	14.3	8.9	< 125	56
USS0828	3.12	8.52007	19.1365	12.5	10.3	3.3	< 36	22
USS0828	2.21	8.52524	19.1062	28.7	17.2	7.8	< 69	47
USS0828	1.68	8.50535	19.3616	32.6	15.0	8.9	< 63	57
USS0828	3.19	8.50936	19.1568	10.9	9.6	3.0	< 55	21
USS0828	3.14	8.51836	19.1470	10.6	9.3	3.0	< 56	20
USS0828	3.12	8.51842	19.2229	9.8	8.5	2.7	< 31	19
USS0828	2.11	8.52294	19.3736	27.2	16.1	7.6	< 154	54
USS0828	3.08	8.51178	19.2713	9.8	8.5	2.8	< 32	19
USS0828	3.08	8.52057	19.1623	11.0	9.6	3.1	< 27	21
USS0828	3.09	8.51017	19.2324	9.7	8.5	2.8	< 41	19
USS0828	2.91	8.50760	19.2888	12.4	10.3	3.5	< 90	24
USS1558	-0.43	16.01853	-0.5616	69.1	-0.8	1.9	168	21
USS1558	6.18	16.01574	-0.4412	12.8	11.8	1.9	< 99	21
USS1558	4.67	16.02623	-0.5791	11.8	10.7	2.3	< 76	24
USS1558	4.27	16.01759	-0.4926	8.8	7.8	1.8	< 12	20
USS1558	4.22	16.02684	-0.4537	8.8	7.8	1.9	< 36	20
USS1558	4.00	16.02558	-0.3331	12.5	11.1	2.8	< 36	29
USS1558	3.63	16.02841	-0.3256	16.0	13.6	3.7	< 139	39
USS1558	3.68	16.01881	-0.4971	7.6	6.7	1.8	< 46	20
USS1558	3.83	16.01664	-0.5494	8.0	7.5	1.9	< 26	21
USS1558	3.21	16.03336	-0.4571	15.2	12.1	3.8	< 142	39
USS1558	3.64	16.01477	-0.5549	8.6	7.8	2.2	< 5	23
USS1558	3.69	16.02628	-0.4718	7.2	6.7	1.8	< 85	20
USS1558	3.77	16.02106	-0.5752	7.8	7.5	2.0	< 59	21
USS1558	3.70	16.02513	-0.4446	7.1	6.7	1.8	< 67	20
USS1558	3.52	16.01790	-0.3723	8.1	7.5	2.1	< 80	23
USS1558	3.48	16.01199	-0.5260	9.4	8.5	2.5	< 74	28
USS1558	3.54	16.02015	-0.5641	7.3	6.7	1.9	< 35	21
USS1558	3.53	16.02880	-0.4496	8.1	7.5	2.1	< 24	22
USS1558	3.45	16.02921	-0.4704	8.2	7.5	2.2	< 57	23
USS1558	3.49	16.01826	-0.4504	6.9	6.4	1.8	< 76	20
USS1558	3.34	16.01905	-0.3767	7.5	6.7	2.0	< 46	22
USS1558	3.40	16.01557	-0.5405	7.3	6.7	2.0	< 54	21
USS1558	2.69	16.02382	-0.2847	17.3	12.9	4.8	< 105	52
USS1558	3.28	16.02960	-0.3881	9.8	8.9	2.7	< 32	28
USS1558	3.15	16.03080	-0.3842	11.4	10.0	3.2	< 81	32
USS1558	3.08	16.01490	-0.3362	11.6	10.0	3.2	< 138	37
USS1558	2.99	16.02230	-0.3031	11.9	10.0	3.3	< 83	37
USS1558	3.30	16.01716	-0.4054	6.9	6.4	1.9	< 77	21
USS1558	3.30	16.02749	-0.4429	6.8	6.4	1.9	< 37	21
LBDS53	4.24	17.37900	50.0851	12.2	11.1	2.6	< 40	25
LBDS53	4.08	17.38091	50.0487	12.4	11.1	2.7	< 60	26
LBDS53	3.30	17.37313	49.9264	22.0	16.5	5.0	< 129	47
LBDS53	3.97	17.37489	50.0673	11.4	10.3	2.6	< 9	25
LBDS53	3.09	17.36405	50.1318	26.9	19.0	6.1	< 47	51
LBDS53	3.67	17.37053	50.0470	11.8	10.3	2.8	< 56	26
LBDS53	1.61	17.37502	50.2916	32.9	13.2	8.2	< 143	86
LBDS53	3.52	17.37821	50.0537	10.3	9.3	2.6	< 38	25
LBDS53	3.23	17.36849	50.0668	12.4	10.3	3.2	< 34	29
LBDS53	2.74	17.36434	50.1182	20.7	14.7	5.4	< 132	47
LBDS53	3.45	17.37333	50.1966	11.6	10.3	3.0	< 79	28
LBDS53	3.03	17.38347	50.2052	15.5	12.1	4.0	< 98	41
LBDS53	1.99	17.37020	50.2744	32.6	17.2	8.6	< 180	91
LBDS53	2.75	17.36475	50.0454	19.7	14.3	5.2	< 138	45
LBDS53	3.12	17.36790	50.1507	13.2	11.1	3.5	< 76	32
LBDS53	2.96	17.38695	50.0715	15.3	12.1	4.1	< 53	44
LBDS53	2.25	17.38779	50.0164	24.5	15.0	6.7	< 87	71

LBDS53	3.14	17.37113	50.0014	11.6	10.0	3.2	< 76	29
LBDS53	3.23	17.37802	49.9970	10.5	9.3	2.9	< 75	27
LBDS53	2.13	17.36455	50.1646	23.9	13.9	6.5	< 121	56
LBDS53	3.26	17.37548	50.0387	9.6	8.5	2.6	< 60	25
LBDS53	2.87	17.37376	50.2391	14.4	11.4	4.0	< 100	38
LBDS53	3.04	17.38530	50.0815	12.3	10.3	3.4	< 22	34
LBDS53	2.78	17.37617	50.2594	15.8	12.5	4.5	< 108	46
LBDS53	3.25	17.37943	50.0509	9.2	8.5	2.6	< −22	25
TNJ1338	4.71	13.63865	-19.7088	11.5	10.0	2.1	68	21
TNJ1338	4.38	13.63735	-19.6287	11.1	10.0	2.3	< 29	22
TNJ1338	3.41	13.65106	-19.7880	19.0	15.0	4.4	< 176	47
TNJ1338	2.74	13.62795	-19.7457	23.2	15.4	5.6	< −20	58
TNJ1338	3.44	13.64484	-19.8555	14.5	12.1	3.5	< 87	37
TNJ1338	3.66	13.63703	-19.6723	8.7	7.8	2.1	< 53	21
TNJ1338	3.44	13.63607	-19.6198	9.8	8.5	2.5	< 87	24
TNJ1338	2.54	13.65236	-19.6140	26.9	17.5	6.9	< 73	67
TNJ1338	3.55	13.64437	-19.6454	8.5	7.8	2.2	< 53	22
TNJ1338	3.21	13.63053	-19.6212	15.9	13.2	4.1	< 87	42
TNJ1338	3.20	13.63223	-19.5898	15.5	12.9	4.0	< 37	40
TNJ1338	3.31	13.64398	-19.6979	8.2	7.1	2.1	< 69	21
TNJ1338	3.31	13.63487	-19.6254	9.9	8.5	2.6	< 86	25
TNJ1338	3.33	13.63722	-19.6846	8.1	7.1	2.1	< 26	21
TNJ1338	3.33	13.64067	-19.6904	8.1	7.1	2.1	< 79	21
TNJ1338	2.63	13.62868	-19.7655	18.9	13.2	5.0	< 149	51
TNJ1338	3.27	13.64706	-19.7894	10.1	8.9	2.7	< 89	27
TNJ1338	3.19	13.64419	-19.8191	9.9	8.5	2.7	< 103	27
TNJ1338	3.33	13.64382	-19.7938	8.7	7.8	2.3	< 61	23
TNJ1338	3.17	13.63707	-19.5806	10.8	9.3	2.9	< 63	28
TNJ1338	2.95	13.62997	-19.7735	14.3	11.4	3.9	< 99	40
TNJ1338	2.85	13.63696	-19.5325	17.5	13.6	4.8	< 145	45
TNJ1338	3.21	13.64293	-19.6295	8.0	7.1	2.2	< 45	22
TNJ1338	3.24	13.63865	-19.6340	7.9	7.1	2.2	< 55	22
TNJ1338	3.32	13.63676	-19.7060	7.7	7.1	2.1	< 52	21
TNJ1338	1.76	13.65327	-19.7718	24.6	12.1	6.9	< 209	76
TNJ1338	3.33	13.63878	-19.7249	7.5	7.1	2.1	< 41	21
TNJ1338	3.24	13.63481	-19.6059	10.1	9.3	2.9	< 52	27
TNJ1338	2.27	13.63166	-19.7382	9.9	6.4	2.8	< 65	28
TNJ1338	3.14	13.63692	-19.6109	8.7	7.8	2.5	< 47	24
8C1435	4.89	14.61358	63.4061	12.5	11.8	2.4	< 75	24
8C1435	4.30	14.60769	63.2801	10.3	9.6	2.2	< 55	22
8C1435	3.53	14.60255	63.1940	19.5	15.4	4.4	< 72	39
8C1435	3.97	14.61877	63.2804	12.0	10.7	2.7	< 110	27
8C1435	3.15	14.61966	63.1842	24.0	17.2	5.5	< 135	57
8C1435	3.61	14.61315	63.1831	12.9	11.1	3.1	< 83	29
8C1435	2.99	14.60235	63.1834	20.9	15.0	5.0	< 110	44
8C1435	2.95	14.60187	63.1770	24.8	17.9	6.1	< 68	52
8C1435	3.24	14.61960	63.4244	15.0	12.1	3.7	< 155	40
8C1435	3.49	14.61028	63.3191	8.9	7.8	2.2	< 62	22
8C1435	3.51	14.60428	63.2785	10.0	8.9	2.5	< 28	24
8C1435	2.61	14.59887	63.2473	23.5	15.7	6.0	< 65	56
8C1435	3.31	14.61021	63.4061	9.1	7.8	2.4	< 54	23
8C1435	3.56	14.61792	63.2913	9.6	8.9	2.5	< 37	25
8C1435	3.35	14.60997	63.2779	8.5	7.5	2.2	< 59	22
8C1435	2.50	14.59753	63.3040	28.5	18.6	7.5	< 117	71
8C1435	3.33	14.60835	63.1942	10.9	9.6	2.9	< 49	27
8C1435	3.39	14.60939	63.3949	8.7	7.8	2.3	< 53	23
8C1435	3.32	14.61382	63.3708	8.5	7.5	2.2	< 102	22
8C1435	3.24	14.60820	63.4027	9.0	7.8	2.4	< 66	24
8C1435	3.29	14.61855	63.3924	10.8	9.6	2.9	< 75	30
8C1435	2.60	14.60769	63.1323	20.3	14.3	5.5	< 158	50
8C1435	3.07	14.60665	63.1617	14.5	12.1	4.0	< 56	36
8C1435	3.36	14.61182	63.2904	8.1	7.5	2.2	< 33	22
8C1435	2.22	14.59798	63.2846	24.2	14.7	6.6	< 94	62
8C1435	3.19	14.61969	63.2295	13.1	11.4	3.6	< 94	38
8C1435	2.78	14.61814	63.4550	14.7	11.4	4.1	< 69	44
8C1435	3.40	14.61667	63.3944	9.3	8.9	2.6	< 7	26
8C1435	3.19	14.61788	63.3185	8.7	7.8	2.5	< 50	24
RCJ0311	6.33	3.19169	5.0591	16.6	15.4	2.4	< 120	27
RCJ0311	4.83	3.19503	5.2579	13.5	12.1	2.5	< 96	28
RCJ0311	4.57	3.19538	5.2721	13.8	12.5	2.7	< 98	31
RCJ0311	3.89	3.20480	5.1306	12.2	10.3	2.7	< 82	27
RCJ0311	3.41	3.20952	5.0883	28.5	21.1	6.2	< 119	61

RCJ0311	3.66	3.18643	5.2065	16.2	13.2	3.6	< 113	44
RCJ0311	3.44	3.18964	5.2754	17.5	13.9	4.1	< 124	47
RCJ0311	2.85	3.19710	4.9396	29.7	19.7	6.9	< 212	74
RCJ0311	2.78	3.20313	4.9613	28.7	18.6	6.7	< 179	73
RCJ0311	3.73	3.18925	5.1928	11.4	10.0	2.7	< 80	30
RCJ0311	3.90	3.19351	5.2031	9.4	8.5	2.2	< 46	24
RCJ0311	3.79	3.20209	5.0797	10.0	8.9	2.3	< 28	25
RCJ0311	3.70	3.20300	5.1962	9.9	8.9	2.4	< 46	26
RCJ0311	3.47	3.19718	5.0883	8.8	7.5	2.1	< 47	23
RCJ0311	3.38	3.20398	5.0380	12.8	10.7	3.2	< 106	32
RCJ0311	3.25	3.19125	5.0225	11.6	9.6	3.0	< 98	32
RCJ0311	3.47	3.20163	5.2345	10.0	8.9	2.6	< 65	27
RCJ0311	3.35	3.20650	5.1398	11.6	10.3	3.1	< 27	31
RCJ0311	3.22	3.19175	5.0489	9.5	8.2	2.5	< 60	28
RCJ0311	3.37	3.19067	5.0536	9.9	8.9	2.6	< 47	29
RCJ0311	3.02	3.20565	5.2540	15.1	12.5	4.1	< 123	41
RCJ0311	2.99	3.19837	5.2812	10.8	8.9	3.0	< 91	32
RCJ0311	3.23	3.20324	5.1231	8.3	7.5	2.3	< 74	24
RCJ0311	3.15	3.20591	5.1751	10.9	9.6	3.1	< 50	31
RCJ0311	3.15	3.18697	5.2020	11.7	10.3	3.3	< 78	40
RCJ0311	3.12	3.20068	5.2879	11.8	10.3	3.3	< 74	36
RCJ0311	3.32	3.19644	5.1311	7.6	7.1	2.1	< 37	23
RCJ0311	2.53	3.20320	4.9766	19.0	13.6	5.4	< 117	56
RCJ0311	2.70	3.18645	5.0975	12.2	9.3	3.4	< 75	40
RCJ0311	3.00	3.20761	5.0780	13.8	11.8	3.9	< 88	41
RCJ0311	2.40	3.20070	4.9521	21.4	14.7	6.1	< 163	66

A.2 850 μm Maps

Here, I show (Figure A.1) the 850 μm maps of the the 14 HzRG fields presented in chapter 7. All sources found by the CLEAN source extraction are marked: those with S/N>3.5 after deboosting are indicated with cyan circles, all others with red circles. In the case of USS1558 there is a very bright source which is multiply detected in the source extraction. Further investigation suggests that this is the Hubble Space Telescope guide star GSC 0503200868 at RA, Dec= $16^{\rm h}01^{\rm m}05^{\rm s}\!.741$, $-00^\circ32'34''\!.52$. While included in the plots here 'sources' associated with the star were removed from the rest of the analysis. In the source list in Table A.1 it is identified by the negative S/N and deboosted flux.

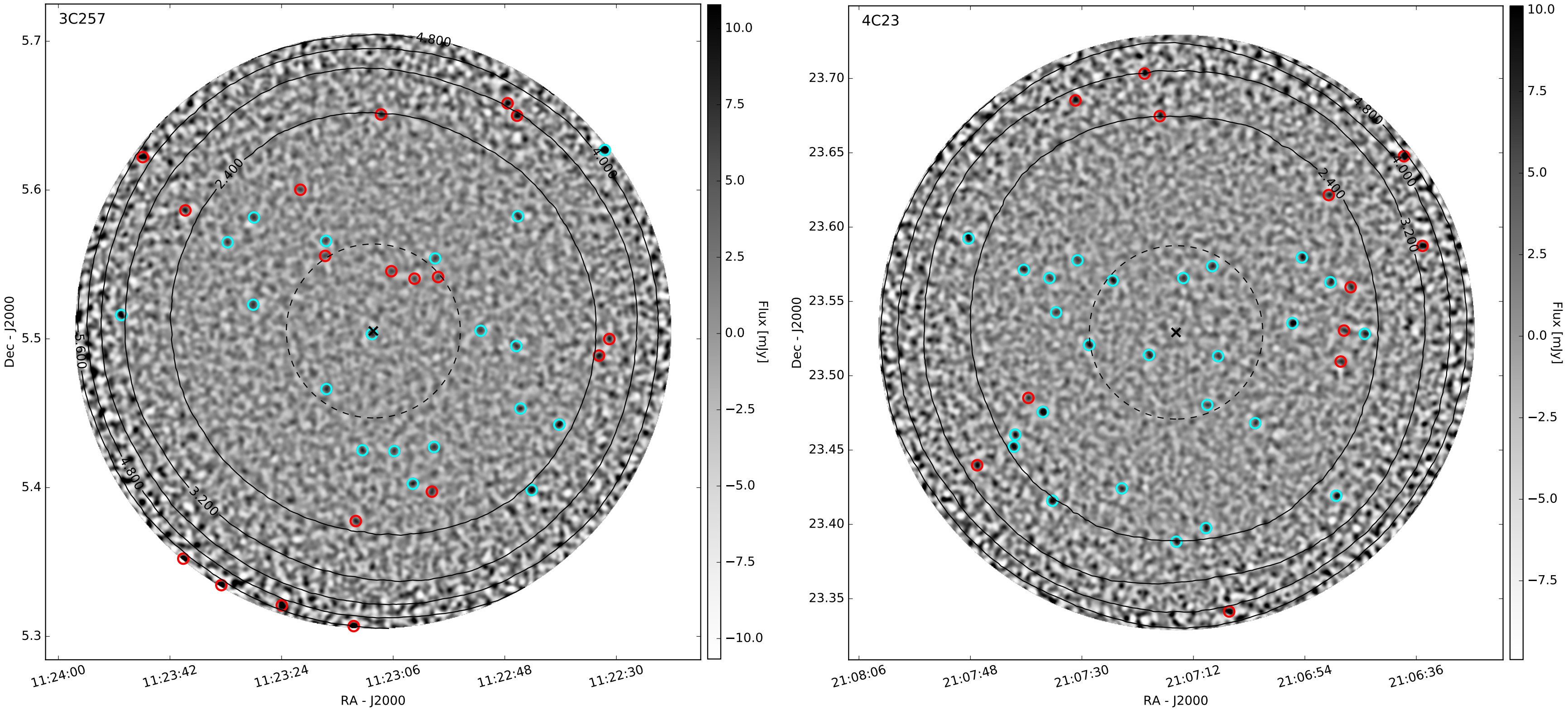

Figure A.1: 850 μm maps with $> 3.5\sigma$ sources circled. Red indicates sources which were initially above 3.5σ, but fell below the cutoff after flux deboosting; cyan those which remained above the cutoff and are included in the rest of the analysis. Contours mark the 850 μm rms noise levels in mJy as indicated. Dashed circles indicate the 6 Mpc comoving radius at the redshift of the HzRG. Maps are not to the same colour scale.

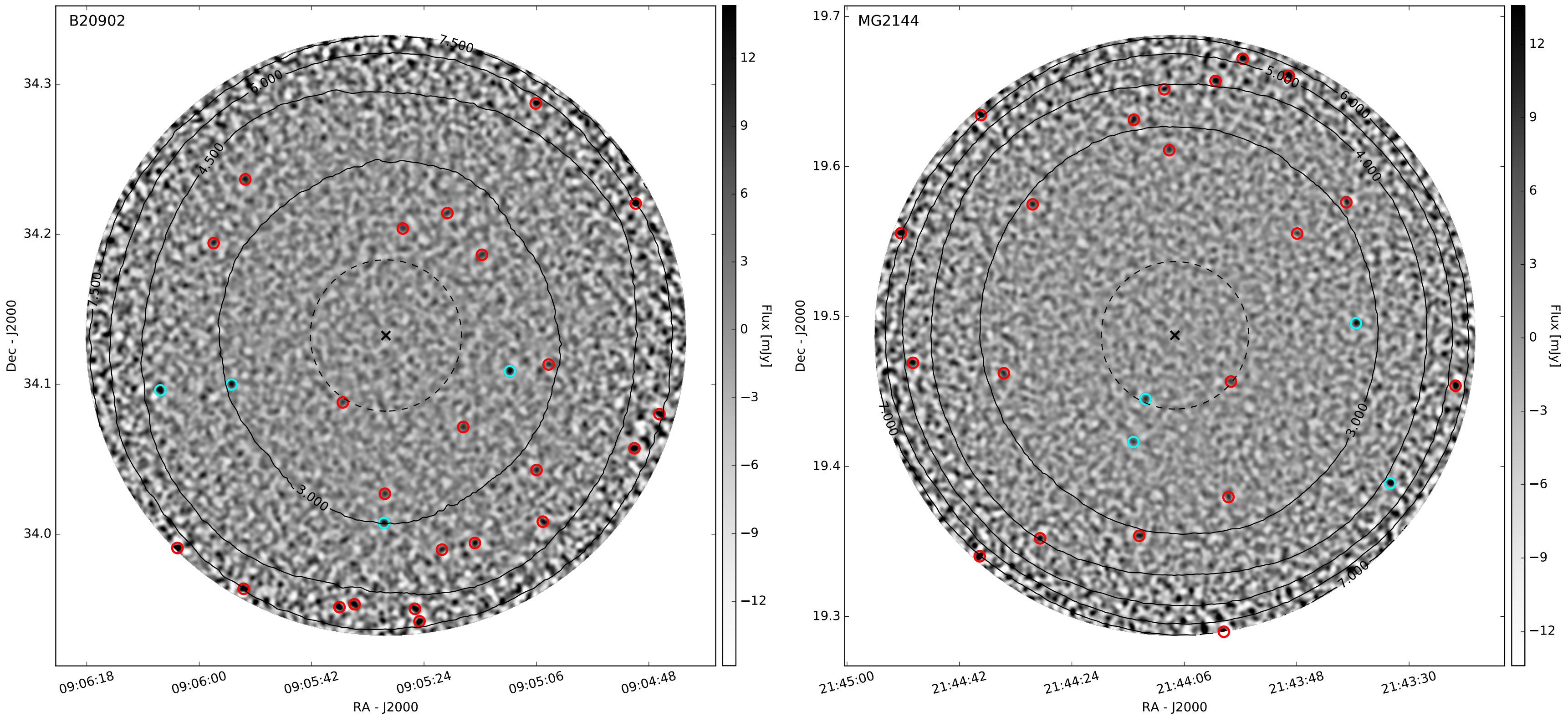

Figure A.1 (continued)

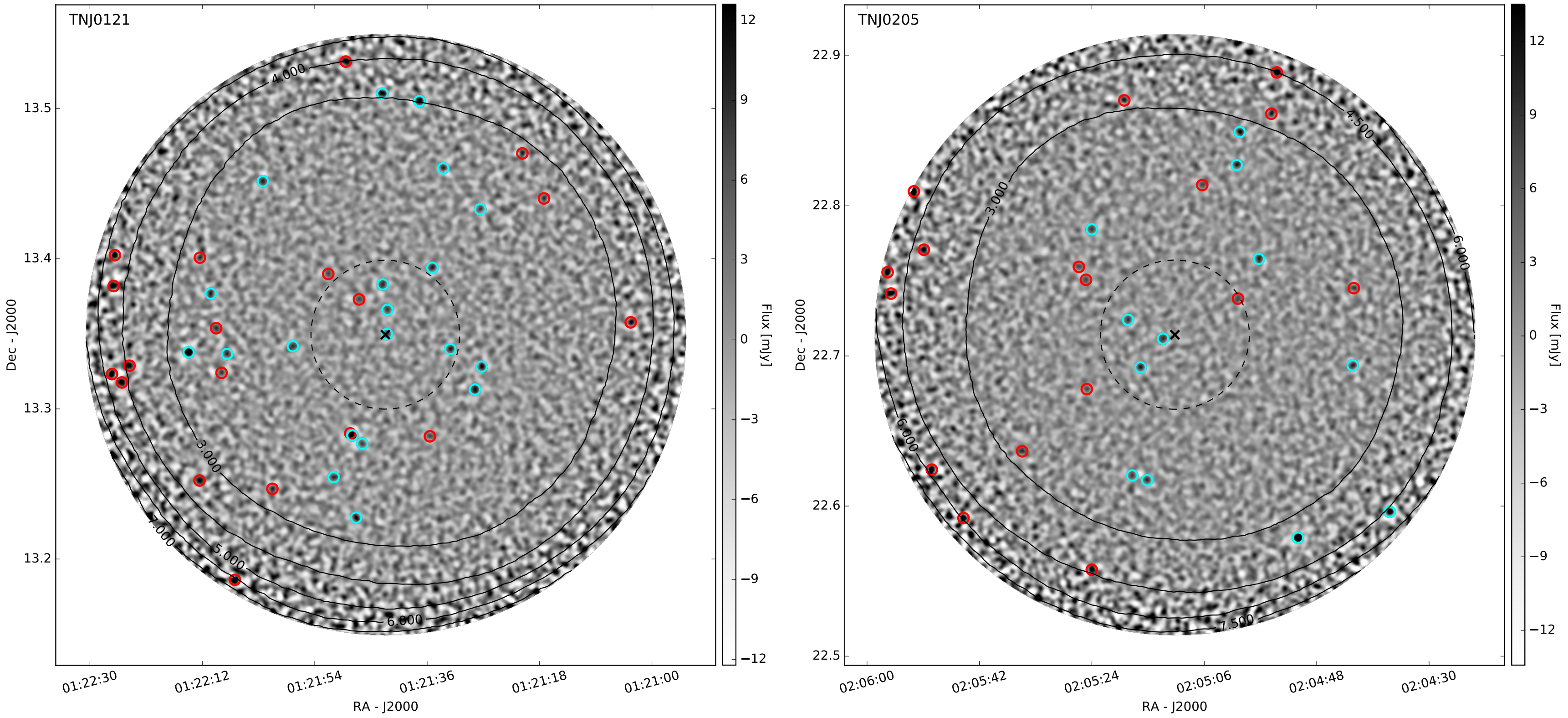

Figure A.1 (continued)

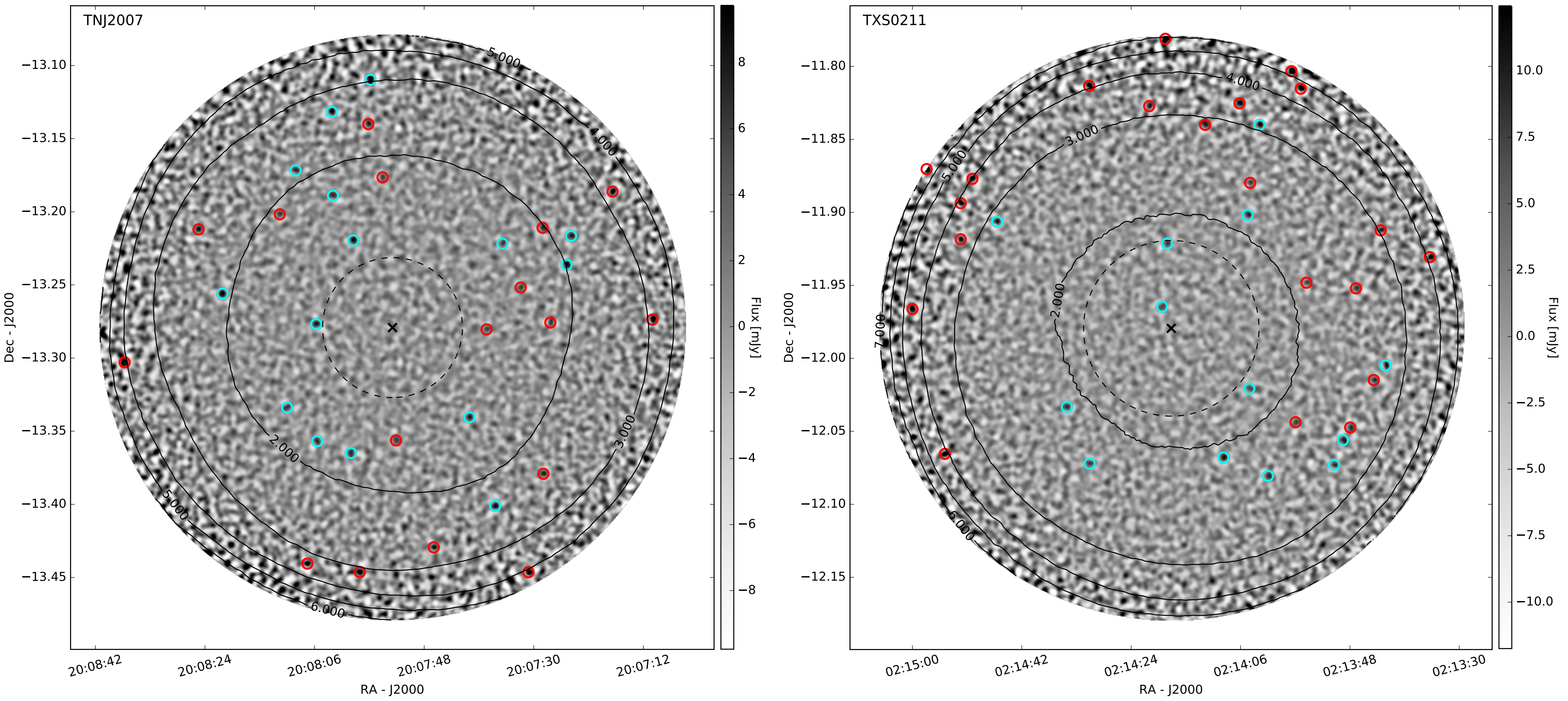

Figure A.1 (continued)

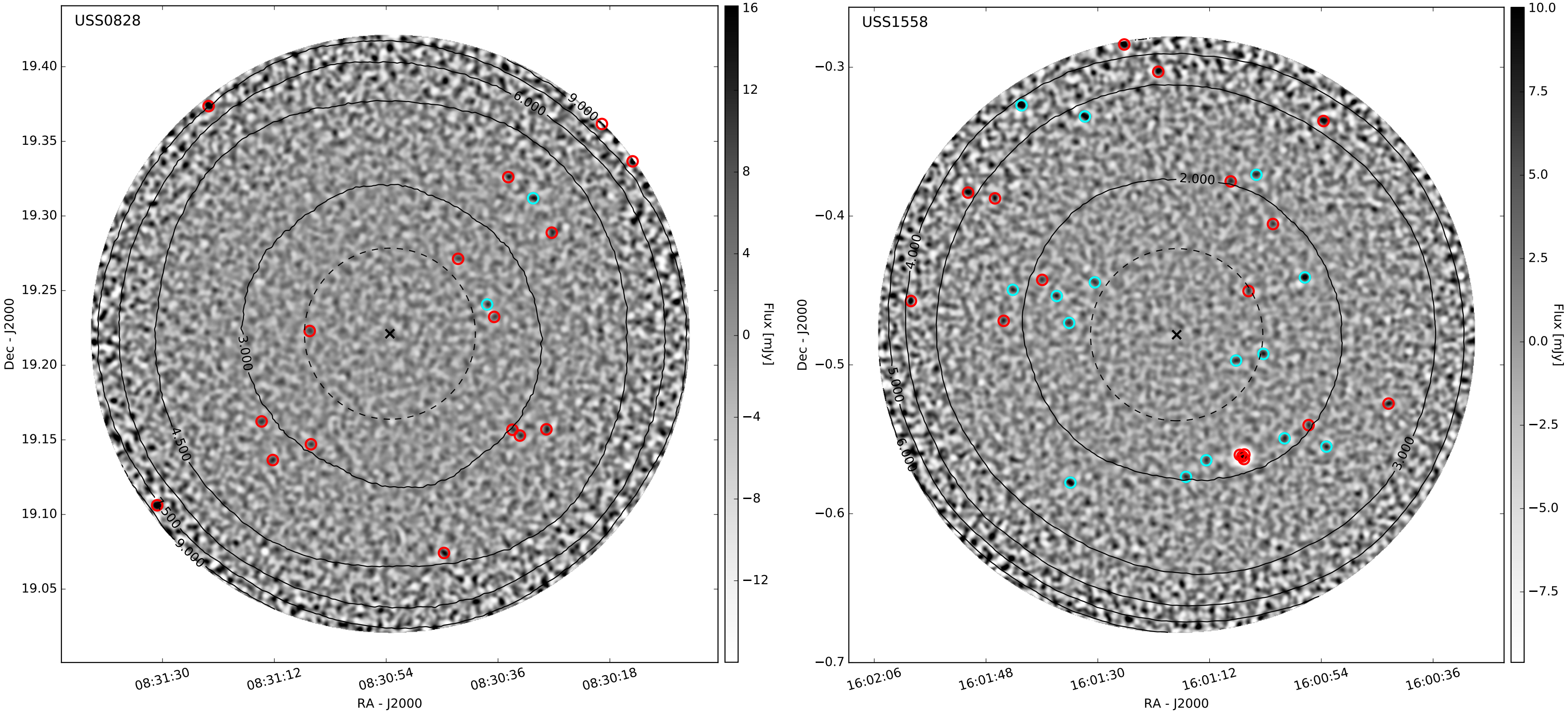

Figure A.1 (continued)

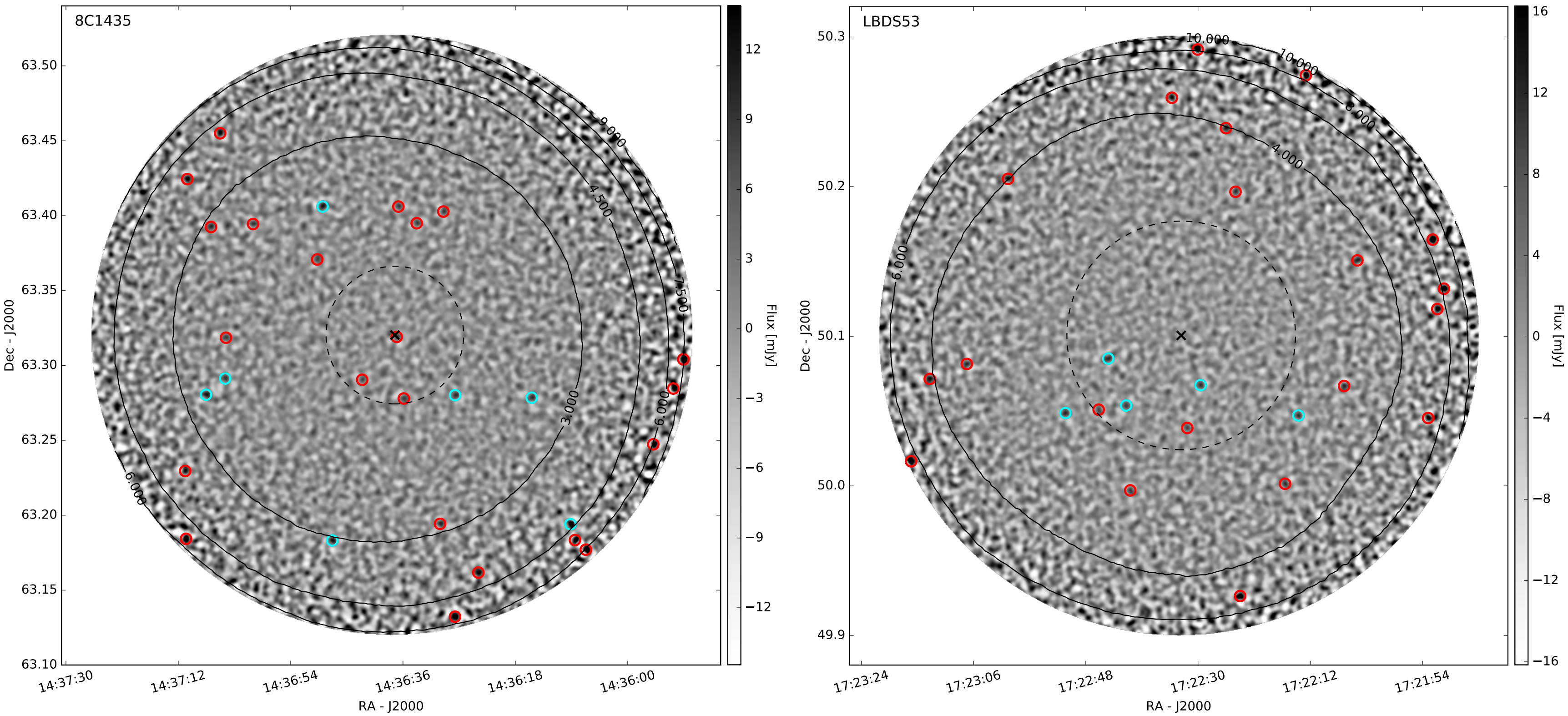

Figure A.1 (continued)

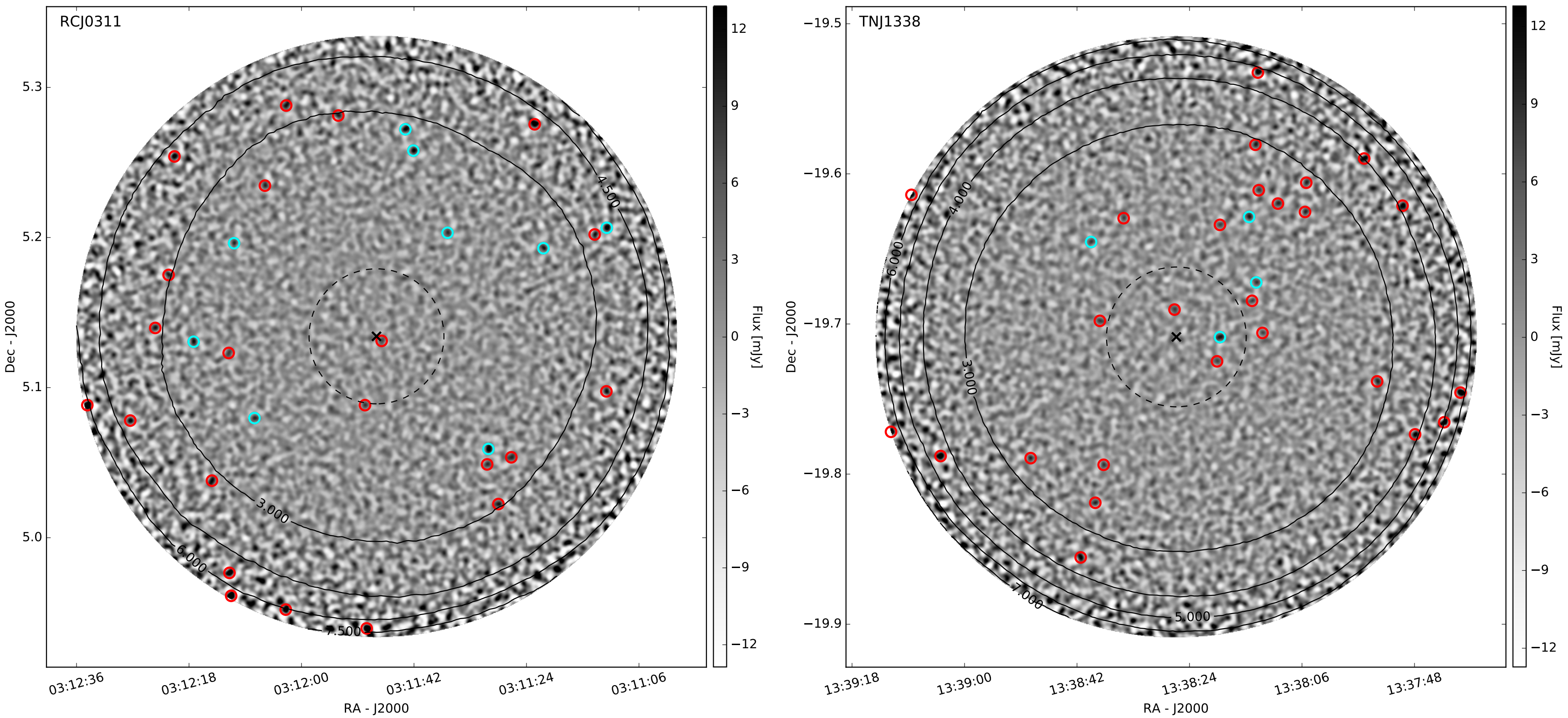

Figure A.1 (continued)

A.3 Field Pixel S/N Histograms

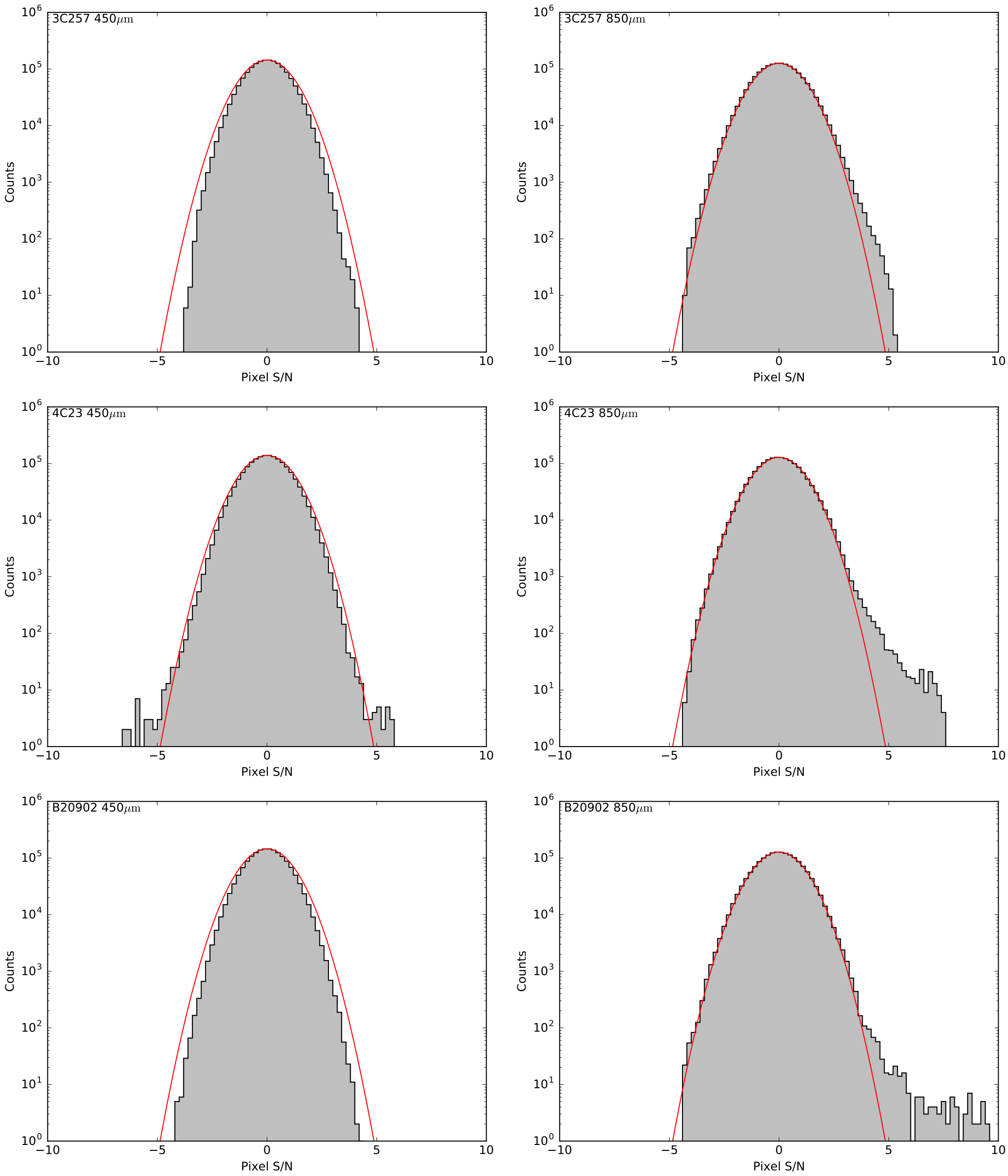

Figure A.2: S/N histograms for the matched-filtered HzRG fields from chapter 7, with clear signs of real sources detected in the positive S/N excess. In the case of USS1558 the negative S/N excess is due to negative bowling around the extremely bright extended local source.

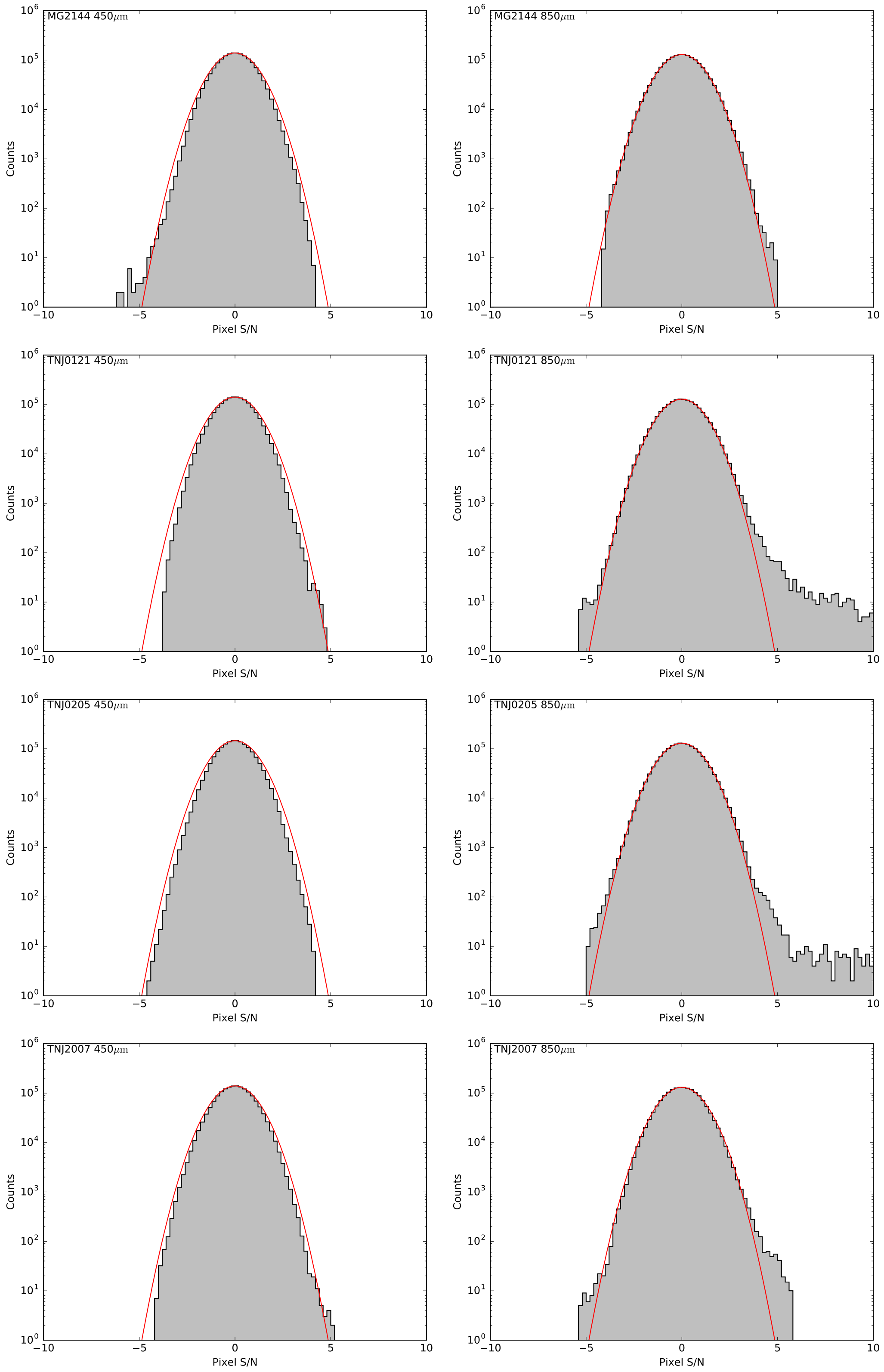

Figure A.2 (continued)

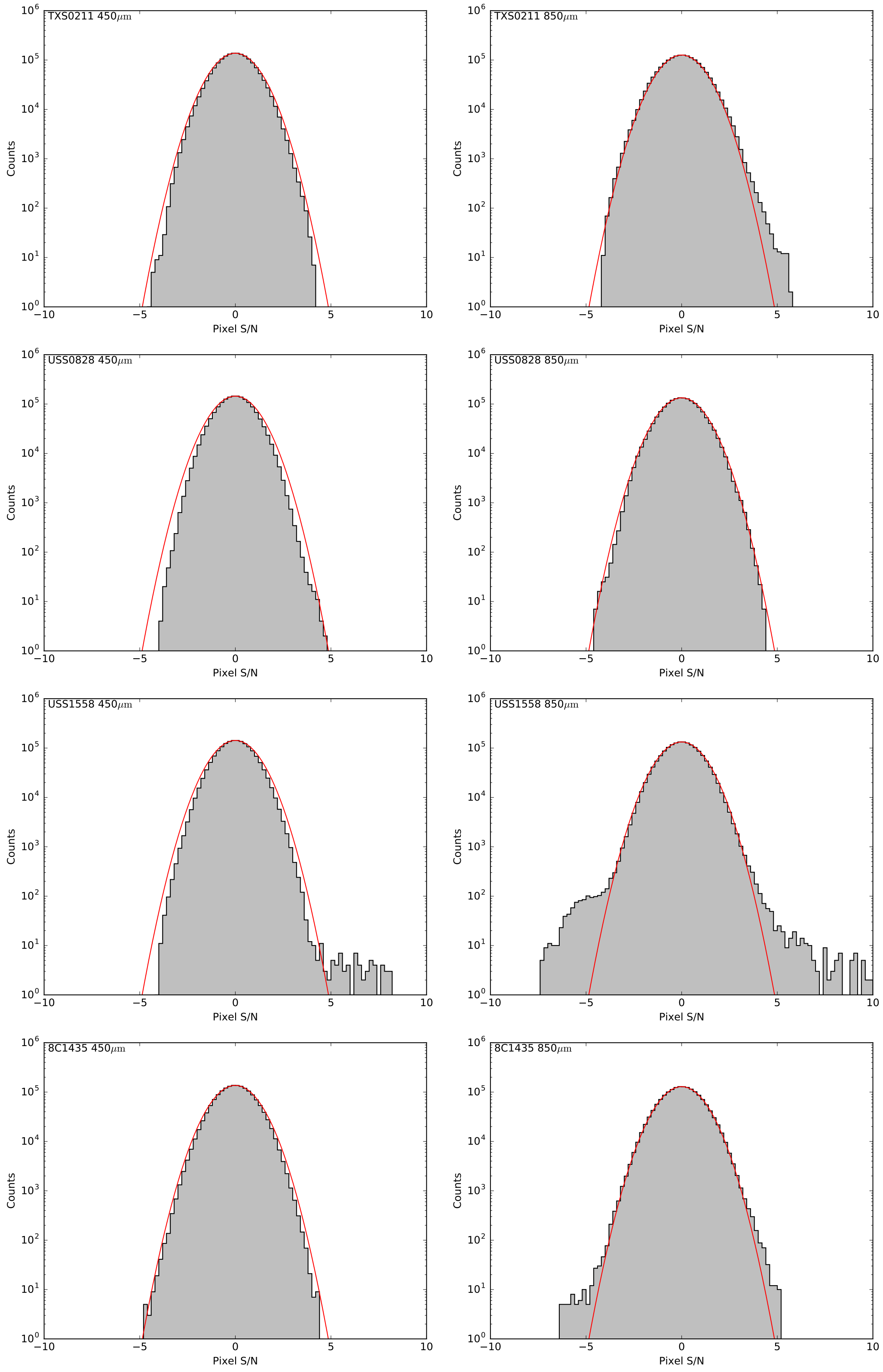

Figure A.2 (continued)

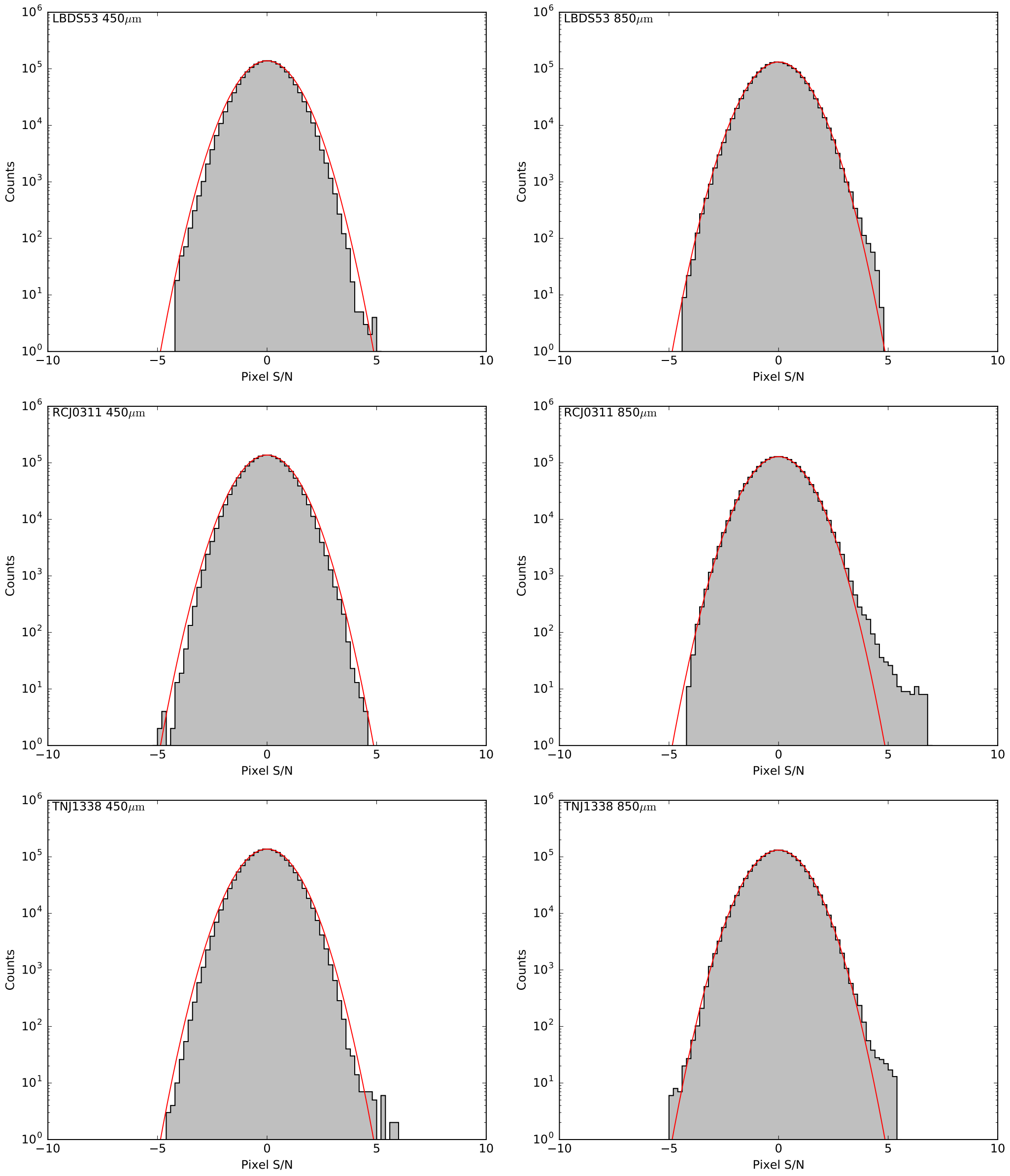

Figure A.2 (continued)

Bibliography

Aalto, S., Garcia-Burillo, S., Muller, S., et al. 2012, A&A, 537, A44

Aalto, S., Polatidis, A. G., Hüttemeister, S., & Curran, S. J. 2002, A&A, 381, 783

Aalto, S., Spaans, M., Wiedner, M. C., & Hüttemeister, S. 2007, A&A, 464, 193

Aalto, S., Wilner, D., Spaans, M., et al. 2009, A&A, 493, 481

Aalto, S., Garcia-Burillo, S., Muller, S., et al. 2015a, A&A, 574, A85

Aalto, S., Martín, S., Costagliola, F., et al. 2015b, A&A, 584, A42

Adams, W. S. 1941, ApJ, 93, 11

Aird, J., Coil, A. L., Moustakas, J., et al. 2012, ApJ, 746, 90

Aladro, R., Martín, S., Martín-Pintado, J., et al. 2011, A&A, 535, A84

Aladro, R., Viti, S., Bayet, E., et al. 2013, A&A, 549, A39

Aladro, R., Martín, S., Riquelme, D., et al. 2015, A&A, 579, A101

Alaghband-Zadeh, S., Chapman, S. C., Swinbank, A. M., et al. 2012, MNRAS, 424, 2232

Alonso-Herrero, A. 2013, ArXiv e-prints, arXiv:1302.2033

Amblard, A., Cooray, A., Serra, P., et al. 2011, Nature, 470, 510

Aravena, M., Bertoldi, F., Carilli, C., et al. 2010, ApJL, 708, L36

Archibald, E. N., Dunlop, J. S., Hughes, D. H., et al. 2001, MNRAS, 323, 417

Armus, L., Bernard-Salas, J., Spoon, H. W. W., et al. 2006, ApJ, 640, 204

Armus, L., Mazzarella, J. M., Evans, A. S., et al. 2009, PASP, 121, 559

Athreya, R. M., Kapahi, V. K., McCarthy, P. J., & van Breugel, W. 1998, A&A, 329, 809

Bachiller, R., & Pérez Gutiérrez, M. 1997, ApJL, 487, L93

Baldwin, J. A., Phillips, M. M., & Terlevich, R. 1981, PASP, 93, 5

Barger, A. J., Cowie, L. L., Sanders, D. B., et al. 1998, Nature, 394, 248

Barger, A. J., Cowie, L. L., Chen, C.-C., et al. 2014, ApJ, 784, 9

Batejat, F., Conway, J. E., Hurley, R., et al. 2011, ApJ, 740, 95

Bayet, E., Gerin, M., Phillips, T. G., & Contursi, A. 2006, A&A, 460, 467

Bayet, E., Viti, S., Williams, D. A., & Rawlings, J. M. C. 2008, ApJ, 676, 978

Beelen, A., Cox, P., Benford, D. J., et al. 2006, ApJ, 642, 694

Beltrán, M. T., Codella, C., Viti, S., Neri, R., & Cesaroni, R. 2009, ApJL, 690, L93

Bertoldi, F., Menten, K. M., Kreysa, E., Carilli, C. L., & Owen, F. 2002, Highlights of Astronomy, 12, 473

Bertoldi, F., Carilli, C. L., Menten, K. M., et al. 2000, A&A, 360, 92

Best, P. N., Longair, M. S., & Roettgering, H. J. A. 1998, MNRAS, 295, 549

Bigiel, F., Leroy, A. K., Blitz, L., et al. 2015, ApJ, 815, 103

Bigiel, F., Leroy, A. K., Jiménez-Donaire, M. J., et al. 2016, ApJL, 822, L26

Blain, A. W. 1999, in Astronomical Society of the Pacific Conference Series, Vol. 191, Photometric Redshifts and the Detection of High Redshift Galaxies, ed. R. Weymann, L. Storrie-Lombardi, M. Sawicki, & R. Brunner, 255

Blain, A. W., & Longair, M. S. 1993, MNRAS, 264, 509

Blain, A. W., Smail, I., Ivison, R. J., Kneib, J.-P., & Frayer, D. T. 2002, Physics Reports, 369, 111

Blumenthal, G. R., Faber, S. M., Primack, J. R., & Rees, M. J. 1984, Nature, 311, 517

Boger, G. I., & Sternberg, A. 2005, ApJ, 632, 302

Bolatto, A. D., Wolfire, M., & Leroy, A. K. 2013, Ann. Rev. Astr. Astrophys., 51, 207

Bond, J. R., & Szalay, A. S. 1983, ApJ, 274, 443

Borys, C., Chapman, S., Halpern, M., & Scott, D. 2003, MNRAS, 344, 385

Bothwell, M. S., Maiolino, R., Cicone, C., Peng, Y., & Wagg, J. 2016, ArXiv e-prints, arXiv:1606.04102

Bothwell, M. S., Chapman, S. C., Tacconi, L., et al. 2010, MNRAS, 405, 219

Bothwell, M. S., Smail, I., Chapman, S. C., et al. 2013, MNRAS, 429, 3047

Bouwens, R., Aravena, M., Decarli, R., et al. 2016, ArXiv e-prints, arXiv:1606.05280

Brinch, C., & Hogerheijde, M. R. 2010, A&A, 523, A25

Brinchmann, J., Charlot, S., White, S. D. M., et al. 2004, MNRAS, 351, 1151

Brodwin, M., Dey, A., Brown, M. J. I., et al. 2008, ApJL, 687, L65

Buchner, J., Georgakakis, A., Nandra, K., et al. 2015, ApJ, 802, 89

Buckle, J. V., Hills, R. E., Smith, H., et al. 2009, MNRAS, 399, 1026

Calcutt, H., Viti, S., Codella, C., et al. 2014, MNRAS, 443, 3157

Capak, P. L., Riechers, D., Scoville, N. Z., et al. 2011, Nature, 470, 233

Carilli, C. L., Hodge, J., Walter, F., et al. 2011, ApJL, 739, L33

Carilli, C. L., Owen, F. N., & Harris, D. E. 1994, AJ, 107, 480

Carilli, C. L., Röttgering, H. J. A., van Ojik, R., et al. 1997, ApJSS, 109, 1

Carilli, C. L., & Walter, F. 2013, Ann. Rev. Astr. Astrophys., 51, 105

Carilli, C. L., Bertoldi, F., Rupen, M. P., et al. 2001, ApJ, 555, 625

Carilli, C. L., Solomon, P., Vanden Bout, P., et al. 2005, ApJ, 618, 586

Carilli, C. L., Daddi, E., Riechers, D., et al. 2010, ApJ, 714, 1407

Carrera, F. J., Page, M. J., Stevens, J. A., et al. 2011, MNRAS, 413, 2791

Casella, G., & George, E. I. 1992, The American Statistician, 46, 167

Caselli, P., Hasegawa, T. I., & Herbst, E. 1993, ApJ, 408, 548

Caselli, P., Walmsley, C. M., Zucconi, A., et al. 2002, ApJ, 565, 331

Casey, C. M., Narayanan, D., & Cooray, A. 2014, Physics Reports, 541, 45

Casey, C. M., Hodge, J. A., Lacy, M., et al. 2015, ArXiv e-prints, arXiv:1510.06411

Casoli, F., Dupraz, C., & Combes, F. 1992, A&A, 264, 55

Castor, J. I. 1970, MNRAS, 149, 111

Chapin, E. L., Berry, D. S., Gibb, A. G., et al. 2013, MNRAS, 430, 2545

Chapman, S. C., Blain, A. W., Smail, I., & Ivison, R. J. 2005, ApJ, 622, 772

Chernin, L. M., Masson, C. R., & Fuller, G. A. 1994, ApJ, 436, 741

Cheung, A. C., Rank, D. M., Townes, C. H., Thornton, D. D., & Welch, W. J. 1968, Physical Review Letters, 21, 1701

Chung, A., Narayanan, G., Yun, M. S., Heyer, M., & Erickson, N. R. 2009, AJ, 138, 858

Chyba, C. F., Thomas, P. J., Brookshaw, L., & Sagan, C. 1990, Science, 249, 366

Cicone, C., Maiolino, R., Sturm, E., et al. 2014, A&A, 562, A21

Combes, F. 2013, in Astronomical Society of the Pacific Conference Series, Vol. 476, New Trends in Radio Astronomy in the ALMA Era: The 30th Anniversary of Nobeyama Radio Observatory, ed. R. Kawabe, N. Kuno, & S. Yamamoto, 23

Condon, J. J., Cotton, W. D., Greisen, E. W., et al. 1998, AJ, 115, 1693

Coppin, K., Chapin, E. L., Mortier, A. M. J., et al. 2006, MNRAS, 372, 1621

Coppin, K., Pope, A., Menéndez-Delmestre, K., et al. 2010, ApJ, 713, 503

Costagliola, F., & Aalto, S. 2010, A&A, 515, A71

Costagliola, F., Aalto, S., Rodriguez, M. I., et al. 2011, A&A, 528, A30

Costagliola, F., Sakamoto, K., Muller, S., et al. 2015, ArXiv e-prints, arXiv:1506.09027

da Cunha, E., Walter, F., Decarli, R., et al. 2013, ApJ, 765, 9

da Cunha, E., Walter, F., Smail, I. R., et al. 2015, ApJ, 806, 110

Daddi, E., Dickinson, M., Morrison, G., et al. 2007, ApJ, 670, 156

Daddi, E., Dannerbauer, H., Stern, D., et al. 2009, ApJ, 694, 1517

Daddi, E., Bournaud, F., Walter, F., et al. 2010, ApJ, 713, 686

Dannerbauer, H., Kurk, J. D., De Breuck, C., et al. 2014, A&A, 570, A55

Davies, R., Mark, D., & Sternberg, A. 2012, A&A, 537, A133

Dayou, F., & Balança, C. 2006, A&A, 459, 297

De Breuck, C., van Breugel, W., Röttgering, H. J. A., & Miley, G. 2000, A&AS, 143, 303

De Breuck, C., Seymour, N., Stern, D., et al. 2010, ApJ, 725, 36

de Jong, T., Dalgarno, A., & Chu, S.-I. 1975, ApJ, 199, 69

Debuhr, J., Quataert, E., & Ma, C.-P. 2011, MNRAS, 412, 1341

Deguchi, S. 1981, ApJ, 249, 145

Dempsey, J. T., Friberg, P., Jenness, T., et al. 2013, MNRAS, 430, 2534

Dey, A., van Breugel, W., Vacca, W. D., & Antonucci, R. 1997, ApJ, 490, 698

Dopita, M. A., Groves, B. A., Fischera, J., et al. 2005, ApJ, 619, 755

Downes, D., & Eckart, A. 2007, A&A, 61, 2

Downes, D., & Solomon, P. M. 1998, ApJ, 507, 615

Dressler, A. 1980, ApJ, 236, 351

Drouart, G., De Breuck, C., Vernet, J., et al. 2014, A&A, 566, A53

Dumouchel, F., Faure, A., & Lique, F. 2010, MNRAS, 406, 2488

Eales, S., Lilly, S., Gear, W., et al. 1999, ApJ, 515, 518

Eales, S. A., Wynn-Williams, C. G., & Duncan, W. D. 1989, ApJ, 339, 859

Eastman, J., Martini, P., Sivakoff, G., et al. 2007, ApJL, 664, L9

Efstathiou, G. 2000, MNRAS, 317, 697

Egami, E., Neugebauer, G., Soifer, B. T., et al. 2000, ApJ, 535, 561

Elbaz, D., Daddi, E., Le Borgne, D., et al. 2007, A&A, 468, 33

Elbaz, D., Dickinson, M., Hwang, H. S., et al. 2011, A&A, 533, A119

Ellis, R. S., McLure, R. J., Dunlop, J. S., et al. 2013, ApJL, 763, L7

Emerson, J. P., Clegg, P. E., Gee, G., et al. 1984, Nature, 311, 237

Engel, H., Davies, R. I., Genzel, R., et al. 2011, ApJ, 729, 58

Engel, H., Tacconi, L. J., Davies, R. I., et al. 2010, ApJ, 724, 233

Fabian, A. C. 2012, Ann. Rev. Astr. Astrophys., 50, 455

Fanaroff, B. L., & Riley, J. M. 1974, MNRAS, 167, 31P

Fedoseev, G., Cuppen, H. M., Ioppolo, S., Lamberts, T., & Linnartz, H. 2015, MNRAS, 448, 1288

Feroz, F., Hobson, M. P., Cameron, E., & Pettitt, A. N. 2013, ArXiv e-prints, arXiv:1306.2144

Ferrarese, L., & Merritt, D. 2000, ApJL, 539, L9

Feruglio, C., Fiore, F., Maiolino, R., et al. 2013, A&A, 549, A51

Fischer, J., Satyapal, S., Luhman, M. L., et al. 1997, in ESA Special Publication, Vol. 419, The first ISO workshop on Analytical Spectroscopy, ed. A. M. Heras, K. Leech, N. R. Trams, & M. Perry, 149

Flower, D. R. 1999, MNRAS, 305, 651

Fuente, A., García-Burillo, S., Gerin, M., et al. 2005, ApJL, 619, L155

Fuente, A., Martin-Pintado, J., & Gaume, R. 1995, ApJL, 442, L33

Gaibler, V., Khochfar, S., Krause, M., & Silk, J. 2012, MNRAS, 425, 438

Galametz, A., Stern, D., De Breuck, C., et al. 2012, ApJ, 749, 169

Gao, Y., Carilli, C. L., Solomon, P. M., & Vanden Bout, P. A. 2007, ApJL, 660, L93

Gao, Y., & Solomon, P. M. 2004a, ApJSS, 152, 63

—. 2004b, ApJSS, 152, 63

Gao, Y., & Solomon, P. M. 2004, ApJ, 606, 271

García-Burillo, S., Martín-Pintado, J., Fuente, A., & Neri, R. 2000, A&A, 355, 499

García-Burillo, S., Martín-Pintado, J., Fuente, A., & Neri, R. 2001, ApJL, 563, L27

García-Burillo, S., Usero, A., Alonso-Herrero, A., et al. 2012, A&A, 539, A8

García-Burillo, S., Combes, F., Hunt, L. K., et al. 2003, A&A, 407, 485

García-Burillo, S., Graciá-Carpio, J., Guélin, M., et al. 2006, ApJL, 645, L17

García-Burillo, S., Usero, A., Fuente, A., et al. 2010, A&A, 519, A2

García-Burillo, S., Combes, F., Usero, A., et al. 2014, A&A, 567, A125

Geach, J. E., Smail, I., Moran, S. M., et al. 2011, ApJL, 730, L19

Genzel, R., Tacconi, L. J., Gracia-Carpio, J., et al. 2010, MNRAS, 407, 2091

Gilman, R. C. 1969, ApJL, 155, L185

Ginsburg, A., Walsh, A., Henkel, C., et al. 2015, A&A, 584, L7

Goldreich, P., & Scoville, N. 1976, ApJ, 205, 144

Goldsmith, P. F., & Langer, W. D. 1999, ApJ, 517, 209

González-Alfonso, E., Fischer, J., Sturm, E., et al. 2012, A&A, 541, A4

González-Alfonso, E., Smith, H. A., Fischer, J., & Cernicharo, J. 2004, ApJ, 613, 247

González-Alfonso, E., Fischer, J., Bruderer, S., et al. 2013a, A&A, 550, A25

—. 2013b, A&A, 550, A25

Gordy, W., & Cook, R. L. 1984, Microwave molecular spectra (Intersciencs Publishers)

Görür, D., & Teh, Y. W. 2011, Journal of Computational and Graphical Statistics, 20, 670

Graciá-Carpio, J., García-Burillo, S., & Planesas, P. 2008a, Ap&SS, 313, 331

Graciá-Carpio, J., García-Burillo, S., Planesas, P., Fuente, A., & Usero, A. 2008b, A&A, 479, 703

Greaves, J. S., & Church, S. E. 1996, MNRAS, 283, 1179

Green, S., & Thaddeus, P. 1974, ApJ, 191, 653

Greve, T. R., Hainline, L. J., Blain, A. W., et al. 2006, AJ, 132, 1938

Greve, T. R., Ivison, R. J., Bertoldi, F., et al. 2004, MNRAS, 354, 779

Greve, T. R., Papadopoulos, P. P., Gao, Y., & Radford, S. J. E. 2009, ApJ, 692, 1432

Greve, T. R., Leonidaki, I., Xilouris, E. M., et al. 2014, ApJ, 794, 142

Gueth, F., Guilloteau, S., & Bachiller, R. 1998, A&A, 333, 287

Guillet, V., Jones, A. P., & Pineau Des Forêts, G. 2009, A&A, 497, 145

Guilloteau, S., & Lucas, R. 2000, in PASP Conf. Ser., Vol. 217, Imaging at Radio through Submillimeter Wavelengths, ed. J. G. Mangum & S. J. E. Radford, 299

Gültekin, K., Richstone, D. O., Gebhardt, K., et al. 2009, ApJ, 698, 198

Hackwell, J. A., Gerhz, R. D., & Woolf, N. J. 1970, Nature, 227, 822

Hagiwara, Y., Baan, W. A., & Klöckner, H.-R. 2011, AJ, 142, 17

Hanson, K. M. 2001, in Medical Imaging 2001, International Society for Optics and Photonics, 456–467

Harada, N., Herbst, E., & Wakelam, V. 2010, ApJ, 721, 1570

Harada, N., Thompson, T. A., & Herbst, E. 2013, ApJ, 765, 108

Hardcastle, M. J., Ching, J. H. Y., Virdee, J. S., et al. 2013, MNRAS, 429, 2407

Harris, G. J., Larner, F. C., Tennyson, J., et al. 2008, MNRAS, 390, 143

Harrison, C. M., Alexander, D. M., Mullaney, J. R., & Swinbank, A. M. 2014, MNRAS, 441, 3306

Hastings, W. K. 1970, Biometrika, 57, 97

Hayward, C. C., Kereš, D., Jonsson, P., et al. 2011, ApJ, 743, 159

Heavens, A., Panter, B., Jimenez, R., & Dunlop, J. 2004, Nature, 428, 625

Henkel, C., Downes, D., Weiß, A., Riechers, D., & Walter, F. 2010, A&A, 516, A111

Henkel, C., Asiri, H., Ao, Y., et al. 2014, A&A, 565, A3

Herbert, P. D., Jarvis, M. J., Willott, C. J., et al. 2010, MNRAS, 406, 1841

—. 2011, MNRAS, 410, 1360

Hodge, J. A., Carilli, C. L., Walter, F., et al. 2012, ApJ, 760, 11

Högbom, J. A. 1974, A&AS, 15, 417

Hogerheijde, M., & van der Tak, F. 2000, RATRAN: Radiative Transfer and Molecular Excitation in One and Two Dimensions, Astrophysics Source Code Library, ascl:0008.002

Holland, W. S., Bintley, D., Chapin, E. L., et al. 2013, MNRAS, 430, 2513

Hopkins, P. F., Hernquist, L., Cox, T. J., et al. 2005, ApJ, 630, 705

—. 2006, ApJSS, 163, 1

Hughes, D. H., Serjeant, S., Dunlop, J., et al. 1998, Nature, 394, 241

Hwang, H. S., Elbaz, D., Dickinson, M., et al. 2011, A&A, 535, A60

Imanishi, M., Dudley, C. C., Maiolino, R., et al. 2007a, ApJSS, 171, 72

Imanishi, M., Nakanishi, K., & Izumi, T. 2016, ArXiv e-prints, arXiv:1605.00644

Imanishi, M., Nakanishi, K., & Kohno, K. 2006, AJ, 131, 2888

Imanishi, M., Nakanishi, K., Tamura, Y., Oi, N., & Kohno, K. 2007b, AJ, 134, 2366

Imanishi, M., Nakanishi, K., Tamura, Y., & Peng, C.-H. 2009, AJ, 137, 3581

Intema, H. T., Venemans, B. P., Kurk, J. D., et al. 2006, A&A, 456, 433

Iono, D., Wilson, C. D., Takakuwa, S., et al. 2007, ApJ, 659, 283

Isaak, K. G., Chandler, C. J., & Carilli, C. L. 2004, MNRAS, 348, 1035

Ivison, R. J., Dunlop, J. S., Smail, I., et al. 2000, ApJ, 542, 27

Ivison, R. J., Papadopoulos, P. P., Smail, I., et al. 2011, MNRAS, 412, 1913

Izumi, T., Kohno, K., Martín, S., et al. 2013, PASJ, 65, 100

Izumi, T., Kohno, K., Aalto, S., et al. 2016a, ApJ, 818, 42

—. 2016b, ApJ, 818, 42

Jackson, J. M., Paglione, T. A. D., Ishizuki, S., & Nguyen-Q-Rieu. 1993, ApJL, 418, L13

Jarrett, T. H., Cohen, M., Masci, F., et al. 2011, ApJ, 735, 112

Jarvis, M. J., Rawlings, S., Eales, S., et al. 2001, MNRAS, 326, 1585

Jennings, D. A., Evenson, K. M., Zink, L. R., et al. 1987, Journal of Molecular Spectroscopy, 122, 477

Jiménez-Serra, I., Caselli, P., Tan, J. C., et al. 2010, MNRAS, 406, 187

Jones, P. A., Burton, M. G., Cunningham, M. R., et al. 2012, MNRAS, 419, 2961

Jones, S. F., Blain, A. W., Lonsdale, C., et al. 2015, MNRAS, 448, 3325

Juneau, S., Dickinson, M., Alexander, D. M., & Salim, S. 2011, ApJ, 736, 104

Juneau, S., Bournaud, F., Charlot, S., et al. 2014, ApJ, 788, 88

Kamenetzky, J., Rangwala, N., Glenn, J., Maloney, P. R., & Conley, A. 2014, ApJ, 795, 174

—. 2015, ArXiv e-prints, arXiv:1508.05102

Kamenetzky, J., Glenn, J., Maloney, P. R., et al. 2011, ApJ, 731, 83

Kamijo, F. 1963, PASJ, 15, 440

Kampakoglou, M., Trotta, R., & Silk, J. 2008, MNRAS, 384, 1414

Kapahi, V. K., & Kulkarni, V. K. 1990, AJ, 99, 1397

Karim, A., Schinnerer, E., Martínez-Sansigre, A., et al. 2011, ApJ, 730, 61

Karim, A., Swinbank, A. M., Hodge, J. A., et al. 2013, MNRAS, 432, 2

Kartaltepe, J. S., Dickinson, M., Alexander, D. M., et al. 2012, ApJ, 757, 23

Kauffmann, G., Li, C., Fu, J., et al. 2012, MNRAS, 422, 997

Kennicutt, Jr., R. C. 1989, ApJ, 344, 685

Kepley, A. A., Leroy, A. K., Frayer, D., et al. 2014, ApJL, 780, L13

Keto, E., Caselli, P., & Rawlings, J. 2015, MNRAS, 446, 3731

Kewley, L. J., Groves, B., Kauffmann, G., & Heckman, T. 2006, MNRAS, 372, 961

Kewley, L. J., Maier, C., Yabe, K., et al. 2013, ApJL, 774, L10

Kewley, L. J., Zahid, H. J., Geller, M. J., et al. 2015, ApJL, 812, L20

Kim, D.-C. 1995, PhD thesis, University of Hawaii

Kirkpatrick, A., Pope, A., Sajina, A., et al. 2015, ApJ, 814, 9

Kirkpatrick, A., Pope, A., Alexander, D. M., et al. 2012, ApJ, 759, 139

Knacke, R. F., Gaustad, J. E., Gillett, F. C., & Stein, W. A. 1969, ApJL, 155, L189

Knudsen, K. K., van der Werf, P. P., & Kneib, J.-P. 2008, MNRAS, 384, 1611

Kohno, K. 2003, in Astronomical Society of the Pacific Conference Series, Vol. 289, The Proceedings of the IAU 8th Asian-Pacific Regional Meeting, Volume 1, ed. S. Ikeuchi, J. Hearnshaw, & T. Hanawa, 349–352

Kohno, K. 2005, in American Institute of Physics Conference Series, Vol. 783, The Evolution of Starbursts, ed. S. Hüttmeister, E. Manthey, D. Bomans, & K. Weis, 203–208

Kohno, K., Matsushita, S., Vila-Vilaró, B., et al. 2001, in Astronomical Society of the Pacific Conference Series, Vol. 249, The Central Kiloparsec of Starbursts and AGN: The La Palma Connection, ed. J. H. Knapen, J. E. Beckman, I. Shlosman, & T. J. Mahoney, 672

Komossa, S., Burwitz, V., Hasinger, G., et al. 2003, ApJL, 582, L15

Kramer, C., Alves, J., Lada, C. J., et al. 1999, A&A, 342, 257

Krips, M., Neri, R., García-Burillo, S., et al. 2008, ApJ, 677, 262

Kurk, J. D., Röttgering, H. J. A., Pentericci, L., et al. 2000, A&A, 358, L1

Lacey, C., & Cole, S. 1993, MNRAS, 262, 627

Lacy, M., Storrie-Lombardi, L. J., Sajina, A., et al. 2004, ApJSS, 154, 166

Lada, E. A. 1992, ApJL, 393, L25

Langer, W. D., Graedel, T. E., Frerking, M. A., & Armentrout, P. B. 1984, ApJ, 277, 581

Langer, W. D., & Penzias, A. A. 1993, ApJ, 408, 539

Langer, W. D., Wilson, R. W., Henry, P. S., & Guelin, M. 1978, ApJL, 225, L139

Larson, K. L., Sanders, D. B., Barnes, J. E., et al. 2016, ArXiv e-prints, arXiv:1605.05417

Leroy, A. K., Walter, F., Sandstrom, K., et al. 2013, AJ, 146, 19

Leroy, A. K., Murphy, E., Armus, L., et al. 2015, ArXiv e-prints, arXiv:1510.06431

Li, C., & White, S. D. M. 2009, MNRAS, 398, 2177

Link, W. A., Cam, E., Nichols, J. D., & Cooch, E. G. 2002, The Journal of Wildlife Management, 66, 277

Lintott, C., & Viti, S. 2006, ApJL, 646, L37

Lique, F., Spielfiedel, A., & Cernicharo, J. 2006, A&A, 451, 1125

Liu, D., Gao, Y., Isaak, K., et al. 2015a, ApJL, 810, L14

Liu, H. B., Galván-Madrid, R., Jiménez-Serra, I., et al. 2015b, ApJ, 804, 37

Liu, T., Wu, Y., & Zhang, H. 2013, ApJL, 775, L2

Loison, J.-C., Wakelam, V., & Hickson, K. M. 2014, MNRAS, 443, 398

Lonsdale, C. J., Farrah, D., & Smith, H. E. 2006, Ultraluminous Infrared Galaxies (Springer Praxis Books), 285

Lonsdale, C. J., Smith, H. E., Rowan-Robinson, M., et al. 2003, PASP, 115, 897

Lutz, D., Sturm, E., Genzel, R., et al. 2003, A&A, 409, 867

Madau, P. 1997, in American Institute of Physics Conference Series, Vol. 393, American Institute of Physics Conference Series, ed. S. S. Holt & L. G. Mundy, 481–490

Madau, P., Ferguson, H. C., Dickinson, M. E., et al. 1996, MNRAS, 283, 1388

Madau, P., Pozzetti, L., & Dickinson, M. 1998, ApJ, 498, 106

Magdis, G. E., Rigopoulou, D., Hopwood, R., et al. 2014, ApJ, 796, 63

Magorrian, J., Tremaine, S., Richstone, D., et al. 1998, AJ, 115, 2285

Maloney, P. R., Hollenbach, D. J., & Tielens, A. G. G. M. 1996, ApJ, 466, 561

Mangum, J. G., Darling, J., Henkel, C., et al. 2013, ApJ, 779, 33

Mannucci, F., Cresci, G., Maiolino, R., Marconi, A., & Gnerucci, A. 2010, MNRAS, 408, 2115

Martín, S., Krips, M., Martín-Pintado, J., et al. 2011, A&A, 527, A36

Martín, S., Kohno, K., Izumi, T., et al. 2015, A&A, 573, A116

Martín, S., Aalto, S., Sakamoto, K., et al. 2016, A&A, 590, A25

Martin-Pintado, J. 1992, A&A, 254, 315

Matsushita, S., Iono, D., Petitpas, G. R., et al. 2009, ApJ, 693, 56

Mayo, J. H., Vernet, J., De Breuck, C., et al. 2012, A&A, 539, A33

McConnell, N. J., & Ma, C.-P. 2013, ApJ, 764, 184

McDowell, J. C., Clements, D., Lamb, S., et al. 2003, ApJ, 591, 154

McKellar, A. 1940, PASP, 52, 187

McMullin, J. P., Waters, B., Schiebel, D., Young, W., & Golap, K. 2007, in Astronomical Society of the Pacific Conference Series, Vol. 376, Astronomical Data Analysis Software and Systems XVI, ed. R. A. Shaw, F. Hill, & D. J. Bell, 127

Meier, D. S., & Turner, J. L. 2005, ApJ, 618, 259

—. 2012, ApJ, 755, 104

Meier, D. S., Walter, F., Bolatto, A. D., et al. 2015, ApJ, 801, 63

Meijerink, R., & Spaans, M. 2005, A&A, 436, 397

Meijerink, R., Spaans, M., & Israel, F. P. 2006, ApJL, 650, L103

—. 2007, A&A, 461, 793

Meijerink, R., Spaans, M., Loenen, A. F., & van der Werf, P. P. 2011, A&A, 525, A119

Meijerink, R., Kristensen, L. E., Weiß, A., et al. 2013, ApJL, 762, L16

Mendez, A. J., Coil, A. L., Aird, J., et al. 2013, ApJ, 770, 40

Menéndez-Delmestre, K., Blain, A. W., Swinbank, M., et al. 2013, ApJ, 767, 151

Metropolis, N., Rosenbluth, A. W., Rosenbluth, M. N., Teller, A. H., & Teller, E. 1953, J. Chem. Phys., 21, 1087

Milam, S. N., Savage, C., Brewster, M. A., Ziurys, L. M., & Wyckoff, S. 2005, ApJ, 634, 1126

Miley, G. 1980, Ann. Rev. Astr. Astrophys., 18, 165

Miley, G., & De Breuck, C. 2008, A&A Rev., 15, 67

Mitchell, G. F. 1984, ApJSS, 54, 81

Müller, H. S., Schlöder, F., Stutzki, J., & Winnewisser, G. 2005, Journal of Molecular Structure, 742, 215

Mundell, C., Ferruit, P., & Pedlar, A. 2001, ApJ, 560, 168

Murphy, E. J., Chary, R.-R., Dickinson, M., et al. 2011, ApJ, 732, 126

Nakanishi, K., Okumura, S. K., Kohno, K., Kawabe, R., & Nakagawa, T. 2005, PASJ, 57, 575

Narayanan, D., Cox, T. J., Hayward, C. C., Younger, J. D., & Hernquist, L. 2009, MNRAS, 400, 1919

Narayanan, D., Hayward, C. C., Cox, T. J., et al. 2010, MNRAS, 401, 1613

Narayanan, D., & Krumholz, M. R. 2014, MNRAS, 442, 1411

Nguyen, Q.-R., Jackson, J. M., Henkel, C., Truong, B., & Mauersberger, R. 1992, ApJ, 399, 521

Noeske, K. G., Weiner, B. J., Faber, S. M., et al. 2007, ApJL, 660, L43

Olsen, K. P., Greve, T. R., Narayanan, D., et al. 2015, ArXiv e-prints, arXiv:1507.00362

Osterbrock, D. E., & Ferland, G. J. 2006, Astrophysics of gaseous nebulae and active galactic nuclei (University Science Books)

Papadopoulos, P. P. 2007, ApJ, 656, 792

Papadopoulos, P. P., Isaak, K., & van der Werf, P. 2010a, ApJ, 711, 757

—. 2010b, ApJ, 711, 757

Papadopoulos, P. P., Röttgering, H. J. A., van der Werf, P. P., et al. 2000, ApJ, 528, 626

Papadopoulos, P. P., Thi, W.-F., Miniati, F., & Viti, S. 2011, MNRAS, 414, 1705

Papadopoulos, P. P., van der Werf, P., Isaak, K., & Xilouris, E. M. 2010c, ApJ, 715, 775

Papadopoulos, P. P., van der Werf, P., Xilouris, E., Isaak, K. G., & Gao, Y. 2012, ApJ, 751, 10

Papadopoulos, P. P., Zhang, Z.-Y., Xilouris, E. M., et al. 2014, ApJ, 788, 153

Peebles, P. J. E. 1982, ApJL, 263, L1

Peng, Y.-j., Lilly, S. J., Kovač, K., et al. 2010, ApJ, 721, 193

Pentericci, G. K., & Venemans, B. P., L. M. 2007, in Astronomical Society of the Pacific Conference Series, Vol. 380, Deepest Astronomical Surveys, ed. J. Afonso, H. C. Ferguson, B. Mobasher, & R. Norris, 219

Pentericci, L., Van Reeven, W., Carilli, C. L., Röttgering, H. J. A., & Miley, G. K. 2000, A&AS, 145, 121

Pérez-González, P. G., Rieke, G. H., Villar, V., et al. 2008, ApJ, 675, 234

Peters, T., Longmore, S. N., & Dullemond, C. P. 2012, MNRAS, 425, 2352

Planck Collaboration, Ade, P. A. R., Aghanim, N., et al. 2014, A&A, 571, A16

Pope, A., Borys, C., Scott, D., et al. 2005, MNRAS, 358, 149

Pope, A., Chary, R.-R., Alexander, D. M., et al. 2008, ApJ, 675, 1171

Rangwala, N., Maloney, P. R., Glenn, J., et al. 2011, ApJ, 743, 94

Reddy, N. A., & Steidel, C. C. 2009, ApJ, 692, 778

Remijan, A. J., Markwick-Kemper, A., & ALMA Working Group on Spectral Line Frequencies. 2007, in Bulletin of the American Astronomical Society, Vol. 39, American Astronomical Society Meeting Abstracts, 132.11

Reuland, M., Röttgering, H., van Breugel, W., & De Breuck, C. 2004, MNRAS, 353, 377

Riechers, D. A., Walter, F., Carilli, C. L., & Bertoldi, F. 2007, ApJL, 671, L13

Riechers, D. A., Walter, F., Carilli, C. L., et al. 2006, ApJ, 650, 604

Riffel, R. A., & Storchi-Bergmann, T. 2011, MNRAS, 417, 2752

Rigby, E. E., Best, P. N., & Snellen, I. A. G. 2008, MNRAS, 385, 310

Rigby, E. E., Snellen, I. A. G., & Best, P. N. 2007, MNRAS, 380, 1449

Rigby, E. E., Hatch, N. A., Röttgering, H. J. A., et al. 2014, MNRAS, 437, 1882

Ripple, F., Heyer, M. H., Gutermuth, R., Snell, R. L., & Brunt, C. M. 2013, MNRAS, 431, 1296

Ritchey, A. M., Federman, S. R., & Lambert, D. L. 2011, ApJ, 728, 36

Rocca-Volmerange, B., Le Borgne, D., De Breuck, C., Fioc, M., & Moy, E. 2004, A&A, 415, 931

Rocca-Volmerange, B., Drouart, G., De Breuck, C., et al. 2013, MNRAS, 429, 2780

Rodighiero, G., Daddi, E., Baronchelli, I., et al. 2011, ApJL, 739, L40

Rodríguez Zaurín, J., Tadhunter, C. N., González Delgado, R. M., & Zaurín, J. R. 2008, MNRAS, 384, 875

Rosenberg, M. J. F., van der Werf, P. P., Aalto, S., et al. 2015, ApJ, 801, 72

Rosenbrock, H. H. 1960, The Computer Journal, 3, 175

Roueff, E., Loison, J. C., & Hickson, K. M. 2015, A&A, 576, A99

Rydbeck, O. E. H., Ellder, J., Sume, A., Hjalmarson, A., & Irvine, W. M. 1974, A&A, 34, 479

Saintonge, A., Kauffmann, G., Kramer, C., et al. 2011a, MNRAS, 415, 32

Saintonge, A., Kauffmann, G., Wang, J., et al. 2011b, MNRAS, 415, 61

Saintonge, A., Lutz, D., Genzel, R., et al. 2013, ApJ, 778, 2

Sajina, A., Yan, L., Armus, L., et al. 2007, ApJ, 664, 713

Sakamoto, K., Aalto, S., Evans, A. S., Wiedner, M. C., & Wilner, D. J. 2010, ApJL, 725, L228

Sakamoto, K., & Scoville, N. 1999, ApJ, 20, 68

Sakamoto, K., Wang, J., Wiedner, M. C., et al. 2008, ApJ, 684, 957

Sakamoto, K., Aalto, S., Wilner, D. J., et al. 2009, ApJ, 700, L104

Salim, S., Rich, R. M., Charlot, S., et al. 2007, ApJSS, 173, 267

Salter, C. J., Ghosh, T., Catinella, B., et al. 2008, AJ, 136, 389

Sanders, D. B., Mazzarella, J. M., Kim, D.-C., Surace, J. A., & Soifer, B. T. 2003, AJ, 126, 1607

Sanders, D. B., & Mirabel, I. F. 1996, Ann. Rev. Astr. Astrophys., 34, 749

Sanders, D. B., Scoville, N. Z., & Soifer, B. T. 1991, ApJ, 370, 158

Schiminovich, D., Ilbert, O., Arnouts, S., et al. 2005, ApJL, 619, L47

Schiminovich, D., Wyder, T. K., Martin, D. C., et al. 2007, ApJSS, 173, 315

Schmidt, M., & Green, R. F. 1983, ApJ, 269, 352

Schuster, K.-F., Boucher, C., Brunswig, W., et al. 2004, A&A, 423, 1171

Scott, S. E., Dunlop, J. S., & Serjeant, S. 2006, MNRAS, 370, 1057

Scott, S. E., Fox, M. J., Dunlop, J. S., et al. 2002, MNRAS, 331, 817

Scoville, N., Yun, M., & Bryant, P. 1997, ApJ, 484, 702

Scoville, N., Sheth, K., Walter, F., et al. 2015, ApJ, 800, 70

Scoville, N. Z., Sargent, A. I., Sanders, D. B., & Soifer, B. T. 1991, ApJL, 366, L5

Scoville, N. Z., & Solomon, P. M. 1974, ApJL, 187, L67

Secrest, N. J., Dudik, R. P., Dorland, B. N., et al. 2015, ApJSS, 221, 12

Seymour, N., Stern, D., De Breuck, C., et al. 2007, ApJSS, 171, 353

Seymour, N., Altieri, B., De Breuck, C., et al. 2012, ApJ, 755, 146

Shirley, Y. L. 2015, ArXiv e-prints, arXiv:1501.01629

Silk, J. 1977, ApJ, 211, 638

Silk, J., & Mamon, G. A. 2012, Research in Astronomy and Astrophysics, 12, 917

Silk, J., & Rees, M. J. 1998, A&A, 331, L1

Smail, I., Ivison, R. J., & Blain, A. W. 1997, ApJL, 490, L5

Smail, I., Ivison, R. J., Gilbank, D. G., et al. 2003, ApJ, 583, 551

Sobolev, V. V. 1960, Moving envelopes of stars (Cambridge: Harvard University Press)

Soifer, B. T., Helou, G., Lonsdale, C. J., et al. 1984, in Bulletin of the American Astronomical Society, Vol. 16, Bulletin of the American Astronomical Society, 470

Soifer, B. T., Neugebauer, G., & Houck, J. R. 1987a, Ann. Rev. Astr. Astrophys., 25, 187

Soifer, B. T., Neugebauer, G., Matthews, K., et al. 1999, ApJ, 513, 207

Soifer, B. T., Sanders, D. B., Madore, B. F., et al. 1987b, ApJ, 320, 238

Soifer, B. T., Neugebauer, G., Matthews, K., et al. 2000, AJ, 119, 509

Solomon, P. M., Downes, D., & Radford, S. J. E. 1992, ApJL, 398, L29

Solomon, P. M., Downes, D., Radford, S. J. E., & Barrett, J. W. 1997, ApJ, 478, 144

Solomon, P. M., Rivolo, A. R., Barrett, J., & Yahil, A. 1987, ApJ, 319, 730

Solomon, P. M., & Sage, L. J. 1988, ApJ, 334, 613

Solomon, P. M., & Vanden Bout, P. A. 2005, Ann. Rev. Astr. Astrophys., 43, 677

Spoon, H. W. W., Marshall, J. A., Houck, J. R., et al. 2007, ApJL, 654, L49

Stern, D., Eisenhardt, P., Gorjian, V., et al. 2005, ApJ, 631, 163

Sternberg, A., Genzel, R., & Tacconi, L. 1994, ApJL, 436, L131

Stevens, J. A., Jarvis, M. J., Coppin, K. E. K., et al. 2010, MNRAS, 405, 2623

Stevens, J. A., Ivison, R. J., Dunlop, J. S., et al. 2003, Nature, 425, 264

Swinbank, A. M., Bower, R. G., Smith, G. P., et al. 2006, MNRAS, 368, 1631

Swings, P., & Rosenfeld, L. 1937, ApJ, 86, 483

Szűcs, L., Glover, S. C. O., & Klessen, R. S. 2014, MNRAS, 445, 4055

Tacconi, L. J., Genzel, R., Blietz, M., et al. 1994, ApJL, 426, 77

Tacconi, L. J., Genzel, R., Tecza, M., et al. 1999, ApJ, 524, 732

Tacconi, L. J., & Young, J. S. 1987, ApJ, 322, 681

Tacconi, L. J., Neri, R., Chapman, S. C., et al. 2006, ApJ, 640, 228

Tacconi, L. J., Genzel, R., Smail, I., et al. 2008, ApJ, 680, 246

Tacconi, L. J., Genzel, R., Neri, R., et al. 2010, Nature, 463, 781

Tacconi, L. J., Neri, R., Genzel, R., et al. 2013, ApJ, 768, 74

Tafalla, M., Myers, P. C., Caselli, P., Walmsley, C. M., & Comito, C. 2002, ApJ, 569, 815

Tecza, M., Genzel, R., Tacconi, L. J., et al. 2000, ApJ, 537, 178

Tennyson, J. 2003, Molecules in Space, Vol. 3 (John Wiley & Sons)

Tennyson, J., & Yurchenko, S. N. 2012, MNRAS, 425, 21

Thronson, H., & Shull, J., eds. 1990, The Interstellar Medium in Galaxies, Vol. 161 (Springer)

Tielens, A. G. G. M., & Hollenbach, D. 1985, ApJ, 291, 722

Toft, S., Smolčić, V., Magnelli, B., et al. 2014, ApJ, 782, 68

Tremaine, S., Gebhardt, K., Bender, R., et al. 2002, ApJ, 574, 740

Trouille, L., Barger, A. J., & Tremonti, C. 2011, ApJ, 742, 46

Tsuboi, M., Miyazaki, A., & Uehara, K. 2015, PASJ, 67, 90

Tunnard, R., & Greve, T. R. 2016, ApJ, 819, 161

Tunnard, R., Greve, T. R., Garcia-Burillo, S., et al. 2015a, ApJ, 815, 114

—. 2015b, ApJ, 800, 25

Usero, A., García-Burillo, S., Fuente, A., Martín-Pintado, J., & Rodríguez-Fernández, N. J. 2004, A&A, 419, 897

Usero, A., García-Burillo, S., Martín-Pintado, J., Fuente, A., & Neri, R. 2006, A&A, 448, 457

Usero, A., Leroy, A. K., Walter, F., et al. 2015, AJ, 150, 115

van Breugel, W. J. M., Stanford, S. A., Spinrad, H., Stern, D., & Graham, J. R. 1998, ApJ, 502, 614

van der Tak, F. F. S., Black, J. H., Schöier, F. L., Jansen, D. J., & van Dishoeck, E. F. 2007, A&A, 468, 627

van der Werf, P. P., Isaak, K., Meijerink, R., et al. 2010, Astronomy & Astrophysics, 518, L42

Vázquez-Semadeni, E., Ballesteros-Paredes, J., & Rodríguez, L. F. 1997, ApJ, 474, 292

Veilleux, S., Rupke, D. S. N., Kim, D.-C., et al. 2009, ApJSS, 182, 628

Venemans, B. P., Kurk, J. D., Miley, G. K., et al. 2002, ApJL, 569, L11

Venemans, B. P., Röttgering, H. J. A., Overzier, R. A., et al. 2004, A&A, 424, L17

Venemans, B. P., Röttgering, H. J. A., Miley, G. K., et al. 2005, A&A, 431, 793

—. 2007, A&A, 461, 823

Véron-Cetty, M.-P., & Véron, P. 2006, A&A, 455, 773

Viero, M. P., Ade, P. A. R., Bock, J. J., et al. 2009, ApJ, 707, 1766

Viti, S., Natarajan, S., & Williams, D. A. 2002, MNRAS, 336, 797

Viti, S., García-Burillo, S., Fuente, A., et al. 2014, A&A, 570, A28

W. R. Gilks, P. W. 1992, Journal of the Royal Statistical Society. Series C (Applied Statistics), 41, 337

Wagg, J., Wilner, D. J., Neri, R., Downes, D., & Wiklind, T. 2005, ApJL, 634, L13

Wang, J., Zhang, J., Shi, Y., & Zhang, Z. 2013, ApJL, 778, L39

Wang, J., Zhang, Z., & Shi, Y. 2011, MNRASL, 416, L21

Wang, J., Nardini, E., Fabbiano, G., et al. 2014, ApJ, 781, 55

Ward, J. S., Zmuidzinas, J., Harris, A. I., & Isaak, K. G. 2003, ApJ, 587, 171

Watson, W. D., Anicich, V. G., & Huntress, Jr., W. T. 1976, ApJL, 205, L165

Weaver, H., Dieter, N. H., & Williams, D. R. W. 1968, ApJSS, 16, 219

Weaver, H., Williams, D. R. W., Dieter, N. H., & Lum, W. T. 1965, Nature, 208, 29

Weinreb, S., Meeks, M. L., & Carter, J. C. 1965, Nature, 208, 440

Weiß, A., Downes, D., Neri, R., et al. 2007, A&A, 467, 955

Weiß, A., Walter, F., & Scoville, N. Z. 2005, A&A, 438, 533

Weiß, A., Kovács, A., Coppin, K., et al. 2009, ApJ, 707, 1201

Weiß, A., De Breuck, C., Marrone, D. P., et al. 2013, ApJ, 767, 88

White, R. L., & Becker, R. H. 1992, ApJSS, 79, 331

White, R. L., Becker, R. H., Gregg, M. D., et al. 2000, ApJSS, 126, 133

Widmann, F., Beuther, H., Schilke, P., & Stanke, T. 2016, A&A, 589, A29

Williams, D. A., & Viti, S. 2013a, Observational Molecular Astronomy (CUP)

—. 2013b, Observational Molecular Astronomy (Cambridge University Press)

Willott, C. J., Rawlings, S., Jarvis, M. J., & Blundell, K. M. 2003, MNRAS, 339, 173

Wilson, C. D., Harris, W. E., Longden, R., & Scoville, N. Z. 2006, ApJ, 641, 763

Wilson, C. D., Rangwala, N., Glenn, J., et al. 2014, ApJ, arXiv:in press

Wilson, R. W., Jefferts, K. B., & Penzias, A. A. 1970, ApJL, 161, L43

Wilson, T. L., Rohlfs, K., & Hüttemeister, S. 2009, Tools of Radio Astronomy (Springer-Verlag), doi:10.1007/978-3-540-85122-6

Wright, E. L. 2006a, PASP, 118, 1711

—. 2006b, PASP, 118, 1711

Wright, E. L., Eisenhardt, P. R. M., Mainzer, A. K., et al. 2010, AJ, 140, 1868

Wu, J., Evans, II, N. J., Gao, Y., et al. 2005, ApJL, 635, L173

Wu, J., Evans, II, N. J., Shirley, Y. L., & Knez, C. 2010, ApJSS, 188, 313

Wylezalek, D., Galametz, A., Stern, D., et al. 2013a, ApJ, 769, 79

Wylezalek, D., Vernet, J., De Breuck, C., et al. 2013b, MNRAS, 428, 3206

Xue, Y. Q., Brandt, W. N., Luo, B., et al. 2010, ApJ, 720, 368

Yamada, M., Wada, K., & Tomisaka, K. 2007, ApJ, 671, 73

Yan, R., Ho, L. C., Newman, J. A., et al. 2011, ApJ, 728, 38

Yang, B., Stancil, P. C., Balakrishnan, N., & Forrey, R. C. 2010, ApJ, 718, 1062

Young, J. S., Kenney, J., Lord, S. D., & Schloerb, F. P. 1984, ApJL, 287, L65

Yun, M. S., & Carilli, C. L. 2002, ApJ, 568, 88

Yun, M. S., Reddy, N. A., & Condon, J. J. 2001, ApJ, 554, 803

Zamojski, M., Yan, L., Dasyra, K., et al. 2011, ApJ, 730, 125

Zhang, Q., Wang, K., Lu, X., & Jiménez-Serra, I. 2015, ApJ, 804, 141

Zhang, Z.-Y., Papadopoulos, P. P., Ivison, R. J., et al. 2016, ArXiv e-prints, arXiv:1605.03885

Zhang, Z.-Y., Henkel, C., Gao, Y., et al. 2014, A&A, 568, A122

“There is no real ending. It’s just the place where you stop the story.”

Frank Herbert